AJNR

AMERICAN JOURNAL OF NEURORADIOLOGY

DECEMBER 2014
VOLUME 35
NUMBER 12
WWW.AJNR.ORG

THE JOURNAL OF DIAGNOSTIC AND INTERVENTIONAL NEURORADIOLOGY

Physician self-referral and image use appropriateness
Kyphoplasty vs. vertebroplasty: randomized trial
3T intraoperative MRI in pediatric brain tumors

Official Journal ASNR • ASFNR • ASHNR • ASPNR • ASSR

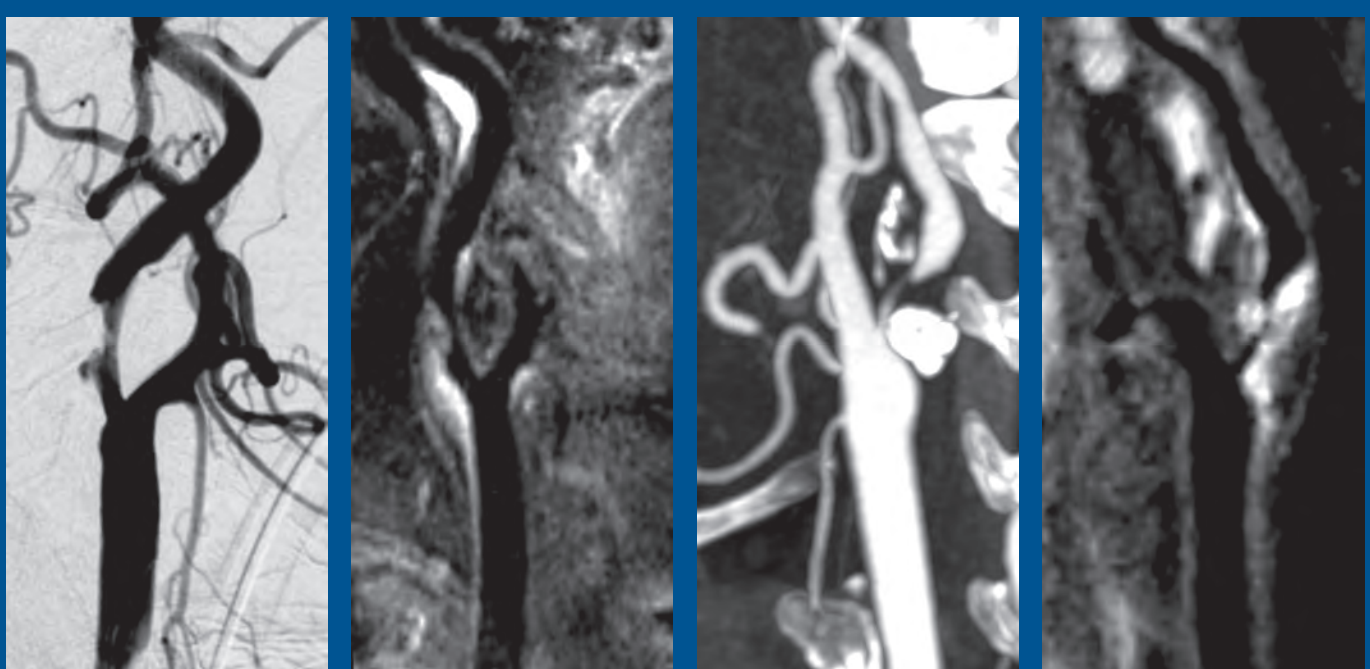

Advanced

by MicroVention

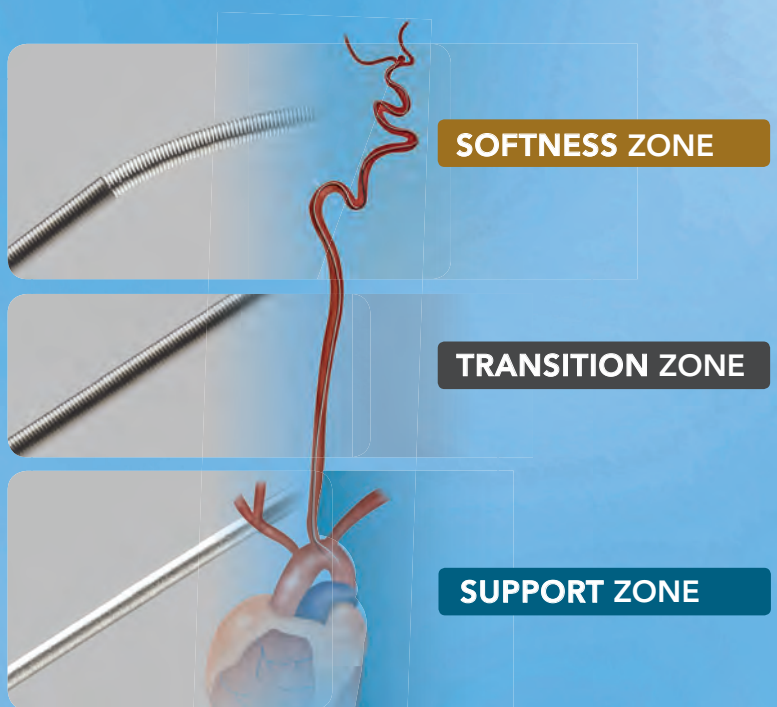

V-Trak® Advanced Coil System

ENHANCED CONTROL TO MAXIMIZE COIL PERFORMANCE

The **V-Trak® Advanced Coil System**, the next generation to power the performance of our most technically advanced line of coils. Offering the optimal combination of support and flexibility.

microvention.com

Support
by MicroVention

LVIS® Intraluminal Support Device

LVIS® Jr. Intraluminal Support Device

LOW-PROFILE VISUALIZED INTRALUMINAL SUPPORT

The **LVIS® and LVIS® Jr. devices** are the next generation technology for optimal intraluminal support and coverage for stent-assist coil procedures.

Used with Headway® Microcatheter

**Humanitarian Device:*
Authorized by Federal Law for use in the treatment of wide-necked aneurysms in the neurovasculature. The effectiveness of this device for this use has not been demonstrated.

For more information or a product demonstration, contact your local MicroVention representative:

MicroVention® TERUMO

MicroVention, Inc.
Worldwide Headquarters PH +1.714.247.8000
1311 Valencia Avenue
Tustin, CA 92780 USA
MicroVention UK Limited PH +44 (0) 191 258 6777
MicroVention Europe, S.A.R.L. PH +33 (1) 39 21 77 46
MicroVention Deutschland GmbH PH +49 211 210 798-0

BARRICADE™ COIL SYSTEM

PERFORMANCE AND VALUE DELIVERED

BLOCKADE MEDICAL

18 TECHNOLOGY DRIVE #169, IRVINE CA 92618 | **P** 949.788.1443
WWW.BLOCKADEMEDICAL.COM

MADE IN AMERICA

CE 0297

MKTG-020 REV. B

AJNR

AMERICAN JOURNAL OF NEURORADIOLOGY

DECEMBER 2014
VOLUME 35
NUMBER 12
WWW.AJNR.ORG

Publication Preview at www.ajnr.org features articles released in advance of print. Visit www.ajnrblog.org to comment on AJNR content and chat with colleagues and AJNR's News Digest at http://ajnrdigest.org to read the stories behind the latest research in neuroimaging.

Indicates Editor's Choices selection

Indicates Fellows' Journal Club selection

Indicates open access to non-subscribers at www.ajnr.org

Indicates article with supplemental on-line table

Indicates article with supplemental on-line photo

Indicates article with supplemental on-line video

Indicates Evidence-Based Medicine Level 1

Indicates Evidence-Based Medicine Level 2

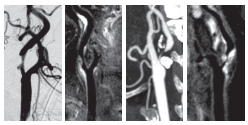

Needle position for cement salvage of instrumentation-associated vertebral fractures.

MR CLEAN: Expanding Clinical Evidence for Stent Retrievers

stryker® Neurovascular

Stryker Neurovascular congratulates the MR CLEAN Investigators[1]

Full study protocol is available at www.mrclean-trial.org

1. Results of the Multicenter Randomized Clinical trial of Endovascular treatment for Acute ischemic stroke in the Netherlands, as presented at the 9th Annual World Stroke Congress, October 25, 2014.

Complete Stroke Care®

Stroke: *Our Only Focus. Our Ongoing Promise.*

ASNR 53rd Annual Meeting & The Foundation of the ASNR Symposium 2015

ASFNR ASHNR ASPNR ASSR SNIS

THE FOUNDATION OF THE ASNR

Just released!! Check out the innovative cutting edge programming at The Foundation of the ASNR Weekend Symposium 2015: "Skull Base: Bridging the Gap…….". World-renowned speakers will be presenting the latest and greatest in clinical and imaging advances, and emphasizing the translation of this information into your daily clinical practice.

Also, the Sunday afternoon Foundation Symposium will continue by introducing new "Neuroradiologist-Clinician-Patient multidisciplinary symposiums" on mild TBI, head & neck cancer, brain cancer and more. Neuroradiologists and clinicians will be discussing the role of imaging and advances in treatment in the care of their patients, while patients and public representatives/ambassadors share their own personal experiences and journeys living with their disease.

What's New for the ASNR 53rd Annual Meeting?

- The Foundation of the ASNR Symposium 2015 "Skull Base: -Bridging the Gap……." on Saturday, April 25 & Sunday morning, April 26, 2015
- **New**…On Sunday afternoon, April 26 - "Neuroradiologist-Clinician-Patient Multidisciplinary Symposiums"
- Enjoy some fun on Sunday late afternoon with an ASNR Game of Jeopardy
- **Note**…For those submitting oral abstracts more slots will be available to present oral papers in Chicago
- Annual Meeting focuses on Value-Based Neuroradiology and much, much more…

ASNR 2015 Program Chair/President Elect Laurie A. Loevner, MD

Programming developed in cooperation with the:

American Society of Functional Neuroradiology (ASFNR)
Pratik Mukherjee, MD, PhD

American Society of Head and Neck Radiology (ASHNR)
Richard H. Wiggins, III, MD

American Society of Pediatric Neuroradiology (ASPNR)
Thierry A.G.M. Huisman, MD

American Society of Spine Radiology (ASSR)
Adam E. Flanders, MD

American Society of Neuroradiology (ASNR)
Health Policy Committee
Robert M. Barr, MD, FACR

Society of NeuroInterventional Surgery (SNIS)
Donald F. Frei, Jr. MD

Online Meeting Registration & Housing for ASNR 2015 coming soon…

Request Programming and Registration Materials for the ASNR 53rd Annual Meeting, Contact:

ASNR 53rd Annual Meeting
c/o American Society of Neuroradiology
800 Enterprise Drive, Suite 205
Oak Brook, Illinois 60523-4216

Phone: 630-574-0220
Fax: 630-574-0661
Email: meetings@asnr.org
Website: www.asnr.org/2015

Scan now to visit our website

SAVE THE DATES….April 25-30, 2015

AJNR

CALL FOR AJNR EDITORIAL FELLOWSHIP CANDIDATES

ASNR and AJNR are pleased once again to join efforts with other imaging-related journals that have training programs on editorial aspects of publishing for trainees or junior staff (3–5 years after training), including Radiology (Olmsted fellowship), AJR (Figley and Rogers fellowships), and Radiologia.

2015 Candidate Information and Requirements

GOALS

- Increase interest in "editorial" and publication-related activities in younger individuals.
- Increase understanding and participation in the AJNR review process.
- Incorporate into AJNR's Editorial Board younger individuals who have previous experience in the review and publication process.
- Fill a specific need in neuroradiology not offered by other similar fellowships.
- Increase the relationship between "newer" generation of neuroradiologists and more established individuals.
- Increase visibility of AJNR among younger neuroradiologists.

ACTIVITIES OF THE FELLOWSHIP

- Serve as Editorial Fellow for one year. This individual will be listed on the masthead as such.
- Review at least one manuscript per month for 12 months. Evaluate all review articles submitted to AJNR.
- Access to our electronic manuscript review system will be granted so that the candidate can learn how these systems work.
- Be involved in the final decision of selected manuscripts together with the Editor-in-Chief.
- Participate in all monthly Senior Editor telephone conference calls.
- Participate in all meetings of the Editors and Publications Committee during the annual meetings of ASNR and RSNA as per candidate's availability. AJNR/ASNR will not provide funding for this activity but may offer a discounted fee for its annual meeting.
- Evaluate progress and adjust program to specific needs in biannual meeting or telephone conference with the Editor-in-Chief.
- Write at least one editorial for AJNR.
- Embark on an editorial scientific or bibliometric project that will lead to the submission of an article to AJNR or another appropriate journal as determined by the Editor-in-Chief. This project will be presented by the Editorial Fellow at the ASNR annual meeting.
- Serve as liaison between AJNR and ASNR's Young Professionals Network and the 3 YPs appointed to AJNR as special consultants. Participate in meetings and telephone calls with this group. Design one electronic survey/year polling the group regarding readership attitudes and wishes.
- Recruit trainees as reviewers as determined by the Editor-in-Chief.
- Participate in Web improvement projects.
- Potentially become a member of AJNR's Editorial Board at the end of the fellowship.
- Invite Guest Editors for AJNR's News Digest to cover a variety of timely topics.

QUALIFICATIONS

- Be a fellow in neuroradiology from North America, including Canada (this may be extended to include other countries).
- Be a junior faculty neuroradiology member (< 3 years) in either an academic and private environment.
- Provide an "end" of fellowship report to AJNR's Editor-in-Chief and ASNR's Publications Committee.
- Be an "in-training" or member of ASNR in any other category.

APPLICATION

- Include a short letter of intent with statement of goals and desired research project. CV must be included.
- Include a letter of recommendation from the Division Chief or fellowship program director. A statement of protected time to perform the functions outlined is desirable.
- Applications will be evaluated by AJNR's Senior Editors and the Chair of the Publications Committee prior to the ASNR meeting. The name of the selected individual will be announced at the meeting.
- Applications should be received by March 3, 2015 and sent to Ms. Karen Halm, AJNR Managing Editor, electronically at khalm@asnr.org.

AJNR

AMERICAN JOURNAL OF NEURORADIOLOGY

Publication Preview at www.ajnr.org features articles released in advance of print. Visit www.ajnrblog.org to comment on AJNR content and chat with colleagues and AJNR's News Digest at http://ajnrdigest.org to read the stories behind the latest research in neuroimaging.

DECEMBER 2014 • VOLUME 35 • NUMBER 12 • WWW.AJNR.ORG

AJNR (Am J Neuroradiol ISSN 0195–6108) is a journal published monthly, owned and published by the American Society of Neuroradiology (ASNR), 800 Enterprise Drive, Suite 205, Oak Brook, IL 60523. Annual dues for the ASNR include $170.00 for journal subscription. The journal is printed by Cadmus Journal Services, 5457 Twin Knolls Road, Suite 200, Columbia, MD 21045; Periodicals postage paid at Oak Brook, IL and additional mailing offices. Printed in the U.S.A. POSTMASTER: Please send address changes to American Journal of Neuroradiology, P.O. Box 3000, Denville, NJ 07834, U.S.A. Subscription rates: nonmember $380 ($450 foreign) print and online, $305 online only; institutions $440 ($510 foreign) print and basic online, $875 ($940 foreign) print and extended online, $365 online only (basic), extended online $790; single copies are $35 each ($40 foreign). Indexed by PubMed/Medline, BIOSIS Previews, Current Contents (Clinical Medicine and Life Sciences), EMBASE, Google Scholar, HighWire Press, Q-Sensei, RefSeek, Science Citation Index, and SCI Expanded.

PUBLICATION METRICS

AMERICAN JOURNAL OF NEURORADIOLOGY

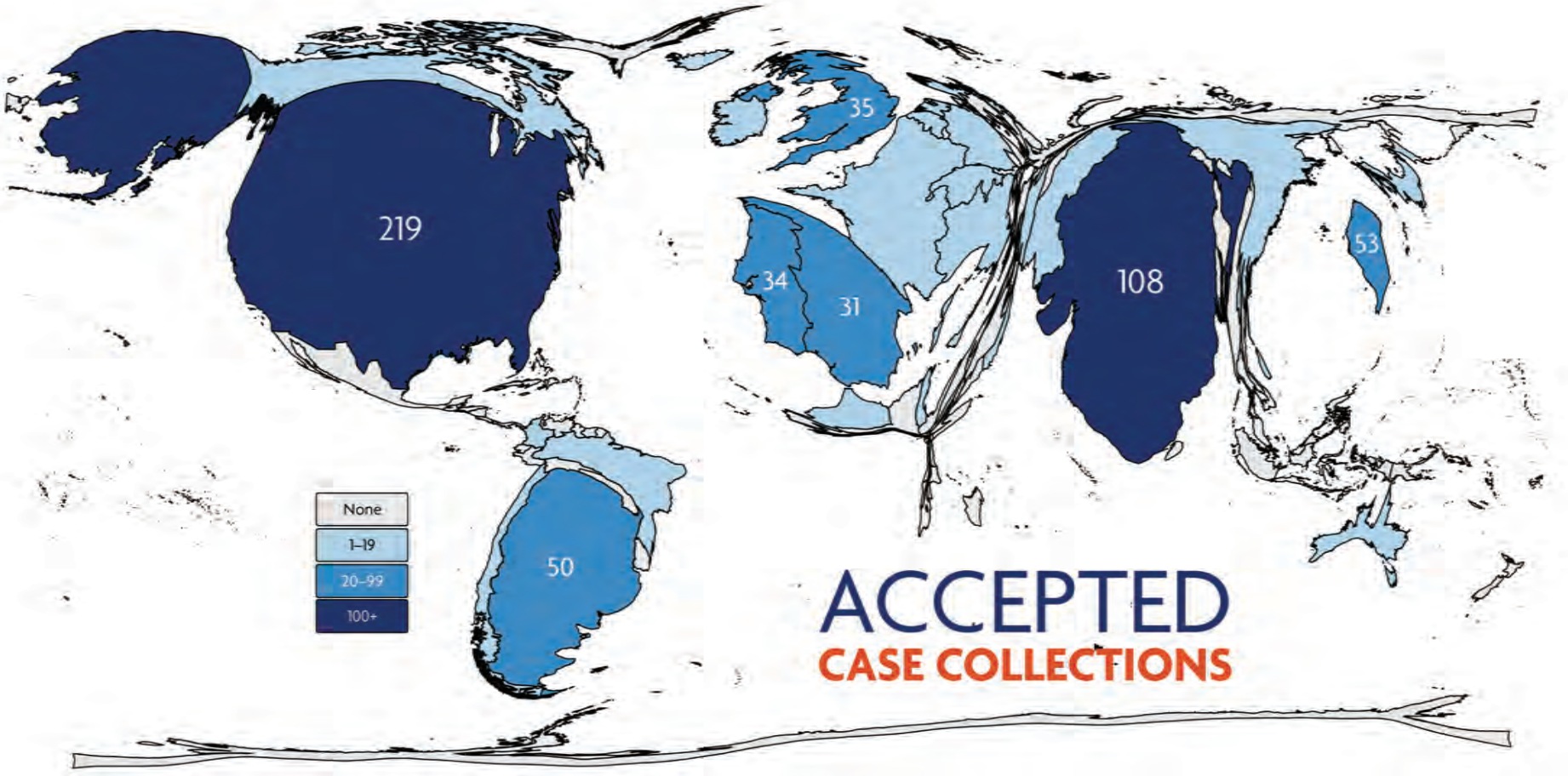

Data (Publication Dates)

Case of the Week: Feb. 23, 2009 to Aug. 31, 2015
Classic Case: May 9, 2011 to Nov. 10, 2014
Case of the Month: Nov. 2011 to Dec. 2014
Clinical Correlation: Oct. 2013 to Aug. 2014

Cartogram created using ScapeToad
www.scapetoad.choros.ch

Basemap from DIVA-GIS
www.diva-gis.org

Graphic by
Jason Gantenberg

The Social Network of Loneliness

M. Castillo, *Editor-in-Chief*

Unlike other countries, we Americans like our heroes to be lonely, and some that come to mind immediately are cowboys, explorers, and scientists patiently working in their laboratories while remaining decontextualized from their surroundings, and perhaps the loneliest of them all: astronauts. Thus, it should come as no surprise that in some of the better recent movies, *Gravity* (Sandra Bullock) and *All Is Lost* (Robert Redford), the main characters find themselves completely alone, and at the end, they are portrayed as heroes. As our social exchange structure changes, Americans are more lonely than ever before, despite our increasing population and our ability to communicate with each other more often and faster.

Although one can argue about the differences and similarities of the following terms: aloneness, isolation, retreat, and seclusion, what I would like to briefly address here is "loneliness," which I take to mean a lack of companionship that may occur even when surrounded by or "connected" to others. Nowadays, our connections are basically electronic and, to many my age or younger, accomplished through Facebook and other "social media."

As of this writing, our main modern social communication tool, Facebook, had 1.31 billion subscribers and 680 million mobile users.[1] Here are some more Facebook statistics that amaze me: 640 billion minutes per month are spent on it, nearly 50% of those 18–34 years of age use it, and it has more than 1 trillion page views per month and 2.7 billion "likes" every day. At the time of this writing, the *American Journal of Neuroradiology* (*AJNR*) had 5461 "likes" and *Radiology* had 28,521 "likes" on their Facebook pages. Thus, it seems that we radiologists are indeed, true Facebook aficionados. For those who like a more concise communication, it will be a relief to learn that Twitter is not doing badly at all. It has nearly 646 million users and hosts nearly 10,000 tweets per second,[2] and just to be fair to Google, I need to mention that its social network (Google+) now has more than 300 million monthly users who upload 1.5 billion pictures every week.[3]

As our electronic social media grow, we seem to get lonelier. The number of US households tripled between 1940 and 2010, but while in 1940, 90% of them contained families, in 2010 only 66% did.[4] About 27% of households have only 1 person, a number 3 times higher than 50 years ago, and 33% of households now have childless couples.

Is loneliness biologic? Cole et al[5] from the University of California, Los Angeles (UCLA) published, in 2007, an interesting article on this topic. He and his coauthors suggested that changes in genes that are related to inflammation also drive chronic high levels of feelings of isolation and loneliness. This study revealed that the levels of gene expressions may be different depending not only on how many people you know but also related to the number of those you feel close to. Intuitively, a relationship between feeling lonely and one's immune system makes sense to me. The greater the number of close friends one has, the more your immune system must be ready to combat the germs they carry. Conversely, a lesser number of friends may result in a lazier immune system, making your health more fragile; it is well-known that the lonely have precarious health. The way the brain perceives and reacts is also different in the lonely. When examined with fMRI, lonely individuals showed less activation of the ventral striatum, which correlated with a feeling of being less rewarded by social stimuli.[6] Nonlonely people showed higher activation of this region, implying that social interactions resulted in a pleasurable event. Lonely individuals also appeared to be more drawn to the distress of others. These studies and others seem to indicate that a lack of perceived pleasure from social interactions is at the core of loneliness.

To avoid loneliness, one must have personal relationships—that is, having a lot of friends on Facebook will not relieve one's feelings of isolation. Conversely, it could be that lonely individuals spend all of their time on Facebook trying to build up a large network of "friends." Moira Burke from the Carnegie Mellon University studied Facebook users and concluded that only those for whom Facebook served as a conduit to establishing direct communications with other individuals leading to friendship seemed to avoid feelings of loneliness.[7] That is, having a large number of friends write on your Facebook wall or communicating with them by terse Twitter-like exchanges will not decrease loneliness. Another study concluded that if one has a lot of friends in real life, one will also have a lot of them on Facebook and be a successful user of it.[8] Simply consuming and broadcasting trivial life events on social media makes one more, not less lonely. The popularity of Facebook may reflect the increasing desire to find oneself among friends (31% in 2010 versus 37% today). Groups of individuals who make and keep friends easier are the Millennial generation (47%), Hispanics (47%), and never-married adults (44%).[9]

To measure loneliness, one of the most popular methods is the UCLA scale. This 20-question scale is easy to use and apparently reproducible. You may find it at http://www.tactileint.com/portfolio/uclalone.html, and when I took the test, I scored a 19, which is the average score for school teachers (I guess I must share with them some frustrations and feelings of isolation perhaps even leading to loneliness). Using this scale, the American Association for Retired Persons (AARP) has found that 35% of adults consider themselves lonely, especially those in poor health, the socially isolated, those with a new residence (less than 1 year), and females; but it also concluded that as we get older overall we feel less and not more lonely.[10] With respect to electronic communications, AARP found that those using e-mail felt that they had fewer deep friendships than before. Not surprisingly, AARP also reported that isolation and loneliness increase a person's risk of death. Loneliness increases circulating cortisol levels that may contribute to brain and cerebrovascular disease and affect sleep patterns that may lead to depression. The common threads between heart and brain vascular disease could be related to the fact

http://dx.doi.org/10.3174/ajnr.A3964

that the lonely have an increased incidence of hypertension and smoke more (on average, 15 cigarettes per day).

Is loneliness genetic in nature? Some studies suggest a strong genetic effect, but because loneliness is highly influenced by environmental situations, its expressions vary from childhood to adulthood and from individual to individual. In 1 highly regarded study, loneliness was assessed in 8387 twins.[11] The conclusions of the study were that heritability of differences in feelings of loneliness was 48%, no unique environmental influences were discernible, genetic contributions to loneliness were similar in children and adults, and the heritability of loneliness showed no sex differences. The authors suggested that individuals are unable to control their loneliness as a response to external stimuli.

Why does loneliness hurt? One hears others saying that "they are so lonely it hurts." Because social exclusion is a type of loneliness, one fMRI study assessed the brains of individuals who were excluded from a specific activity.[12] The results paralleled those from studies of physical pain. That is, the anterior cingulate cortex was less active during exclusion and correlated with self-reported distress. The right ventral prefrontal cortex was active during exclusion, suggesting that it regulates feelings of loneliness by excluding the function of the anterior cingulate cortex. From a developmental standpoint, the same authors believe that the loneliness system "borrowed" its computations from the pain system to prevent its harmful effects.

Perhaps some of the loneliest moments may be experienced within a marriage. Married people are healthier, live longer, and are less lonely but only if their spouses are confidants. This is, again, loneliness is related to the quality of the relationship and not to the relationship per se. One's immediate circle of confidants also extends to one's best friends. Nevertheless, how often you do hear American adults say they have a best friend to confide in? The answer is not often. In 1985, the number of confidants a person had was close to 3; in 2004, it had decreased to 2; and today 25% of Americans claim to have no one to confide in.[13] This seems to be paradoxical when the average American has 634 electronic social ties, but the truth is that most if not all of these ties are superficial and eventually meaningless. When Facebook data are analyzed, it has been found that the largest single group (22%) of "friends" a user has consists of people he or she knew in high school followed by extended family and coworkers. I personally feel that the connection between myself and those I went to high school with is now basically nonexistent, but then, I do not have a Facebook page (I do have a Facebook account that I use to check *AJNR's* page) and do not respond to any Facebook invitations. What is even worse is that up to 7% of Facebook "friends" are strangers whom the user has not and will never meet.

Since our ever-expanding dependency on electronic communications seems to be making us lonelier, it seems ironic that several sites, such as the Web of Loneliness, offer on-line help via chat rooms and blogs and other types of virtual support groups, many through Facebook and Twitter. Another such site is the UK's Campaign to End Loneliness, which, again, contains a plethora of posts (most are useless) and some pictures of their followers, mostly octogenarians whom I doubt know how to use Twitter or Facebook. These sites state that 5 million older British individuals have, as their sole companion, their television. Of course, many of these sites have a scamlike scent and accept donations via Pay Pal, but some like the UK one are supported by philanthropic foundations.

As in many other situations in our lives, loneliness is multifactorial. Our pursuit of space and individualism (an idea ingrained in American culture) and the desire to be alone drove city populations into the suburbs and beyond. So do as country music legend Willie Nelson says: "Mamas, don't let your babies grow up to be cowboys, they'll never stay home and they're always alone, make'em be doctors and lawyers and such. . . ." Moreover, I should add: keep them away from Facebook and Twitter.

REFERENCES

1. STATISTIC BRAIN. Facebook Statistics. http://www.statisticbrain.com/facebook-statistics. Accessed March 19, 2014
2. STATISTIC BRAIN. Twitter Statistics. http://www.statisticbrain.com/twitter-statistics. Accessed March 19, 2014
3. Barr A. **Google's social network sees 58% jump in users.** *USA TODAY*. October 29, 2013. http://www.usatoday.com/story/tech/2013/10/29/google-plus/3296017. Accessed November 11, 2013
4. Jacobsen LA, Mather M, Dupuis B. Population Reference Bureau. Household change in the United States. http://www.prb.org/Publications/Reports/2012/us-household-change.aspx. Accessed November 11, 2013
5. Cole SW, Hawkely LC, Arevalo JM, et al. **Social regulation of gene expression in human leucocytes.** *Genome Biol* 2007;8:R189
6. Cacioppo JT, Norris CJ, Decety J, et al. **In the eye of the beholder: individual differences in perceived social isolation predict regional brain activation to social stimuli.** *J Cogn Neurosci* 2009;21:83–92
7. Burke M, Kraut R, Marlow C. **Social capital on Facebook: differentiating uses and users.** *CHI* 2011. May: 7–12, 2011. http://citeseerx.ist.psu.edu/viewdoc/download?doi=10.1.1.227.6644&rep=rep1&type=pdf. Accessed May 5, 2014
8. Quercia D, Lambiotte R, Stillwell D, et al. **The personality of popular Facebook users.** http://dl.acm.org/citation.cfm?id=2145346. Accessed April 24, 2014
9. BarnaGroup. How the last decade changed American life. https://www.barna.org/barna-update/culture/624-how-the-last-decade-changed-american-life#.UoEdduKO51N. Accessed April 24, 2014
10. Anderson G. **Loneliness among older adults: a national survey of adults 45+.** http://www.aarp.org/personal-growth/transitions/info-09-2010/loneliness_2010.html. Accessed November 11, 2013
11. Boomsma DI, Willemsen G, Dolan CV, et al. **Genetic and environmental contributions to loneliness in adults: the Netherlands twin registry study.** *Behav Genet* 2005;35:745–52
12. Eisenberger NI, Lieberman MD, Williams KD. **Does rejection hurt? An fMRI study of social exclusion.** *Science* 2003;302:290–92
13. Kornblum J. **Study: 25% of Americans have no one to confide in.** *USA TODAY*. June 22, 2006. http://usatoday30.usatoday.com/news/nation/2006-06-22-friendship_x.htm. Accessed March 19, 2014

Delayed Cerebral Ischemia in Aneurysmal Subarachnoid Hemorrhage: Proposal of an Evidence-Based Combined Clinical and Imaging Reference Standard

P.C. Sanelli, S. Kishore, A. Gupta, H. Mangat, A. Rosengart, H. Kamel, and A. Segal

ABSTRACT

SUMMARY: Aneurysmal subarachnoid hemorrhage is associated with high morbidity and mortality, with delayed neurologic deficits from delayed cerebral ischemia contributing to a large portion of the adverse outcomes in this patient population. There is currently no consensus reference standard for establishing the diagnosis of delayed cerebral ischemia either in the research or clinical settings, ultimately limiting strategies for preventing delayed infarction and permanent neurologic deficits. There are currently both clinical and imaging-based criteria for the diagnosis of delayed neurologic deficits and vasospasm, respectively, however, neither clinical nor angiographic assessment alone has been shown to identify patients who develop adverse outcomes from delayed infarction. Thus, the purpose of this work is to propose a 3-tiered combined imaging and clinical reference standard based on evidence from the literature to standardize the diagnosis of delayed cerebral ischemia, both to allow consistency across research studies and to ultimately improve outcomes in the clinical setting.

ABBREVIATIONS: aSAH = aneurysmal subarachnoid hemorrhage; DCI = delayed cerebral ischemia; MRP = MR perfusion

Aneurysmal subarachnoid hemorrhage (aSAH) is associated with high morbidity and mortality.[1,2] The first 2 weeks following aSAH are critical in the management of these patients because they are prone to develop several life-threatening complications, including delayed neurologic deficits,[3] which often arise from delayed cerebral ischemia (DCI), a major contributor to the adverse outcomes in this population.[3-5] Delayed cerebral ischemia manifests in approximately 30% of patients with aSAH and typically occurs between days 4 and 9 after the initial hemorrhage, though it can range from 3 to 14 days.

There remains a lack of standard criteria for defining DCI in the clinical setting,[3,6,7] with a recent literature review describing at least 8 terms to define the concept of DCI in aSAH.[6] Debate over the role of clinical and imaging assessments in defining DCI has occurred for both clinical and research purposes.[3,6,8-10] For example, although the terms "DCI" and "vasospasm" have been used interchangeably, attempts have been made to distinguish DCI from vasospasm, with the former often determined clinically, and the latter, radiographically,[6] because not all patients with clinical neurologic deficits have angiographic vasospasm and not all patients with angiographic vasospasm have neurologic deficits that correspond to the arterial territory of vasospasm.[11,12] Additionally, while severe vasospasm may cause decreased cerebral perfusion, a substantial percentage of patients develop infarction without evidence of vasospasm, suggesting that DCI should be defined as a pathologic process, of which vasospasm may represent a contributing factor.[12,13]

Thus, the aim of this article is to propose an evidence-based reference standard for DCI that incorporates both clinical assessments of neurologic deterioration and imaging assessments of vasospasm, perfusion deficits, and infarction to provide a consistent, uniform standard across a wide range of clinical and research applications. The classification of levels of evidence supporting this reference standard is based on the Levels of Evidence criteria proposed by the Oxford Centre of Evidence Based Medicine (www.cebm.net).[14] Two independent reviewers assessed levels of evidence for each tier, and in the case of discordance, evidence level assignments were made by consensus.

From the Departments of Radiology, Division of Neuroradiology (P.C.S., S.K., A.G.); Public Health (P.C.S.); and Neurology, Division of Stroke and Critical Care (H.M., A.R., H.K., A.S.), NewYork-Presbyterian Hospital–Weill Cornell Campus, New York, New York.

P. Sanelli and S. Kishore are co-first authors.

This work was supported by grant 5K23NS058387 from the National Institute of Neurological Disorders and Stroke, a component of the National Institutes of Health.

The views herein are solely the responsibility of the authors and do not necessarily represent the official view of the National Institute of Neurological Disorders and Stroke or the National Institutes of Health.

Please address correspondence to Pina C. Sanelli, MD, MPH, Department of Radiology, Weill Cornell Medical College, NewYork-Presbyterian Hospital, 525 East 68th St, Starr Pavilion, Box 141, New York, NY 10065; e-mail: pcs9001@med.cornell.edu

http://dx.doi.org/10.3174/ajnr.A3782

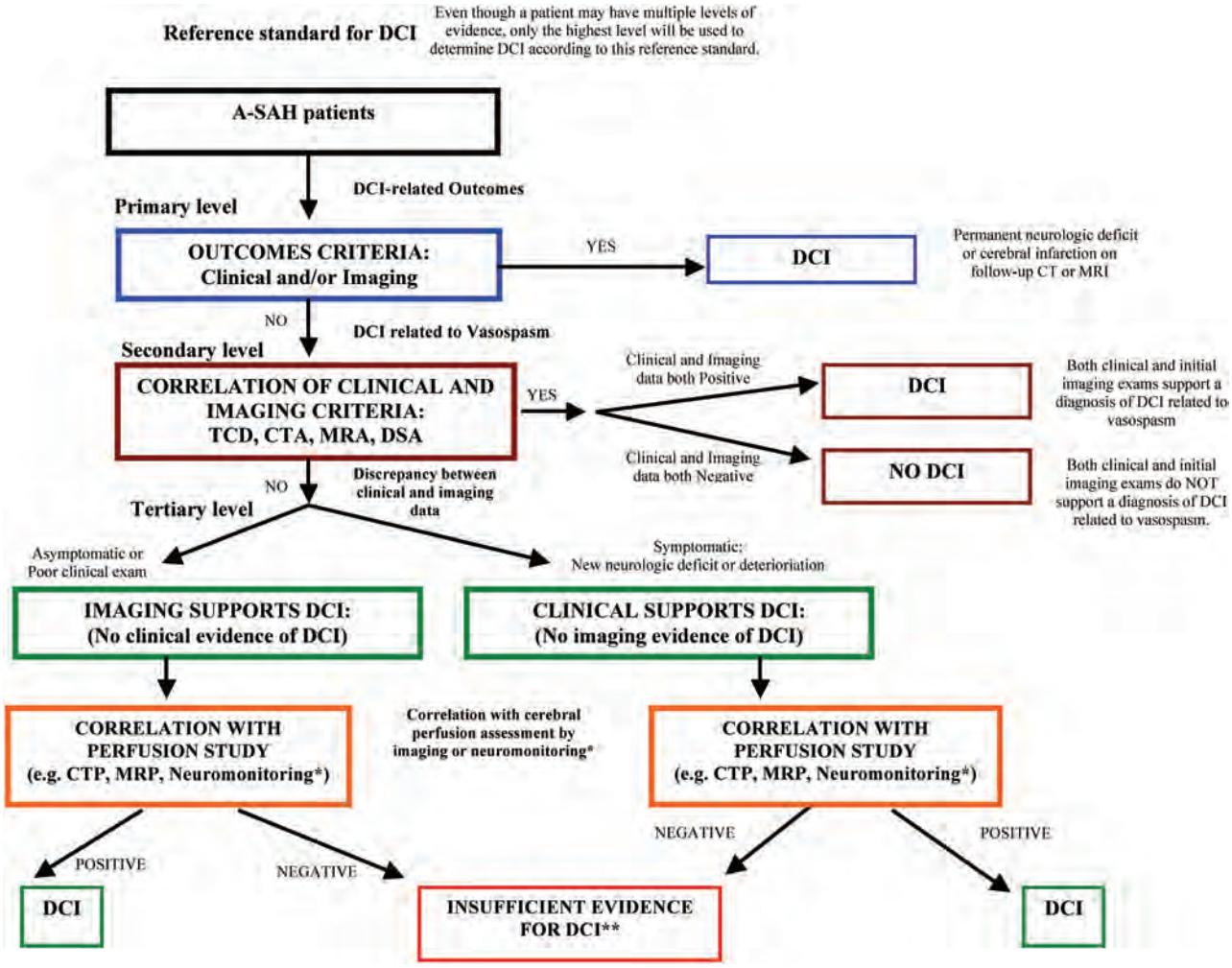

FIG 1. Proposed multitiered reference standard in DCI. Three-tiered DCI reference standard algorithm, ordered from top to bottom. Asterisk indicates neuromonitoring devices such as cerebral microdialysis and oximetry. Double asterisks indicate whether the reference standard is used for clinical assessment and treatment decisions based on the risk/benefit ratio for treatment. If there is low risk, treatment for DCI is recommended. If there is high risk, the patient should re-enter the algorithm.

DESCRIPTION OF THE COMBINED CLINICAL AND IMAGING REFERENCE STANDARD

(Algorithm displayed in Fig 1)

Primary Level: Outcome-Based Criteria

Summary. The primary level classifies patients as having DCI if a new infarction on imaging or new permanent neurologic deficit develops. A new infarction on imaging is determined on CT or MR imaging within 6 weeks after aSAH ictus that was not present on imaging up to 48 hours after aneurysm occlusion and was not attributable to other causes such as surgical clipping, endovascular treatment, ventricular catheter placement, intraparenchymal hematoma, or cerebral herniation. A new permanent neurologic deficit is determined on clinical examination as a new neurologic deficit distinct from the baseline examination performed immediately after aneurysm rupture or aneurysm occlusion and not attributable to other causes. Baseline neurologic examination must be considered after full cardiorespiratory, hemodynamic, and metabolic resuscitation as well as treatment of other factors such as seizures and hydrocephalus. Patients who do not meet either criterion are referred to the secondary level, as described in a subsequent section.

Evidence: Level 1A evidence exists to support these proposed outcomes-based criteria for determining DCI.

An ideal reference standard should reliably identify patients with a high risk of poor outcomes who may benefit from intervention. In large prospective cohort studies, the greatest predictors of severe disability or death at 3 months were a new focal neurologic deficit, a new infarction on follow-up imaging, or both.[6,15,16] Additionally, a large systematic review and meta-analysis of all randomized placebo-controlled trials evaluating the efficacy of protective strategies in aSAH concluded that a reduced incidence of cerebral infarction is significantly associated with improved functional outcome.[17] In fact, new cerebral infarction alone was as strongly correlated with poor 3-month functional outcome as the combination of a new neurologic deficit and corresponding ischemic changes on follow-up neuroimaging.[6] Furthermore, cerebral infarction on noncontrast CT was the primary outcome measure in the early trials of nimodipine, an agent with strong evidence for neuroprotection of DCI.[18]

While angiographic vasospasm has traditionally been the primary focus of interventions and prediction of outcomes, the lack of evidence demonstrating improved outcomes with vasospasm prevention[13,19] has led to incorporating this criterion combined with clinical correlation in the secondary level below.

Secondary Level: Correlation of Clinical and Vascular Imaging Criteria

Summary. The secondary level classifies patients as having DCI if both clinical deterioration and angiographic vasospasm occur. Clinical deterioration is determined by bedside examination and comprises the development of a new neurologic deficit (such as hemiparesis, hemiplegia, aphasia, depressed consciousness, and so forth), a decrease of at least 2 points on the Glasgow Coma Scale, or a decrease of at least 1 point in the motor score, lasting >1 hour at any point after aneurysm occlusion and not attributable to other causes. Vascular imaging for the evaluation of vasospasm includes imaging modalities, such as transcranial Doppler sonography, CTA, MRA, and DSA. Patients with neurologic deterioration and 1 imaging test supporting a diagnosis of vasospasm are classified as having DCI. On the other hand, patients without neurologic deterioration and 1 imaging test without findings of vasospasm are classified as not having DCI. However, patients with either positive clinical or imaging findings that do not correlate with each other are referred to the tertiary level, as described in a subsequent section.

Evidence: Level 1B evidence exists to support using clinical and vascular imaging data for determining DCI.

Evaluation of patients for DCI at the secondary level is most valuable in the clinical setting at the point of care when treatment decisions are made. The primary goal of treatment is to prevent cerebral infarction and permanent neurologic deficits. Thus, traditionally, imaging assessment of vasospasm has been used as a surrogate marker to assist in the diagnosis of DCI, especially given that neurologic deterioration is poorly evaluated in sedated or obtunded patients. Angiographic vasospasm, seen on DSA or CTA, is perhaps the most commonly used surrogate imaging marker in this patient population. Vasospasm has been shown to be strongly associated with DCI, cerebral infarction, poor outcome, and increased mortality within several retrospective and prospective cohort studies, including a post hoc analysis of data from the CONSCIOUS (Clazosentan to Overcome Neurological Ischemia and Infarct Occurring after Subarachnoid Hemorrhage)-1 trial.[11,20-23] However, an analysis of data from 2 systematic reviews and a post hoc analysis did not demonstrate an improvement in outcome with a reduction in angiographic vasospasm.[19] Evidence from both prospective and retrospective cohort studies suggests that patients with angiographic vasospasm and correlated symptoms have worse hospital complications and subsequent disability compared with angiographic vasospasm alone.[9,16] However, there is less evidence to demonstrate the prognostic importance of angiographic vasospasm correlated with symptoms, thus placing this criterion at the secondary level. Although relatively inferior in terms of sensitivity and specificity, transcranial Doppler sonography evaluations of the intracranial vessels can also be performed at bedside to identify arterial narrowing in patients who may be too unstable for more advanced angiographic techniques such as CTA, MRA, or DSA.[24,25]

Tertiary Level: Correlation of Physiologic Data with Clinical or Imaging Criteria

Summary. The tertiary level classifies patients as having DCI if physiologic data correlates with either clinical deterioration or vasospasm. Patients with either clinical deterioration or vasospasm alone may undergo additional physiologic assessment of cerebral hemodynamics, either in the form of imaging such as CTP and MR perfusion (MRP) or neuromonitoring devices such as cerebral blood flow, oxygen tension monitoring, and cerebral microdialysis. Patients with findings suggestive of regional cerebral hypoperfusion or hypoxia that correlate with either clinical deterioration or vasospasm are classified as having DCI. Patients with clinical deterioration or vasospasm but normal physiologic data do not have sufficient evidence to be classified as having DCI.

Evidence: Levels of evidence to support using physiologic data for determining DCI range from 2A to 3B, depending on the technique.

While there is at least moderate evidence supporting the importance of symptomatic vasospasm in DCI at the secondary level, the importance of isolated image-based diagnoses of vasospasm in the absence of clinical findings is somewhat controversial, especially in the absence of infarction. However, a subset of patients with asymptomatic vasospasm will develop asymptomatic ischemia and subsequent infarction. A large prospective cohort identified asymptomatic infarction in approximately 20% of patients with aSAH, and furthermore, these patients had a higher frequency of death and moderate-to-severe disability at 3 months relative to patients with symptomatic infarction.[26] Thus, there may be a subset of patients with apparently asymptomatic vasospasm who are at high risk of eventually developing clinical evidence of DCI, especially those who are comatose or have a ventriculostomy catheter, small-volume aSAH, or ischemia in noneloquent brain[26,27]—all representing complicating factors that are not infrequently encountered in the intensive care setting. Identifying this high-risk subset of patients with asymptomatic vasospasm may prompt measures to implement therapies to prevent the eventual development of DCI.

Conversely, the identification of patients with DCI and clinical deterioration in the absence of vasospasm poses a different important diagnostic challenge. While neurologic deterioration is likely multifactorial in these patients, a subset will go on to develop infarction without vasospasm. A retrospective study of infarction patterns in patients with aSAH found that approximately 17% of patients developed infarcts without imaging evidence of vasospasm, and even in patients with imaging positive for vasospasm, infarcts also developed in areas away from the vasospastic territories.[28] Thus, this level in the algorithm would attempt to identify ischemia in patients with asymptomatic vasospasm or neurologic deterioration without evidence of large-vessel vasospasm.

Perfusion imaging such as CTP and MRP or less common modalities such as xenon-CT provide physiologic imaging assessments of cerebral hypoperfusion and ischemia that could identify patients at risk for infarction. In a retrospective cohort of 96 pa-

tients with aSAH, new CTP deficits seen as prolonged MTT and reduced CBF were significantly associated with subsequent infarction and permanent neurologic deficits.[29] A smaller prospective study evaluating the test characteristics of CTP, CTA, and noncontrast CT obtained at baseline and after the onset of clinical deterioration determined that CTP had the best test performance for the subsequent diagnosis of DCI at discharge.[30] Subsequently, systematic reviews evaluating CTP in aSAH within the broader context of diagnosing vasospasm and DCI found that relative CBF and MTT values correlated highly with subsequent DCI.[25,31] Thus, there is level 2A evidence to support the role of CTP in the diagnosis of DCI.

Evidence to support the use of other imaging modalities to evaluate DCI is more limited. There are limited data evaluating the role of MRP in DCI; however, several small prospective cohort studies demonstrated that CTP, particularly CBF, correlates with MRP-derived values in the same patients within a close time interval, suggesting that MR imaging could also be used in this setting in case CTP is not performed.[32,33] The data for the use of xenon-CT in DCI are even more limited; however, a small prospective cohort study in patients with poor-grade aSAH found that CBF reduction on xenon-CT was only moderately predictive of infarction in these patients and that not all reductions in CBF by this technique resulted in infarction.[34] Thus, there is at best level 2B and 3B evidence for MRP and xenon-CT, respectively, for the diagnosis of ischemia in patients with aSAH. However, these imaging modalities are challenging to perform in this patient population due to scanner accessibility and patient contraindications.

Not all patients with aSAH undergo imaging to assess ischemia, particularly those who are unstable or have poor-grade conditions. Thus, noninvasive and invasive bedside monitoring devices such as cerebral microdialysis, brain tissue oxygenation monitoring (eg, the Licox system, Integra LifeSciences, Plainsboro, New Jersey), and other similar devices have been used to stratify patients at risk of ischemia. A systemic review evaluating the use of microdialysis in the assessment of cerebral ischemia in patients with aSAH found that while the use of the technology is increasing, there is substantial study heterogeneity, thereby limiting the evidence to support its utility.[35] Nonetheless, a small prospective cohort of 44 patients found that a 2-fold increase in ischemia-related metabolites from baseline at the time of acute neurologic deterioration was significantly associated with subsequent infarction and permanent neurologic deficits.[36] Data for cerebral tissue oxygen monitoring are more limited, particularly in patients with aSAH. Several small prospective cohort studies demonstrated the potential utility of detecting hypoxia in aSAH by using tissue oxygenation monitoring.[37-39] Thus, there is level 3A evidence in support of cerebral microdialysis and level 3B evidence to support cerebral oxygen monitoring in patients with aSAH.

Strengths and Limitations of Each Level

Primary Level. The main strength of the primary level is its strong evidence using outcome-based criteria supported by systematic reviews and large observational cohort studies.[3,15,17,19] Thus, the primary level captures patients with the highest mortality and morbidity associated with DCI. Most important, this level emphasizes specificity over sensitivity to accurately identify patients with DCI for treatment decisions. Additionally, patients with DCI who do not develop infarction or neurologic deficits cannot be misclassified at this level because these patients advance to the secondary level for further evaluation. Another strength at this level is the reproducibility in assessing patients with these well-defined outcome measures that are less prone to interobserver variability.

The main limitation at the primary level is the reduced applicability in guiding treatment decisions. In clinical practice, the goal of managing patients with aSAH is to avoid these devastating outcomes of infarction and functional disability. At this level, patients are classified as having DCI according to these criteria, thus limiting improvement in patient outcomes with treatment.

Secondary Level. The main strength of the secondary level is the combination of new neurologic deficits with imaging findings suggestive of angiographic vasospasm that have been shown to correlate with functionally relevant outcomes.[9] Because these criteria can, in some cases, be evaluated before development of infarction and functional disability (ie, at a stage in which impending DCI is still preventable), classification of patients with DCI at this level should theoretically provide maximal benefit from treatment. The combination of both new neurologic deficits and evidence of angiographic vasospasm improves the specificity for identifying patients with DCI, given that neurologic assessment in patients with aSAH can be challenging and angiographic vasospasm does not necessarily correlate with DCI.

A limitation of the secondary level is that patients without new neurologic deficits and without angiographic vasospasm can be misclassified as having no DCI. Comatose or heavily sedated patients have limited clinical assessment and may have suboptimal imaging, resulting in false-negatives for DCI. Although the agreement of clinical and imaging findings improves the specificity for identifying patients with DCI for treatment, the sensitivity may not be optimized at this level for a subset of patients. The probability of correlation is dependent on the quality of each respective evaluation, and both the clinical and imaging assessments at this level are subject to interobserver variability.[10,40,41]

Tertiary Level. The main strength of the tertiary level is improving the sensitivity of the DCI diagnosis by further evaluating discordant clinical and imaging findings from the secondary level, such as in patients with asymptomatic vasospasm or neurologic decline without angiographic vasospasm. Most important, this level allows further evaluation of comatose patients with suboptimal clinical assessments who have angiographic vasospasm as well as symptomatic patients who have suboptimal imaging. These patients often have worse outcomes in comparison with patients with symptomatic DCI, possibly related to delayed treatment.[26] At this level, all patients undergo physiologic assessment of cerebral perfusion and hypoxia to correlate with either clinical or imaging findings suggesting DCI. Thus, this level will include patients who may have been excluded from the diagnosis due to lack of sufficient evidence at the other 2 levels.

A potential limitation of the tertiary level is that the breadth of modalities used to assess ischemia—ranging from noninvasive imaging to invasive tissue monitoring—has variable strength of

evidence to support their use. From an imaging standpoint, CTP has the strongest evidence to support its use in diagnosing DCI; clinically, cerebral microdialysis has some evidence to support its use despite inconclusive results from a systematic review of the literature. There is limited evidence to support the use of the remaining modalities in diagnosing DCI in patients with aSAH.

Future Directions

While there is no perfect reference standard for this complex disease process, this multitiered algorithm attempts to capture the complexity of clinical and imaging findings in DCI according to evidence-based criteria. Specificity is emphasized in this multitiered reference standard with respect to evidence-based clinically relevant outcomes at the primary level, which are particularly valuable in the research setting to potentially improve translation of research findings into clinical practice. Most important, this reference standard approach also incorporates levels of evidence with greater sensitivity for use in clinical settings. The model is heavily weighted toward criteria with supportive statistical evidence and, through a multitiered algorithm, aims to limit the heterogeneity and controversy in defining DCI for research and, potentially, clinical application, combining both imaging and clinical assessments in the determination of DCI. The future direction for validation of this proposed reference standard through prospective studies may help to move forward both clinical care and research in this field.

Disclosures: Pina Sanelli—*RELATED*: *Grant*: National Institute of Neurological Disorders and Stroke, a component of the National Institutes of Health, grant 5K23NS058387. Ajay Gupta—*UNRELATED*: *Grants/Grants Pending*: Association of University Radiologists GE Radiology Research and Academic Fellowship.* *Money paid to the institution.

REFERENCES

1. Hop JW, Rinkel GJ, Algra A, et al. **Case-fatality rates and functional outcome after subarachnoid hemorrhage: a systematic review.** *Stroke* 1997;28:660–64
2. Stegmayr B, Eriksson M, Asplund K. **Declining mortality from subarachnoid hemorrhage: changes in incidence and case fatality from 1985 through 2000.** *Stroke* 2004;35:2059–63
3. Diringer MN, Bleck TP, Claude Hemphill J 3rd, et al. **Critical care management of patients following aneurysmal subarachnoid hemorrhage: recommendations from the Neurocritical Care Society's Multidisciplinary Consensus Conference.** *Neurocrit Care* 2011;15:211–40
4. Roos YB, de Haan RJ, Beenen LF, et al. **Complications and outcome in patients with aneurysmal subarachnoid haemorrhage: a prospective hospital based cohort study in the Netherlands.** *J Neurol Neurosurg Psychiatry* 2000;68:337–41
5. Hijdra A, Van Gijn J, Stefanko S, et al. **Delayed cerebral ischemia after aneurysmal subarachnoid hemorrhage: clinicoanatomic correlations.** *Neurology* 1986;36:329–33
6. Vergouwen MD, and Participants in the International Multi-Disciplinary Consensus Conference on the Critical Care Management of Subarachnoid Hemorrhage. **Vasospasm versus delayed cerebral ischemia as an outcome event in clinical trials and observational studies.** *Neurocrit Care* 2011;15:308–11
7. van der Schaaf IC, Ruigrok YM, Rinkel GJ, et al. **Study design and outcome measures in studies on aneurysmal subarachnoid hemorrhage.** *Stroke* 2002;33:2043–46
8. Reichman M, Gold R, Greenberg E, et al. **Validation of a new reference standard for the diagnosis of vasospasm.** *Acad Radiol* 2010;17:1083–89
9. Sanelli PC, Anumula N, Gold R, et al. **Outcomes-based assessment of a new reference standard for delayed cerebral ischemia related to vasospasm in aneurysmal subarachnoid hemorrhage.** *Acad Radiol* 2012;19:1066–74
10. Vergouwen MD, Vermeulen M, van Gijn J, et al. **Definition of delayed cerebral ischemia after aneurysmal subarachnoid hemorrhage as an outcome event in clinical trials and observational studies: proposal of a multidisciplinary research group.** *Stroke* 2010;41:2391–95
11. Vergouwen MD, Ilodigwe D, Macdonald RL. **Cerebral infarction after subarachnoid hemorrhage contributes to poor outcome by vasospasm-dependent and -independent effects.** *Stroke* 2011;42:924–29
12. Dankbaar JW, Rijsdijk M, van der Schaaf IC, et al. **Relationship between vasospasm, cerebral perfusion, and delayed cerebral ischemia after aneurysmal subarachnoid hemorrhage.** *Neuroradiology* 2009;51:813–19
13. Etminan N, Vergouwen MD, Ilodigwe D, et al. **Effect of pharmaceutical treatment on vasospasm, delayed cerebral ischemia, and clinical outcome in patients with aneurysmal subarachnoid hemorrhage: a systematic review and meta-analysis.** *J Cereb Blood Flow Metab* 2011;31:1443–51
14. Centre For Evidence Based Medicine. OCEBM Levels of Evidence Working Group. Oxford levels of evidence 1. http://www.cebm.net/index.aspx?o=5653. Accessed March 29, 2013
15. Kreiter KT, Mayer SA, Howard G, et al. **Sample size estimates for clinical trials of vasospasm in subarachnoid hemorrhage.** *Stroke* 2009;40:2362–67
16. Frontera JA, Fernandez A, Schmidt JM, et al. **Defining vasospasm after subarachnoid hemorrhage: what is the most clinically relevant definition?** *Stroke* 2009;40:1963–68
17. Vergouwen MD, Etminan N, Ilodigwe D, et al. **Lower incidence of cerebral infarction correlates with improved functional outcome after aneurysmal subarachnoid hemorrhage.** *J Cereb Blood Flow Metab* 2011;31:1545–53
18. Pickard JD, Murray GD, Illingworth R, et al. **Effect of oral nimodipine on cerebral infarction and outcome after subarachnoid haemorrhage: British aneurysm nimodipine trial.** *BMJ* 1989;298:636–42
19. Etminan N, Vergouwen MD, Macdonald RL. **Angiographic vasospasm versus cerebral infarction as outcome measures after aneurysmal subarachnoid hemorrhage.** *Acta Neurochir Suppl* 2013;115:33–40
20. Fisher CM, Roberson GH, Ojemann RG. **Cerebral vasospasm with ruptured saccular aneurysm–the clinical manifestations.** *Neurosurgery* 1977;1:245–48
21. Rabinstein AA, Friedman JA, Weigand SD, et al. **Predictors of cerebral infarction in aneurysmal subarachnoid hemorrhage.** *Stroke* 2004;35:1862–66
22. Fergusen S, Macdonald RL. **Predictors of cerebral infarction in patients with aneurysmal subarachnoid hemorrhage.** *Neurosurgery* 2007;60:658–67, discussion 667
23. Crowley RW, Medel R, Dumont AS, et al. **Angiographic vasospasm is strongly correlated with cerebral infarction after subarachnoid hemorrhage.** *Stroke* 2011;42:919–23
24. Wintermark M, Ko NU, Smith WS, et al. **Vasospasm after subarachnoid hemorrhage: utility of perfusion CT and CT angiography on diagnosis and management.** *AJNR Am J Neuroradiol* 2006;27:26–34
25. Washington CW, Zipfel GJ, and Participants in the International Multi-Disciplinary Consensus Conference on the Critical Care Management of Subarachnoid Hemorrhage. **Detection and monitoring of vasospasm and delayed cerebral ischemia: a review and assessment of the literature.** *Neurocrit Care* 2011;15:312–17
26. Schmidt JM, Wartenberg KE, Fernandez A, et al. **Frequency and clinical impact of asymptomatic cerebral infarction due to vasospasm after subarachnoid hemorrhage.** *J Neurosurg* 2008;109:1052–59
27. Unterberg AW, Sakowitz OW, Sarrafzadeh AS, et al. **Role of bedside**

microdialysis in the diagnosis of cerebral vasospasm following aneurysmal subarachnoid hemorrhage. *J Neurosurg* 2001;94:740–49
28. Wagner M, Steinbeis P, Guresir E, et al. **Beyond delayed cerebral vasospasm: infarct patterns in patients with subarachnoid hemorrhage.** *Clin Neuroradiol* 2013;23:87–95
29. Sanelli PC, Anumula N, Johnson CE, et al. **Evaluating CT perfusion using outcome measures of delayed cerebral ischemia in aneurysmal subarachnoid hemorrhage.** *AJNR Am J Neuroradiol* 2013; 34:292–98
30. Dankbaar JW, de Rooij NK, Velthuis BK, et al. **Diagnosing delayed cerebral ischemia with different CT modalities in patients with subarachnoid hemorrhage with clinical deterioration.** *Stroke* 2009;40: 3493–98
31. Greenberg ED, Gold R, Reichman M, et al. **Diagnostic accuracy of CT angiography and CT perfusion for cerebral vasospasm: a meta-analysis.** *AJNR Am J Neuroradiol* 2010;31:1853–60
32. Wintermark M, Reichhart M, Cuisenaire O, et al. **Comparison of admission perfusion computed tomography and qualitative diffusion- and perfusion-weighted magnetic resonance imaging in acute stroke patients.** *Stroke* 2002;33:2025–31
33. Schramm P, Schellinger PD, Klotz E, et al. **Comparison of perfusion computed tomography and computed tomography angiography source images with perfusion-weighted imaging and diffusion-weighted imaging in patients with acute stroke of less than 6 hours' duration.** *Stroke* 2004;35:1652–58
34. Chieregato A, Tanfani A, Noto A, et al. **Cerebral blood flow thresholds predicting new hypoattenuation areas due to macrovascular ischemia during the acute phase of severe and complicated aneurysmal subarachnoid hemorrhage: a preliminary study.** *Acta Neurochir Suppl* 2008;102:311–16
35. Peerdeman SM, van Tulder MW, Vandertop WP. **Cerebral microdialysis as a monitoring method in subarachnoid hemorrhage patients, and correlation with clinical events–a systematic review.** *J Neurol* 2003;250:797–805
36. Sarrafzadeh A, Haux D, Sakowitz O, et al. **Acute focal neurological deficits in aneurysmal subarachnoid hemorrhage: relation of clinical course, CT findings, and metabolite abnormalities monitored with bedside microdialysis.** *Stroke* 2003;34:1382–88
37. Cerejo A, Silva PA, Vilarinho A, et al. **Intraoperative brain oxygenation monitoring and vasospasm in aneurysmal subarachnoid hemorrhage.** *Neurol Res* 2012;34:181–86
38. Yokose N, Sakatani K, Murata Y, et al. **Bedside assessment of cerebral vasospasms after subarachnoid hemorrhage by near infrared time-resolved spectroscopy.** *Adv Exp Med Biol* 2010;662:505–11
39. Yokose N, Sakatani K, Murata Y, et al. **Bedside monitoring of cerebral blood oxygenation and hemodynamics after aneurysmal subarachnoid hemorrhage by quantitative time-resolved near-infrared spectroscopy.** *World Neurosurg* 2010;73:508–13
40. Anderson GB, Ashforth R, Steinke DE, et al. **CT angiography for the detection of cerebral vasospasm in patients with acute subarachnoid hemorrhage.** *AJNR Am J Neuroradiol* 2000;21:1011–15
41. Wintermark M, Dillon WP, Smith WS, et al. **Visual grading system for vasospasm based on perfusion CT imaging: comparisons with conventional angiography and quantitative perfusion CT.** *Cerebrovasc Dis* 2008;26:163–70

Gadolinium Contrast Agents for CNS Imaging: Current Concepts and Clinical Evidence

E. Kanal, K. Maravilla, and H.A. Rowley

SUMMARY: The aim of this article was to review the properties of the various gadolinium-based contrast agents used for CNS imaging along with the clinical evidence and published data that highlight the impact these different properties can have on diagnostic performance. In addition, approaches to optimizing image acquisition that take into account the different properties of specific gadolinium-based contrast agents and an extensive review of the safety profiles of the various agents are presented.

ABBREVIATIONS: CE = contrast-enhanced; CNR = contrast-to-noise ratio; GBCA = gadolinium-based contrast agent; Gd = gadolinium; NSF = nephrogenic systemic fibrosis; rCBV = relative cerebral blood volume; rCBF = relative cerebral blood flow

Of the 9 gadolinium-based contrast agents (GBCAs) approved by the United States FDA for contrast-enhanced (CE) MR imaging, 7 (gadoterate meglumine, Dotarem, Guerbet, Aulnay-sous-Bois, France; gadobutrol, Gadavist, Bayer HealthCare Pharmaceuticals, Wayne, New Jersey; gadopentetate dimeglumine, Magnevist, Bayer HealthCare; gadobenate dimeglumine, MultiHance, Bracco Diagnostics, Princeton, New Jersey; gadodiamide, Omniscan, GE Healthcare, Milwaukee, Wisconsin; gadoversetamide, OptiMARK, Covidien, Dublin, Ireland; gadoteridol, ProHance, Bracco Diagnostics) are approved specifically for CE-MR imaging of the CNS.[1-7] The 2 agents not approved for CE-MR imaging of the CNS (gadofosveset trisodium, Ablavar, Lantheus Medical Imaging, North Billerica, Massachusetts; and gadoxetic acid, Bayer HealthCare Pharmaceuticals [Eovist or Primovist]) have distinct properties that render them unsuitable for this indication; Ablavar[8] is an intravascular "blood-pool" agent approved for MR angiography of the aortoiliac vessels, whose strong binding to serum albumin (and resulting large effective molecular size) restricts permeability across the open blood-brain barrier, which limits suitability for CNS applications, while Eovist[9] is an approved liver-specific agent inappropriate for CNS applications because 50% of the injected dose is taken up and eliminated by hepatocytes.

Although numerous studies published in high-ranking peer-reviewed journals have confirmed the safety and efficacy of the 7 GBCAs approved for CNS imaging, differences among these agents and the impact these differences may have on diagnostic sensitivity and clinical decision-making remain underappreciated and sometimes misunderstood.

The aim of this article was to review the properties of the various GBCAs used for CNS imaging together with the clinical evidence and published data that highlight the impact these different properties can have on diagnostic performance. In addition, approaches to optimizing image acquisition that take into account the different properties of specific GBCAs and an extensive review of the safety profiles of the various agents will be presented.

For the purposes of the present review, brand names rather than chemical names have been used throughout to refer to the various GBCAs. Although chemical names would ordinarily be used in a review article such as this, it was thought that because the actual practitioners of MR imaging are typically more familiar with brand names than with chemical names, the use of brand names would help avoid the possibility of obfuscation and thereby enhance clarity in this field. Moreover, because generic formulations of these agents are not available in the United States, these brand names are clinically relevant designations. We have therefore elected to specifically use the same brand names for the various agents with which the reader will be most familiar.

GBCAS: WHAT THEY ARE AND WHAT THEY DO

As a heavy metal in the lanthanide series, elemental free gadolinium (Gd) is toxic to humans. GBCAs are formed by chelation of gadolinium to organic ligands to decrease its toxicity and render it

From Magnetic Resonance Services (E.K.), Department of Radiology, University of Pittsburgh Medical Center, Pittsburgh, Pennsylvania; Research Laboratory (K.M.), University of Washington, Seattle, Washington; and Departments of Radiology, Neurology, and Neurosurgery (H.A.R.), University of Wisconsin, Madison, Wisconsin.

Please address correspondence to Howard A. Rowley, MD, Department of Radiology, University of Wisconsin, 600 Highland Ave, Mail code 3252, Madison, WI 53792; e-mail: HRowley@UWHealth.org

Indicates open access to non-subscribers at www.ajnr.org

Indicates article with supplemental on-line tables.

http://dx.doi.org/10.3174/ajnr.A3917

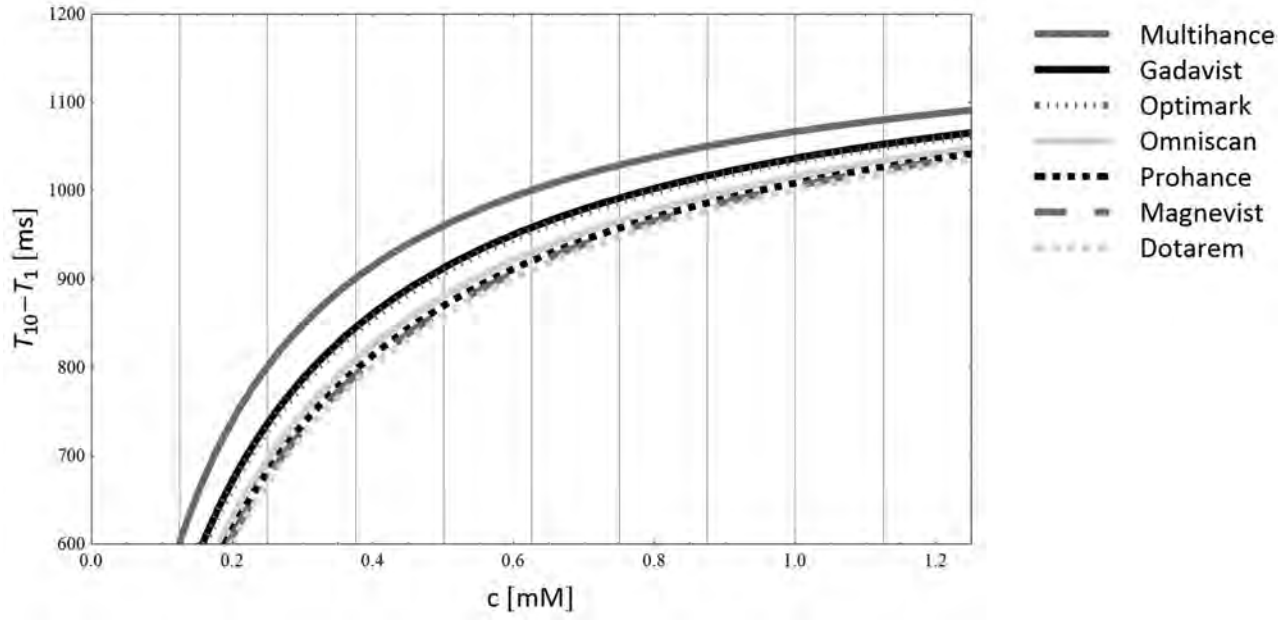

FIG 1. Comparison of T1 shortening of GBCAs as a function of Gd concentration, calculated from the *r1*-relaxivities in blood reported by Rohrer et al in 2005.[11]

safe for human use. Structurally, there are 2 distinct categories of GBCAs: 1) macrocyclic molecules in which the Gd^{3+} ion is caged within the cavity of the ligand, and 2) open-chain or "linear" molecules (On-line Table 1). Within each category, there are both ionic and nonionic GBCAs. Despite their different molecular structures and physicochemical properties, all GBCAs used for CE-MR imaging of the CNS have an identical mechanism of action involving shortening of the T1, T2, and T2* relaxation time constants of adjacent water protons in tissues[10] and similar biodistribution profiles because all are extracellular agents that do not cross the intact blood-brain barrier. The fundamental ability of GBCAs to selectively shorten T1 relaxation within a lesion compared with normal tissue is the basis for the most commonly applied usage of contrast agents in clinical practice today.

The extent to which the time constants are shortened, and hence the effectiveness of a specific GBCA in clinical practice, depends on the local concentration of the GBCA (Fig 1) and on the relaxivity values r_i (with i = 1, 2, 2*) of the agent. Relaxivities are defined as the slope of the linear regression generated from a plot of the measured relaxation rate ($1/T_i$) versus the concentration of the GBCA:

$$\frac{1}{T_i} = \frac{1}{T_{i(0)}} + r_i \times [\text{GBCA}]$$

where T_i denotes the longitudinal (T1) or transverse (T2, T2*) relaxation times of a solution containing GBCA and $T_{i(0)}$, the relaxation time of the solvent without GBCA.[11] Agents with higher *r1, r2,* and *r2** values will shorten the T1, T2, and T2* relaxation times of tissues to a greater extent, resulting in greater signal-intensity enhancement on T1-weighted images or greater signal-intensity loss on T2- and T2*-weighted images, respectively.

Molecules normally tumble or rotate in space at a rate that is dependent on many factors, not the least of which is their molecular mass. This tumbling rate can also be represented as the inverse of the so-called molecular correlation time. The closer the tumbling rate of the gadolinium-containing chelate molecule to the resonant frequency of water molecules, the greater is the relaxivity or relaxation enhancement. The molecules of each of the 7 FDA-approved CNS gadolinium chelates are all relatively small and therefore have exceedingly high tumbling rates that exceed the resonant frequencies of water molecules at the clinically used MR imaging field strengths. However, as the molecular tumbling rates between the paramagnetic contrast agent and the target water-based molecules become closer, energy exchange between the 2 molecules is facilitated and longitudinal magnetization is enhanced (ie, the target tissue T1 shortens).

One of the approved CNS agents, MultiHance, interacts weakly and transiently with serum albumin in vivo. This interaction slows the molecular tumbling rate of the complex, rendering it closer to the resonant frequency of water molecules at the field strength at which they are being imaged. This increases the (enhanced) tissue rotational correlation time (ie, slows its tumbling rate) and therefore brings it closer to matching that of water. The result is greater relaxivities/*r1* values and stronger relaxation enhancement effects.[3,12,13] Thus, the *r1* of MultiHance measured in human plasma at 37°C has been reported to be as high as 7.9 L × $mmol^{-1}$ × s^{-1} at 1.5T,[14] whereas the reported *r1* values of GBCAs that do not significantly interact with serum albumin range from approximately 3.6 L × $mmol^{-1}$ × s^{-1} at 1.5T for Dotarem to 5.2 L × $mmol^{-1}$ × s^{-1} at 1.5T for Gadavist.[11,14] However, reported relaxivity values may vary somewhat between investigating groups due to measurements being made under different conditions. For example, the *r1* and *r2* values reported by Rohrer et al[11] were obtained by using nonsterile bovine blood plasma, while those reported by Pintaske et al[14] were obtained by using human blood plasma.

Six of the 7 GBCAs approved for neuroradiologic imaging are

formulated as 0.5 mol/L concentrations, while 1 agent, Gadavist, is formulated at 1.0 mol/L. The physicochemical properties of this latter GBCA resemble those of the other conventional GBCAs, and its molecular structure differs from that of ProHance in that a hydroxypropyl group on the ProHance molecule is replaced by a trihydroxybutyl group on the Gadavist molecule.[15] Thus, the slightly higher relaxivity of Gadavist can be ascribed mainly to the slightly larger size and hence slightly slower molecular tumbling rate of the Gadavist molecule itself. Notably, the magnitude of the slowing of the molecular tumbling rate is smaller than that observed for GBCAs approved for neuroradiologic applications that interact with serum albumin as well as non-neuroradiologic agents such as Ablavar for which powerful protein binding is observed.

The degree of tissue T1 (and T2 and T2*) shortening by any GBCA is determined by the local concentration of the agent within the tissue being imaged in combination with the relative relaxivity of the agent. Varied concentrations of administered GBCAs can be theorized to result in varied rates of uptake of the agent into the extracellular fluid of the tissues being imaged, with faster tissue uptake expected with a GBCA formulated at a greater concentration. Theoretically, albeit not demonstrated clinically, in routine T1-weighted steady-state imaging, the higher concentration of Gadavist might impact the "ideal" postcontrast imaging time for this agent versus others with lower molarity. Recalling, however, that intravenous administration requires that all administered boluses pass through the heart and lungs before being distributed to the rest of the body, it would seem that any concentration difference per time among the various neuroradiologic GBCAs, other than possibly first-pass effects, would be quite small and likely not clinically discernable in steady-state. In addition, one should recognize that even if the contrast agent may theoretically accumulate faster in the target lesion, enhancing background tissues would also be expected to similarly accumulate that same amount more rapidly. Notwithstanding these theoretic considerations, in daily clinical practice, it appears that the ultimate steady-state concentrations in the tissues being imaged are sufficiently similar for all GBCAs regardless of the administered concentration and that the final concentration in tissues in steady-state is most likely determined predominantly by the total administered dose, based on the similarity of observed contrast enhancement when corrected for differences in relative relaxivity of the different agents as discussed later in this review. Thus, for routine, equidose, postcontrast T1-weighted steady-state imaging, enhanced signal intensities are dominated predominantly by the relative relaxivity values of the agents being compared. Therefore, the higher the *r1* value, the greater will be the contrast between the lesion and nonenhancing background tissues.

Dynamic phase imaging (as is used in perfusion-weighted imaging and in contrast-enhanced MR angiographic studies) differs from the above in that the target tissue of interest is the blood—the same "tissue" into which the agent is directly injected. Thus, per the equation above, higher GBCA concentration and/or higher relaxivity could each produce increases in signal intensity of the intravascular blood for T1-weighted imaging, or greater signal loss for T2- or T2*-weighted imaging. For dynamic bolus CE-MRA examinations, a principal objective is to time the bolus arrival within the vessels of interest to coincide with acquisition of the lowest order phase-encoding steps in *k*-space to obtain maximum vessel enhancement. Because all 7 GBCAs approved for neuroradiologic imaging are approved at identical administered total doses of 0.1 mmol/kg body weight, this means that the higher the concentration of the administered agent, the smaller the volume injected. Thus, a standard administered dose to a 70-kg patient would be 14 mL of any of the 6 GBCAs formulated at 0.5 mol/L, while it would be 7 mL for Gadavist formulated at 1.0 mol/L. However, the result of a smaller injected volume is that the timing window of opportunity during which to catch the higher concentration Gadavist in the vessels of interest is shortened by as much as one-half, making bolus timing more difficult and potentially more error-prone. This can possibly be offset by halving the injection rate when administering higher concentration agents or by diluting them with normal saline before administration. However, these approaches would negate any theoretic advantage of using a higher concentration agent.

The relatively recent FDA approval of GBCAs formulated at different concentrations but approved at identical administered doses provides opportunities for comparison among such agents. However, such attempts at comparison should use identical FDA-approved doses; comparisons should not be performed by using arbitrarily defined equivalent volumes because this would result in "double-dosing" of the higher concentration agent. Such studies evaluating agents of different concentrations would be useful because the ideal time to image is dependent on many factors, which include blood vessel size, flow rate and transit time in the case of CE-MRA, perfusion dynamics (vascularity and permeability) of the anatomy/pathology to be imaged in the case of perfusion MR, the concentration and relaxivities of the administered agent, and the design of the MR imaging pulse sequence to be used to acquire the postcontrast images. Furthermore, "ideal" timing will also be highly dependent on whether first-pass, dynamic contrast information is sought as opposed to steady-state images. "Ideal" timing tends to be spread over far longer windows of opportunity for steady-state acquisitions, while the window for first-pass, dynamic contrast information is quite short and is far more significantly impacted by such factors as the manner in which *k*-space is filled and the temporal resolution of the acquired images. Imaging parameters and timing that might be ideal for one agent might prove to be quite different for another GBCA with different concentration or relaxivity.

CLINICAL EVIDENCE FOR THE ROLE OF RELAXIVITY ON DIAGNOSTIC PERFORMANCE

Methodologic Considerations

Early studies to compare contrast agents for diagnostic efficacy were designed exclusively as interindividual parallel group studies in which each patient (with varying disease entities) was randomly assigned to receive just 1 of the 2 contrast agents.[16-25] Unfortunately, studies of this type are subject to wide interpatient and interlesion variability, resulting in disparate variations within each arm of the study. Such studies do not permit reliable demonstrations of relevant differences between study groups and agents. Indeed, such parallel group studies can only demonstrate equivalence between study groups for equivalent doses of different GBCAs and not superiority or inferiority, even among GBCAs with widely varying relaxivity values.[24,25]

Direct comparison among different agents is accomplished more objectively with an intraindividual crossover study in which each patient receives both GBCAs in random order in 2 identical MR imaging examinations separated by just a few days. Such studies are better designed to isolate the GBCA as the only variable being assessed. Thus, variations due to patient-, disease-, or examination-related factors are eliminated or, at least, minimized. In such studies, any differences in findings can be attributed solely to the GBCA because all other variables are identical for the 2 examinations.

Summarized below are the findings of several such intraindividual crossover studies performed in human subjects for CNS evaluation of various GBCAs. In organizing this discussion, we realized that there is no standardized definition for use of the term, "high relaxivity." It is the opinion of these authors that "high relaxivity" should be defined not numerically alone, but rather by an objectively proved ability of an agent to deliver increased clinical utility as measured by clinically relevant increases in signal enhancement (rather than merely small but statistically significant signal increases) or, preferably, an objectively measured increase in lesion number or lesion extent compared with other "standard" GBCAs.

Steady-State Imaging. To analyze the possible differential roles of relaxivity and concentration in imaging performance, findings are presented for studies that compared the following: 1) Dotarem, Magnevist, Omniscan, OptiMARK, and ProHance (which all possess similar [standard] relaxivity values and are formulated at standard [0.5 mol/L] concentrations), 2) Gadavist (the GBCA with slightly higher relaxivity and the highest concentration [1 mol/L]), and 3) MultiHance (the GBCA with the highest relaxivity and formulated at standard concentration).

1) Intraindividual Crossover Studies Comparing GBCAs with Standard Relaxivity/Standard Concentration (Dotarem, Magnevist, Omniscan, OptiMARK, ProHance). To the authors' knowledge, Greco et al[26] performed the only intraindividual crossover study that compared GBCAs with standard relaxivity/standard concentration. In that study, 2 blinded readers intraindividually compared Magnevist (*r1*-relaxivity at 1.5T: 3.9–4.1 $L \times mmol^{-1} \times s^{-1}$)[11,14] with ProHance (*r1*-relaxivity at 1.5T: 4.1 $L \times mmol^{-1} \times s^{-1}$ measured in bovine plasma at 37°C)[11] in 80 subjects for the presence of disease, degree of enhancement, location and number of lesions, and additional information gained (definition of lesion borders, improved visualization, distinction of edema, disease classification, determination of recurrent tumor, and so forth). Neither reader noted any significant differences in terms of GBCA preference (readers 1 and 2 preferred ProHance over Magnevist in 2 and 4 cases, respectively, and Magnevist over ProHance in 1 and 2 cases, respectively), and no differences were noted between agents in terms of the additional information provided on postcontrast images (On-line Table 2).

2) Intraindividual Crossover Studies Comparing a GBCA with Slightly Higher Relaxivity and High Concentration versus Standard Relaxivity/Standard Concentration Agents (Gadavist versus Either Dotarem, Magnevist, Omniscan, OptiMARK, or ProHance). To date, 5 published reports have described intraindividual crossover comparisons of Gadavist with standard relaxivity GBCAs.[27-31] Three of these looked specifically at the potential benefit of Gadavist versus Magnevist[27,28] or ProHance[29] for the detection and visualization of cerebral metastases and concluded, in each case, that Gadavist is advantageous for lesion detection primarily because of improved lesion conspicuity (On-line Table 2). However, the conclusions in a study by Anzalone et al[27] were based solely on subjective assessment of images from 27 patients by 2 neuroradiologists in consensus, but unfortunately, no quantitative assessment of lesion enhancement was reported. Kim et al[28] reported improved quantitative enhancement (lesion/brain contrast-to-noise ratio [CNR]) with Gadavist, but this study was retrospective and only compared double (0.2 mmol/kg body weight) doses of Gadavist and Magnevist. Furthermore, GBCA administration was not random (all patients received Magnevist for the first examination and Gadavist for the second). In the third study in patients with brain metastases, Katakami et al[29] evaluated a larger number of patients by using a prospective design and concluded that a single 0.1-mmol/kg dose of Gadavist is noninferior to a double 0.2-mmol/kg dose of ProHance for lesion detection. However, despite administering a single 0.1-mmol/kg dose of ProHance as part of the study design, no assessment of single-dose ProHance images was performed. Thus, it is not possible to say whether a single dose of ProHance would have proved noninferior to a single dose of Gadavist by using their study design, sample size, and assessment methodology.

In a more recent single-center study in 51 patients with either primary or secondary brain tumors, 2 blinded readers each preferred Gadavist to ProHance in more patients in terms of subjective "preference in contrast enhancement," "overall preference," and "preference in diagnostic quality."[30] However, differences in quantitative enhancement were inconsistent and sequence-dependent, with a higher SNR for Gadavist noted only on a second T1-FLASH sequence at approximately 10 minutes postinjection, with no differences between agents seen on T1-spin echo or MPRAGE sequences. Indeed, Bayer HealthCare (manufacturer of gadobutrol, Gadavist) reported to the FDA that the performances of 0.1-mmol/kg doses of Gadavist and ProHance for brain tumor imaging are similar.[2,31] In a prospective multicenter phase III study performed in 419 patients for the FDA approval of Gadavist for CNS imaging, 3 blinded readers each reported similar contrast enhancement, lesion border delineation, and lesion internal morphology and a similar overall accuracy of diagnosis when these 2 agents were administered at an equivalent dose of 0.1 mmol/kg body weight. The conclusion of the study was that Gadavist is noninferior to ProHance.[2,31]

Another recent report presented findings from a study that prospectively compared single-dose Gadavist (*r1*-relaxivity: 4.7–5.2 $L \times mmol^{-1} \times s^{-1}$ in plasma at 37°C[11,14]) with single-dose Dotarem (*r1*-relaxivity: 3.6 $L \times mmol^{-1} \times s^{-1}$) in 136 patients with cerebral neoplastic enhancing lesions.[32] In this study, significant preference for Gadavist compared with Dotarem was noted by 2 of 3 blinded readers for overall reader preference. However, none of the 3 readers considered Gadavist superior to Dotarem for lesion delineation, while only 1 blinded reader noted a minimally significant preference for Gadavist for the definition of lesion internal structure. Quantitatively, the percentage lesion enhancement following Gadavist was approximately 9% higher than

that following Dotarem, as expected from the differences in their respective relaxivities, but this yielded no significant difference between the 2 agents for measured CNR. Most important, no differences in the number of lesions detected with either agent were observed.

3a) Intraindividual Crossover Studies Comparing the GBCA with the Highest Relaxivity/Standard Concentration versus GBCAs with Standard Relaxivity/Standard Concentration (MultiHance versus Dotarem, Magnevist, Omniscan, OptiMARK, or ProHance). Numerous multicenter studies have compared MultiHance with standard GBCAs by using an intraindividual crossover study design with blinded image evaluation by fully independent experienced neuroradiologists.[33-41] All of these studies were designed to demonstrate superiority rather than noninferiority, and the findings of all concluded that MultiHance is significantly superior in terms of both qualitative enhancement (global diagnostic preference, lesion border delineation, definition of disease extent, visualization of lesion internal morphology, lesion contrast enhancement) and quantitative enhancement (CNR, lesion-to-background ratio) (On-line Table 2). In each of these studies, the authors concluded that the superiority of MultiHance was due to its higher *r1* value.

3b) Intraindividual Crossover Study to Compare the Highest Relaxivity GBCA versus the GBCA Formulated at the Highest Concentration (MultiHance versus Gadavist). A recent study by Seidl et al[41] directly addressed the relative merits of high relaxivity versus high gadolinium concentration. In their randomized, double-blind, intraindividual crossover study, 123 patients each underwent 1 examination with 0.1-mmol/kg MultiHance and 1 examination with 0.1-mmol/kg Gadavist. Three blinded readers consistently demonstrated a highly significant ($P < .0001$) preference for MultiHance for all qualitative end points with good interreader agreement for all evaluations (On-line Table 2). In addition, significant superiority was noted for all quantitative assessments with a mean difference of approximately 22% in percentage lesion enhancement between MultiHance and Gadavist.

This study demonstrated that gadolinium concentration has little-to-no practical clinical impact on steady-state morphologic imaging and that at identical approved (0.1 mmol/kg) doses, the relaxivity of the GBCA is the dominant characteristic determining the degree of enhancement.

Perfusion Imaging. Cerebral perfusion assessment by dynamic susceptibility contrast MR imaging is frequently used for evaluation of brain tumors, stroke, and degenerative diseases such as dementia. The technique is based on rapid intravenous injection of a GBCA and subsequent bolus tracking by using a fast susceptibility-weighted imaging sequence that uses the T2* relaxing properties of the GBCA. Following tracer kinetic modeling, parametric maps of mean transit time, regional cerebral blood volume (rCBV), and regional cerebral blood flow (rCBF) can be calculated by unfolding tissue concentration curves and the concentration curve of the feeding artery.

Compared with conventional morphologic (static) imaging, (dynamic) perfusion imaging is more dependent on the shape of the injected contrast bolus and thus on the rate at which GBCAs are injected. Additionally, higher administered GBCA concentration and higher relaxivity might each be beneficial in augmenting the signal loss associated with the first-pass contrast bolus through the tissues of interest.

Although interindividual parallel group studies have compared Gadavist with Magnevist at 1.5T,[42,43] comparatively few intraindividual crossover studies have been performed to compare GBCAs for perfusion imaging. Those that have been performed have compared Gadavist with either Magnevist at 3T[44] or MultiHance at 1.5T[45] or 3T.[46,47]

1) Inter- and Intraindividual Crossover Studies Comparing GBCAs with Standard Relaxivity/High Concentration versus Standard Relaxivity/Standard Concentration (Gadavist versus Magnevist). An interindividual parallel group comparison of Gadavist with Magnevist was first performed by Griffiths et al,[42] who compared 10- and 20-mL injections of Gadavist with 20-mL injections of Magnevist (all at 5 mL/s, resulting in overall injection times of 2 and 4 seconds, respectively) in 6 groups of 6 patients (36 patients overall) at 1.5T to determine whether the higher Gd concentration of Gadavist was beneficial when using thinner sections (4 mm as opposed to 7 mm) for single-shot, gradient-recalled echo-planar imaging. They compared time-intensity curves calculated at regions of interest in the hemispheric white matter and thalamus in terms of maximum signal reduction (ie, the difference between mean baseline and minimum value on the time-intensity curve), full width at half minimum, and signal-to-noise measurements. No significant differences were found between 20 mL of Magnevist and 10 mL of Gadavist in terms of the maximum signal changes observed in either anatomic area and at either section thickness. On the other hand, the signal changes nearly doubled when 20-mL Gadavist was compared with 20-mL Magnevist (ie, when a 2-fold higher dose of Gadavist was used), indicating that the total amount (ie, dose) of Gd was the dominant factor in determining signal response rather than the administered concentration per se.

A second interindividual parallel group comparison of Gadavist and Magnevist at 1.5T was subsequently performed by the same group when investigating whether 2 gadolinium perfusion studies of the whole brain could be performed during the same table occupancy without degradation of the derived data in the second study.[43] In this study, 12 patients each received 2 injections at a fixed rate of 5 mL/s of either 20-mL Magnevist (6 patients) or 10-mL Gadavist (6 patients), with each administration separated by 8 minutes. Although the study was not designed specifically to compare the 2 agents directly, the authors nevertheless showed no significant differences in either the maximum signal change or full width at half maximum with 10-mL Gadavist compared with 20-mL Magnevist.

A small-scale intraindividual crossover comparison of these 2 GBCAs was recently performed at 3T by Giesel et al[44] in 11 patients (6 with intra-axial tumors, 5 with extra-axial tumors), who each underwent examinations with 5-mL Gadavist and 10-mL Magnevist by using a T2*-weighted, gradient recalled-echo, echo-planar technique. As in the studies by Griffiths et al,[42,43] the injection rate for both agents was 5 mL/s. However, unlike Griffiths et al, the authors reported significantly higher maximal signal changes for Gadavist in both gray and white matter and noted that Gadavist depicted a larger number of "hot spots" (areas with higher blood perfusion in the tumor) on color-coded maps than

Magnevist in most of the 6 intra-axial tumors. The authors concluded that the higher concentration of Gadavist offers advantages over standard-concentration Magnevist for delineation of gray and white matter and for the demarcation of highly vascularized tumor tissue and that these advantages are due to an improved bolus effect with increased intravascular concentration during the first pass.

2) Intraindividual Crossover Studies Comparing High Relaxivity/Standard Concentration versus Standard Relaxivity/High Concentration (MultiHance versus Gadavist). Early intraindividual crossover studies to compare Gadavist and MultiHance were performed independently by Essig et al[45] and Thilmann et al[46] in healthy volunteers at 1.5T and 3T, respectively. In the study by Thilmann et al,[46] 16 healthy volunteers each underwent 3 DSC-MR imaging examinations separated by at least 3 days, receiving a single (0.1-mmol/kg; 7-mL) dose of Gadavist, a double (14-mL) dose of Gadavist, and a single (14-mL) dose of MultiHance, each at an injection rate of 5 mL/s (ie, resulting in injection times of 1.4, 2.8, and 2.8 seconds, respectively). Quantitative determinations based on signal intensity/time curves were made at regions of interest on gray and white matter and specific arteries selected for perfusion analysis. Additionally, gray-scale and color-coded maps of regional cerebral blood volume and regional cerebral blood flow were calculated and compared.

Quantitative analysis revealed nearly identical signal intensity/time curves for the 2 single-dose examinations. No differences were noted in terms of maximal relative signal drop, full width at half maximum, or signal-to-noise ratio of the concentration curve at maximum concentration. Likewise, qualitative evaluation of rCBV and rCBF maps by 2 experienced blinded radiologists revealed no differences between the 2 single-dose examinations with no advantage noted for either of the 2 GBCAs. More pronounced signal drops (52% versus 32%) and better quality perfusion maps (rCBV and rCBF) were obtained with double-dose Gadavist compared with either single-dose examination, though both single-dose examinations were considered suitable for diagnostic purposes.

More recently, Wirestam et al[47] performed further evaluations of data acquired by Thilmann et al[46] and confirmed that double-dose Gadavist results in higher absolute CBV, CBF, and mean transit time than single-dose Gadavist and that no significant differences are apparent between single-dose Gadavist and single-dose MultiHance.

Similar findings and conclusions to those of Thilmann et al[46] were made by Essig et al[45] in a study comprising 12 healthy male volunteers who each underwent 4 highly standardized perfusion MR imaging examinations with 0.1- and 0.2-mmol/kg doses of Gadavist and MultiHance, each administered at 5 mL/s. As in the study by Thilmann et al,[46] a single dose of both agents was shown to be sufficient to achieve high-quality, diagnostically valid perfusion maps. Again, no differences were noted between single doses of the 2 agents for any quantitative parameter (susceptibility effect [percentage signal drops of approximately 30%], rCBV, and rCBF values) apart from full width at half maximum, which was significantly greater for MultiHance. Likewise, 2 off-site blinded readers found no significant differences between Gadavist and MultiHance in terms of image quality, adequacy of white-to-gray matter differentiation, or subjective preference for 1 agent or the other in terms of CBV and CBF image sets. Better overall image quality was noted with double (0.2 mmol/kg) doses of the 2 agents, for which a slightly higher susceptibility effect was seen with Gadavist. Nevertheless, the authors considered that double doses of the 2 agents provided no clinical benefit over single-dose examinations. The authors also concluded that single doses of both agents were effective at inducing sufficient signal drop on T2* EPI sequences to permit robust and reproducible quantification of perfusion parameters. Moreover, they concluded that the greater volume of injection of MultiHance had no disadvantage and gave comparable perfusion values to those obtained with the more highly concentrated Gadavist.

Contrast-Enhanced MR Angiography. Similar to perfusion imaging, dynamic bolus contrast-enhanced MR angiography is a rapid imaging technique in which images are acquired during the first pass of a GBCA through the vessels of interest. However, unlike DSC perfusion imaging, the level of enhancement is dependent on the *r1* of the agent rather than the *r2** value. Accordingly, image quality and diagnostic performance are dependent not only on the image acquisition parameters but also on the contrast-injection protocol. Thus, while advances in sequence design can lead to marked improvements in the spatial and temporal resolution of vessel images, it remains fundamental that bolus timing and the peak concentration of intraluminal contrast coincide with the acquisition of the lower order phase-encoding steps of *k*-space image acquisition. To achieve MR angiograms with adequate homogeneous arterial contrast and without image artifacts, contrast bolus timing must achieve high concentration and a relatively constant plateau during acquisition of the central part of *k*-space, which contributes most of the image contrast. In addition, evidence appears to support the need to maintain a high level of Gd in the vessels during much of the higher order phase-encoding acquisition to minimize vessel edge blurring that can reduce vessel detail and visualization of smaller vessels.[48]

For the purposes of the present article, the focus will mainly be on studies comparing GBCAs for CE-MRA of the intracranial and supra-aortic vessels. However, the underlying principles of GBCA administration and image acquisition are common to all CE-MRA examinations across all vascular territories.

Intraindividual Crossover Studies Comparing GBCAs for CE-MRA of the Supra-Aortic Vessels

Of the few intraindividual crossover studies performed in the supra-aortic vessels, most have compared MultiHance with Magnevist.[49-51] In a very early study of 12 patients referred for CE-MRA of the carotid arteries, Pediconi et al[49] compared a single 0.1-mmol/kg dose of MultiHance with a double (0.2-mmol/kg) dose of Magnevist and found superior quantitative and qualitative enhancement with MultiHance for carotid time-resolved CE-MRA. Both doses of GBCAs were administered at a fixed rate of 2 mL/s, and the better imaging performance was ascribed to the higher *r1* of MultiHance. In that study, a single 0.1-mmol/kg dose of MultiHance would have been administered during 7.5 seconds for a 75-kg patient. Conversely, the double 0.2-mmol/kg dose of Magnevist would have been administered during 15 seconds, potentially resulting in exclusion of a portion of the increased Magn-

evist dose from the central part of the *k*-space during the MRA acquisition. On the other hand, the extended injection time for double-dose Magnevist would have provided double the window of opportunity to correctly "catch" the highest intraluminal GBCA concentration and may have contributed to better vessel wall sharpness, though this was not evaluated in the study. Empiric adjustments to optimize signal by using a specific pulse sequence, gadolinium agent, acquisition timing, and injection parameters are, therefore, critical in achieving best image quality.

A recent study by Li et al[50] in 46 patients compared single-dose MultiHance and double-dose Magnevist. In this study, the 2-fold greater volume of Magnevist required to achieve a double dose was injected at a 2-fold faster rate to achieve comparable bolus geometry for the 2 examinations in each patient. Three blinded readers in the study found no differences between single-dose MultiHance and double-dose Magnevist for any qualitative parameter (vessel anatomic delineation, detection/exclusion of pathology, and global preference) or for quantitative measures of contrast enhancement (SNR, CNR). Indirect support for the findings of Li et al[50] comes from a study by Bültmann et al,[51] who compared single 0.1-mmol/kg doses of MultiHance and Magnevist across 19 arteries/arterial segments (comprising the internal carotid arteries; anterior, middle, and posterior cerebral arteries; vertebral arteries; and basilar artery) in 12 healthy volunteers at 3T. Maximum-intensity-projection images acquired with MultiHance were found to be markedly superior in terms of mean technical quality and vessel delineation to those acquired with Magnevist. Likewise the relative CNR was significantly greater with MultiHance, with overall increases of 23.3%, 26.7%, and 28.5% noted for the internal carotid, middle cerebral, and basilar arteries, respectively.

More recently, Kramer et al[52] compared Gadavist with both MultiHance and Dotarem in 20 healthy volunteers at 3T. Although the total dose of each GBCA administered was 0.1 mmol/kg body weight, at variance with previous studies, the authors acquired both static CE-MRA and dynamic (time-resolved) CE-MRA images with 0.07 mmol/kg injected initially for the acquisition of static images followed by a further 0.03 mmol/kg for the acquisition of dynamic MRA. A fixed injection rate of 2 mL/s was used for both injections with all 3 GBCAs, and determinations were made of both quantitative and qualitative end points. Qualitative assessment of static images by 3 blinded readers found Gadavist to be not significantly different from MultiHance but superior to Dotarem, while few differences were noted between MultiHance and Dotarem. In terms of quantitative assessment of static images, a higher SNR with Gadavist was noted in the proximal ICA but not in the distal ICA, while the CNR with Gadavist was not significantly different from that with MultiHance but significantly superior to that with Dotarem. Similar findings were obtained for dynamic MRA. Finally, no differences were noted between the different GBCAs in terms of vessel sharpness.

The manner in which the contrast agents were administered for this study is not one routinely used in clinical practice. Nevertheless, it supports the advantages potentially gained with increased GBCA concentration if data acquisition can be appropriately timed to the shortened first pass of contrast bolus.

SAFETY

With recognition of the association between Gd and nephrogenic systemic fibrosis (NSF) in 2006, there has been a sharply increased focus on GBCA safety. The 7 GBCAs currently approved by the FDA for CNS imaging have nearly identical pharmacokinetic (biodistribution and blood half-lives) profiles and mechanisms of action, and 6 of the 7 have similar clearance pathways almost exclusively through the kidneys. MultiHance differs in that a small fraction of the injected dose (approximately 3%–5%) is taken up by normally functioning hepatocytes and excreted into the bile.

Nephrogenic Systemic Fibrosis

NSF is a rare, potentially life-threatening disease that has been linked to the administration of some GBCAs in patients with severe renal impairment. In the peer-reviewed literature, approximately 78% of all unconfounded, single-agent cases of NSF have been associated with Omniscan, while a further 20% have been associated with Magnevist, and <2%, with OptiMARK.[53] Very few single-agent cases (0.5%) have been associated with the macrocyclic agent Gadavist, while no unconfounded cases have been reported for Dotarem, MultiHance, or ProHance.[53] Similarly, no unconfounded cases have been reported for the 2 GBCAs not approved for CNS imaging (Ablavar, Eovist). Of note, GBCAs associated with the lowest number of putative cases of NSF, if any, are characterized either by a macrocyclic structure with high kinetic stability (Dotarem, Gadavist, ProHance) or a unique ability to interact with or bind to plasma proteins (Ablavar, Eovist, MultiHance). With the latter group, it has been proposed that the aromatic moiety on these complexes, in addition to being responsible for the protein-binding characteristics, may also increase the stability of the molecule by improving their kinetic inertia. This is possibly due to the steric effect of the bulky substituents that slightly hinders unwrapping of the ligand around the gadolinium.[54]

The introduction of specific recommendations such as patient prescreening for renal disease, the contraindication of less stable so-called high-risk GBCAs (Magnevist, Omniscan, and OptiMARK) in patients at risk of NSF, restricting the use of GBCAs to the lowest dose needed to provide the required diagnostic information, and a drastic reduction in the number of cases in which the recommended single dose is exceeded, has resulted in a markedly reduced incidence of NSF. Indeed, these measures have resulted in the number of new NSF cases dropping close to zero.[55]

Adverse Reactions

Although the tolerability of GBCAs is very good, adverse reactions are observed after the administration of all agents as reported in the prescribing information approved by regulatory authorities. On the basis of published data, rates of adverse reactions following GBCA administration range between 0.03% and 2.4%.[56-65] Of these reactions, >74% are transient and mild in intensity. Reactions of moderate or severe intensity have been reported to range from <1% to 19% of cases.[56,58,61-66] Life-threatening and fatal reactions are very rare, with 40 deaths per 51 million administered GBCA doses reported between 2004 and 2009.[65]

Adverse drug reactions fall into 2 major categories. The first

includes reactions that can occur in any patient, such as drug overdose and drug interactions; the second includes reactions that are restricted to susceptible patients, such as drug toxicity/augmented effects (ie, drug idiosyncrasy or reduced tolerance) and hypersensitivity reactions that are either allergic or pseudoallergic in nature.[67] These latter 2 reactions are clinically indistinguishable because their symptomatic presentations are very similar; however, they differ vastly mechanistically. Although true allergic reactions to GBCAs have been reported,[68,69] the available evidence suggests that most adverse reactions to GBCAs are pseudoallergic in nature and are not associated with immunologic specificity.[57]

Acute reactions typically affect susceptible patients and occur within the first hour after GBCA injection. Mild reactions, such as nausea and vomiting, are usually self-limiting and do not require treatment.[57,70] Patients who experience mild reactions should be monitored for at least 30 minutes post-GBCA exposure to ensure that there is no progression of signs and symptoms.[57] Moderate reactions consist of more severe symptoms than mild reactions, or they can appear as other clinically significant reactions that require specific treatment. The vital signs of patients suspected of experiencing a moderate reaction should be monitored closely to make certain that progression to a severe event is avoided. Severe reactions, though quite rare, are significant in that they can present life-threatening situations; thus, immediate recognition and treatment are warranted. In many cases, life-threatening events begin with mild signs and symptoms, and then evolve rapidly. As a result, it is imperative that practitioners monitor all patients receiving a GBCA during their MR imaging procedure, with particular attention paid to asthmatic and atopic patients and patients with allergic respiratory phenomena because these patients are considered more "at risk" of an adverse event. Recent legal action and findings confirm the seriousness with which the Centers for Medicare and Medicaid Services approaches the mandate that GBCA administration be under direct physician supervision.[71]

Regulatory authorities have not differentiated among commercially available GBCAs in terms of acute adverse-reaction profiles. Most published reports consider GBCAs to have comparable adverse event profiles for mild reactions such as nausea and for severe anaphylactoid reactions.[72] To remain objective and scientifically sound, comparisons of adverse event rates across agents should ensure that the mode of data collection (study design, prospective versus retrospective) and population (sex, clinical profile, body area) are taken into account. Variations in these factors alone can result in up to 100-fold differences in apparent event rates.[63-65,73-75] When differences in incidence rates among GBCAs are encountered, such differences are sometimes attributable to methodologic bias or to the so-called Weber or Lalli effects.[76,77]

The Weber effect occurs when a new medication introduced to the clinical market leads to heightened safety vigilance on the part of practitioners and, as a consequence, more frequent reporting of adverse reactions.[56,76,78] After experience is accumulated by using a given product, previously noteworthy reactions are perceived as being predictable and less noteworthy and, therefore, may be reported less frequently.[56,76,78] Thus, the Weber effect is characterized by a transient increase in adverse event reporting that tends to peak in the second year following introduction of a new agent, with a subsequent return to the original baseline reaction rate observed before the introduction of the new agent.[76] Such an effect was recently reported with GBCAs by Davenport et al,[79] who described the impact of an abrupt switch from Magnevist to MultiHance on the incidence of immediate allergic-type adverse events. After MultiHance was substituted for Magnevist, a significant transient increase in the frequency of reported allergic-like reactions occurred that peaked in the second year postswitch and then declined, suggestive of the Weber effect. The subsequent reaction rate during last 3 calendar quarters of the monitoring period did not differ significantly from the original baseline reaction rate with Magnevist.[79] However, the authors did note that the study was underpowered to confirm noninferiority among different GBCAs with respect to severe reactions.

Another confounder in the comparison of adverse events among various GBCAs is the Lalli effect, which occurs when practitioners unintentionally project their feelings about a new product onto patients, inducing fear and anxiety. This may result in unpredictable, idiosyncratic reactions of varying severity.[77]

Both of these effects have been observed with contrast agents[56,77,79]; however, true differences between agents in terms of severe acute reaction rates have not been demonstrated in well-controlled, statistically powered, prospective, randomized, blinded studies.[78] The main reason for the lack of such studies is their complexity, duration, and cost due to the low incidence of adverse events. For an idea about the estimated sample size, a randomized, parallel-group study aimed at comparing the safety of agent A versus agent B with expected rates of allergic-type severe adverse reactions of 1/20,000 and 1/100,000, respectively, would require 350,000 patients per agent—that is, 700,000 patients for 85% statistical power by using 2 group Fisher exact tests with an α of .05 and a 2-sided significance level. Such a sample size would be required for a 5-fold difference in the rate of adverse reactions. If you assume that agent A has a reaction rate of 1/50,000 and agent B has a reaction rate of 1/100,000, the number of patients per group for the same 85% power would rise to 2,890,000.

Several reports have claimed to show differences across GBCAs.[65,66] However, these reports have largely been retrospective surveys or observational studies with major methodologic flaws, such as reliance on the accuracy of historic recordkeeping by busy health care providers, lack of randomization, presence of unbalanced study groups, possible selection bias, potential for confounding data, and inappropriate analysis. In contrast, more reliable data are derived from prospective development studies. Unfortunately, most development studies are noncomparative and, when comparative, are typically too small to allow robust and unequivocal conclusions.[78]

DISCUSSION

Morphologic Imaging

One major conclusion to be drawn from intraindividual crossover studies performed to compare GBCAs at approved doses (0.1 mmol/kg body weight) for morphologic imaging of brain lesions (mostly tumors) is that *r1*-relaxivity is the primary determining

factor for contrast efficacy. Thus, large-scale, well-controlled, prospective clinical studies have found no differences between GBCAs with similar *r1* values (Magnevist versus ProHance,[26] Gadavist versus ProHance,[31]), while differences have been observed between GBCAs with higher *r1*-relaxivity versus GBCAs with "standard" *r1*-relaxivity (Gadavist versus Dotarem[32]; MultiHance versus Dotarem, Magnevist, Omniscan, Gadavist[33-41]). Moreover, the studies performed so far suggest that the magnitude of the superiority reflects the magnitude of the difference in *r1*-relaxivity. Thus, the difference in percentage lesion enhancement of approximately 9% for Gadavist compared with Dotarem[32] reflects only a slightly greater *r1*-relaxivity of Gadavist compared with Dotarem, while the larger differences of 22%–27% for MultiHance compared with Gadavist[41] and Magnevist,[37] respectively, reflect the larger differences in *r1*-relaxivity between these agents. Notably, small differences in percentage lesion enhancement have not been demonstrated to add significant clinical efficacy,[31,32] while larger differences have been shown to result in significantly superior depiction of tumor morphologic features, lesion extent, and border delineation.[33-41] The previously cited studies also support our earlier hypothesis that in steady-state postcontrast T1-weighted imaging typically used for conventional CNS imaging, in which postcontrast acquisition times are delayed at least 2–5 minutes following contrast agent injection, the administered Gd concentration of the agent does not play a significant clinical role when the different GBCAs are delivered at equal FDA-approved doses.

Perfusion Imaging

The magnitude of signal drop in DSC perfusion imaging is largely, if not solely, dependent on the *r2** value of the GBCA together with the local concentration of Gd. The *r1* and *r2* values of GBCAs play no detectable role in DSC perfusion. Thus, at least theoretically, the higher concentration of Gadavist should be advantageous for perfusion imaging compared with standard-concentration GBCAs when administered at equivalent doses at a fixed injection rate. Hence, while a 75-kg patient administered a standard Gadavist dose of 0.1 mmol/kg body weight at a rate of 5 mL/s would receive a total volume of 7.5 mL in 1.5 seconds, the same patient administered an equivalent gadolinium dose of standard concentration GBCA at the same rate would receive a total volume of 15 mL during 3 seconds. In this setting the possibility of injecting an equivalent number of Gd molecules in a shorter time, giving a sharper contrast bolus, might be expected to result in more Gd molecules in the tissue of interest during image acquisition and thus a greater susceptibility effect, as suggested by Giesel et al.[44] However, the experimental results of Thilmann et al[46] and Essig et al[45] revealed no significant differences for similar injected doses of Gadavist and MultiHance (identical signal intensity/time curves obtained for single-dose examinations with both GBCAs). These findings suggest that bolus dispersion (ie, physiologic widening [dilution] of the contrast bolus during the first pass through the lungs and heart) leads to normalization of the resulting bolus shape to a point where the local intravascular concentration of Gd is similar for injections of equal total dose. Dilution of the contrast bolus in this manner appears to obviate any benefit of higher Gd concentration at the short injection times (typically <5 seconds) required for perfusion imaging.[46] In this case, the susceptibility perfusion effect is determined primarily by the administered GBCA dose, rather than by administered GBCA molarity.[46] There is support for this possibility in a study by van Osch et al,[80] which reported the altered results of perfusion measurements obtained when varying parameters, including injection rate, injection volume, and injection time, even when using the same total Gd dose.

Contrast-Enhanced MR Angiography

When injected under comparable conditions (ie, with identical bolus geometry), the greater *r1*-relaxivity of MultiHance has been shown to be beneficial for CE-MRA of the supra-aortic arteries, giving superior quantitative and qualitative enhancement when administered at an equivalent dose to Magnevist[51] and equivalent enhancement and diagnostic performance, when a single dose of MultiHance is compared with a double dose of Magnevist.[50] These findings in the supra-aortic arteries are supported by the findings of numerous intraindividual crossover studies in other vascular territories.[81-86]

It is reasonable to conclude that increased GBCA concentration (as seen in Gadavist) and significant increases in *r1*-relaxivities (to the magnitude seen with MultiHance) would each be beneficial for increased vascular signal intensity for CE-MRA, though the benefit obtained from higher concentrations may be accompanied by a concomitant shortening of the optimal image-acquisition timing window when both agents are injected at similar rates. Attempting to increase the likelihood of successfully matching the timing window of the lowest order phase-encoding steps with the first passage of the contrast agent by slower injection rates or by dilution of the administered agent may help offset any such timing problems but may simultaneously serve to negate any potential benefit that the higher concentration agent might have introduced.

CONCLUSIONS

The use of GBCAs in neurorardiologic applications has revolutionized the field since their introduction 25 years ago. Clinical applications in steady-state parenchymal imaging, MR angiography, and perfusion are developing rapidly. Radiologists should be aware in detail of the characteristics of the various agents including relaxivity, concentration, and chelate stability along with how these affect diagnostic efficacy and patient safety. In this review, we have attempted to present these in a manner that will, hopefully, enable the physician user to optimize agent selection and imaging parameters to achieve the best results for any given clinical situation.

Disclosures: Emanuel Kanal—*UNRELATED*: *Consultancy*: Guerbet, *Comments*: prior to their having a GBCA approved by the FDA, *Grants/Grants Pending*: Bracco Diagnostics,* *Comments*: unrestricted grant funding to support the following project: "In Vitro Serial Dilution Study to Measure the Effects of Comparative Relaxivities among GBCA." Kenneth Maravilla—*UNRELATED*: *Consultancy*: Bracco, Guerbet, *Grants/Grants Pending*: Bracco, Bayer, Guerbet, *Payment for Lectures (including service on Speakers Bureaus)*: Bracco, Guerbet. Howard A. Rowley—*RELATED*: *Grant*: Bayer,* Bracco,* Guerbet,* GE Healthcare,* *Comments*: clinical trials and research support, *Consulting Fee or Honorarium*: Bayer, Bracco, Guerbet, GE Healthcare, *Comments*: consulting fees related to contrast or contrast applications, *Support for Travel to Meetings for the Study or Other Purposes:* Bayer, Bracco, Guerbet, GE Healthcare, *Comments*: travel reimbursement related to consulting, *UNRELATED*: *Consultancy*:

Gore, Eli Lilly, Genentech, Abbott Labs, Lundbeck, Paion, Forest Labs, National Institutes of Health, *Comments*: clinical trial safety monitoring boards, consulting for protocols which incorporated contrast use in some cases, *Payment for Lectures (including service on* Speakers Bureaus*)*: Bracco, GE Healthcare, Continuing Medical Education organizations, *Patents (planned, pending or issued)*: GE Healthcare,* *Comments*: MRI pulse sequence, joint patent pending, *Royalties*: Wisconsin Alumni Research Foundation, *Comments*: CT patent that incorporates contrast. *Money paid to the institution.

REFERENCES

1. Dotarem product label. http://www.accessdata.fda.gov/drugsatfda_docs/label/2013/204781s000lbl.pdf. Accessed May 10, 2013
2. Gadavist product label. http://www.accessdata.fda.gov/drugsatfda_docs/label/2011/201277s000lbl.pdf. Accessed May 10, 2013
3. Magnevist product label. http://www.accessdata.fda.gov/drugsatfda_docs/label/2012/019596s051lbl.pdf. Accessed May 10, 2013
4. MultiHance product label. http://www.accessdata.fda.gov/drugsatfda_docs/label/2010/021357s009lbl.pdf. Accessed May 10, 2013
5. Omniscan product label. http://www.accessdata.fda.gov/drugsatfda_docs/label/2010/020123s037lbl.pdf. Accessed May 10, 2013
6. OptiMARK product label. http://www.accessdata.fda.gov/drugsatfda_docs/label/2010/020937s016lbl.pdf. Accessed 10 May 10, 2013
7. ProHance product label. http://www.accessdata.fda.gov/drugsatfda_docs/label/2010/020131s024lbl.pdf. Accessed May 10, 2013
8. Ablavar product label. http://www.accessdata.fda.gov/drugsatfda_docs/label/2010/021711s003lbl.pdf. Accessed May 10, 2013
9. Eovist product label. http://www.accessdata.fda.gov/drugsatfda_docs/label/2010/022090s004lbl.pdf. Accessed May 10, 2013
10. Bellin MF, Van Der Molen AJ. **Extracellular gadolinium-based contrast media: an overview.** *Eur J Radiol* 2008;66:160–67
11. Rohrer M, Bauer H, Mintorovitch J, et al. **Comparison of magnetic properties of MRI contrast media solutions at different magnetic field strengths.** *Invest Radiol* 2005;40:715–24
12. Cavagna FM, Maggioni F, Castelli PM, et al. **Gadolinium chelates with weak binding to serum proteins: a new class of high-efficiency, general purpose contrast agents for magnetic resonance imaging.** *Invest Radiol* 1997;32:780–96
13. Giesel FL, von Tengg-Kobligk H, Wilkinson ID, et al. **Influence of human serum albumin on longitudinal and transverse relaxation rates (R1 and R2) of magnetic resonance contrast agents.** *Invest Radiol* 2006;41:222–28
14. Pintaske J, Martirosian P, Graf H, et al. **Relaxivity of gadopentetate dimeglumine (Magnevist), gadobutrol (Gadavist), and gadobenate dimeglumine (MultiHance) in human blood plasma at 0.2, 1.5, and 3 Tesla.** *Invest Radiol* 2006;41:213–21, Erratum in *Invest Radiol* 2006;41:859
15. Laurent S, Elst LV, Muller RN. **Comparative study of the physicochemical properties of six clinical low molecular weight gadolinium contrast agents.** *Contrast Media Mol Imaging* 2006;1:128–37
16. Yuh WT, Fisher DJ, Engelken JD, et al. **MR evaluation of CNS tumors: dose comparison study with gadopentetate dimeglumine and gadoteridol.** *Radiology* 1991;180:485–91
17. Myhr G, Rinck PA, Børseth A. **Gadodiamide injection and gadopentetate dimeglumine: a double-blind study in MR imaging of the CNS.** *Acta Radiol* 1992;33:405–09
18. Balériaux D, Matos C, De Greef D. **Gadodiamide injection as a contrast medium for MRI of the central nervous system: a comparison with gadolinium-DOTA.** *Neuroradiology* 1993;35:490–94
19. Valk J, Algra PR, Hazenberg CJ, et al. **A double-blind, comparative study of gadodiamide injection and gadopentetate dimeglumine in MRI of the central nervous system.** *Neuroradiology* 1993;35:173–77
20. Brugières P, Gaston A, Degryse HR, et al. **Randomised double blind trial of the safety and efficacy of two gadolinium complexes (Gd-DTPA and Gd-DOTA).** *Neuroradiology* 1994;36:27–30
21. Akeson P, Jonsson E, Haugen I, et al. **Contrast-enhanced MRI of the central nervous system: comparison between gadodiamide injection and gadolinium-DTPA.** *Neuroradiology* 1995;37:229–33
22. Oudkerk M, Sijens PE, van Beek EJ, et al. **Safety and efficacy of Dotarem (Gd-DOTA) versus Magnevist (Gd-DTPA) in magnetic resonance imaging of the central nervous system.** *Invest Radiol* 1995;30:75–78
23. Grossman RI, Rubin DI, Hunter G, et al. **Magnetic resonance imaging in patients with central nervous system pathology: q comparison of OptiMARK (Gd-DTPA-BMEA) and Magnevist (Gd-DTPA).** *Invest Radiol* 2000;35:412–19
24. Runge VM, Armstrong MR, Barr RG, et al. **A clinical comparison of the safety and efficacy of MultiHance (gadobenate dimeglumine) and Omniscan (gadodiamide) in magnetic resonance imaging in patients with central nervous system pathology.** *Invest Radiol* 2001;36:65–71
25. Runge VM, Parker JR, Donovan M. **Double-blind, efficacy evaluation of gadobenate dimeglumine, a gadolinium chelate with enhanced relaxivity, in malignant lesions of the brain.** *Invest Radiol* 2002;37:269–80
26. Greco A, Parker JR, Ratcliffe CG, et al. **Phase III, randomized, double blind, crossover comparison of gadoteridol and gadopentetate dimeglumine in magnetic resonance imaging of patients with intracranial lesions.** *Australas Radiol* 2001;45:457–63
27. Anzalone N, Gerevini S, Scotti R, et al. **Detection of cerebral metastases on magnetic resonance imaging: intraindividual comparison of gadobutrol with gadopentetate dimeglumine.** *Acta Radiol* 2009;50:933–40
28. Kim ES, Chang JH, Choi HS, et al. **Diagnostic yield of double-dose gadobutrol in the detection of brain metastasis: intraindividual comparison with double-dose gadopentetate dimeglumine.** *AJNR Am J Neuroradiol* 2010;31:1055–58
29. Katakami N, Inaba Y, Sugata S, et al. **Magnetic resonance evaluation of brain metastases from systemic malignances with two doses of gadobutrol 1.0M compared with gadoteridol: a multicenter, phase II/III study in patients with known or suspected brain metastases.** *Invest Radiol* 2011;46:411–18
30. Koenig M, Schulte-Altedorneburg G, Piontek M, et al. **Intra-individual, randomised comparison of the MRI contrast agents gadobutrol versus gadoteridol in patients with primary and secondary brain tumours, evaluated in a blinded read.** *Eur Radiol* 2013;23:3287–95
31. Center for Drug Evaluation and Research. FDA Advisory Committee Briefing Document. New Drug Application 201–277. http://www.fda.gov/downloads/drugs/developmentapprovalprocess/developmentresources/ucm255169.pdf. Accessed February 6, 2014
32. Anzalone N, Scarabino T, Venturi C, et al. **Cerebral neoplastic enhancing lesions: multicenter, randomized, crossover intraindividual comparison between gadobutrol (1.0M) and gadoterate meglumine (0.5M) at 0.1 mmol Gd/kg body weight in a clinical setting.** *Eur J Radiol* 2013;82:139–45
33. Colosimo C, Ruscalleda J, Korves M, et al. **Detection of intracranial metastases: a multicenter, intrapatient comparison of gadobenate dimeglumine-enhanced MRI with routinely used contrast agents at equal dosage.** *Invest Radiol* 2001;36:72–81
34. Knopp MV, Runge VM, Essig M, et al. **Primary and secondary brain tumors at MR imaging: bicentric intraindividual crossover comparison of gadobenate dimeglumine and gadopentetate dimeglumine.** *Radiology* 2004;230:55–64
35. Colosimo C, Knopp MV, Barreau X, et al. **A comparison of Gd-BOPTA and Gd-DOTA for contrast-enhanced MRI of intracranial tumours.** *Neuroradiology* 2004;46:655–65
36. Essig M, Tartaro A, Tartaglione T, et al. **Enhancing lesions of the brain: intra-individual crossover comparison of contrast enhancement after gadobenate dimeglumine versus established gadolinium comparators.** *Academic Radiology* 2006;13:744–51
37. Maravilla KR, Maldjian JA, Schmalfuss IM, et al. **Contrast enhancement of central nervous system lesions: multicenter intraindividual crossover comparative study of two MR contrast agents.** *Radiology* 2006;240:389–400
38. Kuhn MJ, Picozzi P, Maldjian JA, et al. **Evaluation of intraaxial enhancing brain tumors on magnetic resonance imaging: intraindividual crossover comparison of gadobenate dimeglumine and**

gadopentetate dimeglumine for visualization and assessment, and implications for surgical intervention. *J Neurosurg* 2007;106:557–66
39. Rowley HA, Scialfa G, Gao PY, et al. **Contrast-enhanced MR imaging of brain lesions: a large-scale intraindividual crossover comparison of gadobenate dimeglumine versus gadodiamide.** *AJNR Am J Neuroradiol* 2008;29:1684–91
40. Rumboldt Z, Rowley HA, Steinberg F, et al. **Multicenter, double-blind, randomized, intra-individual crossover comparison of gadobenate dimeglumine and gadopentetate dimeglumine in MRI of brain tumors at 3 Tesla.** *J Magn Reson Imaging* 2009;29:760–67
41. Seidl Z, Vymazal J, Mechl M, et al. **Does higher gadolinium concentration play a role in the morphologic assessment of brain tumors? Results of a multicenter intraindividual crossover comparison of gadobutrol versus gadobenate dimeglumine (the MERIT Study).** *AJNR Am J Neuroradiol* 2012;33:1050–58
42. Griffiths PD, Wilkinson ID, Wels T, et al. **Brain MR perfusion imaging in humans.** *Acta Radiol* 2001;42:555–59
43. Griffiths PD, Pandya H, Wilkinson ID, et al. **Sequential dynamic gadolinium magnetic resonance perfusion-weighted imaging: effects on transit time and cerebral blood volume measurements.** *Acta Radiol* 2006;47:1079–84
44. Giesel FL, Mehndiratta A, Risse F, et al. **Intraindividual comparison between gadopentetate dimeglumine and gadobutrol for magnetic resonance perfusion in normal brain and intracranial tumors at 3 Tesla.** *Acta Radiol* 2009;50:521–30
45. Essig M, Lodemann KP, Le-Huu M, et al. **Intraindividual comparison of gadobenate dimeglumine and gadobutrol for cerebral magnetic resonance perfusion imaging at 1.5 T.** *Invest Radiol* 2006;41:256–63
46. Thilmann O, Larsson EM, Björkman-Burtscher IM, et al. **Comparison of contrast agents with high molarity and with weak protein binding in cerebral perfusion imaging at 3 T.** *J Magn Reson Imaging* 2005;22:597–604
47. Wirestam R, Thilmann O, Knutsson L, et al. **Comparison of quantitative dynamic susceptibility-contrast MRI perfusion estimates obtained using different contrast-agent administration schemes at 3T.** *Eur J Radiol* 2010;75:e86–91
48. Beranek-Chiu J, Froehlich JM, Wentz KU, et al. **Improved vessel delineation in keyhole time-resolved contrast-enhanced MR angiography using a gadolinium doped flush.** *J Magn Reson Imaging* 2009;29:1147–53
49. Pediconi F, Fraioli F, Catalano C, et al. **Gadobenate dimeglumine (Gd-BOPTA) vs gadopentetate dimeglumine (Gd-DTPA) for contrast-enhanced magnetic resonance angiography (MRA): improvement in intravascular signal intensity and contrast to noise ratio.** *Radiol Med* 2003;106:87–93
50. Li Y, Li X, Li D, et al. **Multicenter, intraindividual comparison of single-dose gadobenate dimeglumine and double-dose gadopentetate dimeglumine for MR angiography of the supra-aortic arteries (the Supra-Aortic Value Study).** *AJNR Am J Neuroradiol* 2013;34:847–54
51. Bültmann E, Erb G, Kirchin MA, et al. **Intra-individual crossover comparison of gadobenate dimeglumine and gadopentetate dimeglumine for contrast-enhanced MR angiography of the supraaortic vessels at 3 Tesla.** *Invest Radiol* 2008;43:695–702
52. Kramer JH, Arnoldi E, François CJ, et al. **Dynamic and static magnetic resonance angiography of the supra-aortic vessels at 3.0 T: intraindividual comparison of gadobutrol, gadobenate dimeglumine, and gadoterate meglumine at equimolar dose.** *Invest Radiol* 2013;48:121–8
53. Pirovano G, Munley J, Schultz C, et al. **Nephrogenic systemic fibrosis: a review of published cases and results from three prospective observational studies.** *Insights Imaging* 2012;3(suppl 1):S293
54. Idée JM, Port M, Robic C, et al. **Role of thermodynamic and kinetic parameters in gadolinium chelate stability.** *J Magn Reson Imaging* 2009;30:1249–58
55. Bennett CL, Qureshi ZP, Sartor AO, et al. **Gadolinium-induced nephrogenic systemic fibrosis: the rise and fall of an iatrogenic disease.** *Clin Kidney J* 2012;5:82–88
56. Abujudeh HH, Kosaraju VK, Kaewlai R. **Acute adverse reactions to gadopentetate dimeglumine and gadobenate dimeglumine: experience with 21,659 injections.** *AJR Am J Roentgentol* 2010;194:430–34
57. American College of Radiology. Manual on Contrast Media. Version 9. 2013. http://www.acr.org. Accessed January 4, 2013
58. Bruder O, Schneider S, Nothnagel D, et al. **Acute adverse reactions to gadolinium-based contrast agents in CMR: multicenter experience with 17,767 patients from the EuroCMR Registry.** *JACC Cardiovasc Imaging* 2011;4:1171–76
59. Cochran ST, Bomyea K, Sayre JW. **Trends in adverse events after IV administration of contrast media.** *AJR Am J Roentgenol* 2001;176:1385–88
60. Forsting M, Palkowitsch P. **Prevalence of acute adverse reactions to gadobutrol: a highly concentrated macrocyclic gadolinium chelate: review of 14,299 patients from observational trials.** *Eur J Radiol* 2010;74:e186–92
61. Murphy KP, Szopinski KT, Cohal RH, et al. **Occurrence of adverse reactions to gadolinium-based contrast material and management of patients at increased risk: a survey of the American Society of Neuroradiology Fellowship Directors.** *Acad Radiol* 1999;6:656–64
62. Li A, Wong CS, Wong MK, et al. **Acute adverse reactions to magnetic resonance contrast media: gadolinium chelates.** *Br J Radiol* 2006;79:368–71
63. Dillman JR, Ellis JH, Cohan RH, et al. **Frequency and severity of acute allergic-like reactions to gadolinium-containing I.V. contrast media in children and adults.** *AJR Am J Roentgenol* 2007;189:1533–38
64. Hunt CH, Hartman RP, Hesley GK. **Frequency and severity of adverse effects of iodinated and gadolinium contrast materials: retrospective review of 456,930 doses.** *AJR Am J Roentgenol* 2009;193:1124–27
65. Prince MR, Zhang H, Zou Z, et al. **Incidence of immediate gadolinium contrast media reactions.** *AJR Am J Roentgenol* 2011;196:W138–43
66. Jung JW, Kang HR, Kim MH, et al. **Immediate hypersensitivity reaction to gadolinium-based MR contrast media.** *Radiology* 2012;264:414–22
67. Vervloet D, Durham S. **Adverse reactions to drugs.** *BMJ* 1998;316:1511–14
68. Hasdenteufel F, Luyasu S, Renaudin JM, et al. **Anaphylactic shock after first exposure to gadoterate meglumine: two case reports documented by positive allergy assessment.** *J Allergy Clin Immunol* 2008;121:527–28
69. Schiavino D, Murzilli F, Del Ninno M, et al. **Demonstration of an IgE-mediated immunological pathogenesis of a severe reaction to gadopentetate dimeglumine.** *J Invest Allergol Clin Immunol* 2003;13:140–42
70. European Society on Urogenital Radiology (ESUR). ESUR Guidelines on Contrast Media. Version 8.1. http://www.esur.org/esur-guidelines/. Accessed January 4, 2013
71. United States of America ex rel. Lynch vs. Imagimed LLC, et al. (N.D. N.Y.); as reported on http://www.justice.gov/opa/pr/2013/August/13-civ-958.html. Accessed September 14, 2013
72. Runge V. **Safety of approved MR contrast media for intravenous injection.** *J Magn Reson Imaging* 2000;12:205–13
73. Bleicher AG, Kanal E. **Assessment of adverse reaction rates to a newly approved MRI contrast agent: review of 23,553 administrations of gadobenate dimeglumine.** *AJR Am J Roentgenol* 2008;191:W307–11
74. Shellock FG, Parker JR, Venetianer C, et al. **Safety of gadobenate dimeglumine (MultiHance): summary of findings from clinical studies and postmarketing surveillance.** *Invest Radiol* 2006;41:500–09
75. Shellock FG, Parker JR, Pirovano G, et al. **Safety characteristics of gadobenate dimeglumine: clinical experience from intra- and interindividual comparison studies with gadopentetate dimeglu-**

mine. *J Magn Reson Imaging* 2006;24:1378–85, Erratum in *J Magn Reson Imaging* 2007;26:217
76. Weber JC. **Epidemiology of adverse reactions to nonsteroidal anti-inflammatory drug.** In: Rainsford KD, Velo GP, eds. *Side Effects of Antiinflammatory/Analgesic Drugs Advances in Inflammation Research*. Vol. 6. New York: Raven Press; 1984:1–7
77. Lalli AF. **Urographic contrast media reactions and anxiety.** *Radiology* 1974;112:267–71
78. Semelka RC, Hernandes Mde A, Stallings CG, et al. **Objective evaluation of acute adverse events and image quality of gadolinium-based contrast agents (gadobutrol and gadobenate dimeglumine) by blinded evaluation: pilot study.** *Magn Reson Imaging* 2013;31:96–101
79. Davenport MS, Dillman JR, Cohan RH, et al**. Effect of abrupt substitution of gadobenate dimeglumine for gadopentetate dimeglumine on rate of allergic-like reactions.** *Radiology* 2013;266:773–82
80. van Osch MJ, Vonken EJ, Wu O, et al. **Model of the human vasculature for studying the influence of contrast injection speed on cerebral perfusion MRI.** *Magn Reson Med* 2003;50:614–22
81. Prokop M, Schneider G, Vanzulli A, et al. **Contrast-enhanced MR angiography of the renal arteries: blinded multicenter crossover comparison of gadobenate dimeglumine and gadopentetate dimeglumine.** *Radiology* 2005;234:399–408
82. Gerretsen SC, le Maire TF, Miller S, et al. **Multicenter, double-blind, randomized, intraindividual crossover comparison of gadobenate dimeglumine and gadopentetate dimeglumine for MR angiography of peripheral arteries.** *Radiology* 2010;255:988–1000
83. Knopp MV, Giesel FL, von Tengg-Kobligk H, et al. **Contrast-enhanced MR angiography of the run-off vasculature: intraindividual comparison of gadobenate dimeglumine with gadopentetate dimeglumine.** *J Magn Reson Imaging* 2003;17:694–702
84. Stein PD, Chenevert TL, Fowler SE, et al. **Gadolinium-enhanced magnetic resonance angiography for pulmonary embolism: a multicenter prospective study (PIOPED III).** *Ann Intern Med* 2010;152:434–43, W142–43
85. Woodard PK, Chenevert TL, Sostman HD, et al. **Signal quality of single dose gadobenate dimeglumine pulmonary MRA examinations exceeds quality of MRA performed with double dose gadopentetate dimeglumine.** *Int J Cardiovasc Imaging* 2012;28:295–301
86. Wang J, Yan F, Liu J, et al. **Multicenter, intra-individual comparison of single dose gadobenate dimeglumine and double dose gadopentetate dimeglumine for MR angiography of the peripheral arteries (the peripheral VALUE study)**. *J Magn Reson Imaging* 2013;38:926–37

A Randomized Trial Comparing Balloon Kyphoplasty and Vertebroplasty for Vertebral Compression Fractures due to Osteoporosis

M. Dohm, C.M. Black, A. Dacre, J.B. Tillman, G. Fueredi, on behalf of the KAVIAR investigators

ABSTRACT

BACKGROUND AND PURPOSE: Several trials have compared vertebral augmentation with nonsurgical treatment for vertebral compression fractures. This trial compares the efficacy and safety of balloon kyphoplasty and vertebroplasty.

MATERIALS AND METHODS: Patients with osteoporosis with 1–3 acute fractures (T5–L5) were randomized and treated with kyphoplasty ($n = 191$) or vertebroplasty ($n = 190$) and were not blinded to the treatment assignment. Twelve- and 24-month subsequent radiographic fracture incidence was the primary end point. Due to low enrollment and early withdrawals, the study was terminated with 404/1234 (32.7%) patients enrolled.

RESULTS: The average age of patients was 75.6 years (77.4% female). Mean procedure duration was longer for kyphoplasty (40.0 versus 31.8 minutes, $P < .001$). At 12 months, 7.8% fewer patients with kyphoplasty (50/140 versus 57/131) had subsequent radiographic fracture, and there were 8.6% fewer at 24 months (54/110 versus 64/111). The results were not statistically significant ($P > .21$). When we used time to event for new clinical fractures, kyphoplasty approached statistical significance in longer fracture-free survival (Wilcoxon, $P = .0596$). Similar pain and function improvements were observed. CT demonstrated lower cement extravasation for kyphoplasty (157/214 versus 164/201 levels treated, $P = .047$). For kyphoplasty versus vertebroplasty, common adverse events within 30 postoperative days were procedural pain (12/191, 9/190), back pain (14/191, 28/190), and new vertebral fractures (9/191, 17/190); similar 2-year occurrence of device-related cement embolism (1/191, 1/190), procedural pain (3/191, 3/190), back pain (2/191, 3/190), and new vertebral fracture (2/191, 2/190) was observed.

CONCLUSIONS: Kyphoplasty and vertebroplasty had similar long-term improvement in pain and disability with similar safety profiles and few device-related complications. Procedure duration was shorter with vertebroplasty. Kyphoplasty had fewer cement leakages and a trend toward longer fracture-free survival.

ABBREVIATIONS: AE = adverse event; BKP = balloon kyphoplasty; EQ-5D = EuroQol-5-Domain; KAVIAR = Kyphoplasty and Vertebroplasty In the Augmentation and Restoration of vertebral body compression fractures; MedDRA = Medical Dictionary for Regulatory Activities; ODI = Oswestry Disability Index; RCT = randomized controlled trial; VCF = vertebral compression fracture; VP = vertebroplasty

Vertebral compression fractures (VCFs) are clinically recognized in 1.4 million individuals worldwide annually,[1] often resulting in pain, disability, vertebral deformity,[2] and considerable negative economic impact.[3] Balloon kyphoplasty (BKP) and vertebroplasty (VP) are percutaneous procedures aimed at reducing pain and providing fracture stability. Balloon kyphoplasty uses orthopedic inflatable bone tamps before bone cement injection in an attempt to correct vertebral deformity and control cement distribution.[4-6] Vertebroplasty is similar, using needles to deliver bone cement without orthopedic balloons.[7] When Kyphoplasty and Vertebroplasty In the Augmentation and Restoration of vertebral body compression fractures (KAVIAR) was initiated, no comparative randomized controlled trials (RCTs) existed, and evidence remains limited.[8] Several RCTs demonstrated better clinical outcomes for kyphoplasty and vertebroplasty compared with nonsurgical management.[4,7,9-11] The KAVIAR study objectives were to document and compare BKP and VP safety and effectiveness in patients with osteoporosis with VCF. The primary end point, subsequent radiographic

Received June 15, 2014; accepted after revision August 25.

From the Department of Orthopaedic Surgery, University of Arizona College of Medicine (M.D.), Tucson, Arizona; Utah Valley Interventional Associates and Utah Valley Regional Medical Center (C.M.B.), Provo, Utah; OrthoMontana (A.D.), Billings, Montana; Medtronic Spine (J.B.T.), Sunnyvale, California; and Aurora Memorial Hospital of Burlington (G.F.), Burlington, Wisconsin.

This work was sponsored and funded by Medtronic Spine.

Please address correspondence to Michael Dohm, MD, Department of Orthopaedic Surgery, University of Arizona College of Medicine, 2800 E Ajo Way, Suite 200, PO Box 245005, Tucson, AZ 85724; e-mail: mdohm@ortho.arizona.edu

Indicates open access to non-subscribers at www.ajnr.org

Indicates article with supplemental on-line table.

Evidence-Based Medicine Level 1.

http://dx.doi.org/10.3174/ajnr.A4127

VCF incidence, was selected because stabilization and deformity correction may have an effect on new VCF occurrence.[12] Secondary end points included pain, disability, and quality-of-life assessments.

MATERIALS AND METHODS

Patients

A protocol steering committee, established before study enrollment (see the "Acknowledgments"), comprised kyphoplasty and vertebroplasty experts, to reduce the potential for bias and provide critical input to study design elements.

Participants had 1–3 acute, painful, VCFs from T5 to L5 due to osteoporosis and had correlative clinical findings with edema on MR imaging, uptake on radionuclide bone scans, or acute vertebral height loss within 6 months by CT, MR imaging, or x-ray. Patients were excluded if back pain was not attributable to VCF, they had >3 acute fractures, had VCFs >6 months old, had fractures due to cancer or high-energy trauma, required procedures other than BKP or VP for fracture stabilization, they had contraindications such as irreversible coagulopathy or known allergies to bone cement or contrast, or had evidence of local or systemic infection. In the absence of cancer or trauma (see exclusions above), the presence of VCF is a hallmark of osteoporosis[13]; therefore, the decision to perform diagnostic bone mineral attenuation examinations was determined by treating physicians and was not a study requirement. Before enrollment, participants gave written informed consent, which included risks for both procedures. The protocol and consent forms were approved by the institutional review board for enrolling sites.

Research Design

Patients were randomized to kyphoplasty ($n = 199$) or vertebroplasty ($n = 205$) by computer by using a dynamic minimization technique stratified by the number of prevalent VCFs, etiology, and study center; patients were not blinded—that is, on randomization, they were aware of the treatment assignment.

Investigator requirements were 50 lifetime procedures or 20 in the last year for each procedure. Investigators qualified for only 1 procedure could participate as a team—that is, they could partner with an investigator qualified in the other technique to treat patients randomized to the alternative treatment. Treating physicians partnering as a team were to consult on patient screening (before enrollment and randomization) to ensure agreement that the patient could be treated with either VP or BKP. Tools and polymethylmethacrylate bone cement used were approved or cleared by the FDA for treating VCFs by using BKP and VP, respectively. BKP was performed by using a bilateral approach as previously described (Kyphon Osteo Introducer Systems, Inflatable Bone Tamps, HV-R Bone Cement, Bone Filler Devices, and other BKP devices were manufactured by Medtronic Spine, Sunnyvale, California).[4-6,14] VP was performed according to local practices.

The primary end points were 12- and 24-month new radiographic VCF (including any new or worsening index fracture) incidence by using the method of Genant et al.[15] Originally, the 1234 enrollment goal stemmed from an 8.7% difference in subsequent radiographic fracture (40% in VP, 31.3% in BKP), 20% withdrawal, 80% power, and 5% α. Due to high unanticipated withdrawal (38%) and limited enrollment, the sponsor, unaware of outcomes, terminated the study with only 404/1234 patients enrolled. This decision was discussed with the protocol steering committee and data safety monitoring board members (see the "Acknowledgments") with subsequent investigator notification. Enrolled patients were terminated without additional follow-up except that any not reaching the 1-month visit were followed to collect 30-day safety data. Investigators reviewed and signed case report forms in an Electronic Data Capture system (Outcome, Cambridge, Massachusetts), and data were 100% source-verified.

All adverse events (AEs) were collected, reported, and evaluated by investigators for device and procedure relationship. AEs were systematically classified into preferred terms and system organ class according to the Medical Dictionary for Regulatory Activities (MedDRA)[16] by using the verbatim language reported by investigators into Electronic Data Capture. An independent data safety monitoring board reviewed safety data and associated MedDRA coding for the trial. New clinical fractures were defined as subsequent, painful vertebral fractures coming to clinical attention. Data were derived from specific, subsequent fracture and adverse event data entered by sites in the Electronic Data Capture.

Secondary outcomes at 1, 3, 12, and 24 months included the SF-36 Physical Component Summary,[17] the EuroQol-5-Domain (EQ-5D) questionnaire,[18] a numeric rating scale for back pain,[19] and the Oswestry Disability Index (ODI) (Section 8, regarding sexual activity, was removed from the ODI questionnaire and therefore not asked of these typically elderly patients).[20] Back pain was also assessed 7 days postoperatively. For EQ-5D, US utilities were applied.[21]

Standing lateral spine radiographs were obtained at baseline, postoperatively, and at 3, 12, and 24 months. Standing lateral images were used for determining new radiographic fracture by using the method of Genant et al[15]; and vertebral kyphotic angulation, by using quantitative morphometry.[22] The angle formed by lines drawn parallel to the caudal and cranial fractured vertebral body endplates determined the kyphotic angulation. A postprocedural CT scan was obtained through treated levels and was used for determining cement volume and leakage. All images were read centrally (Synarc, Newark, California) by a blinded radiologist. Cement volume was determined by cement injected intraoperatively as reported by investigators, and an independent radiologist used postoperative CTs and computer-assisted segmentation of vertebrae, with cement defined as voxels >850. Image segments were inspected, and voxels >850 were removed if clearly part of native bone.

Statistical Methods

Modified intention to treat was used, including all data available from the 381 patients randomized and treated. Eight patients with BKP and 15 with VP enrolled, withdrew before surgery, and were therefore not analyzed. All other subjects underwent surgery as assigned. Four patients with BKP and 7 with VP underwent a crossover surgery for a subsequent VCF. For any subject having surgery for a new VCF, the last observation before surgery was carried forward to later visits. Continuous variables were analyzed by ANCOVA by using the baseline as a covariate. For categoric

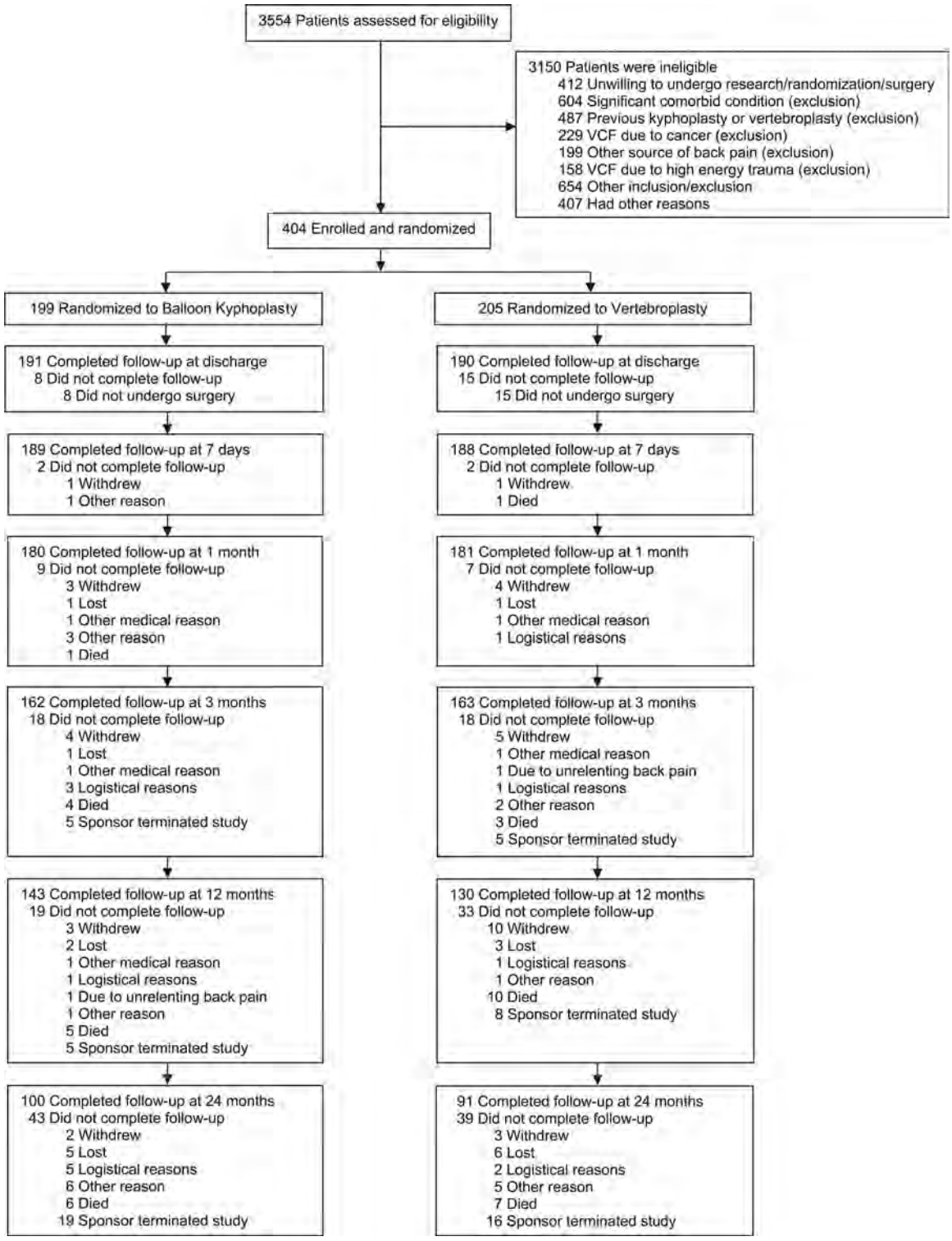

FIG 1. Patient accountability.

variables, between-group comparisons were assessed by using the χ^2 or Fisher exact test. For cement leakage, cement volume, and kyphotic angulation, analyses were based on treated levels. $P \leq .05$ was statistically significant.

Funding Source

Medtronic Spine sponsored this study and contributed to study design, data monitoring, statistical analysis, and reporting of results and paid for independent core laboratory and data safety-monitoring board services.

RESULTS

Patient Disposition and Demographics

Patients were enrolled and randomized between October 2006 and May 2011. Figure 1 shows patient disposition.

The average age of patients was 75.6 years, 77.4% were women,

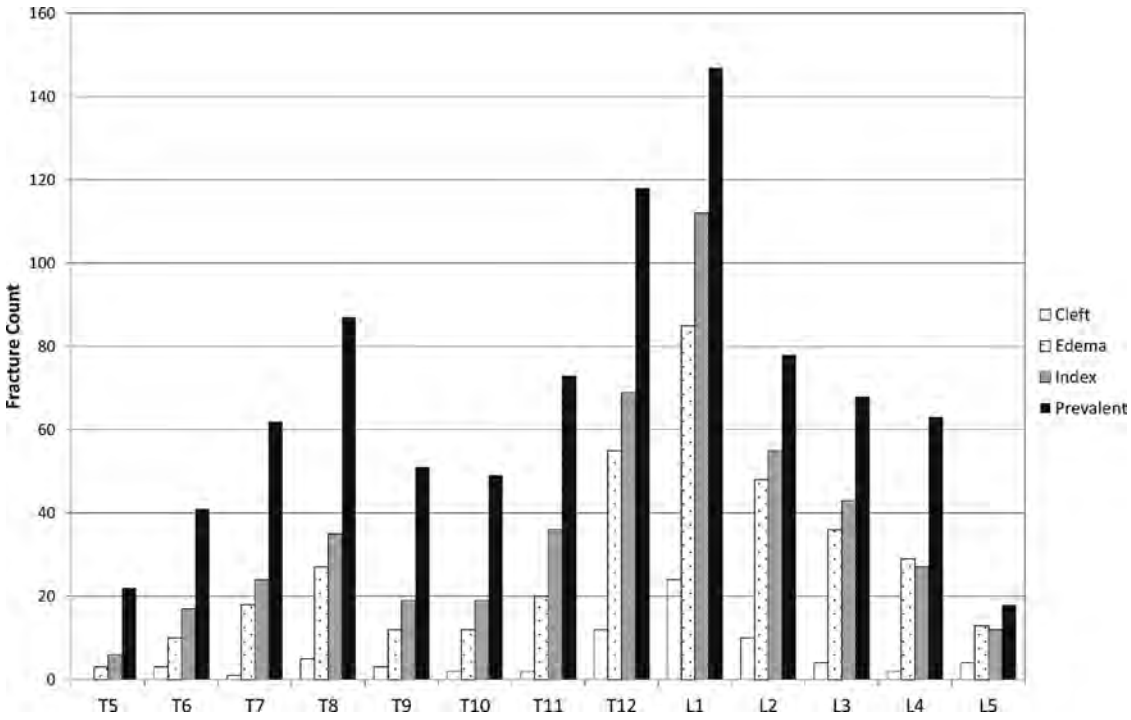

FIG 2. Distribution of index and prevalent fractures and those with edema and vacuum cleft for the BKP and VP groups combined. Index levels (those identified as treatment levels) and prevalent fractures (all radiographic fractures assessed by the core laboratory) are shown, identified from standing lateral x-ray films with 379 of 381 treated patients contributing data. The distribution of levels with edema and those with vacuum cleft is shown on the basis of available MR imaging at baseline (294 of 381 treated patients).

and 78.5% had single fractures treated (On-line Table). The baseline proportion of patients using bisphosphonates, calcium, and vitamin D is shown in the On-line Table; 151/261 (57.9%), 212/261 (81.2%), and 214/261 (82.0%) were using bisphosphonates, calcium, and vitamin D at 12 months respectively; and 93/191 (48.7%), 149/191 (78.0%), and 151/191 (79.1%), at 24 months. Use of these medications was not statistically significant between groups.

There was a higher radiographic fracture prevalence than identified clinically, and most treated fractures had active lesions confirmed on MR imaging (Fig 2). Most fractures occurred at T12 and L1.

Procedure Characteristics

Most patients (70.3%) had local anesthesia with conscious sedation (Table 1). Fewer radiologists performed kyphoplasty (150/191, 78.5%) compared with vertebroplasty (165/190, 86.8%). Vertebroplasty had a shorter mean procedure duration (BKP, 40.0 minutes; VP, 31.8 minutes; $P < .001$) and median hospitalization duration (BKP, 22 hours; VP, 8 hours; $P = .010$). For vertebroplasty, 152/189 (80.4%) procedures were performed by using an injector kit. Kyphoplasty had statistically significantly higher cement volumes assessed by CT (Table 1).

Subsequent Vertebral Fracture

Regarding the primary end points (Table 2), 7.8% fewer patients with BKP had subsequent radiographic fractures compared with those who had VP at 12 months ($P = .21$), and 8.6% fewer, at 24 months ($P = .23$); but results were not statistically significant. Because subsequent radiographic fractures included any worsening index fractures, we analyzed those separately; 4 of 140 (2.9%) subjects with BKP and 10 of 131 (7.6%) subjects with VP had worsening index fractures ($P = .10$) at 12 months. No additional worsening index fractures were detected at 24 months.

Kaplan-Meier analysis of new clinically identified fractures (Fig 3) approached statistical significance for longer fracture-free survival in the BKP group (Wilcoxon test, $P = .0596$). For the 88 subjects with new clinically recognized fractures (Fig 3), 85 of 88 (96.6%) were specifically associated with new-onset pain. Sixty-three (71.6%) subjects had a VCF confirmed by MR imaging; 15 (17.0%) had VCF confirmed by using x-ray only, which consisted of a change of at least 1 Genant grade. Six (6.8%) had CT, 2 (2.2%) had bone scans, and 2 (2.2%) had an imaging technique not specified. With regard to subsequent treatment, 70 (79.5%) had vertebral augmentation for at least 1 VCF, 16 (18.1%) had nonsurgical care alone, 1 (1.1%) had subsequent fusion surgery with instrumentation, and 1 (1.1%) had therapy not identified.

Pain, Disability, and Quality of Life

Kyphoplasty and vertebroplasty groups had similar baseline back pain, SF-36 Physical Component Summary, and EQ-5D quality-of-life and ODI scores. For each outcome, statistically significant improvements from baseline were observed for each group, but differences between treatment groups were not significant (Fig 4). Concomitant with pain relief, use of opioid medications dropped from 73.9% (122/165) of patients at baseline (On-line Table) to 17.6% (25/142) for BKP and from 74.6% (126/169) to 23.9% (34/142) for VP at 6 months ($P = .24$). Results were 17.6% (16/91) for BKP and 25.6% (21/82) for VP at 24 months ($P = .26$).

Table 1: Procedure characteristics

	Kyphoplasty (*n* = 191)	Vertebroplasty (*n* = 190)	*P* Value
Surgery as randomized (No.)	191	190	
Physician type (m) (%)			.019
Interventional radiologist	117 (61.3)	138 (72.6)	
Interventional neuroradiologist	33 (17.3)	27 (14.2)	
Orthopedic surgeon	41 (21.5)	23 (12.1)	
Neurosurgeon	0	2 (1.1)	
Anesthesia (m) (%)			.086
Local with conscious sedation	125 (65.4)	143 (75.3)	
General	55 (28.8)	37 (19.5)	
Other	11 (5.8)	10 (5.3)	
Hospitalization (m) (%)			.014
Outpatient	109 (57.1)	132 (69.5)	
Inpatient	82 (42.9)	58 (30.5)	
Postural reduction performed (m) (%)	154 (80.6)	142 (75.1)	.217
Procedure duration (min) (mean) (SD)	40.0 (22.0)	31.8 (19.3)	<.001
Fluoroscopy duration (min) (mean) (SD)	10.0 (6.3)	8.5 (4.9)	.008
Duration of stay (hr) (median) (IQR)	22.0 (6.0–26.0)	8.0 (5.0–24.0)	.010
Fractures treated	*n* = 244	*n* = 235	
Procedure (m) (%)			<.001
Bilateral	242 (99.2)	151 (65.1)	
Unilateral	2 (0.8)	81 (34.9)	
Total cement volume (mL) (median) (IQR)[a]	4.6 (3.4–6.0)	4.0 (3.0–6.0)	.053
Fractures scanned by CT[b]	*n* = 214	*n* = 201	
Vertebral body volume (mL) (median) (IQR)	25.7 (19.3–31.4)	25.1 (19.4–31.9)	.74
Cement volume (mL) (median) (IQR)	5.2 (3.8–6.3)	4.6 (2.9–6.5)	.037
Cement/vertebral ratio (median) (IQR)	0.21 (0.16–0.26)	0.19 (0.13–0.25)	.008

Note:—(m) indicates numerator (No.) in category; IQR, interquartile range.

[a] For BKP, all patients were treated with HV-R bone cement (Kyphon; Medtronic Spine, Sunnyvale, California). For VP, 46 (24.3%) patients were treated with Spineplex (Stryker, Kalamazoo, Michigan); 43 (22.8%), with Parallax (ArthroCare, Austin, Texas); 34 (18.0%), with AVAtex (CareFusion, San Diego, California); 14 (7.4%), with Confidence (DePuy Spine, Raynham, Massachusetts); 11 (5.8%), with HV-R (Kyphon); 10 (5.3%), with Visioplast (Tecres, Verona, Italy); and 10 (5.3%), with Vertefix (Cook, Bloomington, Indiana). The remaining 21 (11.1%) were treated with other bone cements.

[b] CT assessments were made by the core radiographic laboratory.

Table 2: Patients with new radiographic fractures[a]

	Kyphoplasty	Vertebroplasty	*P* Value
0–3 Mo			
None	115 (76.7%)	106 (72.6%)	.43
All subsequent	35 (23.3%)	40 (27.4%)	
0–12 Mo[b]			
None	90 (64.3%)	74 (56.5%)	.21
All subsequent	50 (35.7%)	57 (43.5%)	
0–24 Mo[b]			
None	56 (50.9%)	47 (42.3%)	.23
All subsequent	54 (49.1%)	64 (57.7%)	

[a] Radiographic fractures identified by a core laboratory.

[b] Co-primary end point.

Secondary Radiographic End Points

Investigators were to attempt vertebral deformity correction, regardless of treatment; 154/191 (80.6%) patients with BKP and 142/189 (75.1%) with VP had perioperative postural reduction. Compared with the preoperative condition, average postoperative kyphotic correction was statistically significant at each time point for both the BKP and VP groups (Table 3). Postoperatively, the ANCOVA estimate of mean difference between groups was 0.21° (95% CI, −0.73°–1.14°) and was not statistically different ($P = .663$). At 24 months, kyphosis correction was better in the BKP group with a mean difference between groups of 1.42° (95% CI, 0.10°–2.74°), which was statistically significant ($P = .036$).

Safety

The most common AEs (classified according to MedDRA) within 30 days of surgery were procedural pain (BKP: 12/191, VP: 9/190), back pain (BKP: 14/191, VP: 28/190), and new symptomatic fracture (BKP: 9/191, VP: 17/190). Common during 2 years were bronchitis (BKP: 10/191, VP: 10/190), pneumonia (BKP: 15/191, VP: 12/190), urinary tract infection (BKP: 11/191, VP: 19/190), falls (BKP: 47/191, VP: 46/190), procedural pain (BKP: 12/191, VP: 9/190), arthralgia (BKP: 18/191, VP: 12/190), back pain (BKP: 49/191, VP: 59/190), lumbar vertebral facture (BKP: 9/191, VP: 13/190), and thoracic vertebral fracture (BKP: 20/191, VP: 21/190). Device- and procedure-related AEs during 2 years are detailed in Table 4; most were observed within 30 days postsurgery. All AEs are posted on www.clinicaltrials.gov (NCT00323609). A few AEs, including procedural pain (BKP: 3/191, VP: 3/190), back pain (BKP: 2/191, VP: 3/190), new fractures (BKP: 2/191, VP: 2/190), cement embolism (BKP: 1/191, VP: 1/190), muscle spasm (BKP: 1/191, VP: 0/190), arthralgia (BKP: 1/191, VP: 0/190), bone marrow edema (BKP: 0/191, VP: 1/190), and implant-site extravasation (BKP: 0/191, VP: 1/190), were specifically considered to be device-related (Table 4). Five BKP AEs (constipation, procedural nausea, procedural hypotension, hallucination, exacerbated chronic obstructive pulmonary disease) and 5 VP AEs (hypersensitivity, mental status changes, hypoxia, respiratory failure, hematoma) were considered anesthesia- or procedure-related (Table 4). No deaths were noted as device- or procedure-related.

Overall cement extravasation, assessed by postoperative CT (Fig 5), was lower ($P = .047$) for BKP (157/214 levels treated) compared with VP (164/201 levels treated). There was lower intravascular extravasation for BKP (59/214 levels treated) compared with VP (76/201 levels treated, $P = .028$). As indicated in Table 4, 1 patient with BKP and 1 with VP each presented with symptoms and were found to have cement embolism. One patient with VP had a new symptomatic fracture occur within 2 days postoperatively (inferior to the index level), with inferior cement leakage that was considered possibly bone cement–related.

DISCUSSION

This was the first large-scale RCT of BKP and VP with long-term follow-up. Both treatments provided similar sustained improvement from baseline in pain, disability, and quality of life that lasted for 2 years. These improvements were statistically significant and clinically relevant but were not statistically different between groups. Safety data support the safe use of both BKP and VP. Kyphoplasty trended toward fewer fractures, had lower ce-

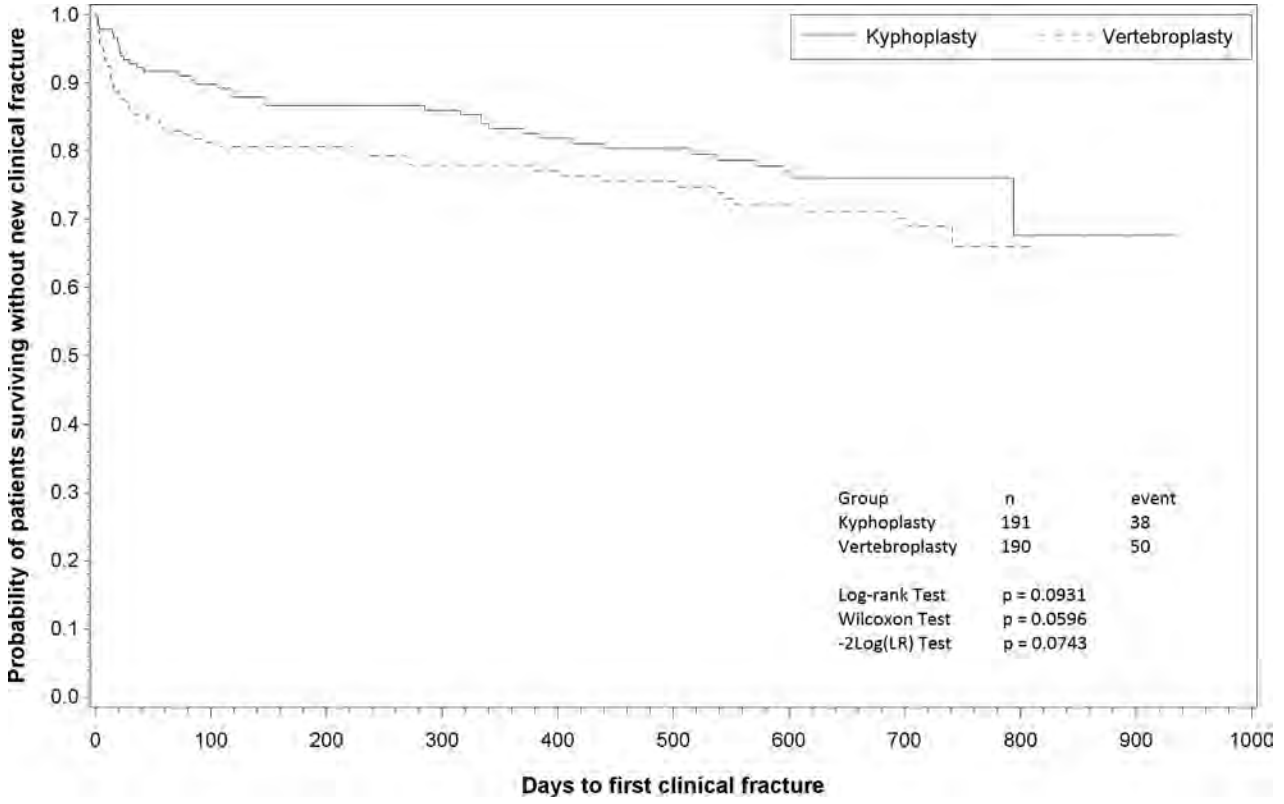

FIG 3. Kaplan-Meier survival analysis for new clinical fractures.

ment extravasation, and more kyphotic deformity correction at 24 months. With vertebroplasty, there was slightly more local anesthesia use, more outpatient procedures, and a shorter duration of stay; it is likely that these findings are due to the different physician profiles performing the procedures (Table 1) and associated practice patterns.[23,24] Differences in physician profile likely stem from the study design allowing investigators to participate as a team (see Material and Methods). Shorter procedure and fluoroscopy duration for VP may be related to more unipedicular vertebral access during VP treatment (Table 1).

Minimally clinically important differences are commonly used thresholds to estimate the clinical significance of outcomes.[25] Improvements from baseline in the SF-36 Physical Component Summary were >7.5 points at 12 and 24 months for both groups, exceeding the estimated minimally clinically important difference of 3.5–4.3 points.[25] Similarly, improvements of ≥4 points exceeded the 1- to 2.5-point threshold for back pain,[19,25] improvements of >25 points exceeded the 10- to 15-point threshold for ODI,[20,25] and improvements of ≥0.28 points exceeded the 0.08 threshold for EQ-5D.[26]

Cumulative evidence demonstrates that kyphoplasty and vertebroplasty provide better outcome than nonsurgical management in RCTs and meta-analyses[4,5,7,9-11,27,28] and acceptable cost-effectiveness ratios.[11,29-31] Several large retrospective studies using claims data, investigating BKP, VP, and nonsurgical management, provide additional evidence.[32-35] Although 2 blinded RCTs concluded that vertebroplasty was similar to a local anesthetic "sham" intervention,[36,37] these trials have several important limitations, including atypically broad inclusion criteria, allowance of chronic fractures, small sample size, and, in 1 study, high crossover, all of which preclude definitive conclusions.[28,38,39] For example, in 1 study, higher crossover in the sham group compared with vertebroplasty (51% versus 13%, $P < .001$) at 3 months suggests that any short-term effects of the sham intervention are not long-lasting.[36] Here, and in several other RCTs, kyphoplasty and vertebroplasty had statistically significant and sustained clinical improvement from baseline in pain, disability, and quality-of-life outcomes for 1 and 2 years; and compared with nonsurgical management, benefits persisted throughout 1 and 2 years for several outcomes.[7,9-11] Such results are inconsistent with placebo effects.

Currently, there is 1 small randomized study showing similar pain outcomes for BKP and VP but statistically significantly better height restoration for BKP.[8] Nonrandomized comparisons show similar results.[40,41] Here, postsurgery kyphotic angulation correction was similar between groups. There was some loss of correction in both groups at 3 months; however, for VP, the trend was more loss, with a statistically significant 24-month difference between groups (Table 3). Our postoperative results of approximately 3° of kyphosis correction are consistent with 2 other BKP RCTs[5,6]; one with long-term follow-up reported minimal correction loss during 2 years.[5] Postural reduction has been shown to provide deformity correction for vertebroplasty,[42,43] achievable in 35%–50% of acute fractures that have dynamic mobility.[6,43] Likewise, in several BKP studies, substantial postural reduction with additional inflatable bone tamp contributions of 27%–100% has been documented.[6,44,45] With KAVIAR, 75% of patients with VP had postural reduction, accounting for deformity correction in the VP group, and this finding may explain less postoperative correction in VP (compared to BKP) reported in other studies.[8,40,41]

The subsequent radiographic fracture rate is similar to that in

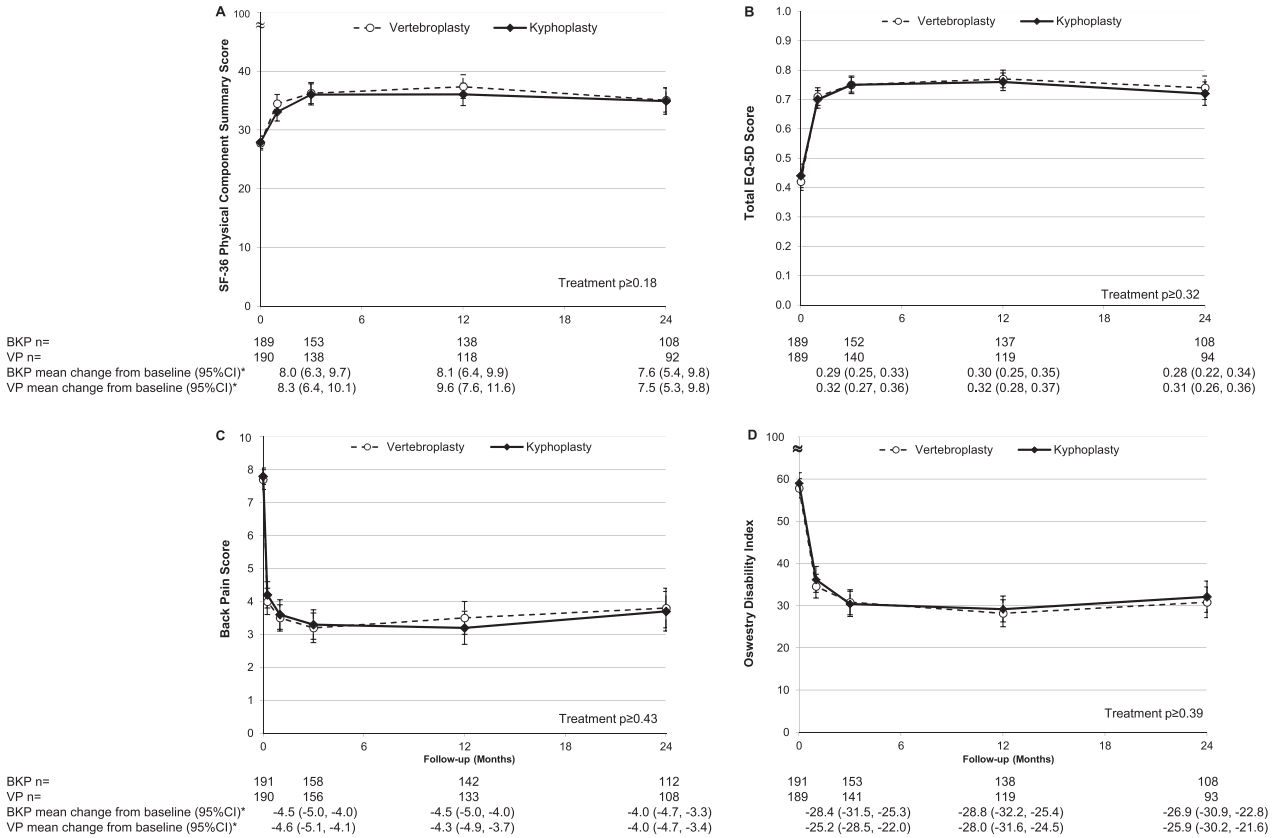

FIG 4. Quality-of-life, disability, and pain assessments at baseline and after balloon kyphoplasty or vertebroplasty. Means and 95% confidence intervals are shown for balloon kyphoplasty (*solid lines*) and vertebroplasty (*dashed lines*) for the SF-36 Physical Component Summary (scale 0–100) (*A*); the total EQ-5D scores (scale 0–1) (*B*); back pain (scale 0–10) (*C*); and the Oswestry Disability Index (scale 0–100) (*D*). The treatment *P* value in each panel indicates the comparison between groups. Below each panel, the *n* for each group is shown for baseline, 3, 12, and 24 months and the group average for change from baseline and 95% CI for 3, 12, and 24 months. The *asterisk* indicates $P < .001$ for all change from baseline scores.

Table 3: Index vertebral body kyphotic angulation correction

	Levels (No.)		Raw Data Change from Baseline in Degrees (Mean) (95% CI)[a]		ANCOVA Change from Baseline in Degrees (LS Mean) (95% CI)		ANCOVA Estimate of Mean Difference (95% CI)	ANCOVA *P* Value
	BKP	VP	BKP	VP	BKP	VP		
Post-op	213	195	3.10 (2.39–3.80)	3.41 (2.61–4.21)	3.34 (2.70–3.99)	3.14 (2.47–3.81)	0.21 (−0.73–1.14)	.663
3 Mo	168	155	1.78 (0.98–2.58)	2.28 (1.37–3.19)	2.00 (1.27–2.72)	2.04 (1.28–2.80)	−0.04 (−1.10–1.01)	.933
12 Mo	154	127	1.97 (1.11–2.82)	1.51 (0.58–2.44)	2.18 (1.47–2.89)	1.26 (0.48–2.04)	0.92 (−0.14–1.98)	.089
24 Mo	99	92	2.09 (0.90–3.28)	1.43 (0.39–2.47)	2.46 (1.55–3.37)	1.04 (0.09–1.98)	1.42 (0.10–2.74)	.036

Note:—Post-op indicates postoperative; LS, least squares.

[a] On the basis of the paired *t* test, changes from baseline results at each time point within each group (BKP and VP) were statistically significant ($P \leq .007$).

another RCT[5,10] and is likely due to the high number of prevalent fractures at baseline, a potent risk factor.[13] This finding underscores the importance of additional therapeutic measures such as pharmacologics to help reduce fracture risk. Because randomization was stratified by baseline fracture prevalence, BKP and VP groups were well-balanced. Although not statistically significant, likely due to lack of statistical power, the BKP group was 7.8%–8.6% lower in 1- and 2-year radiographic fracture rates, consistent with the prespecified protocol originally powered to detect an 8.7% difference. Furthermore, the Kaplan-Meier analysis of new clinically recognized fractures approached statistical significance for a longer time to first clinical fracture within the BKP group. These results are consistent with several meta-analyses showing fewer new VCFs in BKP.[46-48]

Kyphoplasty and vertebroplasty were found to be safe in this population, having similar safety profiles (Table 4). A similar number of patients in each group had device-related cement embolism (1 BKP, 1 VP), back pain (2 BKPs, 3 VPs), procedural pain (2 BKPs, 3 VPs), and new fractures considered to be related to the procedure (2 BKPs, 2 VPs). Several meta-analyses suggested that while both procedures have a low complication rate, BKP may have a lower rate of serious and symptomatic complications.[47-49] The similar safety profile observed here may be due to highly experienced physicians required by the protocol.

CT assessment showed significantly less cement extravasation in BKP- (73%) versus VP-treated (82%) vertebrae ($P = .047$). These rates are higher than those in most reports, likely relating to use of CT, but are consistent with leakage being lower in BKP.[46-49] Most other studies reported cement leakage on the basis of investigator assessment, by using reviews of conventional x-ray images,

Table 4: Device/procedure/anesthesia–related adverse events during 2 years

No. of Patients[a]		Kyphoplasty (*n* = 191)	Vertebroplasty (*n* = 190)
With procedure/device/anesthesia-related (or possibly) AEs		12	11
Blood and lymphatic disorders	Bone marrow edema	0	1[b]
Gastrointestinal disorders	Constipation	1[c]	0
Immune system disorders	Hypersensitivity	0	1[c]
Injury or procedural complications	Cement embolism	1[d]	1[d]
	Implant site extravasation	0	1[e]
	Mental status changes postoperative	0	1[c]
	Procedural hypotension	1[c]	0
	Procedural nausea/vomiting	1[c]	0
	Procedural pain	3[f]	3[f]
	Spinal fracture	1[g]	0
Musculoskeletal disorders	Arthralgia	1[g]	0
	Back pain	2[g]	3[g]
	Muscle spasm	1[g]	0
	Symptomatic vertebral fracture	1[g]	2[g]
Psychiatric disorders	Hallucination	1[c]	0
Respiratory disorders	COPD	1[c]	0
	Hypoxia	0	1[c]
	Respiratory failure	0	1[c]
Vascular disorders	Hematoma	0	1[h]

Note:—COPD indicates chronic obstructive pulmonary disease.

[a] Patients may have had multiple AEs; all system organ class categories are listed when there was an event considered related (or possibly related) to device/procedure/anesthesia.

[b] In 1 patient, 1 event was considered nonserious and possibly related to bone cement.

[c] In 1 patient, 1 event was considered serious and related (or possibly related) to anesthesia and was resolved with medical intervention.

[d] In 1 patient, 1 event each was considered serious and bone cement–related (or possibly related). In each case, the event occurred after the surgical treatment of a subsequent fracture; the BKP event was resolved with oxygen, and the VP event was ongoing at final follow-up.

[e] In 1 patient, 1 event was considered bone cement–related and nonserious. A spinal canal leak was detected intraoperatively; CT was immediately performed without significant canal stenosis observed with no medical intervention given.

[f] Three patients in each group with 3 (2 serious) and 4 (all serious) events in the BKP and VP groups, respectively, were considered device-related (or possibly related) but were resolved.

[g] The number of patients reflected in the Table had events that were considered serious and related (or possibly related) to the device.

[h] In 1 patient, 1 event was nonserious and possibly related to the procedure (likely a prone position on the operating table).

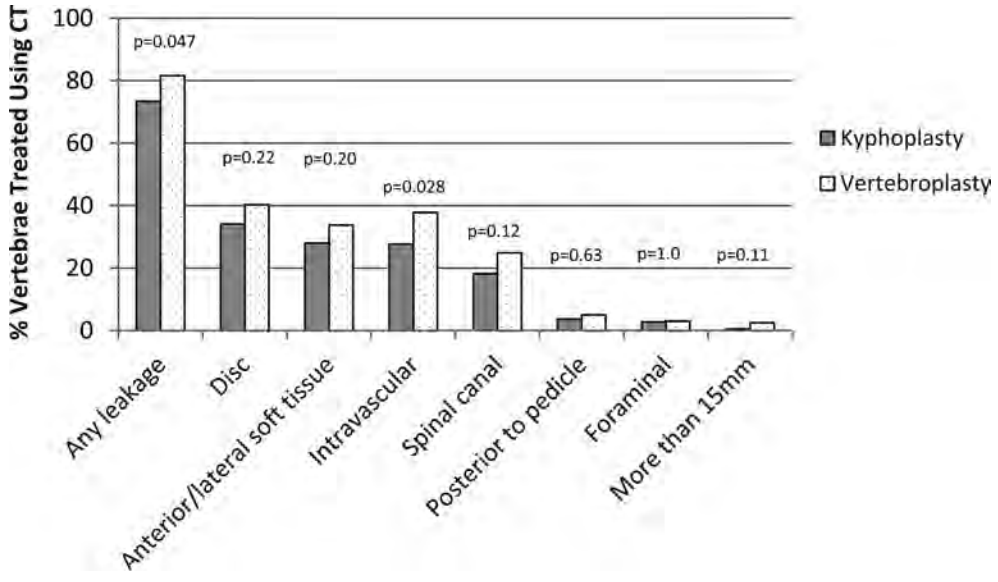

FIG 5. Cement extravasation. The percentage of treated vertebrae in each treatment group having cement extravasation, measured by using postoperative CT, is shown; results are based on evaluable CT data for 168/191 patients with BKP and 160/190 with VP, accounting for 214/244 and 201/233 levels, respectively. Fischer exact *P* values comparing the 2 treatment groups for each category are shown.

which are prone to interpretation bias and are less sensitive. These results are similar to those in another study using CT, also reporting less leakage in BKP (49%) versus VP (87%).[50] Leakage into the perispinal vasculature was significantly less ($P = .028$) for BKP. Meta-analyses of complications suggest that BKP results in fewer symptomatic cement leakages, which include embolism and spinal cord compression.[46-48]

The primary limitations in this study were the lack of patient blinding, substantial loss to follow-up, and early termination, which resulted in lack of statistical power for the primary end point. Verte-

broplasty treatment was not standardized among centers. This lack of standardization may be viewed as a limitation and likely accounts for observed differences between groups in bilateral treatment and may, at least partially, account for differences in cement volumes and leakage. Differences in bilateral treatment, in turn, may have had an effect on the statistically significant changes between groups in kyphotic angulation at 24 months. However, because there is no established standard for vertebroplasty, for generalizability, every study center was asked to provide care consistent with local practices. Nonetheless, the strengths are the randomized, multicenter design, a relatively large sample size, and long-term follow-up. The results of this trial confirm the effectiveness of vertebral body cement augmentation for patients with osteoporosis with ongoing pain at index levels correlated by physical examination and imaging. Our results are consistent with recently updated guidelines published by the National Institute for Health and Care Excellence in the United Kingdom.[51]

CONCLUSIONS

Kyphoplasty and vertebroplasty had similar statistically significant sustained clinical improvement in pain and disability with similar AE profiles. Procedure duration and hospitalization were shorter with vertebroplasty. Kyphoplasty had fewer cement leakages, a trend of longer fracture-free survival, and less loss of kyphotic-deformity correction during 2 years.

ACKNOWLEDGMENTS

The authors are indebted to all participating staff at the investigational centers and the patients who consented to participate in the KAVIAR trial, and they thank Li Ni, PhD, and Feng Tang, PhD, (Medtronic Spine) for contributions to statistical analysis. The authors gratefully acknowledge the KAVIAR protocol steering committee members, Drs Jacques Dion, Michael Ford, Joshua Hirsch, Mary Jensen, Reginald Knight, Isador Lieberman, James Lindley, Mark Myers, Wayne Olan, Frank Phillips, and Gregg Zoarski for contributions to the study design and the data safety monitoring board members, Drs Gunnar Andersson, Harry Cloft, Deborah Kado, Kern Singh, and Joel Verter, for contributions in monitoring patient safety throughout the trial.

APPENDIX

KAVIAR Investigators

Principal investigator, city, state (number of patients enrolled), for enrolling centers:

United States. G. Fueredi, Burlington, Wisconsin (42); G. So, Torrance, California (39); M. Dohm, Grand Junction, Colorado (36); L. Haikal, Huntington, West Virginia (28); C. Black, Provo, Utah (26); J. Milburn, New Orleans, Louisiana (22); R. DiSalle, Toledo, Ohio (21); A. Dacre, Billings, Montana (20); J. Neil, Scottsdale, Arizona (19); N. Cooper, Atlanta, Georgia (19); P. Chesis, Kansas City, Missouri (17); D. Sacks, Reading, Pennsylvania (17); S. Pledger, Middletown, Ohio (17); J. Small, Temple Terrace, Florida (16); P. Minor, Milwaukee, Wisconsin (12); H. Haykal, Houston, Texas (9); M. Montgomery, Temple, Texas (5); C. Kazmierczak, Royal Oak, Michigan (5); S. Bukata, Rochester, New York (4); A. Padidar, San Jose, California (4); P. Schloesser, Murray, Utah (4); B. Ward, Bend, Oregon (3); V. Lewis, Roanoke, Virginia (3); D. Beall, Oklahoma City, Oklahoma (3); C. Graham, Columbia, South Carolina (1).

Canada. C. Guest, Barrie, Ontario (12).

Disclosures: Michael Dohm—*RELATED*: *Fees for Participation in Review Activities such as Data Monitoring Boards, Statistical Analysis, Endpoint Committees, and the Like*: Medtronic Spine,* *Comments*: The Western Slope Study Group was compensated for study-specific data collection related to this study only. I received no money because the Western Slope Study Group is a quality-improvement organization, 501 (c) 3, and I am not a paid employee. I received no compensation at any time, in any form from Medtronic. Carl M. Black—*RELATED*: *Grant*: Kyphon/Medtronic,* *Comments*: Utah Valley Regional Medical Center received remuneration for administrative support during the research trial; *Support for Travel to Meetings for the Study or Other Purposes*: Kyphon/Medtronic, *Comments*: for inservice and training on research protocol; *Provision of Writing Assistance, Medicines, Equipment, or Administrative Support*: Kyphon/Medtronic*, *Comments*: data collection and statistical support; *Other*: As a study investigator, my institution received compensation from Medtronic Spine for study-specific data collection. Alan Dacre—*RELATED*: *Provision of Writing Assistance, Medicines, Equipment, or Administrative Support*: Kyphon/Medtronic,* *Comments*: to support the collection of data for the study; *Other*: As a study investigator, my institution received compensation from Medtronic Spine for study-specific data collection; *UNRELATED*: *Consultancy*: Medtronic, *Comments*: I have an agreement but have not done any remunerable work. John B. Tillman—*RELATED*: *Other*: Medtronic, *Comments*: employed as a Clinical Program Director; *UNRELATED*: *Stock/Stock Options*: Medtronic. George Fueredi—*RELATED*: *Grant*: Aurora Medical Group*; *Other*: As a study investigator, my institution received compensation from Medtronic Spine for study-specific data collection and has received compensation for consulting for Medtronic Spine. *Money paid to the institution.

REFERENCES

1. Johnell O, Kanis JA. **An estimate of the worldwide prevalence and disability associated with osteoporotic fractures.** *Osteoporos Int* 2006;17:1726–33
2. Silverman S. **The clinical consequences of vertebral compression fracture.** *Bone* 1992;13:S27–31
3. Lindsay R, Burge RT, Strauss DM. **One year outcomes and costs following a vertebral fracture.** *Osteoporos Int* 2005;16:78–85
4. Berenson J, Pflugmacher R, Jarzem P, et al. **Balloon kyphoplasty versus non-surgical fracture management for treatment of painful vertebral body compression fractures in patients with cancer: a multicentre, randomised controlled trial.** *Lancet Oncol* 2011;12:225–35
5. Van Meirhaeghe J, Bastian L, Boonen S, et al. **A randomized trial of balloon kyphoplasty and non-surgical management for treating acute vertebral compression fractures: vertebral body kyphosis correction and surgical parameters.** *Spine (Phila Pa 1976)* 2013;38:971–83
6. Bastian L, Schils F, Tillman JB, et al. **A randomized trial comparing 2 techniques of balloon kyphoplasty and curette use for obtaining vertebral body height restoration and angular-deformity correction in vertebral compression fractures due to osteoporosis.** *AJNR Am J Neuroradiol* 2013;34:666–75
7. Farrokhi MR, Alibai E, Maghami Z. **Randomized controlled trial of percutaneous vertebroplasty versus optimal medical management for the relief of pain and disability in acute osteoporotic vertebral compression fractures.** *J Neurosurg Spine* 2011;14:561–69
8. Liu JT, Liao WJ, Tan WC, et al. **Balloon kyphoplasty versus vertebroplasty for treatment of osteoporotic vertebral compression fracture: a prospective, comparative, and randomized clinical study.** *Osteoporos Int* 2010;21:359–64
9. Wardlaw D, Cummings SR, Van Meirhaeghe J, et al. **Efficacy and safety of balloon kyphoplasty compared with non-surgical care for vertebral compression fracture (FREE): a randomised controlled trial.** *Lancet* 2009;373:1016–24
10. Boonen S, Van Meirhaeghe J, Bastian L, et al. **Balloon kyphoplasty for the treatment of acute vertebral compression fractures: 2-year results from a randomized trial.** *J Bone Miner Res* 2011;26:1627–37

11. Klazen CA, Lohle PN, de Vries J, et al. **Vertebroplasty versus conservative treatment in acute osteoporotic vertebral compression fractures (Vertos II): an open-label randomised trial.** *Lancet* 2010;376:1085–92
12. Briggs AM, Wrigley TV, van Dieen JH, et al. **The effect of osteoporotic vertebral fracture on predicted spinal loads in vivo.** *Eur Spine J* 2006;15:1785–95
13. Lindsay R, Silverman SL, Cooper C, et al. **Risk of new vertebral fracture in the year following a fracture**. *JAMA* 2001;285:320–23
14. Wardlaw D, Van Meirhaeghe J, Ranstam J, et al. **Balloon kyphoplasty in patients with osteoporotic vertebral compression fractures.** *Expert Rev Med Devices* 2012;9:423–36
15. Genant HK, Wu CY, van Kuijk C, et al. **Vertebral fracture assessment using a semiquantitative technique.** *J Bone Miner Res* 1993;8:1137–48
16. MedDRA term selection: points to consider. ICH endorsed guide for MedDRA users. Release 4.2, based on MedDRA Version 14.1, October 2011. http://www.meddra.org/sites/default/files/guidance/file/9491-1410_termselptc_r4_2_sep2011.pdf. Accessed July 2, 2014
17. Ware J, Kosinski M, Dewey J. *How to Score Version 2 of the SF-36 Health Survey*. Lincoln: QualityMetric; 2000
18. *EQ-5D User Guide*. Rotterdam, the Netherlands: EuroQol Group; 1996
19. Farrar JT, Young JP Jr, LaMoreaux L, et al. **Clinical importance of changes in chronic pain intensity measured on an 11-point numerical pain rating scale.** *Pain* 2001;94:149–58
20. Fairbank JC, Pynsent PB. **The Oswestry Disability Index.** *Spine* 2000;25:2940–52
21. Agency for Healthcare Research and Quality. U.S. Valuation of the EuroQol EQ-5D Health States. January 2012. http://www.ahrq.gov/professionals/clinicians-providers/resources/rice/EQ5Dproj.html. Accessed June 7, 2013
22. Eastell R, Cedel SL, Wahner HW, et al. **Classification of vertebral fractures.** *J Bone Miner Res* 1991;6:207–15
23. Goz V, Koehler SM, Egorova NN, et al. **Kyphoplasty and vertebroplasty: trends in use in ambulatory and inpatient settings.** *Spine J* 2011;11:737–44
24. Mehio AK, Lerner JH, Engelhart LM, et al. **Comparative hospital economics and patient presentation: vertebroplasty and kyphoplasty for the treatment of vertebral compression fracture.** *AJNR Am J Neuroradiol* 2011;32:1290–94
25. Copay AG, Glassman SD, Subach BR, et al. **The minimum clinically important difference in lumbar spine surgery patients: a choice of methods using the Oswestry Disability Index, Medical Outcomes Study Questionnaire Short Form 36, and Pain Scales.** *Spine J* 2008;8:968–74
26. Walters SJ, Brazier JE. **Comparison of the minimally important difference for two health state utility measures: EQ-5D and SF-6D.** *Qual Life Res* 2005;14:1523–32
27. Papanastassiou ID, Phillips FM, Van Meirhaeghe J, et al. **Comparing effects of kyphoplasty, vertebroplasty, and non-surgical management in a systematic review of randomized and non-randomized controlled studies.** *Eur Spine J* 2012;21:1826–43
28. Anderson PA, Froyshteter AB, Tontz WL Jr. **Meta-analysis of vertebral augmentation compared to conservative treatment for osteoporotic spinal fractures.** *J Bone Miner Res* 2013;28:372–82
29. Strom O, Leonard C, Marsh D, et al. **Cost-effectiveness of balloon kyphoplasty in patients with symptomatic vertebral compression fractures in a UK setting.** *Osteoporos Int* 2010;21:1599–608
30. Svedbom A, Alvares L, Cooper C, et al. **Balloon kyphoplasty compared to vertebroplasty and nonsurgical management in patients hospitalised with acute osteoporotic vertebral compression fracture: a UK cost-effectiveness analysis.** *Osteoporos Int* 2013;24:355–67
31. Edidin AA, Ong KL, Lau E, et al. **Cost-effectiveness analysis of treatments for vertebral compression fractures.** *Appl Health Econ Health Policy* 2012;10:273–84
32. Edidin AA, Ong KL, Lau E, et al. **Mortality risk for operated and nonoperated vertebral fracture patients in the Medicare population.** *J Bone Miner Res* 2011;26:1617–26
33. McCullough BJ, Comstock BA, Deyo RA, et al. **Major medical outcomes with spinal augmentation vs conservative therapy.** *JAMA Intern Med* 2013;173:1514–21
34. Lange A, Kasperk CP, Alvares L, et al. **Survival and cost comparison of kyphoplasty and percutaneous vertebroplasty using German claims data.** *Spine (Phila Pa 1976)* 2014;39:318–26
35. Chen AT, Cohen DB, Skolasky RL. **Impact of nonoperative treatment, vertebroplasty, and kyphoplasty on survival and morbidity after vertebral compression fracture in the Medicare population.** *J Bone Joint Surg Am* 2013;95:1729–36
36. Kallmes DF, Comstock BA, Heagerty PJ, et al. **A randomized trial of vertebroplasty for osteoporotic spinal fractures.** *N Engl J Med* 2009;361:569–79
37. Buchbinder R, Osborne RH, Ebeling PR, et al. **A randomized trial of vertebroplasty for painful osteoporotic vertebral fractures.** *N Engl J Med* 2009;361:557–68
38. Bono CM, Heggeness M, Mick C, et al. **North American Spine Society: newly released vertebroplasty randomized controlled trials—a tale of two trial**s. *Spine J* 2010;10:238–40
39. Clark W, Lyon S, Burnes J, et al. **Trials of vertebroplasty for vertebral fractures.** *N Engl J Med* 2009;361:2097–98
40. Li X, Yang H, Tang T, et al. **Comparison of kyphoplasty and vertebroplasty for treatment of painful osteoporotic vertebral compression fractures: twelve-month follow-up in a prospective nonrandomized comparative stud**y. *J Spinal Disord Tech* 2012;25:142–49
41. Grohs JG, Matzner M, Trieb K, et al. **Minimal invasive stabilization of osteoporotic vertebral fractures: a prospective nonrandomized comparison of vertebroplasty and balloon kyphoplasty**. *J Spinal Disord Tech* 2005;18:238–42
42. Chin DK, Kim YS, Cho YE, et al. **Efficacy of postural reduction in osteoporotic vertebral compression fractures followed by percutaneous vertebroplasty.** *Neurosurgery* 2006;58:695–700; discussion 695–700
43. McKiernan F, Jensen R, Faciszewski T. **The dynamic mobility of vertebral compression fractures.** *J Bone Miner Res* 2003;18:24–29
44. Voggenreiter G. **Balloon kyphoplasty is effective in deformity correction of osteoporotic vertebral compression fractures.** *Spine* 2005;30:2806–12
45. Shindle MK, Gardner MJ, Koob J, et al. **Vertebral height restoration in osteoporotic compression fractures: kyphoplasty balloon tamp is superior to postural correction alone.** *Osteoporos Int* 2006;17:1815–19
46. Eck JC, Nachtigall D, Humphreys SC, et al. **Comparison of vertebroplasty and balloon kyphoplasty for treatment of vertebral compression fractures: a meta-analysis of the literature.** *Spine J* 2008;8:488–97
47. Taylor RS, Taylor RJ, Fritzell P. **Balloon kyphoplasty and vertebroplasty for vertebral compression fractures: a comparative systematic review of efficacy and safety.** *Spine* 2006;31:2747–55
48. Lee MJ, Dumonski M, Cahill P, et al. **Percutaneous treatment of vertebral compression fractures: a meta-analysis of complications.** *Spine* 2009;34:1228–32
49. Hulme PA, Krebs J, Ferguson SJ, et al. **Vertebroplasty and kyphoplasty: a systematic review of 69 clinical studies.** *Spine* 2006;31:1983–2001
50. Lee IJ, Choi AL, Yie MY, et al. **CT evaluation of local leakage of bone cement after percutaneous kyphoplasty and vertebroplasty.** *Acta Radiol* 2010;51:649–54
51. National Institute for Health and Care Excellence. NICE technology appraisal guidance 279: percutaneous vertebroplasty and percutaneous balloon kyphoplasty for treating osteoporotic vertebral compression fractures. April 2013. http://www.nice.org.uk/guidance/ta279/resources/guidance-percutaneous-vertebroplasty-and-percutaneous-balloon-kyphoplasty-for-treating-osteoporotic-vertebral-compression-fractures-pdf. Accessed September 16, 2014

Pilot Study of Radiation Dose Reduction for Pediatric Head CT in Evaluation of Ventricular Size

S. Gabriel, L.J. Eckel, D.R. DeLone, K.N. Krecke, P.H. Luetmer, C.H. McCollough, J.G. Fletcher, and L. Yu

ABSTRACT

BACKGROUND AND PURPOSE: CT is a ubiquitous, efficient, and cost-effective method to evaluate pediatric ventricular size, particularly in patients with CSF shunt diversion who often need emergent imaging. We therefore sought to determine the minimum dose output or CT dose index required to produce clinically acceptable examinations.

MATERIALS AND METHODS: Using a validated noise insertion method and CT projection data from 22 patients, standard pediatric head CT images were reconstructed with weighted filtered back-projection and sinogram-affirmed iterative reconstruction corresponding to routine, 25%, and 10% dose. Reconstructed images were then evaluated by 3 neuroradiologists (blinded to dose and reconstruction method) for ventricular size, diagnostic confidence, image quality, evidence of hemorrhage, and shunt tip location, and compared with the reference standard.

RESULTS: There was no significant difference in the ventricular size ranking, and the sensitivity for moderate to severe hydrocephalus was 100%. There was no significant difference between the full-dose level and the ventricular size rankings at the 25% or the 10% dose level for either reconstruction kernel ($P > .979$). Diagnostic confidence was maintained across doses and kernel. Hemorrhage was more difficult to identify as image quality degraded as dose decreased but was still seen in a majority of cases. Shunts were identified by all readers across all doses and reconstruction methods.

CONCLUSIONS: CT images having dose reductions of 90% relative to routine head CT examinations provide acceptable image quality to address the specific clinical task of evaluating ventricular size.

ABBREVIATION: mGy = milligray

Before the advent of ventricular CSF shunt devices for the treatment of hydrocephalus, patients had a poor prognosis with a very high mortality rate. In 1949, Nulsen and Spitz[1] were the first to prove the efficacy of placing a shunt with a 1-way valve into the venous system of a patient with hydrocephalus to free outflow of CSF into the venous system. The eventual introduction of the Spitz-Holter valve in 1956 made ventricular shunting the standard treatment for hydrocephalus.[2] Since then, significant technical advancements in CSF diversion devices have continued; however, device complications remain fairly common even today. One study estimated that an episode of ventricular shunt failure will occur in 85% of patients within 15 years of device insertion[3] with 30%–40% of ventricular shunts failing after the first year of insertion.[4] Kim et al[5] reported a ventricular shunt mortality rate of 2.2%. The clinical diagnosis of shunt malfunction is further complicated by nonspecific clinical signs, which can be attributed to other common pediatric ailments.[5,6]

CT evaluation of ventricular size, in conjunction with clinical symptoms, is the primary means of assessing ventricular CSF shunt failure/malfunction in pediatric patients with closed fontanelles.[5] However, concerns were expressed regarding the use of CT in children,[7] primarily because they are more sensitive than adults for some cancers, one of which is radiation-induced brain tumor.[8] In some cases, these concerns have prevented judicious use of CT imaging.[9]

Rapid sequence MR imaging may also be used for evaluation of ventricular size; however, it is not routinely available at large medical centers during off hours, or at small hospitals that do not have MR imaging units. In addition, MR imaging is more time consuming and costly, sometimes requires sedation of young children, and is associated with rare but existing

Received April 10, 2014; accepted after revision June 4.

From the Department of Radiology (S.G.), University of California Los Angeles, Los Angeles, California; and Department of Radiology (L.J.E., D.R.D., K.N.K., P.H.L., C.H.M., J.G.F., L.Y.), Mayo Clinic, Rochester, Minnesota.

Please address correspondence to Laurence J. Eckel, MD, 200 First St SW, Rochester, MN 55905; e-mail: eckel.laurence@mayo.edu

http://dx.doi.org/10.3174/ajnr.A4056

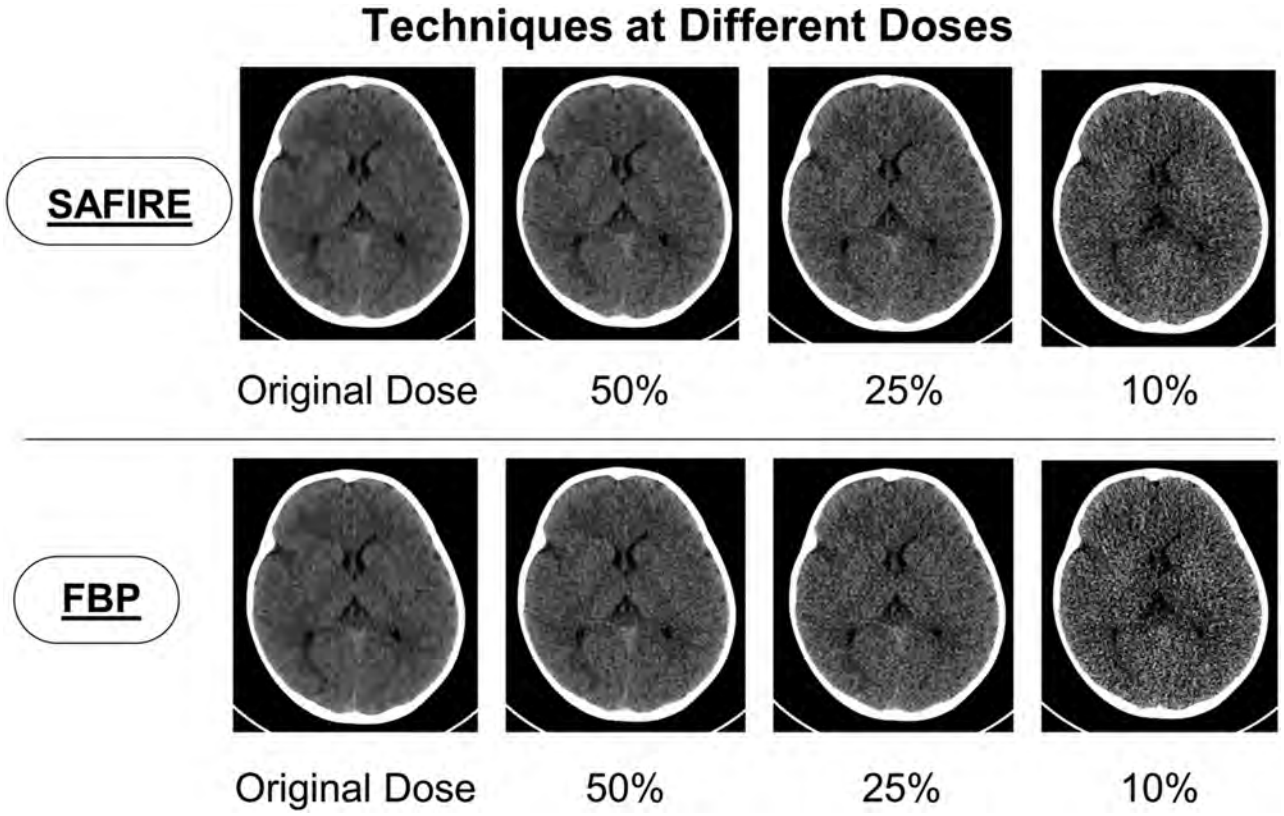

FIG 1. An actual subject from our study showing the full dose, 50% dose, 25% dose, and 10% dose using sinogram-affirmed iterative reconstruction and filtered back-projection reconstructions.

safety risks associated with strong magnetic fields and radiofrequency electromagnetic emissions.[10-12]

Shunted pediatric patients will require episodic imaging throughout the life of a shunt to ensure proper functionality, and given the wide availability of CT across our large (and often rural) health care network, CT is the principal imaging technique used. However, repeated use of CT in children has recently come into question, with some providers advocating use of MR imaging, despite its associated limitations, because MR imaging does not use ionizing radiation. To allay concerns regarding radiation, we have initiated educational programs for providers and patients that put the very small potential risk associated with a CT examination into proper perspective. In addition, our practice carefully evaluates our scanning protocols to use the lowest doses of radiation necessary to answer the specific diagnostic question.

Because assessment of ventricular size does not require the same level of image quality as a routine head CT examination, we hypothesized that the radiation dose could be greatly reduced for this diagnostic task without compromising diagnostic accuracy. Therefore, the purpose of this specific work was to determine the minimum radiation dose required to produce clinically acceptable head CT examinations for the evaluation of ventricular shunt malfunction. As part of this evaluation, we also examined whether the use of newer image reconstruction algorithms designed to facilitate dose reduction, commonly referred to as iterative reconstruction, were required for accurate diagnoses.[11,13]

MATERIALS AND METHODS

Our Institutional Review Board approved this study with a waiver of informed consent. Minnesota Research Authorization was obtained for each study subject. This study used CT projection data from pediatric head CT using 1 of 2 emergency department CT scanners at our institution. All examinations included in this study were performed as the standard of care; the images were retrospectively processed and evaluated. This study was in complete compliance with the Health Insurance Portability and Accountability Act.

Patient Population

Twenty-two pediatric subjects who underwent noncontrast head CT studies at our institution from August 2012 to March 2013 were included in this study. Inclusion criteria included: patient <18 years of age, acquisition of head CT without contrast using our routine head CT protocol, and ability to retrieve and archive CT projection data. CT projection data were collected consecutively on all pediatric patients. Patients were excluded if CT projection data were deleted off the scanner image reconstruction system before archiving or if the patient was without the Minnesota Research Authorization. Some of our study subjects had a ventriculostomy device to treat hydrocephalus.

Image Acquisition and Reconstruction

Patients were scanned using our regular pediatric head CT protocol on a 128-section CT scanner (Definition Flash; Siemens, Erlangen, Germany). Each examination was acquired with a rotation time of

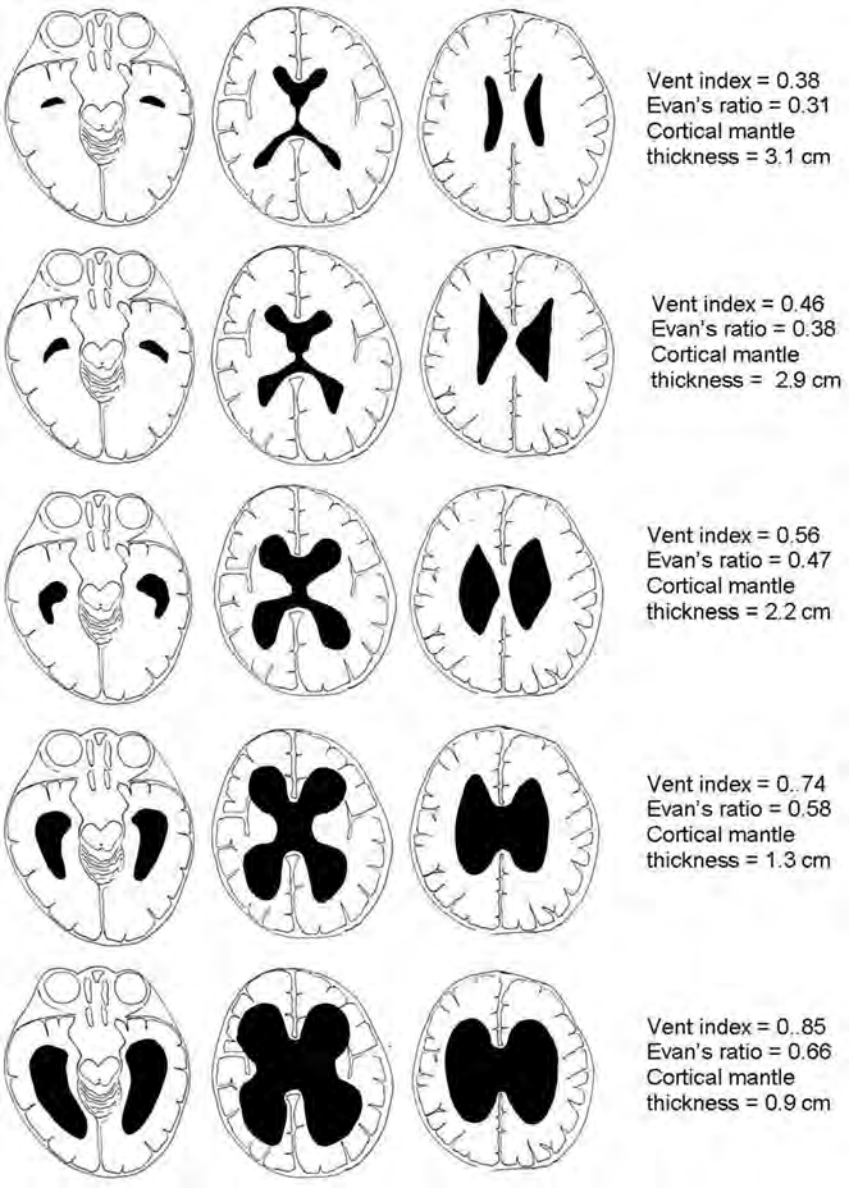

FIG 2. Ventricular size was classified using a previously published visual scale. Reprinted with permission from Dias MS, Shaffer ML, Iantosca MR, et al. Variability among pediatric neurosurgeons in the threshold for ventricular shunting in asymptomatic children with hydrocephalus. *J Neurosurg Pediatr* 2011;7:134–42.

0.5 seconds, a helical pitch of 0.8, a tube energy of 120 kV, a quality reference mAs of 220, and a detector configuration of 128 × 0.6 mm. The automatic exposure control (CARE Dose 4D; Siemens) was used. Because the automatic exposure control setting on this scanner uses an adult-size reference patient for pediatric patients, the actual effective mAs (mAs/pitch) was much lower than 220 because of the adaptation of the mAs to the pediatric head size. There were 5 trauma patients scanned with a slightly higher quality reference mAs at 275 and 4 patients scanned with an adult technique (250 effective mAs, CARE Dose 4D off) because they were older than 6 years according to our clinical protocols.

Using a validated noise insertion program[14] that takes into account both the automatic exposure control and the bow-tie filter of the scanner, noise was inserted into the CT projection data of each patient to result in new CT projection data for each patient that corresponded to 25% and 10% of the original routine dose (ie, 75% and 90% dose reduction). Images from these lower-dose CT projection data were reconstructed using a 5-mm section thickness and 5-mm interval with 2 reconstruction kernels used at each dose level, a routine head kernel with weighted filtered back projection (H30), and a head kernel using sinogram-affirmed iterative reconstruction (Siemens) called J30 with a strength setting of 2 (Fig 1).

Image Interpretation

Three board- and Certificate of Added Qualification–certified neuroradiologists with 8, 22, and 23 years of experience (L.J.E., P.H.L., K.N.K.) were asked to evaluate each CT dataset for ventricular size, diagnostic confidence, image quality, evidence of hemorrhage, and shunt tip location using a standard form. Readers were blinded to clinical history, dose level, and reconstruction kernel. A blocked reader design was used so that the neuroradiologist readers were presented with each patient's examination (using a unique dose level/reconstruction method combination) once in every 22 examinations. CT image datasets were presented to the reader in random order, with images evaluated on a computer workstation (Advantage Windows Version 4.3–05; GE Healthcare, Milwaukee, Wisconsin). Ventricular size was graded as normal, mild hydrocephalus, moderate hydrocephalus, or severe hydrocephalus based on a previously published visual scale shown in Fig 2 that was reproduced on the data form, with the two largest ventricle sizes classified as severe. Diagnostic confidence was rated along a 5-point scale similar to comparable previous studies[15-17]: 1 = nondiagnostic, cannot identify or rule out ventricular enlargement and shunt tube tip location; 2 = will potentially miss mild ventricular enlargement and shunt tube tip location; 3 = will probably not miss ventricular enlargement and shunt tube tip location; 4 = most likely will identify all abnormalities with respect to ventricular enlargement and shunt tube tip; 5 = can detect ventricular enlargement and shunt tube tip without diagnostic compromise. Image quality was also graded along a similar 5-point scale: 1 = nondiagnostic because of excessive noise/artifacts; 2 = diagnosis questionable because of excessive noise/artifacts; 3 = diagnostic with moderate but acceptable noise/artifacts; 4 = mild noise, no change in diagnostic confidence; 5 = routine diagnostic image quality.

Radiologists were also asked to identify intracranial hemor-

rhage of any type (ie, present, not present, cannot ascertain). If hemorrhage was present, they were asked to identify the location. They were also asked to record the shunt tube tip if present. In addition, readers were given an opportunity to notate additional observations or comments.

Reference Standard

A reference standard for ventricular size for each patient was determined using reader agreement rules. These rules defined the reference standard ventricular size to be the ventricular size determined by at least 2 of the 3 readers when examining the routine-dose head CT using the standard commercial iterative reconstruction kernel (J30). For these 22 routine-dose datasets, all 3 readers rated ventricular size identically in 15 (68%). In the remaining 7 cases, 2 of 3 readers always agreed with the outlying reader ventricular size rank differing by only 1 severity rank.

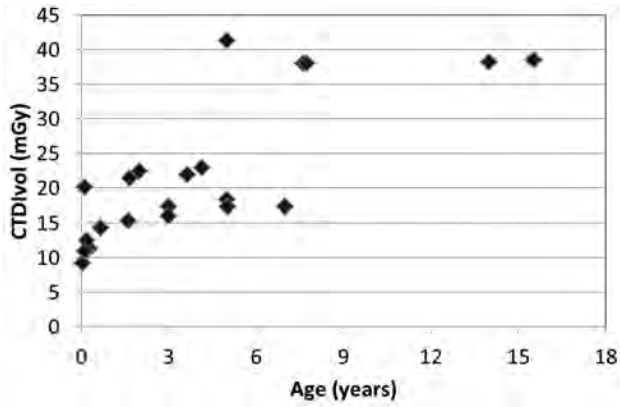

FIG 3. Distribution of volume CT dose index for the 22 patients in their original full-dose examinations (mean, 21.6 ± 10.3 mGy; range, [9.2 mGy, 41.3 mGy]). The volume CT dose index was based on a 16-cm CT dose index phantom.

Statistical Analysis

The accuracy of each reader's ventricular size rankings were compared with the reference standard for each dose level and reconstruction method. The sensitivity and accuracy for moderate and severe hydrocephalus were also determined using ventricular size of 3 or 4 versus ventricular size 1 or 2. Descriptive statistics (ie, mean, standard deviation) were used to report diagnostic confidence and image quality for each dose level and reconstruction method. Wilcoxon rank sum test was performed to determine whether diagnostic confidence and image quality for the reduced dose differed from those in the routine-dose head CT examinations. Reader agreement was calculated for all doses and kernels using a multirater κ statistic.

RESULTS

Twenty-two patients underwent pediatric head CT with subsequent reconstruction of reduced-dose compared with standard head CT images corresponding to 25% and 10% of the original dose. Patient ages ranged from 1 month to 16 years (median 3 years). Indications for examination included evaluation for hydrocephalus ($n = 8$), trauma ($n = 9$), and general assessment ($n = 5$). Of the 22 total patients evaluated in this study, 12 of the children were seen in our emergency department, 2 were being seen in the outpatient clinic and later scanned in the emergency department, and 8 patients were inpatients at the time of the scan.

The mean volume CT dose index in the original 22 full-dose examinations was 21.6 milligray (mGy) ± 10.3 mGy (minimum: 9.2 mGy; maximum: 41.3 mGy), as shown in Fig 3. The mean dose-length product was 370 ± 216 mGy × cm (minimum: 98 mGy × cm; maximum: 778 mGy × cm). Using an age-corrected conversion factor from dose-length product to effective dose,[18] the estimated mean effective dose was 1.8 ± 0.5 millisievert (mSv) (minimum: 1.0 mSv; maximum: 2.9 mSv). The estimated mean effective dose corresponding to the 10% dose level would be 0.18 ± 0.05 mSv.

According to reference standard assessment of ventricular size, there were 12 patients with normal ventricular size, 7 patients with mild hydrocephalus, 2 patients with moderate hydrocephalus, and 1 patient with severe hydrocephalus. There was substantial agreement between the 3 readers when determining ventricular size with a multirater κ of 0.73, which indicates substantial agreement.

The accuracy for an exact match of reference standard ventricular size and each reader's ventricular size rankings for each dose level and reconstruction method are given in Table 1. The accuracy for the full-dose examinations ranged from 86% to 95% across readers, from 73% to 95% at the 25% dose level, and from 77% to 91% at the 10% dose level. The 95% confidence intervals for accuracy of ventricular assessment were virtually identical for each reader (Table 1). Except for 1 case for each reader at the 10% dose level with each reconstruction method, all disagreements at the lower dose levels for either reconstruc-

Table 1: Accuracy of ventricular size rank for exact match between reader and reference standard

	100% Dose	25% Dose		10% Dose	
	J30	J30	H30	J30	H30
Reader 1	19/22 86[b] (65–97)	19/22 86[b] (65–97)	19/22 86[b] (65–97)	19/22 86[a] (65–97)	19/22 86[a] (65–97)
Reader 2	19/22 86[b] (65–97)	16/22 73[b] (50–89)	19/22 86[b] (65–97)	17/22 77[a] (55–92)	17/22 77[a] (55–92)
Reader 3	21/22 95[b] (77–100)	21/22 95[b] (77–100)	21/22 95[b] (77–100)	20/22 91[a] (71–99)	20/22 91[a] (71–99)

[a] Indicates that all incorrect ventricular size rankings were discrepant by 1 rank.
[b] Indicates that all cases except for 1 at the lower dose levels were categorized within 1 rank ventricular size, when compared with the reference standard.

Table 2: Accuracy for identification of moderate and severe hydrocephalus (ie, rank 3 or 4 versus rank 1 or 2) per reader compared with reference standard

	100% Dose	25% Dose		10% Dose	
	J30	J30	H30	J30	H30
Reader 1	22/22 100 (85–100)	22/22 100 (85–100)	21/22 95 (77–100)	22/22 100 (85–100)	21/22 95 (77–100)
Reader 2	20/22 91 (71–99)	20/22 91 (71–99)	21/22 95 (77–100)	21/22 95 (77–100)	20/22 91 (71–99)
Reader 3	22/22 100 (85–100)	22/22 100 (85–100)	22/22 100 (85–100)	22/22 100 (85–100)	22/22 100 (85–100)

tion method were within 1 rank of ventricular size compared with the reference standard.

The sensitivity for the identification of moderate to severe hydrocephalus was 100% for all 3 readers across all radiation dose levels and reconstruction methods (3 of 3; 95% confidence interval 29%–100%). The accuracy for the identification of moderate or severe hydrocephalus is shown in Table 2 and ranged from 95% to 100% for reader 1, from 91% to 95% for reader 2, and 100% for reader 3.

Radiologists reported their diagnostic confidence on a 5-point scale (Table 3). For all 3 readers, the diagnostic confidence was very high (mean rank = 4.88) on the original dose scan and similar for the 25% dose scans, regardless of reconstruction method ($P > .3$ except for Reader 2's 25% dose + filtered back-projection, where $P = .02$). For 1 reader, diagnostic confidence was significantly lower at the 10% dose level, and was worse for the reconstruction kernel without iterative reconstruction (mean confidence rank = 1.18 and 1.09, respectively, for the J30 and H30 kernel). At the 10% dose level, diagnostic confidence was significantly degraded for the filtered back-projection ($P < .003$ for all readers), but this difference was small in magnitude for 2 of 3 readers who had mean confidence scores of 4.6 and 4.7. With iterative reconstruction, 1 reader no longer had significantly lower confidence scores at the 10% dose level ($P = .16$), but findings were unchanged for the other 2 ($P < .005$).

Table 4 reports the overall perceived image quality by each reader across dose levels and reconstruction methods. As expected, each reader perceived significantly degraded image quality and more noise artifacts at the lower dose levels, regardless of reconstruction method ($P < .002$ for all comparisons). At the 25% dose level, 2 of 3 readers rated image quality as significantly better with iterative reconstruction compared with filtered back-projection ($P = .02$, $P = .001$). At the 10% dose level, only 1 reader rated iterative reconstruction significantly better ($P = .013$).

Although the study and examination was not designed to identify intracranial hemorrhage, there were 3 cases by reference standard, with 2 of 3 readers identifying it at all doses (Fig 4). There were 7 cases with intracranial shunts with shunt tip locations correctly identified by all 3 readers.

Table 3: Diagnostic confidence per reader for evaluation of ventricular size

	100% Dose	25% Dose		10% Dose	
	J30	J30	H30	J30	H30
Reader 1	5.0 ± 0.0	5.0 ± 0.0	5.0 ± 0.2	4.7 ± 0.5	4.6 ± 0.5
Reader 2	5.0 ± 0.2	4.8 ± 0.5	4.6 ± 0.6	3.9 ± 0.9	3.3 ± 1.2
Reader 3	5.0 ± 0.0	5.0 ± 0.0	5.0 ± 0.0	4.9 ± 0.5	4.7 ± 0.6

Note:—5-point scale: 1 indicates nondiagnostic, cannot identify or rule out ventricular enlargement and shunt tube tip location; 2, will potentially miss mild ventricular enlargement and shunt tube tip location; 3, will probably not miss ventricular enlargement and shunt tube tip location; 4, most likely will identify all abnormalities with respect to ventricular enlargement and shunt tube tip; 5, can detect ventricular enlargement and shunt tube tip without diagnostic compromise.

Table 4: Overall image quality per reader using the 5-point scale described above

	100% Dose	25% Dose		10% Dose	
	J30	J30	H30	J30	H30
Reader 1	4.9 ± 0.4	4.1 ± 0.4	3.8 ± 0.5	3.5 ± 0.5	3.2 ± 0.4
Reader 2	3.8 ± 1.1	2.3 ± 0.7	1.6 ± 0.6	1.2 ± 0.5	1.1 ± 0.3
Reader 3	4.1 ± 0.7	3.5 ± 0.6	3.4 ± 0.6	2.2 ± 0.5	1.8 ± 0.4

DISCUSSION

Pediatric patients with CSF shunts are often repeatedly scanned to evaluate for shunt malfunction. Most of these repeat scans are evaluating ventricular morphology, most specifically ventricular size stability, shunt location, and in some cases CSF shunt complications. In our study, we simulated doses that were 25% and 10% of the original dose. We showed that simulated reduction to 10% of the standard dose was diagnostically acceptable. In this blinded study, neuroradiologists were able to accurately detect moderate to severe hydrocephalus across all dose levels and reconstruction kernels without compromising diagnostic performance. As expected, the overall image quality decreased at lower doses; however, this did not compromise the diagnostic accuracy for this specific indication. The resultant volume CT dose index was reduced from 21.6 to 2.2 mGy. The corresponding estimated effective dose was reduced from 1.8 to roughly 0.18 mSv, which is negligible relative to the annual background radiation in the United States from naturally occurring sources (mean, 3.0 mSv; range, 1–10 mSv).

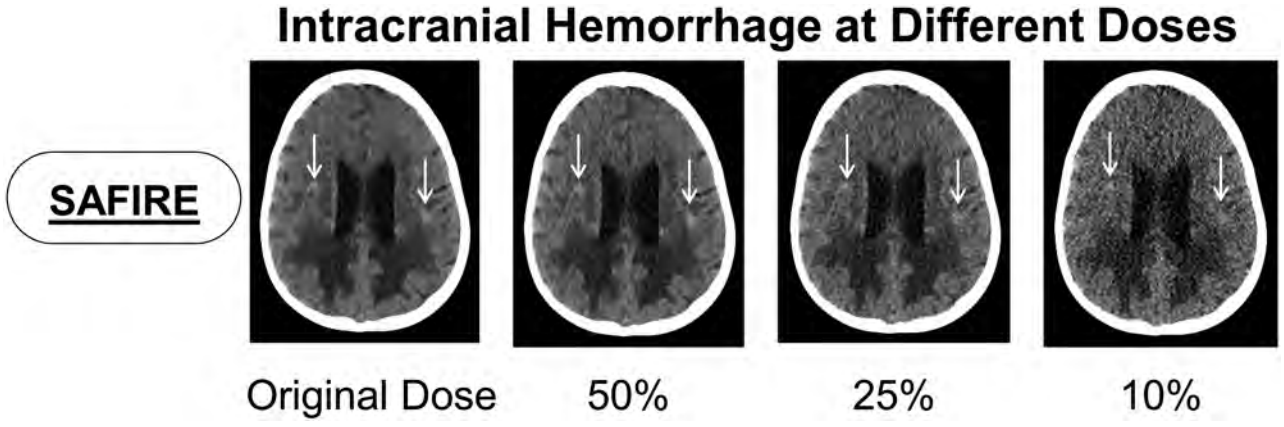

FIG 4. Although the study was not designed to identify intracranial hemorrhage, it could be occasionally identified. Images from an actual subject in our study showing intracranial hemorrhage (*arrow*) at the full, 25%, and 10% dose using sinogram-affirmed iterative reconstruction. As subtle hemorrhage may not be identified at lower doses, the technique should not be used in cases where identification of hemorrhage is suspected or critical.

Using validated, reduced dose compared with standard simulation techniques,[14] our study demonstrated that a 90% reduction in dose relative to a routine head CT examination was clinically acceptable for the evaluation of ventricular size. In addition, iterative reconstruction is not required to keep observer performance high at the lower doses, so our results can be easily translated across a broad range of CT scanner models of various makes and models.

All 7 cases of intracranial shunts were accurately identified by all readers. This 100% accuracy in identifying shunt position is far more favorable than the literature available for rapid-sequence MR imaging where it is reportedly lower. In 2 studies, from 42%[11] to 60%[13] of reviews for catheter positions were graded as nondiagnostic or poor in at least 1 sequence. O'Neill et al[11] found that insufficient shunt-catheter visualization was especially associated with small ventricles when using half-Fourier acquisition single-shot turbo rapid-sequence MR imaging.

Based on this evaluation study, we have already implemented a reduced-dose technique in our practice for pediatric patients with shunts since March 2013. A quality reference mAs of 25 was used instead of the original 220 quality reference mAs. Image quality continues to be deemed sufficient for the diagnostic task of evaluating potential shunt malfunction.

There were several limitations to our study. This was a pilot retrospective review, and our study was underpowered to perform noninferiority testing. We consequently reported and compared ratios and 95% confidence intervals for accuracy of ventricular size rank. Because of obvious differences in technique (Fig 1), blinded readers were likely able to distinguish the original-dose studies from the reconstructed lower-dose studies at 25% and 10% of the original dose. This could have resulted in bias during subjective image quality evaluation, despite being blinded to technical data. In addition, the design of our questionnaire may have prompted the blinded radiologists to look closer for shunt tube tips and intracranial hemorrhage more than they otherwise would have without prompting.

CONCLUSIONS

The accuracy of detection of moderate and severe hydrocephalus was maintained across all dose levels and reconstruction methods. As expected, diagnostic confidence was generally maintained, with image quality decreased at lower dose levels.

CT images at 10%–25% of the dose level of routine head CT examinations provide acceptable image quality to address the specific clinical task of evaluating ventricular size. Extremely low-dose CT examinations for the evaluation of ventricular size and shunt malfunction are a reasonable alternative to emergent MR imaging and avoid the increased cost, workflow inefficiencies, frequent need for sedation, and safety concerns associated with MR imaging. The promising results of this study have already resulted in implementation of this very low-dose head CT protocol at our institution.

ACKNOWLEDGMENTS

The authors would like to express their appreciation to Maria M. Shiung and Michael R. Bruesewitz, RT, for their contributions to this work. We would also like to thank Amy L. Nordstrom for assistance in preparation of the manuscript.

Disclosures: Cynthia McCollough—*UNRELATED: Grants/Grants Pending:* Siemens Medical Solutions*; *Travel/Accommodations/Meeting Expenses Unrelated to Activities Listed:* Siemens Healthcare AG, *Comments*: Travel to present research results for sponsored research unrelated to this work. Joel Fletcher—*UNRELATED: Grants/Grants Pending:* Siemens Healthcare,* *Comments*: My institution receives a grant from Siemens Healthcare, which manufactures the iterative reconstruction kernel used in this study. This grant includes personnel time for me as a coinvestigator. Lifeng Yu—*UNRELATED: Other:* Siemens Healthcare, *Comments*: The authors and Mayo Clinic have intellectual property rights related to a technology that is not used in the current research. *Money paid to the institution.

REFERENCES

1. Nulsen FE, Spitz EB. **Treatment of hydrocephalus by direct shunt from ventricle to jugular vein.** *Surg Forum* 1951:399–403
2. Boockvar JA, Loudon W, Sutton LN. **Development of the Spitz-Holter valve in Philadelphia.** *J Neurosurg* 2001;95:145–47
3. Stone JJ, Walker CT, Jacobson M, et al. **Revision rate of pediatric ventriculoperitoneal shunts after 15 years.** *J Neurosurg* 2013;11:15–19
4. George KJ, Roy D. **A low radiation computed tomography protocol for monitoring shunted hydrocephalus.** *Surg Neurol Int* 2012;3:103
5. Kim TY, Stewart G, Voth M, et al. **Signs and symptoms of cerebrospinal fluid shunt malfunction in the pediatric emergency department.** *Pediatr Emerg Care* 2006;22:28–34
6. Madikians A, Conway EE. **Cerebrospinal fluid shunt problems in pediatric patients.** *Pediatr Ann* 1997;26:613–20
7. Brenner DJ, Elliston CD, Hall EJ, et al. **Estimated risks of radiation-induced fatal cancer from pediatric CT.** *AJR Am J Roentgenol* 2001;176:289–96
8. United Nations Scientific Committee on the Effects of Atomic Radiation. *Sources, effects and risks of ionizing radiation UNSCEAR 2013 Report.* New York: United Nations Scientific Committee on the Effects of Atomic Radiation; 2013
9. McCollough CH. **Defending the use of medical imaging.** *Health Phys* 2011;100:318–21
10. Kanal E, Barkovich AJ, Bell C, et al. **ACR guidance document on MR safe practices: 2013.** *J Magn Reson Imaging* 2013;37:501–30
11. O'Neill BR, Pruthi S, Bains H, et al. **Rapid sequence magnetic resonance imaging in the assessment of children with hydrocephalus.** *World Neurosurg* 2013;80:e307–12
12. Chaljub G, Kramer LA, Johnson RF, et al. **Projectile cylinder accidents resulting from the presence of ferromagnetic nitrous oxide or oxygen tanks in the MR suite.** *AJR Am J Roentgenol* 2001;177:27–30
13. Ashley WW, McKinstry RC, Leonard JR, et al. **Use of rapid-sequence magnetic resonance imaging for evaluation of hydrocephalus in children.** *J Neurosurg* 2005;103:124–30
14. Yu LF, Shiung M, Jondal D, et al. **Development and validation of a practical lower-dose-simulation tool for optimizing computed tomography scan protocols.** *J Comput Assist Tomogr* 2012;36:477–87
15. Prakash P, Kalra MK, Kambadakone AK, et al. **Reducing abdominal CT radiation dose with adaptive statistical iterative reconstruction technique.** *Invest Radiol* 2010;45:202–10
16. Fletcher JG, Grant KL, Fidler JL, et al. **Validation of dual-source single-tube reconstruction as a method to obtain half-dose images to evaluate radiation dose and noise reduction: phantom and human assessment using CT colonography and sinogram-affirmed iterative reconstruction (SAFIRE).** *J Comput Assist Tomogr* 2012;36:560–69
17. Froemming AT, Kawashima A, Takahashi N, et al. **Individualized kV selection and tube current reduction in excretory phase computed tomography urography: potential for radiation dose reduction and the contribution of iterative reconstruction to image quality.** *J Comput Assist Tomogr* 2013;37:551–59
18. American Association of Physicists in Medicine. **The measurement, reporting and management of radiation dose in CT: report of AAPM Task Group 23 of the Diagnostic Imaging Council CT Committee.** AAPM report no. 96; 2008. https://www.aapm.org/pubs/reports/RPT_96.pdf. Accessed May 28, 2014

Radiation Dose Reduction in CT-Guided Spine Biopsies Does Not Reduce Diagnostic Yield

K.A. Shpilberg, B.N. Delman, L.N. Tanenbaum, S.J. Esses, R. Subramaniam, and A.H. Doshi

ABSTRACT

BACKGROUND AND PURPOSE: CT-guided biopsy is the most commonly used method to obtain tissue for diagnosis in suspected cases of malignancy involving the spine. The purpose of this study was to demonstrate that a low-dose CT-guided spine biopsy protocol is as effective in tissue sampling as a regular-dose protocol, without adversely affecting procedural time or complication rates.

MATERIALS AND METHODS: We retrospectively reviewed all patients who underwent CT-guided spine procedures at our institution between May 2010 and October 2013. Biopsy duration, total number of scans, total volume CT dose index, total dose-length product, and diagnostic tissue yield of low-dose and regular-dose groups were compared.

RESULTS: Sixty-four patients were included, of whom 31 underwent low-dose and 33 regular-dose spine biopsies. There was a statistically significant difference in total volume CT dose index and total dose-length product between the low-dose and regular-dose groups ($P < .0001$). There was no significant difference in the total number of scans obtained ($P = .3385$), duration of procedure ($P = .149$), or diagnostic tissue yield ($P = .6017$).

CONCLUSIONS: Use of a low-dose CT-guided spine biopsy protocol is a practical alternative to regular-dose approaches, maintaining overall quality and efficiency at reduced ionizing radiation dose.

ABBREVIATIONS: CTDIvol = volume CT dose index; DLP = dose-length product; kVp = peak kilovoltage; mGy = milligray

Imaging-guided biopsy is a commonly used method to obtain a tissue diagnosis in suspected cases of malignancy. In particular, CT guidance is often used for precise localization of a lesion before and during biopsy. It provides the operator with great anatomic detail for biopsy planning and execution and allows for confirmation of needle placement into the area of concern. CT guidance is the preferred method of biopsy for osseous lesions within the vertebrae.[1-4] Even though CT guidance has become increasingly used for various procedures, there is concern over the amount of radiation exposure to the patient.[5-8]

Radiation dose reduction is commonly used in routine diagnostic CT scanning. Pediatric patients and patients who receive multiple scans for acute disease follow-up, chronic conditions, and screening purposes often undergo CT with modified scanning protocols to reduce dose.[9-14] This type of protocol modification has also been used in CT-guided interventions to limit radiation dose when performing multiple scans during the procedure.[8,15-18] Given the increased desire to reduce radiation dose to patients, we transitioned our protocols for CT-guided spine biopsies to use a lower dose.

The purpose of this study was to demonstrate that a low-dose protocol for CT-guided spine biopsies is as effective in tissue sampling without an increase in procedural time or an increase in complication rates compared with our legacy higher-dose approaches.

MATERIALS AND METHODS

After obtaining Institutional Review Board approval, we retrospectively reviewed all patients who underwent CT-guided spine procedures at our institution between May 2010 and October 2013. The total number of charts reviewed was 132.

Patients who underwent disk space aspirations and biopsies for suspected diskitis/osteomyelitis were excluded because of limited availability of surgical pathology data as most specimens were

Received April 29, 2014; accepted after revision June 5.

From the Department of Radiology, Icahn School of Medicine, Mount Sinai Health System, New York, New York.

Paper previously presented as an oral presentation at: American Society of Spine Radiology Annual Symposium, February 23–26, 2014; Miami Beach, Florida and Annual Meeting of the American Society of Neuroradiology, May 17–22, 2014; Montreal, Québec, Canada.

Please address correspondence to Amish Doshi, MD, Mount Sinai Hospital, Department of Radiology, Box 1234, 1 Gustave L Levy Pl, New York, NY 10029; e-mail: doshia@gmail.com, amish.doshi@mountsinai.org

http://dx.doi.org/10.3174/ajnr.A4053

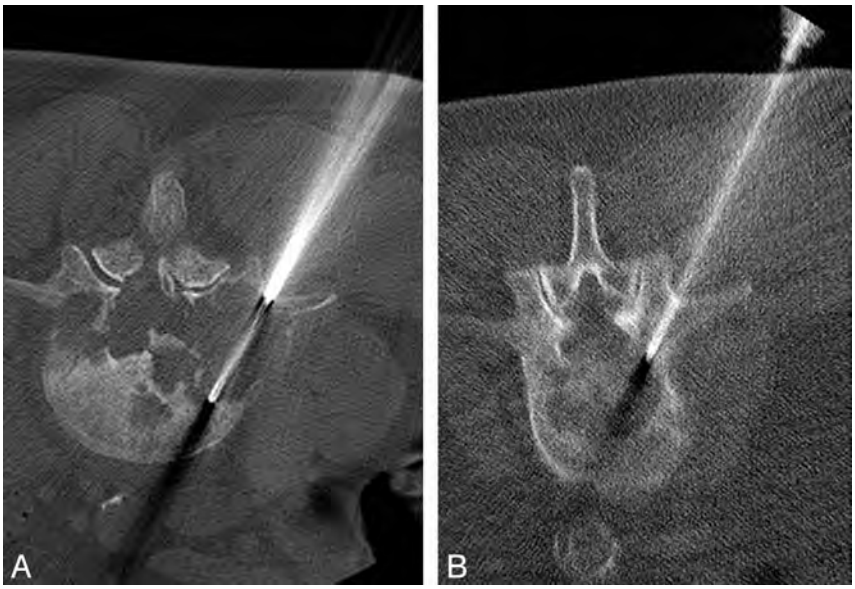

FIG 1. *A*, Axial CT performed with the regular-dose technique (kVp 120, mAs 250) demonstrates a biopsy needle within a lytic lesion in L3 vertebral body. *B*, Axial CT performed with the low-dose technique (kVp 80, mAs 60) demonstrates a biopsy needle within a lytic lesion in L2 vertebral body. Both the lesion and the biopsy needle including its tip are sufficiently conspicuous.

only submitted for microbiology analysis. CT-guided pain management procedures such as facet cyst ruptures and epidural injections were also excluded. Patients for whom dose reports were not available in our institution's PACS were excluded.

Ultimately, 64 patients were included in this analysis. Two lesions were biopsied in 2 patients and 1 lesion in the remaining 62 patients, yielding a total of 66 lesions. All the biopsies were performed by 1 Certificate of Added Qualification–certified neuroradiologist (A.H.D.) with 6 years of experience. The low-dose protocol was initiated in February 2012 and has been almost exclusively used since November 2012.

Procedure

All CT-guided spine biopsies were performed on a 4-channel CT scanner (Volume Zoom; Siemens, Erlangen, Germany) or 8-section CT scanner (LightSpeed Ultra; GE Healthcare, Milwaukee, Wisconsin) in helical mode based on availability. The 8-section scanner was used to guide 50 biopsies (78.1%) and 4-section scanner for the remaining 14 biopsies (21.9%). CT fluoroscopy was not available. Patients all followed a standard course for these biopsies. Each was positioned prone for the procedures. Vital signs were monitored. Mild to moderate conscious sedation was used in 60 patients (93.8%), monitored anesthesia care in 2 patients (3.1%), and local anesthetic only in 2 patients (3.1%). A Fast Find Grid (Webb Manufacturing, Philadelphia, Pennsylvania) was placed over the general biopsy site for localization. In each patient, 1 preprocedure CT scan was obtained using a regular-dose protocol (120 peak kilovoltage [kVp]) and 200 mAs) for planning. Skin was prepped and draped in normal sterile fashion. One percent lidocaine was infiltrated into tissues for local and deep anesthesia. An 11-, 12-, or 13-gauge bone biopsy needle set (Osteo-Site; Cook, Bloomington, Indiana, or Bonopty; AprioMed, Londonderry, New Hampshire) was advanced into the lesion with CT images obtained after each needle advancement. Once the needle was confirmed within the lesion, CT scans were performed after each biopsy pass. In each patient, 1 final postbiopsy scan was obtained after the needle was removed using regular-dose parameters to assess for postprocedural complications. Patients were then transferred to a recovery area to be monitored before discharge or return to their hospital room.

Data Collection and Scanning Parameters

Data from PACS and dose reports were collected, including age, sex, location, and characteristics of lesion biopsied, kVp, mAs, pitch, volume CT dose index (CTDIvol) per series (milligray [mGy]), CTDIvol total (mGy), scan range (mm), dose-length product (DLP) per series (mGy·cm), total DLP (mGy·cm), number of biopsy-guiding scans, number of pre- and postbiopsy diagnostic scans, number of needle passes, total number of scans, duration of each biopsy (defined as time from the first prebiopsy scan to last postbiopsy scan), and complications. Pathology results were obtained for each patient from electronic medical records.

Low-dose biopsies were defined as those with a kVp of 80 and mAs of 40–60. Regular-dose biopsies were defined as those with a kVp of 120 and mAs >200. Scans performed at kVp and mAs parameters outside the above-mentioned criteria of low-dose or regular-dose biopsies were classified based on average CTDIvol (CTDIvol <10 mGy for low dose; CTDIvol >10 mGy for regular dose) as previously described by Kröpil et al.[19] They defined low-dose CTs as having a CT dose index <10 mGy. For example, 2 patients whose biopsies were started as low-dose protocol were switched to regular-dose protocol at the operator's discretion because of insufficient conspicuity of subtle lesions and were classified as "regular-dose" because the average CTDIvol was 17.1 mGy in one and 20.3 mGy in the other. Figure 1 demonstrates representative images from regular-dose and low-dose CT-guided spine biopsies.

Diagnostic tissue yield was classified as "positive for malignancy," "specific benign diagnosis," and "negative for malignancy without a specific benign diagnosis." Lesions were classified as lytic, sclerotic, or mixed. The location of lesions was recorded as cervical, thoracic, lumbar, or sacral.

Age, biopsy duration, total number of scans (including prebiopsy and postbiopsy scans), total CTDIvol (including that used for prebiopsy and postbiopsy scans), and total DLP (including that used for prebiopsy and postbiopsy scans) of low-dose and regular-dose groups were compared using an unpaired *t* test (GraphPad Prism software; GraphPad Software, San Diego, California). Diagnostic tissue yield and the distribution of lesions by type and location of low-dose and regular-dose biopsies were

compared using Fisher exact test (GraphPad Software). *P* value < .05 was considered statistically significant.

RESULTS

Of the 64 patients who underwent CT-guided spine biopsies from 2010 to 2013, 29 patients (45.3%) underwent the procedure using a low-dose protocol and 35 patients (54.7%) using a regular-dose protocol. Table 1 demonstrates the mean and ranges for age, number of scans, duration of procedure, total CTDIvol, and total DLP for low-dose protocol; Table 2 denotes the same for regular-dose protocol.

Demographics

There was no significant difference between the 2 groups in patient age (63.86 ± 13.67 years for low dose versus 59.49 ± 14.6 years for regular dose; $P = .2239$) or in sex distribution (14 of 29 or 48.3% women for low dose versus 19 of 35 or 54.3% women for regular dose; $P = .802$).

Table 1: Low-dose biopsy group results

	Range	Mean ± Standard Deviation
Age (years)	29–87	63.86 ± 13.67
Total number of scans	5–22	11.38 ± 4.354
Duration (minutes)	19–76	34.31 ± 12.19
Total CTDIvol (mGy)	29.98–147.9	69.47 ± 24.76
Total DLP (mGy·cm)	239.3–1206	601.5 ± 237.7

Table 2: Regular dose biopsy group results

	Range	Mean ± Standard Deviation
Age (years)	24–86	59.49 ± 14.6
Total number of scans	6–29	12.46 ± 4.527
Duration (minutes)	21–58	38.17 ± 8.92
Total CTDIvol (mGy)	98.77–761.9	285.2 ± 132.6
Total DLP (mGy·cm)	523.6–3062	1541 ± 648.1

Dose and Scanning Time

There was a statistically significant difference between low-dose and regular-dose groups in total CTDIvol (69.47 ± 24.76 mGy for low dose versus 285.2 ± 132.6 mGy for regular dose; $P < .0001$) and total DLP (601.5 ± 237.7 mGy·cm for low dose versus 1541 ± 648.1 mGy·cm for regular dose; $P < .0001$) (Fig 2).

There was no significant difference in total number of scans obtained (11.38 ± 4.354 for low dose versus 12.46 ± 4.527 for regular dose; $P = .3385$) and duration of procedure (34.31 ± 12.19 minutes for low dose versus 38.17 ± 8.92 minutes for regular dose; $P = .149$) between the 2 groups (Fig 2).

Several outliers were noted, falling greater or less than 2 standard deviations from the mean. One patient in the low-dose group who had 2 lesions (one mixed and one sclerotic) biopsied had significantly more scans, longer duration of the procedure and higher total DLP than average. Two patients in the regular-dose group had significantly more scans than average (25 and 29) because of difficulty in accessibility of small vertebral body lesions, which resulted in significantly higher than average total CTDIvol (761.86 mGy) in one and total DLP (3062.46 mGy·cm) in the other.

Biopsy Results

There was no significant difference between the 2 groups in the proportion of cases positive for malignancy (20 of 29 or 69.0% for low dose versus 21 of 35 or 60% for regular-dose; $P = .6017$), those with a specific benign diagnosis (2 of 29 or 6.9% for low dose versus 6 of 35 or 17.1% for regular dose; $P = .2754$), and those whose pathology was negative for malignancy without a specific benign diagnosis (7 of 29 or 24.1% for low dose versus 8 of 35 or 22.9% for regular dose; $P = 1.00$).

Of the 66 lesions that were biopsied, 39 (59.1%) were lytic, 15 (22.7%) were sclerotic, and 12 (18.2%) were mixed. There was no statistically significant difference in lesion type between the low-dose and regular-dose groups (*P* values ranging from .1174 to .7694).

Most of the lesions that underwent biopsy were located within the lumbar spine (29 of 66; 44%). This was followed by the thoracic spine (28 of 66; 42.4%), sacrum (7 of 66; 10.6%) and cervical spine (2 of 66; 3%). There was no statistically significant difference in the location of lesions between the low-dose and regular-dose groups (*P* values ranging from .4334 to 1.00).

There were sufficient specimens for diagnosis in all patients in both biopsy groups. Overall, there was only 1 minor complication characterized by bleeding from the cannula, which was successfully

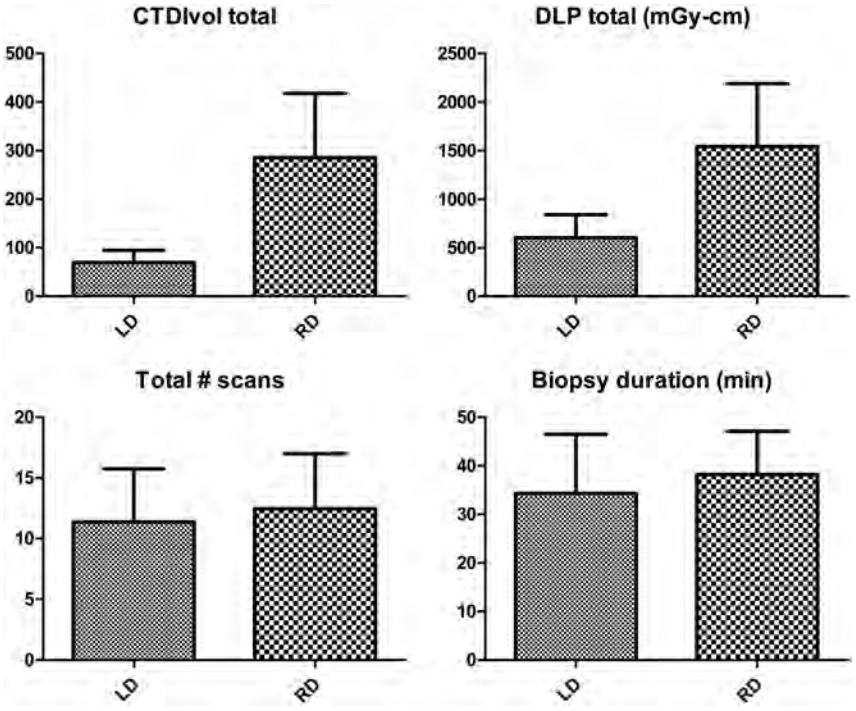

FIG 2. Graphs of means with standard deviations comparing radiation dose (total CTDIvol and DLP), total number of scans, and biopsy duration between low-dose and regular-dose groups.

treated with Gelfoam (Pfizer, New York, New York), in a low-dose group patient whose biopsy yielded metastatic renal cell carcinoma. No major complications were reported.

DISCUSSION

Imaging guidance for biopsy is a commonly used procedure in patients with imaging findings concerning for malignancy. In particular, CT guidance has been used for biopsy of a variety of sites within the body.[1-4,8,15,16,20-23] This is largely attributed to an improved ability of the operator to identify the lesion and plan a trajectory for biopsy. CT-guided biopsy has been shown to be an effective tool in identifying pathology with relatively low risk and cost compared with open biopsy.[4,22,24] However, a frequently cited concern with CT scanning is the potential consequences of ionizing radiation, and there is much emphasis on limiting radiation to as low as reasonably achievable to obtain the necessary results whenever possible.[8,25]

Previous studies have demonstrated the utility of a low-dose CT technique for a variety of interventional procedures. Meng et al[15] performed biopsies of lung lesions at lower doses and found that a reduction in the measure of radiation dose, CT dose index, and DLP were possible without sacrificing diagnostic yield. Smith et al[8] were able to reduce the radiation dose to the chest during CT-guided percutaneous lung biopsies by greater than 95% (from DLP of 677.5 mGy·cm to 18.3 mGy·cm) without decreasing technical success or patient safety. Pediatric CT-guided bone biopsies have been performed using lower mAs and kVp techniques producing acceptable image quality and providing similar diagnostic yield compared with standard techniques.[16] A low-dose CT protocol has also been used in spinal pain interventions. One study found that a change in CT parameters to lower radiation dose resulted in an 86% reduction in total DLP (from 1458 mGy·cm to 199 mGy·cm) for CT-guided spine injection procedures for pain.[17] Artner et al[18] demonstrated that the dose related to CT-guided sacroiliac joint injections can be significantly reduced to levels of pulsed fluoroscopy without compromising needle placement into the joint.

In this study, we found a significantly reduced radiation dose as expressed by CTDIvol and DLP in patients undergoing CT-guided spine biopsies using a low-dose protocol compared with a regular-dose protocol. There was no significant difference in the total number of biopsy scans, procedure time, or in the diagnostic yield between the groups. To our knowledge, this is the first study demonstrating a significantly reduced patient exposure to ionizing radiation during CT-guided spine biopsies without sacrificing the quality, efficiency, and diagnostic yield of the procedure.

Although there was a significantly lower radiation exposure in the low-dose biopsy group compared with the regular-dose group, we predict that a DLP might be lowered even further by reducing tube voltage (mAs) and/or current (kVp), increasing the pitch and decreasing the scan range in the z-axis.[20,26-29] Intermittent axial scanning mode rather than helical mode and the use of a stationary CT table may further contribute to radiation dose reduction.[24,30]

A substantial proportion of radiation exposure comes from pre- and postbiopsy scans because they are designed to optimize soft tissue visualization for needle guidance and to exclude postbiopsy traumatic sequelae. In fact, 1 study showed that up to 90% of the total patient dose during biopsies was administered during the helical planning stage.[29] Therefore, prebiopsy diagnostic imaging should be carefully reviewed beforehand to determine whether repeat conventional dose scanning may be avoided during the procedure.[31] If a prebiopsy scan is necessary, a grid can be placed over the spinal level of interest before the first series of scans based on known anatomic landmarks.[31] Chintapalli et al[31] suggest that in low-risk CT-guided interventions, which may include some spine biopsies, regular-dose postbiopsy scans can be eliminated at the discretion of the radiologist. A low-dose protocol, as well as techniques to further reduce dose, should be familiar to the radiologist performing the procedures and technologist acquiring the images.[31]

Newer techniques have recently emerged to address image quality when reducing CT dose. These include iterative reconstruction models such as adaptive statistical iterative reconstruction and model-based iterative reconstruction.[9-14,32-40] Although these imaging algorithms provide an additional method for dose reduction in CT-guided procedures, their availability is currently limited to newer CT scanners for routine diagnostic CT imaging. The greater availability of the iterative reconstruction software over time may allow for increased operator comfort when evaluating low-dose images during CT-guided procedures, potentially further reducing the radiation dose.

This retrospective study did have some limitations. It was not randomized, and a single operator performed most of the CT-guided spine biopsies. Therefore, the reproducibility of the results using the low-dose protocol cannot be fully assessed in this study. In addition, it would be difficult to determine whether increasing comfort with the procedure may have contributed to a slightly greater efficiency of the procedure using a low-dose protocol. The retrospective nature of this study also limits assessment of factors related to operator scanning protocol adjustments in challenging biopsy cases.

CONCLUSIONS

Radiation exposure to patients undergoing CT-guided spinal biopsies can be optimized to reduce the overall dose during the examination. Low-dose CT-guided spine biopsies have a significantly lower total cumulative radiation exposure compared with regular-dose CT biopsies without significantly affecting procedural time or diagnostic tissue yield. A simple dose-reduction protocol can use reduction in mAs and kVp during the procedure. A number of additional modifications to image acquisitions can be made to reduce the dose. Our data show that a low-dose protocol should be considered as an alternative to regular-dose protocol when performing CT-guided spinal biopsies, allowing the operator to reduce ionizing radiation dose while maintaining overall quality and efficiency of the procedure.

ACKNOWLEDGMENTS

The authors thank Idoia Corcuera-Solano, MD, for help with statistical analysis.

Disclosures: Bradley Delman—*UNRELATED: Consultancy:* Bayer Medrad,* *Comments*: Consultancy for contrast injection systems. Lawrence Tanenbaum—

UNRELATED: Payment for Lectures (including service on Speakers Bureaus): GE, Siemens. *Money paid to the institution.

REFERENCES

1. Brugieres P, Revel MP, Dumas JL, et al. **CT-guided vertebral biopsy. A report of 89 cases.** *J Neuroradiol* 1991;18:351–59
2. Lis E, Bilsky MH, Pisinski L, et al. **Percutaneous CT-guided biopsy of osseous lesion of the spine in patients with known or suspected malignancy.** *AJNR Am J Neuroradiol* 2004;25:1583–88
3. Kornblum MB, Wesolowski DP, Fischgrund JS, et al. **Computed tomography-guided biopsy of the spine. A review of 103 patients.** *Spine (Phila Pa 1976)* 1998;23:81–85
4. Rimondi E, Staals EL, Errani C, et al. **Percutaneous CT-guided biopsy of the spine: results of 430 biopsies.** *Eur Spine J* 2008;17:975–81
5. Coursey C, Frush D. **CT and radiation: what radiologists should know.** *Appl Radiol* 2008;37:22–29
6. Brenner DJ, Hall EJ. **Computed tomography—an increasing source of radiation exposure.** *N Engl J Med* 2007;357:2277–84
7. Huda W, Mettler FA. **Volume CT dose index and dose-length product displayed during CT: what good are they?** *Radiology* 2011;258:236–42
8. Smith JC, Jin DH, Watkins GE, et al. **Ultra-low-dose protocol for CT-guided lung biopsies.** *J Vasc Interv Radiol* 2011;22:431–36
9. Corcuera-Solano I, Doshi AH, Noor A, et al. **Repeated head CT in the neurosurgical intensive care unit: feasibility of sinogram-affirmed iterative reconstruction-based ultra-low-dose CT for surveillance.** *AJNR Am J Neuroradiol* 2014;35:1281–87
10. Mathieu KB, Ali H, Fox PS, et al. **Radiation dose reduction for CT lung cancer screening using ASIR and MBIR: a phantom study.** *J Appl Clin Med Phys* 2014;15:4515
11. Flicek KT, Hara AK, Silva AC, et al. **Reducing the radiation dose for CT colonography using adaptive statistical iterative reconstruction: a pilot study.** *AJR Am J Roentgenol* 2010;195:126–31
12. Kambadakone AR, Chaudhary NA, Desai GS, et al. **Low-dose MDCT and CT enterography of patients with Crohn disease: feasibility of adaptive statistical iterative reconstruction.** *AJR Am J Roentgenol* 2011;196:W743–52
13. Shuman WP, Green DE, Busey JM, et al. **Model-based iterative reconstruction versus adaptive statistical iterative reconstruction and filtered back projection in liver 64-MDCT: focal lesion detection, lesion conspicuity, and image noise.** *AJR Am J Roentgenol* 2013;200:1071–76
14. Becce F, Ben Salah Y, Verdun FR, et al. **Computed tomography of the cervical spine: comparison of image quality between a standard-dose and a low-dose protocol using filtered back-projection and iterative reconstruction.** *Skeletal Radiol* 2013;42:937–45
15. Meng XX, Kuai XP, Dong WH, et al. **Comparison of lung lesion biopsies between low-dose CT-guided and conventional CT-guided techniques.** *Acta Radiol* 2013;54:909–15
16. Patel AS, Soares B, Courtier J, et al. **Radiation dose reduction in pediatric CT-guided musculoskeletal procedures.** *Pediatr Radiol* 2013;43:1303–08
17. Shepherd TM, Hess CP, Chin CT, et al. **Reducing patient radiation dose during CT-guided procedures: demonstration in spinal injections for pain.** *AJNR Am J Neuroradiol* 2011;32:1776–82
18. Artner J, Cakir B, Reichel H, et al. **Radiation dose reduction in CT-guided sacroiliac joint injections to levels of pulsed fluoroscopy: a comparative study with technical considerations.** *J Pain Res* 2012;5:265–69
19. Kröpil P, Lanzman RS, Walther C, et al. **Dose reduction and image quality in MDCT of the upper abdomen: potential of an adaptive post-processing filter** [in German]. *Rofo* 2010;182:248–53
20. Kloeckner R, dos Santos DP, Schneider J, et al. **Radiation exposure in CT-guided interventions.** *Eur J Radiol* 2013;82:2253–57
21. Monfardini L, Preda L, Aurilio G, et al. **CT-guided bone biopsy in cancer patients with suspected bone metastases: retrospective review of 308 procedures.** *Radiol Med* 2014;119:852–60
22. Gogna A, Peh WC, Munk PL. **Image-guided musculoskeletal biopsy.** *Radiol Clin North Am* 2008;46:455–73, v
23. Hau A, Kim I, Kattapuram S, et al. **Accuracy of CT-guided biopsies in 359 patients with musculoskeletal lesions.** *Skeletal Radiol* 2002;31:349–53
24. Leng S, Christner JA, Carlson SK, et al. **Radiation dose levels for interventional CT procedures.** *AJR Am J Roentgenol* 2011;197:W97–103
25. Lucey BC, Varghese JC, Hochberg A, et al. **CT-guided intervention with low radiation dose: feasibility and experience.** *AJR Am J Roentgenol* 2007;188:1187–94
26. Kalra MK, Maher MM, Toth TL, et al. **Strategies for CT radiation dose optimization.** *Radiology* 2004;230:619–28
27. Tsalafoutas IA, Tsapaki V, Triantopoulou C, et al. **CT-guided interventional procedures without CT fluoroscopy assistance: patient effective dose and absorbed dose considerations.** *AJR Am J Roentgenol* 2007;188:1479–84
28. Smith AB, Dillon WP, Lau BC, et al. **Radiation dose reduction strategy for CT protocols: successful implementation in neuroradiology section.** *Radiology* 2008;247:499–506
29. Sarti M, Brehmer WP, Gay SB. **Low-dose techniques in CT-guided interventions.** *Radiographics* 2012;32:1109–19; discussion 1119–20
30. Chang AL, Schoenfeld AH, Brook AL, et al. **Radiation dose for 345 CT-guided interlaminar lumbar epidural steroid injections.** *AJNR Am J Neuroradiol* 2013;34:1882–86
31. Chintapalli KN, Montgomery RS, Hatab M, et al. **Radiation dose management: part 1, minimizing radiation dose in CT-guided procedures.** *AJR Am J Roentgenol* 2012;198:W347–51
32. McKnight CD, Watcharotone K, Ibrahim M, et al. **Adaptive statistical iterative reconstruction: reducing dose while preserving image quality in the pediatric head CT examination.** *Pediatr Radiol* 2014;44:997–1003
33. Hara AK, Paden RG, Silva AC, et al. **Iterative reconstruction technique for reducing body radiation dose at CT: feasibility study.** *AJR Am J Roentgenol* 2009;193:764–71
34. Silva AC, Lawder HJ, Hara A, et al. **Innovations in CT dose reduction strategy: application of the adaptive statistical iterative reconstruction algorithm.** *AJR Am J Roentgenol* 2010;194:191–99
35. Yanagawa M, Gyobu T, Leung AN, et al. **Ultra-low-dose CT of the lung: effect of iterative reconstruction techniques on image quality.** *Acad Radiol* 2014;21:695–703
36. Deák Z, Grimm JM, Treitl M, et al. **Filtered back projection, adaptive statistical iterative reconstruction, and a model-based iterative reconstruction in abdominal CT: an experimental clinical study.** *Radiology* 2013;266:197–206
37. Pickhardt PJ, Lubner MG, Kim DH, et al. **Abdominal CT with model-based iterative reconstruction (MBIR): initial results of a prospective trial comparing ultralow-dose with standard-dose imaging.** *AJR Am J Roentgenol* 2012;199:1266–74
38. Sagara Y, Hara AK, Pavlicek W, et al. **Abdominal CT: comparison of low-dose CT with adaptive statistical iterative reconstruction and routine-dose CT with filtered back projection in 53 patients.** *AJR Am J Roentgenol* 2010;195:713–19
39. Prakash P, Kalra MK, Kambadakone AK, et al. **Reducing abdominal CT radiation dose with adaptive statistical iterative reconstruction technique.** *Invest Radiol* 2010;45:202–10
40. Mitsumori LM, Shuman WP, Busey JM, et al. **Adaptive statistical iterative reconstruction versus filtered back projection in the same patient: 64 channel liver CT image quality and patient radiation dose.** *Eur Radiol* 2012;22:138–43

Physician Self-Referral and Imaging Use Appropriateness: Negative Cervical Spine MRI Frequency as an Assessment Metric

T.J. Amrhein, B.E. Paxton, M.P. Lungren, N.T. Befera, H.R. Collins, C. Yurko, J.D. Eastwood, and R.K. Kilani

ABSTRACT

BACKGROUND AND PURPOSE: Imaging self-referral is increasingly cited as a contributor to diagnostic imaging overuse. The purpose of this study was to determine whether ownership of MR imaging equipment by ordering physicians influences the frequency of negative cervical spine MR imaging findings.

MATERIALS AND METHODS: A retrospective review was performed of 500 consecutive cervical spine MRIs ordered by 2 separate referring-physician groups serving the same geographic community. The first group owned the scanners used and received technical fees for their use, while the second group did not. Final reports were reviewed, and for each group, the percentage of negative study findings and the frequency of abnormalities were calculated. The number of concomitant shoulder MRIs was recorded.

RESULTS: Five hundred MRIs meeting inclusion criteria were reviewed (250 with financial interest, 250 with no financial interest). Three hundred fifty-two had negative findings (190 with financial interest, 162 with no financial interest); there were 17.3% more scans with negative findings in the financial interest group ($P = .006$). Among scans with positive findings, there was no significant difference in the mean number of lesions per scan, controlled for age (1.90 with financial interest, 2.19 with no financial interest; $P = .23$). Patients in the financial interest group were more likely to undergo concomitant shoulder MR imaging (24 with financial interest, 11 with no financial interest; $P = .02$).

CONCLUSIONS: Cervical spine MRIs referred by physicians with a financial interest in the imaging equipment used were significantly more likely to have negative findings. There was otherwise a highly similar distribution and severity of disease between the 2 patient samples. Patients in the financial interest group were more likely to undergo concomitant shoulder MR imaging.

ABBREVIATIONS: FI = financial interest; NFI = no financial interest; OEDS = order entry decision support

United States health care expenditures grew 3.9% in 2011, reaching $2.7 trillion or an estimated 17.9% of the gross domestic product.[1] Health care spending is projected to continue to grow in 2012 and 2013 at 4.2% and 3.8%, respectively.[2] Diagnostic imaging costs remain a large component of annual health care expenditures and have, therefore, been targeted in an effort to contain costs. While the proportion of growth in health care expenditures attributable to diagnostic imaging use has decreased considerably in recent years, medical imaging use among nonradiologist physicians continues to increase at a growth rate twice that of radiologists and remains a significant contributor to higher imaging use and cost.[3]

Imaging self-referral is defined as physicians referring their own patients for imaging to facilities in which they or their partners have financial interests.[4-6] In 1991, Medicare fraud-and-abuse legislation was passed in an effort to curb the rising tide of medical imaging self-referral. Commonly referred to as the "Stark II law" after the primary author Representative Fortney "Pete" Stark (Democrat, California), the legislation bans physician referrals to entities in which they have a financial relationship.[7] However, the inclusion of an in-office ancillary services exception (created with patient convenience in mind) permits physicians to both order and provide advanced imaging services for patients in their office. As a result, despite the presence of the Stark law, physician self-referral of medical imaging has continued to grow substantially.[8]

Received April 21, 2014; accepted after revision June 2.

From the Department of Radiology (T.J.A., B.E.P., N.T.B., C.Y., J.D.E., R.K.K.), Duke University Medical Center, Durham, North Carolina; Department of Radiology (M.P.L.), Stanford University School of Medicine, Stanford, California; and Center for Biomedical Imaging (H.R.C.), Medical University of South Carolina, Charleston, South Carolina.

Please address correspondence to Timothy J. Amrhein, MD, Department of Radiology, Duke University Medical Center, DUMC Box 3808, Durham, NC 27710; e-mail: timothy.amrhein@duke.edu

http://dx.doi.org/10.3174/ajnr.A4076

Critics of the practice of self-referral have asserted that it leads to overuse of diagnostic imaging and is, therefore, an important contributor to rising health care costs. In support of this argument, several previously published studies have demonstrated that the practice of imaging self-referral is increasing, that physicians who own diagnostic imaging equipment are more likely to refer their patients for imaging at facilities in which they have a financial interest, and that self-referral by nonradiologist physicians leads to higher overall imaging use.[9-18] However, despite the growing body of literature documenting these findings, the conclusion that self-referral leads to inappropriate medical imaging use, or overuse, remains a topic of debate. This is, in part, secondary to the inherent challenges researchers face in demonstrating the similarity between 2 compared groups of patients, particularly with regard to rates and severity of disease, insurance status, and clearly discerning the financial arrangements of imaging equipment ownership.

Criticisms of prior studies linking imaging self-referral to overuse have focused on their inadequate consideration of use appropriateness. Determining the appropriateness of medical imaging use is a complex and challenging task confounded by multiple factors, including patient population (payer and insurance status and regional geographic differences), clinical setting (hospital versus outpatient practice), disease prevalence (young versus elderly), referral biases (eg, specialist versus primary care), diagnostic interpretation inhomogeneity (discordant "grading" of lesions) and terminology, or skill differences among interpreting radiologists. In many scenarios, these factors become uncontrollable variables that complicate attempts to compare the appropriateness of referrals for medical imaging between groups of physicians, including between groups with and without financial relationships to the medical imaging equipment. Prior effort has evaluated differences in the volume of patients referred for medical imaging between the 2 groups based on International Classification of Diseases-9 diagnosis codes and use per patient encounter. This approach has flaws because both the proportion of examinations with normal findings and the differences in prevalence and severity of disease between the 2 compared groups are not evaluated. Without this additional information, comparisons of relative use may be feasible, but not the appropriateness of imaging use.

Comparing the proportion of imaging examinations with negative findings, after controlling for potential confounding variables, would allow an accurate assessment of the differences in imaging referral patterns between the 2 physician groups (financially incentivized and nonfinancially incentivized). This would not only validate previously published studies on imaging appropriateness but also add to the existing body of literature addressing the issue of self-referral. Furthermore, an analysis of the prevalence and severity of imaging-confirmed pathology between these groups may serve as a surrogate for disease prevalence and overall severity within the 2 different patient populations, because groups with equal disease prevalence and severity should manifest an equivalent number of positive imaging findings.

The purpose of this study was to determine whether ownership of MR imaging equipment by an ordering physician group affects the use of cervical spine MR imaging. This was accomplished by comparing the likelihood of negative cervical spine MR imaging findings and the cervical spine MR imaging pathology rates between the 2 groups. We wished to test the null hypothesis that no such difference exists and that usage patterns are the same. This was accomplished via evaluation of 2 subordinate hypotheses: 1) There is no difference in the rate of examinations with negative findings between self-referred and non-self-referred MR imaging examinations, and 2) among examinations with positive findings, there are no differences in the prevalence of individual pathology subtypes between the 2 groups. We considered that no difference in the first would indicate that no excess ordering of examinations occurred in either group and that no difference in the second would mean that the 2 patient groups were highly similar with regard to the rate and type of pathology.

MATERIALS AND METHODS

This retrospective Health Insurance Portability and Accountability Act–compliant study was approved by the institutional review board of the appropriate medical center, and a waiver of informed consent was granted. Chronologically consecutive cervical spine MR imaging reports were reviewed from February to September of 2009 in 1 academic musculoskeletal imaging practice, consisting of 5 attending radiologists. Each interpreting radiologist was a subspecialty-trained musculoskeletal imager, with a mean of 14 years (range, 5–23 years) of experience exclusively in musculoskeletal radiology. MR imaging examinations that met the inclusion criteria were analyzed from each of 2 groups in tandem so that each cohort would, by design, have the same number of studies. The first group was ordered by orthopedists who had imaging performed on MR imaging equipment owned by that same orthopedic group (financial interest [FI]). The second group of scans was ordered by a different group of orthopedists in the same community who did not own or have other financial interest in the MR imaging equipment used (no financial interest [NFI]). The physical locations of the referring physician group outpatient clinical practices were recorded. The residency training institution and years in practice of the referring physicians were also recorded for each group. The source of the data base, all physician groups, and identifying details including locations are purposely kept anonymous.

All cervical spine MR imaging examinations from both referring physician groups (FI and NFI) were performed at 1.5T field strength using identical protocols and were interpreted by the same subspecialty musculoskeletal radiology practice. The interpreting radiology practice had no financial interest in the imaging equipment used for either patient group. Patients with prior cervical spine surgery or prior cervical spine MR imaging examinations were excluded to help eliminate the potential confounding effects of prior surgery and postoperative changes and to control for any differences in the follow-up practice patterns between the 2 groups. Inclusion criteria were first-time cervical spine MR imaging examinations performed as an outpatient. Final reports were reviewed and examinations with the following findings were considered positive: "moderate-to-severe" or "severe" spinal canal stenosis, moderate-to-severe or severe neuroforaminal narrowing, moderate-to-severe or severe facet degenerative changes, moderate-to-severe or severe disk herniation contacting the cord,

Distribution of sex

Sex	Financial Interest	No Financial Interest
Female	162	146
Male	88	104
Total	250	250

and osseous abnormalities (the most common being fracture). These findings were chosen because they represent significant pathology that is more likely to be an etiology of neck pain for which treatment may be considered. The number of disk interspace levels exhibiting ≥1 of the above findings was recorded. Patient age and sex were recorded, as was the acquisition of concomitant shoulder MR imaging examinations.

The percentage of scans with negative findings was tabulated for each group. Because it was possible for scans with positive findings to contain multiple lesions and that each of these lesions could represent an etiology for neck pain or radicular symptoms, the total number of lesions per scan was calculated for each of the examinations with positive findings in each group.

Statistical Analysis

Using a significance threshold of $\alpha = .05$, 2-tailed, we performed a power analysis that showed that we would have >90% power to detect a difference in rates of scans with negative findings of 50% ($n = 250$) and 35% ($n = 250$) in conditions comparing financial interest with no financial interest.

In 2-sample comparisons when covarying for age was not needed, χ^2 tests were used for the binomial variables; Fisher exact tests, for comparisons with fewer than 5 observations in a cell; and *t* tests, for the continuous variables. Logistic regression was used to predict negative scan outcomes by using age as a covariate. ANCOVA was used to identify mean differences in characteristics of scans with positive findings with age as a covariate. χ^2 and *t* test *P* values reported in this article are 2-tailed, and statistical significance was considered at a threshold of $P < .05$. All statistical analyses were conducted by using SPSS 21 and 22 (IBM, Armonk, New York).

RESULTS

Five hundred examinations (250 in the FI group and 250 in the NFI group) that met the inclusion criteria during the study period were evaluated. There was no statistically significant difference in the distribution of sex between the 2 groups ($P = .14$) (Table). There was a statistically significant difference in mean patient age between the 2 groups, 48.4 years (range, 13–78 years) for FI and 54.3 years (range, 15–86 years) for NFI ($P < .001$). Given this difference and the known propensity for increased frequency and severity of degenerative changes with increased age, ANCOVA subanalyses were conducted by using age as a covariate.

Negative Examination Findings

Among the 500 examinations, 352 had negative findings (190 in FI and 162 in NFI). There were 17.3% more scans with negative findings in the FI group, a difference that was statistically significant ($P = .006$) (Fig 1).

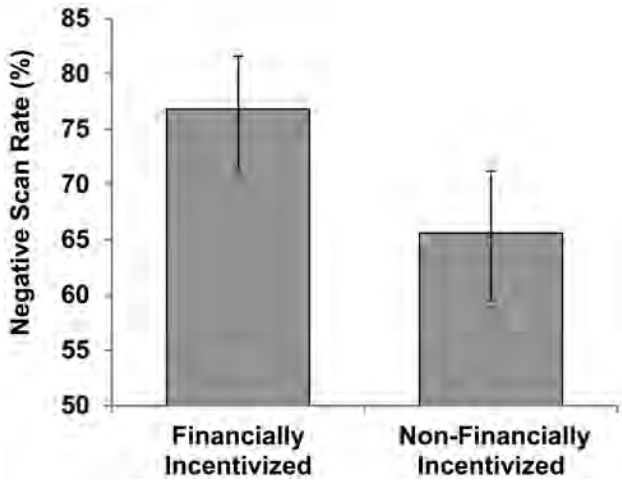

FIG 1. Negative cervical spine MR imaging rates (with 95% CIs). There was a 17.3% increase in the negative examination rate in the FI group ($P = .006$).

Positive Examination Findings

Among examinations with positive findings, there was no statistically significant difference in the mean number of lesions per scan between the NFI ($n = 2.19$) and FI ($n = 1.90$) groups ($P = .23$) or in the mean number of positive levels per scan between the 2 groups (NFI = 1.59, FI = 1.56, $P = .80$), adjusted for age. If one compared the frequencies of the evaluated abnormality subtypes, there was no significant difference in the mean number of neuroforaminal stenoses (NFI = 1.09, FI = 0.87; $P = .32$), disk abnormalities (NFI = 0.75, FI = 0.81; $P = .68$), or facet degenerative changes (NFI = 0.26, FI = 0.23; $P = .81$) per scan, adjusted for age. The number of examinations containing descriptors of canal stenosis was too small for meaningful analysis (NFI = 5, FI = 1).

Concurrent Shoulder MR Imaging

Patients in the FI group were significantly more likely to undergo concurrent shoulder MR imaging while undergoing cervical spine MR imaging than those in the NFI group: 24 and 11, respectively ($P = .02$) (Fig 2). Among patients undergoing concomitant shoulder MRI, there was a proportionally greater number of patients with cervical spine MRIs with normal findings in the FI group (23 of 24, 95.8%) in comparison with the NFI group (8 of 11, 72.7%) ($P = .08$). A greater percentage of concurrent shoulder MRIs obtained in the FI group had negative findings (FI: 8 of 24, 33.3%; NFI: 1 of 11, 9.1%) ($P = .22$). When patients underwent concurrent shoulder and cervical spine MR imaging and the cervical spine MR imaging findings were negative, all of the NFI group shoulder scans had positive findings (8 of 8), while only 14 of the 23 FI cases had positive findings ($P = .003$).

Referring Physician Characteristics

Most orthopedic clinics for the FI and NFI groups were within close geographic proximity to each other, because all were located within the same 50-mile radius. Nearly equal percentages of the referring clinicians from each group (54% FI, 53% NFI) trained at a single common orthopedic residency program ($P = 1.0$). Both groups had similar proportions of physicians with subspecialty or fellowship training ($P = .076$), and both were similar in size. Fi-

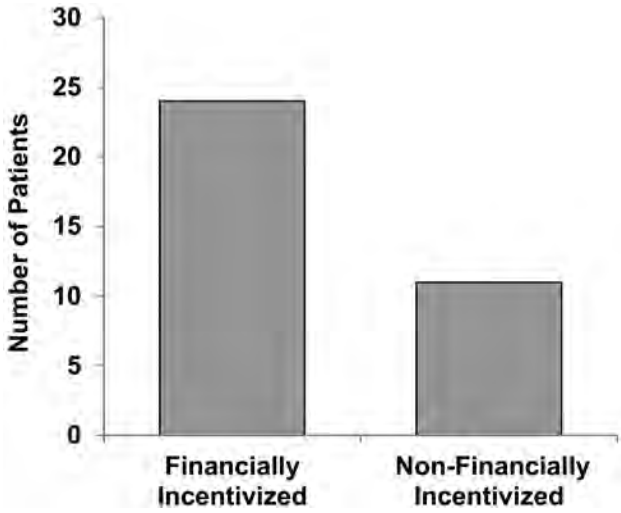

FIG 2. The number of concurrent shoulder MR imaging scans obtained. Patients in the FI group were significantly more likely to undergo concurrent shoulder MR imaging ($P = .02$).

nally, there were comparable mean years of practice between both groups (14.2 years for NFI, 14.1 years for FI; $P = .526$).

DISCUSSION

The purpose of this study was to evaluate the differences in the use of cervical spine MR imaging between 2 groups of physicians, 1 with a financial interest in the imaging equipment used and 1 without. Our results demonstrate a 17.3% increased negative examination rate among patients referred by the physician group with a financial interest in the imaging equipment used ($P = .006$). Therefore, we reject the null hypothesis number 1. This suggests that there may be a reduced threshold for obtaining cervical spine MR imaging in the presence of a financial incentive, whether conscious or unconscious.

A wealth of literature exists on the topic of physician imaging self-referral. Many of these prior studies have attempted to compare use between 2 physician groups based on Medicare billing data.[19,20] Criticism of this method has often centered on an inability to adequately assess the appropriateness of imaging use and on the failure of the method to account for the many complexities driving use, such as differences in disease severity between patient groups. Indeed, accurately evaluating the relationship between imaging self-referral and financial incentive is extremely challenging and would require consideration of a multitude of factors including patient populations, referral biases (specialist versus primary care), clinical setting (outpatient versus hospital), disease prevalence, variations in diagnostic standards (discordant "grading" of severity), differences in imaging protocols and equipment, and differences in terminology used by interpreting radiologists.

Our study used a recently developed method to examine imaging self-referral that is focused on use appropriateness rather than a simple count of use per patient. Rather than reviewing billing data or imaging indications, we analyzed the final diagnoses on imaging examinations, thereby helping to control for differences in the severity of disease between different referring physician groups (FI and NFI). This method for comparing patient cohort similarity was used in several prior publications.[21-23] Furthermore, a single small academic radiology group interpreted all examinations from both referring physician groups; this helps to control for radiologist interreader variation. Additionally, because this radiology group did not own any of the imaging equipment, there was no confounding financial interest.

We found no statistically significant difference in the average number of abnormalities per study with positive findings or in the number of positive levels per scan between the NFI and FI groups. Additionally, there was no significant difference in the rates of neuroforaminal stenosis, disk bulge, or facet degenerative change. This similarity in the abnormality rate per positive scan confirms the null hypothesis number 2 and suggests that the 2 patient groups had a comparable prevalence of pathology. Assuming that abnormalities found on studies with positive findings act as surrogates for the disease prevalence within both patient populations, the 2 groups appear to significantly differ only in their rates of cervical spine MR imaging studies with negative findings. We suspect that the divergent negative examination rate may reflect differences in decision-making in patients presenting with cervicalgia, particularly in regard to the threshold for acquiring imaging.

It is of particular interest that the FI group patients were more likely to receive concomitant shoulder MR imaging ($P = .02$). Because it is often challenging to differentiate between a cervicogenic and rotator cuff etiology for upper extremity pain, this clinical challenge was likely present in both patient populations.[24] If patients in the FI group had a larger prevalence of shoulder pathology than the NFI group, this might lead to an increased rate of positive concomitant shoulder MR imaging findings. However, this was not the case. In fact, patients in the FI group were more likely to have normal findings on shoulder MRI (33.3% for FI versus 9.1% for NFI, $P = .22$). Furthermore, comparing the subgroups of patients that underwent both cervical spine and shoulder MR imaging revealed that FI patients were also more likely to have negative cervical spine MR imaging findings. Finally, 9 patients in the FI group had negative findings on both examinations versus no patients in the NFI group. These findings, while somewhat limited by the small sample size, demonstrate increased use of concomitant shoulder MR imaging in the FI group and suggest a trend toward considerably increased negative examination rates in keeping with the cervical spine MR imaging data.

There were several limitations to this investigation. First, the inherent complexities of both cervicalgia and cervical spine degenerative changes make it difficult to define a "true-positive" examination. This challenge is pervasive throughout daily clinical practice. For instance, confirming a causal relationship between suspected imaging findings and a patient's pain often requires feedback in the form of targeted treatment. While even "mild" degenerative changes can be symptomatic, an objective demarcation for positive examination findings was a prerequisite to investigation. It is possible that establishing a different threshold for positive examination findings or considering alternative pathologies could have led to different results. However, we chose to define severe degenerative change as positive because these findings are more likely to be causes of pain that are clinically important and result in therapy, such as steroid injections or surgery. A second limitation is the relatively limited number of concurrent

shoulder MR imaging examinations, hindering the ability to achieve statistical significance in the analysis of components of this subset of our data. Additionally, we did not compare insurance status, ethnicity, or socioeconomic status between the 2 groups because these data were not available for review. Finally, there was a statistically significant difference in age between the 2 groups (54.3 for NFI, 48.4 for FI). This required the use of ANCOVA with age as a covariate to account for the known increased prevalence of spine degenerative changes with advanced age.

Despite these limitations, this study clearly demonstrates an increased negative examination rate in the physician group that collected technical fees for the imaging equipment used. We believe that this apparent bias, whether conscious or unconscious, is an important consideration when health care costs, more specifically medical imaging costs, are analyzed. An excessive negative scan rate on the order of 15%–20% is a considerable financial burden when extrapolated nationally. To date, the across-the-board cuts to imaging reimbursements have done nothing to address this bias and have, instead, placed future access to advanced imaging in jeopardy. Similar findings have previously been reported in the lumbar spine, shoulder, and knee.[21-23] These findings require validation across other geographic regions and medical practices.

The observed bias toward increased use of cervical spine MR imaging does not, by itself, prove intended overuse for profit. It is possible that other factors are at play influencing 1 physician group to image more frequently. Such considerations might include an imaging-intensive practice pattern less reliant on physical examination findings, perhaps secondary to differences in training. Similarly, one might purport that younger physicians may be more familiar with the use of MR imaging in diagnostic evaluations because it was part of their training, while more senior physicians may be more comfortable with alternative diagnostic methodologies (physical examination, myelography). Many of these physician-related considerations may not be significant factors in this study because the 2 groups were highly similar in terms of mean years of practice and number of trained subspecialists and had nearly equal percentages of physicians who trained at the same residency program.

Physician order entry decision support (OEDS) software has been proposed as a mechanism for decreasing the incidence of unnecessary imaging examinations. OEDS has proved success and could potentially reduce the rate of negative examination findings in both referral groups by providing recommendations according to the American College of Radiology appropriateness criteria for cervical spine MR imaging.[25] However, in most cases, OEDS software does not include "hard stops" but rather allows referring physicians to override recommendations. Therefore, the FI and NFI groups would be able to continue to order examinations as they think appropriate. Furthermore, if practice patterns for either group involve order placement by clinic office staff, the appropriateness recommendations may be blindly overridden to follow attending physician requests.[26] For these reasons, it is difficult to discern how the addition of OEDS would influence the ordering practice patterns of our referral groups.

CONCLUSIONS

This study demonstrates a significantly increased negative cervical spine MR imaging rate in patients referred by physicians with a financial interest in the imaging equipment used in comparison with those patients referred by physicians without such an interest. This increased negative examination rate occurred despite similar referring physician characteristics, patient demographics, and cervical spine pathology burden. Further study is warranted among a larger sample of physician practices and in different geographic regions to ascertain the extent of the issue and to further investigate the utility of comparing pathology frequencies between practices as a metric for imaging use appropriateness.

REFERENCES

1. Hartman M, Martin AB, Benson J, et al. **National health spending in 2011: overall growth remains low, but some payers and services show signs of acceleration.** *Health Aff (Millwood)* 2013;32:87–99
2. Centers for Medicare and Medicaid Services. National Health Expenditure Projections 2011–2021. http://www.cms.gov/Research-Statistics-Data-and-Systems/Statistics-Trends-and-Reports/NationalHealthExpendData/Downloads/Proj2011PDF.pdf. Accessed April 4, 2014
3. Levin DC, Rao VM, Parker L, et al. **Bending the curve: the recent marked slowdown in growth of noninvasive diagnostic imaging.** *AJR Am J Roentgenol* 2011;196:W25–29
4. Mitchell JM. **Utilization trends for advanced imaging procedures: evidence from individuals with private insurance coverage in California.** *Med Care* 2008;46:460–66
5. Armstrong D. **MRI and CT centers offer doctors way to profit on scans.** *The Wall Street Journal*. May 5, 2005. http://online.wsj.com/news/articles/SB111498587452921637. Accessed March 6, 2012
6. Thompson DF. **Understanding financial conflicts of interest.** *N Engl J Med* 1993;329:573–76
7. Omnibus Budget Reconciliation Act of 1989. Pub L No. 101–239, §6204, 103 Stat 2106, 2236–43 (1989)
8. Hillman BJ, Goldsmith J. **Imaging: the self-referral boom and the ongoing search for effective policies to contain it.** *Health Aff (Millwood)* 2010;29:2231–36
9. Medicare Payment Advisory Commission. *A DATA BOOK: Healthcare Spending and the Medicare Program*. Washington, DC: MedPAC; 2008
10. United States. General Accounting Office. *Referrals to Physician-Owned Imaging Facilities Warrant HCFA's Scrutiny: Government Accounting Office (GAO)—Report to the Chairman, Subcommittee on Health, Committee on Ways and Means, House of Representatives/United States General Accounting Office*. Washington, DC: GAO/HEHS; 1994
11. Gazelle GS, Halpern EF, Ryan HS, et al. **Utilization of diagnostic medical imaging: comparison of radiologist referral versus same-specialty referral.** *Radiology* 2007;245:517–22
12. Hillman BJ, Joseph CA, Mabry MR, et al. **Frequency and costs of diagnostic imaging in office practice: a comparison of self-referring and radiologist-referring physicians.** *N Engl J Med* 1990;323:1604–08
13. Hillman BJ, Olson GT, Griffith PE, et al. **Physicians' utilization and charges for outpatient diagnostic imaging in a Medicare population.** *JAMA* 1992;268:2050–54
14. Kouri BE, Parsons RG, Alpert HR. **Physician self-referral for diagnostic imaging: review of the empiric literature.** *AJR Am J Roentgenol* 2002;179:843–50
15. Levin DC, Rao VM. **Turf wars in radiology: updated evidence on the relationship between self-referral and the overutilization of imaging.** *J Am Coll Radiol* 2008;5:806–10
16. Levin DC, Rao VM, Parker L, et al. **Ownership or leasing of MRI facilities by nonradiologist physicians is a rapidly growing trend.** *J Am Coll Radiol* 2008;5:105–09
17. Litt AW, Ryan DR, Batista D, et al. **Relative procedure intensity with**

self-referral and radiologist referral: extremity radiography. *Radiology* 2005;235:142–47
18. Radecki SE, Steele JP. **Effect of on-site facilities on use of diagnostic radiology by non-radiologists.** *Invest Radiol* 1990;25:190–93
19. Sharpe RE, Nazarian LN, Parker L, et al. **Dramatically increased musculoskeletal ultrasound utilization from 2000 to 2009, especially by podiatrists in private offices.** *J Am Coll Radiol* 2012;9:141–46
20. Hughes DR, Sunshine JH, Bhargavan M, et al. **Physician self-referral for imaging and the cost of chronic care for Medicare beneficiaries.** *Med Care* 2011;49:857–64
21. Amrhein TJ, Lungren MP, Paxton BE, et al. **Journal Club: shoulder MRI utilization—relationship of physician MRI equipment ownership to negative study frequency.** *AJR Am J Roentgenol* 2013; 201:605–10
22. Lungren MP, Amrhein TJ, Paxton BE, et al. **Physician self-referral: frequency of negative findings at MR imaging of the knee as a marker of appropriate utilization.** *Radiology* 2013;269:810–15
23. Paxton BE, Lungren MP, Srinivasan RC, et al. **Physician self-referral of lumbar spine MRI with comparative analysis of negative study rates as a marker of utilization appropriateness.** *AJR Am J Roentgenol* 2012;198:1375–79
24. Pateder DB, Berg JH, Thal R. **Neck and shoulder pain: differentiating cervical spine pathology from shoulder pathology.** *J Surg Orthop Adv* 2009;18:170–74
25. Blackmore CC, Mecklenburg RS, Kaplan GS. **Effectiveness of clinical decision support in controlling inappropriate imaging.** *J Am Coll Radiol* 2011;8:19–25
26. Rosenthal DI, Weilburg JB, Schultz T, et al. **Radiology order entry with decision support: initial clinical experience.** *J Am Coll Radiol* 2006;3:799–806

Genetics of Amyotrophic Lateral Sclerosis

J. Gorodenker and L.M. Levy

ABBREVIATIONS: ALS = amyotrophic lateral sclerosis; UMN = upper motor neuron; LMN = lower motor neuron; fALS = familial amyotrophic lateral sclerosis; sALS = sporadic amyotrophic lateral sclerosis

Amyotrophic lateral sclerosis (ALS) reflects a heterogeneous group of neurodegenerative disorders unified by loss of motor neurons in the primary motor cortex, brain stem, and spinal cord, resulting in progressive muscle weakness. Typical ALS (representing 80% of cases) is a limb-predominant disease characterized by a combination of upper motor neuron (UMN) and lower motor neuron (LMN) symptoms predominantly affecting the extremities. ALS may also present in a bulbar form (20%), with early symptoms involving muscles innervated by the lower brain stem, affecting articulation, chewing, and swallowing. While the disease may chronically persist in such form, it usually progresses to the generalized muscle weakness of typical ALS.[1,2]

Patients with ALS are more often male and typically present in late middle age. ALS is often rapidly progressive, and most patients die within 3–5 years of onset; however considerable variability exists. ALS is divided into sporadic and familial forms and may be classified by body region of onset, relative mix of UMN and LMN involvement, and rate of progression. Many well-characterized genetic variants exist, and subtypes can vary significantly in usual presentation, including age of onset, rate of progression, and degree of cognitive impairment.[1,3]

The overall incidence of the disease is approximately 1–2 cases per 100,000 individuals per year, and the prevalence is 4–6 cases per 100,000 worldwide. ALS is diagnosed clinically by El Escorial (World Federation of Neurology) Criteria, with neuroimaging and neurophysiologic studies predominantly used to exclude other diagnostic entities.[4,5] Management is largely supportive; however, delay in progression and ventilator dependence has been achieved in selected patients by use of riluzole, an indirect glutamate receptor antagonist and selective blocker of TTX-sensitive sodium channels.[1]

From George Washington University Medical Center, Washington, DC.

Please address correspondence to Joseph Gorodenker, MD, Diagnostic Radiology, George Washington University Hospital, 900 23rd St NW, Washington, DC 20037; e-mail: josephgoro@gmail.com

http://dx.doi.org/10.3174/ajnr.A3831

The phenotypic heterogeneity of ALS presents several difficulties; the diagnosis of ALS is made on clinical grounds and is fundamentally uncertain, ranging from "suspected" to "possible," to "probable" to "definite." There currently is no stated role for neuroimaging to support the diagnosis of ALS; however, diagnosis requires absence of neuroimaging evidence of other disease processes that may explain the observed clinical and electrophysiological signs.[4,5]

Absence of a sensitive and specific test for ALS often results in significant delay of diagnosis, which ranges from 13–18 months from onset of the disease or longer in patients who present with isolated LMN signs.[5] Furthermore, delayed diagnosis restricts the inclusion of patients in clinical trials and limits early initiation of potential neuroprotective treatments. The variability of ALS progression also limits assessment of potential treatment effects.

TDP-43 is an emergent diagnostic marker of ALS. The presence of TDP-43–positive inclusions in degenerating motor neurons appears to be a specific (>95%) albeit modestly sensitive (<60%) diagnostic feature of ALS; however, this biomarker remains investigational. The pathologic significance of TDP-43 aggregates is unknown and may reflect misfolding or altered trafficking.[6]

WHAT IS THE PATHOPHYSIOLOGY OF ALS?

The underlying pathophysiology of ALS is not well understood. Extensive research has outlined several plausible molecular pathways that may contribute to motor neuron degeneration in ALS. These pathways, which continue to be actively investigated, include the roles of oxidative stress and glutamate excitotoxicity, abnormal neurofilament function, protein misfolding, impairment of RNA processing, defects in axonal transport, changes in endosomal trafficking, and mitochondrial dysfunction.[3,7] Recently, forms of ALS and frontotemporal dementia have been found to share common molecular pathophysiology, a prionlike self-propagating dysregulation in RNA processing, and protein homeostasis.[3] This highlights the interplay of genetic and environmental interaction in disease initiation and propagation.

WHAT ARE THE GENETICS OF ALS?

Most (90%) of ALS cases are sporadic (sALS), with unknown genetic linkage. The remaining 10% of cases are familial (fALS), and at least 15 genes have been identified that are implicated in approximately one-third of fALS cases.[1,3] These may be inherited in an autosomal dominant, autosomal recessive, or X-linked pattern.[1] These genes include *SOD-1* (20% of fALS cases), *C9ORF72* (30% of fALS cases), *TARDBP*, *FUS*, *Alsin, FIG-4*, *SIGMAR1,* and *UBQLN2*. Each gene is associated with a well-characterized pattern of disease, for example, an *Alsin* mutation is associated with a slowly progressive disease, with predominantly UMN signs, whereas a mutation in *FIG-4,* which encodes phosphoinositide-5-phosphatase, is associated with a rapidly progressive disease with prominent corticospinal tract signs. An autosomal recessive mutation in *SIGMAR1* is associated with a juvenile-onset typical ALS as well as frontotemporal dementia.[1,3]

In contrast, the genetic underpinnings of most sALS cases are unknown, though some of the above genes noted for fALS including *SOD1*, *FUS*, *C9ORF72*, and several others, have been linked to sALS cases as well. These genes may be affected by abnormal copy number, single nucleotide polymorphisms, polyglutamine repeats, and deletion or insertion mutations. Examples include polyglutamine repeats in *ATXN2*, which codes for Ataxin-2 protein (locus 12q24.12), and SNP associations in *APEX1*, which codes for Apurinic Endonuclease DNA repair enzyme 1 (locus 14q11.2), a protein that protects cells from the effects of oxidative stress.[1,3]

WHAT IS THE ROLE OF CONVENTIONAL NEUROIMAGING IN ALS?

Conventional anatomic imaging of the brain and spinal cord is helpful in excluding diseases that may mimic the UMN and LMN signs of ALS. Specifically (per the revised criteria of the World Federation of Neurology Research Group on Motor Neuron Diseases), conventional imaging may be useful in "clinically probable" or "possible ALS." Notably, conventional MR imaging is not required in cases of "clinically definite" disease with a bulbar or a pseudobulbar onset.[4,5]

Differential pathology that may be uncovered includes lesions of multiple sclerosis and cerebrovascular disease, masses, spondylotic or other forms of myelopathy, or radiculopathy.[5]

In patients with ALS, signal intensity changes on proton attenuation, T2-weighted, and FLAIR sequences may be seen anywhere along the cerebrospinal tract, from the centrum semiovale to the brain stem.[2,5] Typical changes in the brain are often best appreciated on coronal imaging and appear as areas of bilateral symmetric increased signal intensity.[8] The frequency of cerebrospinal tract lesions in patients with ALS ranges widely across studies (from 15–76%), with combination imaging approaching a sensitivity above 60%.[8] Symmetric T2 signal intensity changes have also been described in the anterior temporal subcortical white matter in patients with ALS and dementia.[8] These lesions correspond to loss of myelin, white matter degeneration, and gliosis.

Other findings noted in patients with ALS include lower whole-brain volume as compared with healthy control subjects, though global brain atrophy is relatively mild and nonspecific, and a characteristic T2 dark rim that is probably related to iron deposition in the precentral cortex (reflecting death of Betz cells) may be present; however, this, too, may be seen in healthy control subjects.[5,8] T2 and T1 hyperintensities of the anterolateral columns of the cervical cord have been described in ALS and may have higher specificity than signal intensity changes on brain MR images. Moreover, such changes have been associated with a younger age at onset and a rapid disease progression.[5] However, signal changes frequently do not correspond with clinical findings and are overall nonspecific; cerebrospinal tract hyperintensities have been described in healthy subjects and in patients with various other diseases.[5]

Given the overall limitations, the traditional role of conventional structural imaging is to support electrophysiologic studies and exclude alternate diagnoses.[2,4]

IS THERE A ROLE FOR ADVANCED NEUROIMAGING TECHNIQUES IN ALS?

Advanced neuroimaging techniques, which elaborate on microstructure (structural MRI and DTI), metabolism (hydrogen spectroscopy MR and PET), and neural network integrity (resting-state functional connectivity MRI) have been useful in elucidating the pathophysiology of ALS. These may play a future clinical role but for now remain largely investigational.[2]

High-resolution structural MR imaging allows for detailed analysis of focal atrophy and regional gray-white matter differences and may be combined with computer-aided segmentation, voxel-based morphometry, and surface-based morphometry.[2,5,8]

Current DTI techniques, which evaluate the integrity of white matter tracts, have overall low sensitivity (0.65) and specificity (0.67), and are at present unsuitable for clinical application in the diagnosis of ALS.[9] Hydrogen spectroscopy MR metrics, which allow for ratio and absolute quantification of metabolites, demonstrate changes across motor neuron diseases; typically decreased NAA, decreased glutamate, and increased choline. These metrics correlate with measures of disease severity and UMN function but are generally nonspecific.[2] Resting-state functional connectivity MRI and PET studies have demonstrated γ-Aminobutyric acid system dysfunction in ALS, suggesting a pathophysiologic process possibly mediated by glutamate excitotoxicity.[2] Of note, advanced machine learning tools have been shown to achieve promising (>70%) accuracy for disease state classification by use of these techniques in combination.[10]

REFERENCES

1. Chen S, Sayana P, Zhang X, et al. **Genetics of amyotrophic lateral sclerosis: an update.** *Mol Neurodegen* 2013:8:28
2. Foerster BR, Welsh RC, Feldman EL. **25 years of neuroimaging in amyotrophic lateral sclerosis.** *Nat Rev Neurol* 2013;9:513–24
3. Ling S, Polymenidou M, Cleveland DW. **Converging mechanisms in ALS.** *Neuron* 2013;79:416–38
4. Brooks BR, Miller RG, Swash M, et al. **El Escorial revisited: revised criteria for the diagnosis of amyotrophic lateral sclerosis.** *Amyotroph Lateral Scler Other Motor Neuron Disord* 2000;1:293–99
5. Agosta F, Chiò A, Cosottini M, et al. **The present and the future of neuroimaging in amyotrophic lateral sclerosis.** *AJNR Am J Neuroradiol* 2010;31:1769–77
6. Upadhyayula S, Gearing M, Jonathan Glass J. **TDP-43 inclusions in**

the spinal cord: sensitivity and specificity for the diagnosis of sporadic ALS (meeting abstracts). *Neurology* 2013;80:P02.171
7. Ferraiuolo L, Kirby J, Grierson AJ, et al. **Molecular pathways of motor neuron injury in amyotrophic lateral sclerosis.** *Nat Rev Neurol* 2011;7:616–30
8. Kwan JY, Jeong SY, Van Gelderen P, et al. **Iron accumulation in deep cortical layers accounts for MRI signal abnormalities in ALS: correlating 7 Tesla MRI and pathology.** *PLoS One* 2012;7:e35241
9. Foerster BR, Dwamena BA, Petrou M, et al. **Diagnostic accuracy of diffusion tensor imaging in amyotrophic lateral sclerosis: a systematic review and individual patient data meta-analysis.** *Acad Radiol* 2013;20:1099–100
10. Welsh RC, Jelsone-Swain LM, Foerster BR, et al. **The utility of independent component analysis and machine learning in the identification of the amyotrophic lateral sclerosis diseased brain.** *Front Hum Neurosci* 2013;7:251

Subcortical Atrophy Is Associated with Cognitive Impairment in Mild Parkinson Disease: A Combined Investigation of Volumetric Changes, Cortical Thickness, and Vertex-Based Shape Analysis

E. Mak, N. Bergsland, M.G. Dwyer, R. Zivadinov, and N. Kandiah

ABSTRACT

BACKGROUND AND PURPOSE: The involvement of subcortical deep gray matter and cortical thinning associated with mild Parkinson disease remains poorly understood. We assessed cortical thickness and subcortical volumes in patients with Parkinson disease without dementia and evaluated their associations with cognitive dysfunction.

MATERIALS AND METHODS: The study included 90 patients with mild Parkinson disease without dementia. Neuropsychological assessments classified the sample into patients with mild cognitive impairment ($n = 25$) and patients without cognitive impairment ($n = 65$). Volumetric data for subcortical structures were obtained by using the FMRIB Integrated Registration and Segmentation Tool while whole-brain, gray and white matter volumes were estimated by using Structural Image Evaluation, with Normalization of Atrophy. Vertex-based shape analyses were performed to investigate shape differences in subcortical structures. Vertex-wise group differences in cortical thickness were also assessed. Volumetric comparisons between Parkinson disease with mild cognitive impairment and Parkinson disease with no cognitive impairment were performed by using ANCOVA. Associations of subcortical structures with both cognitive function and disease severity were assessed by using linear regression models.

RESULTS: Compared with Parkinson disease with no cognitive impairment, Parkinson disease with mild cognitive impairment demonstrated reduced volumes of the thalamus ($P = .03$) and the nucleus accumbens ($P = .04$). Significant associations were found for the nucleus accumbens and putamen with performances on the attention/working memory domains ($P < .05$) and nucleus accumbens and language domains ($P = .04$). The 2 groups did not differ in measures of subcortical shape or in cortical thickness.

CONCLUSIONS: Patients with Parkinson disease with mild cognitive impairment demonstrated reduced subcortical volumes, which were associated with cognitive deficits. The thalamus, nucleus accumbens, and putamen may serve as potential biomarkers for Parkinson disease–mild cognitive impairment.

ABBREVIATIONS: MCI = mild cognitive impairment; MDS = Movement Disorder Society; PD = Parkinson disease; PD-MCI = Parkinson disease with mild cognitive impairment; PD-NCI = Parkinson disease with no cognitive impairment; SDGM = subcortical deep gray matter; SIENAX = Structural Image Evaluation, with Normalization of Atrophy

Parkinson disease (PD) has traditionally been considered a motor disorder. However, the presence of cognitive dysfunction is increasingly recognized and known to occur even at early stages, and most patients develop dementia during the course of the disease. Recently, it has emerged that patients with PD show a wide and variable spectrum of cognitive deficits involving multiple domains such as executive function, attention, memory, visuospatial, and, less frequently, language.[1,2] While traditionally believed to occur only in advanced stages of PD, recent studies suggest that approximately 30%–35% of patients with early PD experience cognitive disturbances,[3,4] which have been defined as mild cognitive impairment (MCI).[5] The Movement Disorder Society (MDS) Task Force reported a mean prevalence of Parkinson disease with mild cognitive impairment (PD-MCI) at 27%, ranging from 19% to 38%.[6] Furthermore, the impact of MCI and dementia in pa-

Received November 8, 2013; accepted after revision May 28, 2014.

From the Department of Neurology (E.M., N.B., M.G.D., R.Z.), Buffalo Neuroimaging Analysis Center, and MR Imaging Clinical Translational Research Center (R.Z.), School of Medicine and Biomedical Sciences, University at Buffalo, State University of New York, Buffalo, New York; Department of Neurology (E.M., N.K.), National Neuroscience Institute, Singapore; and Istituto de Ricovero e Cura a Carattere Scientifico "S. Maria Nascente," Don Gnocchi Foundation (N.B.), Milan, Italy.

This work was supported by the Singapore National Research Foundation and Singapore Ministry of Health's National Medical Research Council and by the Buffalo Neuroimaging Analysis Center neuroimaging fellowship to Elijah Mak.

Please address correspondence to Robert Zivadinov, MD, PhD, FAAN, Department of Neurology, School of Medicine and Biomedical Sciences, Jacobs Neurological Institute, 100 High St, Buffalo, NY 14203; e-mail: rzivadinov@bnac.net; or Nagaendran Kandiah, MBBS, MRCP (UK), FAM, Department of Neurology, National Neuroscience Institute, 11 Jalan Tan Tock Seng, Singapore 308433; e-mail: nagaendran_kandiah@nni.com.sg

Indicates open access to non-subscribers at www.ajnr.org

Indicates article with supplemental on-line table.

http://dx.doi.org/10.3174/ajnr.A4055

tients with PD at any given stage of the disease is substantial, with adverse consequences for functioning,[7] psychiatric morbidity, caregiver burden,[8] and mortality.[9] At present, there is much to be elucidated with regard to the etiology of cognitive impairment in PD.

Initially, dementia in PD was described as subcortical. Cognitive dysfunction in patients without dementia has also been attributed to dopaminergic depletion disrupting the frontostriatal circuit[10] or dopamine-acetylcholine synaptic imbalance.[11] Nevertheless, recent investigations by using structural MR imaging suggest that specific cognitive deficits, such as memory deficits, and dementia in PD may also be accompanied by structural cerebral abnormalities. In this regard, MR imaging studies have demonstrated cortical atrophy in patients with PD with dementia. A recent meta-analysis revealed regional gray matter reductions of the medial temporal lobe and the basal ganglia,[12] while other areas, including the caudate,[13] hippocampus,[14] and amygdala,[15] have also been implicated. However, present findings on GM atrophy in patients without dementia with PD are inconclusive. While a few studies have demonstrated atrophy in the medial temporal lobes,[16] amygdala,[17] and frontal and parietal regions,[18] others have reported no significant GM reductions in PD populations without dementia.[19]

In addition, cortical thinning in PD represents a relatively new area of research, and it has been reported to be more sensitive than voxel-based morphometry.[20] Recent studies have shown that cortical thinning occurs in PD without dementia.[21] A longitudinal study also reported that patients with early PD presented with a more aggressive rate of cortical thinning in the frontotemporal regions compared with healthy controls.[22]

These mixed neuroimaging findings could be due, in part, to cognitively heterogeneous groups of patients, particularly in studies in which patients with MCI were not distinguished from those with normal cognition. Therefore, to systematically compare the pattern of GM atrophy in mild PD and its impact on specific cognitive domains, we used the recent MDS Task Force criteria to classify patients with PD with MCI or as cognitively normal (PD-NCI). We estimated the volumes of the amygdala, hippocampus, nucleus accumbens, caudate nucleus, putamen, pallidum, and thalamus in a cohort of patients with PD by using the FMRIB Integrated Registration and Segmentation Tool (FIRST; http://fsl.fmrib.ox.ac.uk/fsl/fslwiki/FIRST).

Furthermore, we assessed differences in subcortical deep gray matter (SDGM) structures between PD-MCI and PD-NCI and further examined associations between individual structures and cognitive performances across multiple domains. Because vertex analysis directly measures changes in geometry without any smoothing of the image data, it might have the potential to more precisely detect regional alterations of the subcortical GM than the conventional voxel-based morphometry approach.[23] Therefore, we used a vertex-based shape-analysis method to investigate potential shape differences of SDGM structures between PD-MCI and PD-NCI. Last, vertex-wise cortical thickness analysis was performed by using FreeSurfer (http://surfer.nmr.mgh.harvard.edu) to assess and compare patterns of regional cortical alterations between both PD groups.

MATERIALS AND METHODS

Subjects

The present study included 90 patients with mild PD (65.08 ± 7.71 years of age; disease duration, 5.26 ± 3.90 years; and Hoehn and Yahr stage = 1.88 ± 0.39) recruited from August 2011 to March 2012 from a tertiary neurology center. PD was diagnosed by neurologists trained in movement disorders according to the National Institute of Neurologic Disorders and Stroke criteria.[24] Patients with dementia and serious medical and psychiatric comorbidities were excluded.

Clinical Assessment

Demographic, clinical, and vascular risk factor data were collected, and a comprehensive clinical assessment was conducted to ascertain cognitive status and functional ability. The severity and stage of the patient's parkinsonism was evaluated by using the Unified Parkinson's Disease Rating Scale motor subscore[25] and the modified Hoehn and Yahr stage.[26] To standardize data on medication use, we converted dosages of PD medications to total daily levodopa-equivalent doses. This calculation was based on the conversion formulae reported by Tomlinson et al.[27] The study was approved by the centralized institutional review boards of the participating institutions, and informed consent was obtained from patients or their legal caregivers.

Neuropsychological Assessment

Cognitive performance was evaluated by trained psychologists by using a standardized neuropsychological battery. To ensure standardization and integrity of data, we evaluated patients during their "on" medication state. Global cognition was evaluated by using the Mini-Mental State Examination[28] and the Montreal Cognitive Assessment.[29] In line with the recommendations of the MDS Task Force, specific cognitive domains including memory, executive function, visuospatial function and language, and attention/working memory were also assessed.[30] In this regard, patients were evaluated with the following subtests from the Alzheimer Disease Assessment Scale-Cognitive[31]: Word-List Immediate, Delayed and Recognition Recall for episodic memory; the Frontal Assessment Battery and the 10-Point Clock Test for executive function; a figure copy test and test for the number of errors made on a maze for visuospatial function; a 20-point object-naming test and a fruit-naming fluency test for language assessment; and digit span, color trails 2, and a test for time taken on a maze for attention/working memory.[31-33] Performances on individual tasks were transformed into z scores. Subsequently, a composite summary index for each cognitive domain was derived from the corresponding averages of the respective individual neuropsychological tests.

MCI Classification

To qualify PD-MCI for MDS level 2 criteria, we analyzed performance on the suggested 5 cognitive domains (attention/working memory, executive, language, episodic memory, and visuospatial). Cutoff scores for the various cognitive tests were based on locally validated norms when available, and for those without, international ones were used. The performance on a cognitive test was considered abnormal if the score was 1.5 SDs below the norm.

Impairment on at least 2 neuropsychological tests, represented by either 2 tests showing impairment in 1 cognitive domain or 1 test showing impairment in 2 different cognitive domains, was required. Patients with PD who did not fulfill the criteria for PD-MCI or PD-dementia were classified as PD-NCI.

Image Acquisition

All subjects underwent MR imaging on a 3T whole-body system (Achieva 3.0; Philips Healthcare, Best, the Netherlands). A high-resolution volumetric 3D T1-weighted magnetization-prepared rapid acquisition of gradient echo sequence (axial acquisition: TR, 7.1 ms; TE, 3.3 ms; TI, 850 ms; FOV, 240 × 240 mm^2; matrix, 256 × 256; section thickness, 1 mm; total, 180 sections; scanning time, 5 minutes and 13 seconds) and a whole-brain 3D fluid-attenuated inversion recovery sequence (turbo spin-echo: TR, 8000 ms; TE, 340 ms; TI, 2400 ms; FOV, 240 × 240 mm^2; matrix, 256 × 256; section thickness, 1 mm; total, 170 sections; scanning time, 10:24) were acquired for all patients. Both clinical testing and MR imaging were performed on the same day for all patients.

Image Analysis

Quantitative image analyses were performed at the Buffalo Neuroimaging Analysis Center, Buffalo, New York.

Quantification of GM and WM Volumes. For each subject, we obtained GM, white matter, and a volumetric scaling factor by using Structural Image Evaluation, with Normalization of Atrophy (SIENAX, Version 2.6; FMRIB Software Library, http://www.fmrib.ox.ac.uk/fsl/).[34]

Quantification of Subcortical Deep Gray Matter Volumes. Before we used the T1-weighted images for subsequent analysis, the analysis was modified by an in-house-developed in-painting technique to avoid the impact of WM hyperintensities on GM volume as previously described.[35] WM hyperintensities were outlined on each axial FLAIR image section by using a reproducible, semiautomated local threshold technique (Jim, Version 5.0; Xinapse Systems, Northamptonshire, UK). All WM hyperintensity masks were created by a single rater (E.M.), blinded to clinical characteristics and tests results, with similar reproducibility as previously reported.[36]

Subsequently, FIRST was used to segment the amygdala, hippocampus, nucleus accumbens, pallidum, caudate nucleus, putamen, and thalamus from the in-painted T1.[23] The reproducibility of FIRST has been previously reported.[37] Examples of subcortical segmentation of a subject classified as having PD-MCI and of a subject classified as having PD-NCI are presented in Fig 1. In subsequent volumetric analyses, the normalization factor from SIENAX was included to reduce the effects of interindividual variability due to head size.[34]

Vertex Analysis for Assessment of SDGM Shape Alterations. FIRST creates a surface mesh for each subcortical structure

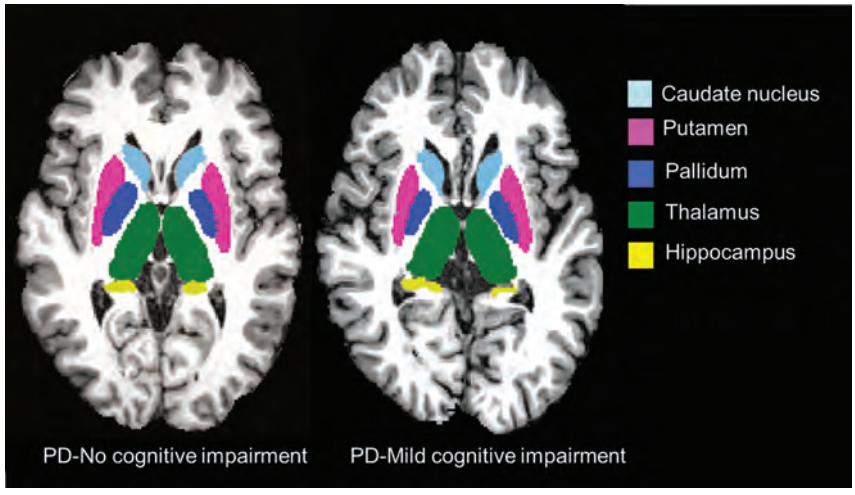

FIG 1. Representative FIRST segmentation of subcortical structures in patients with PD-MCI (left) and PD-NCI (right).

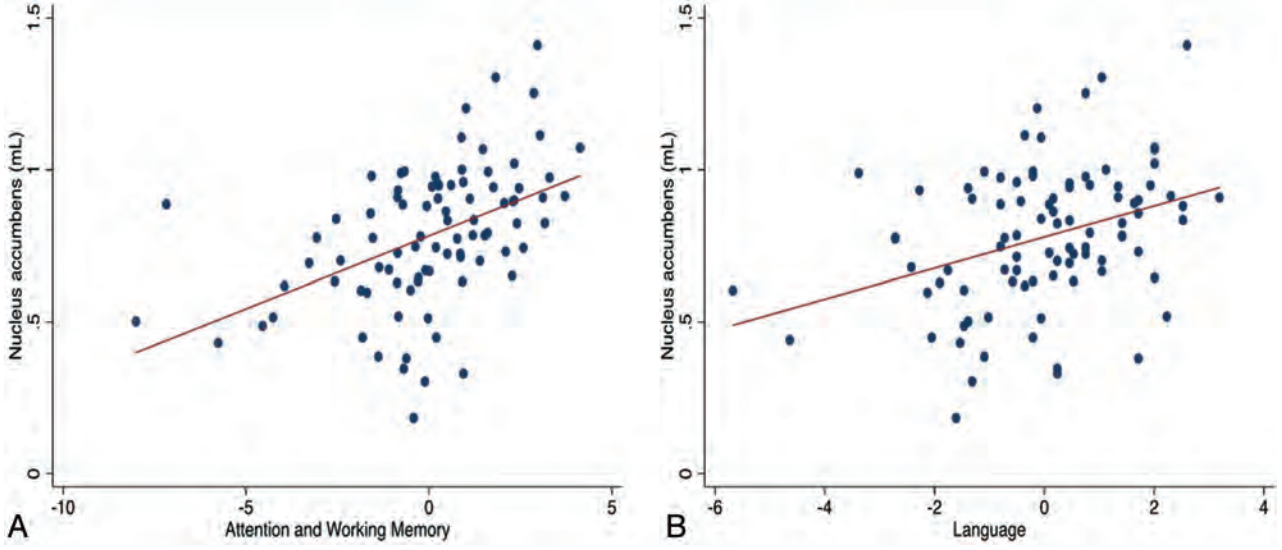

FIG 2. Scatterplot showing the associations between the nucleus accumbens and attention and working memory (*A*) and language domains (*B*).

Table 1: Demographic, clinical, and white matter hyperintensity characteristics between patients with Parkinson disease with and without mild cognitive impairment

Demographic and Clinical Variables	PD-NCI (*n* = 65)	PD-MCI (*n* = 25)	*P* Value
Age (yr) (mean) (SD)	63.4 (7.6)	69.4 (6.4)	.001[a,b]
Sex (male) (No.) (%)	46 (72.3)	18 (76.0)	.723[c]
Education (yr) (mean) (SD)	11.0 (3.1)	9.3 (3.5)	.032[a,d]
Hoehn and Yahr (mean) (SD)	1.9 (0.4)	1.8 (0.4)	.357[d]
Disease duration (yr) (mean) (SD)	5.4 (4.3)	5.0 (2.7)	.910[d]
UPDRS (mean) (SD)	17.5 (7.0)	20.0 (8.4)	.167[b]
Levodopa equivalent dose (mg) (mean) (SD)	557.4 (375.7)	510.2 (299.0)	.767[d]
Cardiovascular risk factors (No.) (%)			
Diabetes	5 (7.8)	8 (32.0)	.004[a,c]
Hypertension	20 (31.3)	13 (52.0)	.069[c]
Hyperlipidemia	20 (31.3)	14 (56.0)	.031[a,c]
Smoking	15 (23.4)	6 (24.0)	.955[c]
White matter hyperintensities			
Total WMH volume (mm) (mean) (SD)	4.2 (5.8)	12.3 (10.3)	<.001[a,e]

Note:—UPDRS indicates Unified Parkinson's Disease Rating Scale, subscore III; WMH, white matter hyperintensities.
[a] Significant differences at $P < .05$ level.
[b] Student *t* test.
[c] χ^2 test.
[d] Mann-Whitney *U* test.
[e] Analysis of covariance test, corrected for age, sex, and education.

by using a deformable mesh model. The mesh is composed of a set of triangles, and the apex of adjoining triangles is called a vertex. The number of vertices for each structure is fixed so that corresponding vertices can be compared across individuals and between groups.[38] Vertex analysis was performed, and shape alterations of SDGM were assessed on a per-vertex basis. Regional changes in the vertices of SDGM structures between PD-MCI and PD-NCI were assessed by using a generalized linear model with age, sex, and education as nuisance covariates. The results were then corrected for multiple comparisons by using the false discovery rate ($P < .05$).

Cortical Thickness Analysis. T1 images of the subjects were processed with the volume and surface pipeline of FreeSurfer. The technical details of cortical reconstruction and volumetric segmentation procedures have been described previously.[39]

Statistical Analysis

General Analyses. Group comparisons of demographics, neuropsychological variables, and regional volumetric data were performed by using STATA 12 (StataCorp, College Station, Texas). The Student *t* test or the nonparametric Mann-Whitney rank sum test was used to investigate differences between groups, depending on the normality of the distributions. The χ^2 test was used for categoric variables (sex and vascular risk factors). Left and right volumes of the SDGM structures were highly correlated (data not shown). Therefore, to minimize the total number of comparisons, we combined left and right SDGM structures to yield a single structural volume. Mean regional GM volumetric differences between PD-MCI and PD-NCI groups were investigated while controlling for age, sex, education, and head size (by using the volumetric scaling factor from SIENAX) by ANCOVA.

Subsequently, for each SDGM structure showing a significant volumetric difference, a linear regression model was designed to assess associations with different cognitive domains separately. In addition, we also tested for associations between the SDGM structures and disease characteristics (disease duration and Unified Parkinson's Disease Rating Scale motor scores). Age, sex, and years of education were also added as independent variables in these models because of their expected influence on cognitive test scores, while the volumetric scaling factor was included to control for differences in head size between patients. For all analyses, 2-tailed *P* values were used and $P < .05$ was considered significant.

Image-Based Analyses. Statistical maps were generated by using the Query, Design, Estimate, Contrast application in FreeSurfer. Briefly, Query, Design, Estimate, Contrast fits a generalized linear model at each surface vertex to explain the data from all subjects in the study. A surface-based Gaussian smoothing kernel of full width at half maximum of 10 mm was applied to the data before subsequent analyses. Using a generalized linear model, we compared cortical thickness variations between PD-MCI and PD-NCI, controlling for age, sex, and years of education. Correlations between regional cortical thickness and disease and cognitive measures were also modeled. The level of significance was set at $P < .05$ corrected for multiple comparison by using the false discovery rate.[40]

RESULTS

Subject Demographic and Clinical Characteristics

The group comparisons of demographic and cognitive characteristics of the study cohort are shown in Tables 1 and 2, respectively. Within the PD group, 25 were classified as having PD-MCI; 65, as having PD-NCI, and none as having PD-dementia. The PD-MCI group was significantly older than PD-NCI group, while the PD-NCI group was more educated. Both groups were comparable in terms of duration of disease, Unified Parkinson's Disease Rating Scale motor scores, and Hoehn and Yahr staging. Comparisons of the various cardiovascular risk factors demonstrated a significantly higher prevalence of patients with PD-MCI having diabetes mellitus ($P = .004$) and hyperlipidemia ($P = .031$), compared with patients with PD-NCI.

Cognitive Performance

Patients with PD-MCI had significantly lower scores on global cognition compared with those with PD-NCI (Mini-Mental State Examination, $P = .016$; Montreal Cognitive Assessment, $P < .018$; Global Index, $P = .008$) after correcting for age, sex, and years of education. Comparisons of individual neuropsychological tests are shown in Table 2. With the exception of visuospatial ability and episodic memory domains, the PD-MCI group performed significantly poorer in executive functioning, attention and working memory, and language abilities (all, $P \leq .023$).

SDGM Comparisons

Group comparisons of mean volumes for all SDGM structures are shown in Table 3. ANCOVA analyses, controlling for age, sex, education, and head size revealed significant reductions in volumes of the thalamus ($P = .03$) and nucleus accumbens ($P = .04$) of patients with PD-MCI compared with PD-NCI.

Table 2: Comparison of neuropsychological measures between patients with Parkinson disease with and without mild cognitive impairment

Neuropsychological Measures	PD-NCI (Mean) (SD)	PD-MCI (Mean) (SD)	Adjusted *P* Value
Global cognition (mean) (SD)			
MMSE	28.4 (1.6)	26.7 (2.6)	.016[a,b]
MOCA	27.0 (2.9)	24.5 (2.4)	.018[a,b]
ADAS11	6.8 (4.2)	9.8 (3.5)	.071[a,b]
Global Index	0.1 (0.5)	−0.3 (0.3)	.008[a,b]
Cognitive tests (mean) (SD)			
Clock drawing	9.31 (1.25)	8.48 (1.47)	.126
Frontal Assessment Battery	16.69 (1.38)	15.28 (2.09)	.027
Digit Span	17.42 (3.50)	15.04 (2.24)	.015
Digit Cancellation	19.86 (6.54)	15.08 (6.45)	.063
Color Trail 1	80.48 (37.59)	137.24 (82.08)	.008
Color Trail 2	138.94 (60.75)	229.58 (103.31)	.002
Maze	18.63 (10.59)	30.80 (17.83)	.005
Maze errors	0.06 (0.30)	0.04 (0.20)	.942
ADAS: Immediate and Delayed Recall	5.08 (2.69)	7.04 (3.28)	.090
ADAS: Recognition	1.55 (2.22)	2.00 (2.50)	.644
ADAS: Language	1.15 (1.37)	2.00 (1.71)	.168
Fruit Fluency	14.11 (3.29)	11.24 (2.80)	.029
Cognitive domains (mean) (SD)			
Executive function	0.4 (1.5)	−1.0 (2.0)	.023[a,b]
Attention/working memory	0.8 (1.7)	−2.0 (2.4)	<.000[a,b]
Visuospatial	0.0 (1.8)	−0.1 (1.4)	.919[d]
Episodic memory	0.3 (1.6)	−0.6 (1.5)	.193[b]
Language	0.4 (1.4)	−1.0 (1.5)	.018[a,b]

Note:—MMSE indicates Mini-Mental State Examination; MOCA, Montreal Cognitive Assessment; ADAS11, Alzheimer Disease Assessment Scale-Cognitive.

[a] Significant differences at $P < .05$ level.

[b] Analysis of covariance test, corrected for age, sex, and education.

Table 3: Volumetric comparisons between patients with Parkinson disease with and without mild cognitive impairment

SDGM Structures[a]	PD-NCI (Mean) (SD)	PD-MCI (Mean) (SD)	Adjusted *P* Value
Amygdala	2.13 (0.51)	2.23 (0.36)	.220[b]
Hippocampus	7.65 (0.97)	7.18 (0.79)	.198[b]
Nucleus accumbens	0.83 (0.22)	0.64 (0.19)	.044[b]
Caudate nucleus	6.37 (0.76)	5.96 (0.76)	.327[b]
Putamen	9.51 (1.41)	8.62 (1.17)	.058[b]
Pallidum	3.72 (0.66)	3.60 (0.84)	.876[b]
Thalamus	13.94 (1.65)	12.71 (1.09)	.025[b]
Normalized gray matter	688.76 (34.86)	661.92 (28.24)	.035[b]
Normalized white matter	654.43 (41.49)	633.10 (46.04)	.618[b]

[a] All volumes are reported in milliliters. Significant difference is at the $P < .05$ level.

[b] Analysis of variance adjusting for age, sex, education, and head size.

Table 4: Mean global and hemispheric cortical thickness between patients with Parkinson disease with and without mild cognitive impairment

Cortical Thickness[a]	PD-NCI (Mean) (SD)	PD-MCI (Mean) (SD)	Adjusted *P* Value
Left hemisphere	2.20 (0.10)	2.13 (0.11)	.095[b]
Right hemisphere	2.19 (0.10)	2.13 (0.10)	.264[b]
Global mean cortical thickness	4.40 (0.19)	4.26 (0.21)	.151[b]

[a] Cortical thickness is expressed in millimeters. Significant difference is at the $P < .05$ level.

[b] Analysis of variance adjusting for age, sex, education.

Vertex-Wise Shape Comparisons of SDGM Structures

Vertex analysis did not reveal any significant differences in the shapes of SDGM structures between PD-MCI and PD-NCI.

Cortical Thickness Comparisons

Global mean and hemispheric cortical thickness values are shown in Table 4. Vertex-wise group comparisons of regional cortical thickness showed no significant differences between PD-MCI and PD-NCI in any cortical area.

Association between SDGM Structures and Cognitive Impairment

β regression coefficients of the correlations between volumes of SDGM structures and the main cognitive tests scores are shown in the On-line Table. The total volume of the nucleus accumbens was significantly correlated with a range of cognitive variables, including overall scores of attention/working memory ($\beta = 0.28$, $r^2 = 0.32$, $P = .02$) and language ($\beta = 0.25$, $r^2 = 0.29$, $P = .04$) (Fig 2). Furthermore, there was a trend toward the associations between nucleus accumbens and global cognition ($\beta = 0.23$, $r^2 = 0.2292$, $P = .06$) and executive function ($\beta = 0.23$, $r^2 = 0.2575$, $P = .06$). Putaminal volume was correlated with overall scores of attention/working memory ($\beta = 0.31$, $r^2 = 0.34$, $P = .005$). These correlations did not survive correction for multiple comparisons.

Association between SDGM Structures and Disease Characteristics

β regression coefficients of the correlations between volumes of SDGM structures and the indices of disease characteristics (Unified Parkinson's Disease Rating Scale and disease duration) are shown in the On-line Table. Putamen volume was correlated with the Unified Parkinson's Disease Rating Scale ($\beta = -0.33$, $r^2 = 0.12$, $P = .009$). This correlation did not survive correction for multiple comparisons.

DISCUSSION

At present, the pathophysiologic relationship between neurodegeneration processes and cognitive dysfunction in PD remains unclear, and ongoing investigations to identify structural biomarkers of cognitive impairment in patients with PD without dementia have yielded inconclusive results. Varying degrees of atrophy have been reported in patients with PD without dementia,[41-43] with mixed evidence of an association between atrophy and neuropsychological measures.[44] Within a cohort of 90 patients with mild PD without dementia, we investigated SDGM volumes and cortical thickness and examined their associations with cognitive functioning and disease severity. To date, only a few studies have directly examined the patterns of GM atrophy in well-delineated cognitive subgroups of PD. PD-MCI exhibited significantly reduced total volumes in a number of SDGM regions, including the thalamus and nucleus accumbens, and there was a trend toward the putamen, relative to PD-NCI.

These volumetric reductions suggest that a pattern of subcortical atrophy can be detected at an early stage of cognitive decline

in mild stages of PD. The finding of thalamic atrophy in PD-MCI is novel, and warrants further consideration. Traditionally, the thalamus has been conceptualized as a relay center, involved in both sensory and motor functions.[45] It is increasingly recognized as an important site for neuropathologic inclusions, including Lewy bodies in patients with PD. The relationship between thalamic degeneration and cognitive impairment has also been investigated in previous studies. Volumetric loss in the thalamus has been proposed as a predictor of dementia,[46] while studies have demonstrated thalamic atrophy in PD with dementia compared with healthy individuals.[14,16] Previous studies have also demonstrated the relation of thalamic atrophy to cognitive performance in other neurologic disorders, including Alzheimer disease,[47] Huntington disease,[48] and multiple sclerosis.[49] Considered in light of those findings, the volumetric reduction of the thalamus observed in our PD-MCI group may reflect an intermediary stage of cognitive dysfunction. Of note, we did not find any significant alteration of the shapes of SDGM structures in PD-MCI relative to PD-NCI. Further studies are needed to examine the clinical significance of shape alterations in SDGM structures and their utility as potential biomarkers of cognitive impairment and dementia in PD.

Additionally, a number of associations between the nucleus accumbens and putamen and cognitive test scores were also found. While the results were controlled for age, sex, years of education, and head size, they were not corrected for multiple comparisons. Performance on attention and working memory was associated with reduced volumes of the nucleus accumbens and putamen. Additionally, the nucleus accumbens was also significantly correlated with performance in the language domain. A possible explanation for our findings might be offered by previous evidence linking the nucleus accumbens to memory and learning processes.[50] Furthermore, a previous population-based study demonstrated that accumbens volume is predictive of cognitive decline in the elderly.[51] At this time, very little is known about the putaminal role in cognition. Despite the traditional role of the putamen in motor functions, the finding of an association between reduced putaminal volumes and cognitive scores on the attention and working memory domain in the present study is consistent with a previous report that demonstrated a signification association between putaminal 6-[^{18}F]-fluoro-L-dopa uptake and measures for executive functioning, memory, and fluency in a group of 28 patients with PD without dementia.[52]

At present, the literature concerning the role of cortical thinning in cognitive deterioration in PD remains inconclusive. We did not find significant thinning of the cortex in PD-MCI compared with PD-NCI in any region. A previous study found significant associations between the Mini-Mental State Examination and cortical thickness in their PD cohort.[53] In addition, they found significant cortical thinning in patients with moderate PD without dementia compared with healthy controls and in PD with dementia compared with moderate PD without dementia. Considered together, the absence of cortical thinning in our PD-MCI group might be attributed to the finer distinction of cognitive statuses in our PD cohort.

The strengths of this study include the use of the MDS Task Force diagnostic criteria and a comprehensive neuropsychological evaluation to characterize PD-MCI. However, we acknowledge the possible involvement of executive functions in the interpretation of the fluency test findings that was used to characterize language in our cohort. In-painted T1 images also improved the quality of the subcortical segmentation due to the known effect of tissue misclassification due to lesion-induced T1 hypointensities in the WM. Preprocessing of images to correct for such pathology is now highly recommended.

Our study was limited by the absence of patients with PD with established dementia and healthy controls for comparison. This constraint prevented us from exploring the associations between SDGM volumes and cognitive dysfunction across a broader range of cognitive stages in PD. As such, these findings need to be confirmed in larger prospective studies with an additional group of well-matched healthy controls. In this regard, a recent study has also demonstrated subcortical atrophy in PD without dementia compared with healthy controls, particularly in the putamen, nucleus accumbens, and hippocampus.[54] In addition, the present findings must be interpreted by taking into account the lack of correction for multiple comparisons and that the sample size between PD-NCI ($n = 65$) and PD-MCI ($n = 25$) was imbalanced. Thus, to check against a potential violation of the assumption of equal variances across groups in ANOVA, we performed the Bartlett test to ensure homoscedasticity. Another limitation of the study could be related to performance of testing during the "on" medication state. Moreover, we did not have volumetric data on the substantia nigra, an area with extensive projections to limbic and cortical regions. In fact, an earlier study found a significant correlation between the severity of dementia in patients with PD and neuronal loss in the medial part of the substantia nigra.[55] Finally, we aim to extend this study by incorporating a longitudinal design that will allow us to elucidate the trajectory of brain atrophy in PD-MCI and examine its potential involvement in progression to PD dementia.

CONCLUSIONS

Due to the growing recognition of PD-MCI as a clinically significant condition in PD, our findings warrant the continued concerted effort to validate biomarkers of neurodegeneration associated with MCI. The early delineation of PD-MCI from PD-NCI will help elucidate the processes underlying cognitive decline in PD, while longitudinal research can investigate the contributions of SDGM structures to cognitive dysfunction as the disease progresses.

Disclosures: Michael G. Dwyer—*UNRELATED*: *Consultancy*: Claret Medical, EMD Serono, *Comments*: served on scientific advisory board for EMD Serono and has done image analysis consulting work for Claret Medical. Robert Zivadinov—*UNRELATED*: *Consultancy*: Biogen Idec, EMD Serono, Teva Pharmaceuticals, Genzyme-Sanofi, Novartis, Claret Medical; *Grants/Grants Pending*: Biogen Idec,* EMD Serono,* Teva Pharmaceuticals,* Novartis,* Genzyme-Sanofi,* Claret Medical*; *Payment for Lectures (including service on Speakers Bureaus)*: Biogen Idec, EMD Serono, Teva Pharmaceuticals, Genzyme-Sanofi, Novartis. Nagaendran Kandiah—*RELATED*: *Grant*: National Medical Research Council of Singapore*; *UNRELATED*: *Grants/Grants Pending*: National Medical Research Council of Singapore,* Biomedical Research Council of Singapore,* Singhealth Foundation,* Media Development Authority of Singapore*; *Travel/Accommodations/Meeting Expenses Unrelated to Activities Listed*: Novartis,* Eisai,* Lundbeck*; *Other*: N.K. has received an honorarium and Continuing Medical Education sponsorship from Lundbeck.* *Money paid to the institution.

REFERENCES

1. Muslimovic D, Post B, Speelman JD, et al. **Cognitive profile of patients with newly diagnosed Parkinson disease.** *Neurology* 2005;65:1239–45
2. Sollinger AB, Goldstein FC, Lah JJ, et al. **Mild cognitive impairment in Parkinson's disease: subtypes and motor characteristics.** *Parkinsonism Relat Disord* 2010;16:177–80
3. Poletti M, Emre M, Bonuccelli U. **Mild cognitive impairment and cognitive reserve in Parkinson's disease.** *Parkinsonism Relat Disord* 2011;17:579–86
4. Kandiah N, Narasimhalu K, Lau PN, et al. **Cognitive decline in early Parkinson's disease.** *Mov Disord* 2009;24:605–08
5. Caviness JN, Driver-Dunckley E, Connor DJ, et al. **Defining mild cognitive impairment in Parkinson's disease.** *Mov Disord* 2007; 22:1272–77
6. Litvan I, Aarsland D, Adler CH, et al. **MDS task force on mild cognitive impairment in Parkinson's disease: critical review of PD-MCI.** *Mov Disord* 2011;26:1814–24
7. Bronnick K, Ehrt U, Emre M, et al. **Attentional deficits affect activities of daily living in dementia-associated with Parkinson's disease.** *J Neurol Neurosurg Psychiatry* 2006;77:1136–42
8. Aarsland D, Bronnick K, Ehrt U, et al. **Neuropsychiatric symptoms in patients with Parkinson's disease and dementia: frequency, profile and associated care giver stress.** *J Neurol Neurosurg Psychiatry* 20062007;78:36–42
9. Levy G, Tang MX, Louis ED, et al. **The association of incident dementia with mortality in PD.** *Neurology* 2002;59:1708–13
10. Owen AM. **Cognitive dysfunction in Parkinson's disease: the role of frontostriatal circuitry.** *Neuroscientist* 2004;10:525–37
11. Calabresi P, Picconi B, Parnetti L, et al. **A convergent model for cognitive dysfunctions in Parkinson's disease: the critical dopamine-acetylcholine synaptic balance.** *Lancet Neurol* 2006;5:974–83
12. Pan PL, Shi HC, Zhong JG, et al. **Gray matter atrophy in Parkinson's disease with dementia: evidence from meta-analysis of voxel-based morphometry studies.** *Neurol Sci* 2013;34:613–19
13. Almeida OP, Burton EJ, McKeith I, et al. **MRI study of caudate nucleus volume in Parkinson's disease with and without dementia with Lewy bodies and Alzheimer's disease.** *Dement Geriatr Cogn Disord* 2003;16:57–63
14. Burton EJ, McKeith IG, Burn DJ, et al. **Cerebral atrophy in Parkinson's disease with and without dementia: a comparison with Alzheimer's disease, dementia with Lewy bodies and controls.** *Brain* 2004;127:791–800
15. Junqué C, Ramirez-Ruiz B, Tolosa E, et al. **Amygdalar and hippocampal MRI volumetric reductions in Parkinson's disease with dementia.** *Mov Disord* 2005;20:540–44
16. Summerfield C, Junque C, Tolosa E, et al. **Structural brain changes in Parkinson disease with dementia: a voxel-based morphometry study.** *Arch Neurol* 2005;62:281–85
17. Bouchard TP, Malykhin N, Martin WR, et al. **Age and dementia-associated atrophy predominates in the hippocampal head and amygdala in Parkinson's disease.** *Neurobiol Aging* 2008;29:1027–39
18. Nishio Y, Hirayama K, Takeda A, et al. **Corticolimbic gray matter loss in Parkinson's disease without dementia.** *Eur J Neurol* 2010;17:1090–97
19. Tessa C, Giannelli M, Della Nave R, et al. **A whole-brain analysis in de novo Parkinson disease.** *AJNR Am J Neuroradiol* 2008;29:674–80
20. Pereira JB, Ibarretxe-Bilbao N, Marti MJ, et al. **Assessment of cortical degeneration in patients with Parkinson's disease by voxel-based morphometry, cortical folding, and cortical thickness.** *Hum Brain Mapping* 2012;33:2521–34
21. Tinaz S, Courtney MG, Stern CE. **Focal cortical and subcortical atrophy in early Parkinson's disease.** *Mov Disord* 2011;26:436–41
22. Ibarretxe-Bilbao N, Junque C, Segura B, et al. **Progression of cortical thinning in early Parkinson's disease.** *Mov Disord* 2012;27:1746–53
23. Patenaude B, Smith SM, Kennedy DN, et al. **A Bayesian model of shape and appearance for subcortical brain segmentation.** *Neuroimage* 2011;56:907–22
24. Gelb DJ, Oliver E, Gilman S. **Diagnostic criteria for Parkinson disease.** *Arch Neurol* 1999;56:33–39
25. Movement Disorder Society Task Force on Rating Scales for Parkinson's Disease. **The Unified Parkinson's Disease Rating Scale (UPDRS): status and recommendations**. *Mov Disord* 2003;18: 738–50
26. Hoehn MM, Yahr MD. **Parkinsonism: onset, progression, and mortality.** *Neurology* 1967;17:427–42
27. Tomlinson CL, Stowe R, Patel S, et al. **Systematic review of levodopa dose equivalency reporting in Parkinson's disease.** *Mov Disord* 2010;25:2649–53
28. Folstein MF, Robins LN, Helzer JE. **The Mini-Mental State Examination.** *Arch Gen Psychiatry* 1983;40:812
29. Dalrymple-Alford JC, MacAskill MR, Nakas CT, et al. **The MoCA: well-suited screen for cognitive impairment in Parkinson disease.** *Neurology* 2010;75:1717–25
30. Litvan I, Goldman JG, Tröster AI, et al. **Diagnostic criteria for mild cognitive impairment in Parkinson's disease: Movement Disorder Society Task Force guidelines.** *Mov Disord* 2012;27:349–56
31. Rosen WG, Mohs RC, and Davis KL. **A new rating scale for Alzheimer's disease.** *Am J Psychiatry* 1984;141:1356–64
32. Dubois B, Slachevsky A, Litvan I, et al. **The FAB: a frontal assessment battery at bedside.** *Neurology* 2000;55:1621–26
33. Sunderland T, Hill JL, Mellow AM, et al. **Clock drawing in Alzheimer's disease: a novel measure of dementia severity.** *J Am Geriatr Soc* 1989;37:725–29
34. Jenkinson M, Beckmann CF, Behrens TE, et al. **FSL.** *Neuroimage* 2012;62:782–90
35. Gelineau-Morel R, Tomassini V, Jenkinson M, et al. **The effect of hypointense white matter lesions on automated gray matter segmentation in multiple sclerosis.** *Hum Brain Mapping* 2012;33: 2802–14
36. Zivadinov R, Heininen-Brown M, Schirda CV, et al. **Abnormal subcortical deep-gray matter susceptibility-weighted imaging filtered phase measurements in patients with multiple sclerosis: a case-control study.** *Neuroimage* 2012;59:331–39
37. Batista S, Zivadinov R, Hoogs M, et al. **Basal ganglia, thalamus and neocortical atrophy predicting slowed cognitive processing in multiple sclerosis.** *J Neurol* 2012;259:139–46
38. Hughes EJ, Bond J, Svrckova P, et al. **Regional changes in thalamic shape and volume with increasing age.** *Neuroimage* 2012;63: 1134–42
39. Fischl B. **FreeSurfer.** *Neuroimage* 2012;62:774–81
40. Genovese CR, Lazar NA, and Nichols T. **Thresholding of statistical maps in functional neuroimaging using the false discovery rate.** *Neuroimage* 2002;15:870–78
41. Lyoo CH, Ryu YH, and Lee MS. **Topographical distribution of cerebral cortical thinning in patients with mild Parkinson's disease without dementia.** *Mov Disord* 2010;25:496–99
42. Melzer TR, Watts R, MacAskill MR, et al. **Grey matter atrophy in cognitively impaired Parkinson's disease.** *J Neurol Neurosurg Psychiatry* 2012;83:188–94
43. Song SK, Lee JE, Park HJ, et al. **The pattern of cortical atrophy in patients with Parkinson's disease according to cognitive status.** *Mov Disord* 2011;26:289–96
44. Dalaker TO, Zivadinov R, Larsen JP, et al. **Gray matter correlations of cognition in incident Parkinson's disease.** *Mov Disord* 2010; 25:629–33
45. Herrero MT, Barcia C, Navarro JM. **Functional anatomy of thalamus and basal ganglia.** *Childs Nerv Syst* 2002;18:386–404
46. de la Monte SM, Wells SE, Hedley-Whyte T, et al. **Neuropathological distinction between Parkinson's dementia and Parkinson's plus Alzheimer's disease.** *Ann Neurol* 1989;26:309–20
47. de Jong LW, van der Hiele K, Veer IM, et al. **Strongly reduced volumes of putamen and thalamus in Alzheimer's disease: an MRI study.** *Brain* 2008;131:3277–85
48. Kassubek J, Juengling FD, Ecker D, et al. **Thalamic atrophy in Hun-**

tington's disease co-varies with cognitive performance: a morphometric MRI analysis. *Cereb Cortex* 2005;15:846–53
49. Benedict, RH, Hulst HE, Bergsland N, et al. **Clinical significance of atrophy and white matter mean diffusivity within the thalamus of multiple sclerosis patients.** *Mult Scler* 2013;19:1478–84
50. Goldenberg G, Schuri U, Gromminger O, et al. **Basal forebrain amnesia: does the nucleus accumbens contribute to human memory?** *J Neurol Neurosurg Psychiatry* 1999;67:163–68
51. de Jong LW, Wang Y, White LR, et al. **Ventral striatal volume is associated with cognitive decline in older people: a population based MR-study.** *Neurobiol Aging* 2012;33:424.e1–10
52. van Beilen M, Leenders KL. **Putamen FDOPA uptake and its relationship to cognitive functioning in PD.** *J Neurol Sci* 2006;248:68–71
53. Zarei M, Ibarretxe-Bilbao N, Compta Y, et al. **Cortical thinning is associated with disease stages and dementia in Parkinson's disease.** *J Neurol Neurosurg Psychiatry* 2013;84:875–81
54. Lee HM, Kwo, KY, Kim MJ, et al. **Subcortical grey matter changes in untreated, early stage Parkinson's disease without dementia.** *Parkinsonism Relat Disord* 2014;20:622–26
55. Rinne JO, Mlic JR, Paljärvi L, et al. **Dementia in Parkinson's disease is related to neuronal loss in the medial substantia nigra.** *Ann Neurol* 1989;26:47–50

Early Reperfusion Rates with IV tPA Are Determined by CTA Clot Characteristics

S.M. Mishra, J. Dykeman, T.T. Sajobi, A. Trivedi, M. Almekhlafi, S.I. Sohn, S. Bal, E. Qazi, A. Calleja, M. Eesa, M. Goyal, A.M. Demchuk, and B.K. Menon

ABSTRACT

BACKGROUND AND PURPOSE: An ability to predict early reperfusion with IV tPA in patients with acute ischemic stroke and intracranial clots can help clinicians decide if additional intra-arterial therapy is needed or not. We explored the association between novel clot characteristics on baseline CTA and early reperfusion with IV tPA in patients with acute ischemic stroke by using classification and regression tree analysis.

MATERIALS AND METHODS: Data are from patients with acute ischemic stroke and proximal anterior circulation occlusions from the Calgary CTA data base (2003–2012) and the Keimyung Stroke Registry (2005–2009). Patients receiving IV tPA followed by intra-arterial therapy were included. Clot location, length, residual flow within the clot, ratio of contrast Hounsfield units pre- and postclot, and the M1 segment origin to the proximal clot interface distance were assessed on baseline CTA. Early reperfusion (TICI 2a and above) with IV tPA was assessed on the first angiogram.

RESULTS: Two hundred twenty-eight patients (50.4% men; median age, 69 years; median baseline NIHSS score, 17) fulfilled the inclusion criteria. Median symptom onset to IV tPA time was 120 minutes (interquartile range = 70 minutes); median IV tPA to first angiography time was 70.5 minutes (interquartile range = 62 minutes). Patients with residual flow within the clot were 5 times more likely to reperfuse than those without it. Patients with residual flow and a shorter clot length (≤15 mm) were most likely to reperfuse (70.6%). Patients with clots in the M1 MCA without residual flow reperfused more if clots were distal and had a clot interface ratio in Hounsfield units of <2 (36.8%). Patients with proximal M1 clots without residual flow reperfused 8% of the time. Carotid-T/-L occlusions rarely reperfused (1.7%). Interrater reliability for these clot characteristics was good.

CONCLUSIONS: Our study shows that clot characteristics on CTA help physicians estimate a range of early reperfusion rates with IV tPA.

ABBREVIATIONS: CART = classification and regression tree; cirHU = clot interface ratio in Hounsfield units; IA = intra-arterial; IQR = interquartile range; TCD = transcranial Doppler

Acute ischemic stroke treatment is primarily focused on dissolving clots within the arterial tree by using thrombolytic agents administered intravenously or by endovascular techniques. Since the approval of IV tPA for thrombolysis, effort has been made to identify clot characteristics on imaging that predict recanalization with IV tPA. The "hyperattenuated" sign on NCCT is a marker of intracranial clot.[1-3] Its location (MCA versus Sylvian) plays an important role in determining clinical outcome.[4-8] In addition, the length of the hyperattenuated segment on NCCT, especially with ultrathin-section nonenhanced CT reconstructions, correlates with recanalization and good clinical outcome.[9,10] Clot characteristics on CTA that predict recanalization include location and burden.[11-13] Residual flow on transcranial Doppler (TCD) is an imaging marker of recanalizing clot.[14,15]

Current evidence supports the role of early reperfusion in improving clinical outcome in patients with acute ischemic stroke.[16,17] If clinicians are able to estimate early reperfusion rates with IV tPA, they can make decisions favoring rescue intra-arterial (IA) therapy in patients with a low likelihood of early reperfusion with IV tPA.

Received January 19, 2014; accepted after revision May 6.

From the Departments of Clinical Neurosciences (S.M.M., T.T.S., A.T., M.A., E.Q., M.E., M.G., A.M.D., B.K.M.), Radiology (J.D., M.A., M.E., M.G., A.M.D., B.K.M.), and Community Health Sciences (T.T.S., B.K.M.), University of Calgary, Calgary, Alberta, Canada; Department of Neurology (S.I.S.), Dongsan Medical Center, Keimyung University, Daegu, South Korea; Faculty of Medicine (M.A.), King Abdulaziz University, Jeddah, Saudi Arabia; Department of Neurology (S.B.), University of Manitoba, Winnipeg, Manitoba, Canada; Department of Neurology (A.C.), Hospital Clinico Universitario, University of Valladolid, Valladolid, Spain; Seaman Family MR Center (M.A., E.Q., M.E., M.G., A.M.D., B.K.M.), Calgary, Alberta, Canada; and Hotchkiss Brain Institute (T.T.S., M.G., A.M.D., B.K.M.), Calgary, Alberta, Canada.

Paper previously presented at: International Stoke Conference, February 11–14, 2014; San Diego, California.

Please address correspondence to Bijoy K. Menon, MD, Department of Clinical Neurosciences and Radiology, University of Calgary, Hotchkiss Brain Institute, Seaman Family MR Center, Foothills Medical Centre, 1403 29th St NW, Calgary, Alberta, Canada T2N2T9; e-mail: docbijoymenon@gmail.com

http://dx.doi.org/10.3174/ajnr.A4048

Table 1: Baseline demographics and CTA clot characteristics stratified by the 2 populations that form part of the overall study

	Calgary CTA Data Base (*n* = 165)	Keimyung Stroke Registry (*n* = 63)	*P* Value
Age (yr) (mean)	66.4 ± 14.3	69.5 ± 9.96	.12
Sex (male) (%)	49.1%	53.9%	.5
Baseline NIHSS (median) (IQR)	18 (8)	14 (6)	.01
Onset to IV tPA time (minutes) (median) (IQR)	112 (73)	125 (57)	.18
IV tPA initiation to first angiography run time (minutes) (median) (IQR)	53 (45)	139 (75)	.01
Site of occlusion (No.) (%)			
Carotid-T/-L	13 (8%)	1 (1.6%)	.09
Tandem occlusions	38 (23%)	23 (36.5%)	
M1 MCA	86 (52.1%)	31 (49.2%)	
M2 MCA	28 (17%)	8 (12.7%)	
Very early arterial-weighted CTA (preclot HU < 150 and preclot HU ≥ HU at the torcula) (No.) (%)	0 (0%)	2 (3.2%)	.07
Very late venous phase CTA (preclot HU < 150 and preclot HU < HU at the torcula) (No.) (%)	1 (0.6%)	2 (3.2%)	.19
Residual flow (%)	21.8%	4.8%	.01
Clot length (mm) (median) (IQR)	22.3 (34.5)	50 (30.6)	.01
cirHU (median) (IQR)	1.5 (0.85)	2.8 (1.5)	.01
M1 MCA origin to proximal clot interface distance (mm) (median) (IQR)	10.6 (7.6)	9.6 (11.3)	.74

In this study, we report early reperfusion rates with IV tPA stratified by several clot characteristics measured on CTA. Using classification and regression tree analysis (CART), we then derived an algorithm to help clinicians estimate early reperfusion rates with IV tPA in patients with proximal clots.[18]

MATERIALS AND METHODS

Data are from patients presenting with acute ischemic stroke and proximal anterior circulation occlusions from the Calgary CTA data base (2003–2012) and the Keimyung Stroke Registry (2005–2009). Details of both registries have been described in previous publications.[10,19] Similarities and differences in baseline characteristics of patients in these registries are described in Table 1.

Data from both registries were combined for the present analysis to have a sufficient sample size for robust statistical analyses and to increase the generalizability of results. All patients underwent an NCCT of the head at admission followed by CTA of the head and neck. Only patients who received IV tPA followed by a conventional cerebral angiography (DSA) for IA therapy were included in our study. Information on demographic and clinical characteristics was collected at baseline. Stroke severity was assessed by using the NIHSS at baseline, at discharge, and at 90 days. Functional status was assessed by using the mRS at similar timepoints. Interval times from stroke-symptom onset to presentation in the emergency department, imaging, thrombolysis, and endovascular procedures were also collected. The local ethics boards approved both studies.

Image Acquisition and Analysis

Standard nonhelical NCCT scanning was performed on a multisection scanner with a 5-mm section thickness. NCCT was followed by CTA with a helical scan technique. Coverage was from the arch to the vertex with continuous axial sections parallel to the orbitomeatal line of 0.625- to 1.25-mm section thickness. Acquisitions were obtained after a single bolus intravenous contrast injection of 70–120 mL of nonionic contrast media into an antecubital vein at 3–5 mL/s, autotriggered by the appearance of contrast in a region of interest manually placed in the ascending aorta. Differences in protocol between the centers included the following: 1) the use of a scanner (HD75; GE Healthcare, Milwaukee, Wisconsin) versus a Somatom Sensation scanner (Siemens, Erlangen, Germany), and 2) CTA acquisition autotriggered by the appearance of contrast in the arch of the aorta versus the common carotid artery. Patients were taken to the angiography suite for revascularization after receiving IV tPA. The first angiogram of the ipsilesional arterial tree on DSA was used to identify early reperfusion with IV tPA. Baseline and follow-up imaging was analyzed at the imaging core lab of the Calgary Stroke Program. OsiriX, Version 4 (http://www.osirix-viewer.com) was used to reconstruct 2D multiplanar reconstruction images in axial, coronal, and sagittal planes by using 24-mm-thick slabs. An independent reader (M.A.) assessed reperfusion on the first DSA run and final angiography.[17]

Clot Characteristics

The following clot characteristics on baseline CTA were studied while the reader was blinded to conventional angiogram and clinical data.

Clot Location. Clot location was divided into 4 groups: carotid-T/-L, tandem (cervical ICA and M1 MCA occlusions with a patent intracranial ICA), M1 MCA, and proximal M2 MCA occlusions. M1 MCA was defined as a vessel extending from the ICA bifurcation to the origin of the first major branch in the Sylvian sulcus.

Clot Length. Clot length was measured on CTA by using 3-mm multiplanar reconstructions in the axial plane (Fig 1). Whenever the proximal or distal end of clot could not be identified, clot length was imputed to 50 mm. This imputation happened most frequently with ICA clots in which the proximal end was in the neck. We chose 50 mm as our imputation value because no clots that were measurable had lengths of >50 mm. Our use of nonparametric statistics ensures that this imputation does not affect results.

Residual Flow within the Clot. Residual flow within the clot has been described in the TCD literature but never before by using CTA.[14,15] If we saw clearly visibly increased contrast attenuation through the clot compared with surrounding brain parenchyma, it was classified as the presence of residual flow (Fig 2). Clots that are hyperattenuated on NCCT could have increased signal attenuation on CTA; we found no correlation between the presence of the hyperattenuated sign on NCCT and what we classified as residual flow on CTA source images (Fisher exact test; *P* value = .76), thus suggesting that residual flow on CTA is not due to hyperattenuated clots on NCCT. We then graded residual flow within clot as follows— grade 0: clot with no contrast permeation and attenuation similar to that in surrounding brain parenchyma; grade I: clot appearing denser than surrounding brain parenchyma, with contrast potentially permeating through the clot; grade II: hairline or streak of well-defined contrast across the partial or complete length of the clot. Patients with intravascular nonocclusive thrombus on baseline CTA were considered as having early reperfusion at baseline and therefore excluded from analyses.

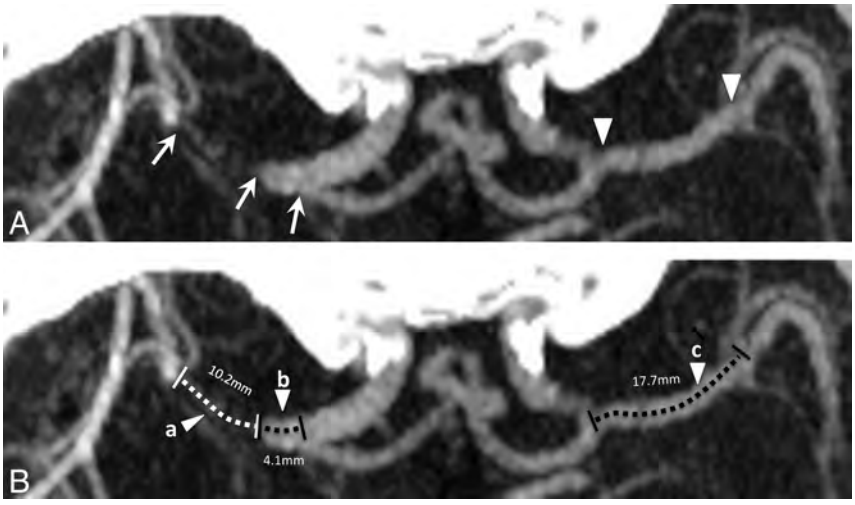

FIG 1. *A*, M1 MCA occluded segment (*white arrows*) with patent proximal M1 MCA on the right and the contralateral M1 MCA (*white arrowheads*). *B*, Clot length (*broken white line*; segment a) and distance from M1 MCA origin to proximal clot interface (*broken black line*; segment b). Measurement of the contralateral M1 MCA segment is shown for reference (segment c).

Clot Interface Ratio in Hounsfield Units. Residual flow within the clot may not always be visible to the naked eye due to partial volume effects on CTA. If, however, contrast signals at the proximal and distal clot

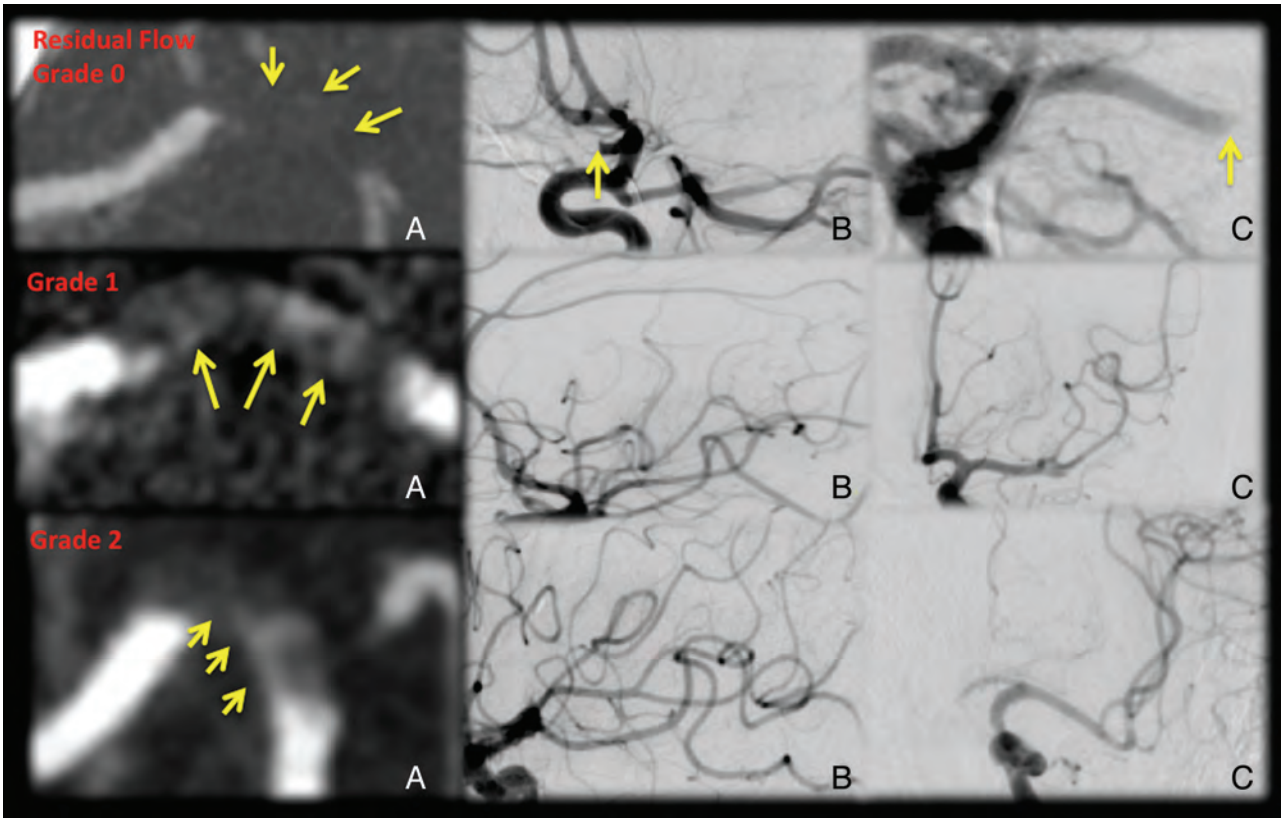

FIG 2. Residual flow on baseline CT angiography along with early reperfusion with IV tPA assessed on the first angiogram of the ipsilesional arterial tree. The top panel shows a patient with a left M1 MCA clot and no residual flow (*A*, grade 0 residual flow, *yellow arrows*, density similar to that of surrounding brain parenchyma). The first angiogram shows no recanalization (*B* and *C*). The middle panel shows a left M1 MCA clot with grade 1 residual flow (*A*, *yellow arrows*, denser than surrounding brain parenchyma). The first angiogram shows excellent reperfusion (*B* and *C*). The bottom panel shows a left M1 MCA clot with grade 2 residual flow (*A*, *yellow arrows*, hairline or streak of well-defined contrast across the partial or complete length of the clot). The first angiogram shows excellent reperfusion (*B* and *C*).

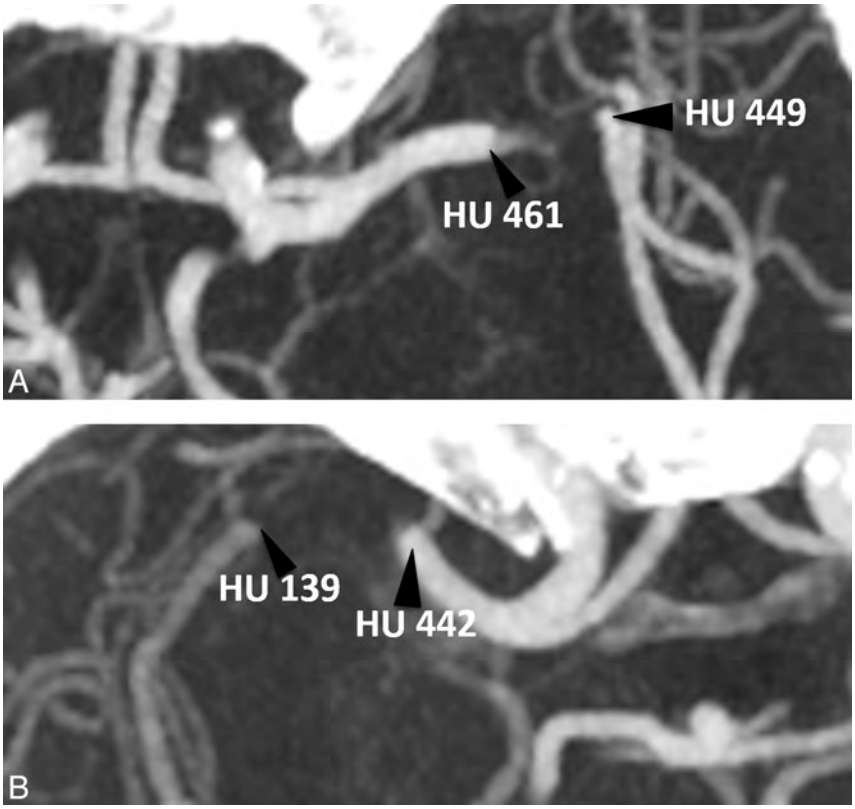

FIG 3. Clot interface Hounsfield unit ratio calculated by measuring the Hounsfield units in a region of interest selected at the proximal and distal clot interface only in scans that are mid- to late arterial- or appropriate venous-weighted. cirHU is calculated by dividing the proximal clot interface Hounsfield unit by the distal clot interface Hounsfield unit. In *A*, a patient with a left M1 MCA clot has a cirHU of 1.05 while in *B*, a patient with a left M1 MCA clot has a cirHU of 3.21.

interface (in an appropriate venous-weighted scan) are similar, the similarity is a potential marker of residual flow through the clot or of good collateral status. If contrast signal at the proximal end of the clot is high but drops at the distal end, it could mean no residual flow and/or poor collateral status. The presence of residual flow and/or good collaterals could be associated with increased reperfusion rates with IV tPA. To test this hypothesis, we calculated the clot interface ratio in Hounsfield units (cirHU) by dividing the proximal clot interface Hounsfield units by the distal clot interface Hounsfield units (Fig 3). CirHU was not calculated whenever proximal or distal clot interface Hounsfield units could not be measured. We decided to exclude from analyses CTAs that were very early arterial weighted (preclot Hounsfield units $<$150 and greater than Hounsfield units at the torcula) because this would affect the validity of our assumptions on cirHU being a marker of residual flow and/or good collaterals.

Distance from the M1 MCA Origin to the Proximal Clot Interface. For M1 MCA occlusions, we studied an additional clot characteristic by measuring the distance from the M1 MCA origin to the proximal clot interface.[20,21] Distal M1 MCA clots may be exposed to more shear stress at the proximal clot interface due to patent flow in the lenticulostriate arteries compared with proximal clots. Additionally, distal M1 clots are potentially smaller than proximal clots. Smaller clots with more shear stress at the clot interface may lyse more with IV tPA.[20,22]

Early Reperfusion

All past and current literature reports recanalization/reperfusion with IV tPA by using either TCD Thrombolysis in Brain Infarction grades or Thrombolysis in Myocardial Infarction grades.[11,14,15] We, therefore, chose to use TICI 2a/2b/3 on the first angiogram of the ipsilesional arterial tree on DSA as our primary measure of reperfusion; this grade is comparable with Thrombolysis in Myocardial Infarction 2 and will therefore give readers an ability to compare the rates we report with those in previous literature. Nonetheless, we also reported reperfusion rates measured as TICI 2b/3 as a secondary outcome measure and performed sensitivity analyses with this latter outcome.

Statistical Analyses

Categoric data are reported by using proportions, ordinal data, and continuous data, with a skewed distribution by using medians and continuous data with a normal distribution by using means. Because the proximal or distal end of the clot was not identified in some patients, an arbitrary value of $>$50 mm was assigned to such patients. Our choice of nonparametric statistics based on ranks for this variable ensured that this imputation did not affect results. Association between clot characteristics and early reperfusion (TICI 2a to 3) was studied by using the Fisher exact test of proportions for categoric data and the Wilcoxon rank sum test for nonparametric data. In addition, we did 3 sensitivity analyses: 1) analyses restricted to M1 MCA occlusions with reperfusion defined as TICI 2a–3; and 2) analyses of the whole sample with reperfusion defined as TICI 2b/3; and finally 3) similar analyses restricted to each of the 2 populations (ie, the Calgary and the Keimyung data) in our sample. A 2-sided $\alpha < .05$ was considered statistically significant. These analyses were performed by using STATA/SE 12.1 software (StataCorp, College Station, Texas).

We then used a recursive partitioning classification and a regression tree (CART, Fig 4) to model the relationship between early reperfusion and various clot characteristics. CART is a distribution-free regression method that builds a tree by recursively partitioning the data into increasingly homogeneous subgroups to maximize the explained variance within each subgroup. At each stage (node), the CART algorithm selects the explanatory variable and splitting value that gives the best discrimination between 2 outcome classes. A full CART algorithm adds nodes until they are homogeneous or contain few observations. Our use of CART as a model-building strategy helped us explore the rich nonlinear interactions between various clot characteristics, determine collinearity, and predict early reperfusion while deriving estimates of reperfusion.[18] Predictor variables included resid-

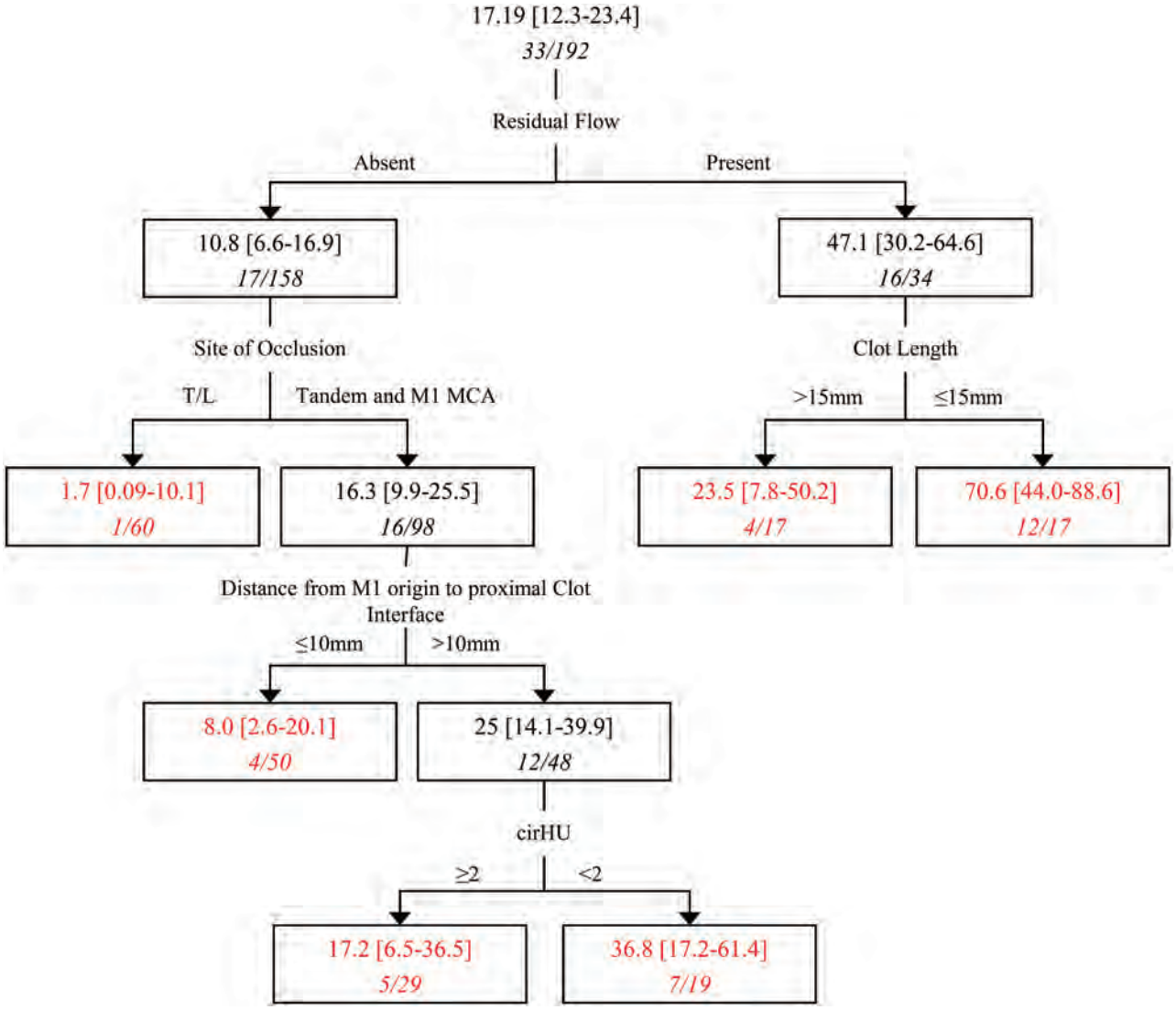

FIG 4. Tree representation of a recursive partitioning model (CART) predicting early reperfusion with IV tPA. Each subgroup (*rectangle*) has the percentage of subjects with early reperfusion (95% confidence interval). The number of subjects reperfused/number of subjects in each subgroup is italicized below each percentage. In all, 33/192 (17.19%) patients with ICA and M1 MCA clots achieved early reperfusion. Tree end points are highlighted in red. Splitting criteria and subgroup characteristics are described along each connecting line.

ual flow (grades 1–2 versus 0), clot length (≤15 mm versus >15 mm), cirHU (≥2 versus <2), and distance from the M1 MCA origin to the proximal clot interface (≤10 mm versus >10 mm; all patients with ICA occlusions had length imputed to 0).

We restricted the model to include only patients with ICA, tandem, and M1 MCA occlusions. This was deliberate because in this population of patients with proximal occlusions, a decision analysis model helps clinicians decide if early reperfusion with IV tPA is so low that rescue IA therapy may be worthwhile. This part of the analysis was performed by using *R* statistical computing software, Version 3.0.1 (http://www.r-project.org). The ANOVA method was chosen so that the nodes would be reported as the proportion of recanalization in each subgroup. Early reperfusion rates, including 95% confidence intervals, were calculated for each of the nodes after the final model was determined. Two readers (S.M.M. and M.E.) assessed all clot characteristics blinded to all follow-up data. Interrater reliability for each clot characteristic and for TICI on the first angiogram of the ipsilesional arterial tree on DSA is reported in 30 patients by using an unweighted κ and was interpreted as per the Landis and Koch template.

RESULTS

We identified 228 patients (50.4% men; median age, 69 years; median baseline NIHSS score, 17) who fulfilled the inclusion criteria. Median symptom onset to IV tPA time was 120 minutes (interquartile range [IQR] = 70 minutes); median IV tPA to first angiography time was 70.5 minutes (IQR = 62 minutes). Baseline demographics and clot characteristics by center are described in Table 1. Early reperfusion rates with IV tPA, final reperfusion rates after IA therapy, and final clinical outcome are reported in Fig 5.

Primary Analysis

In analyses defining early reperfusion as TICI 2a/2b/3, median clot length in the early reperfusers was 19 mm (IQR = 12.9 mm)

Location (number, %)		Median clot length in mm (IQR)	Early reperfusion with IV tPA (n, %)	Final reperfusion post IA (n, %)	90-day mRS 0-2 (n, %)
	T/L 61 (26.7%)	50 (IQR = 0)	1 (1.6%)	25 (41%)	14 (23%)
	Tandem 14 (6.1%)	26.3 (IQR = 32.2)	4 (28.6%)	10 (71.4%)	7 (50%)
	M1 MCA 117 (51.3%)	21.6 (IQR = 20.7)	28 (23.9%)	84 (71.8%)	68 (58.1%)
	M2 MCA 36 (15.8%)	22.4 (IQR = 22.8)	14 (38.9%)	29 (80.5%)	27 (75%)

FIG 5. Clot location and length on baseline CTA along with early reperfusion (TICI 2a/2b/3) rates with IV tPA, final reperfusion (TICI 2b/3) at end of the IA procedure, and 90-day clinical outcome (mRS 0–2).

compared with the nonreperfusers (34.9 mm, IQR = 30.7 mm, $P < .001$). Residual flow was present in 39/228 (17.1%) patients. Early reperfusion was seen in 27/189 (14.3%) patients without any residual flow (grade 0), in 13/30 (43.3%) patients with grade 1 residual flow, and in 7/9 (77.8%) patients with grade 2 residual flow ($P < .001$). CirHU could be measured in 165/228 (72.4%) patients. Median cirHU in the early reperfusers was 1.48 (IQR = 0.64) compared with the nonreperfusers (1.88, IQR = 1.41, $P < .01$). In patients with a cirHU < 2, early reperfusion was seen in 37/101 (36.6%) compared with 9/64 (14.1%) with cirHU ≥ 2 ($P < .01$).

Sensitivity Analyses Restricted to M1 MCA Occlusions

We identified 117 patients with M1 MCA occlusion. Residual flow was present in 28/117 (23.9%) patients. Early reperfusion (TICI 2a/2b/3) was seen in 15/91 (16.5%) patients without any residual flow at the site of the clot (grade 0), in 10/21 (47.6%) patients with grade 1 residual flow, and in 3/5 (60%) patients with grade 2 residual flow ($P = .002$). Median clot length in the early reperfusers was 17.1 mm (IQR = 14.8 mm) compared with the nonreperfusers (22.7 mm, IQR = 19.3, $P = .01$). cirHU could be measured in 116/117 patients. Median cirHU in the early reperfusers was 1.53 (IQR = 6.5) compared with the nonreperfusers (2.05 mm, IQR = 1.5, $P < .01$). In patients with a cirHU < 2, early reperfusion was seen in 23/66 (34.8%) compared with 5/50 (10%) patients with cirHU ≥ 2 ($P = .002$). Median M1 origin to proximal clot interface distance in the early reperfusers was 13.4 mm (IQR = 10.95 mm) compared with 9.3 mm (IQR = 7.7 mm) in the nonreperfusers ($P = .001$). When clots were located >10 mm from the M1 MCA origin, 20/60 (33.3%) showed early reperfusion compared with 8/57 (14%) in clots that were ≤10 mm from the M1 MCA origin ($P = .01$).

Sensitivity Analyses Defining Early Reperfusion as TICI 2b/3

Early reperfusion on the first angiography run was seen in 1/61 (1.6%) of "T/L" type occlusions, in 3/14 (21.4%) of tandem occlusions, in 14/117 (12%) of M1 MCA occlusions, and in 5/36 (14%) of M2 MCA occlusions ($P = .02$). Early reperfusion (TICI 2b/3) was seen in 7/189 (3.7%) patients without any residual flow

Table 2: Interrater reliability of various clot characteristics on CTA and TICI on first-run angiography ($n = 30$)

Clot Characteristics	Agreement	κ	*P* Value
Residual flow (grades 0, 1, 2)	86.7%	0.66	<.0001
Clot length (≤15 vs >15 mm)	100%	1	<.0001
Distance from M1 MCA origin (≤10 vs >10 mm)	100%	1	<.0001
cirHU ≥2 vs <2)	90%	0.78	<.0001
Early reperfusion with IV tPA (TICI 2a–3)	100%	1	<.0001

at the site of the clot (grade 0), in 11/30 (36.7%) patients with grade 1 residual flow, and in 5/9 (55.5%) patients with grade 2 residual flow ($P < .001$). Median clot length in the early reperfusers was 14.6 mm (IQR = 13.8 mm) compared with the nonreperfusers (32 mm, IQR = 30.9 mm, $P < .001$). In patients with a cirHU < 2, early reperfusion was seen in 21/101 (20.8%) compared with 1/64 (1.6%) patients with cirHU ≥ 2 ($P < .001$).

CART Model

When using recursive partitioning (CART) and restricting the analyses to patients with ICA and M1 occlusions only, residual flow within the clot (grades 1–2) was the most discriminative predictor of early reperfusion (TICI 2a–3) followed by clot location, length, distance from M1 origin, and cirHU. In patients with residual flow, 16/34 (47.1%) reperfused compared with 17/158 (10.8%) without residual flow. Among patients with clots having residual flow, those with a shorter clot length (≤15 mm) had a 70.6% rate of early reperfusion compared those with longer clots (>15 mm) with 23.5% early reperfusion. When residual flow was absent, 1.7% of patients with a carotid-T/-L occlusion reperfused early compared with 16.3% of patients with tandem or M1 MCA clots. Of patients without residual flow with tandem/M1 occlusions, if the distance of the clot from the M1 MCA origin was ≤10 mm, 8% of patients reperfused early compared with a 25% early reperfusion rate in patients with clots >10 mm from the M1 MCA origin. Last, in those patients with clots >10 mm from the M1 MCA origin, early reperfusion was seen in 36.8% of patients with cirHU < 2 compared with 17.2% in patients with cirHU ≥ 2. The decision tree derived from recursive portioning along with 95% confidence intervals around estimates of early reperfusion is shown in Fig 4.

Finally, in sensitivity analyses restricted to the Calgary and Keimyung populations, we did not notice any differential effect of clot characteristics on early reperfusion rates (data not shown). Interrater reliability for all clot characteristics and for TICI on the first DSA was substantial (Table 2).

DISCUSSION

In the largest sample to date, we show that clot characteristics on baseline CTA, including location, length, residual flow, and blood flow around the clot (cirHU), can be used to estimate early reperfusion rates with IV tPA (Fig 4). We also show the generalizability of our results by their applicability in 2 different populations. Our results will inform trialists and physicians of patients who could reperfuse early with IV tPA and those who are more likely to require additional IA therapy to achieve early reperfusion.

Our data show that reperfusion rates with IV tPA are lower when clots are longer. This effect of clot length on lysis has been corroborated by previous studies by using other imaging modalities, including NCCT.[3,9] Furthermore, by using CART, we are able to show that early reperfusion with IV tPA is highest in clots having residual flow that are, in addition, short. Residual flow within a clot is associated with less tissue damage in coronary angiography and higher rates of arterial recanalization in patients with stroke by using TCD with IV tPA.[14,23] Residual flow within the clot could be a surrogate for intrinsic clot properties (porous versus impermeable).[22,24] Our study, for the first time, describes a potential imaging marker on CTA for residual flow within a clot. The lack of any significant association between residual flow on CTA and the hyperattenuated sign on NCCT suggests that residual flow grade was not influenced by intrinsic clot attenuation in our study.[24,25]

In vitro studies show that clot lysis increases if more clot surface is exposed to blood.[22] Our study uses a novel measure (cirHU) for the extent of blood flow around the clot. CirHU is a marker of good collateral flow and/or residual flow through the clot. It helps in further discrimination of early reperfusion rates (Fig 4). We also confirm a previously reported association between early recanalization and the distance of the clot from the M1 MCA origin.[20,21]

Our study has limitations. We restricted our analysis of early reperfusion rates with IV tPA to baseline CTA characteristics. Nonetheless, no relationship between hyperdense sign on NCCT and residual flow on CTA in our data attests to the fact that these imaging modalities measure very different clot qualities. Moreover, detailed analysis of clot characteristics on NCCT requires thin sections to which we did not have access.[3] We could not directly measure residual flow within the clot by using another imaging technique like TCD because of the retrospective nature of our study; nonetheless, we show that the imaging marker we propose for residual flow correlates with early reperfusion rates with IV tPA, thus providing a measure of construct validity for our hypothesis. Because we only included patients who were taken to the angiography suite for IA thrombolysis, a selection bias toward patients with larger clots and more severe ischemia is possible in our sample. Finally, our sample includes patients from 2 different centers, one of which is predominantly East Asian. This latter population is known to have higher rates of intracranial atherosclerosis. Besides, differences in CT scanning equipment and acquisition protocol (autotriggering) between the 2 centers could explain the differences in some baseline CTA imaging measures (Table 1). Nonetheless by including data from both centers, we are able to increase our sample size and the generalizability of our findings.[13]

CONCLUSIONS

Our results and the decision analysis (CART) algorithm we describe in Fig 4 need to be validated in a larger prospective cohort of patients. Such a predictive model of early reperfusion by using baseline imaging could help clinical decision-making when administering IV tPA and IA therapy in addition to being used in the targeted design of clinical trials in patients with acute ischemic stroke.

Disclosures: Mayank Goyal—*UNRELATED*: *Consultancy*: Covidien/ev3, *Comments*: for design, conducting, and educating related to acute stroke trials; *Payment for Lectures (including service on Speakers Bureaus)*: Covidien/ev3, *Comments*: education on acute stroke imaging and treatment; *Stock/Stock Options*: Calgary Scientific, NoNo Inc, *Comments*: own stock. Andrew M. Demchuk—*RELATED:* The Calgary CTA database was supported by Heart and Stroke Foundation of Alberta, North West Territories and Nunavut funding, and the Heart and Stroke Foundation Chair in Stroke Research.* *UNRELATED*: *Grants/Grants Pending*: receives grant support from the Canadian Institute of Health Research to study clot characteristics predicting early reperfusion with IV tPA.* Bijoy K. Menon—*UNRELATED*: *Grants/Grants Pending*: Canadian Institute for Health Research,* *Comments*: grant for a prospective study aimed at understanding reperfusion with IV tPA. This project, however, does not use any data from the above-mentioned study. *Money paid to the institution.

REFERENCES

1. von Kummer R, Meyding-Lamade U, Forsting M, et al. **Sensitivity and prognostic value of early CT in occlusion of the middle cerebral artery trunk.** *AJNR Am J Neuroradiol* 1994;15:9–15
2. Leys D, Pruvo JP, Godefroy O, et al. **Prevalence and significance of hyperdense middle cerebral artery in acute stroke.** *Stroke* 1992; 23:317–24
3. Riedel CH, Jensen U, Rohr A, et al. **Assessment of thrombus in acute middle cerebral artery occlusion using thin-slice nonenhanced computed tomography reconstructions.** *Stroke* 2010;41:1659–64
4. Moulin T, Cattin F, Crepin-Leblond T, et al. **Early CT signs in acute middle cerebral artery infarction: predictive value for subsequent infarct locations and outcome.** *Neurology* 1996;47:366–75
5. Tomsick T, Brott T, Barsan W, et al. **Prognostic value of the hyperdense middle cerebral artery sign and stroke scale score before ultraearly thrombolytic therapy.** *AJNR Am J Neuroradiol* 1996;17: 79–85
6. Somford DM, Nederkoorn PJ, Rutgers DR, et al. **Proximal and distal hyperattenuating middle cerebral artery signs at CT: different prognostic implications.** *Radiology* 2002;223:667–71
7. Leary MC, Kidwell CS, Villablanca JP, et al. **Validation of computed tomographic middle cerebral artery "dot" sign: an angiographic correlation study.** *Stroke* 2003;34:2636–40
8. Barber PA, Demchuk AM, Hudon ME, et al. **Hyperdense Sylvian fissure MCA "dot" sign: a CT marker of acute ischemia.** *Stroke* 2001;32:84–88
9. Riedel CH, Zimmermann P, Jensen-Kondering U, et al. **The importance of size: successful recanalization by intravenous thrombolysis in acute anterior stroke depends on thrombus length.** *Stroke* 2011;42:1775–77
10. Shobha N, Bal S, Boyko M, et al. **Measurement of length of hyperdense MCA sign in acute ischemic stroke predicts disappearance after IV tPA.** *J Neuroimaging* 2014;24:7–10
11. Bhatia R, Hill MD, Shobha N, et al. **Low rates of acute recanalization with intravenous recombinant tissue plasminogen activator in ischemic stroke: real-world experience and a call for action.** *Stroke* 2010;41:2254–58
12. Puetz V, Dzialowski I, Hill MD, et al. **Intracranial thrombus extent predicts clinical outcome, final infarct size and hemorrhagic transformation in ischemic stroke: the clot burden score.** *Int J Stroke* 2008;3:230–36
13. Lee KY, Han SW, Kim SH, et al. **Early recanalization after intravenous administration of recombinant tissue plasminogen activator as assessed by pre- and post-thrombolytic angiography in acute ischemic stroke patients.** *Stroke* 2007;38:192–93
14. Saqqur M, Tsivgoulis G, Molina CA, et al. **Residual flow at the site of intracranial occlusion on transcranial Doppler predicts response to intravenous thrombolysis: a multi-center study.** *Cerebrovasc Dis* 2009;27:5–12
15. Ma M, Berger J. **A novel TCD grading system for residual flow in stroke patients.** *Stroke* 2001;32:2446
16. Rha JH, Saver JL. **The impact of recanalization on ischemic stroke outcome: a meta-analysis.** *Stroke* 2007;38:967–73
17. Wintermark M, Albers GW, Broderick JP, et al. **Acute stroke imaging research roadmap II.** *Stroke* 2013;44:2628–39
18. Lemon SC, Roy J, Clark MA, et al. **Classification and regression tree analysis in public health: methodological review and comparison with logistic regression.** *Ann Behav Med* 2003;26:172–81
19. Menon BK, Smith EE, Coutts SB, et al. **Leptomeningeal collaterals are associated with modifiable metabolic risk factors.** *Ann Neurol* 2013;74:241–48
20. Hirano T, Sasaki M, Mori E, et al. **Residual vessel length on magnetic resonance angiography identifies poor responders to alteplase in acute middle cerebral artery occlusion patients: exploratory analysis of the Japan Alteplase Clinical Trial II.** *Stroke* 2010;41:2828–33
21. Saarinen JT, Sillanpaa N, Rusanen H, et al. **The mid-M1 segment of the middle cerebral artery is a cutoff clot location for good outcome in intravenous thrombolysis.** *Eur J Neurol* 2012;19:1121–27
22. Anand M, Rajagopal K, Rajagopal KR. **A model for the formation and lysis of blood clots.** *Pathophysiol Haemost Thromb* 2005;34: 109–20
23. Blanke H, Cohen M, Karsch KR, et al. **Prevalence and significance of residual flow to the infarct zone during the acute phase of myocardial infarction.** *J Am Coll Cardiol* 1985;5:827–31
24. Liebeskind DS, Sanossian N, Yong WH, et al. **CT and MRI early vessel signs reflect clot composition in acute stroke.** *Stroke* 2011;42: 1237–43
25. Moftakhar P, English JD, Cooke DL, et al. **Density of thrombus on admission CT predicts revascularization efficacy in large vessel occlusion acute ischemic stroke.** *Stroke* 2013;44:243–45

Transcranial Sonography of the Substantia Nigra: Digital Image Analysis

D. Školoudík, M. Jelínková, J. Blahuta, P. Čermák, T. Soukup, P. Bártová, K. Langová, and R. Herzig

ABSTRACT

BACKGROUND AND PURPOSE: Increased echogenicity of the substantia nigra is a typical transcranial sonography finding in Parkinson disease. Experimental software for digital analysis of the echogenic substantia nigra area has been developed. The aim of this study was to compare the evaluation of substantia nigra echogenicity by using digital analysis with a manual measurement in patients with Parkinson disease and healthy volunteers.

MATERIALS AND METHODS: One hundred thirteen healthy volunteers were enrolled in the derivation cohort, and 50 healthy volunteers and 30 patients with Parkinson disease, in the validation cohort. The substantia nigra was imaged from the right and left temporal bone window by using transcranial sonography. All subjects were examined twice by using different sonographic machines by an experienced sonographer. DICOM images of the substantia nigra were encoded; then, digital analysis and manual measurement of the substantia nigra were performed. The 90th percentile of the derivation cohort values was used as a cut-point for the evaluation of the hyperechogenic substantia nigra in the validation cohort. The Spearman coefficient was used for assessment of the correlation between both measurements. The Cohen κ coefficient was used for the assessment of the correlation between both measurements and Parkinson disease diagnosis.

RESULTS: The Spearman coefficient between measurements by using different machines was 0.686 for digital analysis and 0.721 for manual measurement ($P < .0001$). Hyperechogenic substantia nigra was detected in the same 26 (86.7%) patients with Parkinson disease by using both measurements. Cohen κ coefficients for digital analysis and manual measurement were 0.787 and 0.762, respectively ($P < .0001$).

CONCLUSIONS: The present study showed comparable results when measuring the substantia nigra features conventionally and by using the developed software.

ABBREVIATIONS: AC1 = first-order agreement coefficient; *I* = intensity; PD = Parkinson disease; SN = substantia nigra; TI = tissue index; TCS = transcranial sonography

Parkinson disease (PD) is a progressive neurodegenerative disorder. Postmortem and neuroimaging studies showed that PD-associated neuronal dysfunction, cell loss, and α-synuclein pathology begin years before clinical symptoms appear and clinical diagnosis is possible.[1-4] This preclinical period may be the most promising time window for successful neuroprotective interventions in PD.[5]

Increased echogenicity of the substantia nigra (SN) is a typical transcranial sonography (TCS) finding in patients with PD. Recent studies reported an enlarged hyperechogenic SN in approximately 90% of patients with PD, by using cutoff values between 0.20 and 0.25 cm^2, depending on the specific sonography system used.[6,7] In contrast, a hyperechogenic enlarged SN is detectable in only approximately 10% of healthy volunteers.[8] Moreover, this feature is already present in prediagnostic disease stages and persists during the course of PD without

Received February 24, 2014; accepted after revision May 26.

From the Faculty of Health Science (D.Š.), Palacký University Olomouc, Olomouc, Czech Republic; Department of Neurology (D.Š., M.J., P.B.), University Hospital Ostrava, Ostrava, Czech Republic; Department of Neurology (M.J.), Hospital, Karviná-Ráj, Karviná, Czech Republic; Institute of Computer Science (J.B., P.Č., T.S.), Faculty of Philosophy and Science, Silesian University in Opava, Opava, Czech Republic; Department of Biophysics (K.L.), Faculty of Medicine and Dentistry, Institute of Molecular and Translational Medicine, Palacký University, Olomouc, Czech Republic; and Department of Neurology (R.H.), Charles University Faculty of Medicine and University Hospital Hradec Králové, Hradec Králové, Czech Republic.

This work was supported by a grant from the Moravian-Silesian Region, No. CZ.1.05/2.1.00/010030.

Paper previously presented as a special oral presentation at: Annual Meeting of the American Academy of Neurology, March 16–23, 2013; San Diego, California.

Please address correspondence to David Školoudík, MD, PhD, FESO, Department of Neurology, University Hospital Ostrava, CZ-708 52 Ostrava, Czech Republic; e-mail: skoloudik@hotmail.com

Indicates open access to non-subscribers at www.ajnr.org

Evidence-Based Medicine Level 2.

http://dx.doi.org/10.3174/ajnr.A4049

significant changes.[9,10] Approximately 60% of healthy volunteers with hyperechogenic SN show a decrease in ^{18}F-DOPA uptake in the striatum,[8] and hyperechogenic SN is more frequently observed in subjects prone to develop extrapyramidal symptoms after neuroleptic therapy.[11]

However, the main limitation of TCS in the evaluation of SN hyperechogenicity is the dependence of image quality on both the sonographer's experience and the quality of the bone window.[12-14] Digital analysis of TCS images of the SN could eliminate this limitation. We developed an experimental application B-mode Assist System with a graphic user interface in Matlab (MathWorks, Natick, Massachusetts), an integrated development environment with a plug-in Image Processing Toolbox, for digital analysis of SN echogenicity.[15,16]

The aim of the study was to compare the manual measurement of SN with digital analysis of SN echogenicity by using the developed software obtained by 2 different sonography machines in patients with PD and healthy volunteers.

MATERIALS AND METHODS

One hundred nineteen healthy volunteers were examined in the neurosonologic laboratory during 1 month for the evaluation of normal values for SN for both manual and automatic measurements of the area: the derivation cohort. Two months later, 52 healthy volunteers and 32 patients with PD were enrolled in the validation study: the validation cohort. Patients with PD were diagnosed in accordance with the UK Parkinson's Disease Society Brain Bank criteria.[17] Subjects who exhibited low quality of the TCS B-mode (due to an insufficient temporal bone window) as tested by the developed software were excluded from the study—6 in the derivation cohort, 2 healthy volunteers, and 2 patients with PD in the validation cohort. The image quality was evaluated by a developed B-mode Assist System as a part of the digital analysis of the image. Images with a mean value of brightness intensity (I) $\geq$ 25 in all 5 $\times$ 5 mm pixels were considered low-quality. The entire study was conducted in accordance with the Declaration of Helsinki of 1975 (as revised in 2004 and 2008). The study was approved by the ethics committee of the University Hospital Ostrava. All patients provided written informed consent.

Transcranial Sonography

The substantia nigra was imaged in all subjects from both the right and left temporal bone windows in the axial mesencephalic plane. Two examinations of the SN were performed by using 2 different machines, My Lab Twice (Esaote, Genova, Italy) with a PA 240 phased array (machine 1) and Vivid 7 Pro (GE Healthcare, Horten, Norway) with a 3S phased array (machine 2) in all subjects during a 2-week period.

The examination was performed through a temporal bone window with the following parameters: for the My Lab Twice: a penetration depth of 16 cm; penetration, high; dynamic range, 7 (50 dB); frequency, 1–4 MHz; enhancement, 3; attenuation, 2; view, 9; persistence, 7; dynamic compression, 0; gain, 36%; gray map, 0; S view, off; 2 focuses in 5 and 10 cm; mechanical index, 0.9; tissue indices (TIs) 1.0, TIB 1.0, and TIC 2.1; for the Vivid 7 Pro: penetration depth, 15 cm; dynamic range, 51 dB; frequency, 1.5–3.6 MHz; persistence, 5.6; frame rate, 24.5/s; filter reject, 2; gain, −10; gray map, J; 2 focuses in 5 and 10 cm; mechanical index, 1.2; TIC, 1.4.

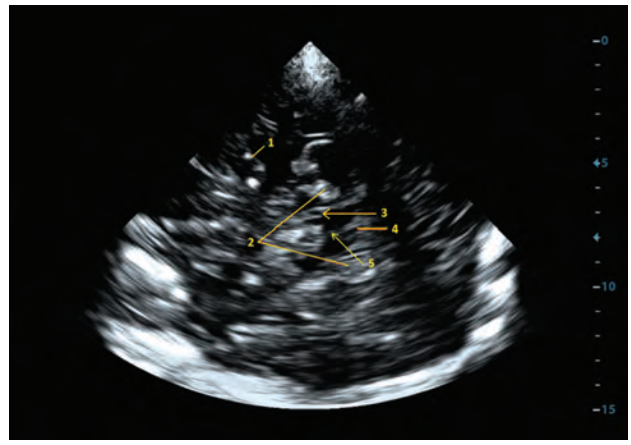

FIG 1. Transcranial sonography: brain stem with the substantia nigra imaged from a transtemporal approach, axial mesencephalic plane. 1) middle cerebral artery, 2) perimesencephalic cisterns, 3) substantia nigra, 4) fourth ventricle, and 5) brain raphe.

The butterfly-shaped structures of the mesencephalic brain stem and the region of the SN were depicted as clearly as possible from the transversal plane (Fig 1). The right and then the left temporal bone windows were used, and both images were saved in DICOM format. Personal data and examination times were deleted, and all acquired images were encoded as anonymized data by using a unique key before manual measurement or digital analysis.

Four images (1 image from the left side and 1 from the right side acquired by using both machines) were obtained from each subject. All examinations were performed by a single sonographer (D.Š.) who was blinded to the patient diagnoses but not to movement disorder symptoms.

Manual and Automatic Measurements

The SN ipsilateral to the insonation was assessed from both sides. Manual SN echogenic size measurements were performed on axial scans automatically after manual encircling of the outer circumference of the echogenic SN area from encoded images by the same experienced sonographer (D.Š.) with 15 years' experience with TCS evaluation of the SN.[18,19] Interinvestigator and intrainvestigator correlations were published previously.[14]

For all subsequent processing steps of the digital analysis and measurement, images without SN-area encircling were converted to 8-bit gray-scale (intensity value I = 0–255). The designed algorithm allowed region-of-interest-based processing on gray-scale images with intensities of 0–255, binary thresholding, and computation of areas inside an elliptic region of interest. The size and shape of the region of interest were based on the histologic image of the SN (Fig 2), and the same region of interest was used for digital analysis of all images.[15,16] Input images were loaded into the application and cropped to a window of 50 $\times$ 50 mm from the native axis of the image. A predefined elliptic region of interest was manually placed in the region of the SN by a single technician (J.B.) trained in TCS image evaluation. The algorithm computed the area for each I (from 0 to 255) inside the total

area = 50 mm^2 of the elliptic region of interest circumscribed in the ipsilateral SN. The echogenicity index as a total sum of areas (area under the curve) was counted for each image. The 90th percentile value from the derivation cohort was set as a border value. The difference between the border value and the counted value of the echogenicity index of each image in the validation cohort was used for differentiation between normal (minus values) and hyperechogenic SNs (plus values) (Fig 3).

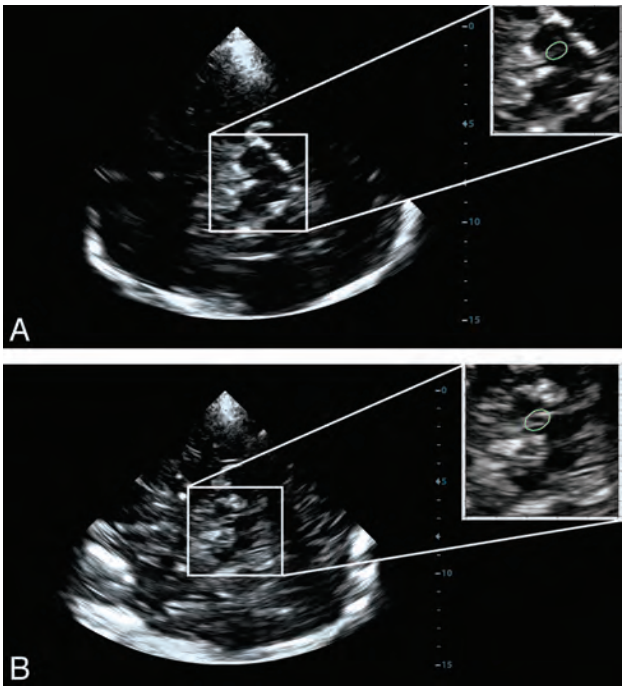

FIG 2. Placement of the region of interest (green) for digital analysis on the TCS brain stem images obtained from a healthy volunteer (*A*) and a patient with Parkinson disease (*B*).

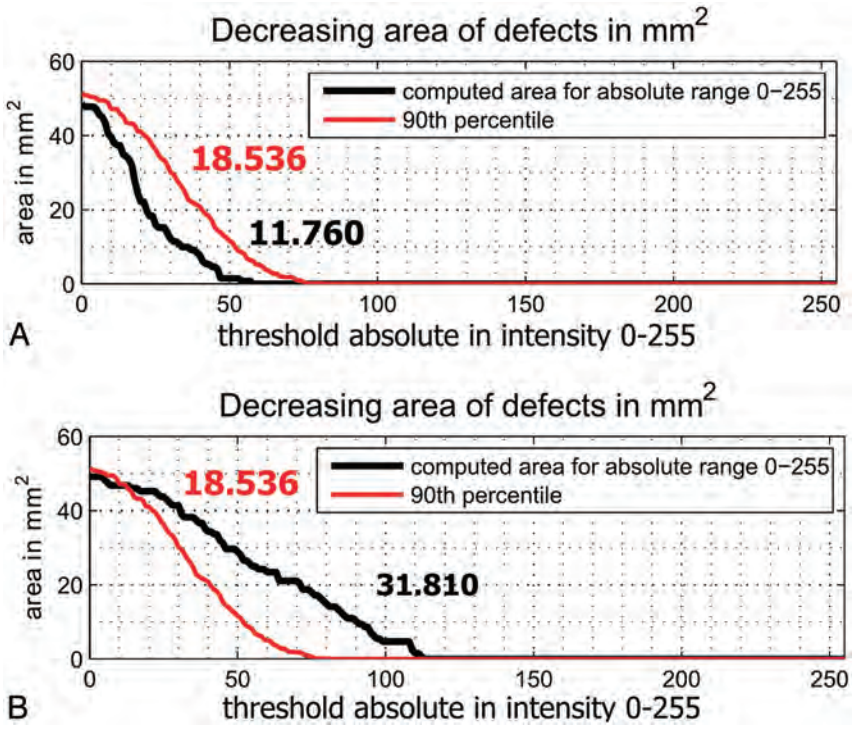

FIG 3. The difference between the 90th percentile of the derivation cohort (*red line*; echogenicity index, 18.536) and the counted value in the validation cohort (black) measured by using machine 1. *A*, Normal echogenicity of the substantia nigra (echogenicity index, 11.760). *B*, Hyperechogenic substantia nigra (echogenicity index, 31.810).

Statistics

The Shapiro-Wilk test was used for the correspondence of calculated parameters to a normal distribution. Data with a normal distribution are reported as mean ± SD. All parameters not fitting a normal distribution are presented as mean, median, and interquartile range. Comparative statistical analysis was performed to calculate the level of linear correlation, with the Spearman correlation coefficient (r), between both manual measurement and digital analysis, right and left temporal bone windows, and different sonographic machines. The Cohen κ and first-order agreement coefficient (AC1) were applied when we statistically assessed the correlation between PD diagnosis and manual measurement or digital analysis results. The higher values of manually measured echogenic SN areas and echogenicity indices obtained by using digital image analysis from the right and left temporal bone windows were used for these statistics. Receiver operating characteristic curves for PD diagnosis by using both measurements with area under the curve and optimal cut-point determination were performed for machine 1. Statistical evaluations were performed by using SPSS, Version 17.0 (IBM, Armonk, New York).

RESULTS

After subjects (healthy volunteers and patients with PD) with a low quality of the TCS B-mode were excluded, 113 healthy volunteers in the derivation cohort and 50 healthy volunteers and 30 patients with PD in the validation cohort were evaluated. Demographic data of the derivation and validation cohorts are presented in Table 1. The 90th percentile values for both machines established from SN images of the derivation cohort are shown in Fig 4. The SN echogenicity index, counted by using digital analysis, was highly correlated between machine 1 and machine 2 ($r = 0.996$, $P < .01$). The values of the 90th percentile of the echogenicity index for machines 1 and 2 were 18.536 and 18.078, respectively. The coefficient of variation between the 2 measurements of the same image with a repeat region-of-interest placement was 1.8%. The manually measured 90th percentile of the SN area was equal for both machines (0.24 cm^2).

The 90th percentile values for both machines and both manual measurement and digital analysis were used as border values in the validation cohort. The bilateral hyperechogenic SN was detected in 4 volunteers by using machine 1 and digital analysis of the TCS image. In the same 4 volunteers, the bilateral hyperechogenic SN was detected by using machine 2 and digital analysis of the TCS image, but only in 2 of

them was an enlarged hyperechogenic SN ≥ 0.24 cm^2 found by using manual measurements in both machines. In the remaining 2 subjects with hyperechogenic SNs in digital analysis, the manually measured SN area was borderline (0.23 and 0.24 cm^2, respectively).

The correlations between the manual measurement and digital analysis for both machines, between images obtained by different machines, and between the right and left SN by using both manual measurement and digital analysis are presented in Table 2.

Cohen κ and AC1 coefficients for digital manual measurement and digital analysis were $\kappa = 0.762$ (95% CI, 0.615–0.909), AC1 = 0.787; and $\kappa = 0.787$ (95% CI, 0.648–0.926), AC1 = 0.812, respectively ($P < .0001$ for both measurements). Receiver operating characteristic curves for PD diagnosis by using both measurements and machine 1 are shown in Fig 5. Areas under the curve for manual measurement and for digital analysis were 0.936 (95% CI, 0.882–0.990) and 0.937 (95% CI, 0.884–0.990), respectively. The optimal cut-point for the echogenic area by using manual measurements was >0.25 cm^2, with 86.7% sensitivity and 96.0% specificity for PD. The optimal cut-point for the echogenicity index by using digital analysis was >18.576 for machine 1 and >18.118 for machine 2, with 86.7% sensitivity and 92.0% specificity for PD.

Table 1: Demographic data of the derivation and validation cohorts

		Validation Cohort	
	Derivation Cohort Healthy Volunteers	Healthy Volunteers	Patients with PD
No. of subjects	113	50	30
Mean age (yr)	52.3 ± 13.1	54.1 ± 12.2	56.9 ± 10.5
Male sex (No.) (%)	58 (51.3)	25 (50.0)	19 (63.3)
Median UPDRS-III (IQR, range)	NA	NA	29.5 (20.5–38.5; 12–47)
Median Hoehn and Yahr stage (IQR, range)	NA	NA	2 (1–3; 1–3)
L-DOPA therapy (No.) (%)	NA	NA	19 (63.3%)
DA therapy (No.) (%)	NA	NA	15 (50.0)
Mean of disease duration (mo) (range)	NA	NA	28.4 ± 12.0 (6–48)

Note:—DA indicates dopamine agonist; IQR, interquartile range; NA, not applicable; UPDRS, Unified Parkinson's Rating Scale.

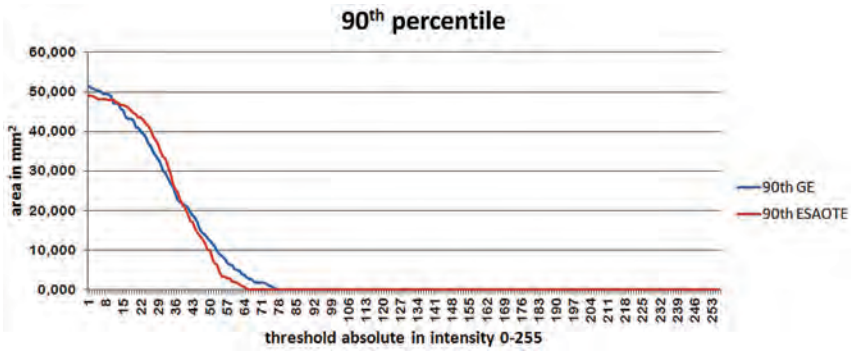

FIG 4. The 90th percentile of the derivation cohort for the Esaote My Lab Twice (machine 1) and GE Healthcare Vivid 7 Pro (machine 2) machines.

DISCUSSION

Correlations between manual measurement and B-mode Assist System digital analysis were high in the presented study, with the Spearman coefficient > 0.6. Both correlations between measurements from images acquired from different machines and between right and left SN were similar when measured manually and digitally. The similar correlation coefficients between measurement of the right and left SN by using both manual measurement and digital analysis showed that both techniques were able to detect the asymmetry in SN echogenicity.

At present, no software for the evaluation of SN hyperechogenicity is routinely used. Contrary to previously tested programs (software) based on image segmentation and consecutive measurement of the hyperechogenic SN area,[20-22] the presented software did not use an arbitrary cutoff value of echogenicity (represented by brightness intensity) for the evaluation of the hyperechogenic SN area. Problems with determination of this cutoff value are the main limitation for routine use of such software because only minor changes of this value lead to a substantial shift in measured SN area. Results of the present study demonstrate the usability of digital analysis of SN echogenicity with the developed B-Mode Assist System software, which counts the SN echogenicity index instead of the SN area measured by previously developed software programs. Thereby, it overcomes the problems with determination of the echogenicity cutoff value.

Despite progress in the quality of TCS images obtained by high-end sonographic machines, the main limitation of sonographic B-mode evaluation is still the dependence on the sonographer's experience and skill, and the results may be biased, especially with less experienced

Table 2: Correlations between manual measurement and digital analysis of substantia nigra echogenicity for both machines, between measurements performed using different machines, and between the right and left substantia nigra using both manual measurement and digital analysis

Correlations	Spearman Coefficient	*P* Value
Between manual measurement and digital analysis for My Lab Twice	0.630	<.0001
Between manual measurement and digital analysis for Vivid Pro 7	0.553	<.0001
Between digital analysis using different machines	0.686	<.0001
Between visual measurements using different machines	0.721	<.0001
Between the right and left substantia nigra using digital analysis and My Lab Twice	0.575	<.0001
Between the right and left substantia nigra using digital analysis and Vivid Pro 7	0.512	.0001
Between the right and left substantia nigra using manual measurement and My Lab Twice	0.494	.0003
Between the right and left substantia nigra using manual measurement and Vivid Pro 7	0.631	<.0001

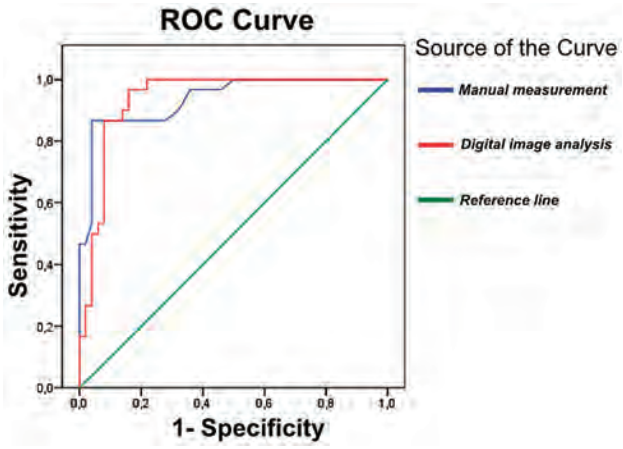

FIG 5. Receiver operating characteristic curve for Parkinson disease diagnosis using manual measurement (blue) and digital analysis (red) of the substantia nigra for machine 1.

investigators.[14,18] In addition, the quality of the TCS examination is dependent on the bone window quality.[12,13,18] In contrast to the second limitation, the first one should be partially eliminated by using the developed software.[15,16]

The 90th percentile of the SN area measured in healthy volunteers is used as a border between normal and hyperechogenic enlarged SNs.[18] This value differs between different machines and sonographers, usually between 0.20 and 0.25 cm^2.[6-8,18,23] In the presented derivation cohort, the 90th percentile for both machines (My Lab Twice and Vivid 7 Pro) was the same (0.24 cm^2). Moreover, the 90th percentile of the echogenicity index using software for the digital analysis of the image was similar for both machines. These results demonstrated the reproducibility of SN features measured by TCS, not only when the same machine is used but also when using 2 different high-end machines (My Lab Twice and Vivid 7 Pro).[7,9,10,18,24-26] Several previous studies showed that TCS is an easily reproducible method and has a high specificity and sensitivity for the diagnosis of PD.[7,9,10,18,24-26] Interinvestigator and intrainvestigator correlations of SN evaluation are high and statistically significant ($r \geq 0.85$, Cohen κ coefficient = 0.83, intraclass correlation coefficient = 0.84–0.96).[9,14,23,26-28] However, semiquantitative TCS evaluation of SN echogenicity and measurement of the SN area are highly dependent on the sonographer's experience, with significant correlations observed only for the experienced physician sonographers ($r \geq 0.85$, $P < .001$) and poor correlations for the sonographic lab assistant or physician without sonographic experience ($r < 0.47$, $P > .05$).[14]

One of the main roles of a digital analysis of SN echogenicity should be the improvement of interinvestigator and intrainvestigator correlations. Nevertheless, its potential use in the detection of changes in SN echogenicity during a course of PD should be tested in the future. Studies with manually measured SN did not show any changes in the hyperechogenic SN area in patients with PD during a 5-year follow up.[9] The results of several animal and postmortem studies demonstrated that SN echogenicity is significantly dependent on its iron content, and increased tissue iron concentration correlates with SN hyperechogenicity.[8,29-31] This, together with an apparently autosomal dominant inheritance of this echo feature in relatives of patients with idiopathic PD, supports the idea of a primary role of disturbed iron metabolism in PD.[32] It is still possible that other factors contribute to SN hyperechogenicity, such as abnormal iron-protein bindings, gliosis, and structural changes of neurons or glial cells (atrophy, morphologic changes of cells) in the SN.[33] Due to overcoming the dependency on a subjective bias when evaluating the echogenic SN area manually, the digital analysis of SN echogenicity should be tested for detection of minor and slow changes in SN echogenicity in patients with PD in future studies.

Several limitations of the present study should be mentioned. First, the TCS examination was performed only by a single well-trained sonographer. Sonographers without TCS experience could have problems with correctly imaging the SN. MR imaging–TCS fusion imaging with virtual navigation technology could be helpful in this case. Second, the quality of the TCS image is influenced by the quality of the sonography machine and its preset parameters. For digital analysis, the optimal quality of the TCS image is evaluated by developed software, but it is very subjective when using manual measurements. Finally, the standard sonography system settings should be used.[33] Especially, changes in settings influencing the image brightness (eg, gain or dynamic range) could lead to a bias. This influence of gain changes can be overcome by also performing the B-mode Assist System digital image analysis for the reference region (eg, thalamus or occipital lobe white matter) and by using the obtained data for a correction of the digital analysis of the SN area. For the future, there is a new technique, MR imaging–TCS fusion imaging with virtual navigation technology, that could be helpful in more accurate TCS diagnostics.[34] This technique enables simultaneous real-time TCS and MR imaging (or CT) of brain structures, with possible overlapping of both images.[35] It allows one to exactly determine several structures on TCS imaging for subsequent analysis (eg, substantia nigra, red nucleus, brain raphe, caudate nucleus, lenticular nucleus, or insular cortex).

CONCLUSIONS

Digital analysis of SN echogenicity by using the B-mode Assist System showed comparable results with conventional manual measurement of the echogenic SN area by an experienced sonographer. The presented digital analysis may overcome the main limitation of TCS evaluation of SN—the dependence on the sonographer's experience.

Disclosures: David Školoudík—*RELATED*: *Grant*: Moravian-Silesian Region.* Petra Bártová—*RELATED*: *Grant*: Moravian-Silesian Region.* *Money paid to the institution.

REFERENCES

1. Fearnley JM, Lees AJ. **Ageing and Parkinson's disease: substantia nigra regional selectivity.** *Brain* 1991;114:2283–301
2. Lees AJ. **When did Ray Kennedy's Parkinson's disease begin?** *Mov Disord* 1992;7:110–16
3. Vingerhoets FJ, Snow BJ, Lee CS, et al. **Longitudinal fluorodopa positron emission tomographic studies of the evolution of idiopathic parkinsonism.** *Ann Neurol* 1994;36:759–64
4. Hilker R, Schweitzer K, Coburger S, et al. **Nonlinear progression of Parkinson disease as determined by serial positron emission tomographic imaging of striatal fluorodopa F 18 activity.** *Arch Neurol* 2005;62:378–82

5. Poewe W. **The need for neuroprotective therapies in Parkinson's disease: a clinical perspective.** *Neurology* 2006;66:S2–9
6. Berg D, Siefker C, Becker G. **Echogenicity of the substantia nigra in Parkinson's disease and its relation to clinical findings.** *J Neurol* 2001;248:684–89
7. Walter U, Wittstock M, Benecke R, et al. **Substantia nigra echogenicity is normal in non-extrapyramidal cerebral disorders but increased in Parkinson's disease.** *J Neural Transm* 2002;109:191–96
8. Berg D, Becker G, Zieler B, et al. **Vulnerability of the nigrostriatal system as detected by transcranial ultrasound.** *Neurology* 1999;53:1026–31
9. Berg D, Merz B, Reiners K, et al. **Five-year follow-up study of hyperechogenicity of the substantia nigra in Parkinson's disease.** *Mov Disord* 2005;20:383–85
10. Gaenslen A, Unmuth B, Godau J, et al. **The specificity and sensitivity of transcranial ultrasound in the differential diagnosis of Parkinson's disease: a prospective blinded study.** *Lancet Neurol* 2008;7:417–24
11. Berg D, Jabs B, Merschdorf U, et al. **Echogenicity of substantia nigra determined by transcranial ultrasound correlates with severity of parkinsonian symptoms induced by neuroleptic therapy.** *Biol Psychiatry* 2001;50:463–67
12. Bogdahn U, Becker G, Schlachetzki F. *Echoenhancers and Transcranial Color Duplex Sonography*. Berlin: Blackwell Science; 1998
13. Kollár J, Schulte-Altedorneburg G, Sikula J, et al. **Image quality of the temporal bone window examined by transcranial Doppler sonography and correlation with postmortem computed tomography measurements.** *Cerebrovasc Dis* 2004;17:61–65
14. Školoudík D, Fadrná T, Bártová P, et al. **Reproducibility of sonographic measurement of the substantia nigra.** *Ultrasound Med Biol* 2007;33:1347–52
15. Blahuta J, Soukup T, Čermák P. **Image processing of medical diagnostic neurosonographical images in MATLAB.** In: *Recent Researches in Computer Science. Proceedings of the 15th World Scientific and Engineering Academy and Society Circuits, Systems, Communications, and Computers Multiconference,* Corfu Island, Greece. July 15–17, 2011:85–90
16. Blahuta J, Soukup T, Jelínková M, et al. **A new program for highly reproducible automatic evaluation of the substantia nigra from transcranial sonographic images.** *Biomed Pap Med Fac Univ Palacky Olomouc Czech Repub* 2013 Apr 22. [Epub ahead of print]
17. Daniel SE, Lees AJ. **Parkinson's Disease Society Brain Bank, London: overview and research.** *J Neural Transm Suppl* 1993; 39:165–72
18. Berg D, Godau J, Walter U. **Transcranial sonography in movement disorders.** *Lancet Neurol* 2008;7:1044–55
19. Ressner P, Skoloudik D, Hlustik P, et al. **Echogenicity of substantia nigra in Parkinson's disease: pilot study.** *J Neuroimaging* 2007; 17:164–67
20. Schreiber J, Sojka E, Licev L, et al. **A new method for the detection of brain stem in transcranial ultrasound images.** In: *Proceedings of The International Joint Conference on Biomedical Engineering Systems and Technologies.* Funchal, Madeira, Portugal. January 28–31, 2008;2:478–83
21. Kier C, Cyrus C, Seidel G, et al. **Segmenting the substantia nigra in ultrasound images for early diagnosis of Parkinson s disease.** *Int J Comput Assist Radiol Surg* 2007;2(suppl 1):S83–85
22. Sakalauskas A, Lukoševičius A, Laučkaitė K, et al. **Automated segmentation of transcranial sonographic images in the diagnostics of Parkinson's disease.** *Ultrasonics* 2013;53:111–21
23. van de Loo S, Walter U, Behnke S, et al. **Reproducibility and diagnostic accuracy of substantia nigra sonography for the diagnosis of Parkinson's disease.** *J Neurol Neurosurg Psychiatry* 2010;81:1087–92
24. Walter U, Dressler D, Probst T, et al. **Transcranial brain sonography findings in discriminating between parkinsonism and idiopathic Parkinson disease.** *Arch Neurol* 2007;64:1635–40
25. Walter U, Hoeppner J, Prudente-Morrissey L, et al. **Parkinson's disease-like midbrain sonography abnormalities are frequent in depressive disorders.** *Brain* 2007;130:1799–807
26. Berg D, Roggendorf W, Schröder U, et al. **Echogenicity of the substantia nigra: association with increased iron content and marker for susceptibility to nigrostriatal injury.** *Arch Neurol* 2002;59:999–1005
27. Becker G, Berg D. **Neuroimaging in basal ganglia disorders: perspectives for transcranial ultrasound.** *Mov Disord* 2001;16:23–32
28. Prestel J, Schweitzer KJ, Hofer A, et al. **Predictive value of transcranial sonography in the diagnosis of Parkinson's disease.** *Mov Disord* 2006;21:1763–65
29. Berg D, Supprian T, Hofmann E, et al. **Depression in Parkinson's disease: brainstem midline alteration on transcranial sonography and magnetic resonance imaging.** *J Neurol* 1999;246:1186–93
30. Berg D, Hochstrasser H, Schweitzer KJ, et al. **Disturbance of iron metabolism in Parkinson's disease: ultrasonography as a biomarker.** *Neurotox Res* 2006;9:1–13
31. Zecca L, Berg D, Arzberger T, et al. **In vivo detection of iron and neuromelanin by transcranial sonography: a new approach for early detection of substantia nigra damage.** *Mov Disord* 2005;20:1278–85
32. Ruprecht-Dörfler P, Berg D, Tucha O, et al. **Echogenicity of the substantia nigra in relatives of patients with sporadic Parkinson's disease.** *Neuroimage* 2003;18:416–22
33. Školoudík D, Walter U. **Method and validity of transcranial sonography in movement disorders.** *Int Rev Neurobiol* 2010;90:7–34
34. Laganá MM, Forzoni L, Viotti S, et al. **Assessment of the cerebral venous system from the transcondylar ultrasound window using virtual navigator technology and MRI.** In: *Proceedings of 33rd Annual International Conference of the Institute of Electrical and Electronics Engineers Engineering in Medicine and Biology Society,* Boston, Massachusetts. August 30–September 3, 2011:579–82
35. Školoudík D, Walter U. *Sonographic Brain Atlas.* Opava: REKESh Comp; 2013

Automatic Quantification of Subarachnoid Hemorrhage on Noncontrast CT

A.M. Boers, I.A. Zijlstra, C.S. Gathier, R. van den Berg, C.H. Slump, H.A. Marquering, and C.B. Majoie

ABSTRACT

BACKGROUND AND PURPOSE: Quantification of blood after SAH on initial NCCT is an important radiologic measure to predict patient outcome and guide treatment decisions. In current scales, hemorrhage volume and density are not accounted for. The purpose of this study was to develop and validate a fully automatic method for SAH volume and density quantification.

MATERIALS AND METHODS: The automatic method is based on a relative density increase due to the presence of blood from different brain structures in NCCT. The method incorporates density variation due to partial volume effect, beam-hardening, and patient-specific characteristics. For validation, automatic volume and density measurements were compared with manual delineation on NCCT images of 30 patients by 2 radiologists. The agreement with the manual reference was compared with interobserver agreement by using the intraclass correlation coefficient and Bland-Altman analysis for volume and density.

RESULTS: The automatic measurement successfully segmented the hemorrhage of all 30 patients and showed high correlation with the manual reference standard for hemorrhage volume (intraclass correlation coefficient = 0.98 [95% CI, 0.96–0.99]) and hemorrhage density (intraclass correlation coefficient = 0.80 [95% CI, 0.62–0.90]) compared with intraclass correlation coefficient = 0.97 (95% CI, 0.77–0.99) and 0.98 (95% CI, 0.89–0.99) for manual interobserver agreement. Mean SAH volume and density were, respectively, 39.3 ± 31.5 mL and 62.2 ± 5.9 Hounsfield units for automatic measurement versus 39.7 ± 32.8 mL and 61.4 ± 7.3 Hounsfield units for manual measurement. The accuracy of the automatic method was excellent, with limits of agreement of −12.9–12.1 mL and −7.6–9.2 Hounsfield units.

CONCLUSIONS: The automatic volume and density quantification is very accurate compared with manual assessment. As such, it has the potential to provide important determinants in clinical practice and research.

ABBREVIATIONS: ICC = intraclass correlation coefficient; LPBA40 = Laboratory of Neuro Imaging Probabilistic Brain Atlas

Despite improvements, the treatment of SAH is associated with high fatality rates and affects fairly young adults: up to half of all cases of SAH are fatal within 30 days, and the mean age of presentation is 55 years.[1-5] There is strong agreement among studies that the amount of subarachnoid blood on initial NCCT has a highly predictive value regarding patient outcome and the incidence of vasospasm and concomitant delayed cerebral ischemia.[3,4,6-9] Hemorrhagic density may be of equal importance in predicting patient outcome, but this has not been validated properly.[3,10-12] Currently several grading systems are used to assess the initial clinical and radiologic features of SAH.[7,8,13-15] However, there is still an ongoing discussion about the optimal method of grading SAH on NCCT.[3,7,16-18] The 2 most commonly used scales of Fisher et al[7] and Hijdra et al[8] have come under criticism; authors referred to these scales as rather gross estimators, difficult to apply, lacking quantification, and cumbersome in the clinical setting.[3,17,19-22] Moreover, hemorrhage density is not considered in these scales. A quantitative volume and density measurement may reduce interobserver variability in comparison with current scales and would provide physicians with a potentially valuable tool for outcome prediction and treatment guidance.[23] As such, the aim of this study was to design and

Received March 11, 2014; accepted after revision May 19.

From the Departments of Radiology (A.M.B., I.A.Z., R.v.d.B., H.A.M., C.B.M.) and Biomedical Engineering and Physics (A.M.B., H.A.M.), Academic Medical Center, Amsterdam, the Netherlands; Institute of Technical Medicine (A.M.B.) and MIRA Institute for Biomedical Technology and Technical Medicine (C.H.S.), University of Twente, Enschede, the Netherlands; and Department of Neurology (C.S.G.), University Medical Centre Utrecht, Utrecht, the Netherlands.

H.A. Marquering and C.B. Majoie contributed equally to this work.

Please address correspondence to Anna M. Boers, MD, Department of Biomedical Engineering and Physics, Academic Medical Center, PO Box 22660, 1100 DD Amsterdam, the Netherlands; e-mail: a.m.boers@amc.uva.nl

http://dx.doi.org/10.3174/ajnr.A4042

Table 1: Clinical and radiographic characteristics of the study population

Characteristics	Test Set (No.) (%)	Training Set (No.) (%)
Sex		
Male	12 (40)	5 (75)
Female	18 (60)	15 (25)
Age (yr)		
45 or younger	7 (23)	5 (25)
46–60	16 (53)	11 (55)
Older than 60	7 (23)	4 (20)
IVH		
Yes	16 (53)	4 (20)
No	14 (47)	16 (80)
ICH		
Yes	19 (63)	12 (60)
No	11 (37)	8 (40)
MCA location		
Left	14 (47)	18 (10)
Right	16 (53)	2 (90)
WFNS at admission		
Grade I	11 (37)	9 (45)
Grade II	2 (7)	2 (10)
Grade III	2 (7)	4 (20)
Grade IV	8 (27)	3 (15)
Grade V	7 (23)	2 (10)
History of hypertension		
Yes	3 (10)	7 (35)
No	22 (73)	13 (65)
Aneurysm size		
≤5 mm	9 (30)	6 (30)
6–10 mm	14 (47)	12 (60)
11–15 mm	3 (10)	2 (10)
>15 mm	3 (10)	–
Signs of DCI		
No	21 (70)	19 (95)
Yes	9 (30)	1 (5)
Paresis	1 (3)	1 (5)
Decreased consciousness	4 (13)	–
Hemiparesis and aphasia	3 (10)	–
Vasospasm	1 (3)	–

Note:—IVH indicates intraventricular hemorrhage; ICH, intracerebral hemorrhage; DCI, delayed cerebral ischemia; WFNS, World Federation of Neurosurgical Societies.

validate a reliable and easy-to-apply automatic measurement for subarachnoid hemorrhage quantification.

MATERIALS AND METHODS

Patient Selection

This study is a substudy of a larger project evaluating the outcome of patients with ruptured middle cerebral artery aneurysms. NCCT image data of 50 consecutive patients with ruptured MCA aneurysms who were admitted to the Academic Medical Center hospital from January 2003 to March 2011 were retrospectively enrolled in this study. A subset of 20 consecutive patients was selected to form a training set for optimization of our method. The remaining 30 patients were used for validation. The inclusion criteria were the following: clinical diagnosis of SAH, available NCCT obtained within 72 hours after initial hemorrhage, and 18 years of age or older. Patients with previous aneurysm treatment by clipping or coiling, craniectomy, or craniotomy were excluded. A summary of the patient clinical and radiographic information is presented in Table 1. Informed consent was waived by the medical ethics committee.

Imaging Protocol

Whole-brain NCCT was performed on a Sensation 64 scanner (Siemens, Erlangen, Germany) and a Sensation 4 scanner (Siemens) with the following parameters: 120 kV, 380 mAs, reconstruction kernel = H40s, and 5-mm section thickness, resulting in volumes with 23–34 sections. The image data were anonymized.

Overview

Our proposed method for detection and quantification of blood after SAH is based on a relative density increase in NCCT images due to the presence of blood. The process started with an atlas-based segmentation to classify different brain structures, followed by a compensation for partial volume effect in the vicinity of the skull. Hereafter, evaluation of density was assessed to set a tissue-specific threshold for density-based segmentation of blood. A region-growing algorithm included subtle attenuated parts of the hemorrhagic areas.

Atlas-Based Segmentation

Atlas-based segmentation requires a reference image with a corresponding atlas, which classifies structures in this image. An experienced neuroradiologist (C.B.M.) selected an NCCT image of a healthy subject as a reference image, ensuring that no pathologies or image artifacts were present. Because the proposed hemorrhage detection method is based on a relative density increase in NCCT images, brain structures with different densities on NCCT images should be recognized. As such, brain tissue was labeled as the following: 1) GM, 2) WM, and 3) CSF.

The Laboratory of Neuro Imaging Probabilistic Brain Atlas (LPBA40)[24] was used for the labeling. The LPBA40 dataset provides the following: 1) average-intensity skull-stripped T1-weighted MR brain image; 2) probabilistic MR imaging tissue maps of WM, GM, and CSF; and 3) probabilistic maps for 56 delineated structures in the brain. The LPBA40 Atlas was registered with the reference image to produce the CT-based atlas.

Skull-Stripping. Because the LPBA40 images are without skull, skull stripping of the NCCT reference image was required before registration. The skull-stripping started with thresholding to select and exclude the skull by using an established threshold of 100 Hounsfield units (HU). This threshold assured that calcifications were excluded and any hemorrhage was included.[25,26] After a 2D erosion with a disk-structuring element in each section, the remaining structures were detected by using 2D-connected component analysis. To discriminate brain tissue from other soft tissues, we excluded connected components with small areas. When multiple connected components were present in a section, the component with its centroid closest to the centroid of the superior section was selected as brain tissue. Here we assume that superior sections only contain a single connected component because of the absence of soft tissues other than brain in the cranial part of the head. After selection of brain tissue, we performed a morphologic closing and dilation, resulting in the final brain mask.

Generation of a CT-Registered Atlas. All registrations were performed by using the open-source software Elastix (Version 4.6; http://elastix.isi.uu.nl).[27] First, the average-density LPBA40 MR

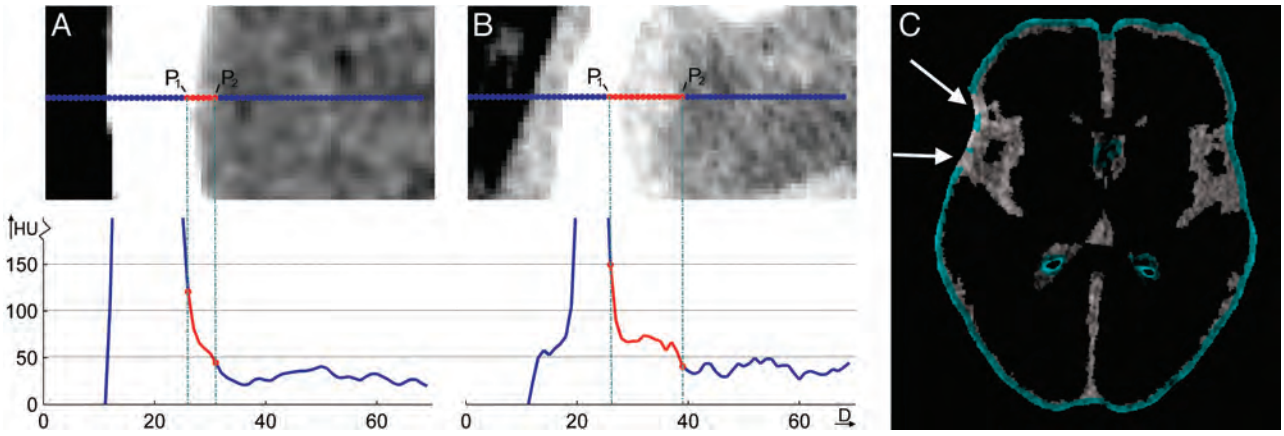

FIG 1. Illustration of differentiation between partial volume effect and hemorrhage in the vicinity of the skull. *A*, Calculation of the density gradient of an NCCT image with high hypodensities near the skull. High gradients are expected to be caused by partial volume effects in contrast to hemorrhages, which result in low gradients as seen in *B* and *C*. The pixels corresponding to low gradients (blue) are excluded from further segmentation. The *white arrows* mark the areas with high gradients present in the CSF image.

brain image was registered to align with the skull-stripped reference image. Because multimodal images needed to align, mutual information was set as a similarity measure for registration. Registration was performed by a rigid and affine transformation first to correct for major differences in position, orientation, and size. Subsequently, a nonrigid B-spline registration was applied to correct for remaining differences in brain shape, and the result was inspected by a trained observer (A.M.B). Using the transformation from this registration, we transformed the anatomically labeled maps of the LBPA40 data with the use of Transformix (Version 4.6; http://elastix.isi.uu.nl)[27] to align with the reference CT image, resulting in the CT-registered atlas images used in the remainder.

Atlas-Based Segmentation of Patient Images. The CT-based atlas was used to label different brain tissue types in all patient images. By registration of the reference image with patient images, the CT-based atlas also aligned with patient data. Similar to the registration of the reference image with the LBPA40 atlas, this process was started with skull stripping. The regions of the patient images were classified by applying this transformation to the CT-based atlas. Because hemorrhages induce density changes, again, mutual information was set as a similarity measure in the registration to label patient NCCT images into GM, WM, and CSF.

Partial Volume Effect

The used image data with relatively thick sections of 5 mm had partial volume effects, resulting in higher density in the skull-brain transition zone. As a result, healthy tissue close to the skull may have density similar to that of blood. This makes it difficult separate images of true hemorrhage near the skull from artifacts, due to partial volume effects. There is however, a noticeable change in the width of the transition zone of healthy brain tissue and skull; this transition is wider in the presence of hemorrhage.

To differentiate hemorrhagic tissue from healthy tissue with partial volume effects, we estimated the density gradient at the transition of skull to healthy brain tissue, in which the gradient for hemorrhagic tissue is lower than that for healthy tissue with partial volume effects. This density gradient (ν) is defined as the density difference (in Hounsfield units) between the skull and healthy brain tissue divided by the Euclidean distance between these points. The location of the points was found by selecting 2 positions on an orthogonal line over the transition of the brain and skull. The pixel closest to the brain tissue with a density of $>$100 HU was selected as the first point (P_1), and the pixels closest to the skull with a density of $<$50 HU, as a second point (P_2). The typical density gradients for partial volume effect and hemorrhagic brain tissue near the skull are illustrated in Fig 1. Using this separation, we excluded voxels with high densities and high gradients from further processing.

Correction for Patient-Specific Density Differences

Relative density differences of normal and hemorrhagic voxels can vary from patient to patient. These variations are mainly caused by partial volume effects in upper and lower sections and beam-hardening but may also be caused by differences in scanner type and brain tissue composition (old infarct, atrophy) and blood composition (age of hemorrhage, hematocrit). Because our method is based on relative density changes, this offset needed to be corrected, to come to an optimal threshold to discriminate blood from normal brain tissue. To estimate these small offsets, we divided recognized tissue types in each section into equal tiles in which the SD of the density was calculated. After visual inspection of an alternating number of tiles, the optimal number of tiles was established ($n = 64$). Tiles with a small SD were expected to be free of blood. The densities in these tiles were used to estimate the mean density of that specific tissue type in that section. This process is illustrated in Fig 2. The "offset" was defined as the difference of the mean density of that tissue type and the values of the reference image. After correction for this offset, a first estimation of hemorrhage was defined as all voxels with a density higher than the adjusted threshold, which was defined by the mean density of the reference image per tissue type $\pm$ the SD.

In the interhemispheric fissure, the falx cerebri can be mistaken for blood and therefore requires additional analysis. The interhemispheric fissure was localized by using anatomic atlas regions adjacent to the midline. A blood-free segment of the falx

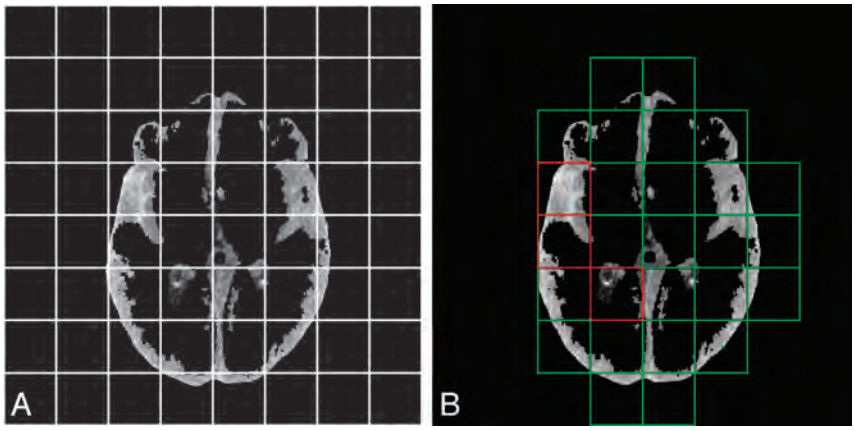

FIG 2. Illustration of the correction for patient-specific density differences. *A*, Each section of a specific tissue type (here CSF) is divided into 64 tiles, and the SDs of the density were calculated. *B*, Green tiles represent those with a low SD of the density and are expected to be free of a substantial amount of extravasated blood and therefore mainly consist of healthy brain tissue, whereas tiles with a high SD (red tiles) are more likely to contain hemorrhage. The densities in the green tiles were included in the calculation of the mean density of that tissue type. Comparison with the mean density of that tissue type in the reference image resulted in a density offset, which was corrected.

was selected as the segment with a small SD of densities. K-means clustering was used to partition the area into 2 structures: normal brain tissue or the falx. Subsequently, the threshold to segment blood in the interhemispheric fissure was adjusted to the normal hyperattenuated falx.

Region Growing

The threshold, as described above, does not include subtle attenuated parts of the hemorrhage. To correct for this underestimation of blood volume, we used initial segmented hemorrhages as seeds for a region-growing algorithm. This algorithm examined all voxels in the vicinity of the initial segmented hemorrhage to determine whether these voxels should be included in the segmentation. A voxel was included if the difference in its density and the average density of the segmented volume was smaller than a predefined threshold of mean density − 1.5 times the SD.

Hemorrhage Volume and Density Estimation

The volume of blood was determined as the multiplication of the segmented voxels by voxel size. For every segmented region of blood, there is a distribution of densities. Because the average density may be sensitive to small overestimations of the segmentation, which would include low-density voxels, the hemorrhage density was defined as the third quartile of the density distribution of the segmented volume.

Manual Hemorrhage Segmentation

The hemorrhage volume of 20 patients with SAH was selected for training and was manually delineated by radiologist I.A.Z. (with 8 years of experience) by using ITK-SNAP 2.4.0 (http://sourceforge.net/projects/itk-snap/files/itk-snap/2.4.0/).[28] The 30 hemorrhage volumes in the test set were delineated twice by radiologists I.A.Z. and R.v.d.B. (with >15 years of experience) and were used for validation. Both observers were blinded to all clinical information and each other's results.

Fisher and Hijdra Grading

Each patient was graded according to the Fisher and Hijdra scales by I.A.Z. and C.S.G. Both observers were blinded to all clinical data and reached a consensus. The sum score of the ventricles and cisterns was combined to obtain the final Hijdra score, ranging from 0 to 42.

Statistical Analysis

The manual measurements of a single observer (I.A.Z.) were used as a reference standard to evaluate the accuracy of the automatic method. The difference in hemorrhage volume between the automatic and manual assessment and the interobserver variability of the manual hemorrhage segmentation was evaluated by a number of tests. At first, scatterplots were presented, and the interclass correlation coefficient (ICC) and its 95% CI with absolute agreement definition were calculated. The ICC was assessed according to the case 3 form of Shrout and Fleiss,[29] in which a 2-way ANOVA model is used for analysis. Additionally, a Bland-Altman analysis was performed to assess the bias and limits of agreement, in which the "bias" was defined as the mean paired difference and limits of agreement.[30] Furthermore, the Dice coefficient[31] was calculated to determine the overlap of the volumes, and the ICC and its 95% CI of the hemorrhage density were assessed.

In addition, Fisher and Hijdra scale scores were compared with manual-delineated and automatic-determined volumes by constructing scatterplots and calculating, respectively, the Spearman rank correlation coefficient and the Pearson correlation coefficient and their 95% CIs.

RESULTS

The test set included 30 patients, with a mean age of 55 ± 12 years, and 60% were women. The mean SAH volume was 39.71 ± 32.84 mL and 39.33 ± 31.49 mL, according to the manual and automatic methods, respectively. The ICC of the volume measurement between the automatic and manual measurements was 0.98 (95% CI, 96%–99%). The ICC of the volume-measurement interobserver agreement was 0.97 (95% CI, 77%–99%). Bland-Altman analysis indicated an average difference in SAH volume of −0.39 mL between the automatic and manual measurements, with limits of agreement ranging from −12.90 to 12.10 mL. For the 2 observers, the Bland-Altman analysis resulted in a bias of −6.22 mL, with limits of agreement ranging from −18.70 to 6.20 mL. The Dice coefficient of the manual and automatic measurements was 0.55 ± 0.24 and ranged from 0.00 to 0.83, in comparison with 0.64 ± 0.20 between the 2 observers.

The interobserver and accuracy measures are shown in Table 2 and Fig 3. The mean SAH density was 61.43 ± 7.26 HU and 62.23 ± 5.89 HU, according to the manual and automatic methods, respectively. The ICC of the hemorrhage density between the observers was 0.98 (95% CI, 89%–99%) and 0.80 (95%

Table 2: Interobserver variability of manual SAH volume measurement and comparison of the manual and automatic methods

	ICC Volume[a] (95% CI)	Bland-Altman Volume Limits of Agreement (mL)	ICC Density[a] (95% CI)	Bland-Altman Density Limits of Agreement (HU)	Dice Coefficient (Mean and Range)	No.[b]
Automatic interobserver	0.98 (0.96–0.99)	−12.90–12.13	0.80 (0.62–0.90)	−7.58–9.18	0.55 (0.00–0.83)	30
Manual interobserver	0.97 (0.77–0.99)	−18.68–6.24	0.98 (0.89–0.99)[c]	−1.52–3.44[c]	0.64 (0.00–0.86)	30

[a] Case 3 intraclass correlation coefficients using an absolute agreement definition.
[b] Number of NCCT scans included in the calculation.
[c] Number of NCCT scans included for calculation = 29.

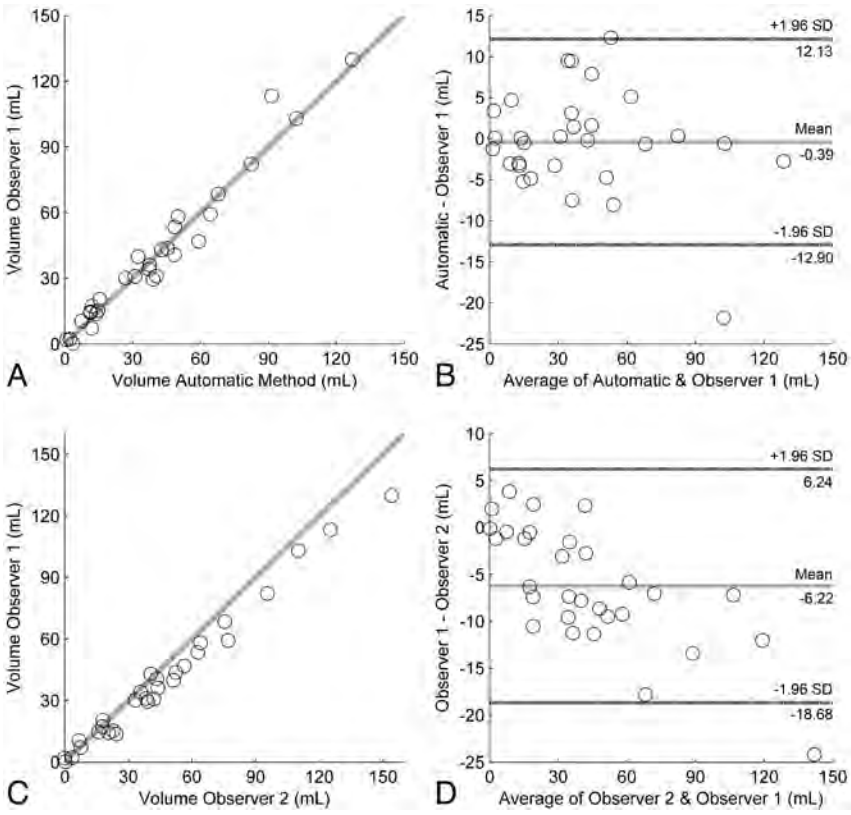

FIG 3. The accuracy of the volume measurement of the automatic method compared with that in observer 1. *A*, Accuracy depicted as a scatterplot. *B*, Accuracy shown by the Bland-Altman plot. Interobserver variability of the manual hemorrhage volume measurement depicted as *C*, scatterplot, and *D*, Bland-Altman analysis.

CI, 62%–90%) for the comparison of the manual reference and automatic method. In 1 case, observer 2 detected no hemorrhage; this case was excluded from the calculation of the manual interobserver variability regarding the density measurement only. Bland-Altman analysis indicated an average difference in SAH density of 0.80 HU between the automatic and manual measurements, with limits of agreement ranging from −7.58 to 9.18 HU. For the 2 observers, the Bland-Altman analysis resulted in a bias of 0.96 HU, with limits of agreement ranging from −1.52 to 3.44 HU.

The Fisher score was 2 in 3 patients (10%), 3 in 4 patients (13%), and 4 in 23 patients (77%). The Hijdra score ranged from 1 to 38, with a median and third quartile of 24 and 29, respectively. The correlation of the hemorrhage volume with the Fisher score and Hijdra score is shown in Fig 4. The Pearson correlation coefficient of the Hijdra score with manual volume measurement was 0.39 (95% CI, 0.04–0.63; $P < .05$), and with automatic measurement, 0.42 (95% CI, 0.08–0.65; $P < .05$). The Spearman rank correlation coefficient of the Fisher score with a manual volume measurement was 0.49 (95% CI, 0.10–0.74; $P < .01$), and with automatic measurement, 0.50 (95% CI, 0.14–0.74; $P < .01$).

DISCUSSION

In this study, we have presented a novel method for automatic hemorrhage volume and density quantification in NCCT scans of patients with SAH. Comparison with manual delineations in 30 patients with SAH with manual assessment showed an excellent agreement in blood volume and a good agreement in blood density.

Despite the general acceptance that the volume of blood after SAH provides information regarding prognostic outcome and guidance for treatment decisions, no method to estimate the real amount of blood so far has been successful. Sato et al[23] proposed an automated measurement on 3D CT to quantify SAH on the basis of thresholding between 40 and 80 HU, which could rapidly measure SAH volume. However, the time needed to manually exclude the scalp and subcutaneous tissue was not taken into account. Furthermore, errors in volume of approximately 10 mL were unavoidable, partly because the volume was calculated by subtracting a mean value for tissues between 40 and 80 HU of healthy subjects from the patient image. Other computer-aided detection methods have been proposed for intracranial hemorrhages; however, these are not suitable to automatically quantify SAH. For instance, the method of Chan[32] is based on the symmetry of the ventricles, which are segmented by thresholding only. Here, the assumption is made that no blood is present in the ventricles, which is often not the case in patients with SAH.

The Fisher scale has become the current historical standard for this purpose on NCCT. It was designed to predict cerebral vasospasm; however, its clinical utility has been questioned.[11,14,19,33] The Fisher scale is not comprehensive enough to serve as a primary grading system for SAH and to predict clinical outcome.[3] In this study, the Fisher scale fails to differentiate among hemorrhages with a small, moderate, or substantial amount of blood by categorizing grade 4 in 77% of the cases within a large range of 12–130 mL. Finding no blood on CT is rare, as is clot <1 mm in

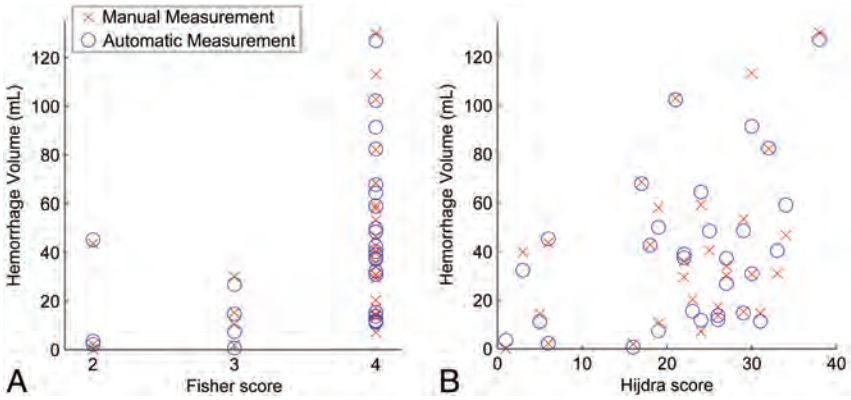

FIG 4. Correlation of the Hijdra score and Fisher score with hemorrhage volume after SAH assessed with scatterplots. *A*, The Fisher score with automatic volume measurement (blue) and manual volume measurement (red). *B*, The Hijdra score with automatic volume measurement (blue) and manual volume measurement (red).

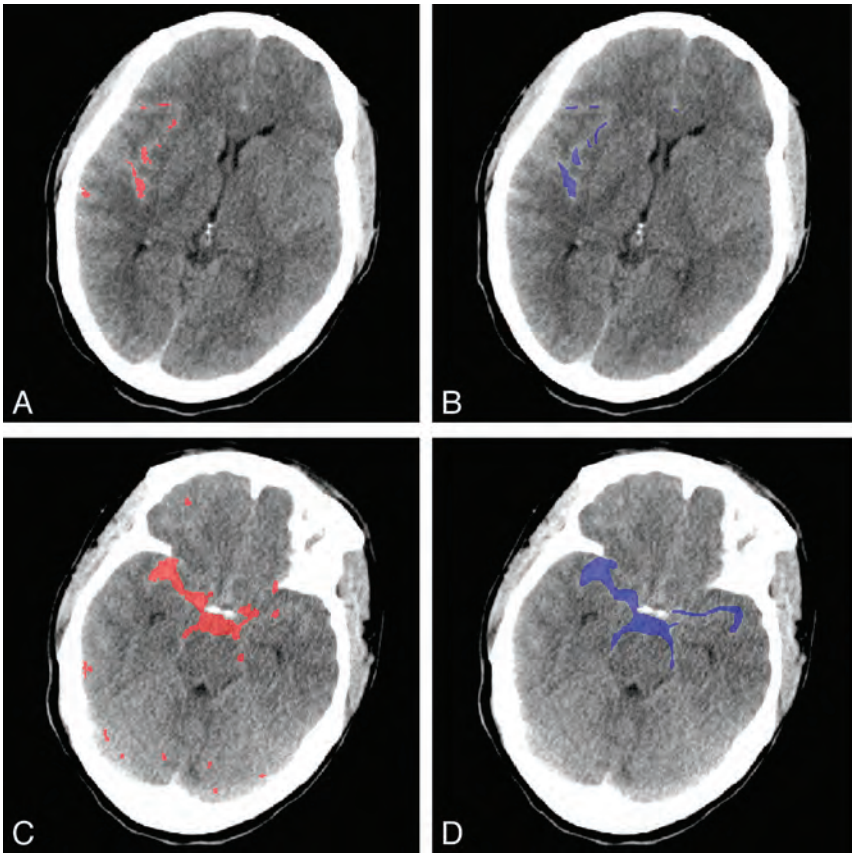

FIG 5. Example of the results of the automatic segmentation of extravasated blood after SAH and manual measurement. *A*, NCCT image, shown in red, with results of the automatic method of a relatively small hemorrhage. *B*, The same NCCT image and hemorrhage as delineated by observer 1 (blue). *C*, NCCT image with beam-hardening in an extreme degree. The automatic method, in red, shows deviations of the hemorrhage volume as delineated by observer 1 (*D*) in blue.

true thickness, making grades 1 and 2 quite uncommon. The correlation of this scale with hemorrhage volume was moderate (0.49). Because there is strong agreement among studies that the amount of subarachnoid blood has highly predictive value regarding patient outcome, we believe that our proposed volumetric measurement has added value above the Fisher scale.[3,4,6-9] Moreover, Fig 4 illustrates the large range of hemorrhage volumes within single Fisher scales. Because of the low number of patients in Fisher grades 1 and 2, we could not perform any valuable statistical analysis.

Even though the method by Hijdra et al[8] is more comprehensive than the Fisher scale, the correlation with the measurements of hemorrhage volume in this study was poor in comparison with our proposed method (0.39 versus 0.98). The Hijdra scale assigns grade 3 to a fissure or cistern when it is completely filled with blood, which does not indicate a certain volume. In addition, assessment of the Hijdra scale is a tedious task and may be impractical in an emergency setting.

Recently, Wilson et al[34] proposed the Barrow Neurological Institute scale, a simple and quantitative method to grade the amount of blood and predict vasospasm. This scale categorized patients with SAH into 5 more evenly distributed classes than the Fisher scale and showed better inter- and intraobserver agreement. However, the clinical value has not been confirmed by other studies. Although this scale appears promising for the prediction of vasospasm, associations with SAH volume have not been reported.

An example of the volume measurements is shown in Fig 5. The concordance of the automatic method with manual reference was excellent, despite a moderate Dice coefficient. This disagreement can partly be attributed to the tortuous shape of the cisterns. The observers perceived an image on the screen and delineated it by hand; this hand method results in smooth edges, whereas the automated method segments the image on a voxel-by-voxel basis, which results in ragged edges.

Another limitation for the current grading scales is that hemorrhage density, which may be equally important, is not considered.[3,10-12] This limitation addresses an additional advantage of the proposed automatic method, which reports a good ICC of the hemorrhage density measurement with the manual reference. This ICC was, however, approximately 18% lower than the interobserver variability. Retrospective analysis showed that this difference was mainly caused by low agreement in patients with small hemorrhage volumes. When we included only SAH volumes >5 mL (3 patients excluded), the ICC of the hemorrhage density of the automatic measurement and manual reference increased to 0.95 (95% CI, 87%–98%). This increase can be partly explained by the difference in procedures regarding small hemorrhages; in

the manual comparison, the observers delineated on the basis of personal experience and by using the contralateral hemisphere for comparison. Here, only slightly hyperattenuated blood could be detected, in contrast to the automatic method, which is threshold-based. No restrictions are to be expected regarding SAH quantification for such small hemorrhages.

In this study, the third quartile was chosen for the hemorrhage-density estimation. We believe that a measurement such as the mean is more sensitive to errors in the segmentation due to the difference in segmentation technique (voxel-by-voxel-based versus delineation by hand). The third quartile is, however, a heuristic approach.

SAH often is accompanied by intraventricular hemorrhage or intracerebral hemorrhage as seen in Table 1. The automatic method in this study was designed to include all blood present in the brain after SAH. Therefore, we believe this method has the potential to serve as a quantification measurement in other types of hemorrhagic strokes. As future work, it could be beneficial to differentiate among locations of hemorrhage to investigate the role of blood distribution in patients with SAH. This study was performed on image data of a population of patients who had SAH due to rupture of an MCA aneurysm. As a result, this study may be affected by a selection bias because these patients, especially, present with bleeding around the temporal and insular regions; however, in most patients, there was extension into the interhemispheric fissure and to the lower pontine cistern. All included NCCT images were obtained on 2 scanner types, with 1 reconstruction kernel. We do, however, expect no problems when using different scanner types because the automatic method corrects for these density differences.

The duration of manual segmentation was recorded for 19 patients only. The manual segmentation ranged between 5 and 23 minutes with a median of 15 minutes, which was considerably longer than the 2–5 minutes required for the Fisher and Hijdra grading. The automatic SAH assessment took an average of 5 minutes per patient on a modern computer. The computation times should be further reduced to make an approach as presented here available for clinical practice.

Furthermore, the automatic method may not recognize aneurysms and large vessels and categorizes them as part of the hemorrhage. Using the proposed method to quantify only the amount of extravasated blood may therefore lead to an overestimation of this volume. A solution for this issue could be to subtract a CTA from the NCCT image.

In this study, a method was designed to correct for partial volume and beam-hardening artifacts, which are more prominent in the anterior fossa near the skull base and in the posterior fossa. Despite these corrections, other CT artifacts, such as patient motion, may cause the automatic SAH quantification to fail. In addition, when beam-hardening is present in an extreme extent, the automatic segmentation may underestimate the hemorrhage volume because the artifacts are approached as a patient-specific density variation as seen in Fig 5. Furthermore, high-attenuated areas may be seen as hemorrhage. Although physics-based artifacts cannot be eliminated, techniques have been developed to correct for these quantitative and visual errors and could be beneficial for improvement of our method.[35,36]

Another point is that the threshold values used in the algorithm are dependent on the standard value in the images. Therefore, the method may be dependent on the image quality. Validation on different scanners and reconstruction techniques is therefore required.

We designed and validated our method to align the real hemorrhage volume and density after SAH. Evaluation with patient outcome is beyond the scope of this study because multiple factors other than radiographic evidence contribute to the prediction of patient outcome, including clinical scales such as those of Hunt and Hess[13] and the World Federation of Neurosurgical Societies.[3,15,37] A future study in which hemorrhage volume and density are combined with other factors is necessary to validate the full utility of this method as a predictor for patient outcome.

CONCLUSIONS

We have presented a fully automatic method for blood volume and density quantification in NCCT scans of patients with SAH. The automatic method showed an excellent accuracy and strong correlation with the manual reference standard. This approach is an easy-to-use (fully automatic) and observer-independent solution in assessing the volume and density and, as such, has the potential to assist in predicting patient outcome, guiding treatment decisions, and standardizing hemorrhage assessment across medical centers in multicenter studies.

Disclosures: Celine S. Gathier—*UNRELATED: Grants/Grants Pending*: I am supported by the Dutch Heart Foundation, grant 2009B046, and the Dutch Brain Foundation, grant KS2009(1)-72. Charles B. Majoie—*UNRELATED: Grants/Grants Pending*: Dutch Heart Foundation,* Nuts Ohra Foundation.* *Money paid to the institution.

REFERENCES

1. Feigin VL, Lawes CM, Bennett DA, et al. **Stroke epidemiology: a review of population-based studies of incidence, prevalence, and case-fatality in the late 20th century.** *Lancet Neurol* 2003;2:43–53
2. Anderson C, Anderson N, Bonita R. **Epidemiology of aneurysmal subarachnoid hemorrhage in Australia and New Zealand: incidence and case fatality from the Australasian Cooperative Research on Subarachnoid Hemorrhage Study (ACROSS).** *Stroke* 2000;31:1843–50
3. Rosen DS, Macdonald RL. **Subarachnoid hemorrhage grading scales: a systematic review.** *Neurocrit Care* 2005;2:110–18
4. van Gijn J, Kerr RS, Rinkel GJ. **Subarachnoid haemorrhage.** *Lancet* 2007;369:306–18
5. Hop JW, Rinkel GJ, Algra A, et al. **Case-fatality rates and functional outcome after subarachnoid hemorrhage: a systematic review.** *Stroke* 1997;28:660–64
6. Bell BA, Kendall BE, Symon L. **Computed tomography in aneurysmal subarachnoid haemorrhage.** *J Neurol Neurosurg Psychiatry* 1980;43:522–24
7. Fisher C, Kistler J, Davis J. **Relation of cerebral vasospasm to subarachnoid hemorrhage visualized by computerized tomographic scanning.** *Neurosurgery* 1980;6:1–9
8. Hijdra A, Brouwers PJ, Vermeulen M, et al. **Grading the amount of blood on computed tomograms after subarachnoid hemorrhage.** *Stroke* 1990;21:1156–61
9. Davis JM, Davis KR, Crowell RM. **Subarachnoid hemorrhage secondary to ruptured intracranial aneurysm: prognostic significance of cranial CT.** *AJR Am J Roentgenol* 1980;134:711–15
10. Sano H, Kanno T, Shinomiya Y, et al. **Prospection of chronic vasospasm by CT findings.** *Acta Neurochir (Wien)* 1982;63:23–30
11. Fujita S. **Computed tomographic grading with Hounsfield number related to delayed vasospasm in cases of ruptured cerebral aneurysm.** *Neurosurgery* 1985;17:609–12

12. Suzuki J, Komatsu S, Sato T, et al. **Correlation between CT findings and subsequent development of cerebral infarction due to vasospasm in subarachnoid haemorrhage.** *Acta Neurochir (Wien)* 1980;55:63–70
13. Hunt WE, Hess RM. **Surgical risk as related to time of intervention in the repair of intracranial aneurysms.** *J Neurosurg* 1968;28:14–20
14. Claassen J, Bernardini GL, Kreiter K, et al. **Effect of cisternal and ventricular blood on risk of delayed cerebral ischemia after subarachnoid hemorrhage: the Fisher scale revisited.** *Stroke* 2001; 32:2012–20
15. **Report of World Federation of Neurological Surgeons Committee on a Universal Subarachnoid Hemorrhage Grading Scale.** *J Neurosurg* 1988;68:985–86
16. Hijdra A, van Gijn J, Nagelkerke NJ, et al. **Prediction of delayed cerebral ischemia, rebleeding, and outcome after aneurysmal subarachnoid hemorrhage.** *Stroke* 1988;19:1250–56
17. Klimo P Jr, Schmidt RH. **Computed tomography grading schemes used to predict cerebral vasospasm after aneurysmal subarachnoid hemorrhage: a historical review.** *Neurosurg Focus* 2006;21:E5
18. Kramer AH, Hehir M, Nathan B, et al. **A comparison of 3 radiographic scales for the prediction of delayed ischemia and prognosis following subarachnoid hemorrhage.** *J Neurosurg* 2008; 109:199–207
19. Smith EE, Rosand J, Greenberg SM. **Imaging of hemorrhagic stroke.** *Magn Reson Imaging Clin N Am* 2006;14:127–40, v
20. Reilly C, Amidei C, Tolentino J, et al. **Clot volume and clearance rate as independent predictors of vasospasm after aneurysmal subarachnoid hemorrhage.** *J Neurosurg* 2004;101:255–61
21. Allen GS, Ahn HS, Preziosi TJ, et al. **Cerebral arterial spasm: a controlled trial of nimodipine in patients with subarachnoid hemorrhage.** *N Engl J Med* 1983;308:619–24
22. van der Jagt M, Hasan D, Bijvoet HW, et al. **Interobserver variability of cisternal blood on CT after aneurysmal subarachnoid hemorrhage.** *Neurology* 2000;54:2156–58
23. Sato T, Sasaki T, Sakuma J, et al. **Quantification of subarachnoid hemorrhage by three-dimensional computed tomography: correlation between hematoma volume and symptomatic vasospasm.** *Neurol Med Chir (Tokyo)* 2011;51:187–94
24. Shattuck DW, Mirza M, Adisetiyo V, et al. **Construction of a 3D probabilistic atlas of human cortical structures.** *Neuroimage* 2008;39:1064–80
25. Tsuruda JS, Bradley WG. **MR detection of intracranial calcification: a phantom study.** *AJNR Am J Neuroradiol* 1987;8:1049–55
26. Kucharczyk W, Henkelman RM. **Visibility of calcium on MR and CT: can MR show calcium that CT cannot?** *AJNR Am J Neuroradiol* 1994;15:1145–48
27. Klein S, Staring M, Murphy K, et al. **Elastix: a toolbox for intensity-based medical image registration.** *IEEE Trans Med Imaging* 2010;29:196–205
28. Yushkevich PA, Piven J, Hazlett HC, et al. **User-guided 3D active contour segmentation of anatomical structures: significantly improved efficiency and reliability.** *Neuroimage* 2006;31:1116–28
29. Shrout PE, Fleiss JL. **Intraclass correlations: uses in assessing rater reliability.** *Psychol Bull* 1979;86:420–28
30. Altman DG, Bland JM. **Measurement in medicine: the analysis of method comparison studies.** *The Statistician* 1983;32:307–17
31. Dice L. **Measures of the amount of ecologic association between species.** *Ecology* 1945;26:297–302
32. Chan T. **Computer aided detection of small acute intracranial hemorrhage on computer tomography of brain.** *Comput Med Imaging Graph* 2007;31:285–98
33. Woertgen C, Ullrich OW, Rothoerl RD, et al. **Comparison of the Claassen and Fisher CT classification scale to predict ischemia after aneurysmatic SAH?** *Zentralbl Neurochir* 2003;64:104–08
34. Wilson DA, Nakaji P, Abla AA, et al. **A simple and quantitative method to predict symptomatic vasospasm after subarachnoid hemorrhage based on computed tomography: beyond the Fisher scale.** *Neurosurgery* 2012;71:869–75
35. Van Gompel G, Van Slambrouck K, Defrise M, et al. **Iterative correction of beam hardening artifacts in CT.** *Med Phys* 2011;38(suppl 1):S36
36. Van de Casteele E, Van Dyck D, Sijbers J, et al. **A model-based correction method for beam hardening artefacts in X-ray microtomography.** *J Xray Sci Technol* 2004;12:43–57
37. Rosengart AJ, Schultheiss KE, Tolentino J, et al. **Prognostic factors for outcome in patients with aneurysmal subarachnoid hemorrhage.** *Stroke* 2007;38:2315–21

Neuromyelitis Optica: A Diffusional Kurtosis Imaging Study

T.M. Doring, F.C.R. Lopes, T.T.A. Kubo, G. Tukamoto, M.C. Kimura, R.M. Strecker, R.C. Domingues, and E.L. Gasparetto

ABSTRACT

BACKGROUND AND PURPOSE: Conventional MR imaging typically yields normal images of the brain or indicates lesions in areas of high aquaporin expression in patients with neuromyelitis optica. Diffusional kurtosis imaging was applied in patients with neuromyelitis optica to determine whether this technique could detect alterations in diffusion and diffusional kurtosis parameters in normal-appearing white matter and to explore the relationship between diffusional kurtosis imaging and DTI parameters.

MATERIALS AND METHODS: Thirteen patients with neuromyelitis optica and 13 healthy controls underwent MR imaging of the brain with conventional and diffusional kurtosis imaging sequences. Tract-based spatial statistics and region-of-interest-based analyses were conducted to identify differences between patients with neuromyelitis optica and controls through conventional DTI and diffusional kurtosis imaging parameters. The parameters were correlated to determine the potential relationship between them.

RESULTS: Compared with healthy controls, several diffusional kurtosis imaging and DTI parameters were altered in various fiber tracts of patients with neuromyelitis optica ($P < .05$). A significant decrease ($P < .05$) in radial kurtosis was observed in the corpus callosum and anterior corona radiata and left optic radiation. Differences ($P < .1$) in mean kurtosis were found in patients with neuromyelitis optica. We found a negative correlation between diffusional kurtosis imaging (radial kurtosis, axial kurtosis, mean kurtosis) and the corresponding DTI parameters (radial diffusivity, axial diffusivity, mean diffusivity). Positive correlations were found for radial kurtosis and mean kurtosis with fractional anisotropy.

CONCLUSIONS: This study demonstrated differences in conventional diffusion and diffusional kurtosis parameters, especially radial kurtosis, in the normal-appearing white matter of patients with neuromyelitis optica compared with healthy controls. Larger studies of patients with neuromyelitis optica should be performed to assess the potential clinical impact of these findings.

ABBREVIATIONS: AD = axial diffusivity; AK = axial kurtosis; CC = corpus callosum; DKI = diffusional kurtosis imaging; FA, fractional anisotropy; MD = mean diffusivity; MK = mean kurtosis; NMO = neuromyelitis optica; OR = optic radiation; RD = radial diffusivity; RK = radial kurtosis; TBSS = tract-based spatial statistics

Neuromyelitis optica (NMO) is a severe, recurrent demyelinating disease that typically affects the optic nerve and spinal cord.[1,2] In patients with NMO, conventional MR imaging typically yields images with normal findings of the brain or indicates lesions in areas of high aquaporin expression.[3] Studies by using diffusion-tensor MR imaging, which depicts several diffusion parameters, have identified extensive damage in the normal-appearing white matter in patients with NMO, affecting the pyramidal tract, optic radiation (OR), and corpus callosum (CC).[4,5]

Diffusional kurtosis imaging (DKI) is an extension of the DTI technique that allows the simultaneous estimation of diffusion and kurtosis parameters.[6] The DTI model assumes that diffusion occurs in a random unrestricted way, following a Gaussian diffusion probability distribution function. However, the complexity of tissue is the reason that water diffusion deviates from that strict Gaussian behavior and occurs in a restricted way. DKI considers this in its model by quantifying this deviation, the diffusional kurtosis; thus, it is a more accurate description of restricted diffusion than DTI and may provide additional biomarkers in various disease states.[7,8] In combined DTI and DKI acquisitions, at least 15 distinct nonlinear diffusion directions (gradients), with at least 3 distinct b-values,[9] are obtained. Typical b-values for DKI in the brain are 0, 1000, and 2000 s/mm^2. An advantage of DKI is that it apparently accounts for fiber-crossing, whereas DTI fails in

Received March 13, 2014; accepted after revision June 2.

From the Universidade Federal Rio de Janeiro (T.M.D., F.C.R.L., G.T., E.L.G.), Rio de Janeiro, Brazil; Clínica de Diagnóstico Por Imagem and Multi-imagem (T.M.D., F.C.R.L., T.T.A.K., G.T., M.C.K., R.C.D., E.L.G.), Diagnósticos da América, Rio de Janeiro, Brazil; and Siemens Healthcare (R.M.S.), São Paulo, Brazil.

This work was supported by Coordenação de Aperfeiçoamento de Pessoal de Nível Superior (CAPES).

Please address correspondence to Thomas Doring, MS, Avenue Das Américas 4666, Sala 323, CEP 22640102 Rio de Janeiro, Brazil; e-mail: thomas.doring@gmail.com

Indicates open access to non-subscribers at www.ajnr.org

Indicates article with supplemental on-line table.

http://dx.doi.org/10.3174/ajnr.A4050

this respect.[10] Q-ball imaging, a previously described technique that also accounts for fiber crossing, requires numerous encoding directions and even greater b-values, resulting in high acquisition times.[11,12] Therefore, DKI might be useful when shorter acquisition times are needed because it requires only 15 independent directions and lower b-values.

Mean kurtosis (MK), which provides a measure of the overall kurtosis, is the main DKI parameter of interest in an isotropic medium. When diffusion becomes anisotropic (eg, within nerve fibers), directional kurtosis metrics, such as axial kurtosis (AK) and radial kurtosis (RK), can be derived. As in conventional DTI, AK is defined as the kurtosis along the principal eigenvector, whereas RK is the kurtosis perpendicular to the principal eigenvector. Kurtosis parameters have been shown to correlate negatively with DTI parameters.[13] In a previous study,[14] the DKI parameters, especially RK, showed high sensitivity to the degree of myelination of the brain in rats. RK was increased due to a more restricted diffusion perpendicular to the axon during myelination. Conversely, it is expected that RK will decrease when diffusion becomes less restricted during demyelination. Lätt et al[15] recently estimated and compared the regional DKI values of healthy brain tissues with DKI values obtained from previous studies of different pathologies. In another study in which DKI was applied after stroke onset,[16] higher MK values were observed in ischemic WM, which eventually progressed to gliosis, compared with ischemic WM that maintained a normal appearance. These findings suggest the usefulness of DKI for predicting the outcome of ischemic tissue. Finally, DKI parameters were found to be more effective than conventional DTI parameters for differentiating high- and low-grade gliomas.[17]

To date, few studies have assessed the clinical application of DKI. The purpose of this study was to evaluate the brains of patients with NMO by DKI, to determine whether DKI can detect differences in DKI parameters compared with healthy controls and to explore the relationship between DKI and conventional DTI parameters.

MATERIALS AND METHODS

Subjects

Thirteen patients diagnosed with NMO (mean age, 35 ± 14 years; age range, 14–64 years; 6 females and 7 males) were selected from the Clinical Demyelinating Disease data base of our university hospital. All patients fulfilled the revised Criteria of 2006 of Wingerchuk et al.[1] Thirteen demographically matched healthy controls (mean age, 37 ± 13 years; age range, 15–57 years), free of neurologic or psychiatric disorders, were also enrolled. All subjects gave written informed consent, and the study was approved by the institutional review board.

MR Imaging Acquisition

All subjects underwent MR imaging at 3T (Tim Trio; Siemens, Erlangen, Germany). In addition to standard sagittal T1WI and axial T2WI (FLAIR) sequences, a work-in-progress DKI sequence was acquired with 30 gradient directions and the following parameters: b-values of 1 $b = 0$ s/mm^2, 30 $b = 1000$ s/mm^2, and 30 $b = 2000$ s/mm^2; TR/TE = 5300/90 ms; FOV = 220 mm; 45 sections; matrix = 82 × 82; section thickness = 2.7 mm; voxel size = 2.7 mm^3 isotropic; bipolar gradient scheme; bandwidth = 3048 Hz/Px; parallel imaging factor = 2; echo spacing = 0.59 ms; no gap.

DTI and DKI Parametric Map Calculations

DKI raw datasets were processed off-line on a workstation. To calculate the diffusion and kurtosis parametric maps, a custom-written software in Matlab (MathWorks, Natick, Massachusetts)[6] was used. The kurtosis model, as described previously,[5,6] was fitted to the diffusion-weighted signal intensities in each voxel by nonlinear least-squares minimization. The fitted kurtosis tensor was used to calculate AK, RK, and MK, as described by Tabesh et al.[6] Fractional anisotropy (FA), mean diffusion (MD), axial diffusion (AD), and radial diffusion (RD) were calculated from the diffusion tensor in the kurtosis model by using conventional equations.[6] After this, parametric maps were constructed for each parameter (Fig 1).

Data Analysis

Tract-Based Spatial Statistics for Group Analysis. First, all subject data were analyzed statistically by using tract-based spatial statistics (TBSS), a software tool within the fMRI of the Brain Software Library (FSL; http://www.fmrib.ox.ac.uk/fsl).[18] All of the FA maps of subjects were aligned by using nonlinear registration. Then, a mean FA image was created and thinned to generate a mean FA skeleton, which represents the center of all tracts common to the group. We registered each subject's parametric diffusion (MD, RD, and AD) and kurtosis images (MK, RK, and AK) into the same space as the FA, applying the same nonlinear registration used for the previously processed FA images, and projected them onto the skeleton. To perform group comparisons (patients with NMO versus healthy controls), we determined voxelwise cross-subject statistics for each parameter, by using permutation-based inference with 5000 permutations and threshold-free cluster enhancement with a threshold of $P < .05$, corrected for multiple comparisons, by using family-wise error correction. Areas with significantly altered parameters in patients with NMO compared with healthy controls were identified by the Johns Hopkins University White Matter Tractography Atlas (http://cmrm.med.jhmi.edu/) (Fig 2).

Region-of-Interest-Based Group Analysis. Second, a region-of-interest-driven analysis was performed by 2 experienced neuroscientists (F.C.R.L. and T.M.D., each with 7 years of experience) by placing hand-drawn ROIs on the splenium and genu of the CC, corticospinal tract in the cerebral peduncles, and ORs on the B0 maps of each subject by using OsiriX (Version 4.1.2; http://www.osirix-viewer.com). The purpose of this second a priori analysis was to corroborate the TBSS analysis, by choosing specific regions where alterations were expected according to a previous report.[4] The ROIs positioned in the CC, corticospinal tract, and OR had areas of 0.25, 0.15, and 0.29 cm^2, respectively. Then the ROIs were automatically propagated within OsiriX software to all DKI and DTI maps.

Statistical analysis was performed with the R statistical computing software (http://www.r-project.org). Normality was tested by applying the Kolmogorov-Smirnov test. The Cronbach α was used to evaluate the interrater reliability. Group analysis (Student t test) was performed to test for differences between the control and NMO groups. $P < .05$ was considered statistically significant.

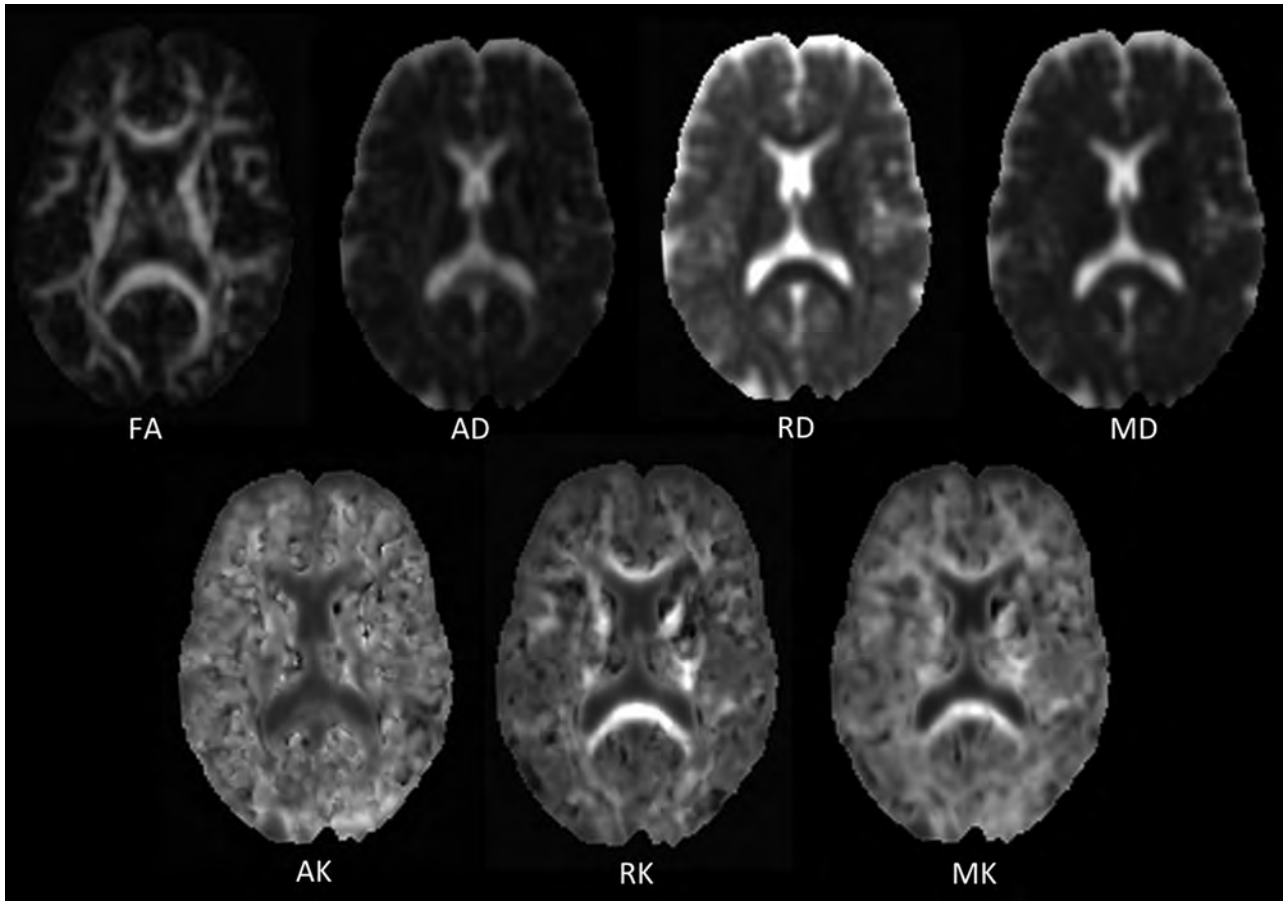

FIG 1. Parametric DKI maps of 1 subject. Common diffusion parameters FA, AD, RD, and MD (upper row). Diffusional kurtosis parameters AK, RK, and MK (lower row).

Correlation between DTI and DKI Parameters. To compare conventional diffusion and DKI parameters, we calculated the Pearson correlation coefficient for all ROIs defined in the second analysis of each subject that were drawn by 1 rater (T.M.D.). A correlation coefficient of $r > 0.7$ was considered a strong correlation, and a coefficient of $0.5 < r < 0.7$ was considered a moderate correlation.

RESULTS

Tract-Based Spatial Statistics

DTI. All results are listed in the On-line Table and illustrated in Fig 2. Reductions in FA were found in the CC (splenium and body), bilateral ORs, inferior fronto-occipital and superior longitudinal fascicules, and left internal capsule (all $P < .05$). MD and RD were increased in the CC (splenium, body, and genu); bilateral ORs; anterior, posterior, and superior corona radiata; inferior fronto-occipital and superior longitudinal fascicules; and bilateral corticospinal tracts in the frontal lobe (all $P < .05$). AD was increased in the CC (splenium, body, and genu), left anterior corona radiata, bilateral superior longitudinal fascicules, and bilateral ORs (all $P < .05$).

DKI. RK was decreased in the splenium, body, and genu of the CC ($P < .05$) and the right anterior corona radiata (Fig 2). A tendency ($P < .1$) for RK reduction was observed in both ORs. Tendencies for MK reduction ($P < .1$) were found in the body and genu of the CC and in the superior corona radiata. AK showed no significant alteration.

Region-of-Interest Analysis

The results of Cronbach α to evaluate the interrater reliability are listed in the Table. All values showed acceptable, good, or excellent interrater reliability ($\alpha \geq 0.7$), expect for 2 values. One value was questionable ($\alpha = .6432$, right corticospinal tract, MD), and one was poor ($\alpha = .5438$, left corticospinal tract, MD).

The On-line Table lists the results of group comparisons. Only regions in which the parameters showed a significant increase or decrease or altered tendency are shown, and only significant P values with an underlying normal distribution are reported.

DTI. Rater 2 found that FA was reduced in the left OR of patients with NMO compared with controls ($P < .05$). Both raters found that MD was increased ($P < .05$) in the genu of the CC in patients with NMO. RD and AD were increased in the same regions ($P < .05$).

DKI. In patients with NMO, both raters found that MK was decreased in the left OR ($P < .05$). Rater 1 found that MK was increased ($P < .05$) in the corticospinal tract of the right peduncle,

whereas rater 2 observed only a tendency of increase ($P = .056$) compared with controls. Both raters found that RK was decreased in the left OR ($P < .05$). Rater 1 found that RK was decreased in the CC splenium ($P < .05$), whereas rater 2 found the same result in the genu of the CC ($P < .05$). No significant alterations in AK were observed.

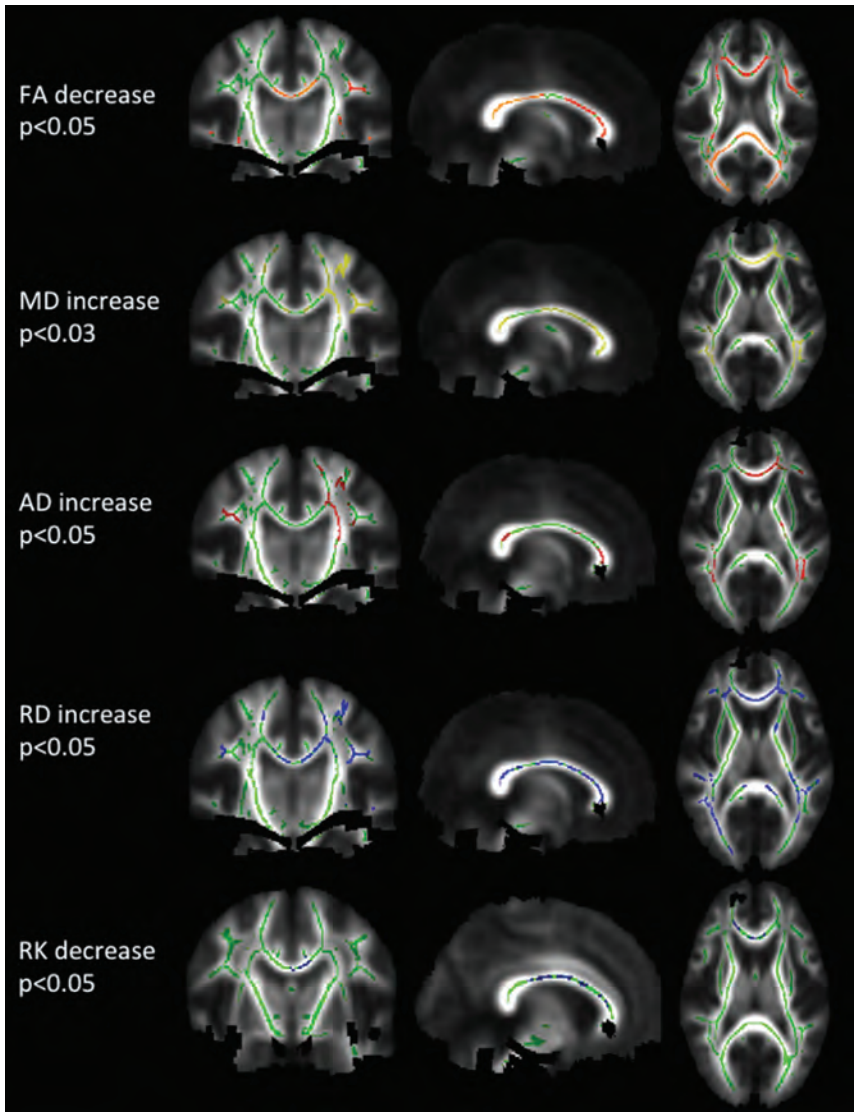

FIG 2. TBSS analysis. Significance *P* maps, corrected for multiple comparison, for DTI and DKI parameters are overlaid color-coded on the skeleton and mean FA image. In green, the mean FA skeleton, where statistical analysis was performed. The following areas are significantly reduced in patients with NMO compared with controls: FA (red-yellow) and RK (blue), or significantly higher, MD (yellow), AD (red), RD (blue).

Correlation between DTI and DKI Parameters Based on Region-of-Interest Analysis

Strong negative correlations were found in the genu and splenium of the CC between RK and MK ($r = -0.709$, $P < .0001$ and $r = -0.881$, $P < .0001$, respectively) and between MD and RD ($r = -0.752$, $P < .0001$ and $r = -0.821$, $P < .0001$, respectively). There was a moderate negative correlation between AK and AD in the bilateral ORs ($r = -0.523$, $P = .006$ and $r = -0.584$, $P = .002$, respectively). A moderate positive correlation was found between FA and MK in the genu and splenium of the CC ($r = 0.549$, $P = .003$ and $r = 0.677$, $P < .0001$, respectively). A strong positive correlation was found between FA and RK in the splenium of the CC ($r = 0.763$, $P < .0001$), and a moderate positive correlation was found in the genu of the CC and the left OR ($r = 0.673$, $P < .0001$ and $r = 0.610$ $P < .001$, respectively). FA and AK were not correlated significantly.

DISCUSSION

In this study, we analyzed the WM in patients with NMO compared with healthy controls by applying the novel DKI technique, by using both TBSS (which requires no a priori hypothesis) and a region-of-interest-driven approach (which uses an a priori hypothesis). Within TBSS, several DTI and DKI parameters were altered significantly in extensive WM tracts, but the only kurtosis parameter that was altered significantly was RK. Within the region-of-interest analysis, the DTI parameters FA, MD, RD, and AD showed significant alterations in some ROIs. The kurtosis parameters RK and MK were altered significantly. Negative correlations were found between several kurtosis and diffusion parameters. A decrease of RK corroborates the presence of demyelination.[14]

Lopes et al[4] previously found significant changes of DTI parameters by a

Interrater reliability test for ROI-based analysis[a]

	CC Genu	CC Splenium	OR R	OR L	CST R	CST L	α	Interpretation
FA	0.9604	0.9958	0.9265	0.9374	0.8504	0.9494	$\alpha \geq .9$	Excellent
MD	0.9110	0.9493	0.8010	0.7811	0.6432	0.5438	$.8 \leq \alpha < .9$	Good
AD	0.9292	0.9299	0.8983	0.9440	0.9290	0.9829	$.7 \leq \alpha < .8$	Acceptable
RD	0.9134	0.9506	0.8401	0.8776	0.8415	0.7905	$.6 \leq \alpha < .7$	Questionable
MK	0.8635	0.9367	0.7894	0.8703	0.9294	0.8332	$.5 \leq \alpha < .6$	Poor
AK	0.9072	0.9526	0.8589	0.7864	0.8164	0.7967	$\alpha < .5$	Unacceptable
RK	0.8968	0.9407	0.8669	0.9446	0.9495	0.9611		

Note:—CST indicates corticospinal tract; R, right; L, left.

[a] The Cronbach α for each ROI, DTI, and DKI parameter is listed.

TBSS analysis in patients with NMO. They observed significant reductions in FA in the CC, ORs, internal and external capsules, corona radiata, and cerebral peduncles and significant increases in RD in the CC, corona radiata, and centrum semiovale. They also found a highly significant negative correlation between FA and RD ($r = -0.976$, $P < .0001$). In the present study, we found a significant FA reduction in those regions, except for the corticospinal tract in the cerebral peduncles. We detected a significant increase in RD in the CC, corona radiata, and centrum semiovale. We found a strong negative correlation between FA and RD in all ROIs, except in the left OR, in which the correlation was moderate and negative. We found a strong positive correlation between FA and RK in the splenium of the CC and moderate positive correlations in the genu of the CC and the left OR. These findings support the hypothesis that the WM damage in patients with NMO is more related to demyelination (RK) than axonal degeneration (AK). This hypothesis was previously stressed in histologic studies,[19,20] which showed that the demyelination process could take place even before axonal death.[20]

Cheung et al[14] demonstrated that RK is highly sensitive to brain maturation due to myelination and, therefore, to its inverse effect, demyelination. Myelin sheath reduction increases the possibility of water diffusion in a direction perpendicular to the nerve fibers, thereby increasing RD and decreasing RK. We observed a significant decrease in RK in the CC and ORs ($P = .028$ and $P = .011$ for raters 1 and 2, respectively, by region-of-interest analysis; $P < .1$ by TBSS). The observed strong negative correlation between RK and RD in the genu and splenium of the CC supports the hypothesis that demyelination is related to a decreased RK and increased RD. Furthermore, MK was increased in the corticospinal tract at the peduncle ($P = .047$ and $P = .56$ by raters 1 and 2, respectively; there was no TBSS result in this area) (without representation on MD maps). This finding might be related to an initial inflammatory process in which high cellularity could restrict overall diffusion, with the diffusion distribution becoming more non-Gaussian and the MK increasing.

Recently, Lätt et al[15] provided estimates of DKI for various cerebral regions in healthy brains and compared them with DTI parameters. They found a strong positive correlation between MK and FA in WM ($r = 0.81$, $P < 10^{-5}$) and a strong negative correlation between RK and RD ($r = -0.95$, $P < 10^{-5}$). In the present study, we found a moderate positive correlation between MK and FA and a strong negative correlation between RK and RD in the splenium and genu of the CC.

Our study had some limitations. During the skull-stripping process by the DKI software, regions in the cerebral peduncle were misclassified as skull in some subjects. In TBSS, after averaging the subject's images to generate a mean FA image, black regions appeared in some cases, and cross-subject statistical analysis was compromised. Unfortunately, the sensibility threshold that determines the degree of skull-stripping was not adjustable within the software version used to reconstruct the DT and DK parametric maps. This aspect of the TBSS analysis might explain why TBSS was unable to detect the significant increase of MK in the right corticospinal tract in the cerebral peduncle.

Another limitation may be the incorrect placements of ROIs during region-of-interest-driven analysis. However, we included this analysis because it is based on a priori data and allowed the comparison with results of previous studies because a TBSS analysis of DKI had not been performed to date, to our knowledge. Moreover, the results of the region-of-interest analysis could verify the TBSS results. The limitation of the region-of-interest analysis (lack of multiple-comparison correction) was overcome by the TBSS analysis by doing a family-wise error multiple comparison correction.

Another limitation was the suboptimal acquisition resulting from the sequence applied, which consisted of b-values of only 1 $b = 0$, 30 $b = 1000$, and 30 $b = 2000$. Noise is a general problem in diffusion MR imaging acquisitions, and its effects have been investigated extensively.[21] Using higher b-values in DKI acquisitions increases the sensitivity of the measurement to noise and, therefore, the possibility that the diffusion and kurtosis parameter estimates will vary from their true values, causing erroneous inferences. A better understanding of the effects of noise on DKI would be helpful in interpreting DKI results. Finally, because NMO is an uncommon disease, the patient population is quite heterogeneous when considering clinical data and treatment options; this heterogeneity is another limitation to our study, and these findings should be replicated in a different group to validate our results.

CONCLUSIONS

This study demonstrated significant differences in diffusion and kurtosis parameters in patients with NMO compared with healthy controls. Conventional diffusion parameters such as FA, MD, RD, and AD were more sensitive to the disease than kurtosis parameters. Only RK was significantly reduced, while MK presented a reduction tendency. AK did not show alterations. Kurtosis parameters were inversely correlated with the corresponding diffusion parameters. RK and MK correlated positively with FA. Further studies are necessary to prove the benefit of DKI parameters as biomarkers for patients with NMO.

ACKNOWLEDGMENTS

The authors would like to thank Dr Ali Tabesh for his technical assistance.

REFERENCES

1. Wingerchuk DM, Lennon VA, Pittock SJ, et al. **Revised diagnostic criteria for neuromyelitis optica.** *Neurology* 2006;66:1485–89
2. Aboul-Enein F, Krssák M, Höftberger R, et al. **Diffuse white matter damage is absent in neuromyelitis optica.** *AJNR Am J Neuroradiol* 2010;31:76–79
3. Pires CE, da Silva CMC, Lopes CRF, et al. **Brain MRI abnormalities in Brazilian patients with neuromyelitis optica.** *J Clin Neurosci* 2012;19:969–74
4. Lopes CRF, Doring TM, Martins C, et al. **The role of demyelination in neuromyelitis optica damage: diffusion tensor MR imaging study.** *Radiology* 2012;263:235–42
5. Rueda-Lopes CR, da Cruz LC, Doring TM, et al. **Diffusion-weighted imaging and demyelinating diseases: new aspects of an old advanced sequence.** *AJR Am J Roentgenol* 2014;202:W34–42
6. Tabesh A, Jensen JH, Ardekani BA, et al. **Estimation of tensors and tensor-derived measures in diffusional kurtosis imaging.** *Magn Reson Med* 2011;65:823–36

7. Jensen JH, Helpern JA, Ramani A, et al. **Diffusional kurtosis imaging: the quantification of non-Gaussian water diffusion by means of magnetic resonance imaging.** *Magn Reson Med* 2005; 53:1432–40
8. Lu H, Jensen JH, Ramani A, et al. **Three-dimensional characterization of non-Gaussian water diffusion in humans using diffusion kurtosis imaging.** *NMR Biomed* 2006;19:236–47
9. Jensen JH, Helpern JA. **MRI quantification of non-Gaussian water diffusion by kurtosis analysis.** *NMR Biomed* 2010;23:698–710
10. Lazar M, Jensen JH, Xuan L, et al. **Estimation of the orientation distribution function from diffusional kurtosis imaging.** *Magn Reson Med* 2008;60:774–81
11. Tuch DS, Reese TG, Wiegell MR, et al. **Diffusion MRI of complex neural architecture.** *Neuron* 2003;40:885–995
12. Tuch DS. **Q-ball imaging.** *Magn Reson Med* 2004;52:1358–72
13. Hui ES, Cheung MM, Qi L, et al. **Towards better MR characterization of neural tissues using directional diffusion kurtosis analysis.** *Neuroimage* 2008;42:122–34
14. Cheung MM, Hui ES, Chan KC, et al. **Does diffusion kurtosis imaging lead to better neural tissue characterization? A rodent brain maturation study.** *Neuroimage* 2009;45:386-92
15. Lätt J, Nilsson M, Wirestam R, et al. **Regional values of diffusional kurtosis estimates in the healthy brain.** *J Magn Reson Imaging* 2013;37:610–18
16. Fung SH, Roccatagliata L, Gonzalez RG, et al. **MR diffusion imaging in ischemic stroke.** *Neuroimaging Clin N Am* 2011;21:345–77, xi
17. Van Cauter S, Veraart J, Sijbers J, et al. **Gliomas: diffusion kurtosis MR imaging in grading.** *Radiology* 2012;263:492–501
18. Smith SM, Johansen-Berg H, Jenkinson M, et al. **Acquisition and voxelwise analysis of multi subject diffusion data with tract-based spatial statistics.** *Nat Protoc* 2007;2:499–503
19. Lucchinetti CF, Mandler RN, McGavern D, et al. **A role for humoral mechanisms in the pathogenesis of Devic's neuromyelitis optica.** *Brain* 2002;125(pt 7):1450–61
20. Marignier R, Nicolle A, Watrin C, et al. **Oligodendrocytes are damaged by neuromyelitis optica immunoglobulin G via astrocyte injury.** *Brain* 2010;133:2578–91
21. Farrell JA, Landman BA, Jones CK, et al. **Effects of signal-to noise ratio on the accuracy and reproducibility of diffusion tensor imaging-derived fractional anisotropy, mean diffusivity, and principal eigenvector measurements at 1.5T.** *J Magn Reson Imaging* 2007;26:756–67

MR Imaging of Subcallosal Artery Infarct Causing Amnesia after Surgery for Anterior Communicating Artery Aneurysm

S. Mugikura, H. Kikuchi, T. Fujii, T. Murata, K. Takase, E. Mori, S. Marinković, and S. Takahashi

ABSTRACT

BACKGROUND AND PURPOSE: During surgery to treat an aneurysm in the anterior communicating artery, injury to the subcallosal artery, a perforator of the anterior communicating artery, may lead to infarction that produces basal forebrain amnesia after surgery. Our purpose was to examine whether 3D MR imaging can detect subcallosal artery infarction in patients with amnesia after surgery for an anterior communicating artery aneurysm.

MATERIALS AND METHODS: We evaluated 3D–T2-weighted MR images obtained a median of 4 months after treatment of anterior communicating artery aneurysm for the presence of infarcted foci in 10 consecutive patients with postoperative amnesia. Because the subcallosal artery and its neighboring perforator, the recurrent artery of Heubner, were considered the most easily affected vessels during that surgery, we focused mainly on 8 regions of the subcallosal artery territory per hemisphere and 5 regions of the recurrent artery of Heubner territory per hemisphere.

RESULTS: All 10 patients had infarcts in the territory of the subcallosal artery (median, 9 regions per patient), and most were bilateral (9 of 10 patients). Five patients had additional infarcted foci in the territory of the recurrent artery of Heubner (median, 1 region per patient), all unilateral. Among the regions perfused by the subcallosal artery, the column of the fornix was involved in all patients; the anterior commissure, in 9; and the paraterminal gyrus, in 8 patients.

CONCLUSIONS: 3D MR imaging revealed subcallosal artery infarction, the distribution of which was mostly bilateral, presumably owing to the unpairedness of that artery, in patients with postoperative amnesia after anterior communicating artery aneurysm repair.

ABBREVIATIONS: ACoA = anterior communicating artery; IQ = full-scale intelligence quotient; MQ = general memory quotient; RAH = recurrent artery of Heubner; VISTA = volumetric isotropic turbo spin-echo acquisition

Since the 1950s, amnesia sufficient to affect quality of life has been repeatedly reported in patients following surgical repair of anterior communicating artery (ACoA) aneurysms.[1-6] On the basis of descriptions from the 1970s of the perforating branches from the ACoA,[7] much indirect evidence indicates that the amnesia is caused by damage or occlusion of the perforators of the ACoA, and this is known as ACoA syndrome.[2,8,9] Gade[10] linked vascular damage of the perforators from the ACoA during surgery with postoperative amnesia not directly, but clearly. In brief, the author found that postoperative amnesia occurred more frequently in cases of trapping the ACoA (82% of 11 patients) than in clipping the aneurysmal neck (16% of 37 patients). The author presumed that trapping the ACoA, which completely disrupted the blood supply through perforators from the ACoA, resulted in a high prevalence of postoperative amnesia. Another report from a postmortem examination of a patient with amnesia following a ruptured and repaired ACoA aneurysm revealed infarctions in the basal forebrain bilaterally, and the author concluded that infarction was caused by an inadvertent sacrifice of the perforators of the ACoA, which presumably was responsible for the patient's amnesia.[11]

Several authors have suspected that the amnesia is caused by occlusion or damage of the subcallosal artery, among the perforating arteries of the ACoA.[12-15] The artery is the largest unpaired

Received March 23, 2014; accepted after revision June 4.

From the Departments of Diagnostic Radiology (S. Mugikura, T.M., K.T., S.T.) and Behavioral Neurology and Cognitive Neuroscience (H.K., T.F., E.M.), Tohoku University, Graduate School of Medicine, Sendai, Japan; and Institute of Anatomy (S. Marinković), School of Medicine, University of Belgrade, Belgrade, Serbia.

Please address correspondence to Shunji Mugikura, MD, PhD, Department of Diagnostic Radiology, Tohoku University, Graduate School of Medicine, 1-1 Seiryo-machi, Aoba-ku, Sendai, Japan 980-8574; e-mail: mugi@rad.med.tohoku.ac.jp

Indicates open access to non-subscribers at www.ajnr.org

Indicates article with supplemental on-line table.

Indicates article with supplemental on-line photo.

http://dx.doi.org/10.3174/ajnr.A4057

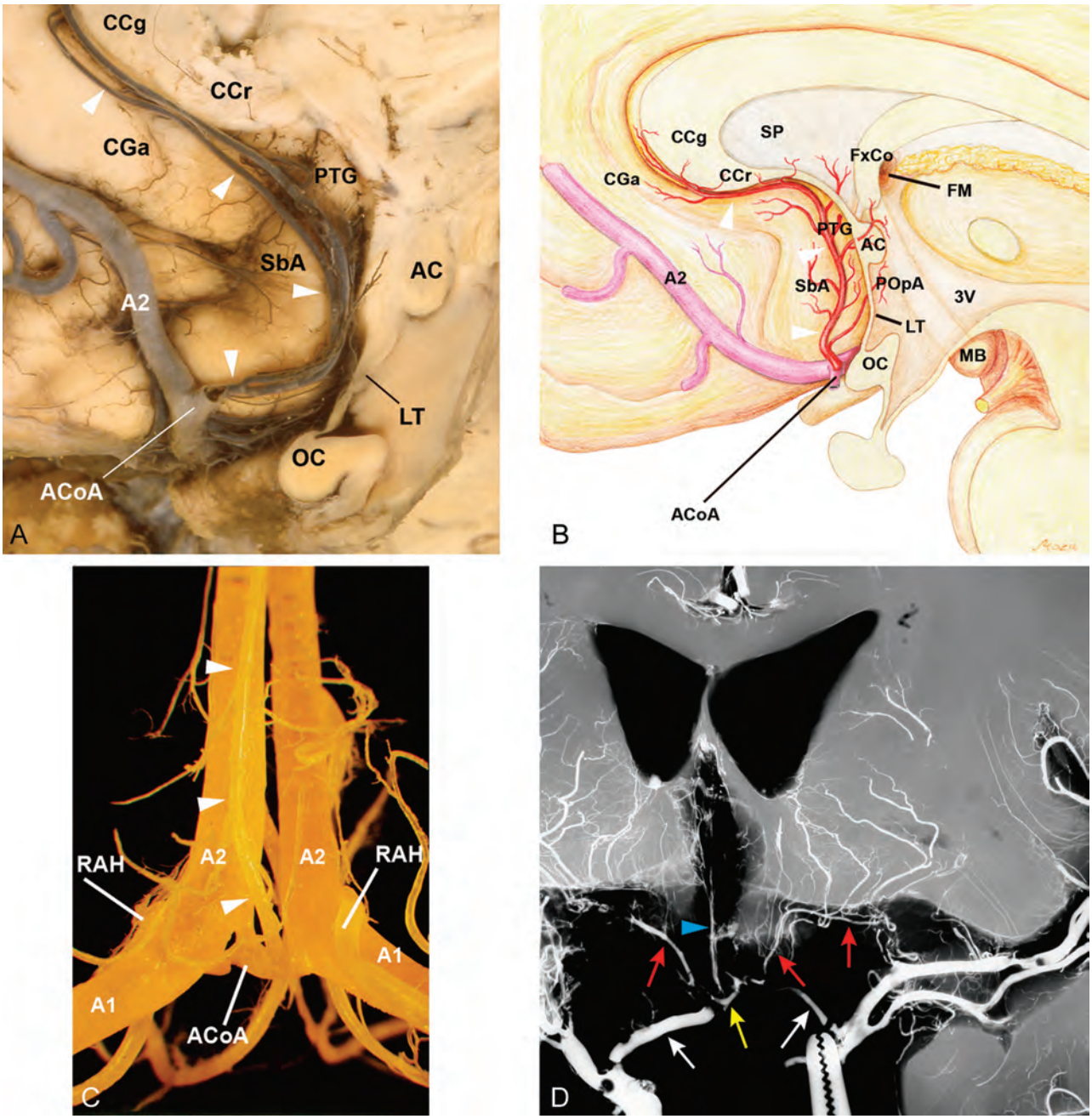

FIG 1. Anatomy of the subcallosal artery and RAH and their supplying basal forebrain regions. *A*, Specimen shows the subcallosal artery. The unpaired subcallosal artery (*arrowheads*) originates from the posterosuperior aspect of the ACoA, divides into 2 stems, and ascends dorsally into the lamina terminalis (LT) cistern, then curves upward and forward along the LT, paraterminal gyrus (PTG), subcallosal area (SbA), the rostrum (CCr) and genu (CCg) of the corpus callosum, and the anterior cingulate gyrus (CGa), thus exhibiting a characteristic S-shaped curve. OC indicates optic chiasm. *B*, Illustrative figure of the subcallosal artery (*arrowheads*) supplying the basal forebrain on the basis of our previous study regarding the microsurgical anatomy of the artery.[16] The subcallosal artery originates from the posterosuperior aspect of the ACoA, ascends dorsally into the LT cistern, and supplies the 8 regions of the basal forebrain as follows: preoptic area (POpA), PTG including a part of the septum pellucidum (SP), SbA, anterior commissure (AC), and column of fornix (FxCo), then curves forward and upward to supply the CCr, CCg, and CGa. FM indicates foramen of Monro; MB, mammillary body; A2, A2 segment of the anterior cerebral artery; 3V, third ventricle. *C*, Specimen of the anterior cerebral and ACoA complex injected with methacrylic resin viewed from the posterior side. The subcallosal artery (*arrowheads*) is seen arising from the ACoA, A1, right and left A1 segments, and A2, right and left A2 segments, of the anterior cerebral arteries. *D*, Coronal microangiogram of the RAH on both sides and the unpaired subcallosal artery (reproduced, with permission, from Takahashi S, Goto K, Fukasawa H, et al. Computed tomography of cerebral infarction along the distribution of the basal perforating arteries. Part I. Striate arterial group. *Radiology* 1985;155:107–18). Both internal carotid arteries have been retracted inferiorly to demonstrate the cisternal course of the RAH (*red arrows*), which follows a curved or tortuous course along the A1 segment of the anterior cerebral artery (*white arrows*). The branches of the RAH are distributed to a part of the basal forebrain. The subcallosal artery (*arrowhead*) is also seen arising from the ACoA (*yellow arrow*).

one with a diameter of approximately 0.5 mm and perfuses the medial and ventral cerebral hemispheres (basal forebrain) bilaterally (Fig 1).[13,16] The proximity between ACoA aneurysms and the origin of this artery suggests the possibility of arterial injury during surgery (On-line Fig 1).

In a review of 17 neurosurgical outcome studies (including

Table 1: Patient demographic data and summary of neuropsychological findings

Patient	1	2	3	4	5	6	7	8	9	10
Age (yr) (sex)	52/M	42/M	39/M	45/M	54/M	45/M	69/M	55/M	39/M	59/F
Ruptured/unruptured	R	R	R	R	R	R	U	R	R	U
CT grade[a]	3	4	3	3	4	3	NA	4	4	NA
Treatment	Trap	Clip	Clip 2nd	Clip	Clip	Clip	Clip	Clip	Clip	Clip
Months from treatment[b]	2	4	4[b]	3	13	3	3	5	3	4
MMSE[c]	24	25	26	28	25	28	26	24	23	27
IQ[d]	82	97	111	110	120	106	102	83	89	92
MQ[e]	58	59	68	92	92	87	86	64	68	67
IQ minus MQ	24	38	43	18	28	19	16	19	21	25
Attention/concentration	81	80	114	138	131	115	115	91	94	133
Delayed recall	<50	<50	<50	<50	64	73	62	<50	<50	<50

Note:—R indicates ruptured; U, unruptured; MMSE, Mini-Mental State Examination; IVH, intraventricular hemorrhage in the bilateral lateral ventricles; Trap, trapping; Clip, clipping; NA, not applied; WAIS-III, Wechsler Adult Intelligence Scale III; WMS-R, Wechsler Memory Scale-Revised.

[a] CT grade, proposed by Claassen et al,[39] classifies the severity of aneurysmal subarachnoid hemorrhage on CT scans at onset into 5 grades from 0 to 4, according to the appearance of both of SAH and intraventricular hemorrhage in the bilateral lateral ventricles: grade 0, no SAH or IVH; grade 1, minimal SAH, no IVH; grade 2, minimal SAH, with IVH; grade 3, thick SAH, no IVH; grade 4, thick SAH, with IVH. In this scaling, the definition of "thick" is "completely filling" ≥1 cistern or fissure. In 2 patients with unruptured aneurysm (patients 7 and 10), grading was not applied.

[b] Months after second clipping.

[c] MMSE, used to assess cognitive impairment (full score 30).[40]

[d] IQ evaluated by the Wechsler Adult Intelligence Scale III.[18]

[e] MQ, general memory quotient, attention/concentration quotient, and delayed recall quotient, evaluated by Wechsler Memory Scale-Revised.[19] Each quotient has a mean of 100 in the normal population and an SD of 15. A substantial difference between IQ (by the WAIS-III) and MQ (by the WMS-R) scores indicates that the person with amnesia has a particular impairment in memory—but not in the "intelligence" per se.[20]

504 patients) of ruptured and repaired ACoA aneurysms, the diagnosis of basal forebrain amnesia has been made mainly by neuropsychological examination alone, thereby leading to a large variety of prevalences ranging between 3% and 83%.[17] Meanwhile, in the reports that provided imaging findings in cases with postoperative amnesia of an ACoA aneurysm, most used CT scans and/or 2D MR imaging (with relatively thick section thickness) and did not clarify the exact location of the infarcts inside the basal forebrain, probably because of low image resolution and metallic artifacts from clips placed during surgery.[2,3,5]

Our purpose was to test the hypothesis that 3D MR imaging can detect subcallosal artery infarction in patients with amnesia after ACoA aneurysm surgery.

MATERIALS AND METHODS

Patients

Our institutional review board approved this retrospective observational study, and written informed consent was waived. From December 2007 to March 2013, 14 consecutive patients with amnesia following surgical treatment of an ACoA aneurysm visited the behavioral neurology service of our hospital and underwent 3T 3D MR imaging examinations. Patients were examined by behavioral neurologists and underwent neuropsychological examinations, including the Wechsler Adult Intelligence Scale III[18] and Wechsler Memory Scale-Revised.[19] Of the 14 patients, we enrolled 10 patients who showed a substantial difference between the full-scale intelligence quotient (IQ) on the Wechsler Adult Intelligence Scale III and general memory quotient (MQ) on the Wechsler Memory Scale-Revised scores; IQ − MQ > 15, indicating that the person with amnesia had a particular impairment in memory but not in "intelligence" per se[20] [IQ − MQ = 26 (mean), 18–43 (range), all > 15]. Patient demographic data and a summary of neuropsychological findings are shown in Table 1. The 10 patients included 8 with ruptured and 2 with unruptured ACoA aneurysms.

Neuropsychological examinations and 3D MR images reviewed in this study were performed a median of 4 months (range, 2–13 months) from aneurysm treatment. Each set of examinations was conducted within a month of the other. This delayed timing of examinations was considered desirable for neuropsychological memory assessment because such assessment in the acute phase (from 1 to 6 weeks) after the aneurysmal rupture would hardly be valid, with the diagnosis of amnesia being difficult due to both a state of confusion, including disorientation, and intellectual disturbance.[17] Indeed, amnesia did not manifest for some time in 7 patients after treatment of the ruptured ACoA aneurysms (surgical clipping in 6 patients and trapping of the ACoA in another); however, amnesia became apparent as the patients recovered from acute-stage illness. In contrast, 2 patients with unruptured ACoA aneurysms (patients 7 and 10) developed amnesia immediately after surgery. The tenth patient (patient 3) underwent clipping of an ACoA aneurysm the day following the rupture and was doing well when approximately 3 weeks later, postoperative CT angiography disclosed a remnant of the aneurysm lumen. After a second surgery, the patient immediately presented with amnesia.

MR Imaging Examination

In all 10 patients, MR imaging examinations were performed a median of 4 months (range, 2–13 months) from aneurysmal treatment by using a 3T machine (Achieva 3T Quasar Dual imager; Philips Healthcare, Erlangen, Germany) with an 8-channel sensitivity encoding head coil. All patients underwent a sagittal 3D volumetric isotropic turbo spin-echo acquisition (VISTA) of T2-weighted imaging, axial 3D magnetization prepared rapid acquisition of gradient-echo, conventional axial T1-, T2-, and T2*-weighted, fluid-attenuated inversion recovery imaging, and time-of-flight MR angiography. VISTA provides high-resolution volumetric T2-weighted images with a turbo spin-echo acquisition and produces fewer metallic artifacts from aneurysmal clips than the fast-field echo acquisition.

The parameters for T2WI-VISTA were the following: TR/TE, 4000/180 ms; FOV, foot to head, 224 mm, anterior to posterior,

Table 2: Infarction in each vascular territory on MR imaging for 10 patients[a]

	Patient No. (R/L)																			
	1		2		3		4		5		6		7		8		9		10	
	R	L	R	L	R	L	R	L	R	L	R	L	R	L	R	L	R	L	R	L
Vascular territory																				
Subcallosal ($n = 8$)	+	+	+	+	+	+	+	+	+	+	+	+		+	+	+	+	+	+	+
RAH ($n = 5$)	+								+							+	+		+	
Unspecified ($n = 3$)	+					+					+				+	+	+	+	+	

Note:—R/L indicates right and left hemisphere; +, infarcted focus present in a vascular territory; blank space, sparing of the territory.
[a] For vascular territories of subcallosal, RAH, and unspecified, refer to Fig. 2.

224 mm, right-to-left, 164 mm; acquisition voxel size, foot to head, 0.56 mm, anterior to posterior, 0.56 mm, right-to-left, 0.80 mm; reconstruction voxel size, foot to head, 0.44 mm, anterior to posterior, 0.44 mm, right-to-left, 0.40 mm; echo-train length, 111; number of signal averages, 1. VISTA uses the low-refocusing flip angle scheme to reduce initial signal modulations during the first few echoes by setting the flip angle at 130° for the first refocusing pulse and 80° for succeeding refocusing pulse trains.[21] We used sensitivity encoding or parallel imaging with a speed-up factor of 6.0 (2 in the anterior to posterior, 3 in the right-to-left direction). Total acquisition time was 8 minutes 16 seconds. We obtained T2WI-VISTA images in the sagittal plane for acquisition within a clinically reasonable scanning time.

The parameters for MPRAGE were the following: TR/TE, 6.6/3.0 ms; FOV, foot to head, 176 mm, anterior to posterior, 224 mm, right-to-left, 204 mm; acquisition voxel size, 1/1/1 mm; reconstruction voxel size, 0.5/0.5/0.5 mm; echo-train length, 226; number of signal averages, 1; flip angle, 8°. The total scan duration was 5 minutes 13 seconds.

In addition to the 3D images obtained in the chronic phase as described, 3 patients underwent MR imaging in the acute stage after treatment at outside hospitals by using 1.5T machines (Signa; GE Healthcare, Milwaukee, Wisconsin). The images were sent to us later for review: MR imaging including diffusion-weighted imaging immediately after surgery in 2 patients with unruptured ACoA aneurysms and MR imaging 1 week after a second surgery in another patient.

Evaluation of MR Imaging Findings

On multiplanar reconstruction images, 2 experienced neuroradiologists blinded to neuropsychological assessments, with 25 (S.T.) and 15 (S. Mugikura) years' experience, identified and localized infarctions by consensus.

Basal forebrain anatomy was identified on MPRs such as in On-line Fig 2, by referencing multiple coronal brain specimens with detailed diagrams (with 0.7- to 1.5-mm intersectional gap) by Mai et al.[22] Regarding the vascular territories of infarction, we referenced descriptions of arterial supply of the basal forebrain in the radio-anatomic literature[16,23,24] and specifically focused on the following 16 regions of the basal forebrain per hemisphere: 8 regions of the territory of the subcallosal artery (anterior cingulate gyrus; anterior commissure; column of the fornix; paraterminal gyrus, including a part of the septum pellucidum; preoptic area; rostrum and genu of the corpus callosum; and subcallosal area).[13,16] Because the recurrent artery of Heubner (RAH), which usually originates on both sides around the junction of the ACoA and the anterior cerebral artery (Fig 1),[25,26] is also considered at high risk of injury from treatment of ACoA aneurysms, 5 regions of the territory of the RAH were also included in this analysis (anterior limb of the internal capsule, caudate nucleus, globus pallidus, nucleus accumbens, and putamen).[24,26,27] Three additional neighboring regions with unspecified vascular supply (bed nucleus of the stria terminalis, diagonal band of Broca, and substantia innominata) were reviewed for infarction.

Excluding 4 regions completely obscured by artifacts from aneurysmal clips, we examined 316 unobscured or nearly unobscured regions. As well, we recorded infarctions outside the above 16 regions in the basal forebrain.

We also examined which part of the column of the fornix the infarction affected (ie, the pars libera, including both post- and precommissural fibers, and the pars tecta just posterior to the anterior commissure [On-line Fig 3]).

Atrophy of the mammillary body is known to correlate positively with severity of damage to the ipsilateral column of the fornix from Wallerian degeneration.[28] Therefore, 2 other neuroradiologists, with 15 (T.M.) and 10 (K.T.) years' experience and blinded to the purpose of the evaluation, also examined the mammillary bodies for possible atrophy and its relationship to the presence or absence of infarctions in the column of the fornix.

RESULTS

All 10 patients had infarcted foci in the territory of the subcallosal artery, and 9 patients had bilateral foci (Table 2). In contrast, only 5 patients had infarcted foci in the territory of the RAH, all unilateral (patients 1, 5, 8, 9, and 10). Infarcted foci in the territories of unspecified arteries were found in 6 patients. Foci of 3 patients (patients 2, 4, and 7) were limited to the territory of the subcallosal artery and did not involve the territories of the RAH or unspecified arteries. No patients had infarcted foci in the territory of the RAH alone without foci in the territory of the subcallosal artery.

In 2 patients with unruptured aneurysms, DWI performed the day after the surgery showed acute infarcted foci in the basal forebrain. The foci were later confirmed by the 3D MR imaging to involve the unilateral territory of the subcallosal artery but not of the RAH in 1 patient (patient 7) and the bilateral territories of the subcallosal artery and the unilateral RAH territory in the other (patient 10). In another patient with a second clipping surgery, thin-section CT preoperatively showed no lesions in the basal forebrain but DWI performed 1 week after a second surgery showed acute infarcted foci in the basal forebrain. 3D MR imaging

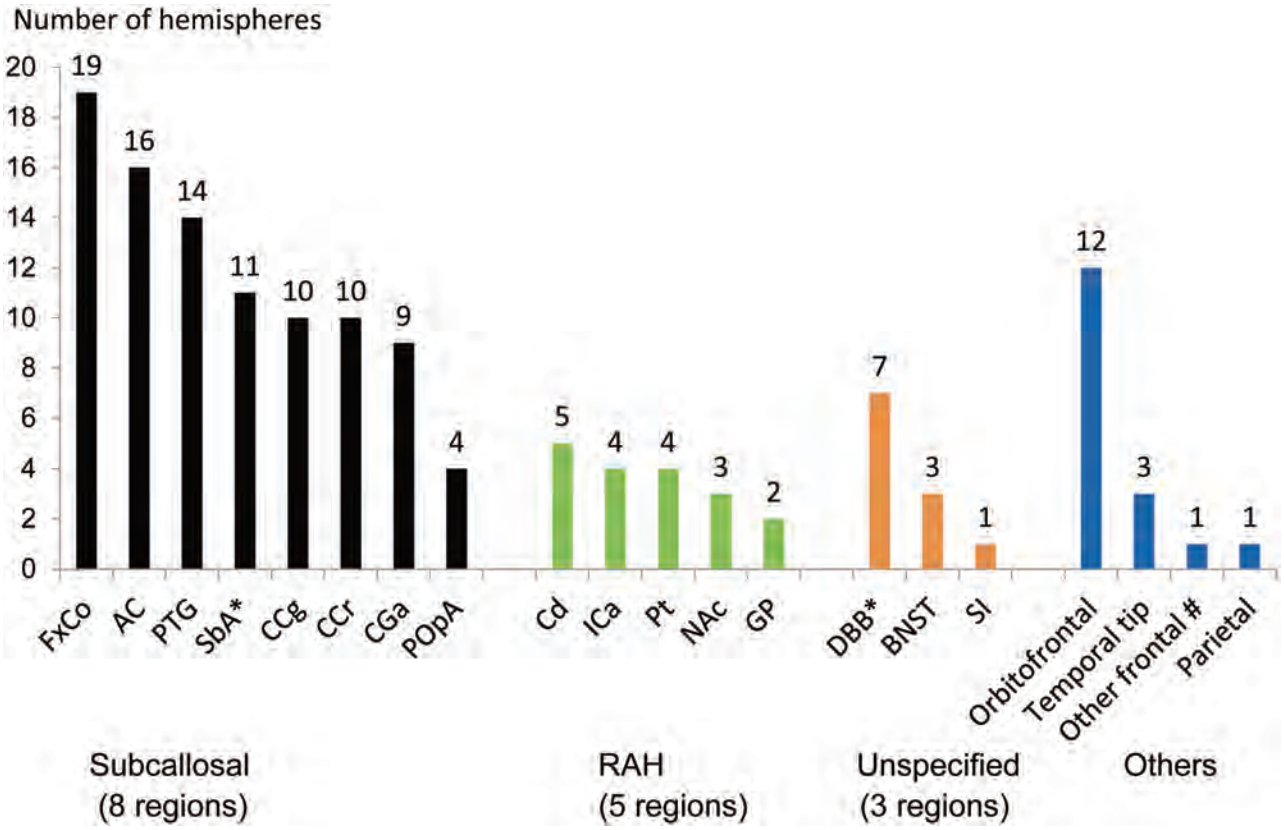

FIG 2. Summary of the infarcted foci on MR images in each region according to the vascular supply. The number on each bar graph represents the number of hemispheres in which infarcted foci of each region were found. Eight regions of the subcallosal artery: column of the fornix (FxCo), anterior commissure (AC), paraterminal gyrus (PTG), subcallosal area (SbA), genu of the corpus callosum (CCg), rostrum of the corpus callosum (CCr), anterior cingulate gyrus (CGa), and preoptic area (POpA). Five regions of the RAH: caudate nucleus (Cd), anterior limb of the internal capsule (ICa), putamen (Pt), nucleus accumbens (NAc), and globus pallidus (GP). Three other regions defined as the regions of unspecified vascular supply: diagonal band of Broca (DBB), bed nucleus of the stria terminalis (BNST), and substantia innominata (SI). The asterisk indicates that metallic artifacts from aneurysmal clips completely obscured the SbA in 2 hemispheres of 2 patients unilaterally and DBB in 1 patient bilaterally. Number sign indicates that "other frontal" represents the frontal lobe other than the orbitofrontal and basal forebrain region.

later disclosed bilateral infarcts in the territory of the subcallosal artery (patient 3).

Infarctions were most common in 3 regions in the territory of the subcallosal artery (Fig 2)—the column of the fornix, anterior commissure, and paraterminal gyrus (detailed MR imaging findings of 10 patients are in the On-line Table). The column of the fornix was involved in all 10 patients (19 hemispheres, bilaterally in 9 patients, unilaterally on the left in 1 patient). In the 19 hemispheres with fornix involvement, the pars libera was affected in all, while the pars tecta was affected in 15 (79% of 19) hemispheres.

Bilateral involvement of the anterior commissure in 7 patients demonstrated a characteristic bow-tie-like appearance (Figs 3 and 4); unilateral involvement in 2 patients showed an incomplete bow-tie-like appearance (On-line Fig 4). All 7 patients with bow-tie-like involvement of the bilateral anterior commissure had infarcts bilaterally in the adjoining pars libera of the column of the fornix, with associated infarcts in the pars tecta that were bilateral in 5 and unilateral in 2. Two patients had a lesion of the anterior commissure on only the left side, which therefore displayed an incomplete bow-tie-like appearance: They also had infarcted foci in the pars libera and pars tecta unilaterally on the left in 1 patient (patient 7, On-line Fig 4) and bilaterally in the other patient (patient 5). One patient had no involvement of the anterior commissure.

The paraterminal gyrus was involved bilaterally in 6 patients and unilaterally in 2, and the subcallosal area was involved bilaterally in 3 and unilaterally in 5 patients.

The corpus callosum was involved in the genu bilaterally in 5 patients and in the rostrum bilaterally in 3 and unilaterally in 4 patients. The anterior cingulate gyrus was involved bilaterally in 2 and unilaterally in 5 patients. These infarcted foci were located along the medial aspect of the brain and almost in line with associated lesions in the paraterminal gyrus and column of the fornix. This anteroposterior extent of involvements was observed on axial and sagittal MR images (Fig 4).

Of 3 regions with the unspecified vascular supply, the diagonal band of Broca was most frequently involved (35%, 7 of 20 hemispheres; 50%, 5 of 10 patients). Of regions outside the basal forebrain, the orbitofrontal region was most frequently involved (60%, 12 of 20 hemispheres; 90%, 9 of 10 patients).

Definite atrophy of the mammillary body was seen in 15 (79%) of 19 hemispheres with infarcted regions in the column of the fornix. We considered the mammillary body to be nonatrophied

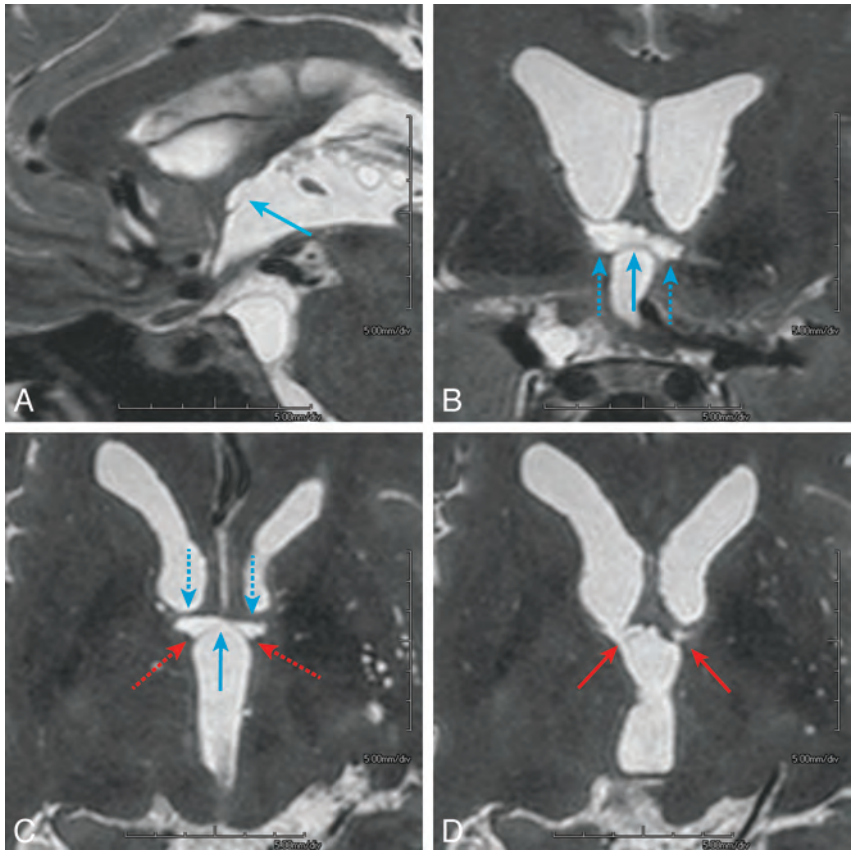

FIG 3. A 45-year-old who man presented with a ruptured aneurysm of the anterior communicating artery. Surgical clipping of the aneurysm was performed the day of onset (patient 4). Neuropsychological examination 3 months after the rupture confirmed amnesia. The imaging anatomy of the basal forebrain is detailed in On-line Fig 2: paramedian sagittal (*A*), coronal (*B*), and axial (*C*) and its next superior section (*D*), volumetric isotropic turbo spin-echo acquisition of T2WI (T2WI-VISTA) images shows infarcted foci in the midline (*light blue arrows*) and paramedian parts (*dashed light blue arrows*) of the anterior commissure along with the pars libera (*red arrows*) and pars tecta (*dashed red arrows*, *C*) of the columns of the fornices. Note that on coronal (*B*) and axial (*C*) images, infarcted foci in the bilateral anterior commissure show a characteristic bow-tie-like appearance and are associated with the infarcted foci in the adjoining bilateral pars libera and pars tecta of the column of the fornix. Other than the columns of the fornix and anterior commissure, no other regions are involved in the basal forebrain. The orbitofrontal region and temporal tip on the left were also involved, presumably damaged by the surgical procedure of the aneurysmal clipping (not shown).

in 2 hemispheres of 2 patients (patients 2 and 4) in which the mammillary body was compressed or deformed by the elongated posterior cerebral artery or the basilar artery. In a patient with unilateral fornix involvement by infarction in the left hemisphere, atrophy of the mammillary body was seen only in the left hemisphere (patient 7).

DISCUSSION

Subcallosal Artery Infarct Causing ACoA Syndrome or Amnesia

We found infarcted foci in the territory of the subcallosal artery in all 10 patients with amnesia following treatment of ACoA aneurysms, and in 9 patients, the infarcted foci were bilateral. Meanwhile, 5 patients had additional infarcted foci in the territory of the RAH, and its involvement was always unilateral. This difference between bilateral and unilateral involvement may be explained by the fact that the subcallosal artery is unpaired, whereas the RAH is present on both sides. Thus, infarct patterns in the cases described in this study are compatible with the suggestion of previous neurosurgical and neuropsychological studies that occlusion of the subcallosal artery could cause postoperative amnesia.

We believe that the relationship between surgical damage of the subcallosal artery and amnesia is particularly apparent in 3 patients who presented with amnesia immediately after surgery. In 2 patients with unruptured aneurysms and another with a second clipping surgery, DWI revealed acute lesions that were confirmed later by 3D MR imaging to involve the territory of the subcallosal artery. In all, the involvement in the basal forebrain was obviously caused by vascular damage during surgery.

This was a small study and may not be considered definitive to conclude that occlusion or damage of the subcallosal artery during surgery causes bilaterally distributed infarction and produces postoperative amnesia. However, this hypothesis would be extremely difficult to prove, unless a correlation was found between preserving a given artery and lack of amnesia. We believe the data that we present in this study are strong and appear to answer, to a reasonable degree, an important clinical question that has persisted for several decades. The causal relationship is apparent if we consider acutely developed amnesia immediately after surgery with postsurgically developed infarcts in the territory of the subcallosal artery in our 3 patients and the presence of infarcted foci in the same vascular territory in all the remaining 7 patients with amnesia following treatment of ACoA aneurysms.

Sites Responsible for Postoperative Amnesia

What structures of the basal forebrain are responsible for postoperative basal forebrain amnesia? This question remains to be answered. Because our study included no control group without amnesia, we cannot draw a definitive conclusion. However, considering the affected regions in our cases, the column of the fornix, a constituent of the Papez neuronal circuit (On-line Fig 3), seems the most likely responsible site for the amnesia. The same hypothesis has been suggested in the literature: Infarction relatively limited to the bilateral columns of the fornices on DWI has been separately reported in 4 patients with spontaneous stroke and acute onset of amnesia,[29-32] in a patient with amnesia following clipping,[33] and in another following coiling of an unruptured ACoA aneurysm.[34]

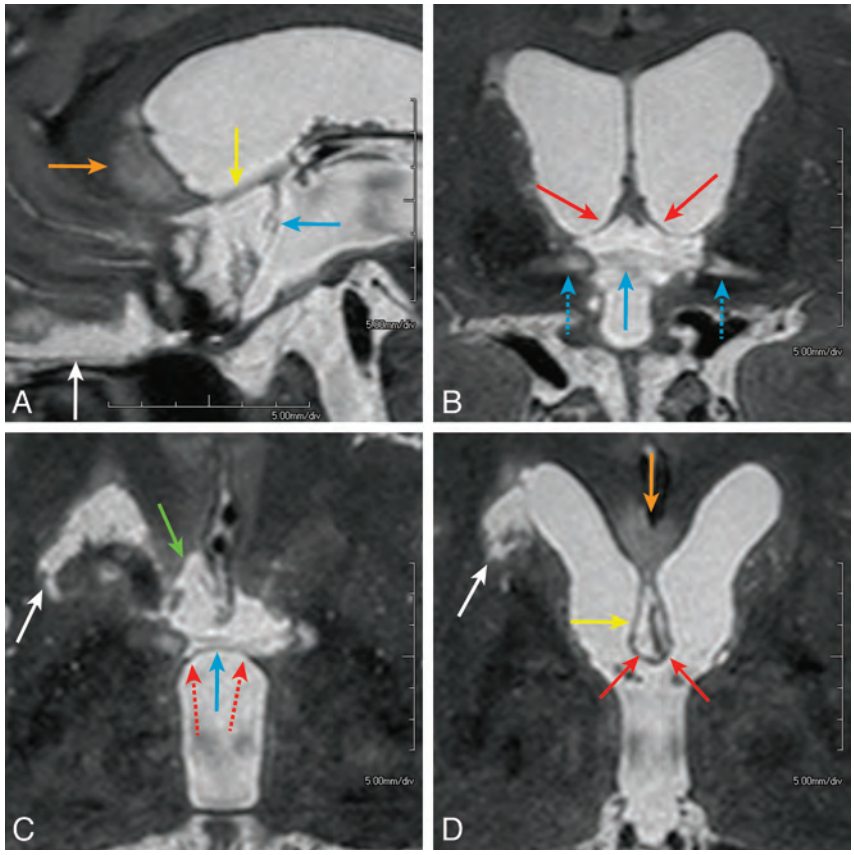

FIG 4. A 52-year-old man presented with a ruptured aneurysm of the anterior communicating artery. Surgical trapping of the ACoA for the ruptured ACoA aneurysm was performed the day of onset (patient 1). Neuropsychological examination 2 months after the rupture confirmed amnesia. Midsagittal (*A*), coronal (*B*), and axial (*C* and *D*) images of T2WI-VISTA show the infarcted foci involving the pars libera of the column of the fornix (*B* and *D*, *solid red arrows*) and anterior commissure (*A–C*, *light blue arrows*), paraterminal gyrus (*A* and *D*, *yellow arrows*), subcallosal area (*C*, *green arrow*), and genu or rostrum of the corpus callosum (*A* and *D*, *orange arrows*). The entire extent of the lesions shows sagittally elongated bandlike infarctions along the medial aspect of the brain, which probably represent the distribution of the characteristic S-shaped course of the subcallosal artery. On coronal (*B*) and axial (*C*) images, infarction in the bilateral anterior commissure shows a bow-tie-like appearance and is associated with infarcted foci in the adjoining pars libera (*solid red arrows*) and pars tecta (*dashed red arrows*) of the bilateral columns of the fornices. Lateral extension of hyperintense lesions along the lateral part of the anterior commissure (*B*, *dashed light blue arrows*) may indicate Wallerian degeneration of the midline infarction in the anterior commissure (*solid light blue arrow*). Infarction in the head of the caudate nucleus on the right is also seen (*white arrows*, *C* and *D*), which presumably represents involvement of the right recurrent artery of Heubner. The orbitofrontal region is also involved (*A*, *white arrow*).

Furthermore, a recent study of diffusion tensor imaging in patients after treatment of a ruptured ACoA aneurysm also speculated that amnesia might be related to injury of the cingulum and the fornix.[35] However, the authors did not analyze the sites of lesions or present the neuropsychological data of their cases. On the contrary, all our patients demonstrated infarction in the column of the fornix and underwent formal neuropsychological tests, which indicated their disproportionate impairment of memory but only limited intellectual decline [IQ − MQ = 26 (mean), all > 15]. We included only patients with relatively preserved intellectual function because diffuse brain damage owing to hydrocephalus and vasospasm could worsen generalized intellectual function with resultant memory impairment. Therefore, our manner of enrolling subjects may be a strength of our study because it enabled us to localize the lesions responsible for basal forebrain amnesia after ACoA aneurysmal treatment.

Still, we noted the high prevalence of infarctions in the orbitofrontal area in our study. The lesions in this area designated as infarction in this study could have included the sequelae of intraparenchymal hemorrhage associated with the aneurysmal rupture and/or partial surgical resection being necessary to visualize the ACoA aneurysmal neck during surgery.[25] Several neuropsychological studies, however, indicated that the lesions in the orbitofrontal area alone did not cause amnesia.[3,36,37]

Alternatively, several reports attributed basal forebrain amnesia to interruption of the cholinergic system.[1,3,11,38] Indeed, in our patients, infarction in the paraterminal gyrus in 8 and in the diagonal band of Broca in 5 suggests likely involvement of the cholinergic system. Additionally, lesions in the pars libera of the column of the fornix, which include cholinergic fibers, in all our patients might also indicate interruption of the cholinergic system.

Diagnostic Value of 3D MR Imaging in Patients with Basal Forebrain Amnesia

Because previous diagnosis of basal forebrain amnesia has been made mainly by the neuropsychological examination alone or by using CT and/or 2D MR imaging, detailed localization of lesions has not been achieved. In our study, in contrast, use of 3T 3D MR imaging enabled identification and localization of small infarcts, and we believe identifying the exact locations of infarcts in the basal forebrain should help clarify the diagnosis of post-treatment amnesia following surgery for ACoA aneurysms.

Specifically, 2 MR imaging signs appeared characteristic: The first, the bow-tie-like appearance of infarcts, seen on both axial and coronal MR images, represents bilateral involvement of the anterior commissure associated with infarcted foci in the column of the fornix (pars libera and pars tecta). The second sign, a sagittally elongated infarction along the medial aspect of the brain on axial or sagittal MR imaging planes that involves the anterior cingulate gyrus, genu, and/or rostrum of the corpus callosum, should represent the sagittally elongated vascular distribution along the characteristic S-shaped course of the subcallosal artery (Fig 1*A*, -*B*). We believe both signs are important MR imaging indicators of amnesia associated with ACoA aneurysm treatment.

Although it may be possible to perform the same analysis by using conventional 2D 2- or 3-mm coronal imaging with/without axial images, we presume that 3D MR imaging by using MPR could more easily identify small structures in the basal forebrain. Indeed, a recent neuropsychological study by Proust et al[5] revealed the high prevalence of verbal memory deficits (58.3%) among 36 patients with variably decreased intellectual function after ACoA clipping. Regarding verbal memory deficits, Guglielmi[14] stated, in his letter to the editor, that ACoA syndrome is likely due to occlusion of the subcallosal artery. In the series of reports by Proust et al using thin-section 1.5T 2D MR imaging (axial FLAIR images, 5-mm-thick; axial T2-weighted images, 2-mm-thick; axial T1-weighted images, 2.5-mm thick; and coronal T2-weighted images centered on the frontal and temporal areas, thickness not shown), the prevalence of the basal forebrain lesions was 33.3% in 36 patients. However, the authors did not clarify the exact location of lesions inside the basal forebrain. We believe that high-resolution 3D T2WI might be desirable for this kind of study.

Limitations

Our study limitations include a small number of patients and lack of a control group without symptoms of amnesia. Another limitation is that DWI was examined in the acute phase in 3 cases only, whereas in the remaining 7 patients with ruptured aneurysms, acute-phase DWI was not performed, presumably because the onset of amnesia after surgery was unnoticed or unrecognized due to associated acute illness. Further studies of a large number of consecutive patients treated surgically or interventionally for ACoA aneurysms, preferably by using both DWI in the acute phase and 3D MR imaging in the chronic phase along with formal neuropsychological examinations, remain to be conducted.

Another limitation is that we did not analyze the more detailed memory test, including retrieval or encoding. This analysis might clarify the relationship between the lesions and neuropsychological characteristics of postoperative amnesia.

The last limitation is the subjective evaluation by 2 examiners of atrophy of the mammillary bodies without volumetry.

CONCLUSIONS

We described 3D MR imaging findings in patients with amnesia following surgical treatment of ACoA aneurysms: infarctions in the territory of the subcallosal artery, mostly with bilateral involvement. In these cases, infarct patterns were compatible with previous neurosurgical and neuropsychological studies suggesting that occlusion of the subcallosal artery could cause postoperative amnesia. From a neurosurgical point of view, our results indicate that preservation of that artery during treatment of an ACoA aneurysm should be crucial, though further studies involving a large number of consecutive patients treated for ACoA aneurysms must be conducted to validate this hypothesis.

ACKNOWLEDGMENTS

We thank our department colleagues Yasuko Tatewaki and Li Li for their important suggestions and helpful discussions and Makoto Obara of Philips Electronics Japan, Tokyo, for technical advice and support in advanced MR imaging.

Disclosures: Shunji Mugikura—*RELATED: Payment for Lectures (including service on Speaker Bureraus)*: Philips Healthcare, Terumo; *UNRELATED: Grants/Grants Pending*: Japan Society for the Promotion of Science Kakenhi*; *Payment for Lectures (including service on Speakers Bureaus)*: Daiichi-Sankyo, Terumo, Philips Healthcare. Shoki Takahashi—*UNRELATED: Grants/Grants Pending*, JSPS Kakenhi,* Daiichi-Sankyo,* Bayer,* Eisai,* Terumo,* Mitsubishi-Tanabe Pharma,* Nihon Medi-physics,* Philips Healthcare,* Siemens,* Toshiba,* *Payment for Lectures (including service on Speakers Bureaus)*: Daiichi-Sankyo, Eisai, Terumo. *Money paid to the institution.

REFERENCES

1. Damasio AR, Graffradford NR, Eslinger PJ, et al. **Amnesia following basal forebrain lesions.** *Arch Neurol* 1985;42:263–71
2. DeLuca J, Diamond BJ. **Aneurysm of the anterior communicating artery: a review of neuroanatomical and neuropsychological sequelae.** *J Clin Exp Neuropsychol* 1995;17:100–21
3. Fujii T. **The basal forebrain and episodic memory.** In: Dere E, Nadel L, Easton A, et al, eds. *Handbook of Episodic Memory*. Amsterdam: Elsevier Science; 2008:343–58
4. Lim C, Alexander MP. **Stroke and episodic memory disorders.** *Neuropsychologia* 2009;47:3045–58
5. Proust F, Martinaud O, Gerardin E, et al. **Quality of life and brain damage after microsurgical clip occlusion or endovascular coil embolization for ruptured anterior communicating artery aneurysms: neuropsychological assessment.** *J Neurosurg* 2009;110:19–29
6. Markowitsch HJ, Staniloiu A. **Amnesic disorders.** *Lancet* 2012;380:1429–40
7. Crowell RM, Morawetz RB. **The anterior communicating artery has significant branches.** *Stroke* 1977;8:272–73
8. Sekhar LN, Natarajan SK, Britz GW, et al. **Microsurgical management of anterior communicating artery aneurysms.** *Neurosurgery* 2007;61:273–90, discussion 290–92
9. Hernesniemi J, Dashti R, Lehecka M, et al. **Microneurosurgical management of anterior communicating artery aneurysms.** *Surg Neurol* 2008;70:8–28, discussion 29
10. Gade A. **Amnesia after operations on aneurysms of the anterior communicating artery.** *Surg Neurol* 1982;18:46–49
11. Phillips S, Sangalang V, Sterns G. **Basal forebrain infarction: a clinicopathologic correlation.** *Arch Neurol* 1987;44:1134–38
12. Türe U, Yasargil MG, Krisht AF. **The arteries of the corpus callosum: a microsurgical anatomic study.** *Neurosurgery* 1996;39:1075–84, discussion 1084–85
13. Serizawa T, Saeki N, Yamaura A. **Microsurgical anatomy and clinical significance of the anterior communicating artery and its perforating branches.** *Neurosurgery* 1997;40:1211–16, discussion 1216–18
14. Guglielmi G. **Coil over clip.** *J Neurosurg* 2009;111:410–11, author reply 411–12
15. Heros RC. **Perforator and secondary branch origin: the importance of perforators in aneurysm surgery.** *World Neurosurg* 2013 Mar 14. [Epub ahead of print]
16. Marinkovic S, Milisavljevic M, Marinković Z. **Branches of the anterior communicating artery: microsurgical anatomy.** *Acta Neurochir (Wien)* 1990;106:78–85
17. von Cramon DY, Muller U. **The septal region and memory.** *Adv Tech Stand Neurosurg* 1998;24:3–40
18. Wechsler D. *Wechsler Adult Intelligence Scale, third edition (WAIS-III)*. San Antonio: Psychological Corporation; 1997
19. Wechsler D. *Wechsler Memory Scale Revised: Manual.* San Antonio: Psychological Corporation; 1987
20. Foster JK. **Memory impairment.** In: Foster JK, ed. *Memory: A Very Short Introduction*. New York: Oxford University Press; 2009:84–100
21. Hennig J, Scheffler K. **Easy improvement of signal-to-noise in RARE-sequences with low refocusing flip angles: rapid acquisition with relaxation enhancement.** *Magn Reson Med* 2000;44:983–85
22. Mai JK, Paxinos G, Voss T. *Atlas of the Human Brain.* New York: Academic Press; 2007
23. Feekes JA, Hsu SW, Chaloupka JC, et al. **Tertiary microvascular territories define lacunar infarcts in the basal ganglia.** *Ann Neurol* 2005;58:18–30
24. Takahashi S. **Intracranial arterial system: basal perforating arteries.**

In: Takahashi S, ed. *Neurovascular Imaging: MRI and Microangiography.* London: Springer-Verlag; 2010:53–130
25. Yaşargil MG, Smith RD, Young PH, et al. **Anterior cerebral artery complex.** In: Yaşargil MG, ed. *Microneurosurgery.* Stuttgart: Georg Thieme Verlag; 1984:92–128
26. Takahashi S, Goto K, Fukasawa H, et al. **Computed tomography of cerebral infarction along the distribution of the basal perforating arteries. Part I. Striate arterial group**. *Radiology* 1985;155:107–18
27. Takahashi S, Suzuki M, Matsumoto K, et al. **Extent and location of cerebral infarcts on multiplanar MR images: correlation with distribution of perforating arteries on cerebral angiograms and on cadaveric microangiograms.** *AJR Am J Roentgenol* 1994;163:1215–22
28. Tsivilis D, Vann SD, Denby C, et al. **A disproportionate role for the fornix and mammillary bodies in recall versus recognition memory.** *Nat Neurosci* 2008;11:834–42
29. Park SA, Hahn JH, Kim JI, et al. **Memory deficits after bilateral anterior fornix infarction.** *Neurology* 2000;54:1379–82
30. Moussouttas M, Giacino J, Papamitsakis N. **Amnestic syndrome of the subcallosal artery: a novel infarct syndrome.** *Cerebrovasc Dis* 2005;19:410–14
31. Renou P, Ducreux D, Batouche F, et al. **Pure and acute Korsakoff syndrome due to a bilateral anterior fornix infarction: a diffusion tensor tractography study.** *Arch Neurol* 2008;65:1252–53
32. Adamovich BL, Gualberto G, Roberts T, et al. **Teaching neuroimages: amnesia due to fornix infarction.** *Neurology* 2009;73:e86
33. Hattingen E, Rathert J, Raabe A, et al. **Diffusion tensor tracking of fornix infarction.** *J Neurol Neurosurg Psychiatry* 2007;78:655–56
34. Mosimann PJ, Saint-Maurice JP, Lenck S, et al. **Fornix infarction and Korsakoff dementia after coiling of a large anterior communicating artery aneurysm.** *Neurology: Clinical Practice* 2012;2:260–62
35. Hong JH, Choi BY, Chang CH, et al. **Injuries of the cingulum and fornix after rupture of an anterior communicating artery aneurysm: a diffusion tensor tractography study.** *Neurosurgery* 2012;70:819–23
36. Böttger S, Prosiegel M, Steiger HJ, et al. **Neurobehavioural disturbances, rehabilitation outcome, and lesion site in patients after rupture and repair of anterior communicating artery aneurysm.** *J Neurol Neurosurg Psychiatry* 1998;65:93–102
37. Fujii T, Suzuki M, Suzuki K, et al. **Normal memory and no confabulation after extensive damage to the orbitofrontal cortex.** *J Neurol Neurosurg Psychiatry* 2005;76:1309–10
38. Fujii T. **Perforating branches of the anterior communicating artery: anatomy and infarction.** In: Taakahashi S, ed. *Neurovascular Imaging: MRI and Microangiography.* London: Springer-Verlag; 2010:189–96
39. Claassen J, Bernardini GL, Kreiter K, et al. **Effect of cisternal and ventricular blood on risk of delayed cerebral ischemia after subarachnoid hemorrhage: the Fisher scale revisited.** *Stroke* 2001; 32:2012–20
40. Dick JP, Guiloff RJ, Stewart A, et al. **Mini-mental state examination in neurological patients.** *J Neurol Neurosurg Psychiatry* 1984;47: 496–99
41. Budson AE, Price BH. **Memory dysfunction.** *N Engl J Med* 2005;352:692–99
42. Shah A, Jhawar SS, Goel A. **Analysis of the anatomy of the Papez circuit and adjoining limbic system by fiber dissection techniques.** *J Clin Neurosci* 2012;19:289–98
43. Duvernoy HM. **Structures, functions, and connections.** In: Duvernoy HM, Cattin F, Risold PY. *The Human Hippocampus: Functional Anatomy, Vascularization and Serial Sections with MRI.* 2nd ed. Berlin: Springer-Verlag; 1998:5–38

Susceptibility-Weighted MR Imaging: A Better Technique in the Detection of Capillary Telangiectasia Compared with T2* Gradient-Echo

U.S. Chaudhry, D.E. De Bruin, and B.A. Policeni

ABSTRACT

BACKGROUND AND PURPOSE: Enhancing lesions on brain MR imaging can present a diagnostic quandary as both benign lesions such as brain capillary telangiectasia and pathologic lesions such as demyelination may appear similar. Stagnation of blood in low-flow venous channels of brain capillary telangiectasias results in susceptibility effect secondary to the increased local deoxyhemoglobin. Both T2* gradient-echo imaging and SWI were demonstrated as valuable in the diagnosis of brain capillary telangiectasia. Because SWI is more sensitive to susceptibility changes than gradient-echo, we aim to demonstrate increased diagnostic value of SWI compared with gradient-echo in making the diagnosis of brain capillary telangiectasia.

MATERIALS AND METHODS: We retrospectively reviewed the MR images of 17 patients with a presumed diagnosis of brain capillary telangiectasia and who were examined from June 2010 to September 2012. All patients underwent MR imaging at 1.5T with T1, T2, FLAIR, gradient-echo, SWI, and gadolinium-enhanced T1 sequences. Lesions were evaluated for the presence or absence of signal abnormality on each particular sequence.

RESULTS: All 17 brain capillary telangiectasias demonstrated distinct signal-intensity loss on SWI compared with 7 of 17 (41%) who showed signal-intensity loss on gradient-echo. The increased frequency of detection using SWI versus gradient-echo is statistically significant ($z = 2.85$, $P < .01$; $\chi^2 = 8.10$, $P < .01$). Six of the lesions showed signal-intensity changes on T1 and/or T2 whereas the remaining lesions were isointense to normal brain.

CONCLUSIONS: Brain capillary telangiectasias are more conspicuous on SWI than gradient-echo imaging and other precontrast MR imaging. SWI is a valuable tool in diagnosing these benign lesions and should serve to increase diagnostic confidence.

ABBREVIATIONS: BCT = brain capillary telangiectasia; GRE = gradient-echo

Brain capillary telangiectasia (BCT) is considered the most benign vascular malformation in the brain.[1] This is usually incidental as it is almost always asymptomatic.[2] It is described as having an inconspicuous appearance on precontrast MR imaging with faint or brush-like enhancement on postcontrast imaging.[3,4] Its importance lies in the fact that it may be confused with much more serious pathologies such as metastasis, acute demyelination, and subacute infarction.[2] This issue is only going to become more of a challenge with increased quality of MR imaging and increasing field strengths, which will increase susceptibility effects. A few previous publications have addressed utility of gradient-echo (GRE) and DWI for BCT diagnosis.[3-5] SWI is a relatively new concept relying on susceptibility effect secondary to the increase in local deoxyhemoglobin.[6] SWI has been shown to be more sensitive to magnetic field susceptibility than GRE.[7] There does remain a need for a study to compare the sensitivity of SWI versus GRE images when it comes to diagnosing a BCT with certainty.

The purpose of the study was to demonstrate an increased diagnostic value of SWI compared with GRE in making the diagnosis of BCT. Comparison to other modalities such as T2-weighted imaging and DWI were also made.

MATERIALS AND METHODS

Subjects were selected using a keyword search for "capillary telangiectasia" on all MR imaging radiology reports with a date range from June 1, 2011 (coinciding with the initial implementation of SWI on our MR scanners) to September 30, 2012. This yielded 209 studies. Individual studies were then reviewed in con-

Received March 28, 2014; accepted after revision May 23.

From the Department of Radiology (U.S.C., D.E.D., B.A.P.) and Section of Neuroradiology (D.E.D., B.A.P.), University of Iowa Hospitals and Clinics, Iowa City, Iowa.

Paper previously presented as electronic poster at: Annual Meeting of the American Society of Neuroradiology, May 18–23, 2013; San Diego, California.

Please address correspondence to Bruno A. Policeni, MD, Department of Radiology, University of Iowa Hospitals and Clinics, 200 Hawkins Dr, Iowa City, IA; e-mail: bruno-policeni@uiowa.edu

http://dx.doi.org/10.3174/ajnr.A4082

sensus by 2 board-certified radiologists, 1 with a Certificate of Added Qualification in neuroradiology. T1, T2, SWI, GRE, and postcontrast images were all reviewed to establish the diagnosis of BCT. A total of 17 patients with lesions meeting diagnostic criteria for BCT who also underwent SWI were found. No patients underwent biopsy or surgical resection of these BCTs.

Imaging was done on 1.5T MR scanners (Avanto; Siemens, Erlangen, Germany). All patients underwent standard MR imaging including axial spin-echo T1- and T2-weighted imaging, FLAIR, DWI, T2*-GRE, SWI, and postcontrast fat-saturated axial T1-weighted imaging. Intravenous gadobenate dimeglumine (MultiHance; Bracco Diagnostics, Princeton, New Jersey) was administered at a concentration of 0.1 mmol/kg.

Table 1: Comparison of detection of capillary telangiectasia among different sequences

Imaging Sequence	No. of Patients Detected (*n* = 17)
T1	1 (5.9%)
T2	6 (35.3%)
FLAIR	6 (35.3%)
GRE	7 (41.2%)
SWI	17 (100%)

Table 2: Distribution of BCT according to location in the study

Location	No. of Patients with BCT (*n* = 17)
Pons	8 (47.0%)
Cerebral hemispheres, excluding gray matter nuclei	6 (35.3%)
Deep supratentorial gray matter nuclei	1 (5.9%)
Cerebellum	1 (5.9%)
Midbrain	1 (5.9%)

RESULTS

Seventeen lesions meeting diagnostic criteria for BCT were identified in 17 patients. All 17 BCTs demonstrated distinct signal-intensity loss on SWI (Table 1). Figure 1–3 represent the spectrum of lesions seen, varying from some seen only on SWI, to some seen in both. Seven of the total 17 (41%) demonstrated signal-intensity loss on GRE imaging. Six of the lesions showed signal-intensity changes on T1 and/or T2, whereas the remaining lesions were isointense to normal brain (Table 1). Most of the lesions were in the pons, 47% (Table 2).

A McNemar test for dependent proportions was used for statistical analysis.[8] Increased frequency of detection by SWI

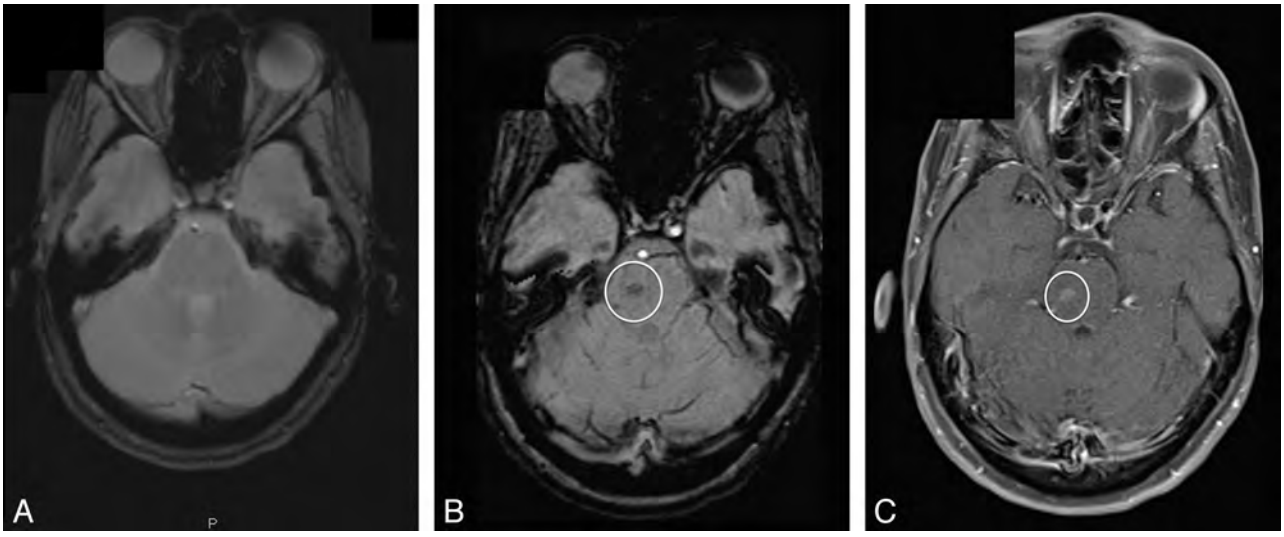

FIG 1. A BCT (*circle*) not seen on GRE image (*A*) but seen on SWI (*B*) and postcontrast T1 image (*C*).

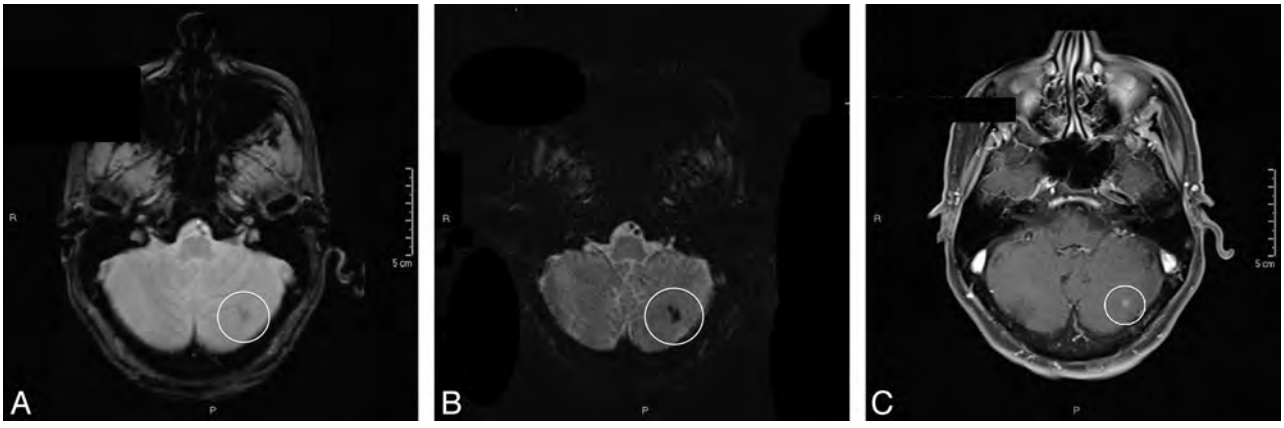

FIG 2. A BCT (*circle*) seen more clearly on SWI. *A*, GRE image; *B*, SWI; *C*, postcontrast T1 image.

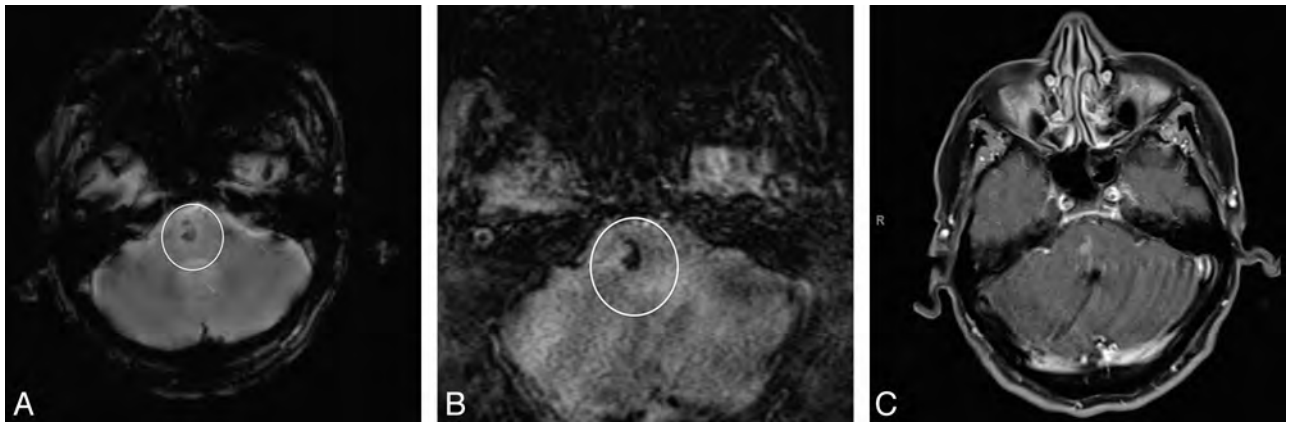

FIG 3. A BCT (*circle*) seen in the pons on both GRE (*A*) and SWI (*B*) and confirmed on postcontrast T1 image (*C*).

versus GRE was statistically significant ($z = 2.85$, $P < .01$; $\chi^2 = 8.10$, $P < .01$).

DISCUSSION

BCT is a benign vascular malformation consisting of a cluster of thin-walled capillaries intermixed with normal brain parenchyma, differentiating it from a cavernous malformation, which has no normal brain parenchyma.[1,9] It is relatively rare, having a reported prevalence of 0.4%, and represents 16%–20% of cerebral vascular malformations.[1,9] These have a predilection for the pons but have been uncommonly reported in other locations.[10] Of our 17 cases, 8 (47.0%) BCTs were in the pons with the others distributed in other locations of the brain (Table 2). Although there are a few case reports of this entity being symptomatic,[2] BCTs are almost invariably asymptomatic.[10] With improvement in MR imaging field strength, the detection of these slow-flowing lesions is increasing, creating an increasing dilemma for differentiating them from other postcontrast enhancing lesions such as demyelination, subacute infarction, and neoplasm.[1,9]

Susceptibility in MR imaging is defined as the magnetic response of a substance when placed in an external magnetic field. SWI, which was first described in 1997, is a high-resolution 3D gradient-echo MR imaging sequence that uses magnitude and phase information to create an image from T2*-contrast and phase changes relying on magnetic susceptibility.[11] BCTs show increased susceptibility effects[9] and signal loss on SWI in a focal lesion, in which enhancement is highly specific for a BCT.[7] As these lesions rarely have hemorrhage or calcifications, slow flow and increased quantities of deoxyhemoglobin are thought to be the causes of increased susceptibility.[10]

Finkenzeller et al[5] showed that GRE sequences were particularly useful in detecting BCTs. Lee et al[6] demonstrated DWI can also be useful for BCT detection. A case report in 2006 by Yoshida et al[12] found a BCT that was occult on GRE but showed signal loss on SWI. A retrospective study in 2012 by El-Koussy et al[13] examined 33 cases of BCT and found that 100% showed signal loss on SWI whereas only 39% showed changes on T1 and T2 images. Our series compared frequency of detection of BCT for SWI versus GRE. In our series, we found no examples of BCT where GRE was positive and SWI was negative. BCTs were more conspicuous on SWI than GRE and other precontrast MR imaging. Of the 17 patients whom we studied, only 7 were diagnosed on GRE imaging. Our findings suggest that diagnostic certainty has the potential to increase for focal enhancement when SWI is performed instead of GRE alone. This is most likely related to the fact that SWI is more sensitive to the susceptibility effects that BCT is known to cause.[10] This is because this sequence additionally relies on phase changes.[11]

Our study was done on 1.5T scanners and recent studies have clearly showed increased susceptibility with increased strength of magnetic field.[14] Future studies can focus on higher field strengths, possibly with 3T and using a bigger number of patients.

CONCLUSIONS

BCT is a potential diagnostic dilemma; increased diagnostic certainty can reduce morbidity and unnecessary testing. In our series, we found no examples of BCT where GRE was positive and SWI was negative. BCTs were more conspicuous on SWI than GRE and, in some cases, were picked up when GRE was negative. SWI therefore appears superior to GRE in the detection of BCT and, though still in its early stages, the initial research shows the addition of SWI has the potential to increase the likelihood of diagnosing BCT and decreasing misdiagnosis.

REFERENCES

1. Nussbaum ES. **Vascular malformations of the brain.** *Minn Med* 2013;96:40–43
2. Scaglione C, Salvi F, Riguzzi P, et al. **Symptomatic unruptured capillary telangiectasia of the brain stem: report of three cases and review of the literature.** *J Neurol Neurosurg Psychiatry* 2001;71:390–93
3. Barr RM, Dillon WP, Wilson CB. **Slow-flow vascular malformations of the pons: capillary telangiectasia?** *AJNR Am J Neuroradiol* 1996;17:71–78
4. Lee RR, Becher MW, Benson ML, et al. **Brain capillary telangiectasia: MR imaging appearance and clinicohistopathologic findings.** *Radiology* 1997;205:797–805
5. Finkenzeller T, Fellner FA, Trenkler J, et al. **Capillary telangiectasias of the pons. Does diffusion-weighted MR increase diagnostic accuracy.** *Eur J Radiol* 2010;74:112–16
6. Lee BCP, Vo KD, Kido DK, et al. **MR high-resolution blood oxygenation level-dependent venography of occult (low-flow) vascular lesions.** *AJNR Am J Neuroradiol* 1999;20:1239–42
7. Sehgal V, Delproposto Z, Haacke EM, et al. **Clinical applications of neuroimaging with susceptibility-weighted imaging.** *J Magn Reson Imaging* 2005;22:439–50
8. McNemar Q. *Psychological Statistics.* 4th ed. New York: Wiley; 1969:54–58

9. Byrne JV. **Cerebrovascular malformations.** *Eur Radiol* 2005;15: 448–52
10. Castillo M, Morrison T, Shaw JA, et al. **MR imaging and histologic features of capillary telangiectasia of the basal ganglia.** *AJNR Am J Neuroradiol* 2001;22:1553–55
11. Dammann P, Barth M, Zhu Y, et al. **Susceptibility weighted magnetic resonance imaging of cerebral cavernous malformations: prospects, drawbacks, and first experience at ultra-high field strength (7-Tesla) magnetic resonance imaging.** *Neurosurg Focus* 2010;29:E5
12. Yoshida Y, Terae S, Kudo K, et al. **Capillary telangiectasia of the brain stem diagnosed by susceptibility-weighted imaging.** *J Comput Assist Tomogr* 2006;30:980–82
13. El-Koussy M, Schroth G, Gralla G, et al. **Susceptibility-weighted MR imaging for diagnosis of capillary telangiectasia of the brain.** *AJNR Am J Neuroradiol* 2012;33:715–20
14. Campbell PG, Jabbour P, Yadla S, et al. **Emerging clinical imaging techniques for cerebral cavernous malformations: a systematic review.** *Neurosurg Focus* 2010;29:E6

Gadolinium Enhancement of Atherosclerotic Plaque in the Middle Cerebral Artery: Relation to Symptoms and Degree of Stenosis

C.-W. Ryu, G.-H. Jahng, and H.S. Shin

ABSTRACT

BACKGROUND AND PURPOSE: High-resolution MR imaging can depict intracranial arterial atherosclerotic plaques. Our aim was to evaluate the relationship between the degree of enhancement of MCA plaques on contrast-enhanced high-resolution MR imaging and ischemic stroke and stenosis severity.

MATERIALS AND METHODS: This study enrolled 36 patients diagnosed with moderate-to-severe atherosclerotic MCA stenosis. A contrast-enhanced T1-weighted volume isotropic turbo spin-echo acquisition sequence was acquired for assessing plaque enhancement. Plaque-to-CSF contrast ratio was calculated after the signal intensity of plaques at the stenotic segment was measured. Univariate comparison and multivariate logistic regression analyses were performed for symptomatic and asymptomatic groups to assess the relationship between symptomatic stenosis and independent variables, including plaque-to-CSF contrast ratio, degree of stenosis, and clinical risk factors. Plaque-to-CSF contrast ratio was compared between the moderate and severe stenosis groups.

RESULTS: Twenty-one patients had symptomatic MCA stenosis, and 15 had asymptomatic stenosis. The plaque-to-CSF contrast ratio was significantly higher in the symptomatic group than in the asymptomatic group (63.6 ± 10.6% versus 54.1 ± 13.5%, respectively; $P < .05$). The degree of stenosis also differed significantly between the 2 groups ($P < .05$). Multivariate analysis revealed that the degree of stenosis was the only independent predictor of ischemic stroke symptoms. The plaque-to-CSF contrast ratio of severe stenosis was significantly higher than that of moderate stenosis (66.8 ± 8.7% versus 55.9 ± 12.8%, respectively; $P < .05$).

CONCLUSIONS: Plaque enhancement was significantly higher in patients with symptomatic plaques and may have been affected by the degree of stenosis. A difference in plaque enhancement according to the degree of stenosis has implications for understanding the development of intracranial atherosclerotic plaques.

ABBREVIATIONS: CR = plaque-to-CSF contrast ratio; Gd = gadolinium; HR-MRI = high-resolution MR imaging; ICAD = intracranial atherosclerotic disease; SI = signal intensity; WASID = Warfarin Aspirin Symptomatic Intracranial Disease

Intracranial atherosclerotic disease (ICAD) is now considered the most common cause of ischemic stroke worldwide.[1,2] It is a challenge for many clinicians to assess vulnerable regions of intracranial artery stenosis by using in vivo methods. As a result, there has been a recent increase in interest in techniques to depict the state of the intracranial artery wall by using high-resolution MR imaging (HR-MRI) with a high magnetic field.

Received January 21, 2014; accepted after revision May 30.

From the Departments of Radiology (C.-W.R., G.-H.J.) and Neurosurgery (H.S.S.), Kyung Hee University Hospital at Gangdong, Kyung Hee University School of Medicine, Seoul, Korea.

This work was supported by a grant from Kyung Hee University in 2012 (KHU-20120760).

Please address correspondence to Chang-Woo Ryu, MD, Department of Radiology, Kyung Hee University Hospital at Gangdong, 149 Sangil-dong, Gangdong-gu, Seoul 134-727, Korea; e-mail: md.cwryu@gmail.com

http://dx.doi.org/10.3174/ajnr.A4038

Inflammation increases vulnerability to plaque rupture by facilitating neovascularization within the plaque and increasing endothelial permeability. Strong contrast enhancement of arterial plaques on MR imaging suggests the presence of a vascular supply and increased endothelial permeability, which facilitate the entry of contrast agents from the blood plasma.[3-6] Several studies have shown that gadolinium (Gd) enhancement of extracranial carotid plaques on MR imaging is associated with plaque neovascularization or increased levels of serum inflammatory markers such as C-reactive protein.[7-10] An association between carotid plaque enhancement and clinical symptoms has been observed in several recent investigations by using Gd-enhanced MR imaging.[9,11]

In contrast to the numerous investigations that have been performed on the carotid artery, only a few studies performed on a small number of patients have focused on the clinical significance of Gd enhancement of plaques in the setting of ICAD.[12-14] These studies identified a significant association between plaque en-

hancement on ICAD and ischemic events. However, there is some debate about whether contrast enhancement is a good predictor of intracranial stenosis in ischemic stroke. Klein et al[15] expressed doubt about the relationship between plaque enhancement and stroke because they found stationary enhancement of basilar plaques regardless of the time elapsed after an acute event.

Several factors are known to be related to ischemic stroke in the territory of the stenotic segment.[16,17] In particular, the severity of stenosis is a strong predictor of subsequent stroke in the territory of the symptomatic stenotic artery. To assess whether Gd enhancement of plaques at the stenotic segment is valuable as a predictor of ischemic stroke, an unbiased assessment of the influence of other independent factors, including the degree of stenosis, should be undertaken. Thus, the purpose of this study was to evaluate whether Gd enhancement of plaques in ICAD is associated with clinical symptoms, independent of other predictive factors for ischemic stroke risk.

MATERIALS AND METHODS

Subjects

This study was approved by the local ethics committee. Patients with acute neurologic symptoms underwent an acute stroke MR imaging protocol and postcontrast HR-MRI between August 2011 and October 2012. Before MR imaging, all subjects provided informed consent to undergo MR imaging with the use of contrast media. The radiologic findings from the MR imaging were reviewed, and those subjects who had unilateral M1 stenosis of >70% on TOF-MRA and ≥2 risk factors for atherosclerosis were enrolled in the study.

After reviewing patient medical records and MR imaging findings, we excluded patients who met the following criteria: 1) a high risk of carotid artery-to-artery embolism (ipsilateral ICA stenosis of >50%); 2) a high risk of cardioembolism (eg, atrial fibrillation, prosthetic cardiac valve); 3) vascular disease of other clinically and/or radiologically suspected etiology, such as Moyamoya disease, vasculitis, or dissection; 4) known coagulopathies (eg, protein C or S deficiency, antiphospholipid antibody syndrome); 5) ipsilateral acute lacunar infarction (single acute ischemic lesion of <2 cm at the basal ganglia or the corona radiata) at sites of MCA stenosis; 6) T1 hyperintensity within the stenotic MCA representing intraplaque hemorrhage and/or intraluminal thrombus on MPRAGE MR imaging; and 7) poor MRA or HR-MRI image quality, making the image nondiagnostic or difficult to analyze quantitatively.

Forty-two subjects met all inclusion criteria. However, 4 patients with ipsilateral cavernous ICA stenosis and 2 patients with ipsilateral cervical carotid stenosis were excluded. None of the patients were excluded due to either intraluminal thrombus or poor image quality. In total, 36 subjects (mean age, 68.69 ± 12.21 years; 17 males) were enrolled in this study.

MR Imaging

MR imaging was performed on a 3T MR imaging system (Achieva; Philips Healthcare, Best, the Netherlands) with a 16-channel phased array neurovascular coil. The MR imaging stroke protocol included the following: T1-weighted MPRAGE sagittal imaging with presaturation of inflowing blood, axial DWI, T2-weighted FLAIR axial imaging, TOF-MRA, and contrast-enhanced neck MRA. To evaluate plaques in the MCA, we added to the stroke protocol postcontrast HR-MRIs that were obtained axially at the circle of Willis, as shown on TOF-MRA. Contrast-enhanced HR-MRIs were acquired with 3D T1-weighted volume isotropic turbo spin-echo acquisition axial imaging with presaturation of inflowing blood to obtain black-blood images. Scans were started with an approximately 4-minute delay time, including the scan time for contrast-enhanced neck MRA after injection of contrast media. We used the following HR-MRI parameters: TR = 350 ms, TE = 19.51 ms, flip angle = 90°, refocusing angle = 120°, acquisition matrix = 240 × 240, FOV = 120 × 120, 3D slab thickness = 13 mm, in-plane pixel size = 0.5 × 0.5 mm, overcontiguous section thickness = 2 mm, reconstruction matrix = 352 × 352, reconstruction voxel size = 0.34 × 0.34 × 1 mm, reconstruction section thickness = 1 mm, foldover direction = anteroposterior, signal average = 2, TSE factor = 3, sensitivity encoding factor = 2 for the phase-encoding direction and 1 for the section-selection direction, number of stacks = 2 for each of the 13 sections, transverse presaturation thickness = 80 mm, total scan time = 184 seconds.

Clinical Data Assessment

Subjects were classified as having either symptomatic stenosis or asymptomatic stenosis according to the presence of recent ischemic stroke consistent with MCA stenosis. Symptomatic stenosis was defined as a diffusion-restrictive lesion seen on DWI in the territory of the stenotic MCA with a corresponding acute neurologic deficit within 2 weeks before MR imaging. Asymptomatic stenosis was diagnosed in patients with nonspecific neurologic symptoms (headache, dizziness, and so forth) that were not localized to the ipsilateral side of the MCA stenosis and who had no observations of any ischemic lesion on DWI. Patients with acute ischemic lesions localized to the territory of the posterior circulation, the anterior cerebral artery, or the contralateral MCA were considered to have asymptomatic MCA stenosis.

Clinical data, including basic demographics and risk factors for atherosclerosis, namely diabetes, hypertension, dyslipidemia, current smoking, obesity, and history of coronary disease, were also recorded.

MR Imaging Assessment

According to the distribution of acute ischemic lesions on DWI, infarctions in the symptomatic group were classified as borderzone, striatocapsular, or pial embolic, according to the previously published topographic definition of DWI.[18] The degree of MCA stenosis was classified as severe or moderate according to TOF-MRA findings. Severe stenosis was defined as a flow signal defect at the stenotic segment (Fig 1). Moderate stenosis was defined as stenosis of >70% that did not meet the criteria for severe stenosis (Fig 2). Although MRA is considered a relatively accurate diagnostic tool for grading intracranial artery stenosis,[19,20] interpretations of MRA generally show a tendency to overestimate the degree of stenosis. The criterion for moderate stenosis based on MRA was therefore set to >70%, thus modifying the Warfarin Aspirin Symptomatic Intracranial Disease (WASID) angiographic criterion for moderate stenosis (>50%).[21] The degree

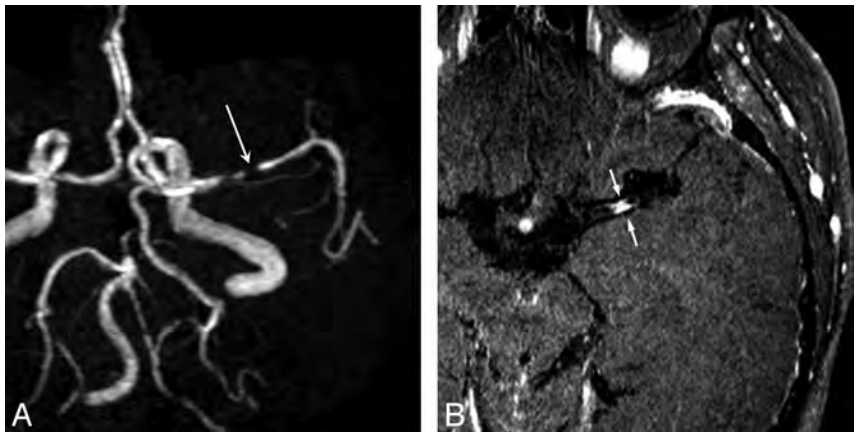

FIG 1. A 73-year-old man with severe MCA stenosis (*A*, *long arrow*) who presented with multifragmented infarctions at the ipsilateral MCA territory. Postcontrast MR image shows attenuated enhancement of the plaque (*B*, *small arrows*).

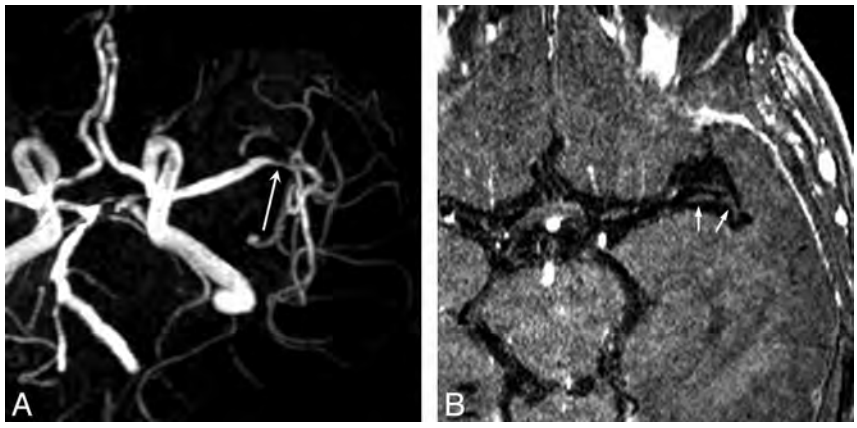

FIG 2. An 88-year-old woman with asymptomatic moderate MCA stenosis (*A*, *long arrow*) has relatively little enhancement of MCA plaques (*B*, *small arrows*).

of stenosis was measured by the WASID method[22] by careful review and consensus of 2 raters (a neuroradiologist and a neurosurgeon).

The degree of enhancement was quantified by drawing ROIs on the contrast-enhanced HR-MRI. ROIs were ovoid or linear and placed to cover the plaques in a manner that was consistent with the stenotic segment of the MCA on MRA by a neuroradiologist. To increase the reliability of the ROIs, the rater measured the signal intensity (SI) 3 times with a region-of-interest drawing and then averaged the SI values. The plaque-to-CSF contrast ratio (CR) was calculated by using the following equation[23]:

$$CR_{plaque\text{-}to\text{-}CSF}\ (\%) = (SI_{plaque} - SI_{CSF}) \times 100/(SI_{plaque} + SI_{CSF}),$$

where SI_{plaque} is plaque SI and SI_{CSF} is CSF SI measured by manual drawing of the round region of interest at the suprasellar cistern or Sylvian cistern. When drawing the region of interest to measure SI_{CSF}, the neuroradiologist was careful not to include any vessels within the cisternal space.

Statistical Analyses

To evaluate the difference between symptomatic and asymptomatic groups, we compared radiologic findings (stenosis degree and CR) and clinical parameters between the 2 groups by using univariate methods (2-sample *t* test or Fisher exact test). Stepwise multivariate logistic regression analysis was used to assess how independent variables, including clinical risk factors, degree of stenosis, and CR, were related to the presence of acute symptoms. CR was compared between moderate and severe stenosis cases by using the 2-sample *t* test. A *P* value $< .05$ was considered statistically significant.

RESULTS

Of the 36 subjects enrolled in our study, 21 (mean age, 69.7 ± 11.9 years; 10 men) were classified as having symptomatic stenosis and 15 (mean age, 67.3 ±12.9 years; 7 men) were classified as having asymptomatic stenosis. Among the 21 cases of symptomatic stenosis, 10 were subcategorized as pial embolic infarctions, 7 were considered borderzone infarctions, and 4 were striatocapsular infarctions. Eleven of the symptomatic cases (52%) had moderate stenosis, and 10 (48%) had severe stenosis. The mean CR for symptomatic stenosis was 63.64 ± 10.56%. Among 15 subjects with asymptomatic stenosis, 8 subjects had acute infarctions in inconsistent areas and 7 did not have any ischemic lesions or symptoms. Thirteen subjects (87%) were considered to have moderate stenosis, and 2 (13%) had severe stenosis. The mean CR for asymptomatic stenosis was 54.09 ± 13.49%.

Univariate comparisons of radiologic and clinical variables showed that the CR of the symptomatic stenosis group was significantly higher than that of the asymptomatic stenosis group ($P = .029$; 95% CI, 0.99–17.27) (Fig 3*A*). The Fisher exact test showed that the frequency of severe stenosis was significantly higher in the symptomatic group than in the asymptomatic group ($P = .039$). Demographic variables and atherosclerotic risk factors were not significantly different between the 2 groups (Table). Multivariate logistic regression analysis revealed that the severity of MCA stenosis was the only statistically significant independent predictor of ischemic stroke symptoms (odds ratio = 7.15; 95% CI, 1.28–39.83; $P = .025$).

In total, there were 24 patients with moderate stenosis and 12 with severe stenosis. The mean CRs of patients with moderate and severe stenosis were 55.91 ± 12.82% and 66.78 ± 8.70%, respectively. The CR for patients with severe stenosis was significantly higher than that of those with moderate stenosis ($P = .010$; 95% CI, 2.74–19.01) (Fig 3*B*).

DISCUSSION

In this study, Gd enhancement of MCA plaques was associated with the degree of stenosis and ischemic stroke in the territory of the stenotic segment; the degree of stenosis was also associated with clinical symptoms. Although there was a positive relation-

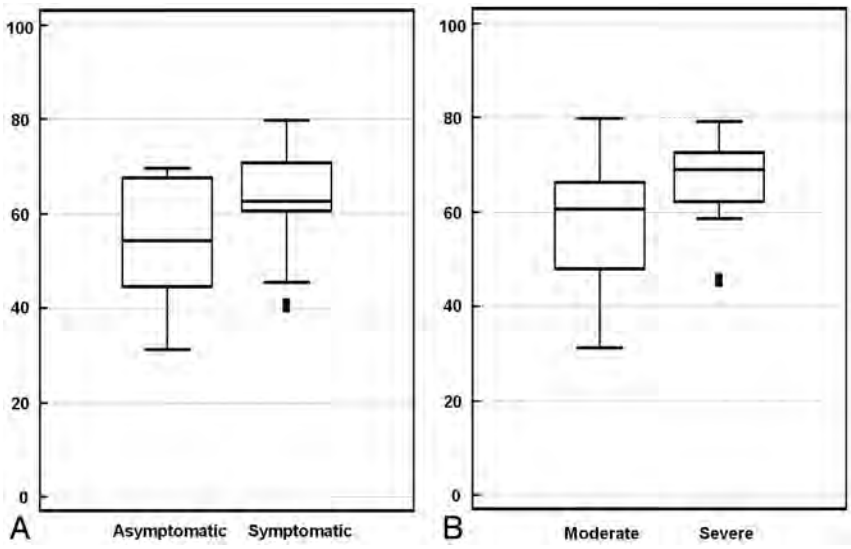

FIG 3. *A*, Comparison of the plaque-to-CSF contrast ratio between asymptomatic and symptomatic stenosis groups. Mean CRs for asymptomatic and symptomatic stenosis are 54.09 ± 13.49% and 63.64 ± 10.56%, respectively. *B*, Comparison of CRs between moderate and severe MCA stenosis. Mean CRs for moderate and severe stenosis are 55.91 ± 12.82% and 66.78 ± 8.70%, respectively.

Comparison of asymptomatic and symptomatic stenosis groups[a]

Characteristics	Symptomatic Stenosis (*n* = 21)	Asymptomatic Stenosis (*n* = 15)	*P* Value[b]
Age (yr)	69.7 ± 11.9	67.3 ± 12.9	.58
Sex, male	10	7	1.00
Risk factor			
HTN	13 (62%)	12 (80%)	.29
DM	8 (38%)	8 (53%)	.49
Dyslipidemia	12 (57%)	11 (73%)	.48
Current smoking	8 (38%)	4 (27%)	.72
Obesity	11 (52%)	5 (33%)	.32
CHD	2 (10%)	2 (13%)	1.00
MCA stenosis			
Site	12 right, 9 left	4 right, 11 left	.09
Degree[c]	11 moderate, 10 severe	13 moderate, 2 severe	<.05
CR (%)	63.64 ± 10.56	54.09 ± 13.49	<.05

Note:—CHD indicates coronary heart disease; DM, diabetes mellitus; HTN, hypertension.

[a] Values are presented as numbers (%). Age and CR are presented as means.

[b] *P* values were calculated by the *t* test and Fisher exact test.

[c] The degree of stenosis was the only independent variable that survived multivariate logistic regression analysis (odds ratio = 7.15; 95% CI, 1.28–39.83; *P* = .025).

ship between plaque enhancement and the presence of acute ischemic lesions in the territory of the MCA, this relationship did not survive multivariate logistic regression analysis.

The degree of stenosis in ICAD is known to be a reliable predictor of ischemic stroke. A prospective study conducted by the WASID trial group in 339 patients with ICAD revealed a strikingly higher prevalence of recurrent stroke in the territory of the stenotic segment in patients with severe stenosis than in patients with moderate stenosis.[16] The fact that symptomatic plaques were more likely to be more severe than asymptomatic plaques in terms of the degree of stenosis introduces a simple bias that could have affected the results: A larger plaque mass is more likely to show greater enhancement or to make enhancement more obvious or detectable given the still-limited resolution of the technique. We were, therefore, not able to confirm that contrast enhancement of plaques is a predictive factor for stroke risk independent of the degree of stenosis. Our findings suggested that higher grades of stenosis had greater enhancement that was not causally related to infarction but was instead simply caused by stenosis. Therefore, in order for Gd plaque enhancement in ICAD to be used as a predictor of ischemic stroke, a prospective trial should be designed in which risk and control groups have similar degrees of stenotic severity, or enhancement should be assessed in patients with equivalently stenotic bilateral plaques in the same location in the setting of unilateral acute infarction.

There was a difference in plaque enhancement in relation to the degree of stenosis. This finding can be explained in 3 ways: First, the role of the vasa vasorum should be considered. Unlike extracranial arteries, which are surrounded by solid tissue, intracranial arteries have little-to-no vasa vasorum.[24,25] This finding is consistent with the hypothesis that the vasa vasorum in the intracranial artery does not necessarily have an obligatory role in lesion development during the early stages of atherosclerosis. As atherosclerosis progresses to an advanced stage, the vasa vasorum develops in the proximal-to-distal segments. The vasa vasorum in the distal segments sometimes develops independently[26] and may play an important role in plaque growth. This hypothetic process is supported by a postmortem study that reported that the vasa vasorum was more frequently developed in aged patients with severe atherosclerosis.[25] Second, inflammatory changes that occur within plaques during plaque growth may also explain the strong enhancement of severe stenosis. A histopathologic-radiologic correlation study of the extracranial carotid artery showed that Gd enhancement was significantly associated with neovascularization, macrophages, and loose fibrosis within plaques.[9] This finding explains the positive relationship between Gd enhancement and both the severity of stenosis and clinical symptoms. Third, CR may increase with increased wall thickness, regardless of inflammatory and neovascular changes, simply by virtue of the decreased volume averaging with the surrounding CSF with an increase in vessel wall thickness.

Weaknesses of this study were the low number of subjects and the retrospective design. The lack of both pathologic correlation and conventional angiography is another major limitation. Because the primary management for ICAD at our institution is medical therapy, pathologic confirmation or diagnostic angiography is strictly limited, even for symptomatic lesions.

CONCLUSIONS

This study demonstrated that the enhancement of plaques in the intracranial artery was closely related to the severity of stenosis. This relationship may be due to different degrees of neovascularity or permeability according to plaque progression. Because stenotic degree may be simultaneously associated with plaque contrast enhancement on MCA and clinical symptoms, the previously reported relationship between plaque enhancement and stroke derived from univariate comparisons should be reconsidered. To settle the debate about the predictive value of plaque enhancement in the setting of intracranial atherosclerosis, further studies are required to compare symptomatic and asymptomatic subjects with similar degrees of stenosis severity.

REFERENCES

1. Chimowitz MI, Lynn MJ, Howlett-Smith H, et al. **Comparison of warfarin and aspirin for symptomatic intracranial arterial stenosis.** *New Engl J Med* 2005;352:1305–16
2. Wong KS, Huang YN, Gao S, et al. **Intracranial stenosis in Chinese patients with acute stroke.** *Neurology* 1998;50:812–13
3. O'Brien KD, Allen MD, McDonald TO, et al. **Vascular cell adhesion molecule-1 is expressed in human coronary atherosclerotic plaques: implications for the mode of progression of advanced coronary atherosclerosis.** *J Clin Invest* 1993;92:945–51
4. O'Brien KD, McDonald TO, Chait A, et al. **Neovascular expression of E-selectin, intercellular adhesion molecule-1, and vascular cell adhesion molecule-1 in human atherosclerosis and their relation to intimal leukocyte content.** *Circulation* 1996;93:672–82
5. Moulton KS, Vakili K, Zurakowski D, et al. **Inhibition of plaque neovascularization reduces macrophage accumulation and progression of advanced atherosclerosis.** *Proc Natl Acad Sci U S A* 2003;100:4736–41
6. Celletti FL, Waugh JM, Amabile PG, et al. **Vascular endothelial growth factor enhances atherosclerotic plaque progression.** *Nat Med* 2001;7:425–29
7. Yuan C, Kerwin WS, Ferguson MS, et al. **Contrast-enhanced high resolution MRI for atherosclerotic carotid artery tissue characterization.** *J Magn Reson Imaging* 2002;15:62–67
8. Kerwin WS, O'Brien KD, Ferguson MS, et al. **Inflammation in carotid atherosclerotic plaque: a dynamic contrast-enhanced MR imaging study.** *Radiology* 2006;241:459–68
9. Millon A, Boussel L, Brevet M, et al. **Clinical and histological significance of gadolinium enhancement in carotid atherosclerotic plaque.** *Stroke* 2012;43:3023–28
10. Lombardo A, Rizzello V, Natale L, et al. **Magnetic resonance imaging of carotid plaque inflammation in acute coronary syndromes: a sign of multisite plaque activation.** *Int J Cardiol* 2009;136:103–05
11. Millon A, Mathevet JL, Boussel L, et al. **High-resolution magnetic resonance imaging of carotid atherosclerosis identifies vulnerable carotid plaques.** *J Vasc Surg* 2013;57:1046–51
12. Skarpathiotakis M, Mandell DM, Swartz RH, et al. **Intracranial atherosclerotic plaque enhancement in patients with ischemic stroke.** *AJNR Am J Neuroradiol* 2013;34:299–304
13. Kim JM, Jung KH, Sohn CH, et al. **Middle cerebral artery plaque and prediction of the infarction pattern.** *Arch Neurol* 2012;69:1470–75
14. Vergouwen MD, Silver FL, Mandell DM, et al. **Eccentric narrowing and enhancement of symptomatic middle cerebral artery stenoses in patients with recent ischemic stroke.** *Arch Neurol* 2011;68:338–42
15. Klein IF, Lavallee PC, Mazighi M, et al. **Basilar artery atherosclerotic plaques in paramedian and lacunar pontine infarctions: a high-resolution MRI study.** *Stroke* 2010;41:1405–09
16. Kasner SE, Chimowitz MI, Lynn MJ, et al. **Predictors of ischemic stroke in the territory of a symptomatic intracranial arterial stenosis.** *Circulation* 2006;113:555–63
17. Jung JM, Kang DW, Yu KH, et al. **Predictors of recurrent stroke in patients with symptomatic intracranial arterial stenosis.** *Stroke* 2012;43:2785–87
18. Lee DK, Kim JS, Kwon SU, et al. **Lesion patterns and stroke mechanism in atherosclerotic middle cerebral artery disease: early diffusion-weighted imaging study.** *Stroke* 2005;36:2583–88
19. Bash S, Villablanca JP, Jahan R, et al. **Intracranial vascular stenosis and occlusive disease: evaluation with CT angiography, MR angiography, and digital subtraction angiography.** *AJNR Am J Neuroradiol* 2005;26:1012–21
20. Choi CG, Lee DH, Lee JH, et al. **Detection of intracranial atherosclerotic steno-occlusive disease with 3D time-of-flight magnetic resonance angiography with sensitivity encoding at 3T.** *AJNR Am J Neuroradiol* 2007;28:439–46
21. Kasner SE, Lynn MJ, Chimowitz MI, et al. **Warfarin vs aspirin for symptomatic intracranial stenosis: subgroup analyses from WASID.** *Neurology* 2006;67:1275–78
22. Samuels OB, Joseph GJ, Lynn MJ, et al. **A standardized method for measuring intracranial arterial stenosis.** *AJNR Am J Neuroradiol* 2000;21:643–46
23. Wattjes MP, Lutterbey GG, Harzheim M, et al. **Imaging of inflammatory lesions at 3.0 Tesla in patients with clinically isolated syndromes suggestive of multiple sclerosis: a comparison of fluid-attenuated inversion recovery with T2 turbo spin-echo.** *Eur Radiol* 2006;16:1494–500
24. Aydin F. **Do human intracranial arteries lack vasa vasorum? A comparative immunohistochemical study of intracranial and systemic arteries.** *Acta Neuropathol* 1998;96:22–28
25. Takaba M, Endo S, Kurimoto M, et al. **Vasa vasorum of the intracranial arteries.** *Acta Neurochirurgica* 1998;140:411–16
26. Atkinson JL, Okazaki H, Sundt TM Jr, et al. **Intracranial cerebrovascular vasa vasorum associated with atherosclerosis and large thick-walled aneurysms.** *Surg Neurol* 1991;36:365–69

Preoperative Prognostic Value of MRI Findings in 108 Patients with Idiopathic Normal Pressure Hydrocephalus

J. Virhammar, K. Laurell, K.G. Cesarini, and E.-M. Larsson

ABSTRACT

BACKGROUND AND PURPOSE: MR imaging is used in the diagnostic evaluation of patients with idiopathic normal pressure hydrocephalus. The aim of this study was to describe the prevalence of several imaging features and their prognostic use in the selection of shunt candidates with idiopathic normal pressure hydrocephalus.

MATERIALS AND METHODS: Preoperative MR imaging scans of the brain were retrospectively evaluated in 108 patients with idiopathic normal pressure hydrocephalus who had undergone a standardized, clinical evaluation before and 12 months after shunt surgery. The MR imaging features investigated were the Evans index, callosal angle, narrow sulci at the high convexity, dilation of the Sylvian fissure, diameters of the third ventricle and temporal horns, disproportionately enlarged subarachnoid space hydrocephalus, flow void through the aqueduct, focal bulging of the roof of the lateral ventricles, deep white matter hyperintensities, periventricular hyperintensities, and focal widening of sulci and aqueductal stenosis.

RESULTS: In logistic regression models, with shunt outcome as a dependent variable, the ORs for the independent variables, callosal angle, disproportionately enlarged subarachnoid space hydrocephalus, and temporal horns, were significant ($P < .05$), both in univariate analyses and when adjusted for age, sex, and previous stroke.

CONCLUSIONS: A small callosal angle, wide temporal horns, and occurrence of disproportionately enlarged subarachnoid space hydrocephalus are common in patients with idiopathic normal pressure hydrocephalus and were significant predictors of a positive shunt outcome. These noninvasive and easily assessed radiologic markers could aid in the selection of candidates for shunt surgery.

ABBREVIATIONS: DESH = disproportionately enlarged subarachnoid space hydrocephalus; DWMH = deep white matter hyperintensities; ICC = intraclass correlation coefficient; iNPH = idiopathic normal pressure hydrocephalus; NPH = normal pressure hydrocephalus; PVH = periventricular hyperintensities; SINPHONI = Study of Idiopathic Normal Pressure Hydrocephalus on Neurological Improvement

Idiopathic normal pressure hydrocephalus (iNPH) is a disease of the elderly population, with symptoms of balance and gait disturbances, dementia, and urinary incontinence; and in approximately 8 of 10 patients, the symptoms are reversible after shunt insertion.[1,2] Several imaging methods have been used in the diagnosis and selection of shunt candidates, but the standard method at present is MR imaging. Even though advanced functional imaging methods are being considered, the clinical evaluation of patients with iNPH still often relies on morphologic findings.

However, whether morphologic findings on preoperative imaging are of prognostic value is controversial, and there is no consensus regarding which MR imaging sequences and variables to evaluate in the selection of shunt candidates. In addition, it is not fully clear how the radiologic features are related to each other and to the symptoms. Previous studies have often involved a limited number of patients and a mixed sample of both idiopathic normal pressure hydrocephalus and normal pressure hydrocephalus (NPH) secondary to a brain insult.

Therefore, we investigated 108 patients who had undergone shunt surgery for iNPH, with the aim of describing the occurrence and prognostic value of 13 different radiologic variables and the relation between MR imaging findings and clinical symptoms.

MATERIALS AND METHODS

Materials

The sample consisted of 108 patients with iNPH who underwent shunt surgery between 2006 and 2010 at the authors' hospital. Median age at the time of surgery was 74 years (range, 54–88 years); 58 (54%) were men and 50 (46%) were women. Inclusion

Received March 30, 2014; accepted after revision May 23.

From the Departments of Neuroscience and Neurology (J.V., K.L.), Neuroscience and Neurosurgery (K.G.C.), and Radiology (E.-M.L.), Uppsala University, Uppsala, Sweden; and Department of Pharmacology and Clinical Neuroscience (K.L.), Östersund, Umeå University, Umeå, Sweden.

Please address correspondence to J. Virhammar, MD, PhD, Department of Neuroscience and Neurology, Uppsala University, Akademiska Sjukhuset, ing 85, 751 85 Uppsala, Sweden; e-mail: johan.virhammar@neuro.uu.se; @johanvirhammar.

http://dx.doi.org/10.3174/ajnr.A4046

criteria were a preoperative MR imaging examination of the brain and a clinical evaluation before and at 12 months after shunt surgery. All patients had ventricular enlargement and gradually evolving symptoms, including a gait disturbance with or without cognitive decline or urinary incontinence. Patients with secondary NPH were excluded. During the follow-up period, 29 patients had various types of shunt complications and 5 patients had complications related to comorbidity. The sample is described in detail in a previous study.[3]

Clinical Evaluation

Patients referred to Uppsala University Hospital because of clinical and radiologic symptoms of NPH were evaluated prospectively before surgery and at follow-up 12 months postoperatively by a multidisciplinary team specialized in hydrocephalus. A neurologist performed a clinical and neurologic evaluation, including a medical history covering intracranial hemorrhage, meningitis, or trauma or other causes of secondary hydrocephalus. All patients were assessed according to a prospective, standardized protocol developed to follow symptoms with time and to measure the outcome after shunt surgery. The cognitive function was tested with the Mini-Mental State Examination; urinary symptoms, with 1 ordinal continence scale[4]; motor function, with 1 ordinal balance scale[4] and 1 ordinal gait scale[4]; and we also used 3 tests in which time and the number of steps were measured. The latter included walking 10 m at a self-chosen speed, a Timed Up and Go Test, and walking backward 3 m.

A shunt responder was defined as a patient improved in any of the following 3 criteria:

1) Motor function of ≥1 level on the gait or balance scale or ≥20% reduction in the time or the number of steps in ≥50% of the 3 tests
2) Cognition ≥4 levels in the Mini-Mental State Examination
3) Continence scale ≥1 level and improvement in the Mini-Mental State Examination score of ≥2 levels.

A dichotomous variable shunt outcome was created and used as a dependent variable in the logistic regression. The modified Rankin Scale was used as a measure of general handicap level.

Imaging

Forty-one (38%) of the preoperative MR imaging examinations were performed at the authors' hospital, and 67 (62%), at the referring hospitals. Ten (9%) were performed on a 3T scanner; 75 (70%), on a 1.5T scanner; 15 (14%), on a 1T scanner; and 8 (7%), on a 0.5T scanner.

Evaluation of MR images was performed retrospectively, with the investigators blinded to the patients' clinical data. Multiplanar reconstruction of the images was used as described below. For continuous variables, 2 investigators analyzed 20 randomly selected patients, and intraclass correlation coefficients (ICCs) were calculated to obtain inter-rater reliability. For the ordinal and dichotomous variables, 2 investigators independently analyzed all patients; and to test reliability, Cohen κ was calculated. In cases of discrepancy in the evaluation, the images were re-evaluated, and a consensus was reached.

The Evans index was measured on transverse images as the ratio between the maximum diameter of the frontal horns of the lateral ventricles and the maximum inner diameter of the skull in the same section (Fig 1*A*).

The callosal angle measured on MR imaging is the angle between the lateral ventricles on a coronal image through the posterior commissure, perpendicular to the anterior/posterior commissure plane (Fig 1*B*).[5]

Compression of the medial and/or high convexity cortex sulci (narrow sulci) was evaluated on coronal and transverse images.[6] It was graded as the following: 0 = normal or wider than normal, 1 = slight compression, 2 = definitive compression (Fig 1*C*, -*D*).

Dilation of the Sylvian fissure was graded in 3 different ways. The first method was described by Kitagaki et al[7] and later illustrated with coronal images by Hashimoto et al.[8] We graded dilation as the following: 0 = normal or narrow, 1 = mildly moderately enlarged, 2 = highly enlarged.[7,8] When we used this method, the reliability between the 2 investigators was not sufficient (κ = 0.36, Fig 2 and Table 1). Therefore, we created a new grading scale, the Sylvian fissure ordinal, an ordinal scale with 3 levels and grading still based on the images of Hashimoto et al but with a more precise definition of how to reconstruct the coronal images to attain a higher reproducibility. The coronal images used for the Sylvian fissure ordinal were reconstructed at the level of the central part of the brain stem and angulated along the brain stem (Fig 2*B*). In the third method, the height of the Sylvian fissure was measured quantitatively on a sagittal image located at the midpoint between the skull and the insular cortex. The height was measured in millimeters in 5 different locations perpendicular to the direction of the Sylvian fissure. The median value of the 5 locations was calculated for each side, and the average of right and left was recorded.

Disproportionately enlarged subarachnoid space hydrocephalus (DESH) refers to a communicating hydrocephalus with enlarged ventricles and a disproportionate distribution of the CSF between the inferior and superior subarachnoid spaces.[8] It was graded as present if both narrow sulci at the high convexity and the Sylvian fissure ordinal were graded as ≥1 (Fig 1*D*).

Flow void phenomenon through the aqueduct and fourth ventricle (flow void) was graded by a modified version of the ordinal scale described by Algin et al.[9] It was graded as follows: 0 = no flow in the aqueduct, 1 = flow void only in the aqueduct, 2 = flow void in the aqueduct and the upper half of the fourth ventricle, 3 = flow void that extends to the caudal part of the fourth ventricle. It was graded on T2-weighted sagittal images without flow compensation. Only examinations from 1 scanner (Avanto 1.5T; Siemens, Erlangen, Germany) were included to avoid scanner differences with regard to flow compensation (n = 36, Fig 1*E*).

Focal bulging of the roof of the lateral ventricles was evaluated on sagittal images and was graded as present or not present (Fig 3).

The diameter of the third ventricle was measured in millimeters on transverse T1-weighted images in the center of the ventricle in the anteroposterior direction but in the widest part in the inferior-superior direction (Fig 1*F*). The maximal diameter of the temporal horns was measured in millimeters on each side on transverse images, and the average of left and right was calculated (Fig 1*G*).

Deep white matter hyperintensities (DWMH) were evaluated

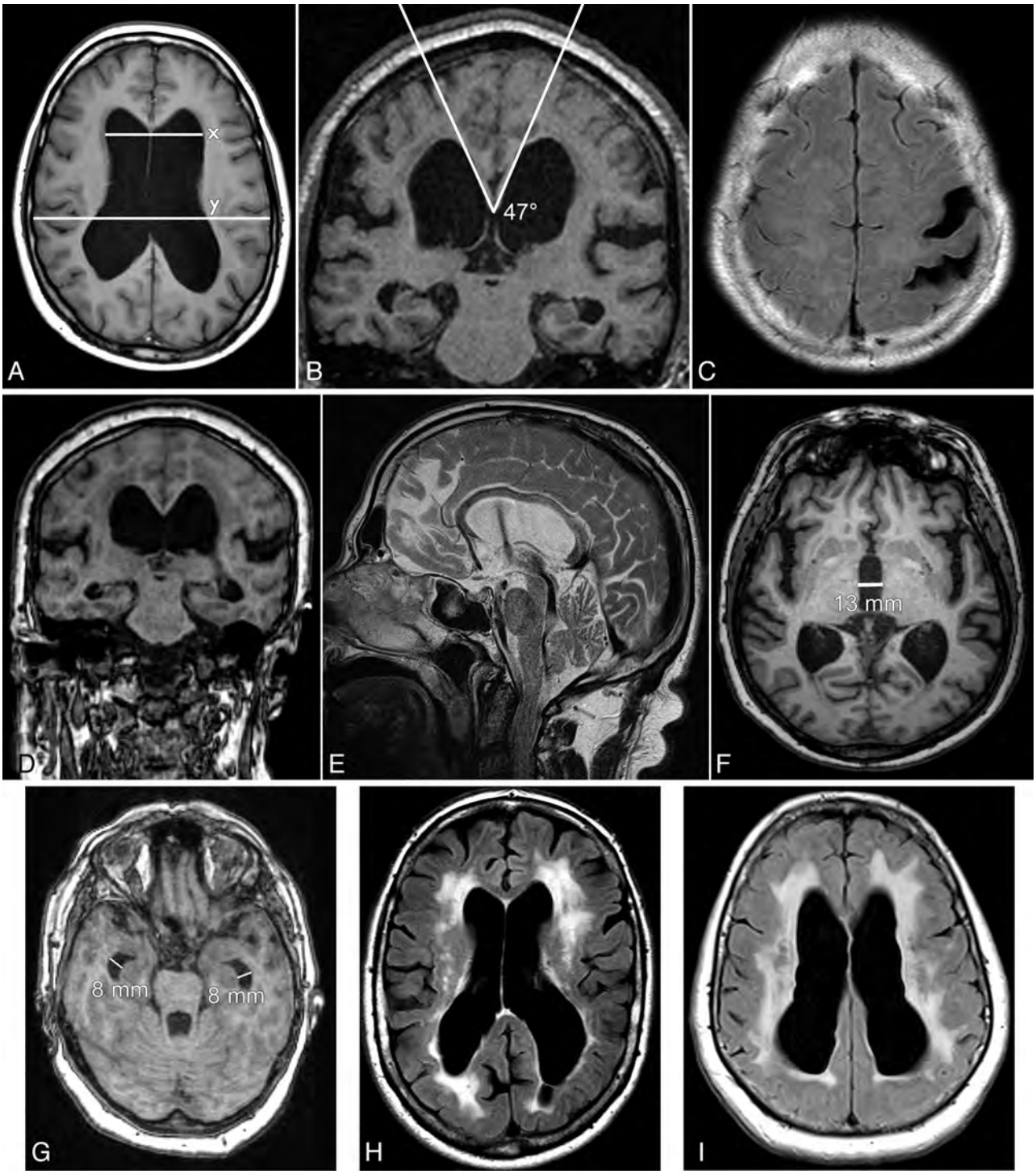

FIG 1. Nine different patients with iNPH. *A*, Evans index = x/y. *B*, Callosal angle. *C*, Narrow medial sulci and 2 focally dilated sulci on the left side. *D*, DESH. *E*, A flow void in the aqueduct and fourth ventricle graded as 2. In addition, a flow void in the foramina of Monro. *F*, Large diameter of the third ventricle. *G*, Dilated temporal horns. *H*, DWMH graded as 3 in a patient who also has PVH. *I*, PVH graded as 2.

on T2 FLAIR images by the ordinal scale described by Fazekas et al[10] as follows: 0 = no lesions, 1 = punctate foci, 2 = beginning confluence of foci, 3 = large confluent areas (Fig 1*H*). All clearly visible single lesions were graded as punctate foci.

Periventricular hyperintensities (PVH) along and always in contact with the frontal and parietal portions of the lateral ventricles were evaluated on T2 FLAIR images. They were graded as follows: 0 = normal (including a "pencil-thin lining" along the ventricular wall and small caps around the frontal horns), 1 = increased PVH, 2 = irregular large symmetric hyperintensities extending out into the deep white matter and, on at least 2 locations, all the way from the ventricles to the cortex (Fig 1*I*).[10]

Accumulation of CSF in focally enlarged sulci, previously called "transport sulci," was evaluated as present or not present (Fig 1*C*).[11,12]

Focal narrowing of the aqueduct with suspicion of aqueductal

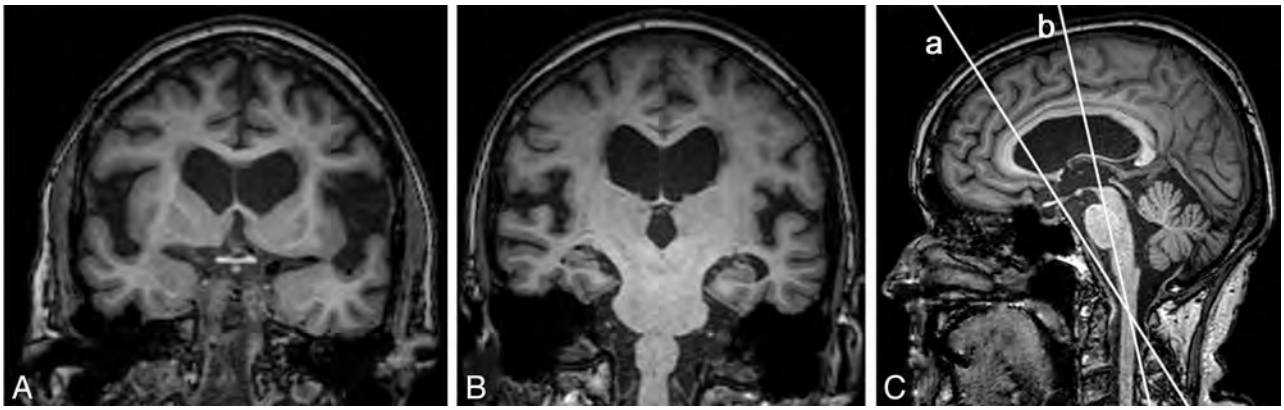

FIG 2. TI-weighted 3D images of a patient with iNPH. *A* and *B*, Coronal images illustrate the different heights of the Sylvian fissure that can be achieved depending on the angulation of the section. *B*, The Sylvian fissure ordinal. *C*, Sagittal image with orientation lines represented by the coronal images *A* and *B*.

Table 1: Interrater reliability between 2 independent investigators for all imaging findings

Imaging Feature	Reliability
Evans index (ICC)	0.93
Callosal angle (ICC)	0.95
Narrow sulci (κ)	0.64
Sylvian fissure original (κ)[a]	0.36
Sylvian fissure ordinal (κ)[b]	0.62
Sylvian fissure height (ICC) (mm)	0.89
DESH[c]	NA
Flow void (κ)	0.33
Focal bulging (κ)	0.28
Third ventricle (ICC)	0.96
Temporal horns (ICC)	0.80
DWMH (κ)	0.67
PVH (κ)	0.72
Focally enlarged sulci (κ)	0.54
Aqueductal stenosis (κ)	0.32

Note:—NA indicates not applicable.
[a] The original method to measure the Sylvian fissure.[7]
[b] Ordinal scale of 0–2.
[c] Calculated from Sylvian fissure ordinal and narrow sulci.

stenosis was evaluated on sagittal and coronal images and graded as present or not present.

Statistics

ICC and κ were used to test for reliability between 2 investigators. Univariate associations and associations adjusted for sex, between shunt outcomes, and all imaging features were assessed with logistic regression models. Imaging markers significant in the univariate analyses were adjusted for age, sex, and previous stroke in multiple logistic regression models. Results from the logistic regression models were presented in a forest plot as estimated ORs with a 95% CI of 1 SD increase for continuous variables and a 1 unit increase for dichotomous and ordinal variables. The difference in the proportion of shunt responders or the level of improvement between patients with or without dichotomous imaging findings was tested with the χ^2 test and the Mann Whitney *U* test, respectively. Correlations were tested by using the Spearman rank correlation coefficient (r) or the ϕ coefficient when appropriate. The correlations tested were exploratory and were not decided before the study, and the level of significance was set at $P < .01$ for correlations. For other analyses, the level of significance was set at $P < .05$. No corrections for multiple analyses were done. Analyses were performed by using SPSS Version 21.0, (IBM, Armonk, New York).

RESULTS

At 12-month follow-up, 82 of the 108 patients (76%) had improved after shunt surgery. Mean values ± SD at preoperative MR imaging were the following: Evans index, 0.38 ± 0.04; callosal angle, 61 ± 17°; diameter of the third ventricle, 12 ± 3 mm; diameter of the temporal horns, 7 ± 2 mm; and the mean height of the Sylvian fissures, 6 ± 3 mm. Prevalence and grading of imaging features measured on ordinal or dichotomous scales are presented in Table 2.

The predictive value of the imaging findings is presented as a sex-adjusted OR in Fig 4. For callosal angle, DESH, and temporal horns, the ORs were significant in the univariate analyses, and when adjusted for sex or when adjusted for sex, age, and previous stroke in the 3 separate multivariate logistic regression models. If only patients without complications ($n = 76$) were included in the logistic regression, the ORs for callosal angle, DESH, and temporal horns were still significant.

There were several correlations among different imaging features at the preoperative MR imaging investigations in the range of $r = 0.26–0.68$ (Table 3).

Patients without PVH performed better at baseline in the modified Rankin Scale and in the stride length in the Timed Up and Go Test and 10 m walk compared with patients with PVH ($P < .05$). Patients without focal bulging performed better in the walking backward 3 m test compared with patients with the imaging feature present ($P < .05$). Patients with normal Sylvian fissures performed better in the modified Rankin Scale ($P < .01$), balance scale ($P < .01$), 10 m walk, and the walking backward 3 m test ($P < .05$) compared with patients with dilated Sylvian fissures. At baseline, Sylvian fissure height (millimeters) correlated with both impaired speed and step length in the walking backward 3 m test at baseline ($r = 0.61$, $P < .001$ and $r = 0.66$, $P < .0001$, respectively). A smaller callosal angle correlated with more impaired scoring in the balance scale ($r = 0.26$, $P < .01$), and the Evans index correlated negatively with the Mini-Mental State Examination score ($r = -0.27$, $P < .01$).

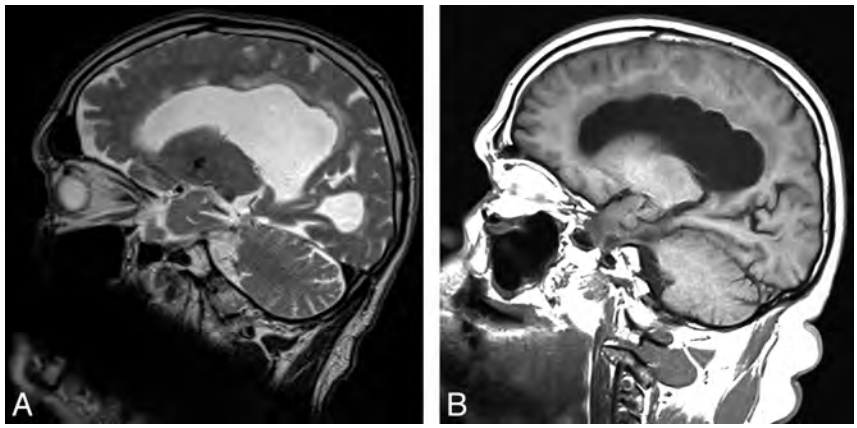

FIG 3. Two patients with focal bulging of the roof of the lateral ventricles. Sagittal images include the most cranial portions of the lateral ventricles. *A*, T2-weighted image. *B*, T1-weighted image.

Table 2: Prevalence and grading of imaging findings measured on dichotomous and ordinal scales

Imaging Feature (Grading Range)	Frequency of Different Grading (No.) (%)[a]				Sample (No.)
	0	1	2	3	
Sylvian fissure ordinal (0–2)	23 (21)	77 (71)	8 (8)	NA	108
DESH (0–1)	36 (33)	72 (67)	NA	NA	108
Flow void (0–3)[b]	0 (0)	0 (0)	9 (25)	27 (75)	36
Narrow sulci (0–2)	24 (22)	22 (20)	62 (58)	NA	108
Focal bulging (0–1)	13 (12)	95 (88)	NA	NA	108
DWMH (0–3)	5 (5)	11 (10)	31 (29)	60 (56)	107
PVH (0–2)	27 (25)	66 (62)	14 (13)	NA	107
Focally enlarged sulci (0–1)	45 (42)	63 (58)	NA	NA	108
Aqueductal stenosis (0–1)	105 (97)	3 (3)	NA	NA	108

Note:—NA indicates not applicable.
[a] Dichotomous variables: 0 = not present, 1 = present.
[b] Flow void in the aqueduct and fourth ventricle.

There was no difference in the proportion of patients with a positive outcome or level of improvement in relation to the Fazekas score among patients with DWMH. The proportion of patients with severe DWMH (Fazekas 3) that improved after shunting was 45/60 (75%) compared with 36/47 (77%) in patients with less severe DWMH.

In Table 1, the interrater reliability is presented. For continuous variables, the reliability had the range of 0.80–0.96 (ICC), and for variables on an ordinal scale, it had a range of 0.33–0.72 (κ). The interrater reliability of dichotomous variables was 0.28–0.67 (κ).

DISCUSSION

In patients with suspected iNPH, MR imaging is used to aid in the diagnosis and selection of shunt candidates. In this retrospective study of 108 patients with iNPH who had undergone shunt surgery and clinical examination before and at 12 months after surgery, a small callosal angle, occurrence of DESH, and wide temporal horns on the preoperative MR imaging scans were significant predictors of positive shunt outcome.

A small callosal angle has previously been described as useful for separating patients with iNPH from those with Alzheimer disease and healthy controls.[5] The results in this and a previous study of a smaller callosal angle in patients who responded to shunt surgery further support its prognostic value.[3] The significant OR < 1 for the callosal angle can be interpreted as showing that patients with a larger angle are less likely to benefit from shunt surgery.

Dilation of the temporal horns of the lateral ventricles is an established finding in hydrocephalus[13,14] and has previously been reported to be more frequent in patients who improve after shunt surgery compared with nonresponders.[12] This finding was strengthened by the results of the present study. The dilation of the temporal horns in iNPH should not be mistaken for atrophy of the medial temporal lobe as is seen in Alzheimer disease,[15] even though there are reports of diminished hippocampus volume in patients with NPH.[16]

In the present study, DESH was a predictor of a positive shunt outcome. The imaging feature was discussed in a publication from the Japanese Study of Idiopathic Normal Pressure Hydrocephalus on Neurological Improvement (SINPHONI), and was described as a morphologic hallmark of iNPH. In the SINPHONI study, a positive outcome was achieved in 80% of 100 patients by using an MR imaging–based diagnostic scheme.[8] In SINPHONI, 96% of the patients had dilated Sylvian fissures and could be classified as having DESH compared with 67% in the present study. Because SINPHONI used narrow supra-Sylvian subarachnoid spaces as an inclusion criterion in contrast to the present study, the prognostic usefulness of DESH could not be calculated in that study. In CT studies, it has been reported that dilated Sylvian fissures are a sign of poor prognosis, and it has been argued that the dilation is caused by atrophy, which is at odds with the findings in the SINPHONI study.[12,17] The difference could be explained by the fact that the Sylvian fissure could only be evaluated on transverse images at that time, and it is much easier to visualize the dilation of Sylvian fissures on reconstructed coronal sections as in modern studies. In the present study, the finding of only dilated Sylvian fissures or only narrow sulci at the high convexity did not predict a positive outcome. Nevertheless, in light of our study and the SINPHONI study, it seems as if DESH is a very common finding in iNPH and that it may aid in the selection of shunt candidates.

Several correlations between imaging findings were seen, and some patterns emerged. As expected, there were correlations between markers of the ventricular width and Evans index, and the temporal horns correlated with the diameter of the third ventricle. DESH correlated with a smaller callosal angle and focal bulging of the ventricular roofs.

There was a significant difference at baseline in the severity of motor symptoms and handicap levels between patients with and without PVH, dilated Sylvian fissures, and focal bulging of the ventricular roofs. Correlations were seen between the severity of

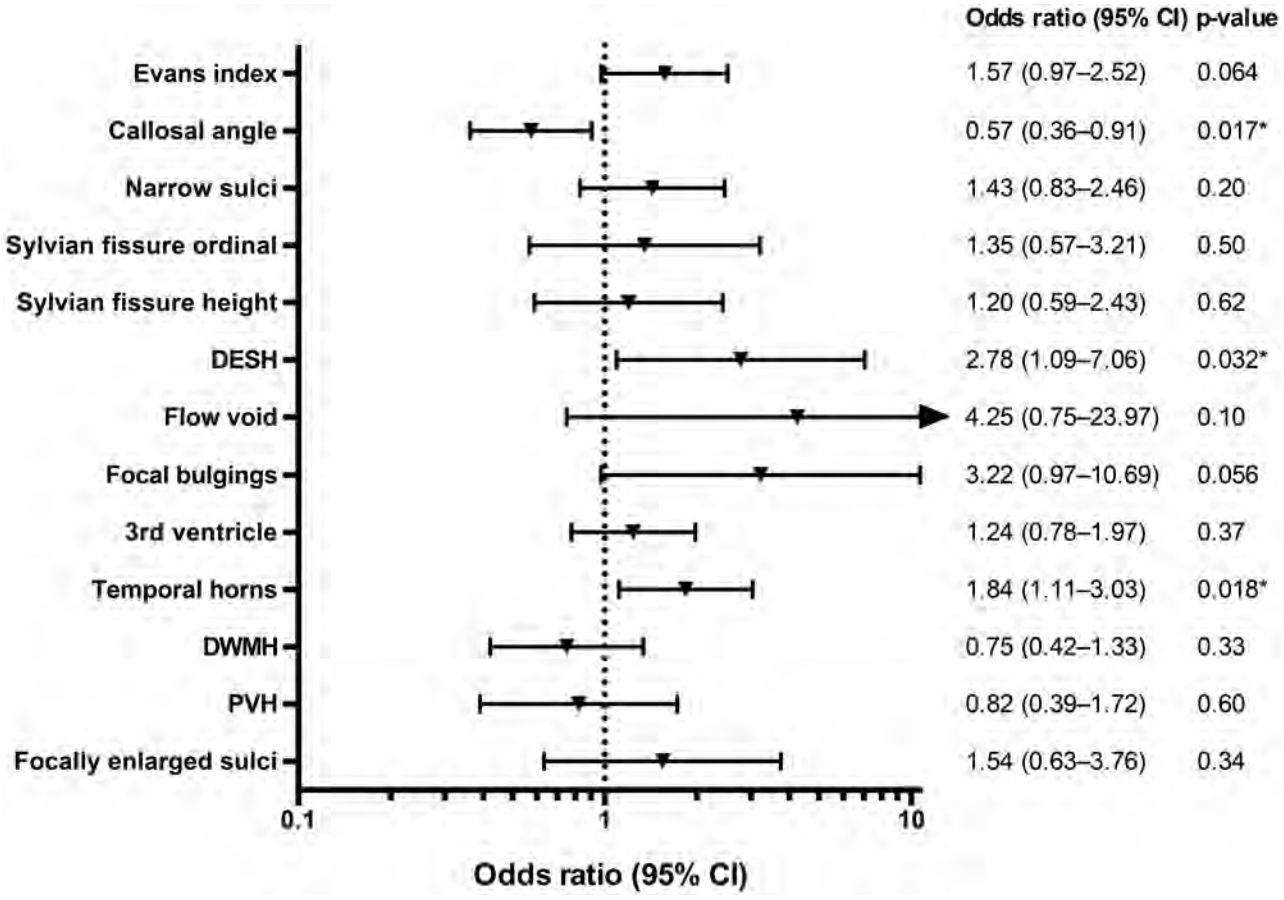

FIG 4. Forest plot with sex-adjusted odds ratios for all imaging features. OR with a 95% CI of 1-SD increase for continuous variables and a 1-U increase for dichotomous and ordinal variables. An *arrow* indicates that the confidence interval extends beyond the range of the plot. The Sylvian fissure ordinal is the ordinal scale 0–2; the Sylvian fissure height is measured in millimeters. The *asterisk* indicates $P < .05$.

Table 3: Correlations among different imaging markers at baseline[a]

Imaging Feature	Significant Correlations
Evans index	Third ventricle ($r = 0.39$[b])
Callosal angle	DESH ($r = -0.27$[c]), focal bulging ($r = -0.28$[c]), temporal horns ($r = -0.33$[d])
DESH	Focal bulging ($r = 0.34$[d]), focally enlarged sulci ($r = 0.32$[d]), callosal angle ($r = -0.27$[c])
Focal bulging	Temporal horns ($r = 0.26$[c]), callosal angle ($r = -0.28$[c]), DESH ($r = 0.34$[d])
Third ventricle	Temporal horns ($r = 0.38$[b])
DWMH	PVH ($r = 0.68$[b])

Note:—*r* indicates Spearman correlation coefficient.

[a] Measurements of Sylvian fissure and narrow sulci at the high convexity were not included because they are components of DESH.

[b] $P < .0001$.

[c] $P < .01$.

[d] $P < .001$.

motor symptoms and a smaller callosal angle or wider Sylvian fissures; and a correlation was seen between a larger Evans index and more impaired cognitive function.

White matter hyperintensities on MR imaging are often divided into PVH, adjacent to the ventricles, and DWMH, located in the deep white matter. Both DWMH and PVH have been reported to be associated with risk factors for vascular disease, such as hypertension and smoking. The origin of the hyperintensities is still debated, and DWMH has been reported to represent gliosis, chronic ischemia, or plasma leakage caused by diffuse cerebrovascular endothelial failure.[18]

In the present study, patients with severe DWMH had a similar positive outcome rate compared with the whole sample, which is in line with the results of Tullberg et al,[19] who concluded that patients must not be excluded from shunt surgery on the basis of the DWMH findings. In NPH, the PVH around the lateral ventricles is probably caused by transependymal CSF passage into the adjacent white matter, and it has, in some studies, been reported to be a good prognostic sign.[20,21] We could not replicate that finding, but patients with PVH had more severe gait disturbances and handicap levels at baseline compared with patients without PVH. Because more severe PVH often extends far from the lateral ventricles into the deep white matter, it can sometimes be almost impossible to differentiate PVH from DWMH. This difficulty could be one explanation behind both the high frequency of severe DWMH and the good outcome rate in these patients. Some patients may have had both DWMH and advanced PVH. This possibility is further supported by a strong correlation between DWMH and PVH.

The focal bulging of the roof of the lateral ventricles is an MR imaging feature that, to our knowledge, has not been described previously in iNPH. We do not know the frequency of this finding in other types of ventricular enlargement, obstructive hydrocephalus, or healthy elderly. The focal bulging is best visualized on sagittal images in the section including the most cranial portions

of the ventricles. The bulging may be caused by CSF pulsations in the lateral ventricles in a weakened spongiotic ependyma and edematous periventricular brain parenchyma,[22] located between periventricular veins.

The interrater reliability between 2 observers of measures of flow void, focal bulging, and aqueductal stenosis was not satisfactory and neither was the reliability of the original description of the grading of the Sylvian fissure.[7,8] We showed that the reliability increased from $\kappa = 0.36$ to $\kappa = 0.62$ by defining the way the sections should be reconstructed and angulated. Dramatic differences in the height of the Sylvian fissure could be obtained depending on which coronal section was used and how it was angulated (Fig 2). All inconsistent grading scores were re-evaluated, and a consensus was reached between the 2 investigators. In accordance with our experience, Ishii et al[5] illustrated differences in the callosal angle, depending on the angulation of the coronal section. These differences are important when these imaging features are used in clinical practice, and only well-defined grading scales with high reliability should be used.

In 3 of the cases in this study, there was a subtle focal narrowing of the Sylvian aqueduct. This did not obstruct the CSF flow and was not considered the cause of the hydrocephalus in these patients. It is advisable to evaluate the aqueduct thoroughly in patients with suspected iNPH—for example, by including a high-resolution, heavily T2-weighted 3D MR imaging sequence in the protocol to exclude obstructive causes of hydrocephalus.

An interesting finding is the diversity of different morphologic features in this study. All patients had similar symptomatology, but 67% had DESH, while 10% had neither dilated Sylvian fissures nor narrow high-convexity sulci; 25% had no PVH at all, while 13% had PVH extending all the way to the cortex. Previous studies in iNPH have found both heterogeneous patterns of metabolic disturbances in the cortex measured with FDG-PET and various patterns of CBF reduction measured with SPECT.[23,24] These findings raise the question: Are the morphologic differences different stages of the same disease or is iNPH a syndrome of several diseases with different etiologies? There were significant differences in symptom severity between patients with or without PVH, focal bulging, and dilated Sylvian fissures, indicating that these imaging features may be involved in the progression of the disease. However, this question should be addressed in a prospective longitudinal study.

It has recently been discussed that in studies of iNPH, it is important to present descriptive data of the sample, including comorbidity, to facilitate comparisons of different studies.[25] It seems to be equally important to also describe the radiologic findings in sufficient detail. Otherwise, we cannot know whether we are investigating and performing surgery in similar patients, and comparisons of studies become difficult.

Despite these findings, callosal angle, DESH, or temporal horns cannot be used to exclude patients from surgery. Of patients with a callosal angle of >90°, 4/7 (57%) improved; 23/36 (64%) patients without DESH improved; and 7/15 (47%) patients with temporal horns of <5 mm improved from shunt surgery. This illustrates one of the greatest problems with studies of prognostic or nonprognostic investigations in iNPH: The number of patients who do not improve after shunting are too few, even in samples as large as in this study, to draw any conclusions regarding in which patients shunting should not be performed.

Some limitations should be addressed. All patients had been diagnosed with iNPH by a specialized team and had undergone shunt surgery, and the MR imaging investigations used in this study had been used in the clinical evaluation of these patients. We had no control group of healthy individuals or patients with Alzheimer disease. Thus, the results in this study must be interpreted in the light of the highly selected sample, and no conclusions about the diagnostic value of the findings can be made. The clinical radiologic diagnosis was made by several different neuroradiologists without a defined protocol, which might have influenced the frequency of some of the retrospectively evaluated imaging findings. For example, all patients had an Evans index of >0.30, and no patient had severe cortical atrophy. However, several of the imaging features investigated in this study were not used clinically at the time of the study at our center. Because of missing sequences in some patients, we could not grade all imaging features in all patients. This gap was most evident for grading of the flow void because we chose to include only investigations from a single scanner to avoid any differences among scanners.[26] Because of the limited number of patients in whom flow void was graded, not a single patient with a small flow void was found, which probably affected the absence of significant correlations between flow void and other MR imaging findings. Although data were collected prospectively in a standardized way, the radiologic measurements and analyses of clinical data for this study were performed retrospectively. This feature limited the possibility of making corrections when specific MR imaging sequences or some clinical data were missing.

CONCLUSIONS

The callosal angle, diameter of the temporal horns, and presence of DESH were predictors of a positive outcome after shunting in this sample of patients with iNPH. We recommend that these noninvasive imaging features be assessed in the preoperative evaluation of patients with iNPH because they may aid in the selection of shunt candidates.

ACKNOWLEDGMENTS

We thank Lisa Wernroth for statistical consultation and the staff of our NPH team at Uppsala University Hospital for their commitment to all the patients.

Disclosures: Johan Virhammar—*RELATED: Grant:* Selanders Stiftelse,* *Comments:* Selanders Stiftelse is an independent foundation in Sweden. The institution received a grant to support the cost of this study. Katarina Laurell—*RELATED: Grant:* Selanders Stiftelse.* *Money paid to the institution.

REFERENCES

1. Adams RD, Fisher CM, Hakim S, et al. **Symptomatic occult hydrocephalus with "normal" cerebrospinal-fluid pressure: a treatable syndrome.** *N Engl J Med* 1965;273:117–26
2. Klinge P, Hellstrom P, Tans J, et al. **One-year outcome in the European multicentre study on iNPH.** *Acta Neurol Scand* 2012;126:145–53
3. Virhammar J, Laurell K, Cesarini KG, et al. **The callosal angle measured on MRI as a predictor of outcome in idiopathic normal-pressure hydrocephalus.** *J Neurosurg* 2014;120:178–84

4. Hellström P, Klinge P, Tans J, et al. **A new scale for assessment of severity and outcome in iNPH.** *Acta Neurol Scand* 2012;126:229–37
5. Ishii K, Kanda T, Harada A, et al. **Clinical impact of the callosal angle in the diagnosis of idiopathic normal pressure hydrocephalus.** *Eur Radiol* 2008;18:2678–83
6. Sasaki M, Honda S, Yuasa T, et al. **Narrow CSF space at high convexity and high midline areas in idiopathic normal pressure hydrocephalus detected by axial and coronal MRI.** *Neuroradiology* 2008;50:117–22
7. Kitagaki H, Mori E, Ishii K, et al. **CSF spaces in idiopathic normal pressure hydrocephalus: morphology and volumetry.** *AJNR Am J Neuroradiol* 1998;19:1277–84
8. Hashimoto M, Ishikawa M, Mori E, et al. **Diagnosis of idiopathic normal pressure hydrocephalus is supported by MRI-based scheme: a prospective cohort study.** *Cerebrospinal Fluid Res* 2010; 7:18
9. Algin O, Hakyemez B, Taskapilioglu O, et al. **Morphologic features and flow void phenomenon in normal pressure hydrocephalus and other dementias: are they really significant?** *Acad Radiol* 2009;16: 1373–80
10. Fazekas F, Chawluk JB, Alavi A, et al. **MR signal abnormalities at 1.5 T in Alzheimer's dementia and normal aging.** *AJR Am J Roentgenol* 1987;149:351–56
11. Holodny AI, George AE, de Leon MJ, et al. **Focal dilation and paradoxical collapse of cortical fissures and sulci in patients with normal-pressure hydrocephalus.** *J Neurosurg* 1998;89:742–47
12. Wikkelsö C, Andersson H, Blomstrand C, et al. **Computed tomography of the brain in the diagnosis of and prognosis in normal pressure hydrocephalus.** *Neuroradiology* 1989;31:160–65
13. Svendsen P, Duru O. **Visibility of the temporal horns on computed tomography.** *Neuroradiology* 1981;21:139–44
14. Tans JT. **Differentiation of normal pressure hydrocephalus and cerebral atrophy by computed tomography and spinal infusion test.** *J Neurol* 1979;222:109–18
15. Scheltens P, Leys D, Barkhof F, et al. **Atrophy of medial temporal lobes on MRI in "probable" Alzheimer's disease and normal ageing: diagnostic value and neuropsychological correlates.** *J Neurol Neurosurg Psychiatry* 1992;55:967–72
16. Golomb J, de Leon MJ, George AE, et al. **Hippocampal atrophy correlates with severe cognitive impairment in elderly patients with suspected normal pressure hydrocephalus.** *J Neurol Neurosurg Psychiatry* 1994;57:590–93
17. Benzel EC, Pelletier AL, Levy PG. **Communicating hydrocephalus in adults: prediction of outcome after ventricular shunting procedures.** *Neurosurgery* 1990;26:655–60
18. Wardlaw JM, Smith C, Dichgans M. **Mechanisms of sporadic cerebral small vessel disease: insights from neuroimaging.** *Lancet Neurol* 2013;12:483–97
19. Tullberg M, Jensen C, Ekholm S, et al. **Normal pressure hydrocephalus: vascular white matter changes on MR images must not exclude patients from shunt surgery.** *AJNR Am J Neuroradiol* 2001;22:1665–73
20. Poca MA, Mataro M, Del Mar Matarin M, et al. **Is the placement of shunts in patients with idiopathic normal-pressure hydrocephalus worth the risk? Results of a study based on continuous monitoring of intracranial pressure.** *J Neurosurg* 2004;100:855–66
21. Børgesen SE, Gjerris F. **The predictive value of conductance to outflow of CSF in normal pressure hydrocephalus.** *Brain* 1982;105: 65–86
22. Milhorat TH, Clark RG, Hammock MK, et al. **Structural, ultrastructural, and permeability changes in the ependyma and surrounding brain favoring equilibration in progressive hydrocephalus.** *Arch Neurol* 1970;22:397–407
23. Ishii K, Hashimoto M, Hayashida K, et al. **A multicenter brain perfusion SPECT study evaluating idiopathic normal-pressure hydrocephalus on neurological improvement.** *Dement Geriatr Cogn Disord* 2011;32:1–10
24. Tedeschi E, Hasselbalch SG, Waldemar G, et al. **Heterogeneous cerebral glucose metabolism in normal pressure hydrocephalus.** *J Neurol Neurosurg Psychiatry* 1995;59:608–15
25. Malm J, Graff-Radford NR, Ishikawa M, et al. **Influence of comorbidities in idiopathic normal pressure hydrocephalus: research and clinical care—a report of the ISHCSF task force on comorbidities in INPH.** *Fluids Barriers CNS* 2013;10:22
26. Bradley WG Jr, Scalzo D, Queralt J, et al. **Normal-pressure hydrocephalus: evaluation with cerebrospinal fluid flow measurements at MR imaging.** *Radiology* 1996;198:523–29

Success Rates for Functional MR Imaging in Children

A. Rajagopal, A. Byars, M. Schapiro, G.R. Lee, and S.K. Holland

ABSTRACT

BACKGROUND AND PURPOSE: Functional MR imaging is widely used for research in functional brain development in healthy children. However, obtaining high-quality brain imaging data from pediatric research participants requires cooperation that is challenging for young children. In this study, we examined success rates for fMRI in typically developing children in both longitudinal and cross-sectional research study designs to inform the recruitment needs of future pediatric brain imaging studies.

MATERIALS AND METHODS: In the cross-sectional study, 459 healthy children (5–18 years of age, 215 girls) were recruited. A subset of 30 healthy children 5–7 years of age from the cross-sectional cohort were selected and scanned for 10 consecutive years in the longitudinal arm of the study. Following anatomic scans, each participant attempted 4 functional MR imaging tasks. Success rate was defined as the proportion of fMRI tasks completed. Differences in success rates across sexes and in cross-sectional-versus-longitudinal cohorts were evaluated by using the Fischer exact test.

RESULTS: In the cross-sectional study, 74% of the children completed all tasks. Success rates for individual tasks ranged from 34% to 67% for children 5–7 years of age and 76%–100% for those 8–18 years of age. In the longitudinal study, 89% of children completed all tasks in all 10 years. We established significance ($P < .0001$) between the cross-sectional and longitudinal cohorts for both 0% and 100% task completion rates. There was no significance between sexes.

CONCLUSIONS: When designing pediatric fMRI studies in children, the sample sizes indicated by power analysis should be scaled up according to age (ie, 33% for ages 8–18 years, 50% for ages 5–7 years).

ABBREVIATIONS: HUSH = hemodynamic unrelated to scanner hardware; SR = success rate

Functional MR imaging is a commonly used noninvasive technique for tracking the changes in blood oxygenation levels that accompany neuronal activity.[1] Clinically, fMRI has been used extensively to identify or locate important brain regions before performing surgery on tumors or removing epileptic foci.[2,3] It is also a widely used research tool for the investigation of brain activity during a wide array of primary somatosensory, language, and other higher level cognitive tasks. Most functional MR images require the subject to be awake and attentive to respond to the experimental paradigms being presented. The main challenges in successfully obtaining MR imaging data are restlessness, claustrophobia, or other anxieties on the part of participants.

The success rate (SR) of scanning children in fMRI paradigms has been examined in 2 studies.[4,5] The study by Byars et al[4] examined the success rate in 209 children between 5 and 18 years of age completing 4 fMRI tasks and 1 anatomic reference scan. In that study, most of the children in the age range of 9 through 18 years completed all 4 functional tasks and the anatomic task. However, the failure rate was higher in younger children 5–7 years of age. The current sample of 459 children included the original group of 200+ subjects from Byars et al in 2002, plus an additional 259 subjects in the cross-sectional cohort.

In another recent study, children in the age range of 10–18 years had a significantly greater scan success rate than those 4–6 years of age. Yerys et al[5] determined that groups with clinical conditions like attention deficit/hyperactivity disorder, autism spectrum disorder, and epilepsy had lower success rates than nonclinical control groups.

Received February 26, 2014; accepted after revision May 6.

From the Pediatric Neuroimaging Research Consortium (A.R., G.R.L., S.K.H.), Department of Radiology, and Department of Neurology (A.B., M.S.), Cincinnati Children's Hospital Medical Center, Cincinnati, Ohio; and Departments of Radiology (S.K.H.), Pediatrics (S.K.H.), Otolaryngology (S.K.H.), Physics (S.K.H.), Neuroscience (S.K.H.), and Biomedical Engineering (S.K.H.), University of Cincinnati, Cincinnati, Ohio.

This work was funded by a grant from the National Institutes of Health (R01-HD38578).

Please address correspondence to Akila Rajagopal, MD, Pediatric Neuroimaging Research Consortium, Cincinnati Children's Hospital Medical Center, MLC 5033, 3333 Burnet Ave, Cincinnati, OH 45219; e-mail: akila.rajagopal@cchmc.org

http://dx.doi.org/10.3174/ajnr.A4062

In the present report, success and failure rates were examined in both cross-sectional and longitudinal cohorts. The longitudinal cohort of $n = 30$ subjects was a subset of the cross-sectional cohort. This group of children was tested annually for 10 years. In the current report, we also include analysis and discussion regarding the reasons that children fail to complete fMRI scans for research. This information may be helpful to the researcher to avoid loss of subjects and data in pediatric neuroimaging studies and to provide a better understanding of the recruitment needs in future studies.

MATERIALS AND METHODS

Subjects

Four hundred fifty-nine healthy children (215 girls) within the age range of 5–18 years were recruited for the cross-sectional fMRI study. The 3 criteria for recruitment were that children be healthy (determined by a questionnaire filled out by the parent), be native English speakers, and have normal findings on neurologic examinations administered by a board-certified pediatric neurologist. Children with any neurologic comorbidity were excluded from the study. From these 459 children, a subset of 30 children (15 girls) within the initial age range of 5–7 years was selected for the longitudinal fMRI study. For this study, the longitudinal study required annual fMRI scanning and testing for 10 consecutive years. The first visit of each longitudinal subject was included in the cross-sectional data analysis described below. Subsequent visits by longitudinal subjects were not included in the cross-sectional analysis. All visits by longitudinal participants are analyzed in the longitudinal trajectories.

MR Imaging

MR imaging was performed on a 3T Biospec MR imaging scanner (Bruker BioSpin MRI, Ettlingen, Germany). The entire scanning session lasted for approximately 45 minutes and included a localizer scan, anatomic scan, multiecho reference scan, and 4 functional MR imaging tasks. The T1-weighted 3D MPRAGE-type anatomic image was acquired in 9 minutes with $1 \times 1.5 \times 1.5$ mm resolution. A T2*-weighted gradient-echo EPI sequence was used to acquire the functional scans. The imaging parameters used for these scans were as follows: TR/TE = 3000/38 ms, bandwidth = 125 kHz, matrix = 64×64, FOV = 25.6×25.6 cm, section thickness = 5 mm. In 5 minutes 30 seconds, 24–32 transverse sections were acquired.

fMRI Paradigms

Four functional tasks examined early and later developing sentential and syntactic language skills: verb-generation, syntactic prosody, picture-matching, and story-processing tasks.[6]

The verb-generation task[7] involved auditory presentation of a series of concrete nouns every 5 seconds, to which the child responded by covertly generating as many verbs as possible associated with the noun during the remainder of the 5-second interval. A bilateral finger-tapping task served as the control task, preventing the child from continuing to generate verbs during the control period and providing a reference area of activation within the motor strip as a means of validating behavioral compliance.

The story-processing task[8] involved an auditory presentation of 5 simple stories, each composed of 10 sentences. The child was instructed to listen to the stories in preparation for answering questions about them after the scans. Random auditory pure tones of various frequencies from 150 to 1000 Hz were presented at unequal intervals of 1–3 seconds during the control task, which was interleaved by the story task.

In the syntactic prosody task,[9] the child had an auditory presentation of a target sentence (selected from the stories in the story-processing task) of a set of sentences that were low-pass-filtered (400 Hz cutoff) so that words were not recognizable, but syntactic prosody was preserved. During the control task, the child was asked to press a button each time a target tone was heard among the other randomly ordered tones of various frequencies.

The word-picture matching task[10] involved simultaneous visual presentations of 2 simple line drawings of common objects. The name of one of the objects was presented via the headphones simultaneously. The child was required to push the button indicating whether the picture on the right or the left matched the word that was heard. The control task was a visual presentation of paired images of unnamable designs.

The prosody and story-processing tasks assess syntax, whereas word-picture matching and verb generation assess semantics.[6] During the first 5 years in the longitudinal study, all children performed these 4 tasks. A nonsignificant rate of change in the lateralization index with age in the first 5 years of the longitudinal study indicated that picture-matching and prosody were early developmental tasks. Hence, in the last 5 years of the longitudinal study, these 2 tasks were replaced by modified versions of the story-processing[11] and verb-generation tasks[12] by using another method called hemodynamic unrelated to scanner hardware (HUSH).[13] This method was designed to facilitate fMRI with auditory stimulation by presenting the stimulus when the scanner is completely silent, and the data are collected through the peak of the hemodynamic response.[11] Other investigators have reported similar approaches.[14]

Desensitization Methods

To improve the success rate due to children being frightened, we used a systematic desensitization method to acclimate children to the MR imaging environment. This process begins with an experienced and child-friendly study coordinator and MR imaging technologist and continues with the following: 1) rewarding children with toys and small gifts for completing each training step, 2) acclimatizing them to the scanner by performing a trial run on the scanner, 3) explaining the procedures in child-friendly but detailed language and letting them hear the noise that the scanner makes, and 4) playing movies during nontask time in the scanner and frequently "checking in" with them by using the audio system while they are in the scanner. These systematic methods add approximately an hour of preparation time in the scanner area before the actual scan. Scanning procedures also last for almost an hour, with additional time between image sequences allocated to interaction with the participants by the study coordinator over the MR imaging–compatible audiovisual system to provide instructions and reassurance about performance and the time left until completion of the scan procedures.

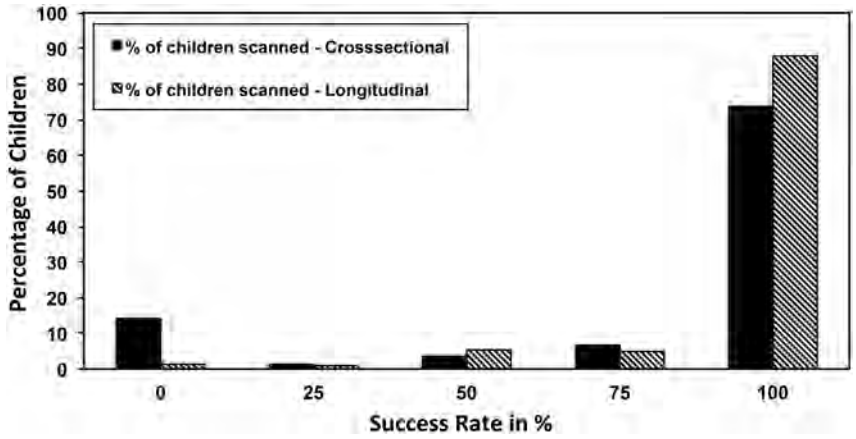

FIG 1. Histogram showing success rates of the percentage of children (y-axis) in the cross-sectional study ($n = 459$) and longitudinal study who were scanned for 10 years ($n = 30$), performing 4 fMRI tasks, and their success rate (x-axis). 100% success rate = 4 tasks completed; 75%, 50%, 25%, and 0% correspond to 3, 2, 1, or no task completed.

Success Rate

The success rate was defined as the ratio of the number of completed and usable fMRI datasets to the total number of fMRI tasks in the study protocol (ie, 4). FMRI data were considered usable if the subject completed the reference scan and anatomic scan with a minimum of motion, along with functional scans.[15] The reference scan was considered important because it helps to perform the geometric correction during reconstruction of the images.[16]

Reasons for Failure

Reasons for children failing to complete MR imaging research protocols are important to understand for optimizing study designs for success. To quantitate reasons for failure, we define the 5 most common reasons for failure and examine the number of failures for each reason. Reasons for failure are defined in order of the largest to smallest number of children reporting this reason for ending participation in the scan session as follows.

1) Children being frightened due to claustrophobia or the noise generated by the scanner

2) No explanations or reasons provided by the subject or the technologists

3) Discomfort or unwillingness to lie still in the scanner

4) Technical errors made by the technologists or researcher. We lost a few data points due to trouble with the scanner or the stimulus-presentation software or video and audio equipment.

5) Motion inside the scanner. Children, especially in the age range of 5–7 years, found it hard to lie still in the scanner for a long time, with head or feet resulting in motion artifacts that caused the operators to stop the scan.

In the case of the longitudinal study, the primary reason for failure was children with braces or retainers, defined as reason 1 for the longitudinal cohort. Braces were exclusion criteria for the neuroimaging study of child language development, and children would not be recruited for the cross-sectional study if braces were discovered during the screening process. However, longitudinal participants who did not have braces when they first enrolled in the study (at age 5–7) were not excluded from continued participation in the longitudinal arm of the study but were not scanned in the years when they had braces. Among the longitudinal participants who continued in the imaging study, failure to complete scans in subsequent years was less common than in the cross-sectional group in general. However, longitudinal participants did fail to complete scans in subsequent years for the same reasons as cross-sectional participants with the 3 most common reasons for failure in the longitudinal study corresponding to items 2, 3, and 5 of the cross-sectional study listed above. The fourth most common reason for failure in the longitudinal study was families not being interested in continuing to participate in the study. Technical faults (4 above) were negligible in the longitudinal study because these "bugs" were eliminated during the first year or 2 of the study.

Statistical Analysis

We compared success/failure rates between boys and girls and also between the cross-sectional and longitudinal cohorts. To test the significance of the differences between the proportions in these groups, we used the Fisher exact test.

RESULTS

Success rate was computed separately for cross-sectional and longitudinal study data. The percentage of children who completed each fMRI task in the cross-sectional and longitudinal studies is plotted as a histogram in Fig 1. The percentages of children who did not complete any of the 4 functional scans, anatomic scan, or reference scan in the cross-sectional and longitudinal study are 14.4% ($n = 66$) and 1.3% ($n = 3$), respectively. In the following sections, the subject groups completing 0% through 100% of the scans will be referred to as SR(0) through SR(100). The number of subjects meeting SR(25), SR(50), SR(75), and SR(100) for the cross-sectional study are as follows: 1.3% ($n = 6$), 3.7% ($n = 17$), 6.8% ($n = 31$), and 73.9% ($n = 339$). The corresponding success rates for the longitudinal study are the following: 0.9% ($n = 2$), 5.2% ($n = 12$), 4.7% ($n = 11$), and 87.9% ($n = 204$), respectively.

Cross-Sectional Cohort

The number of children who completed each task was the following: picture-matching, 374 (81.5%); verb-generation, 376 (81.9%); syntactic prosody, 368 (80.2%); and story-processing task, 370 (80.6%). Table 1 shows the total number of children at each age and the percentage of children (girls and boys) in the cross-sectional study who completed each functional MR imaging task. Table 1 shows that the percentage of children completing each task was >76% in the 8- to 11-year age group and >91% in the 12- to 18-year age group. However, the success rates for the children in the 5- to 7-year age group ranged from 34% to 67%.

Table 1: The total number of girls and boys at every age ranging from 5 to 18 years participating in the cross-sectional study[a]

Age (yr)	Total No. of Children		Tasks Completed							
			Picture (%)		Prosody (%)		Stories (%)		Verbs (%)	
	Girls	Boys	Girls	Boys	Girls	Boys	Girls	Boys	Girls	Boys
5	15	29	60	34.5	60	37.9	67	41.4	60	41.4
6	22	23	63.6	47.8	54.5	39.1	59.1	47.8	54.5	43.5
7	27	22	66.7	50	59.3	50	63	50	67	50
8	15	25	80	88	87	84	80	84	80	92
9	16	17	94	88	81.3	76.5	81.3	82.4	87.5	76.5
10	12	17	100	88	100	94	92	82.4	100	82.4
11	13	17	84.6	100	84.6	94.1	84.6	100	92.3	100
12	14	22	100	100	100	100	100	95.5	100	100
13	21	19	95.2	94.7	95.2	94.7	95.2	94.7	100	94.7
14	14	12	92.8	100	92.8	100	92.8	100	92.8	100
15	12	11	91.7	100	91.7	100	91.7	100	91.7	100
16	11	10	100	90	100	100	100	100	100	100
17	11	12	100	100	100	100	91	100	100	100
18	12	8	100	100	100	100	100	100	100	100

[a] Also tabulated is the number of girls and boys who completed the various functional MRI tasks.

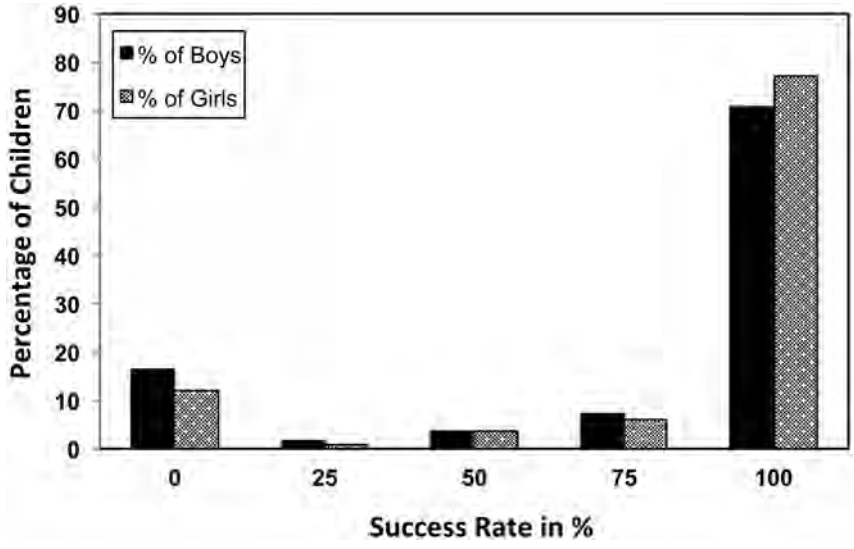

FIG 2. Histogram showing success rates of the percentage of girls ($n = 215$) and boys ($n = 244$) in the cross-sectional study along the y-axis and their success rates along the x-axis. 100% success rate = 4 tasks completed; 75%, 50%, 25%, and 0% correspond to 3, 2, 1, or no task completed.

Figure 2 shows the success rates in the cross-sectional study based on sex. Twelve percent of girls tended to have SR(0), while 16% of boys did not complete any of the tasks. In addition, 77% of the girls completed all the scans, while 71% of the boys completed all the scans.

Longitudinal Cohort

Figure 3 shows the number of children who completed the study annually in the longitudinal study grouped by the age of children in each year. Because the total number of subjects was limited to 30, grouping by age was not performed for each task.

In Table 2, the percentage of children who completed tasks in the longitudinal study for each year for each individual task is tabulated. Table 2 also shows the number of children who were scanned for each year. There are a total of 6 tasks listed in Table 2; however, during the first 5 years of the study, the 4 tasks used were picture, prosody, stories, and verbs. During the last 5 years, the tasks used were stories, verbs, HUSH stories, and HUSH verbs. On the basis of Table 2, it can be seen that the success rate was >89% for the children who returned every year.

Tables 3 and 4 explain the reasons for failure in both cross-sectional and longitudinal studies. The criteria on the basis of which the subjects failed to either complete any task or 1 or 2 or 3 tasks are shown along with the percentage of children who failed for each reason.

Statistical Significance

The Fisher exact test on the success rates in the cross-sectional and longitudinal cohorts yielded a significant difference in the both SR(0) and SR(100) rates ($P < .0001$). The differences at various other success rates, SR(25), SR(50), and SR(75), were not significant. We also tested for statistical significance between girls and boys in the cross-sectional cohort, but there was no significant difference.

DISCUSSION

The percentage of children in SR(100) was 89% for the longitudinal study compared with 74% in the cross-sectional study. The children in the longitudinal study had a better success rate because these children were, in most cases, comfortable with being scanned after the initial scanning and desensitization process. We expected 300 scans for the longitudinal study because we had 30 children recruited who were scanned for 10 years. However, a number of scans were omitted because the children had braces or retainers, and a few families were not interested in continuing to participate in the study or they moved.

From Table 1, it is clear that children 5–7 years of age had the lowest success rate in our study, ranging from 34.5% to 67%. However, there was a drastic improvement in success rates in children 8 and 9 years of age, with success rates ranging from

76.5% to 94%. Children in the 10- to 18-year age group showed success rate ranging from 82.4% to 100%.

Girls tended to have lower failure rates and higher success rates than boys when considering SR(0) and SR (100) (Fig 2). However, both boys and girls had almost the same rate of success in completing 1, 2, and 3 tasks. Although girls had a higher success rate than boys, a Fisher exact test did not find this difference significant. We can conclude that it is reasonable to expect high rates of success in fMRI research studies in both boys and girls as young as 5 years of age.

We have previously shown that task order is not a factor in determining success rate.[15] The main determinant of noncompliance with fMRI task demands by children is the degree of engagement of auditory, visual, and tactile senses, particularly in boys. Even though girls had a higher success rate than boys, the difference was not significant. The current results are consistent with our earlier findings in this regard.[15]

The success rate in the longitudinal study was calculated on the basis of the number of tasks completed by the children compared with the number of children who returned for scans. Children with braces or retainers who could not be scanned were not included in the analysis. On the basis of Table 2, the success rates for years 1 and 4 were >92%, dropped a little in years 2 and 3, but remained >89%. We had 100% success for the years 6, 7, 8, and 10 and >95% success rates for the fifth year. Note that success rates improved as children grew older and had more experience with the procedures.

In Tables 3 and 4, we can see that the primary reasons for failure in the longitudinal study were because the family lost interest or could not be contacted or children had braces in their teenage years. However, the most common reason for failure in the cross-sectional study was that children were afraid to be scanned, quit early, or had excessive motion. This suggests that once children are acclimated to being scanned, they are generally successful in subsequent longitudinal sessions. These Tables provide important information for those interested in conducting pediatric fMRI studies.

Desensitization methods, including a practice run on the MR imaging scanner, continual communication, feedback, and reassurance of children, have been found to be important to our success rates. Even though these procedures add time to the imaging session, they have helped us achieve a better success rate in the cross-sectional study and also to ensure that more children return for scans in the subsequent years of the longitudinal study. Annual holiday greeting cards, birthday cards, and a Facebook group for the longitudinal cohort have also improved our long-term retention as the children enter high school and college.

The results from the cross-sectional study show that 77.3% of the girls and 71% of the boys completed the scans successfully. For a cross-sectional study, recruitment should aim for four-thirds of the desired sample size in children ages 8–18 years and 1.5 times in children ages 5–7 years to meet the power requirements of the study. Oversampling will allow a projected overall success rate of 75%. In the longitudinal study, among the 30 children who were recruited, 3 quit the study either due to moving out of town or not wishing to participate further. On the basis of the numbers from Fig 2, it can be seen that during the fifth, sixth, and seventh years,

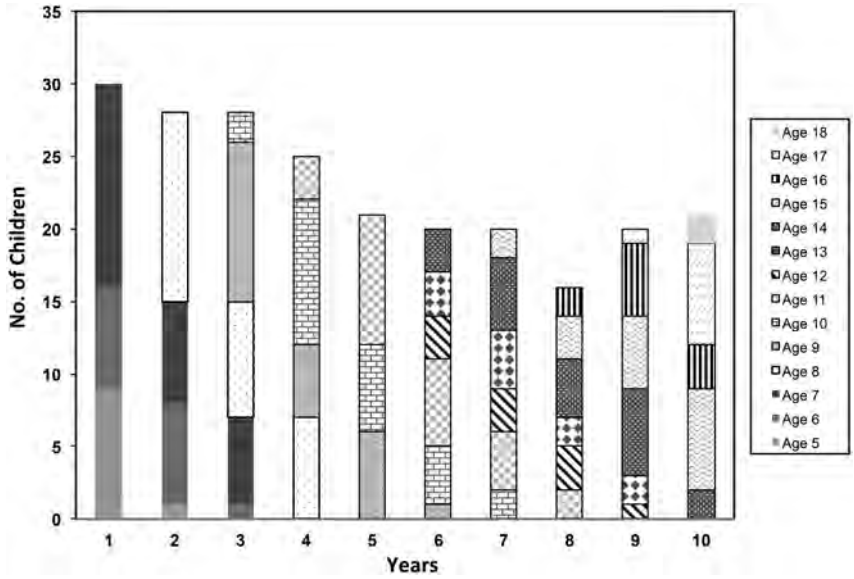

FIG 3. Histogram of the number of children (y-axis) scanned for the longitudinal study annually for 10 years (x-axis). The histogram of the number of children is further sorted on the basis of the age of the children during their visit at each year (gray-scale pattern).

Table 2: Total number of children scanned longitudinally and the tasks completed in the scanner

Study Year	Total Subjects Scanned	Tasks Completed					
		Prosody (%)	Picture (%)	Verbs (%)	Stories (%)	Verbs HUSH (%)	Stories HUSH (%)
1	30	90	86.7	86.7	93.3	NA	NA
2	28	89.3	92.9	96.4	89.3	NA	NA
3	28	89.3	96.4	92.9	92.9	NA	NA
4	25	96	96	96	92	NA	NA
5	21	95.2	100	100	95.2	NA	NA
6	20	NA	NA	100	100	100	100
7	20	NA	NA	100	100	100	100
8	16	NA	NA	100	100	100	100
9	20	NA	NA	100	100	90	95
10	21	NA	NA	100	100	100	100

Note:—NA indicates not applicable.

Table 3: Reasons for failure to complete fMRI tasks for the cross-sectional cohort and the number of children who failed for each reason[a]

	Cross-Sectional			
Criteria	SR(0)	SR(25)	SR(50)	SR(75)
Frightened	36	0	3	2
No details	16	0	0	1
Patient quit	8	4	10	17
Technical fault	0	0	1	7
Motion	3	2	2	5

[a] The subject groups completing 0% through 75% of the scans are referred to as SR(0) through SR(75).

Table 4: Reasons for failure to complete fMRI tasks for the longitudinal cohort and the number of children who failed for each reason[a]

	Longitudinal			
Criteria	SR(0)	SR(25)	SR(50)	SR(75)
Braces	34	0	0	0
No details	20	0	0	0
Not interested	16	0	0	0
Patient quit	0	12	11	4
Motion	2	0	0	0

[a] The subject groups completing 0% through 75% of the scans are referred to as SR(0) through SR(75).

fewer children completed the scans. This finding was mainly due to children in the age range from 11 to 18 having braces or retainers that were not MR imaging–compatible.

Limitations

This study is subject to a few limitations that may restrict its generalizability to other populations and centers. Most important, the study was conducted in healthy children who were recruited specifically for a neuroimaging research protocol. Consequently, these children come from highly motivated families who either have altruistic tendencies or an interest in their child's development. The sample may not be representative of healthy populations as a whole because of the increased motivation of the families to participate in a medical research project. Furthermore, this healthy population of children is most certainly not representative of children with various pathologies such as attention deficit/hyperactivity disorder, autism, epilepsy, or other neurologic or psychiatric disorders. Consequently those designing studies with such populations may not be able to directly extrapolate from the failure rates reported in our study.

Another relevant limitation of the study is that it began in 2000 by using a prototype 3T research MR imaging scanner. Technical advances in clinical MR imaging scanner designs operating at this field strength have resulted in much improved image quality and patient throughput. For example, improved laser alignment and prescan procedures have greatly accelerated the time needed to complete a neuroimaging research protocol. The data acquired for this study between 2000 and 2008 were obtained on a 3T Biospect 30/60 (Bruker) scanner with a 60-cm bore and a quadrature head coil with a 210-mm inner diameter. All of the cross-sectional participants in the study were scanned on this early 3T prototype scanner with an accompanying rate of technical failure and other factors potentially impacting success rates. This configuration also necessitated using video goggles rather than a projection screen for visual presentation, which also may have impacted the failure rates.

In the final 2 years of the study, longitudinal participants were scanned on a more modern 3T Achieva (Philips Healthcare, Best, the Netherlands) MR imaging scanner. As with other modern clinical 3T MR imaging scanners, the system offers a wider bore, more open head coil design with an improved signal-to-noise ratio and image quality. Throughput is improved with better alignment tools and prescanning protocols, resulting in improved success rates for children. These factors are folded into the improved success rates we report for longitudinal subjects in later years and introduce confounding to our analysis.

Finally, with the wider installation of clinical 3T MR imaging scanners in research laboratories and clinical environments, more centers have begun to conduct neuroimaging studies of development in pediatric populations. Several centers, including ours, have developed desensitization protocols that involve pretraining of pediatric participants by introducing them to the noises that MR imaging scanners make for several days before the scanning session and training videos that introduce participants to the MR imaging scanner and laboratory environment before they arrive for their first session.[17] These techniques have proved to work effectively to gain a higher level of cooperation from children. While the current study used some of these methods as we have reported previously,[4,5] our newer methodology may result in better success rates than what we have reported here.

CONCLUSIONS

The success rates provided in this article are relevant for planning future cross-sectional or longitudinal functional imaging studies in normally developing healthy children. On the basis of the success rate analysis by age, when designing fMRI studies involving typical children, the sample size indicated by appropriate power analysis must be increased by 33% in ages older than 8 years and 50% in children 5–7 years of age. This percentage might have to be slightly higher for boys compared with girls because girls tend to comply with the behavioral demands of fMRI scans in the 5- to 18-year age group. While success rates for longitudinal participants are higher than those for the cross-sectional population in general, powering a pediatric neuroimaging study design as outlined above will provide sufficient high-quality data to permit longitudinal data analysis for a study ranging up to 10 years in duration.

Disclosures: Akila Rajagopal—*RELATED*: *Grant*: National Institutes of Health R01-HD38578.* Anna Byars—*RELATED*: *Grant*: National Institutes of Health.* Mark Schapiro—*RELATED*: *Grant*: National Institutes of Health,* *Comments*: I receive support from a National Institutes of Health contract. Gregory R. Lee—*RELATED*: *Grant*: National Institutes of Health: National Institute of Child Health and Human Development, *Comments*: primary source of funding for the study; *Support for Travel to Meetings for the Study or Other Purposes*: National Institutes of Health: National Institute of Child Health and Human Development. Scott K. Holland—*RELATED*: *Grant*: National Institutes of Health R01-HD38578*; *Support for Travel to Meetings for the Study or Other Purposes*: National Institutes of Health,* *Comments*: presentations at Human Brain Mapping, American Society of Neuroradiology, and other meetings; *UNRELATED*: *Grants/Grants Pending*: National Institutes of Health R01-HD38578,* *Comments*: no financial benefit to me personally or to my company. The grant was used exclusively to pay for the research study. *Money paid to the institution.

REFERENCES

1. Ogawa S, Lee TM, Kay AR, et al. **Brain magnetic resonance imaging with contrast dependent on blood oxygenation.** *Proc Natl Acad Sci U S A* 1990;87:9868–72
2. Hingwala D, Thomas B, Radhakrishnan A, et al. **Correlation between anatomic landmarks and fMRI in detection of the sensorimotor cortex in patients with structural lesions.** *Acta Radiol* 2014;55:107–13
3. Zhang J, Mei S, Liu Q, et al. **fMRI and DTI assessment of patients undergoing radical epilepsy surgery.** *Epilepsy Res* 2013;104:253–63
4. Byars AW, Holland SK, Strawsburg RH, et al. **Practical aspects of conducting large-scale functional magnetic resonance imaging studies in children.** *J Child Neurol* 2002;17:885–90
5. Yerys BE, Jankowski KF, Shook D, et al. **The fMRI success rate of children and adolescents: typical development, epilepsy, attention deficit/hyperactivity disorder, and autism spectrum disorders.** *Hum Brain Mapp* 2009;30:3426–35
6. Holland SK, Vannest J, Mecoli M, et al. **Functional MRI of language lateralization during development in children.** *Int J Audiol* 2007;46:533–51
7. Holland SK, Plante E, Weber Byars A, et al. **Normal fMRI brain activation patterns in children performing a verb generation task.** *Neuroimage* 2001;14:837–43
8. Karunanayaka PR, Holland SK, Schmithorst VJ, et al. **Age-related connectivity changes in fMRI data from children listening to stories.** *Neuroimage* 2007;34:349–60
9. Plante E, Holland SK, Schmithorst VJ. **Prosodic processing by children: an fMRI study.** *Brain Lang* 2006;97:332–42
10. Schmithorst VJ, Holland SK, Plante E. **Object identification and lexical/semantic access in children: a functional magnetic resonance imaging study of word-picture matching.** *Hum Brain Mapp* 2007;28:1060–74
11. Vannest JJ, Karunanayaka PR, Altaye M, et al. **Comparison of fMRI data from passive listening and active-response story processing tasks in children.** *J Magn Reson Imaging* 2009;29:971–76
12. Vannest J, Rasmussen J, Eaton KP, et al. **FMRI activation in language areas correlates with verb generation performance in children.** *Neuropediatrics* 2010;41:235–39
13. Schmithorst VJ, Holland SK. **Event-related fMRI technique for auditory processing with hemodynamics unrelated to acoustic gradient noise.** *Magn Reson Med* 2004;51:399–402
14. Birn RM, Bandettini PA, Cox RW, et al. **Event-related fMRI of tasks involving brief motion.** *Hum Brain Mapp* 1999;7:106–14
15. Yuan W, Altaye M, Ret J, et al. **Quantification of head motion in children during various fMRI language tasks.** *Hum Brain Mapp* 2009;30:1481–89
16. Schmithorst VJ, Dardzinski BJ, Holland SK**. Simultaneous correction of ghost and geometrical distortion artifacts in using a multiecho reference scan.** *IEEE Trans Med Imaging* 2001;20:535–39
17. Vannest J. **Behavioral methods for successful non-sedated MRI in infants and young children.** In: *Proceedings of New Horizons in Human Brain Imaging*, Oahu, Hawaii. March 5–7, 2014

A Novel Flow-Diverting Device (Tubridge) for the Treatment of 28 Large or Giant Intracranial Aneurysms: A Single-Center Experience

Y. Zhou, P.-F. Yang, Y.-B. Fang, Y. Xu, B. Hong, W.-Y. Zhao, Q. Li, R. Zhao, Q.-H. Huang, and J.-M. Liu

ABSTRACT

BACKGROUND AND PURPOSE: The Tubridge flow diverter is a novel device developed in China and aimed at reconstructing the parent artery and occluding the aneurysm. We conducted this study to evaluate its feasibility, safety, and efficacy for the treatment of large or giant internal carotid artery aneurysms, which are still challenging with conventional therapy.

MATERIALS AND METHODS: The clinical and angiographic data of 28 patients with 28 large or giant internal carotid artery aneurysms treated with Tubridge flow diverters were prospectively collected and analyzed.

RESULTS: Thirty-three Tubridge flow diverters were successfully implanted except for 1 poor midstent opening; the result was a technical success rate of 97.0% (32/33). Follow-up angiographies were available for 25 aneurysms; the mean follow-up was 9.9 months (5–24 months). Of the 25 aneurysms, 18 (72.0%) were completely occluded, 6 (24.0%) were improved, and 1 (4.0%) was unchanged. All of the visible covered branches and parent arteries were patent, with no stenosis or obliteration. During a follow-up of 6–30 months (mean, 19 months), symptoms were resolved in 13 patients, improved in 6 patients, and unchanged in 4 patients. Five patients experienced transient clinical deterioration due to a postoperative increased mass effect. Procedure-related morbidity and mortality were both zero.

CONCLUSIONS: Our preliminary experience shows that the Tubridge flow diverter is a safe and effective tool for treating large and giant internal carotid artery aneurysms. However, multicenter randomized trials and studies involving a long-term follow-up are necessary.

ABBREVIATIONS: FD = flow diversion; ID = inse diameter

Large and giant aneurysms are associated with much worse outcomes than small ones.[1] The treatment of large and giant aneurysms is challenging for both neurosurgeons and neurointerventionalists, either by conventional endovascular treatment or surgery. Deconstructive approaches, such as ICA occlusion, require sufficient compensation from other blood vessels. Even when this criterion is satisfied, the rate of ischemia has been reported to be as high as 4%–15%.[2] In addition, there is a chance of de novo aneurysm following ICA occlusion.[3] Bypass surgery, especially high-flow bypass, preceding ICA occlusion may help to reduce the occurrence of ischemic complications, but operative complications are not uncommon, though the rate varies in different articles.[4] In contrast, reconstructive approaches aimed at preserving the parent artery were associated with greatly increased recanalization rates that were reported to range from 19.2% to 50%.[2,5]

The Tubridge is a new type of flow-diversion (FD) device developed by MicroPort Medical Company (Shanghai, China) on the basis of our previous hemodynamic studies of intracranial aneurysms,[6] aimed at treating complex aneurysms that were difficult to access via clipping or conventional endovascular treatment, such as large and giant aneurysms, and providing more treatment options for neurointerventionalists and neurosurgeons. After demonstrating its efficacy and safety in animal experiments,[7,8] we obtained the consent of the Ethics Committee and China Food and Drug Administration to initiate the present prospective clinical trial, aimed at evaluating its feasibility, safety, and efficacy for the treatment of large or giant internal carotid artery aneurysms.

Received November 12, 2013; accepted after revision February 3, 2014.

From the Department of Neurosurgery, Changhai Hospital, Second Military Medical University, Shanghai, P.R. China.

Yu Zhou and Peng-Fei Yang contributed equally to this work.

This work was supported by the Subproject of National Technology Supporting Program (2011BAI08B14), Logistics Scientific Research Project (BWS11C008), and the Science and Technology Commission of Shanghai Municipality (10441901902, 10DZ0510800).

Please address correspondence to Qing-Hai Huang, MD, Department of Neurosurgery, Changhai Hospital, Second Military Medical University, 168 Changhai Rd, Shanghai 200433, China; e-mail: ocinhqh@163.com; and Jian-Min Liu, MD, Department of Neurosurgery, Changhai Hospital, Second Military Medical University, 168 Changhai Rd, Shanghai 200433, China; e-mail: Chstroke@163.com

http://dx.doi.org/10.3174/ajnr.A3925

MATERIALS AND METHODS

Patient Selection and Population

After obtaining approval from the Ethics Committee and China Food and Drug Administration, we conducted this prospective study. The inclusion criteria for Tubridge flow-diverter placement were as follows: 1) The subject understands the nature of the procedure and provides written informed consent; 2) the subject is willing to return to the investigational site for the 30-day and 6-month follow-up evaluations, at least; 3) the subject is 18–75 years of age; 4) the subject has ≥1 wide-neck aneurysm (neck diameter of ≥4.0 mm or dome/neck ratio of ≤1); 5) saccular aneurysms are ≥10 mm; 5) the diameter of the parent artery is 2.0–6.5 mm; and 6) the internal carotid artery aneurysm is unruptured. Aneurysms that were ruptured, dissecting, or comorbid with other intracranial diseases were excluded. Recanalized large or giant aneurysms were also included in this study. Therapeutic alternatives, including conventional endovascular treatment or flow-diversion treatment, were considered by the authors of the present article to determine the most appropriate course of treatment. Written consent was obtained from each patient.

Overall, 28 patients with 28 large or giant aneurysms were recruited between August 2010 and August 2012 (2 patients had multiple aneurysms, which were located at the opposite side of the target aneurysms, and were not included in this study). The group comprised 8 men and 20 women; the mean age was 54.8 years (range, 20–73 years). The clinical presentations of these patients varied and included no symptoms ($n = 6$), headache ($n = 11$), recanalization ($n = 3$), oculomotor paralysis ($n = 7$), blurred vision ($n = 3$), blindness ($n = 1$), and amenorrhea ($n = 1$). Endovascular treatments were performed by 2 authors of the present article (J.-M.L. and Q.-H.H), each of whom has >10 years of experience in intracranial stent placement. Of the 3 recanalized aneurysms, 1 case was treated with coils alone, and the remaining 2 cases were treated with stent-assisted coiling with either Neuroform (Stryker Neurovascular, Fremont, California) or LEO (Balt Extrusion, Montmorency, France).

Aneurysm Morphology

Locations of the 28 aneurysms were defined on the basis of the segment of the ICA (according to the classification of Bouthillier et al[9]) where the aneurysm necks were found. Thus, 1 of the 28 aneurysms was located at the petrous segment (the ICA within the carotid canal), 10 were located in the cavernous segment (the ICA from the superior margin of the petrolingual ligament to the proximal dural ring), 7 were located in the paraclinoid segment (the ICA that begins at the proximal dural ring and ends at the distal dural ring where the ICA becomes intradural), 8 were located in the ophthalmic segment (the ICA that begins at the distal dural ring and ends just proximal to the origin of the posterior communicating artery), and 2 were located in the communicating segment (the ICA that begins just proximal to the origin of the posterior communicating artery and ends at the ICA bifurcation). The size of the aneurysms ranged from 11.3 to 44 mm, and the mean size was 21.6 mm. The aneurysms were further classified according to size as large (10–15 mm; $n = 4$), very large (15–25 mm; $n = 16$), or giant (≥25 mm; $n = 8$). The diameters of the proximal parent arteries ranged from 3.6 to 5.8 mm. As described above, 3 aneurysms had been treated with coiling or stent-assisted coiling before, while the others were all treated for the first time.

Description of the Tubridge Flow Diverter and the Procedure

The Tubridge flow diverter is a braided, self-expanding stent-like device with flared ends. Current Tubridge flow diverters are available in various diameters (2.5–6.5 mm) and lengths (12–45 mm). The large Tubridge (diameter, ≥3.5 mm) is a braid of 62 nickel-titanium microfilaments and 2 platinum-iridium radio-opaque microfilaments; the small Tubridge (diameter, <3.5 mm) is composed of 46 nitinol and 2 platinum-iridium microfilaments. All Tubridge flow diverters were designed with a pore size of 0.040–0.050 mm^2 at the nominal diameter to provide high metal coverage (approximately 30.0%–35.0%) at the aneurysmal neck after full opening.

The Tubridge is mounted to a delivery wire and constrained within a removable sheath. The tip of the delivery wire is J-shaped, which is designed to help prevent vascular endothelial cell injury and to facilitate microcatheter removal through previous devices and to deploy a second flow diverter. During the implantation procedure, a Tubridge-compatible standard 0.029 inse diameter (ID) microcatheter was placed in the distal segment (approximately 30 mm) of the aneurysm neck with the assistance of a microwire. Then the Tubridge flow-diversion device was introduced via the microcatheter into the target zone. Manipulation during releasing resembles that in Silk flow diverters (Balt Extrusion). After we placed the Tubridge into position by pushing the delivery wire and simultaneously withdrawing the microcatheter, the device began to expand in the artery and was deployed. To increase the proportion of metal coverage at the aneurysm neck, we deliberately pushed the microcatheter toward the aneurysm neck while the aneurysm neck was partially covered by the stent. Generally, the shortening rate after complete deployment of the Tubridge is approximately <50.0%, depending on the size of the Tubridge relative to the vessel and any discrepancies between the proximal and distal vessel diameters. There is a marker in the middle of the Tubridge; the device can be retracted until released to that point. After one deploys the first one, a second flow diverter would be considered if a disturbed inflow jet was not observed.

Seven of the 25 initially treated aneurysms and all of the 3 recanalized aneurysms were treated by using the Tubridge alone; the remaining 18 aneurysms were treated with the Tubridge flow diverter and loose coiling. In the 18 patients treated with a combination of the Tubridge and coils, all flow diverters were deployed after coiling. In 1 aneurysm with an extremely wide neck, 1 LEO stent was deployed first, which was followed by the telescopic placement of 2 Tubridge flow diverters that were delivered through the LEO stent. After the procedure was completed, DynaCT (Siemens, Erlangen, Germany) reconstruction was performed in each patient to ensure the full opening of the Tubridge. To assess the friction associated with the delivery, after the procedure, the 2 operators were required to record their assessments of the delivery process compared with that in Enterprise stents (Codman & Shurtleff, Raynham, Massachusetts), which were classified as "difficult," "comparable," and "better."

Anticoagulation and Antiplatelet Management

Each patient received systemic heparin after the placement of the sheath. The activated clotting time was maintained at 2–3 times the baseline throughout the procedure. Each patient received dual antiplatelet drugs (300 mg/day aspirin plus 75 mg/day clopidogrel) for at least 3 days before the procedure. A postoperative antiplatelet regimen was administered as follows: <6 weeks: 300 mg aspirin + 75 mg clopidogrel; 6 weeks to 3 months: 100 mg aspirin + 75 mg clopidogrel; ≥3 months: 100 mg aspirin indefinitely.

Clinical and Angiographic Evaluation

According to our protocol, each patient was clinically evaluated at discharge and prescribed follow-up assessments at 1, 3, and 6 months posttreatment and yearly thereafter. An angiographic evaluation consisting of digital subtraction angiography was performed immediately after the procedure, at 6 months posttreatment, and yearly thereafter. For aneurysms treated with the Tubridge flow diverter plus coils, the angiographic results obtained immediately after the procedure were classified according to the Raymond classification system. For aneurysms treated with the Tubridge alone, flow modifications were defined as disrupted inflow jet, slow flow (if the contrast circulation within the aneurysm became slower), or reduced contrast filling (if increased contrast stagnation was observed within the aneurysm at the late venous phase of the angiographic series).[10] At follow-up, the angiographic results were independently interpreted by 2 experienced neurosurgeons who were not involved in this study and compared with the initial results to determinate whether the aneurysms were completely occluded, improved, stable, or recanalized. Branches that were covered by flow diverters were examined to confirm patency. Each patient's clinical symptoms were evaluated and recorded as completely/partially relieved or worsening.

RESULTS

The characteristics of the 28 patients treated with Tubridge flow diverters, including demographic information, clinical presentation, morphologic features of the aneurysms, treatment results, and follow-up data are summarized in Tables 1 and 2.

Immediate Angiographic and Clinical Results

Tubridge delivery was successful in all 28 patients. Thirty-three Tubridge flow diverters were implanted, all of which had a large (diameter, ≥3.5 mm) braid of 64 microfilaments. For 5 aneurysms, 2 overlapping flow diverters were deployed, while the remaining 23 aneurysms were treated with a single flow diverter. No obvious difficulties with device delivery or deployment were encountered, and the amount of friction associated with the delivery was comparable with that of Enterprise stents. However, poor midstent opening was identified in 1 patient (1/33, 3.0%) with an aneurysm in the cavernous segment of the internal carotid artery and a remarkable tortuous parent artery. We attempted to expand the poorly opened stent with a microballoon; however, delivery of the microcatheter though the stent proved to be difficult, and the attempt was abandoned. Fortunately, this patient experienced no untoward effects of the procedure, and close clinical observation was arranged (Fig 1).

Table 1: Clinical, angiographic, and follow-up data in 28 patients with 28 large or giant ICA aneurysms

Characteristics	
Patients (aneurysms) (No.)	28 (28)
Mean age (range) (yr)	54.8 (20–73)
Male/female	8:20
Aneurysm location	
ICA communicating	2
ICA ophthalmic	8
ICA paraclinoid	7
ICA cavernous	10
ICA petrous	1
Presentation	
Asymptomatic	6
Headache	11
Recanalization	3
Oculomotor paralysis	7
Blurred vision	3
Blind	1
Amenorrhea	1
Aneurysm size	
Large (10–15 mm)	4
Very large (15–25 mm)	16
Giant (≥25 mm)	8

Table 2: Clinical, angiographic, and follow-up data in 28 patients with 28 large or giant ICA aneurysms

Treatment	
Treatment strategy	
FD alone	10
FD + loose coiling	18
No. implanted flow diverters	
Two overlapping flow diverters	5
Single flow diverter	23
Technique adverse event	
Poor midstent opening	1
Immediate angiographic results	
Partial occlusion	16
Neck remnant	2
Disrupted inflow jet and slow flow	9
Flow reduction	7
No change	3
Clinical symptoms	
Resolved	13
Improved	6
No change	4
Transient worsening	5
Overall procedure-related morbidity/mortality	0/0
Follow-up angiographic results (n = 25)	
Complete occlusion	18 (72%)
Improvement	6 (24%)
Stable	1 (4%)

For the 18 aneurysms treated with a flow diverter and coiling, the immediate angiographic results included neck remnant in 2 aneurysms and sac residue in the remaining 16 aneurysms. For the 10 aneurysms treated with a flow diverter alone, disrupted inflow jet and slow flow were observed in each patient except for the 1 patient with a poor midstent opening; flow reduction was observed in 7 aneurysms (reduction of <50.0% in 5 patients, reduction of ≥50.0% in 2 patients) (Fig 2), and the remaining 3 aneurysms exhibited no obvious change (1 was due to poor midstent opening as described above). In total, there were 27 visible branches covered by the Tubridge, including 23 ophthalmic ar-

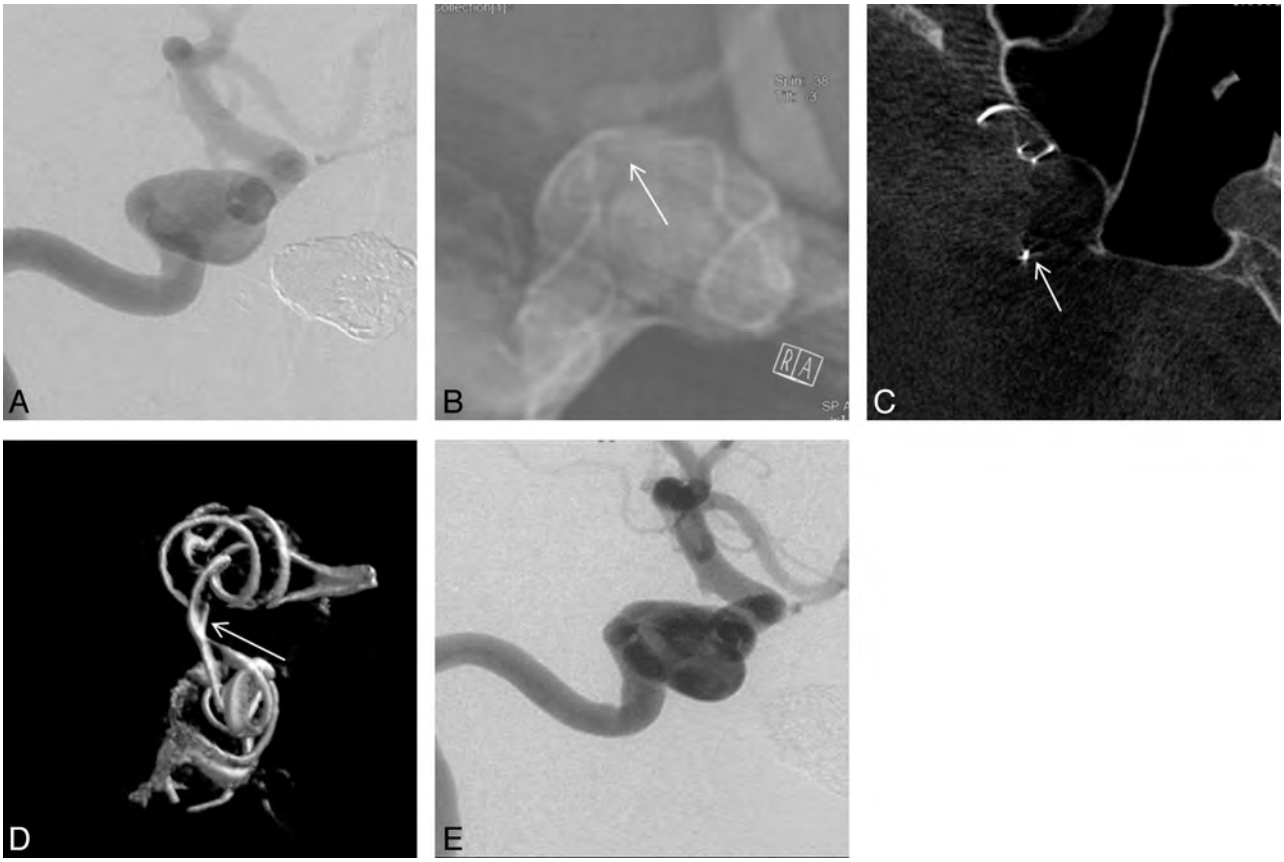

FIG 1. Right internal carotid artery digital subtraction angiography (*A*) revealed a 13-mm wide-neck cavernous segment aneurysm. A Tubridge flow diverter was deployed into the parent artery, aimed at covering the aneurysmal neck, but postoperative DynaCT revealed that the flow diverter was not fully opened (*B*, *white arrow*). Cross-sectional image (*C*, *white arrow*) and 3D reconstruction (*D*, *white arrow*) show poor opening of the device. Fortunately, 18-month follow-up angiography reveals that the aneurysm is stable with a patent artery (*E*).

teries, 2 meningohypophyseal trunks, 1 early frontal branch (in this case, the A1 segment was absent, and the distal part of the Tubridge was deployed into the middle cerebral artery), and 1 posterior communicating artery, all of which were patent following Tubridge deployment.

Clinical Outcome

In all 28 patients, neither ischemic nor hemorrhagic complications occurred. During the follow-up period of 6–30 months (mean, 19.0 months), symptoms were resolved in 13 patients (4 cases of oculomotor paralysis, 9 headaches), improved in 6 patients (3 cases of oculomotor paralysis, 1 case of blurred vision, 2 headaches), and unchanged in 4 patients (2 cases of blurred vision, 1 case of blindness, and 1 case of amenorrhea). Five patients experienced transient clinical deterioration due to a postoperative increase in mass effect. Of these 5, three had moderate headache within 2 weeks after the operation, and 2 experienced worsening oculomotor nerve paralysis within 3 months of the procedure. However, all of these symptoms had resolved by the last follow-up. Thus, there were no instances of procedure-related morbidity or mortality.

Follow-Up Angiographic Results

Twenty-five patients with 25 aneurysms completed a least 1 follow-up cerebral angiography; the remaining patients were unwilling to undergo angiographic follow-up for various reasons. The follow-up periods ranged from 5 to 24 months (mean, 9.9 months). Eighteen of the 25 (72.0%) aneurysms for which follow-up data were available were completely occluded, whereas the 6 (24.0%) in which only a neck remnant was observed (Fig 3) were improved, and 1 (the case in which the stent did not fully open) remained unchanged. Detailed outcomes of aneurysms treated with "FD alone" and "FD plus coiling" are shown in Table 3. In the "FD alone" group, the complete occlusion rate was 75.0%, while that in the "FD plus coiling" group was 70.5%. On the angiograms, parent arteries of all cases were patent, and there was no evidence of intimal hyperplasia or in-stent stenosis. All of the visible covered branches were patent without stenosis or obliteration.

DISCUSSION

In the present article, we report preliminary findings related to the application of Tubridge flow diverters in large or giant ICA aneurysms. Despite the complex morphologies of these aneurysms, the short-term results are satisfactory, with a high technique success rate and minor technique/clinical complications.

Characteristics and Feasibility of Tubridge Flow Diverters

The Tubridge is actually a stentlike vessel-reconstruction device designed with a high metal coverage rate and low porosity. It diverts blood flow away from the aneurysm while preserving normal blood flow of the side branches.

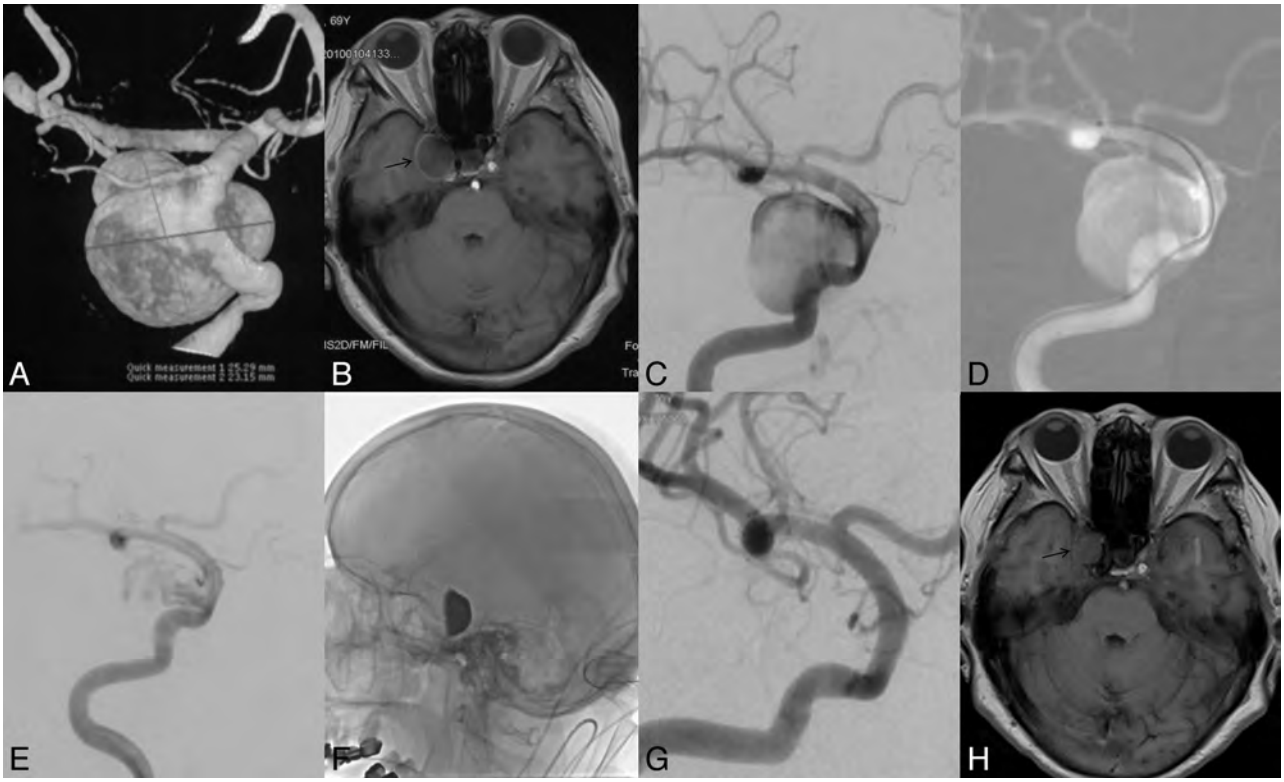

FIG 2. Right internal carotid artery digital subtraction angiography and 3D reconstruction (*A–C*) reveal a giant cavernous segment aneurysm of approximately 25.3 mm. The microcatheter is delivered across the aneurysmal neck (*D*), and 1 Tubridge flow diverter is deployed. Postoperative angiography reveals a disrupted inflow jet, slow flow, and flow reduction (*E* and *F*). The 23-month follow-up angiography reveals that the aneurysm is completely occluded (*G*). *H*, The black arrow points to the patent covered ophthalmic artery during follow-up compared with the preoperative image. MR imaging follow-up shows shrinkage of the aneurysm (*black arrow*).

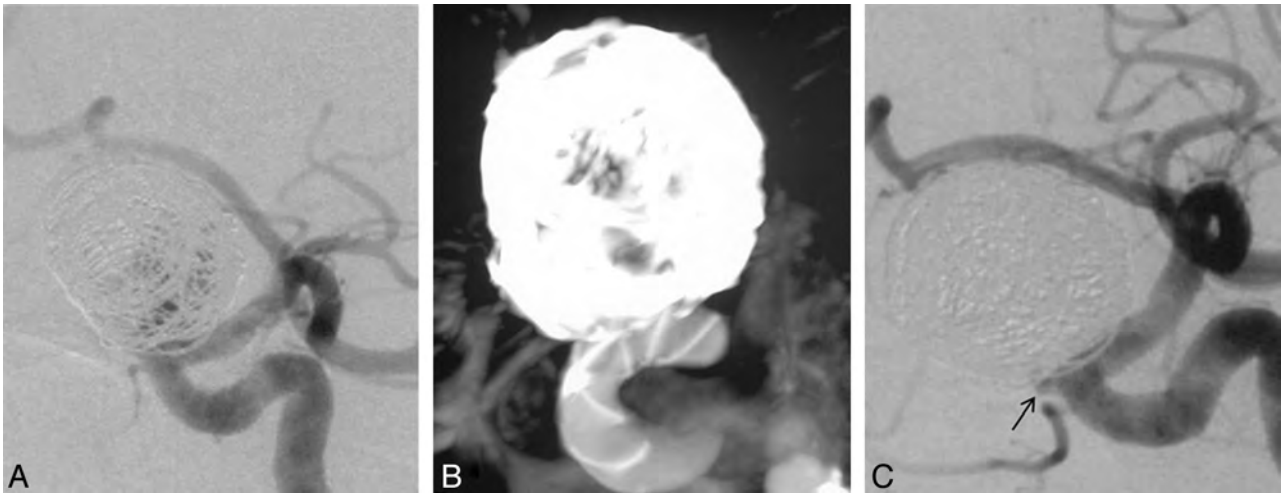

FIG 3. Left internal carotid artery digital subtraction angiography of an aneurysm treated with a Tubridge flow diverter combined with coils, which results in partial occlusion of the aneurysm (*A*). DynaCT reconstruction reveals full opening of the flow diverter (*B*).The 18-month follow-up angiography reveals that the aneurysm has improved, and only a neck remnant is observed (*C*, *black arrow*).

Table 3: Follow-up angiographic outcome of different treatment modalities

	FD Alone	FD Plus Coiling	Total
Complete occlusion	6 (75.0%)	12 (70.5%)	18 (72.0%)
Improved to neck remnant	1 (12.5%)	5 (29.4%)	6 (24.0%)
Unchanged	1 (12.5%)	0	1 (2.0%)
Total	8	17	25

Except for the use of a nickel-titanium alloy (commonly known as nitinol, which exhibits shape-memory and superelasticity) and flared ends, the Tubridge offers multiple structural improvements over the Pipeline Embolization Device (Covidien, Irvine, California) and Silk flow diverters (Table 4). The platinum-iridium material used for the radio-opaque microfilaments improves the visualization of both the diameter and the length during the placement procedure. More important, the use of

Table 4: Structure comparison among different flow diverters

Type	Size (mm)	Braided Microfilaments[a]		Radio-Opaque Microfilaments	Flared End	Metal Coverage	Retrievable
		No.	Material				
Pipeline	3–5.5	48	75% Cobalt chromium and 25% platinum	NA	No	30%–35%	No[b]
Silk	2.5–5	48	Nickel-titanium alloy	4 Platinum wires	Yes	35%–55%	Yes
Surpass	2.5–5	2.5 mm, 36; 3 and 4 mm, 60; 5 mm, 84	Cobalt-chromium	12 Platinum wires	No	30%	NA
Tubridge	2.5–6.5	<3.5 mm, 46; ≥3.5 mm, 62	Nickel-titanium alloy	2 Platinum-iridium wires	Yes	30%–35%	Yes

Note:—NA indicates not applicable.

[a] Braided microfilaments mean those main wires excluding microfilaments especially for radio-opaque usage.

[b] The Pipeline Embolization Device is not retrievable, but at any point up to final deployment, it may be captured and removed from the body.

more braided microfilaments for the large-size flow diverter decreases the shortening rate of the flow diverter after full opening and offers more appropriate pore attenuation compared with the 48-wire design of the Silk or Pipeline flow diverters. Similarly, the recently introduced Surpass flow diverter (Stryker Neurovascular) was also designed with different structures: The 2.5-mm-diameter device has 48 wires, whereas the 3- and 4-mm devices have 72 wires and the 5-mm device is constructed of 96 wires.[11] Moreover, their users experienced neither the complications of device migration nor incomplete neck coverage due to device shortening as reported in early series.[10,12] We believe that these structural improvements combined with extensive operator expertise (both of our operators had practiced the delivery and deployment of the Tubridge on models and gained full knowledge of the Tubridge characteristics before placing it in humans) reduced the chance of technical adverse events in patients treated with FD.

A major concern during Tubridge development was related to theoretic difficulties of placing a device with more braided microfilaments. However, no remarkable delivery difficulties occurred. In the present trial, all flow diverters were successfully deployed except for 1; this outcome resulted in a technical adverse events rate of 3.0%. Additionally, no flow diverters fell into the aneurysmal sac or missed complete neck coverage due to device shortening. These results are comparable with those reported in other FD series; technical adverse events rates for the Pipeline and Silk flow diverters have been reported as 2.3%–13% and 12.3%–23.1%, respectively.[10,12-23]

In theory, a flow diverter can promote healing in aneurysms without additional coiling. However, coils were introduced into the aneurismal sac simultaneously with flow diverter placement in 18 aneurysms of this series. This was done to help the microcatheter cross the neck of extremely wide-neck aneurysms and/or to promote aneurysm thrombosis to prevent early or delayed aneurysm rupture.[20] Additionally, for extremely wide-neck aneurysms, coils may provide good support for implanted flow diverters and help stabilize a flow diverter during deployment. Otherwise, flow diverters may protrude into the aneurismal sac due to the impact of blood flow.

Safety of Tubridge Flow Diverters

Although various articles have reported promising results from treating aneurysms with FD, increasing questions have arisen about this type of treatment. In some prospective studies[13,16,18,19,21-26] and series with large numbers[12] of the Pipeline and Silk devices, the periprocedural complication rate has been reported to generally range from 2.8% to 11%, with a rate of ischemia and SAH/intracerebral hemorrhage ranging from 0.9% to 7.7% and 0% to 6.6%, respectively. Delayed complication rates of ischemia, bleeding, and mass effect were reported to be 0%–11.5%, 0%–4.7%, and 0%–23%, respectively. The overall morbidity and mortality associated with Pipeline and Silk in these studies were 0%–15% and 0%–6.6%, respectively. Ischemic complications are generally due to intrastent thrombosis and/or side branch occlusion. However, intrastent thrombus formation and subsequent parent artery occlusion were always related to poor stent opening.[12-17,26] Resistance to antiplatelets is another possible reason; however, for patients with full opening of the stents, the ischemic event rate was not reported to be higher than that for the self-expansion stent,[12-17,26] though the dose of dual antiplatelet medicine varied in different articles.

To date, most side branch occlusion events have been reported to occur in patients who are treated with more than 2 flow diverters or stents: Szikora et al[22] reported 2 cases of ophthalmic artery occlusion, in which the number of flow diverters implanted was either 3 or 4. One patient in the Pipeline Embolization Device for the Intracranial Treatment of Aneurysms Trial experienced lenticulostriate occlusion after the implantation of 2 Pipeline flow diverters and 1 Neuroform stent.[21] In our series, only 1 instance of poor stent opening occurred, which did not lead to occlusion of the parent artery. Moreover, we did not encounter any other periprocedural or delayed ischemic events by using the present antiplatelet regimen. To ensure subject safety in our series, we implanted no more than 2 flow diverters into any single parent artery. In addition, manipulation of the microcatheter and FD can help decrease the metal coverage rate on the aneurysmal neck and minimize the impact of diversion on the intact vessels and perforators. No visible side-branch occlusions were noted in the present series.

Another severe complication associated with flow diverter implantation is intracranial bleeding. Although the exact reason is unknown, some authors believe that increased intrasaccular pressure and unstable thrombus formation may be involved.[20,27] On the basis of reports of these events, the Balt Extrusion Company released an urgent safety notice in 2010, which advised that coils be used in combination with Silk implantation. However, in the present series, we did not encounter any hemorrhagic complications. This outcome may be due to the implantation of additional coils for selected aneurysms. Additional coils may promote thrombi formation in the aneurysm sac and decrease the risk of aneurysm rupture. However, the low rates of hemorrhagic events

observed in the present study may be due to biases associated with small sample sizes. The necessity of additional coil embolization is under review by various randomized clinical trials such as the Efficacy Trial of Intracranial Aneurysm Treatment Using Two Different Endovascular Techniques.[28] A multicenter prospective trail comparing Tubridge flow-diverting treatments with Enterprise stent-assisted coiling, which is also being conducted in China (registered on the Chinese Clinical Trial Registry: ChiCTR-TRC-13003127), may provide more information about the safety of Tubridge implantation.

Large aneurysms, especially those that are very large or giant, are more often associated with thrombus-induced mass effect or perianeurysm edema following flow diverter implantation. However, most of these complications are transient. Byrne et al[24] reported 4 cases of worsening cranial nerve palsy or brain stem compression symptoms due to delayed aneurysm thrombosis and mass effect in 4 patients. Of these 4 patients, 3 recovered and 1 with a basilar artery aneurysm died. Berge et al[19] reported that 15 patients presented with headaches that were associated with worsening symptoms; however, all of these symptoms were transient and eventually resolved. We also observed this phenomenon in 5 of our patients. However, all symptoms had resolved by the follow-up. Furthermore, we observed partial or complete improvement of the symptoms caused by mass effect in most of our patients, except for cases associated with badly damaged nerves.

Efficacy of Tubridge Flow Diverter Implantation

The concept of flow diversion relies on isolating blood flow away from the aneurysm sac and promoting reconstruction of the parent artery, rather than embolizing the aneurysm sac to make it as compact as possible. The immediate angiographic results often indicate a disturbed flow jet, contrast stagnation, or decreased contrast filling, but not complete occlusion (even in aneurysms treated with FD and coils). However, thrombosis will persist during the follow-up period. The available data suggest that the overall complete occlusion rates beyond 6 months for Pipeline and Silk are 68%–87.8% and 68.4%–94.4%, respectively.[12,16,19,25]

In our series, we observed excellent angiographic results after Tubridge implantation. During the mean follow-up period of 9.9 months, 18 aneurysms were completely occluded. The overall complete occlusion rate was 72%, which is comparable with those of silk flow diverters and the Pipeline Embolization Device and appears to be much better than those rates associated with conventional endovascular treatments.[5,29,30] However, studies with a long-term follow-up and larger series are necessary. De Vries et al[11]recently reported their 6-month follow-up result, which showed a complete occlusion (94%), including 1 case with a 95%–100% occlusion. However, their research contained a high number of small aneurysms, which may influence the occlusion rate. There are still 6 improved aneurysms in our series with only a neck remnant observed. These will be followed up to determine whether they will finally be completely occlude.

In this study, we listed the outcome of aneurysms treated with different modalities (Table 3). The FD-alone group seems to be comparable with the FD-plus coiling group; these results may raise doubts about the necessity of additional coils if there is no safety or delivery consideration as discussed above. However, the sample is small, and further study is needed to draw such conclusions.

Limitations

We acknowledge that the major limitations of this study include the relatively small series size, a short angiographic follow-up period, and lack of randomized comparisons with other potentially efficacious therapies. Patient-selection bias may also exist due to the strict inclusion criteria. However, the data suggest that the Tubridge flow diverter is a safe and effective tool for the treatment of large and giant ICA aneurysms.

Another concern is the application of an antiplatelet regimen for flow diverters. An appropriate regimen should minimize the risk of thromboembolic events, while using as low a dose of antiplatelet drugs as possible to avoid of hemorrhagic complications. However, antiplatelet regimens still vary in the literatures; the dose, the intervals, and even the main drug used are different.[11,13,18,19,23,24] Our regimen is modified according to our previous experience of intracranial stent placement, which still seems to be safe for Tubridge implantation. However, multicenter randomized trials with larger subject numbers and long-term follow-up studies are necessary.

CONCLUSIONS

Our preliminary experience demonstrated that the Tubridge flow diverter is a safe and effective tool for the treatment of large and giant ICA aneurysms. However, multicenter randomized trials and long-term follow-up studies are necessary.

Disclosures: J.-M. Liu—*RELATED*: During the development, I gave some advice about the design of this device and offered some data about our previous hemodynamic studies.

REFERENCES

1. Barrow DL, Alleyne C. **Natural history of giant intracranial aneurysms and indications for intervention.** *Clin Neurosurg* 1995;42:214–44
2. Gonzalez NR, Duckwiler G, Jahan R, et al. **Challenges in the endovascular treatment of giant intracranial aneurysms.** *Neurosurgery* 2006;59:S113–24
3. Zhou Y, Yang P, Zhang Y, et al. **Posterior cerebral artery-posterior communicating artery (PCA-PComA) aneurysms: report of five cases and literature review.** *Neurol India* 2012;60:228–30
4. van Doormaal TP, van der Zwan A, Verweij BH, et al. **Treatment of giant and large internal carotid artery aneurysms with a high-flow replacement bypass using the excimer laser-assisted nonocclusive anastomosis technique.** *Neurosurgery* 2008;62(6 suppl 3):1411–18
5. Gao X, Liang G, Li Z, et al. **A single-centre experience and follow-up of patients with endovascular coiling of large and giant intracranial aneurysms with parent artery preservation.** *J Clin Neurosci* 2012; 19:364–69
6. Huang QH, Yang PF, Zhang X, et al. **Effects of flow diverter with low porosity on cerebral aneurysms: a numerical stimulative study** [in Chinese]. *Zhonghua Yi Xue Za Zhi* 2010;90:1024–27
7. Hong B, Wang K, Huang Q, et al. **Effects of metal coverage rate of flow diversion device on neointimal growth at side branch ostium and stented artery: an animal experiment in rabbit abdominal aorta.** *Neuroradiology* 2012;54:849–55
8. Wang K, Huang Q, Hong B, et al. **Correlation of aneurysm occlusion with actual metal coverage at neck after implantation of flow-diverting stent in rabbit models.** *Neuroradiology* 2012;54:607–13

9. Bouthillier A, van Loveren HR, Keller JT. **Segments of the internal carotid artery: a new classification.** *Neurosurgery* 1996;38:425–32
10. Lubicz B, Collignon L, Raphaeli G, et al. **Pipeline flow-diverter stent for endovascular treatment of intracranial aneurysms: preliminary experience in 20 patients with 27 aneurysms.** *World Neurosurg* 2011;76:114–19
11. De Vries J, Boogaarts J, Van Norden A, et al. **New generation of flow diverter (Surpass) for unruptured intracranial aneurysms: a prospective single-center study in 37 patients.** *Stroke* 2013;44:1567–77
12. O'Kelly CJ, Spears J, Chow M, et al. **Canadian experience with the Pipeline embolization device for repair of unruptured intracranial aneurysms.** *AJNR Am J Neuroradiol* 2013;34:381–87
13. Becske T, Kallmes DF, Saatci I, et al. **Pipeline for uncoilable or failed aneurysms: results from a multicenter clinical trial.** *Radiology* 2013;267:858–68
14. Yeung TW, Lai V, Lau HY, et al. **Long-term outcome of endovascular reconstruction with the Pipeline embolization device in the management of unruptured dissecting aneurysms of the intracranial vertebral artery.** *J Neurosurg* 2012;116:882–87
15. Wagner A, Cortsen M, Hauerberg J, et al. **Treatment of intracranial aneurysms: reconstruction of the parent artery with flow-diverting (Silk) stent.** *Neuroradiology* 2012;54:709–18
16. Velioglu M, Kizilkilic O, Selcuk H, et al. **Early and midterm results of complex cerebral aneurysms treated with Silk stent.** *Neuroradiology* 2012;54:1355–65
17. Tähtinen OI, Manninen HI, Vanninen RL, et al. **The Silk flow-diverting stent in the endovascular treatment of complex intracranial aneurysms: technical aspects and midterm results in 24 consecutive patients.** *Neurosurgery* 2012;70:617–23
18. Fischer S, Vajda Z, Aguilar Perez M, et al. **Pipeline embolization device (PED) for neurovascular reconstruction: initial experience in the treatment of 101 intracranial aneurysms and dissections.** *Neuroradiology* 2012;54:369–82
19. Berge J, Biondi A, Machi P, et al. **Flow-diverter Silk stent for the treatment of intracranial aneurysms: 1-year follow-up in a multicenter study.** *AJNR Am J Neuroradiol* 2012;33:1150–55
20. Turowski B, Macht S, Kulcsar Z, et al. **Early fatal hemorrhage after endovascular cerebral aneurysm treatment with a flow diverter (SILK-stent): do we need to rethink our concepts?** *Neuroradiology* 2011;53:37–41
21. Nelson PK, Lylyk P, Szikora I, et al. **The Pipeline embolization device for the intracranial treatment of aneurysms trial.** *AJNR Am J Neuroradiol* 2011;32:34–40
22. Szikora I, Berentei Z, Kulcsar Z, et al. **Treatment of intracranial aneurysms by functional reconstruction of the parent artery: the Budapest experience with the Pipeline embolization device.** *AJNR Am J Neuroradiol* 2010;31:1139–47
23. Lubicz B, Collignon L, Raphaeli G, et al. **Flow-diverter stent for the endovascular treatment of intracranial aneurysms: a prospective study in 29 patients with 34 aneurysms.** *Stroke* 2010;41:2247–53
24. Byrne JV, Beltechi R, Yarnold JA, et al. **Early experience in the treatment of intra-cranial aneurysms by endovascular flow diversion: a multicentre prospective study.** *PLoS One* 2010;5:e12492
25. Lylyk P, Miranda C, Ceratto R, et al. **Curative endovascular reconstruction of cerebral aneurysms with the Pipeline embolization device: the Buenos Aires experience.** *Neurosurgery* 2009; 64:632–42
26. McAuliffe W, Wycoco V, Rice H, et al. **Immediate and midterm results following treatment of unruptured intracranial aneurysms with the Pipeline embolization device.** *AJNR Am J Neuroradiol* 2012;33:164–70
27. Hassan T, Ahmed YM, Hassan AA. **The adverse effects of flow-diverter stent-like devices on the flow pattern of saccular intracranial aneurysm models: computational fluid dynamics study.** *Acta Neurochir (Wien)* 2011;153:1633–40
28. ClinicalTrials.gov. Multicenter Randomized Trial on Selective Endovascular Aneurysm Occlusion With Coils Versus Parent Vessel Reconstruction Using the SILK Flow Diverter (MARCO POLO Post-Market Clinical Investigation). http://www.clinicaltrials.gov/ct2/show/NCT01084681?term=Marco+Polo&rank=1. Accessed March 17, 2014
29. Ferns SP, Sprengers ME, van Rooij WJ, et al. **Coiling of intracranial aneurysms: a systematic review on initial occlusion and reopening and retreatment rates.** *Stroke* 2009;40:e523–29
30. Sluzewski M, Menovsky T, van Rooij WJ, et al. **Coiling of very large or giant cerebral aneurysms: long-term clinical and serial angiographic results.** *AJNR Am J Neuroradiol* 2003;24:257–62

Cavernous Carotid Aneurysms in the Era of Flow Diversion: A Need to Revisit Treatment Paradigms

O. Tanweer, E. Raz, A. Brunswick, D. Zumofen, M. Shapiro, H.A. Riina, M. Fouladvand, T. Becske, and P.K. Nelson

ABSTRACT

BACKGROUND AND PURPOSE: Recent techniques of endoluminal reconstruction with flow-diverting stents have not been incorporated into treatment algorithms for cavernous carotid aneurysms. This study examines the authors' institutional experience and a systematic review of the literature for outcomes and complications using the Pipeline Embolization Device in unruptured cavernous carotid aneurysms.

MATERIALS AND METHODS: A retrospective search for cavernous carotid aneurysms from a prospectively collected data base of aneurysms treated with the Pipeline Embolization Device at our institution was performed. Baseline demographic, clinical, and laboratory values; intrainterventional data; and data at all follow-up visits were collected. A systematic review of the literature for complication data was performed with inquiries sent when clarification of data was needed.

RESULTS: Forty-three cavernous carotid aneurysms were included in the study. Our mean radiographic follow-up was 2.05 years. On last follow-up, 88.4% of the aneurysms treated had complete or near-complete occlusion. Aneurysm complete or near-complete occlusion rates at 6 months, 12 months, and 36 months were 81.4%, 89.7%, and 100%, respectively. Of patients with neuro-ophthalmologic deficits on presentation, 84.2% had improvement in their visual symptoms. Overall, we had a 0% mortality rate and a 2.3% major neurologic complication rate. Our systematic review of the literature yielded 227 cavernous carotid aneurysms treated with the Pipeline Embolization Device with mortality and morbidity rates of 0.4% and 3.1%, respectively.

CONCLUSIONS: Endoluminal reconstruction with flow diversion for large unruptured cavernous carotid aneurysms can yield high efficacy with low complications. Further long-term data will be helpful in assessing the durability of the cure; however, we advocate a revisiting of current management paradigms for cavernous carotid aneurysms.

ABBREVIATIONS: CCA = cavernous carotid aneurysm; PED = Pipeline Embolization Device

Cavernous carotid aneurysms (CCAs) are a distinct form of extradural intracranial aneurysms. The natural history of CCAs has been studied, with the conclusion that these aneurysms have a low risk of causing major morbidity and mortality.[1-4] However, once they reach the size at which they penetrate or protrude through the dura, they, like other intradural aneurysms, carry the risk of subarachnoid hemorrhage. The overall relatively benign natural history has been weighed against traditional treatment options, including surgical clipping, parent artery occlusion with or without bypass, and endovascular coiling, all of which carry varying risks of major morbidity and mortality. The result has shown that expectant management for most CCAs carries a significantly lower risk than treatment, and this has been the standard of care for most CCAs for the past several decades.

The consensus among practitioners has been that CCAs merit treatment only in narrowly defined circumstances (Table 1).[1-3] Underlying reasons to pursue conservative management also include the low annual rupture rate of CCAs and their tendency to rupture into the cavernous sinus, leading to carotid cavernous fistula formation rather than subarachnoid hemorrhage.

A treatment option that can offer a durable solution with low morbidity and mortality would warrant reconsideration of our current treatment paradigms for CCAs. Recently, flow diversion by using the Pipeline Embolization Device (PED; Covidien,

Received January 29, 2014; accepted after revision May 13.

From the Departments of Neurosurgery (O.T., A.B., D.Z., P.K.N.), Radiology (E.R., D.Z., M.S., H.A.R., T.B., P.K.N.), and Neurology (M.F., T.B., P.K.N.), New York University School of Medicine, New York, New York.

PED devices were provided free by Chestnut Medical for 16 of the described patients as part of the Pipeline Embolization Device for Uncoilable or Failed Aneurysms trial.

Please address correspondence to Peter K. Nelson, MD, Department of Radiology, New York University School of Medicine, 660 First Ave, New York, NY 10016; e-mail: peter.nelson@nyumc.org

http://dx.doi.org/10.3174/ajnr.A4081

Table 1: Generally accepted indications to treat CCAs

Indications
Symptomatic CCAs
Symptomatic mass effect (ophthalmoplegia or intractable retro-orbital pain)
Symptomatic with acute thrombotic changes
Symptomatic or asymptomatic CCAs
Ruptured aneurysms
Bony erosion
Radiographic evidence of projection into subarachnoid space
Underlying coagulopathy
Large aneurysms (>10 mm)
Evidence of growth of aneurysms

Irvine, California)[5] has been introduced and approved by the FDA for treatment of internal carotid artery aneurysms. In early studies, the PED was considered feasible for deployment in most CCAs,[6] and since then, many studies have reported its safety and feasibility for the treatment of anterior circulation aneurysms.[5,7,8] Because the natural history of CCAs is generally favorable, the burden of intervention lies with the success and safety of a device.

We present a single-center study of CCAs treated with the PED and the outcomes and complications. In addition, we review the current literature for morbidity and mortality of CCA treatment with flow diversion. This analysis and accumulation of outcome data may help provide further insight into the ongoing dilemma of management of CCAs.

MATERIALS AND METHODS

The data for this study were collected prospectively but reviewed retrospectively. Our institutional review board approval was obtained prospectively, as part of a larger study. Informed consent was obtained from all participants; the study was compliant with Health Insurance Portability and Accountability Act regulations. From a larger cohort of 126 consecutive subjects treated before December 2011, 43 patients had treatment of a CCA with a PED. Aneurysms of acute dissecting, traumatic, and infectious etiology were excluded.

We recorded the following baseline demographic, clinical, and laboratory values: age, sex, and baseline neuro-ophthalmologic examination (performed by a neuro-ophthalmologist, M.F.). Intrainterventional data recorded were the location of the aneurysm, the size of the aneurysm, and the number of PEDs deployed. At follow-up, the time interval from the procedure, the complete or partial aneurysm occlusion, and ophthalmologic examination (when clinically pertinent) were recorded.

Treatment Protocol

Procedures were performed with the patient under general anesthesia by using 6F or 7F femoral artery access. A 5F or 6F guiding-catheter system was placed into the distal cervical or horizontal petrous segment of the internal carotid artery. A 0.027-inch-inner-diameter microcatheter (Renegade Hi Flo; Boston Scientific, Natick, Massachusetts or Marksman; Covidien) was then manipulated over a 0.014- to 0.016-inch microwire (Transend-14, Transend-18; Stryker Neurovascular or Headliner-16; Terumo, Tokyo, Japan) into a position across the aneurysm neck. Once the microcatheter was in position, the PED was loaded into the hub of the delivery microcatheter and advanced. The device was then deployed through a technique previously described.[6] Once deployed, the delivery microcatheter was advanced over the delivery microwire to recapture the microwire and re-establish its position distal to the aneurysm. If needed, additional PEDs were then deployed by using the same technique. Immediate post-treatment angiography was performed in the working projections for PED reconstruction and in the standard angiographic projections. Neurologic status was assessed before treatment, immediately after treatment, and at discharge.

Periprocedural Medications

Most patients received 75 mg of clopidogrel and 325 mg of acetylsalicylic acid per day starting at least 5 days before the procedure. A small number of patients received loading doses during a 48-hour period, with a minimum total preprocedural clopidogrel dose of 300 mg. During the intervention, patients were anticoagulated by an intravenous bolus of heparin sodium (2000–3000 U). Patients continued clopidogrel (75 mg daily) and acetylsalicylic acid (325 mg daily) for a minimum of 180 days after treatment.

Follow-Up Protocol and Imaging Evaluation

Subjects underwent mandatory clinical follow-up and repeat angiography follow-up to assess aneurysm occlusion, PED positioning, and in-stent stenosis. We considered the longest angiographic follow-up when >1 phase of follow-up was available. All angiograms were reviewed by 3 neurointerventionalists. Radiographic outcome was categorized as either complete occlusion, remnant neck (near-complete occlusion), and residual aneurysm. Because no adjunct coils were used, assessment of radiographic outcome was straightforward with 99% interobserver agreement.

All patients underwent neurologic examination on follow-up visits. The patients who presented with visual symptoms were followed by the Neuro-Ophthamology Department. Complications were grouped into mortality, major morbidity (new post-procedure permanent neurologic deficit), and minor morbidity (transient new deficit).

Systematic Literature Review

To assess multicenter complication rates with flow diversion, we performed a systematic literature review. On-line data bases MEDLINE (PubMed) and EMBASE were searched for English language articles published up to April 2013 containing the following search terms: "intracranial aneurysms" or "cavernous carotid aneurysms" or "flow diverter" or "flow diversion" or "Pipeline Embolization Device" or "Silk." In addition, bibliographies were examined for additional articles. Inclusion criteria were the following: a series of ≥5 patients who had 1) flow diversion for CCA, 2) clinical follow-up of at least 3 months, and 3) neurologic complication and mortality data. Studies reporting a larger cohort of aneurysms were included if data on outcomes specific to CCAs were available. When applicable, inquiries to senior authors of studies requiring further clarification on CCA data were made. Studies in which most patients were included in another study or reported trial were eliminated.

Results are represented as mean ± SD. The Fisher exact test

Table 2: Demographics, patient presentation, and aneurysm characteristics

	No. or Mean
Age (yr)	57 ± 14.2
Female	83.7% (36)
Presenting symptom	
Visual	65.1% (28)
Headaches	16.3% (7)
Thromboembolic event	4.7% (2)
Memory	2.3% (1)
Facial pain/numbness	2.3% (1)
Aneurysm maximum diameter (mm)	24.3 ± 9.7
Small, <10 mm	0
Large, 10–25 mm	23
Giant, ≥25 mm	20
Aneurysm neck (mm)	13.6 ± 11.6
Dome-to-neck ratio	2.2 ± .9

was used for comparison of categoric data, given our sample size. *P* values < .05 were statistically significant.

RESULTS

At our institution, 43 CCAs treated with PEDs were included in our study. These cases represented a consecutive cohort of CCAs treated with PEDs up to December 2011. Sixteen of these patients were included in the Pipeline Embolization Device for Uncoilable or Failed Aneurysms study.[7]

Baseline Patient and Aneurysm Characteristics

Forty-three CCAs were present in 41 patients. The average age of the patient was 57 ± 14.2 years old, and 84.1% were female ($n = 36$). None of these aneurysms were ruptured. The major presenting symptoms were ophthalmologic (diplopia, visual field deficits, or change in visual acuity) in 65% of the patients, headaches in 16.3%, and incidental findings in 9.3%. Most aneurysms were large with wide necks. The average maximum diameter of the treated CCAs was 24.3 ± 9.7 mm; the aneurysm neck was 13.6 ± 11.6 mm. The dome/neck ratios were 2.2 ± 0.88. Three of the aneurysms were treated previously with coils, Onyx embolization (Covidien), and coil plus stent, respectively. Partial thrombosis was noted in 25.6% ($n = 11$) of patients (Table 2).

Procedural Specifics

A total of 165 PEDs were deployed in the treatment of the 43 aneurysms. On average, 3.8 ± 2.1 PEDs were used per aneurysm, and no patient was treated with a single PED (range, 2–10). During this period, the longest PED available was 20 mm, partially accounting for the high PED/aneurysm ratio. All PEDs were deployed without complications, and no instance of PED retraction into the aneurysm sac, dissection, or device migration was noted. An intraoperative ipsilateral subarachnoid hemorrhage was encountered in 1 patient. An avulsion of a small branch arising from the angular division of the right middle cerebral artery with slow extravasation of contrast was seen on angiography, and a parenchymal and Sylvian hematoma was revealed by intraprocedural conebeam CT. This likely was the result of a wire perforation during an exchange technique to bypass the aneurysm neck. The bleeding was controlled with deconstructive embolization with Guglielmi detachable coils (Stryker Neurovascular), leading to hemostasis documented by follow-up CT. The patient was discharged to a subacute nursing facility, and her 1-year mRS was 3.

Adjunctive treatments included coil embolization (1 case) and balloon angioplasties. The single adjunctive coil embolization was performed to obtain distal access through the complex aneurysm neck, where 9 coils were placed and used to deflect the Marksman catheter away from the aneurysm dome. Adjunctive balloon angioplasties, however, were more often used in 32.6% of patients ($n = 14$). The goal of balloon angioplasty was either to dilate severely stenotic perianeurysmal segments of the ICA before PED delivery or, in most instances, to appose the device against the vessel wall in cases in which incomplete device opening was noted, especially in case of excessively tortuous anatomy. No instance of vessel injury, dissection, or rupture was experienced during or after balloon angioplasty. An additional indication for balloon use was as an anchor for distal microcatherization of the parent vessel in 1 case.

Radiographic Follow-Up and Clinical Outcomes

Our mean radiographic follow-up was 2.05 years (range, 0.5–3.5 years). All radiographic follow-up was with DSA except for 1 patient in whom CTA was performed. On last follow-up of all patients, 76.7% had complete occlusion of the aneurysm, 11.6% had entry/neck remnant, and 11.6% had residual filling of their aneurysm. Therefore, 88.4% of the aneurysms treated had complete or near-complete occlusion on last follow-up (See Fig 1 for a representative case). Aneurysm complete or near-complete occlusion rates at 6, 12, and 36 months were 81.4%, 89.7%, and 100%, respectively (Fig 2). No migration of PEDs on follow-up studies was noted. In-stent stenosis higher than 50% was found in 3 of 43 patients at 6-month follow-up, and an additional case of stenosis was found at 1-year follow-up. All of these cases were asymptomatic complete occlusion of the parent vessel along with the aneurysm. In addition, there was no instance of aneurysm expansion in our series.

As mentioned above, 1 instance of major neurologic morbidity was encountered during the periprocedural phase. No other major neurologic morbidity or mortality was reported during our follow-up period. Overall, we had a 0% mortality rate and a 2.3% major neurologic complication rate. Three cases of transient neurologic deficits were encountered. One of these was a small ipsilateral frontal hematoma found at 3 days postprocedure. Of the 19 patients who had neuro-ophthalmologic evaluation before PED placement and continuing follow-up afterward, 84.2% had improvement in their visual symptoms; the rest had no improvement and none had worsening. In addition, there were no cases of SAH after treatment during our follow-up. One case of carotid cavernous fistula was found on 6-month follow-up, presenting as tinnitus on posttreatment day 1; however, the patient did not report this symptom.

Systematic Literature Review

Sixteen studies met our inclusion criteria of having at least 5 patients with CCAs in which morbidity and mortality data for that cohort were available and at least 3-month follow-up to ensure that any delayed complications were included. The se-

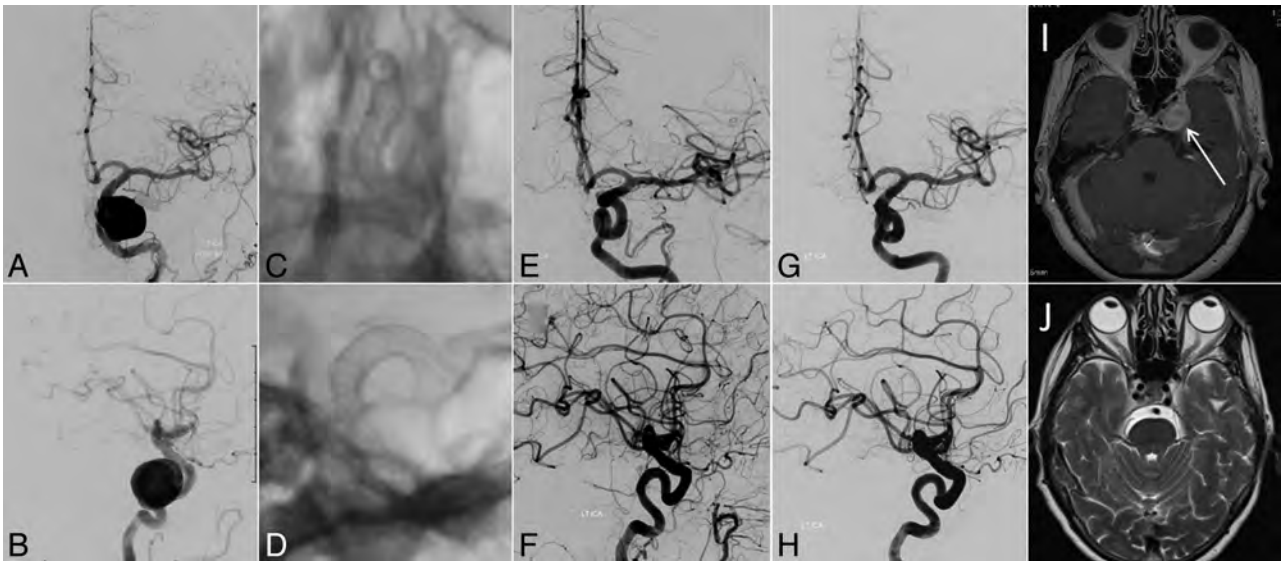

FIG 1. A 65-year-old woman who presented with progressive left-sided ophthalmoparesis due to third and fourth cranial nerve palsy. Digital subtraction angiography in frontal (*A*) and lateral (*B*) views demonstrates a large (19-mm-diameter) aneurysm arising from the cavernous segment of the left internal carotid artery. The patient was treated by endoluminal reconstruction of the LICA with 3 overlapping PEDs (frontal, *C*, and lateral, *D*). One-year follow-up digital subtraction angiography in frontal (*E*) and lateral (*F*) views and 5-year follow-up digital subtraction angiography in frontal (*G*) and lateral (*H*) views confirm stable angiographic cure. Regression of symptoms was correlated with the resolution of aneurysm mass effect as illustrated by comparison of the pretreatment gadolinium-enhanced axial T1-weighted MR image (*I*, *white arrow*) with the 5-year follow-up axial T2-weighted MR image (*J*).

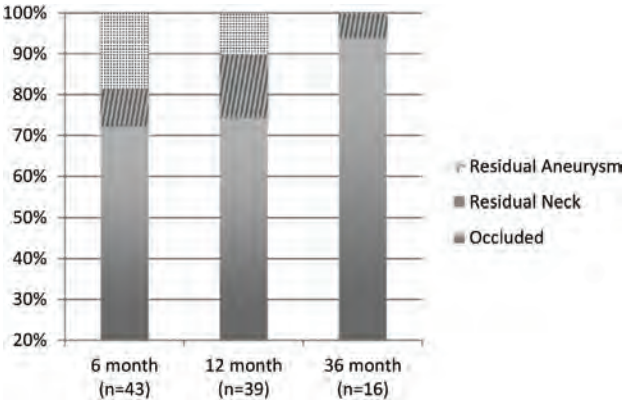

FIG 2. Radiographic outcomes at 6, 12, and 36 months.

nior authors of 6 studies were e-mailed for further clarification of their data, with an 83% response rate with further helpful delineation of their data (Table 3). When we included our data, 296 CCAs treated with flow diversion were found in the literature. A cumulative major morbidity rate was 4.1%, and the mortality rate was 0.7%. A subanalysis looking at studies that used the PED found the morbidity and mortality rates to be only 3.1% and 0.44%, respectively. Studies in which only a Silk flow-diverter stent (Balt Extrusion, Montmorency, France) was used had morbidity and mortality rates of 7.5% and 1.9%, respectively. The greater morbidity seen in Silk studies compared with PED studies trended toward but did not meet statistical significance ($P = .063$).

Table 3: Systematic review of the literature for flow diversion of CCAs

Study	Total Aneurysms in Study	Silk or PED	CCAs (No.)	Major Morbidity (No.)	Mortality (No.)
Berge et al[29]	77	Silk	29	3	0
Becske et al[7,a]	108	PED	28	1	0
Chan et al[30]	13	PED	5	0	0
Chitale et al[31]	42	PED	16	2	0
Cinar et al[32]	55	PED	5	0	0
Fischer et al[33,b]	101	PED	15	1	0
Lubicz et al[34]	34	Silk	5	1	0
Lylyk et al[5]	63	PED	11	0	0
McAuliffe et al[35,c]	57	PED	11	0	0
Nelson et al[6]	31	PED	5	0	0
O'Kelly et al[8]	94	PED	28	0	0
Piano et al[36]	104	Silk	16	1	0
		PED			
Saatci et al[37]	251	PED	28	1	0
Velioglu et al[38,d]	87	Silk	19	0	1
Yu et al[27,e]	178	PED	32	1	1
Current study	43	PED	43	1	0
Total	1338		296	12 (4.1%)	2 (0.7%)
		PED only	227	7 (3.1%)	1 (0.44%)
	0.68	Silk only	53	4 (7.5%)	1 (1.9%)

[a] T. Becske, MD, personal oral communication, April 2013.
[b] H. Henkes, MD, personal e-mail communication, April 2013.
[c] W. McAuliffe, MD, personal e-mail communication, April 2013.
[d] N. Kocer, MD, personal e-mail communication, April 2013.
[e] S.C. Yu, MD, personal e-mail communication, April 2013.

DISCUSSION

In our series of 43 CCAs, we achieved complete or near-complete occlusion of the aneurysm in 88.4% of the patients at last follow-up. By 3 years, 100% of the followed aneurysms achieved complete or near-complete occlusion. This was achieved with 0% mortality and a 2.3% major neurologic complication rate. In addition, 84.2% of the patients with ophthalmologic follow-up had improvement of their presenting visual symptoms. In our systematic review, which included studies from many different centers and countries, the mortality and morbidity rates for treatment of CCAs with PED were 0.44% and 3.1%, respectively.

Natural History of Cavernous Carotid Aneurysms

CCAs, especially when small, rarely rupture. Larger CCAs (>13 mm) had a 5-year rupture rate of 9.4% in the International Study of Unruptured Intracranial Aneurysms trial.[4] When they do rupture, they typically rupture into the cavernous sinus, which leads to carotid cavernous fistula formation. Such a development is far less catastrophic than rupture of intradural aneurysms. However, although rare, SAH from rupture of a CCA with a small intradural component does occur.[1] Unfortunately current imaging is usually unable to clearly distinguish these more dangerous CCAs.[9] There have also been rare case reports of fatal SAH in CCAs judged to be entirely intracavernous.[10]

Several studies have followed the natural history of treated and untreated cohorts of patients with CCA. Stiebel-Kalish et al[3] have published the largest retrospectively reviewed cohort of patients with CCAs. Of 185 patients with CCAs, 74 were treated due to refractory pain, carotid cavernous fistula, sphenoid erosion, diplopia, and compressive optic neuropathy. Among treated patients, pain resolved in 96% of cases. There was no considerable improvement in diplopia, though 61% of patients experienced resolution of symptoms. Of the 111 untreated patients, 2% had stroke, 1% had SAH, 1% had carotid cavernous fistula formation, and 6% developed compressive optic neuropathy; these represented a cumulative 10% adverse event occurrence rate. Quality of life symptoms such as neuro-ophthalmic and refractory pain each resolved spontaneously in 56% of these patients. Moreover, approximately one-third of the untreated patients who were asymptomatic developed symptoms during the course of their 4-year follow-up. The authors also found that those treated by endovascular means (by using preferred methods during a 21-year period) were more likely to experience complications than those not treated. The authors conclude, therefore, that because the risk for major neurologic complications, even in experienced hands, was in the range of 5%–9%, the indications for treatment of CCAs should be carefully considered in each individual case.[3]

Not all studies have come to the same conclusion: A 2003 study compared 21 patients treated for CCAs by using the technology available at the time with 10 not treated and sought to compare outcomes. In the 10 patients followed without intervention, none improved spontaneously, 3 remained the same, and 7 worsened. As a result, the author advocated stronger consideration for treatment.[11]

Treatment Options and Outcomes

Much of the support for the current treatment paradigm is based on the high morbidity and mortality from previously available options for surgical and endovascular intervention. Treatment options are divided into deconstructive and reconstructive approaches. Deconstructive approaches include occlusion of the parent artery with or without a vascular bypass. Reconstructive or constructive approaches aim to preserve the parent artery and include microsurgical clipping, endovascular coiling with or without stents, and now flow diversion with a PED or similar device. Several cohorts of microsurgical clipping have been reported, and even in the best hands, clipping is understandably accompanied by a morbidity and mortality ranging from 14% to 25%.[12-17] Studies of microsurgical carotid occlusion (Hunterian strategies) showed the procedure to be safer, but it still had 9%–22% morbidity and mortality rates.[13,14,16,18]

Studies using endovascular deconstructive carotid occlusion have reported a morbidity and mortality rate ranging from 3% to 8%.[19-23] More recently, van Rooij[24] published his single-center experience with endovascular treatment of CCAs, which demonstrated a low complication rate and high clinical improvement rate. Most procedures being performed were endovascular parent artery occlusion without bypass. During the 15-year span of experience, only 5.8% of the patients had bypasses performed before parent vessel occlusion and approximately 18% of the total CCAs considered for treatment were instead managed conservatively after patients failed balloon test occlusion and did not want to pursue bypass surgery. It is unclear what the follow-up in those 18% of patients was. In another large series of CCAs with Hunterian occlusion, up to 20% required bypass surgery to augment flow.[18]

Although endovascular parent artery occlusion is a relatively easy and inexpensive technique with low morbidity in a selected population, the long-term consequences of altered hemodynamics should be considered. De novo contralateral aneurysm formation is a known sequela of parent artery occlusion, and in a study of case series, there was a 4.5% incidence of new aneurysm formation contralateral to the carotid occlusion at a mean time of 9 years.[25] There was a propensity for large anterior communicating artery flow-related aneurysm formation, which, in the setting of an already occluded ICA, can be a very challenging clinical problem. Because recent treatment outcomes are nearing very low morbidity and mortality (0%–2.3%), the incidence of contralateral aneurysm formation is of important consideration. For these reasons, we advocate preserving normal vascular anatomy whenever possible.

Flow Diversion for CCAs

Numerous cohorts of patients with intracranial aneurysms treated with PEDs have been published in the past several years. A recent meta-analysis of 1654 intracranial aneurysms showed occlusion rates of 76% and procedure-related morbidity and mortality to be 5%.[26] This analysis included posterior circulation aneurysms, which are now well-known to contribute considerable morbidity and mortality. Larger studies stratified by aneurysm location showed that the risk in patients with CCA is low. All studies included in our systematic review reported lower rates of morbidity and mortality compared with their original cohort. In addition, many studies have reported higher occlusion rates among CCA subgroups.[6,27] This extra success afforded to the cavernous segment is likely multifold. Even though this carotid segment is usually tortuous, there were no major bifurcations occurring on it, which resulted in lower wall sheer stress on the vessel wall and less blood flow through the stent. This result likely decreases the chances of an inflow jet and causes more stasis in the aneurysm.

Treatment Paradigms

The high rate of major morbidity and mortality from available treatment options in 2009 led Eddleman et al[1] to elucidate a treatment paradigm widely in use today. This paradigm states that the following CCAs merit treatment: large lesions; symptomatic lesions with acute thrombotic changes; aneurysms with evidence of

growth; symptomatic lesions with mass effect (ophthalmoplegia) or intractable retro-orbital pain; those with considerable local bone erosion due to risk of fatal epistaxis from rupture; lesions with evidence of projection into the subarachnoid space, which usually cannot be demonstrated; ruptured aneurysms with carotid cavernous fistula, which can rarely lead to intracerebral hemorrhage and ocular ischemia[28]; and CCAs in any patient with an underlying coagulopathy.[1]

With the advent of flow diversion, we now have a new and lowered benchmark for treatment risk. This information should play a critical role in patient discussion of expectant management. Patients who present with smaller CCAs and are asymptomatic should understand the benign natural history of their aneurysms. However, these aneurysms have a possibility of growing, and up to one-third of the time, they may become symptomatic.[3] Clinical symptoms, especially when long-standing, may not be relieved with conservative management and can leave the patient with permanent deficits. Smaller CCAs can be treated with less technical difficulty in catheter navigation and PED deployment. Although we do not advocate treatment of small and asymptomatic CCAs, an informed discussion should take place with the patient about all options, and the psychological impact of the diagnosis on the patient should also be considered.

Our institutional preference is to use flow diversion for most unruptured symptomatic CCAs of any size unless they have favorable morphology for complete coil occlusion without stent placement and asymptomatic large complex CCAs, especially in younger patients. Other treatment options such as parent artery occlusion without or with bypass and coil embolization with possible balloon assistance are still reserved for consideration in patients in whom long-term antiplatelet therapy is contraindicated or when other considerations make these options more favorable. The authors believe this is the time for the neurointerventional community to develop a new treatment paradigm for CCAs in the face of favorable outcomes from flow diversion.

Limitations

This study has several important limitations. Although data were collected prospectively, retrospective review imparts inherent bias. In addition, our institutional bias to treat CCAs with flow diversion when possible can skew outcomes. Because during the study period, a limited amount of stent-assisted coiling of CCAs took place, there is no internal cohort with whom to compare our data. Our systematic review also has several limitations: namely, publication bias, heterogeneity of studies, and the retrospective nature of the studies included.

CONCLUSIONS

CCAs have long been considered benign lesions, but even completely extradural CCAs can have catastrophic complications in a small percentage of patients. Unfortunately, these complications are heterogeneous and difficult to anticipate. Any intervention considered in such a setting must have an even lower risk profile than the natural history of the condition being treated. All previous treatment options for CCAs were clearly shown to be more risky for all but a certain small subset of patients with CCA with predictable high-risk profiles. As a result, previous treatment paradigms have been constructed to address only patients at high risk and may fail to offer treatment to patients of moderate risk. We believe that the evidence showing the safety and efficacy of the PED, especially for treating CCAs, merits reconsideration of this existing treatment paradigm.

Disclosures: Andrew Brunswick—*OTHER RELATIONSHIPS*: I am a neurosurgery resident at New York University, and one of our mentors is Peter K. Nelson (in this article), who helped develop the Pipeline Embolization Device. Daniel Zumofen—*RELATED*: *Grant*: Helmut Hartweg Foundation, Swiss Academia of Medical Sciences, *Comments*: personal scholarship. Maksim Shapiro—*UNRELATED*: *Consultancy*: Covidien, *Comments*: I am a proctor and consultant for Covidien, the manufacturer of the Pipeline Embolization Device; *Grants/Grants Pending*: I received Pipeline Embolization Devices from Covidien for benchtop research; *Payment for Development of Educational Presentations*: I am a proctor and consultant for Covidien, the manufacturer of the Pipeline Embolization Device. Mohammad Fouladvand—*RELATED*: *Consulting Fee or Honorarium*: Covidien; *UNRELATED*: *Consultancy*: Covidien. Tibor Becske—*RELATED*: *Consulting Fee or Honorarium*: Covidien; *Support for Travel to Meetings for the Study or Other Purposes*: Covidien; *UNRELATED*: *Consultancy*: Covidien; *Payment for Lectures (including service on Speakers Bureaus)*: Covidien; *Payment for Development of Educational Presentations:* Covidien. Peter K. Nelson—*UNRELATED*: *Consultancy*: Covidien, *Comments*: fees for PED proctoring and activities.

REFERENCES

1. Eddleman CS, Hurley MC, Bendok BR, et al. **Cavernous carotid aneurysms: to treat or not to treat?** *Neurosurg Focus* 2009;26:E4
2. Kupersmith MJ, Stiebel-Kalish H, Huna-Baron R, et al. **Cavernous carotid aneurysms rarely cause subarachnoid hemorrhage or major neurologic morbidity.** *J Stroke Cerebrovasc Dis* 200211:9–14
3. Stiebel-Kalish H, Kalish Y, Bar-On RH, et al. **Presentation, natural history, and management of carotid cavernous aneurysms.** *Neurosurgery* 2005;57:850–57
4. Wiebers D. **Unruptured intracranial aneurysms: natural history, clinical outcome, and risks of surgical and endovascular treatment.** *Lancet* 2003;362:103–10
5. Lylyk P, Miranda C, Ceratto R, et al. **Curative endovascular reconstruction of cerebral aneurysms with the pipeline embolization device: the Buenos Aires experience.** *Neurosurgery* 2009;64:632–42, discussion 642–43, quiz N6
6. Nelson PK, Lylyk P, Szikora I, et al. **The Pipeline embolization device for the intracranial treatment of aneurysms trial.** *AJNR Am J Neuroradiol* 2011;32:34–40
7. Becske T, Kallmes DF, Saatci I, et al. **Pipeline for uncoilable or failed aneurysms: results from a multicenter clinical trial.** *Radiology* 2013;267:858–68
8. O'Kelly CJ, Spears J, Chow M, et al. **Canadian experience with the Pipeline embolization device for repair of unruptured intracranial aneurysms.** *AJNR Am J Neuroradiol* 2013;34:381–87
9. Shapiro M, Becske T, Riina HA, et al. **Toward an endovascular internal carotid artery classification system.** *AJNR Am J Neuroradiol* 2014;35:230–36
10. Lee AG, Mawad ME, Baskin DS. **Fatal subarachnoid hemorrhage from the rupture of a totally intracavernous carotid aneurysm: case report.** *Neurosurgery* 1996;38:596–98, discussion 598–99
11. Goldenberg-Cohen N. **Long term visual and neurological prognosis in patients with treated and untreated cavernous sinus aneurysms.** *J Neurol Neurosurg Psychiatry* 2004;75:863–67
12. Dolenc V. **Direct microsurgical repair of intracavernous vascular lesions.** *J Neurosurg* 1983;58:824–31
13. Dolenc VV. **Extradural approach to intracavernous ICA aneurysms.** *Acta Neurochir Suppl* 1999;72:99–106
14. Heros RC. **Thromboembolic complications after combined internal carotid ligation and extra- to-intracranial bypass.** *Surg Neurol* 1984;21:75–79
15. Heros RC, Nelson PB, Ojemann RG, et al. **Large and giant paraclinoid aneurysms: surgical techniques, complications, and results.** *Neurosurgery* 1983;12:153–63

16. Jafar JJ, Huang PP. **Surgical treatment of carotid cavernous aneurysms.** *Neurosurg Clin N Am* 1998;9:755–63
17. Swearingen B, Heros RC. **Common carotid occlusion for unclippable carotid aneurysms: an old but still effective operation.** *Neurosurgery* 1987;21:288–95
18. Drake CG, Peerless SJ, Ferguson GG. **Hunterian proximal arterial occlusion for giant aneurysms of the carotid circulation.** *J Neurosurg* 1994;81:656–65
19. Niiro M, Shimozuru T, Nakamura K, et al. **Long-term follow-up study of patients with cavernous sinus aneurysm treated by proximal occlusion.** *Neurol Med Chir (Tokyo)* 2000;40:88–96, discussion 96–97
20. Parkinson RJ, Eddleman CS, Batjer HH, et al. **Giant intracranial aneurysms: endovascular challenges.** *Neurosurgery* 2006;59(5 suppl 3):S103–12, discussion S3–13
21. Ponce FA, Albuquerque FC, McDougall CG, et al. **Combined endovascular and microsurgical management of giant and complex unruptured aneurysms.** *Neurosurg Focus* 2004;17:E11
22. van der Schaaf IC, Brilstra EH, Buskens E, et al. **Endovascular treatment of aneurysms in the cavernous sinus: a systematic review on balloon occlusion of the parent vessel and embolization with coils.** *Stroke* 2002;33:313–18
23. Yonas H, Kaufmann A. **Combined extracranial-intracranial bypass and intraoperative balloon occlusion for the treatment of intracavernous and proximal carotid artery aneurysms.** *Neurosurgery* 1995;36:1234
24. van Rooij WJ. **Endovascular treatment of cavernous sinus aneurysms.** *AJNR Am J Neuroradiol* 2012;33:323–26
25. Arambepola PK, McEvoy SD, Bulsara KR. **De novo aneurysm formation after carotid artery occlusion for cerebral aneurysms.** *Skull Base* 2010;20:405–08
26. Brinjikji W, Murad MH, Lanzino G, et al. **Endovascular treatment of intracranial aneurysms with flow diverters: a meta-analysis.** *Stroke* 2013;44:442–47
27. Yu SC, Kwok CK, Cheng PW, et al. **Intracranial aneurysms: midterm outcome of Pipeline embolization device—a prospective study in 143 patients with 178 aneurysms.** *Radiology* 2012;265:893–901
28. van Rooij WJ, Sluzewski M, Beute GN. **Ruptured cavernous sinus aneurysms causing carotid cavernous fistula: incidence, clinical presentation, treatment, and outcome.** *AJNR Am J Neuroradiol* 2006;27:185–89
29. Berge J, Biondi A, Machi P, et al. **Flow-diverter Silk stent for the treatment of intracranial aneurysms: 1-year follow-up in a multicenter study.** *AJNR Am J Neuroradiol* 2012;33:1150–55
30. Chan TT, Chan KY, Pang PK, et al. **Pipeline embolisation device for wide-necked internal carotid artery aneurysms in a hospital in Hong Kong: preliminary experience.** *Hong Kong Med J* 2011;17:398–404
31. Chitale R, Gonzalez LF, Randazzo C, et al. **Single center experience with Pipeline stent: feasibility, technique, and complications.** *Neurosurgery* 2012;71:679–91, discussion 691
32. Çinar C, Bozkaya H, Oran I. **Endovascular treatment of cranial aneurysms with the Pipeline flow-diverting stent: preliminary midterm results.** *Diagn Interv Radiol* 2013;19:154–64
33. Fischer S, Vajda Z, Aguilar Perez M, et al. **Pipeline embolization device (PED) for neurovascular reconstruction: initial experience in the treatment of 101 intracranial aneurysms and dissections.** *Neuroradiology* 2012;54:369–82
34. Lubicz B, Collignon L, Raphaeli G, et al. **Flow-diverter stent for the endovascular treatment of intracranial aneurysms: a prospective study in 29 patients with 34 aneurysms.** *Stroke* 2010;1:2247–53
35. McAuliffe W, Wycoco V, Rice H, et al. **Immediate and midterm results following treatment of unruptured intracranial aneurysms with the Pipeline embolization device.** *AJNR Am J Neuroradiol* 2012;33:164–70
36. Piano M, Valvassori L, Quilici L, et al. **Midterm and long-term follow-up of cerebral aneurysms treated with flow diverter devices: a single-center experience.** *J Neurosurg* 2013;118:408–16
37. Saatci I, Yavuz K, Ozer C, et al. **Treatment of intracranial aneurysms using the Pipeline flow-diverter embolization device: a single-center experience with long-term follow-up results.** *AJNR Am J Neuroradiol* 2012;33:1436–46
38. Velioglu M, Kizilkilic O, Selcuk H, et al. **Early and midterm results of complex cerebral aneurysms treated with Silk stent.** *Neuroradiology* 2012;54:1355–65

Optimized Angiographic CT Using Intravenous Contrast Injection: A Noninvasive Imaging Option for the Follow-Up of Coiled Aneurysms?

P. Gölitz, T. Struffert, I. Kaschka, K. Roessler, F. Knossalla, and A. Doerfler

ABSTRACT

BACKGROUND AND PURPOSE: Because recanalization of coiled cerebral aneurysms is reported to occur, follow-up imaging is mandatory, ideally noninvasively. Our study aimed to evaluate the accuracy of an optimized angiographic CT by using intravenous contrast material injection in the assessment of coiled cerebral aneurysms, compared with MR angiography and digital subtraction angiography, the criterion standard.

MATERIALS AND METHODS: We included 69 patients with 76 coiled cerebral aneurysms. In each patient, we performed an angiographic CT with intravenous contrast material injection with a dual rotational acquisition, a time-of-flight MR angiography, and a DSA. The angiographic CT with intravenous contrast material injection data was postprocessed by using newly implemented reconstructions modes and a dual-volume technique. An aneurysm occlusion rate was assessed in angiographic CT with intravenous contrast material injection and MRA; remnants were measured and correlated with DSA, respectively.

RESULTS: Twenty-eight remnants were revealed by DSA with a mean size of 3.1 × 3.1 mm. Angiographic CT with intravenous contrast material injection demonstrated a sensitivity of 93% and a specificity of 96% in remnant detection. MRA showed almost identical accuracy (sensitivity of 93%, specificity of 100%). Assessment of remnant size by angiographic CT with intravenous contrast material injection and by MRA revealed a high significant correlation with DSA, respectively ($P < .001$).

CONCLUSIONS: Optimized angiographic CT with intravenous contrast material injection and MRA demonstrated accuracy comparable with that of DSA in the follow-up of coiled aneurysms, respectively. The assessment of remnant size showed a high correlation with DSA for both techniques. Due to the lack of radiation exposure, MRA seems to be the preferred technique. However, angiographic CT with intravenous contrast material injection can be considered a reliable, noninvasive alternative in patients with MR imaging contraindications or in cases of compromising artifacts due to metal implants (ie, clips).

ABBREVIATION: ivACT = angiographic CT with intravenous contrast material injection

For treatment of cerebral aneurysms, coil embolization has been established as a widely accepted technique.[1,2] Follow-up evaluation is recommended because recanalization is reported in up to 20% of aneurysms,[3-5] with approximately 10% requiring retreatment. In this instance, DSA is still considered the criterion standard, but it has the disadvantage of being an invasive technique with the risk of procedural complications.[6] Therefore, ideally, a noninvasive imaging technique is desirable as an alternative to DSA. TOF-MRA and contrast-enhanced MRA have demonstrated moderate-to-high diagnostic performance.[7-9] TOF-MRA was superior to contrast-enhanced MRA in terms of coil visibility and is the recommended MR imaging technique.[10] On the other hand, MR imaging may be impossible due to contraindications or lack of availability.

Here, angiographic CT by using intravenous contrast material injection could be an alternative, noninvasive imaging option. Angiographic CT allows the acquisition of high-resolution data from a rotational run of a C-arm-mounted flat panel detector that differs from conventional CT in the material composing it. Angiographic CT with intravenous contrast material injection (ivACT) has recently demonstrated comparable image quality to DSA in visualizing cerebral artery vasculature[11] and has been helpful in aneurysm diagnostics[12] and in the follow-up of clipped aneurysms.[13] Until now, only angiographic CT with intra-arterial contrast material injection has been investigated in the follow-up of coiled aneurysms, providing promising results.[14] With the implementation of new reconstruction

Received January 31, 2014; accepted after revision May 27.

From the Departments of Neuroradiology (P.G., T.S., I.K., A.D.), Neurosurgery (K.R.), and Neurology (F.K.), University of Erlangen, Nuremberg, Germany.

This work was funded by the Medical Valley National Leading Edge Cluster, Erlangen, Germany, Diagnostic Imaging Network, subproject BD 16, research grant No. 13EX1212G, and subproject BD 20, research grant No. 13G 0031A.

Please address correspondence to Philipp Gölitz, MD, Department of Neuroradiology, University of Erlangen-Nuremberg, Schwabachanlage 6, 91054 Erlangen, Germany; e-mail: philipp.goelitz@uk-erlangen.de

http://dx.doi.org/10.3174/ajnr.A4039

modes and enhanced postprocessing algorithms, the image quality of ivACT could be improved and artifacts could be reduced. Our study aimed to evaluate the accuracy of an optimized, noninvasive ivACT in the follow-up of coiled aneurysms compared with MRA and DSA, the criterion standard.

MATERIALS AND METHODS

Sixty-nine consecutive patients, 46 women and 23 men with 76 coiled aneurysms, were prospectively enrolled in our study between March 2012 and August 2013 after ethics committee approval and written informed consent were obtained. The average age was 58 ± 9.3 years (range, 30–79 years). Forty-three patients had subarachnoid hemorrhage. On average, the aneurysms were 6.0 ± 3.0 mm high and 5.4 ± 3.1 mm wide, ranging from 2 to 18 mm, respectively. Twenty-five aneurysms originated from the anterior communicating artery, 5 from the MCA, 16 from the tip of the basilar artery, 8 from the posterior communicating artery, 3 from the anterior choroidal artery, 10 from the paraophthalmic segment of the ICA, 5 from the distal carotid bifurcation, 2 from the posterior inferior cerebellar artery, and 2 from the posterior cerebral artery.

In total, 492 coils were used for treatment: 459 bioactive coils loaded with polyglycolic acid (Cerecyte; Codman Neurovascular, Raynham, Massachusetts), 24 standard bare platinum coils (Guglielmi detachable coil; Stryker, Kalamazoo, Michigan), and 9 volume bare platinum coils (Penumbra Coil 400; Penumbra, Alameda, California). Fifteen aneurysms were treated with additional stent protection (Neuroform; Stryker Neurovascular, Fremont, California).

DSA, including a 3D rotational run, was performed in all patients 6 months after treatment. The day after DSA in every patient, TOF-MRA and, thereafter, ivACT was performed after the serum creatinine level was checked.

DSA

Image acquisition was performed on a biplane flat panel detector angiographic system (Axiom Artis dBA; Siemens, Erlangen, Germany). With standard angiographic methods (transfemoral route), we used a diagnostic catheter for image acquisition. The 3D rotational run was performed with a standard 3D DSA program provided by the manufacturer (5-second DSA run; Siemens). Angiographic data were transferred to a dedicated workstation (Leonardo; Siemens) to generate rotatable, dual-volume images by using commercially available software (iDentify; Siemens). On the basis of the 3D images, targeted 2D series were obtained.

ivACT

ivACT was performed the day after DSA on the same biplane flat panel detector angiographic system by using a dedicated angiographic CT program (10-second DSA; Siemens), including a native and a contrast-enhanced run. The timing for starting the filling run was done with the "bolus-watching" technique.[15] First, 60 mL of contrast material (iomeprol; Imeron 300, Bracco Imaging, Konstanz, Germany) was injected via a needle with a minimal inner diameter of 0.8 mm into an antecubital vein at a rate of 5 mL/s by using a power injector (Accutron HP-D; Medtron, Saarbruecken, Germany) followed by a saline chaser (60 mL; injection rate, 5 mL/s). Data acquisition per run was performed with the following parameters: acquisition time, 10 seconds per run; 70 kV; 512 × 512 matrix; projection on 30 × 40 cm flat panel size; 200° total angle; 0.8°/frame; 250 frames total; dose, 1.2 μGy/frame; CT weighted dose index, approximately 35 mGy. For postprocessing and image evaluation, the data were transferred to a dedicated workstation (Leonardo).

MR Imaging

MR angiography by using the TOF technique was performed with a 3T scanner (Magnetom Trio; Siemens). The parameters of the TOF-MRA were as follows: TR, 22 ms; TE, 3.98 ms; matrix size, 271 × 512; section thickness, 0.7 mm; acquisition time, 5 minutes and 37 seconds. In addition to the source images, MIP reconstructions were generated. For image evaluation, all data were transferred to a dedicated workstation (Leonardo).

Postprocessing and Image Analysis

Image reconstruction of ivACT and 3D DSA was performed by using the mode "native mask," kernel type "HU," and image impression "sharp" for coil delineation. Next, image reconstruction with the newly implemented, commercially available mode "subtraction with motion correction," kernel type "HU", and image impression "very smooth" was performed for visualization of the arteries. Both datasets were fused and loaded into the InSpace function of the workstation by using a commercially available, dual-volume technique (iDentify) to obtain 3D, freely rotatable images.

The reconstructed and source images of ivACT and MRA were anonymized, stored in random order, and evaluated by 2 experienced neuroradiologists in a consensus reading. Both raters were blinded to the results of the DSA. Evaluation of the DSA images was performed independently by a third experienced neuroradiologist who was not involved in the ivACT and MRA evaluation. For DSA evaluation, the 2D and the 3D images, including the source data, were used. For assessment of the occlusion rate, "no remnant" and "any remnant" were differentiated. The category "any remnant" subsumes the categories "neck remnant" and "aneurysm remnant" on the Raymond classification scale.[16] A more detailed remnant classification was spared to avoid possible bias resulting from discrepancies concerning the correct occlusion grading.

The image quality of ivACT and MRA was assessed by using the following grading system: 2 = no interference; 1 = compromised, but sufficient image quality; 0 = not diagnostic.

Statistical analysis was performed by using the software SPSS statistics 20.0 (IBM, Armonk, New York). Mean values and SDs were calculated for aneurysm and remnant size, respectively. The sensitivity and specificity of ivACT and MRA concerning remnant detection were calculated. For analysis of the correlation between the variables, a linear 2-sided correlation (Pearson r) test was performed. The level of significance was set as $P \leq .05$. Observer agreement with DSA was analyzed for ivACT and MRA by using the κ statistic by calculating Cohen κ coefficient. The analysis was based on any remnant/no remnant observation per coiled aneurysm. A value of 0.41–0.60 for the κ coefficient was interpreted as moderate agreement; a value of 0.61–0.80, as substantial agreement; and a value of 0.81–1.00, as almost perfect agreement.

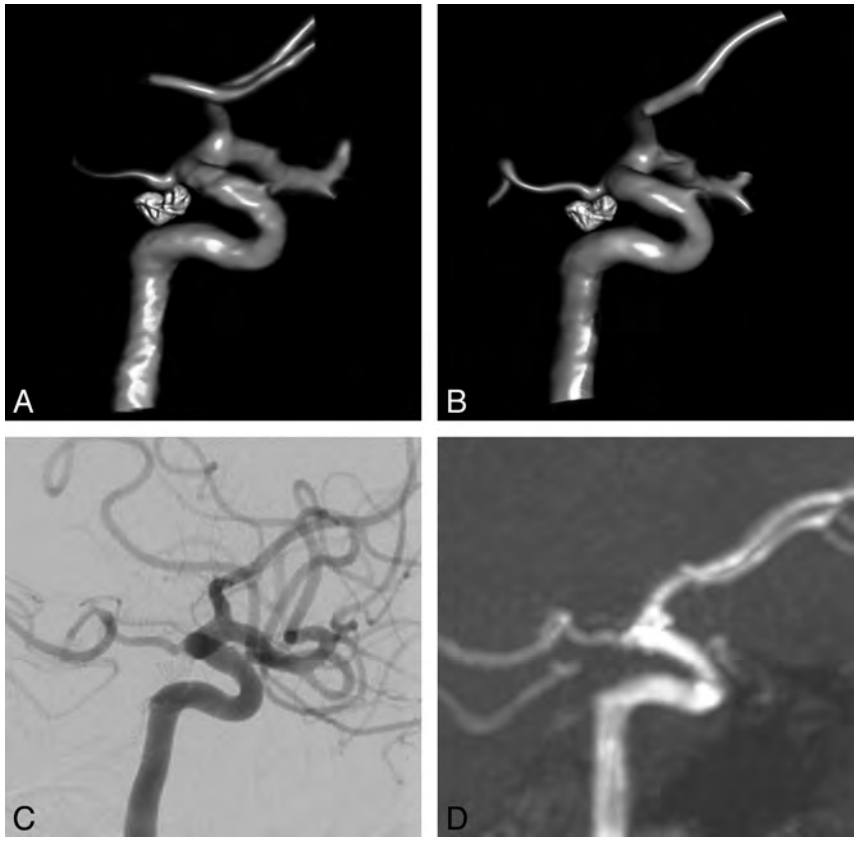

FIG 1. ivACT (*A*) and intra-arterial 3D-DSA (*B*) show, in comparable image quality, complete occlusion after coiling of a posterior communicating artery aneurysm. 2D-DSA (*C*) confirms complete aneurysm occlusion. TOF-MRA (*D*) demonstrates complete occlusion.

RESULTS

Using DSA, we detected a remnant in 28 cases (37%), and saw complete occlusion in 48 cases (63%). On average, aneurysm remnants were 3.1 ± 1.7 mm high and 3.1 ± 2.0 mm wide, based on DSA imaging. Retreatment was considered necessary in 6 aneurysms, meaning an adequate aneurysm occlusion of 92%.

ivACT could be performed in all patients. In 66 aneurysms, image evaluation was possible without interfering artifacts. Image quality was assessed as compromised but sufficient in 10 aneurysms. No case was assessed as nondiagnostic.

By ivACT, complete aneurysm occlusion was assessed correctly in 46 aneurysms, meaning a specificity of 96% (Figs 1 and 2). In 1 of the 2 cases in which remnants were supposed incorrectly, volume bare platinum coils were used, inducing compromising beam-hardening artifacts. In 26 aneurysms, remnants were detected correctly, meaning a sensitivity of 93% (Fig 3). In the 2 cases in which ivACT failed, only small neck remnants without indication for retreatment were missed. Overall, remnants up to a minimal size of 1.0 × 0.9 mm could be revealed by ivACT. Implanted stents caused no substantial artifacts (Fig 4). Measurement of remnants by ivACT demonstrated a significant ($P < .001$) correlation with DSA (Table). Observer agreement with DSA was $\kappa = 0.89$ ($P < .001$; 95% CI, 0.779–0.995), indicating almost perfect agreement.

MRA was performed in 67 patients. In 2 patients, MRA was not viable because of a cardiac pacemaker. In 1 case, MRA was assessed as nondiagnostic due to susceptibility artifacts from an additional aneurysm clip (Fig 5). Image quality was considered compromised by artifacts but sufficient in 4 cases. In the remaining cases, no interfering artifacts were observed.

Remnants were detected correctly in 26 aneurysms, meaning a sensitivity of 93%. All cases of complete aneurysm occlusion were assessed correctly (specificity of 100%). Measurements of remnants by MRA demonstrated a significant ($P < .001$) correlation with DSA (Table). Observer agreement with DSA was found to be $\kappa = 0.91$ ($P < .001$; 95% CI, 0.810–1.010), indicating almost perfect agreement.

In 1 case of a restless patient, both ivACT and MRA failed in remnant detection because of compromising motion artifacts.

DISCUSSION

To the best of our knowledge, ivACT has not yet been evaluated for follow-up of coiled aneurysms. In our study, ivACT demonstrated high sensitivity and specificity in detecting remnants down to a minimal size of 1.0 × 0.9 mm. Assessment of remnant size by ivACT showed a significant correlation with DSA. On the basis of differentiating any remnant and no remnant, agreement of ivACT with DSA was identical in assessing the aneurysmal occlusion rate.

ivACT was performed as a dual rotational 10-second acquisition run by using the bolus-watching technique to obtain the best arterial vessel opacification. Using a dual-volume technique (iDentify) with newly implemented reconstruction modes, one can generate freely rotatable 3D images. Fusing 2 separately reconstructed datasets, 1 optimized for vessel visualization and 1 for coil delineation, allows an improvement in image quality compared with MPR images that are obtained from only 1 reconstruction step.

An advantage compared with DSA is that ivACT allows evaluation of several coiled aneurysms in only 1 examination step (comparison shown in Fig 2). Implanted stents after stent-assisted coiling induced no substantial artifacts (comparison shown in Fig 4). Moreover, the stent lumen can be assessed precisely in ivACT,[17] which is not achievable in MRA. In the case of volume bare platinum coils, ivACT might be less suitable than MRA because these coils seem to induce compromising beam-hardening artifacts. However, our results concerning these coils are limited due to the small sample size, but that might be a subject for further investigations.

In angiographic CT using intra-arterial contrast material injection, substantial "eggshell" artifacts are reported for coil packages larger than 10 mm in diameter, supposedly the result of insufficient reconstruction algorithms.[12] In contrast, in our study by using newly implemented reconstruction algorithms and

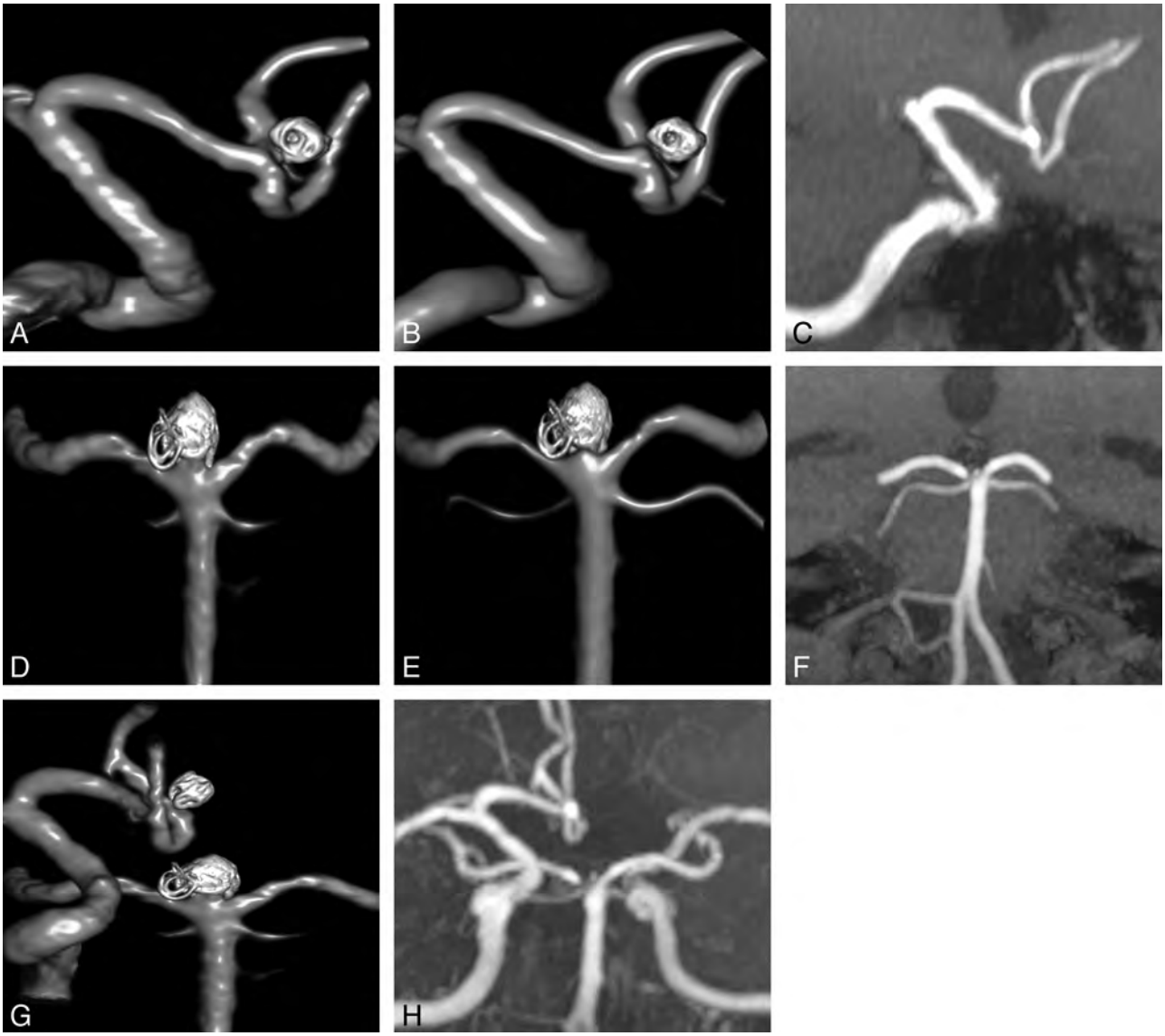

FIG 2. ivACT (*A*) and intra-arterial 3D-DSA (*B*) show, in a comparable way, complete occlusion of an anterior communicating artery aneurysm after coiling. MRA reveals no remnant (*C*). In addition, a second aneurysm located at the tip of the basilar artery was treated by coil embolization. ivACT (*D*) and 3D-DSA (*E*) demonstrate, in nearly identical quality, complete aneurysm occlusion with only mild irregularity at the aneurysm base. In addition, MRA reveals no remnant (*F*). As an advantage of ivACT (*G*) and MRA (*H*), aneurysm evaluation can be performed with only 1 examination step, in contrast to DSA, requiring several vessel catheterizations and contrast material injections.

iDentify instead of MPR reconstructions, we did not observe such artifacts in larger aneurysms. Additionally, image evaluation might be facilitated by injecting the contrast material intravenously, leading to a homogeneous contrast mixing without high-flow artifacts, which can occur with intra-arterial injection.

TOF-MRA also demonstrated high sensitivity and specificity in remnant detection on almost the same level in ivACT. Assessment of remnant size was comparable with that of ivACT and demonstrated a significant correlation with DSA. Stents induced no artifacts substantially compromising aneurysm evaluation, but a reliable assessment of the stent lumen is not viable in MRA.

Our results are in line with those in other MR imaging studies that found substantial agreement between DSA and MRA in evaluating coiled aneurysms. The reported sensitivity and specificity of remnant detection are comparable with our results.[8,18,19] One study found MRA sufficient for therapeutic decision-making in the retreatment of recanalization.[18] On the other hand, evaluation of MRA performed with 3T MR imaging revealed a greater discrepancy with DSA in aneurysms with a small (1–3 mm) residual lumen than in those with a larger lumen because for a small residual lumen, the precise differentiation between subtotal and incomplete occlusion does not seem possible.[8] Similarly, sufficient accuracy of MRA is reported, in general, for the screening of residual flow after coil embolization, but in particular in small aneurysms (<6 mm), the detection of residual flow was limited.[17] Therefore, ivACT might be considered more favorable than MRA in small aneurysms because we found no restrictions with ivACT in evaluating small aneurysms. On the contrary, because ivACT might be limited in evaluating large aneurysms with a maximum diameter of >10 mm, ivACT and MRA could be considered complementary imaging techniques, which might be selected individ-

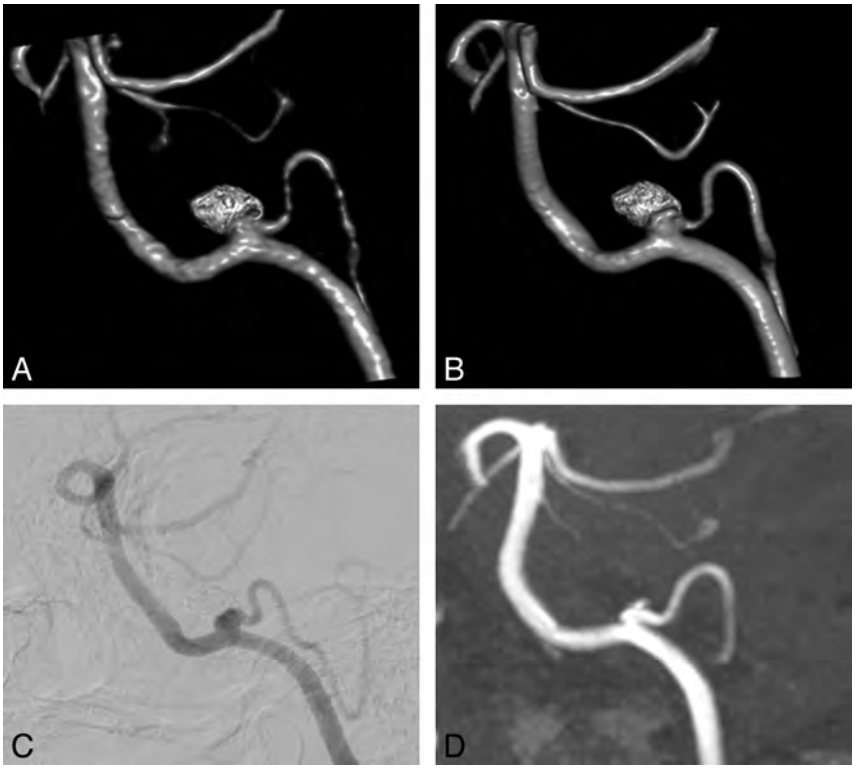

FIG 3. ivACT (*A*) and 3D-DSA (*B*) reveal a small remnant after coiling of a posterior inferior cerebellar artery aneurysm in nearly identical quality. DSA confirms this finding (*C*). TOF-MRA also detects the small remnant (*D*).

ually, depending on aneurysm size or coil material. Here, further investigations with an increased patient population are necessary.

In our study, observer agreement with DSA was almost perfect for both ivACT and MRA. Interobserver variability was not assessed because our study aimed first to demonstrate the feasibility of ivACT and to assess ivACT and MRA as close as possible to the usual clinical setting with only 1 reader. Because MRA and ivACT reached nearly identical accuracy in remnant detection and in the assessment of remnant size, they seem equally capable of a noninvasive follow-up; both may be reliable alternatives to DSA. However, because MRA can be performed without radiation exposure to the patient, it may serve as the preferred technique in routine cases. Nevertheless, in patients with contraindications to MR imaging (heart pacemaker and so forth) or in the case of compromising susceptibility artifacts due to additional metal implants (eg, aneurysm clips, comparison shown in Fig 5), ivACT can be considered a reliable alternative. ivACT could also be an option in

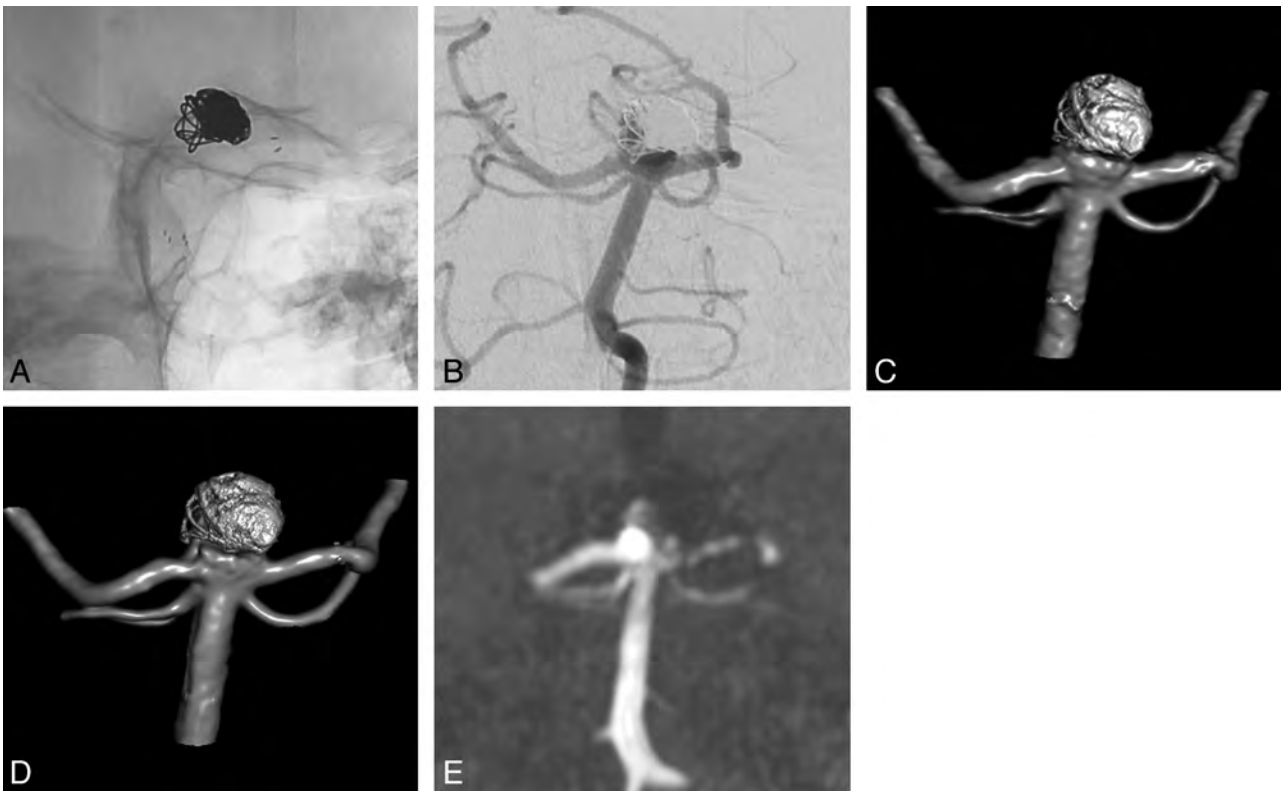

FIG 4. Native (*A*) and DSA images (*B*) after stent-assisted coil embolization of a basilar artery tip aneurysm show a small, laterally located remnant. In ivACT (*C*) and intra-arterial rotational 3D-DSA (*D*), the remnant can be revealed reliably in nearly identical image quality. In TOF-MRA (*E*), the remnant can be delineated clearly, but in contrast to ivACT and 3D-DSA, artifacts are induced by the implanted stent, making stent assessment impossible. In contrast, ivACT allows precise assessment of the stent lumen.

Mean size and SD of aneurysm remnants measured by ivACT and TOF-MRA in correlation with DSA

Remnant	DSA (Mean) (SD)	ivACT (Mean) (SD)	Pearson Correlation Coefficient	TOF-MRA (Mean) (SD)	Pearson Correlation Coefficient
Height	3.1 mm (±1.7)	2.9 mm (±1.8)	0.963 ($P < .001$)	2.8 mm (±1.9)	0.925 ($P < .001$)
Width	3.1 mm (±2.0)	3.1 mm (±2.6)	0.930 ($P < 0.001$)	2.8 mm (±2.1)	0.941 ($P < .001$)

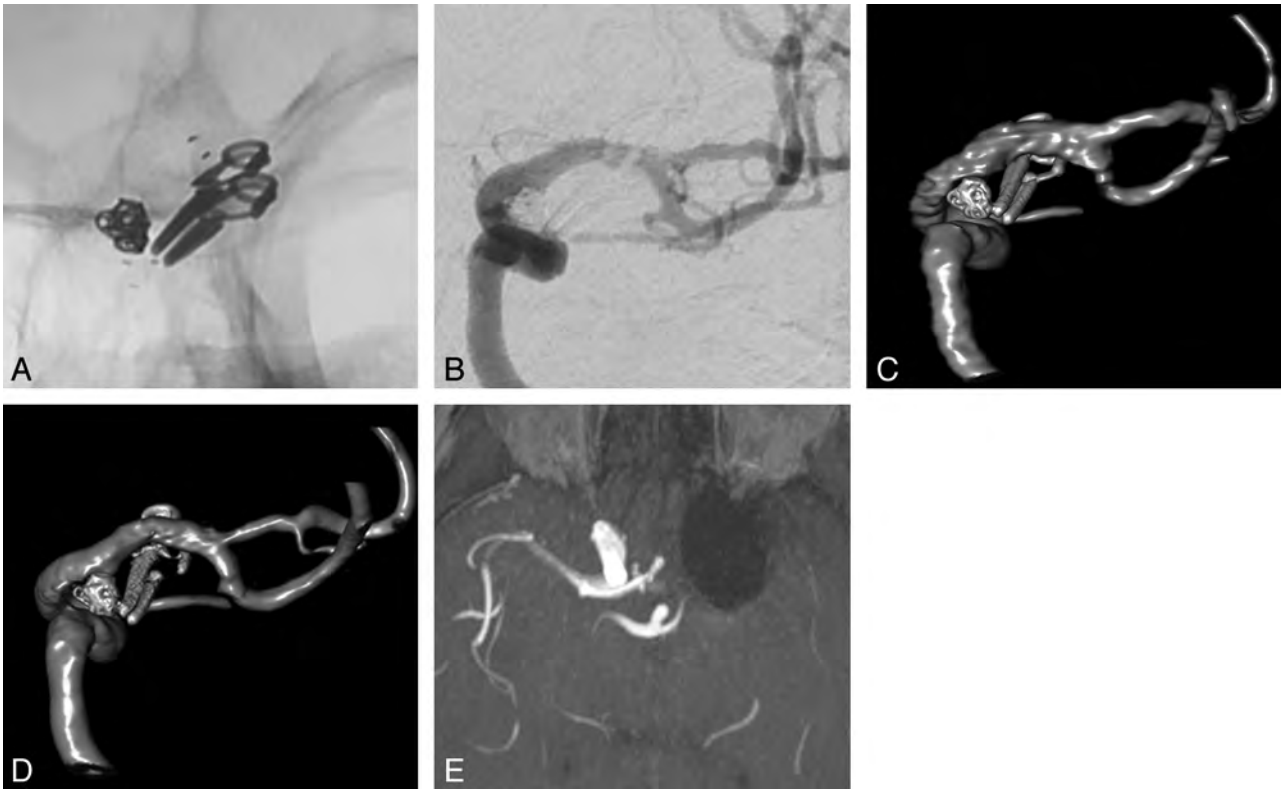

FIG 5. Native (*A*) and contrast-enhanced 2D-DSA (*B*) images show complete occlusion of a posterior communicating artery aneurysm, treated initially by subtotal clipping, followed by stent-assisted coil embolization. ivACT (*C*) and 3D-DSA (*D*) illustrate complete aneurysm occlusion in a comparable quality. In ivACT, no compromising artifacts by the metal implants are observed. MRA fails in delineating the coiled aneurysm because of severe susceptibility artifacts (*E*).

patients treated with ventriculopertioneal shunts to avoid potential maladjustment or damage. The advantages of ivACT are that it has a short acquisition time, it is less time-consuming than DSA and MRA, and it can be performed on an outpatient basis, of interest from an economic point of view.

Concerning radiation exposure, evaluations by using an Alderson-Rando phantom revealed an effective dose of 2.9 mSv for the 10-second run of an ivACT if the entire head was scanned. However, by collimating the FOV on the coil package, the radiation dose can be substantially reduced by up to 0.5 mSv.[20] For comparison, the effective dose of a biplane 2D-DSA series was measured as 1 mSv. Thus, especially in the follow-up of multiple coiled cerebral aneurysms, the use of ivACT could significantly reduce radiation exposure to the patient compared with DSA. Advances in the rapidly developing flat panel detector technology might further contribute to increasing dose effectiveness and improving image quality.

Our findings are limited because mainly 1 type of coil was used for aneurysm treatment in our study population. Moreover, the mean aneurysm size and the mean remnant size were relatively low in our population; thus, an objective for further investigations could be to add more large aneurysms to our series. Head motion and the resulting artifacts lead to a compromised image quality in both modalities, making restless or noncompliant patients less suitable for both imaging techniques. The development of special cups for better head fixation might be helpful for reducing motion artifacts in ivACT. As an objective for further investigations, the implementation of reconstruction modes with automated metal artifact reduction might further contribute to improved ivACT image quality.

CONCLUSIONS

Both, ivACT and MRA, have a high accuracy in detecting remnants after coiling. The accuracy of ivACT as well as of MRA is comparable with the accuracy of DSA. Both noninvasive modalities allowed a reliable assessment of the aneurysm occlusion rate and remnant size. Due to the lack of radiation exposure, MRA seems to be the preferred imaging technique. However, in selected patients, ivACT can be considered an alternative (ie, in patients with contraindications to MR imaging or in the case of compromising artifacts due to metal implants such as aneurysm clips). Moreover, MRA and ivACT might also be considered complementary imaging techniques, which could be selected depending on aneurysm size or coil material. Further investigations in a

larger patient population are needed to substantiate our initial results.

REFERENCES

1. Pierot L, Spelle L, Vitry F, et al. **Immediate clinical outcome of patients harboring unruptured intracranial aneurysms treated by endovascular approach: results of the ATENA study.** *Stroke* 2008;39:2497–504
2. Lanzino G, Murad MH, d'Urso PI, et al. **Coil embolization versus clipping for ruptured intracranial aneurysms: a meta-analysis of prospective controlled published studies.** *AJNR Am J Neuroradiol* 2013:34:1764–68
3. Ferns SP, Sprengers ME, von Rooij WJ, et al. **Coiling of intracranial aneurysms: a systematic review on initial occlusion and reopening and retreatment rates.** *Stroke* 2009;40:e523–29
4. Campi A, Ramzi N, Molyneux AJ, et al. **Retreatment of ruptured cerebral aneurysms in patients randomized by coiling or clipping in the International Subarachnoid Aneurysm Trial (ISAT).** *Stroke* 2007;38:1538–44
5. Pierot L, Delcourt C, Bouquigny F, et al. **Follow-up of intracranial aneurysms selectively treated with coils: prospective evaluation of contrast-enhanced MR angiography.** *AJNR Am J Neuroradiol* 2006;27:744–49
6. Fifi JT, Meyers PM, Lavine SD, et al. **Complications of modern diagnostic cerebral angiography in an academic medical center.** *J Vasc Interv Radiol* 2009;20:442–47
7. Anzalone N, Scomazzoni F, Cirillo M, et al. **Follow-up of coiled aneurysms at 3T: comparison of 3D time-of-flight MR angiography and contrast-enhanced MR angiography.** *AJNR Am J Neuroradiol* 2008;29:1530–36
8. Schaafsma JD, Velthuis BK, Majoie CB, et al. **Intracranial aneurysms treated with coil placement: test characteristics of follow-up MR angiography—multicenter study.** *Radiology* 2010;256:209–18
9. Cho WS, Kim SS, Lee SJ, et al. **The effectiveness of 3T time-of-flight magnetic resonance angiography for follow-up evaluations after the stent-assisted coil embolization of cerebral aneurysms.** *Acta Radiol* 2013;55:604–13
10. Pierot L, Portefaix C, Gauvrit JY, et al. **Follow-up of coiled intracranial aneurysms: comparison of 3D time-of-flight MR angiography at 3T and 1.5T in a large prospective series.** *AJNR Am J Neuroradiol* 2012;33:2162–66
11. Saake M, Breuer L, Goelitz P, et al. **Flat detector computed tomography angiography with intravenous contrast application: feasibility for visualization of cerebral arterial vasculature.** *J Neuroimaging* 2013;23:414–20
12. Gölitz P, Struffert T, Knossalla F, et al. **Angiographic CT with intravenous contrast injection compared with conventional rotational angiography in the diagnostic work-up of cerebral aneurysms.** *AJNR Am J Neuroradiol* 2012;33:982–87
13. Gölitz P, Struffert T, Ganslandt O, et al. **Optimized angiographic computed tomography with intravenous contrast injection: an alternative to conventional angiography in the follow-up of clipped aneurysms?** *J Neurosurg* 2012;117:29–36
14. Buhk JH, Kallenberg K, Mohr A, et al. **Evaluation of angiographic computed tomography in the follow-up after endovascular treatment of cerebral aneurysms: a comparative study with DSA and TOF-MRA.** *Eur Radiol* 2009;19:430–36
15. Struffert T, Kloska S, Engelhorn T, et al. **Optimized intravenous flat detector CT for non-invasive visualization of intracranial stents: first results.** *Eur Radiol* 2011;21:411–18
16. Roy D, Milot G, Raymond J. **Endovascular treatment of unruptured aneurysms.** *Stroke* 2001;32:1998–2004
17. Struffert T, Ott S, Adamek E, et al. **Flat-detector computed tomography in the assessment of intracranial stents: comparison with multi detector CT and conventional angiography in a new animal model.** *Eur Radiol* 2011;21:1779–87
18. Schaafsma JD, Velthuis BK, van den Berg R, et al. **Coil-treated aneurysms: decision making regarding additional treatment based on findings of MR angiography and intraarterial DSA.** *Radiology* 2012;265:858–63
19. Lavoie P, Gariépy JL, Milot G, et al. **Residual flow after cerebral aneurysm coil occlusion: diagnostic accuracy of MR angiography.** *Stroke* 2012;43:740–46
20. Struffert T, Hauer M, Banckwitz R, et al. **Effective dose to patient measurements in flat-detector and multislice computed tomography: a comparison of applications in neuroradiology.** *Eur Radiol* 2014;24:1257–65

Intra-Aneurysmal Flow Patterns: Illustrative Comparison among Digital Subtraction Angiography, Optical Flow, and Computational Fluid Dynamics

O. Brina, R. Ouared, O. Bonnefous, F. van Nijnatten, P. Bouillot, P. Bijlenga, K. Schaller, K.-O. Lovblad, T. Grünhagen, D. Ruijters, and V. Mendes Pereira

ABSTRACT

BACKGROUND AND PURPOSE: Digital subtraction angiography is the gold standard vascular imaging and it is used for all endovascular treatment of intracranial anerysms. Optical flow imaging has been described as a potential method to evaluate cerebral hemodynamics through DSA. In this study, we aimed to compare the flow patterns measured during angiography, by using an optical flow method, with those measured by using computational fluid dynamics in intracranial aneurysms.

MATERIALS AND METHODS: A consecutive series of 21 patients harboring unruptured saccular intracranial aneurysms who underwent diagnostic angiography before treatment was considered. High-frame-rate digital subtraction angiography was performed to obtain an intra-aneurysmal velocity field by following the cardiac-modulated contrast wave through the vascular structures by using optical flow principles. Additionally, computational fluid dynamics modeling was performed for every case by using patient-specific inlet-boundary conditions measured with the optical flow method from both DSA and 3D rotational angiography datasets. Three independent observers compared qualitatively both the inflow direction and the apparent recirculation in regular DSA, optical flow images, and computational fluid dynamics flow patterns for each patient; κ statistics were estimated.

RESULTS: We included 21 patients. In 14 of these 21, the flow patterns were conclusive and matching between the optical flow images and computational fluid dynamics within the same projection view ($\kappa = .91$). However, in only 8 of these 14 patients the optical flow images were conclusive and matching regular DSA images (observer $\kappa = 0.87$). In 7 of the 21 patients, the flow patterns in the optical flow images were inconclusive, possibly due to improper projection angles.

CONCLUSIONS: The DSA-based optical flow technique was considered qualitatively consistent with computational fluid dynamics outcomes in evaluating intra-aneurysmal inflow direction and apparent recirculation. Moreover, the optical flow technique may provide the premises for new solutions for improving the visibility of flow patterns when contrast motion in DSA is not apparent. This technique is a diagnostic method to evaluate intra-aneurysmal flow patterns and could be used in the future for validation and patient evaluation.

ABBREVIATIONS: CFD = computational fluid dynamics; DVF = detector velocity fields; OF = optical flow

While unruptured intracranial aneurysms have become increasingly diagnosed,[1] more questions have been raised about the improvement of patient care management, requiring the knowledge of risks for both treatment and conservative follow-up, which still remain unknown. In particular, the role of hemodynamics in predicting both aneurysm rupture and treatment efficacy for flow-diverter stents still remains ambiguous, despite the sustained research effort.[2,3] Recently, a novel method has been developed based on digital subtraction angiography and 3D rotational angiography images by using optical flow (OF) principles, permitting the observation and measurement of intracranial hemodynamic characteristics in patients with intracranial aneurysms. Bonnefous et al[4] have successfully validated this OF method for measuring the volumetric flow rate by using in vitro experiments, and Pereira et al[5] have validated blood flow rate measurements in patients by using Doppler sonography. This technique has also been applied to quantify flow reduction after

Received May 17, 2014; accepted after revision May 19.

From the Interventional Neuroradiology Unit (O. Brina, R.O., P. Bouillot, K.-O.L., V.M.P.), Service of Neuroradiology, and Service of Neurosurgery (P. Bijlenga, K.S.), University of Geneva Hospitals and Faculty of Medicine, Geneva, Switzerland; Medisys Research Laboratory (O. Bonnefous) and Interventional X-Ray (F.v.N., T.G., D.R.), Philips Healthcare, Zürich, Switzerland; and Division of Neuroradiology (V.M.P.), Department of Medical Imaging, and Division of Neurosurgery (V.M.P.), Department of Surgery, Toronto Western Hospital, University Health Network, Toronto, Ontario, Canada.

This work was supported by the Swiss National Funds–SNF 32003B_141192.

Please address correspondence to Vitor Mendes Pereira, MD, MSc, Division of Neuroradiology, Department of Medical Imaging, and Division of Neurosurgery, Department of Surgery, Toronto Western Hospital, University Health Network, Toronto, Ontario, Canada; e-mail: vitormpbr@hotmail.com

http://dx.doi.org/10.3174/ajnr.A4063

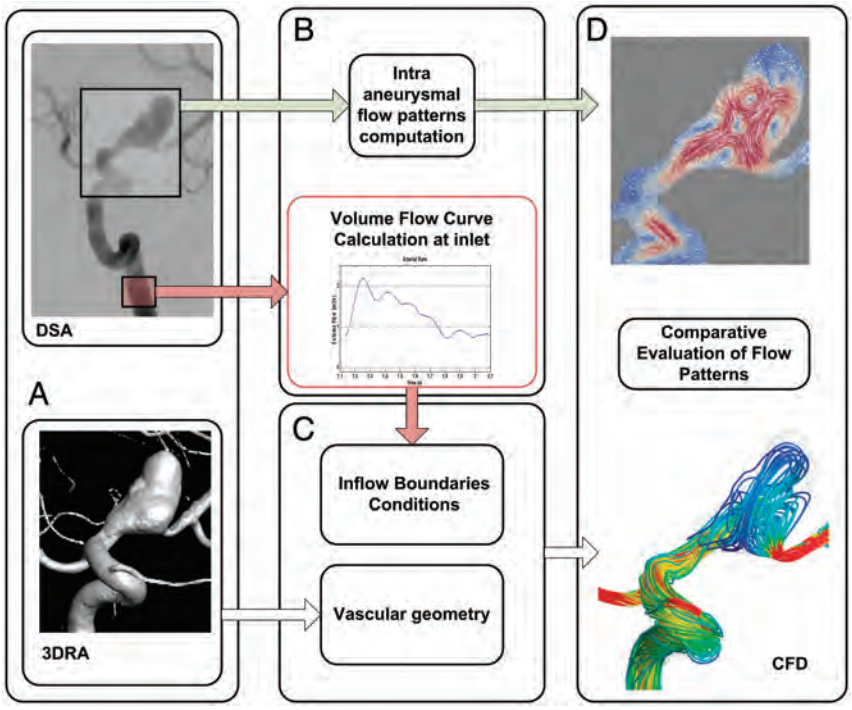

FIG 1. Workflow of the study. *A*, DSA and 3D rotational angiograms. *B*, Optical flow processing provides intra-aneurysmal flow patterns and volumetric flow curves measured in the parent vessel. *C*, Geometry and CFD modeling with the vessel geometry. *D*, Assessment of intra-aneurysmal flow patterns.

flow-diverter stent implantation and seems to be a good predictor of aneurysm thrombosis.[6] The key success factors for this approach include low contrast-injection rates and an adaptive application of OF principles to high-frame-rate angiograms. These prerequisites allowed capturing the physiologic modulation of the contrast attenuation in blood flow, hence providing measurements of conebeam flat panel detector velocity fields (DVF). As a preliminary step ahead of OF in vivo validation in intracranial aneurysms, we propose to qualitatively compare the intra-aneurysmal flow patterns among DSA sequences (showing the qualitative gross flow structures), OF vectors in a 2D plane, and 3D streamlines based on computational fluid dynamics (CFD).

MATERIALS AND METHODS

Patient Selection and Data Collection

We included 21 consecutive patients who presented with unruptured saccular intracranial aneurysms before treatment. Patients with ruptured lesions, partially thrombosed aneurysms, or dissections were excluded from the study. This retrospective study was approved by the Geneva University Hospital ethics committee board (NEC 07–056).

Data Collection

Angiograms were performed by using the Seldinger technique at the level of the femoral artery. A 5F diagnostic catheter was used to selectively catheterize the vessel carrying the aneurysm. The catheter tip was positioned either in the internal carotid artery, 3 cm beyond the bifurcation, or at the V1 segment of the vertebral artery. A 3D rotational angiography was performed by using an angiographic biplane C-arm unit (Allura FD20; Philips Healthcare, Best, the Netherlands) to provide the vascular geometries for CFD modeling and for the inlet volumetric blood flow OF measurement.[5,6] Additionally, the 3D reconstruction was used to determine a suitable DSA projection view. The DSA projection view was chosen to ensure that overlapping the distal arterial branches and parent vessel from the aneurysm bulge was avoided to keep the region of interest free of irrelevant moving patterns that could affect measurements. Subsequently, a high-frame-rate DSA sequence (60 images/s) was acquired with a contrast agent injection rate of 1.5 mL/s during 4 seconds for all patients.

Optical Flow–Based Algorithm

Using an OF method,[4-6] we estimated the detector velocity fields on the basis of analyses of both the temporal and spatial variations of contrast agent attenuation injected during the DSA sequences. The temporal variations are spontaneously created when the injected contrast agent mixes with the blood stream under the pulsatile effect of the cardiac cycle while filling the vessel tree and the aneurysm. Bonnefous et al[4] proposed to decouple the pulsating contrast attenuation from the nonmodulated wash-in/washout component. The contrast wave propagating through the vascular network was thereby captured and processed. The local temporal and spatial contrast attenuation variations were tracked among the successive images of the run. The result was a dynamic representation of DVF or streamlines that preserves their direction and magnitude. In addition, the vector fields were processed by imposing no divergent flow. Detailed descriptions of the postprocessing method can be found in Bonnefous et al[4] and Pereira et al.[6]

Vascular and CFD Modeling

The triangulated surfaces of the vessels were first created from 3D rotational angiograms by using the AneuFuse toolkit (http://www.biomedtown.org).[7] Then, commercial software (ICEM CFD 12.1; ANSYS, Canonsburg, Pennsylvania) was used to produce a high-resolution computational unstructured mesh composed of tetrahedrons in the bulk flow and prism elements near the wall. The mesh element numbers ranged from 4.0 to 5.5 million, with a mesh attenuation of >1700 elements/mm^3. The computational mesh was used in the CFX commercial solver (CFX 12.1; ANSYS) to solve Navier-Stokes equations. Blood was assumed to exhibit the properties of a Newtonian incompressible fluid, and this was specified in the numeric solver. Inlet pulsatile boundary-condition flow curves were measured specifically for each patient by using the OF method coupled with the 3D rotational angiograms (Fig 1).[4-6] These volumetric blood flow measurements were performed in the upstream parent vessel, far enough from the catheter tip to ensure good contrast agent mix-

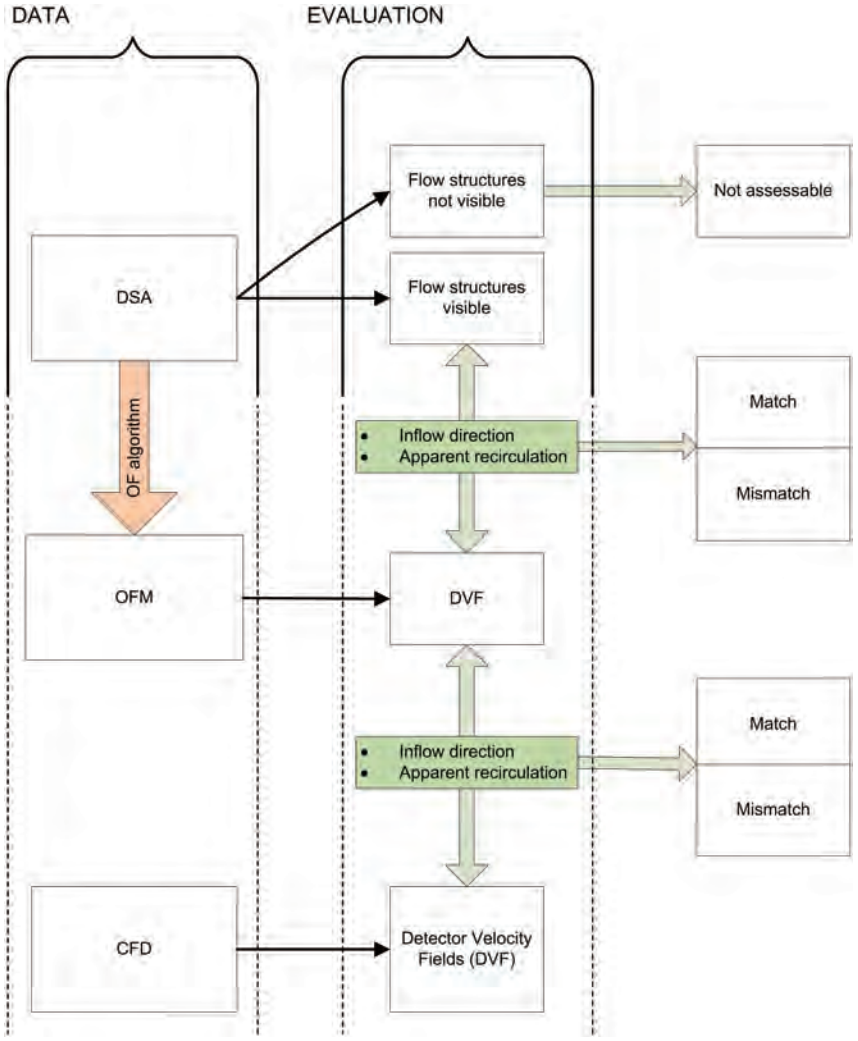

FIG 2. Comparative analysis among the 3 datasets: DSA, OF, and CFD images. The left column represents the 3 types of data work products initiating the illustrative analysis. The "evaluation" process is represented in the second column. The binary evaluation problems are represented in the last column for each defined element of the flow structures.

ing.[4-6] The pressure boundary conditions of the outlets were based on measurements of healthy subjects, as published by Reymond et al.[8] The Womersley analytic solutions, rescaled to the inlet diameter, were used to generate the specific distributions of velocity magnitudes over the artery diameter. The vessel wall was assumed rigid with no-slip boundary features. We simulated 2 cardiac cycles: The first cycle was used to reach solver convergence, and the second was used to collect the hemodynamic results for postprocessing. The Reynolds number ranged from 300 to 500, and the Womersley numbers, from 2.0 to 3.1. The analysis of the results was automated by using both commercial scripts from CFX and customized scripts from Matlab (MathWorks, Natick, Massachusetts).

Comparative Evaluation of Flow Patterns

All image datasets were displayed on the same view in the line of sight of the detector plane. The analysis workflow represented in Fig 2 compares 3 types of datasets:

- High-frame-rate DSA, in which gross intra-aneurysmal contrast motion structures were sought.
- OF images showing the extracted DVF outcomes: To facilitate the visual comparison between DSA and OF images, we specifically integrated DVF to provide short streamlines starting and ending in the aneurysm region of interest (Fig 3, column 2).
- CFD results: The 3D streamlines were viewed with the camera aligned on the line of sight of the detector.

Datasets were visualized on a dedicated workstation and evaluated by 3 independent, experienced observers (V.M.P., O. Brina, and R.O.) blinded to each other's results; the interobserver evaluation agreement was then calculated by using Fleiss κ statistics. For each patient, the 3 image sets were inspected at the systolic and diastolic phases and in the cine loops. Figure 3 shows a subset of flow patterns for the 3 datasets at systole to highlight the convective parts of contrast motion along with all the representation derivatives.

Because the vortical structures cannot be assessed on a planar detector, we restricted the comparative evaluation to inflow direction and apparent recirculation features (Table 1). The planar apparent circulation does not reflect the actual vortical structure on the detector. We evaluated the intra-aneurysmal flow features between the DSA and OF images and compared the DSA-OF images with the CFD outcomes.

RESULTS

Table 2 describes patient and aneurysm features of the 21 patients included in this study. Figure 3 summarizes the matching patterns of various degrees among the DSA, OF images, and CFD outcomes during the systolic phase, represented by 12 distinct aneurysm configurations and divided into 3 groups—Fig 3*A*: conclusive with respect to DSA, DVF, and CFD outcomes (4 of 8 cases were represented); Fig 3*B*: conclusive with respect to DVF and CFD outcomes (4 of 6 were represented); Fig 3*C*: inconclusive with respect to either DSA, DVF, or CFD outcomes (4 of 7 were represented). For all these cases, inlet flow was fed through the internal carotid artery or the vertebral artery. The flow rates ranged between 0.65 (a vertebral case) and 3.95 mL/s (a carotid case).

Comparison of DSA and OF Images

Poor agreement was initially observed between DSA contrast motion patterns and OF velocity vectors because DSA was unable to provide any flow structure information in 13 of the 21 cases, despite the high-frame-rate resolution. These cases were classified as "nonassessable" and mainly involved small-sized aneurysms (Fig 3*B*, -*C*). Alternatively, the patients presenting with larger lesions (>8 mm, $n = 8$) had well-defined DSA flow structures, all match-

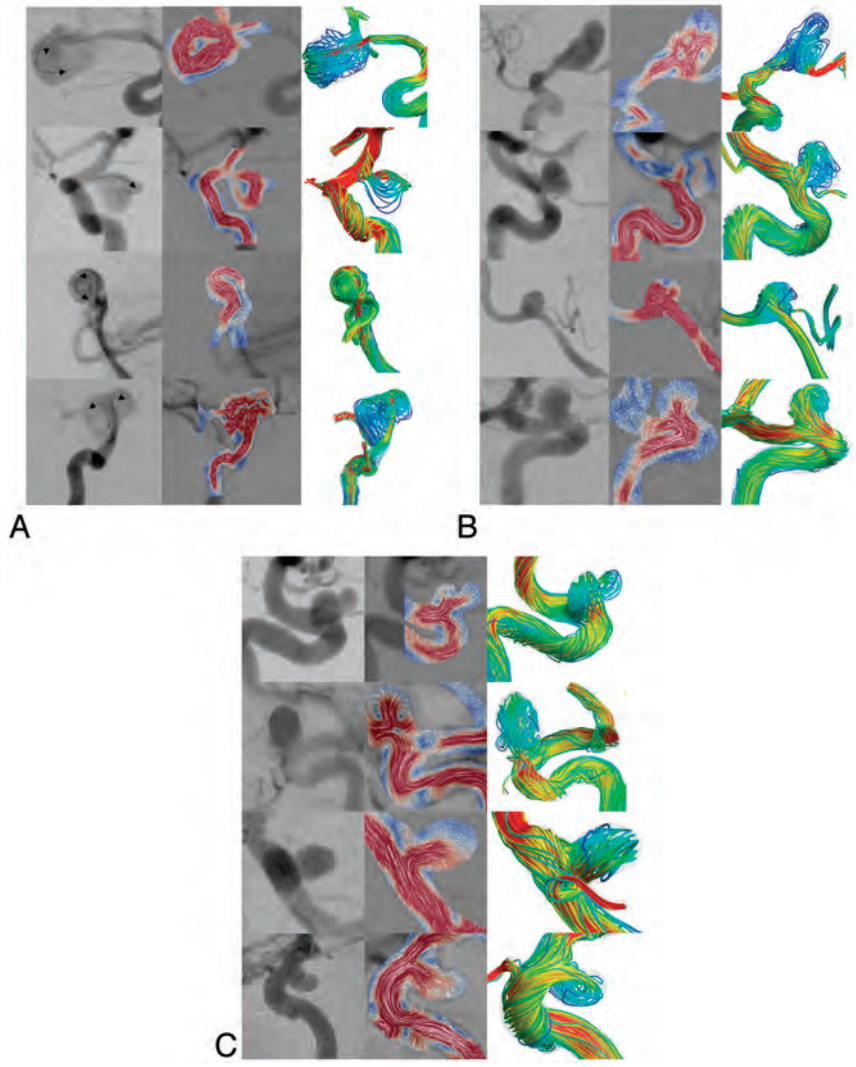

FIG 3. Illustration of the 3 classes of qualitative representations emanating from the 3 techniques: DSA, OF, and CFD. For each section (*A–C*), the 3 columns from left to right represent DSA, DVF, and CFD images, respectively. Each row represents a different patient. Image captures correspond to the systolic phase. *A*, Four cases of 8 with flow patterns conclusively visible on DSA. The *arrows* show flow direction and apparent recirculation. The last 3 rows show perfect matching among DSA, OF images, and CFD, for instance, in patient 11 (row 2) shows a superior narrow inflow jet in a left posterior communicating artery aneurysm with a clockwise vortex. The first row represents patient 15 with a right middle cerebral artery aneurysm with consistent flow structures visible on both DSA and OF images (narrow jet entering the superior part of the aneurysm and creating an anticlockwise vortex). CFD streamlines show a different behavior represented by a medial jet, a narrow impingement area, and a planar vortex orthogonal to the DSA line of sight. This mismatch was essentially produced by fake stenosis generated by the vascular geometry modeling process. *B*, Four cases of 6 with a conclusive OF flow pattern, though "silent" (not visible) on DSA. For instance, DSA of patient 12 in row 3 shows no contrast motion in a left posterior inferior cerebellar artery aneurysm. Contrary to this finding, an inflow jet in the axis of the upstream vertebral artery was visible in the corresponding OF images. This trend was confirmed by CFD streamlines, though the jet deflection was incorrect. *C*, Four cases of 7 are inconclusive with either DSA, OF, or CFD images, all confirming that flow structures could not be visible on the selected plane of the detector. For instance, for the left carotid ophthalmic aneurysm seen in patient 21 and represented in row 2, the flow pattern was not visible in either the DSA, OF, or CFD images. Should the orthogonal projection view be chosen, the flow patterns would have been depicted better, as can be seen on the CFD image.

ing OF inflow direction and apparent recirculation representations (Fig 3*A*). Figure 3*A*, row 2, illustrates a perfect match between DSA and OF images, showing a superior narrow inflow jet along with a clockwise recirculation vortex in a posterior communicating artery aneurysm.

Additionally, even if DVF could be computed from DSA sequences for all the 21 patients, some cases presented OF patterns that could not be classified within the taxonomy of this study (n = 7) on the basis of inflow direction and apparent recirculation features. These cases all had "silent" DSA with no apparent flow structures (Fig 3*C*). Alternatively, Fig 3*B* shows cases in which DSA was also inconclusive (no apparent flow structure), unlike in corresponding OF images (n = 6). All these evaluations were rated by 3 independent observers, with an average interobserver κ estimated to 0.87.

Comparison of the OF Images and the CFD Outcomes

In this step, we compared both inflow direction and apparent recirculation features from OF and CFD outcomes, taking into account the line of sight of the detector plane. The 14 cases that presented clearly defined OF patterns were confirmed by CFD, with the exception of 1 case illustrated in Fig 3*A*, row 1. In this case, CFD streamlines matched neither DVF nor DSA images. This effect was caused by stenosis artifacts in the terminal part of the M1 segment generated by the segmentation process. This stenosis generated an inappropriate inflow jet in the medial part of the aneurysm, which was visible neither in DSA nor in DVF figures. In second row of Fig 3*A*, the strong CFD inflow jet coming through the neck was largely underestimated in OF images, even though its direction was consistent among the 3 datasets. Essentially, this underestimation was due to inappropriate temporal resolution in DSA. For 7 cases, DVF patterns could not be clearly defined (Fig 3*C*) and thereby compared with CFD outcomes. No mismatch was found between both techniques, while CFD streamlines were unable to characterizing DVF flow structures. The lack of OF image-pattern visibility in the line of sight of the detector as confirmed by CFD indicates that another DSA projection view would have been more suitable for flow-pattern visibility. For this OF-CFD comparison, the average interobserver κ was 0.91.

DISCUSSION

In this study, we investigated the qualitative degree of matching between OF-DVF and DSA in intracranial aneurysms with the

Table 1: Inflow direction and apparent recirculation features

Parameters	Description	Label
Inflow direction	Intra-aneurysmal orientation of the penetrating flow/jet	Match nonmatch
Apparent recirculation	Presence of vortical structures/ vortex rotation direction	Match nonmatch

Table 2: Summary of clinical information[a]

Patient	Sex	Age (yr)	Aneurysm Location	Size H/L/W (mm)	Neck Length (mm)	Volume (cm^3)	AR
1	F	70	LMCA	4.6/4.8/4.7	3.90	0.076	1.2
2	F	54	RMCA	8/10.6/8.3	9.90	0.48	0.8
3	F	60	BaTip	6.1/7.1/6.7	5.10	0.2	1.18
4	F	60	RCO	4.9/8.7/5.3	4.60	0.122	1
5	F	58	LCO	6.2/6.2/4.7	3.80	0.124	1.6
6	M	62	LMCA	12.4/8.4/6.8	10.40	0.64	1.2
7	F	62	RCO	6.6/5.6/5.8	3.90	0.115	1.7
8	M	50	LICA cave	4/4.5/6	4.20	0.066	0.95
9	F	67	LPcomA	6.9/7.7.10.8	7.80	0.47	0.9
10	M	40	RICA cave	3.8/4.3/4.2	4.70	0.082	0.8
11	F	47	LPcomA	9.3/9.1/6.2	2.25	0.22	4.15
12	F	55	LPICA	6.6/5.2/6.6	6.10	0.19	0.85
13	F	50	RICA	13.5/17.8/9.9	7.60	1.13	1.77
14	F	53	LCO	5.3/5.5	4.40	0.111	1.2
15	F	54	RMCA	18.3/14.9/13.85	8.50	2.3	2.15
16	F	56	RICA	4.2/5.6/4.5	3.80	0.069	0.9
17	F	45	LCO	5.9/7.7/6.7	3.80	0.173	1.3
18	F	64	RICA	18.3/17/18.5	8.50	3.125	2.2
19	F	56	LICA	3.4/3.2/3	2.90	0.026	1
20	F	56	LCO	5/5.1/5.9	4.50	0.109	1
21	F	52	LCO	8.2/9.6/8.5	4.60	0.353	1.7

Note:—AR indicates aspect ratio; BaTip, basilar artery tip; CO, carotid-ophthalmic; PcomA, posterior communicating artery; PICA, posterior inferior cerebellar artery; L, left; R, right; H/L/W, height/length/width.

[a] Columns represent data for each patient.

help of CFD. The 3 techniques varied greatly in terms of the physical property that they addressed: Digital subtraction angiography essentially measures the absorption of x-rays and contrast motion during the cardiac cycle, the optical flow technique extracts the physical modulation of contrast attenuation over the cardiac cycle out of which in-plane-projected velocity fields (DVF) are assessed, and CFD calculates the 3D velocity field of blood flow by using the inlet boundary conditions provided by both DSA sequences and 3D images. These techniques have been used jointly to improve our interpretation of OF outcomes, which were successfully used to predict flow-diverter stent treatment issues in intracranial aneurysms.[6] Although the OF method has allowed matching between contrast motion and convective flow, the observation of genuine or fake flow structures generally depends on the complexity of flow and the direction of detector plane. Therefore, CFD-computed streamlines were needed to dissipate the above-mentioned ambiguities to avoid any misleading interpretation.

In particular, it was first shown that DVF figures obtained from DSA fairly matched CFD outcomes for both the inflow direction and the apparent recirculation. The complexity of the flow structure, which could be reliably represented by CFD streamlines over the cardiac cycle, helped greatly in drawing conclusive evaluations in the chosen plane of the detector. In our study, 7 of 21 cases were not conclusive as was expected from DSA figures in out-of-focus projection planes. Of the 14 conclusive OF flow structures, only 8 were conclusive with regard to DSA images. The 6 others were not. Nevertheless, their representations of inflow direction and apparent recirculation were compatible with CFD streamlines, independent of aneurysm size, thereby demonstrating that the OF method could possibly unfold genuine flow structures wherever hidden in DSA. The qualitative analysis among DSA, OF images, and CFD was in perfect agreement among the 3 independent observers, as demonstrated by the high κ values of >0.8, confirming that based on the described binary parameters, OF images can provide consistent flow information. Unlike in videos, still images did not necessarily reflect the degree of agreement among the observers.

The clinical benefits of these DVF measurements, readily available during treatment, have not yet been fully established. However, one can foresee several applications in the future: 1) predicting thrombosis in stented aneurysms,[6] and 2) adapting CFD to perioperative patient-specific conditions. Furthermore, an extension of the OF method in 3D would help give more quantitative insight on both the measurements of flow-pattern complexity and related parameters such as wall shear stress in aneurysms, which are believed to play an important role in all aspects of aneurysm growth,[9] rupture,[10] and clotting.[11]

In line with Taylor and Steinman,[12] the OF method was based on vascular anatomic imaging criterion standard DSA, which could bring flow evaluation closer to daily clinical practice. Taylor and Steinman strongly encouraged bringing image-based modeling to the management of vascular diseases rather than innovating with more sophisticated developments that diverge from the clinically oriented approaches. Alternatively, other groups have followed the same lead by using phase-contrast MR angiography and CFD comparisons. Karmonik et al[13] described similar velocity shapes between 2D phase-contrast MR angiography and CFD in anterior communicating artery aneurysms. In 2 canine aneurysm models, Jiang et al[14] also showed favorable agreement of velocity fields between phase-contrast MR angiography and CFD. Other studies compared the flow patterns between DSA and CFD by using virtual angiogram modeling. Cebral et al[15] qualitatively compared the intra-aneurysmal flow structures of 3 patients between conventional DSA and virtual angiograms and were able to predict, with good agreement, the locations and sizes of the inflow jet, outflow, impaction zone, and vortex structures.

Limitations and Further Developments

The single DSA projection view is an unfortunate limitation of our method, which restricted the CFD analysis and consequently precluded the use of qualitative features defined, for instance, by Cebral et al[10] (inflow concentration, impingement zone, flow complexity, and flow stability) to describe the intra-aneurysmal flow. These features were not fully applicable in the context of our DVF study implying the use of simpler parameters. Because the optical flow algorithm measures moving patterns within the regions of interest, overlap of branches and the parent vessel should be avoided as much as possible when choosing the projection views. Moreover, the OF method might introduce fake vortices as a result of projecting laminar flow patterns, which can only be avoided by the extension of the method to 3D images. DVF mag-

nitude can be underestimated for very high velocities due to inappropriate temporal resolution in DSA. In addition to optical flow method boundary condition measurements, segmentation may also impact CFD outcome as has been observed in the first patient in Fig 3*A*. Furthermore, both the seed points and attenuation may influence CFD streamlines.

Moreover, even if the OF method was validated by using Doppler sonography to evaluate the volumetric blood flow in internal carotid arteries, we believe that intra-aneurysmal flow quantification in patients would require further development and carefully conducted validation steps involving, for example, particle imaging velocimetry measurements. In this study, we aimed to demonstrate that a novel method, applicable to the clinical routine, could be used in the future to perform more patient-specific CFD and to characterize potential aneurysm flow patterns related to rupture.

CONCLUSIONS

Velocity field patterns measured in intracranial aneurysms by using the OF method from DSA sequences were reasonably matched with DSA and CFD outcome and could provide, whenever possible, complementary flow pattern structures not visible on DSA. Moreover, the extension of the OF method to 3D images should definitely help in removing fake single-plane flow structures.

Disclosures: Karl Schaller—*UNRELATED*: *Grants/Grants Pending*: Swiss National Science Foundation.* Vitor Mendes Pereira—*RELATED*: *Grant*: Philips,* *Comments*: The grant is to pay the 50% time of a research technician who works locally in our center to collect the data and work on the postprocessing for our daily clinical practice and for the related research projects that we have with Philips. *Money paid to the institution.

REFERENCES

1. Vlak MH, Algra A, Brandenburg R, et al. **Prevalence of unruptured intracranial aneurysms, with emphasis on sex, age, comorbidity, country, and time period: a systematic review and meta-analysis.** *Lancet Neurol* 2011;10:626–36
2. Pereira VM, Brina O, Bijlenga P, et al. **Wall shear stress distribution of small aneurysms prone to rupture: a case-control study.** *Stroke* 2014;45:261–64
3. Pereira VM, Brina O, Gonzalez AM, et al. **Biology and hemodynamics of aneurismal vasculopathies.** *Eur J Radiol* 2013;82:1606–17
4. Bonnefous OP, Pereira VM, Ouared R, et al. **Quantification of arterial flow with digital subtracted angiography (DSA).** *Med Phys* 2012;39:6264–75
5. Pereira VM, Ouared R, Brina O, et al. **Quantification of internal carotid artery flow with digital subtraction angiography: validation of an optical flow approach with Doppler ultrasound.** *AJNR Am J Neuroradiol* 2014;35:156–63
6. Pereira VM, Bonnefous O, Ouared R, et al. **A DSA-based method using contrast-motion estimation for the assessment of the intra-aneurysmal flow changes induced by flow-diverter stents.** *AJNR Am J Neuroradiol* 2013;34:808–15
7. Villa-Uriol MC, Berti G, Hose DR, et al. **@neurIST complex information processing toolchain for the integrated management of cerebral aneurysms.** *Interface Focus* 2011;1:308–19
8. Reymond P, Merenda F, Perren F, et al. **Validation of a one-dimensional model of the systemic arterial tree.** *Am J Physiol Heart Circ Physiol* 2009;297:H208–22
9. Boussel L, Rayz V, McCulloch C, et al. **Aneurysm growth occurs at region of low wall shear stress: patient-specific correlation of hemodynamics and growth in a longitudinal study.** *Stroke* 2008;39:2997–3002
10. Cebral JR, Mut F, Weir J, et al. **Association of hemodynamic characteristics and cerebral aneurysm rupture.** *AJNR Am J Neuroradiol* 2011;32:264–70
11. Ouared R, Chopard B, Rufenacht D, et al. *Thrombosis Engineering in Intracranial Aneurysms Using a Lattice Boltzmann Numerical Method.* Munich: Springer-Verlag; 2009:1538–41
12. Taylor CA, Steinman DA. **Image-based modeling of blood flow and vessel wall dynamics: applications, methods and future directions—Sixth International Bio-Fluid Mechanics Symposium and Workshop, March 28–30, 2008 Pasadena, California.** *Ann Biomed Eng* 2010;38:1188–203
13. Karmonik C, Klucznik R, Benndorf G. **Comparison of velocity patterns in an AComA aneurysm measured with 2D phase contrast MRI and simulated with CFD.** *Technol Health Care* 2008;16:119–28
14. Jiang J, Johnson K, Valen-Sendstad K, et al. **Flow characteristics in a canine aneurysm model: a comparison of 4D accelerated phase-contrast MR measurements and computational fluid dynamics simulations.** *Med Phys* 2011;38:6300–12
15. Cebral JR, Pergolizzi RS Jr, Putman CM. **Computational fluid dynamics modeling of intracranial aneurysms: qualitative comparison with cerebral angiography.** *Acad Radiol* 2007;14:804–13

Forced Arterial Suction Thrombectomy with the Penumbra Reperfusion Catheter in Acute Basilar Artery Occlusion: A Retrospective Comparison Study in 2 Korean University Hospitals

Y.-I. Eom, Y.-H. Hwang, J.M. Hong, J.W. Choi, Y.C. Lim, D.-H. Kang, Y.-W. Kim, Y.-S. Kim, S.Y. Kim, and J.S. Lee

ABSTRACT

BACKGROUND AND PURPOSE: A performance of forced arterial suction thrombectomy was not reported for the treatment of acute basilar artery occlusion. This study compared revascularization performance between intra-arterial fibrinolytic treatment and forced arterial suction thrombectomy with a Penumbra reperfusion catheter in patients with acute basilar artery occlusion.

MATERIALS AND METHODS: Fifty-seven patients with acute basilar artery occlusion were treated with intra-arterial fibrinolysis ($n = 25$) or forced arterial suction thrombectomy ($n = 32$). Baseline characteristics, successful revascularization rate, and clinical outcomes were compared between the groups.

RESULTS: Baseline characteristics, the frequency of patients receiving intravenous recombinant tissue plasminogen activator, and mean time interval between symptom onset and femoral puncture did not differ between groups. The forced arterial suction thrombectomy group had a shorter procedure duration (75.5 minutes versus 113.3 minutes, $P = .016$) and higher successful revascularization rate (88% versus 60%, $P = .017$) than the fibrinolysis group. Fair outcome, indicated by a modified Rankin Scale 0–3, at 3 months was achieved in 34% of patients undergoing forced arterial suction thrombectomy and 8% of patients undergoing fibrinolysis ($P = .019$), and the mortality rate was significantly higher in the fibrinolysis group (25% versus 68%, $P = .001$). Multiple logistic regression analysis identified the forced arterial suction thrombectomy method as an independent predictor of fair outcome with adjustment for age, sex, initial NIHSS score, and the use of intravenous recombinant tissue plasminogen activator (odds ratio, 7.768; 95% CI, 1.246–48.416; $P = .028$).

CONCLUSIONS: In acute basilar artery occlusion, forced arterial suction thrombectomy demonstrated a higher revascularization rate and improved clinical outcome compared with traditional intra-arterial fibrinolysis. Further clinical trials with the newer Penumbra catheter are warranted.

ABBREVIATIONS: BAO = basilar artery occlusion; IA = intra-arterial; FAST = forced arterial suction thrombectomy

The prognosis for acute basilar artery occlusion (BAO) is dismal.[1,2] Early recanalization is one of the most important prognostic factors for an improved outcome in BAO.[3,4] Intravenous infusion of recombinant tissue plasminogen activator is, however, not fully effective for the recanalization of acute BAO.[5,6]

Endovascular treatment is an emerging therapeutic option for acute BAO. Previously, local infusion of fibrinolytic agents was the only available therapy.[2,7,8] Although intra-arterial fibrinolysis achieved a much higher recanalization rate than intravenous rtPA, clinical outcome did not differ between the treatments.[9] Recently, several mechanical thrombectomy devices have been developed and applied in clinical studies.[10-13] However, thus far, no device has been proved to improve clinical outcomes, and the optimal strategy for acute BAO treatment has not yet been established.

The Penumbra System (Penumbra, Alameda, California) is an endovascular device designed to reduce clot burden in acute ischemic stroke due to large cerebral artery occlusion. Although many clinical trials have been conducted using the device, data concerning the use of the Penumbra System in acute BAO are still scarce.[10] Forced arterial suction thrombectomy (FAST), which is a modification of the standard Penumbra System, is used as a mechanical recanalization method for ischemic stroke.[14,15] Unlike the standard Penumbra System, the FAST method involves only a reperfusion catheter. Negative

Received March 28, 2014; accepted after revision May 28.

From the Departments of Neurology (Y.-I.E., J.M.H., J.S.L.) and Radiology (J.W.C., S.Y.K.), Ajou University Medical Center, Suwon, South Korea; Departments of Neurology (Y.-H.H., Y.-W.K.), Neurosurgery (D.-H.K.), and Radiology (D.-H.K., Y.-W.K., Y.-S.K.), Kyungpook National University Hospital, Daegu, South Korea; and Department of Neurosurgery (Y.C.L.), Ajou University Hospital, Daegu, South Korea.

This work was supported by the new faculty research fund of the Ajou University School of Medicine (J.S. Lee).

Please address correspondence to Jin Soo Lee, MD, PhD, Department of Neurology, Ajou University Medical Center, Suwon, South Korea; e-mail: jinsoo22@gmail.com

http://dx.doi.org/10.3174/ajnr.A4045

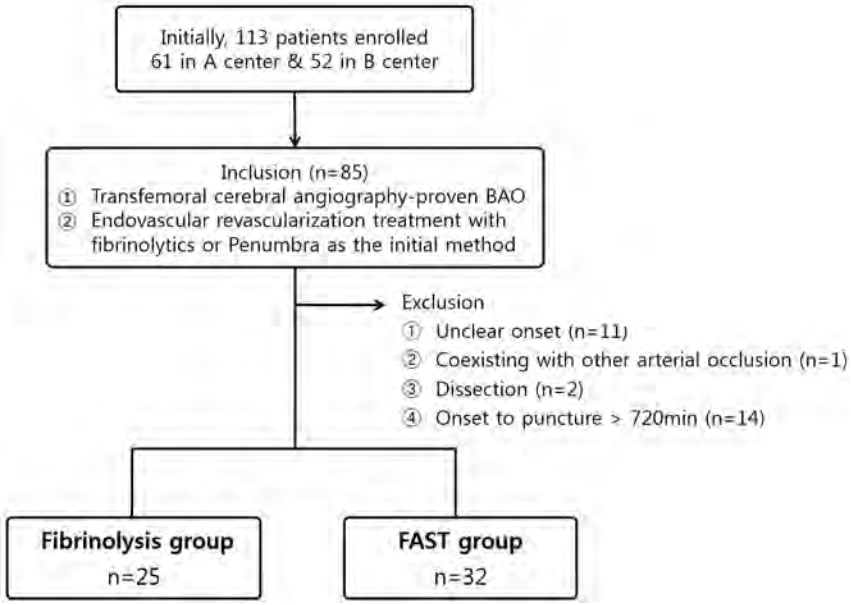

FIG 1. Flow diagram of the current study.

Table 1: Baseline demographics, neurologic deficits, and hyperacute treatment status

	Fibrinolysis Group	FAST Group	*P* Value
No. of patients	25	32	
Age (yr) (mean)	66.6 ± 10.2	68.3 ± 10.7	.549
Male	21 (84%)	22 (69%)	.184
Hypertension	11 (44%)	21 (66%)	.103
Diabetes mellitus	7 (28%)	9 (28%)	.992
Atrial fibrillation	8 (32%)	11 (34%)	.850
NIHSS score on admission (mean)	19.9 ± 8.1	19.8 ± 8.7	.965
TOAST classification			.737
Atherosclerosis	14 (56%)	15 (47%)	
Cardioembolism	7 (28%)	12 (37%)	
Mixed or unknown	4 (16%)	5 (16%)	
Use of intravenous rtPA	7 (28%)	12 (36%)	.35
Time from onset to puncture (min) (mean)	297.0 ± 125.1	281.4 ± 138.3	.662
Primary endovascular treatment			
Urokinase	22 (88%)	–	
rtPA	2 (8%)		
Tirofiban	1 (4%)		
Penumbra	–	32 (100%)	
Rescue treatment methods			
Stenting	7 (28%)	6 (18.8%)	
Tirofiban	2 (8%)	2 (6.3%)	
Abciximab	2 (8%)	–	
Penumbra	2 (8%)		
Solitaire	–	3 (9.4%)	

Note:—TOAST indicates Trial of Org 10172 in Acute Stroke Treatment.[34]

pressure via forceful pulling of a syringe can keep an embolus aspirated at the catheter tip. This method has been reported to be simpler and faster than the standard Penumbra System and has been applied clinically.[14,16,17]

We postulated that the FAST method may improve the clinical outcome of acute BAO compared with the traditional endovascular treatment method of local fibrinolysis. In the present study, we evaluated the revascularization performance and clinical outcomes between intra-arterial (IA) fibrinolytic treatment and the FAST method and compared them with the Penumbra reperfusion catheter in patients with acute BAO.

MATERIALS AND METHODS

Study Population

This retrospective study involved registry data bases and additional imaging analyses. All patients or their caregivers gave informed consent for each endovascular treatment. From registries of 2 university hospitals in Korea, 113 consecutive patients who had BAO with or without continuous vertebral artery occlusion and underwent revascularization treatments between March 2006 and June 2013 were enrolled (Fig 1). Among them, those who had transfemoral cerebral angiography–proved BAO and underwent IA revascularization with either fibrinolysis or mechanical thrombectomy by using FAST as the initial IA treatment method for acute BAO were included. Patients were excluded under the following conditions: 1) their onset of symptoms was unclear, 2) another cerebral artery was occluded, 3) onset-to-puncture time exceeded 720 minutes, or 4) their stroke etiology was dissection. We grouped patients into a fibrinolysis group and a FAST group, depending on the initial method of endovascular treatment. Other endovascular methods for rescue therapy were permitted.

Protocol

Brain parenchyma and cervicocerebral arteries were evaluated by CT or MR imaging as early as possible before IA treatment. The BAO as a treatment target was confirmed by selective cerebral intra-arterial digital subtraction angiography. Patients received either endovascular revascularization treatment following intravenous thrombolysis or endovascular treatment alone. Local intra-arterial fibrinolysis was performed by using an infusion microcatheter inserted into the middle of the clots. Fibrinolytic agents included rtPA, urokinase, abciximab, and tirofiban. All FAST methods were performed by using the Penumbra aspiration catheter (first-generation). Using a transfemoral approach, we placed the guide catheter into the dominant or most navigable vertebral artery. After we placed the reperfusion catheter immediately proximal to the clot, we applied negative pressure at the distal tip by continuous suctioning with a 50-mL syringe. The catheter was then smoothly pulled back. The interventional procedure was terminated when recanalization was achieved or according to a consensus between neurologists and neurointerventionists.

Table 2: Procedural and clinical outcomes

	Fibrinolysis Group	FAST Group	*P* Value
Procedure time (min) (mean)	113.3 ± 65.4	75.5 ± 42.2	.016
Time from onset to final angiography (min) (mean)	419.5 ± 144.7	364.7 ± 145.2	.163
Successful revascularization	15 (60%)	28 (88%)	.017
Intracranial hemorrhage			.157
Hemorrhagic transformation type 1	7 (29%)	4 (13%)	
Hemorrhagic transformation type 2	–	–	
Parenchymal hematoma type 1	–	–	
Parenchymal hematoma type 2	1 (4%)	–	
SAH	2 (8%)	2 (6%)	.797
NIHSS score at discharge (mean)	20.2 ± 11.8	9.2 ± 12.8	.066
Fair outcome at 3 months	2 (8%)	11 (34%)	.019
Mortality	17 (68%)	8 (25%)	.001
Successful revascularization with the primary stand-alone technique	13 of 21 (61.9%)	24 of 26 (92.3%)	.011
Procedure time of the primary stand-alone technique (min) (mean)	91.1 ± 44.6	66.2 ± 34.0	.037
Fair outcome at 3 months with the primary stand-alone technique	1 of 21 (4.8%)	10 of 26 (38.5%)	.007

Outcome Measurements

Baseline patient data, including vascular risk factors, stroke etiology, laboratory and imaging variables, and initial neurologic severity scales, were retrieved from each stroke registry data base and electronic health records. Imaging data were collected from the PACS of each hospital. Procedural duration was defined as the time between the placement of a guide catheter proximal to the target artery and final angiography of the target artery. Revascularization was measured by the Thrombolysis in Cerebral Infarction score. Successful revascularization was defined as a TICI score of 2b (perfusion ≥ 50%) or 3. Functional outcomes were measured by using the modified Rankin Scale and mortality at 3 months. Fair outcome at 3 months was defined as an mRS score of 0–3.

Statistical Analysis

Univariate analyses were performed by using the *t* test for continuous variables and the χ^2 test for nonparametric variables. Logistic regression analysis was used to evaluate whether the FAST method was an independent predictor of fair outcomes at 3 months. Two-sided *P* values < .05 were considered significant. Statistical analyses were performed by using a commercially available software package (SPSS, Version 17.0 for Windows; IBM, Armonk, New York).

RESULTS

Ultimately, 57 patients were included in the study: 25 in the fibrinolysis group and 32 in the FAST group. Baseline characteristics were similar between groups (Table 1). Mean age, the frequency of males, and the mean initial National Institutes of Health Stroke Scale score did not differ significantly between groups. The frequency of patients who underwent intravenous rtPA and the mean time interval between symptom onset and femoral puncture also did not differ between groups.

Procedural and clinical outcomes are presented in Table 2. Urokinase was most frequently used for primary IA fibrinolysis (88%; mean, 240,000 U). Tirofiban and rtPA were used in a small number of patients who underwent primary IA fibrinolysis. In patients who underwent the primary FAST procedure, the Penumbra reperfusion catheter 041 was most frequently used (29 cases), followed by the Penumbra reperfusion catheter 032 (3 cases). Furthermore, the Penumbra reperfusion catheter 026 (2 cases) was used only for rescue therapy in the fibrinolysis group. A separator was not used in any of the cases in both the hospitals. The median number of passes performed with the Penumbra reperfusion catheter was 2 (interquartile range, 1–3). The mean procedural duration was significantly shorter in the FAST group than in the fibrinolysis group (76 minutes versus 113 minutes, $P = .016$). Successful revascularization was achieved at a higher rate in the FAST group than in the fibrinolysis group (88% versus 60%, $P = .017$). The rate of fair outcome at 3 months was significantly higher in the FAST group than in the fibrinolysis group (36% versus 8%, $P = .015$), while the mortality rate was significantly higher in the fibrinolysis group (23% versus 68%, $P = .001$; Fig 2). A multiple logistic regression model revealed that the FAST method was an independent predictor of fair outcome with adjustment for age, sex, initial NIHSS score, and the infusion of intravenous rtPA (odds ratio, 7.768; 95% CI, 1.246–48.416; $P = .028$; Table 3).

Notably, our cohort demonstrated unique characteristics concerning etiology, with atherosclerosis accounting for 50% of pa-

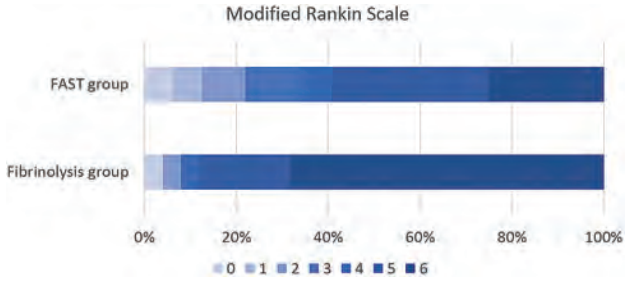

FIG 2. Modified Rankin Scale of each group. Mortality was significantly reduced when patients underwent endovascular treatment with the FAST method compared with local fibrinolysis.

Table 3: Multiple logistic regression model for fair outcome at 3 months

Variables	OR (95% CI)	*P* Value
Age	0.951 (0.881–1.027)	.199
Sex	0.135 (0.013–1.389)	.092
Initial NIHSS score	0.914 (0.828–1.009)	.073
Intravenous rtPA	3.749 (0.685–20.512)	.128
FAST method	7.768 (1.246–48.416)	.028
Successful revascularization	4.339 (0.266–70.698)	.303

Table 4: List of revascularization treatment studies for acute basilar artery occlusion

Reference	Method	No. of Patients	Age (yr)	NIHSS on Admission	Good Outcome	Fair Outcome	Mortality	TIMI 2–3	TICI 2b-3	sICH	SAH
Arnold et al (2004)[31]	Urokinase	40	58 (median)	18 (median)	35%	47%	42%	60%	–	5%	–
Lutsep et al (2008)[13]	Merci	27	58 (median)	22 (median)	33%	41%	44%	78%	–	19%	11%
Roth et al (2011)[10]	Standard Penumbra System	12	70 (median)	28 (median)	33%[a]	50%[a]	33%[a]	83%[b]	–	–	–
Mourand et al (2014)[30]	Solitaire	31	61 (mean)	38 (median)	35%	–	32%	–	74%	16%	–
Espinosa de Ruedz et al (2013)[28]	Solitaire, Trevo	18	68 (mean)	20 (mean)[c]	50%	–	22%	–	94.4%	–	6%
Current study, fibrinolysis	Urokinase, rtPA, tirofiban	25	67 (mean)	20 (mean)	8%	8%	68%	–	36%	4%	8%
Current study, FAST	FAST method	33	68 (mean)	20 (mean)	22%	35%	21%	–	79%	0%	6%

Note:—TIMI indicates Thrombolysis in Myocardial Infarction; sICH, symptomatic intracerebral hemorrhage.
[a] Scales were evaluated before discharge.
[b] Definition of recanalization was not clearly documented.
[c] NIHSS score on admission was evaluated only in nonintubated patients (12 of 18).

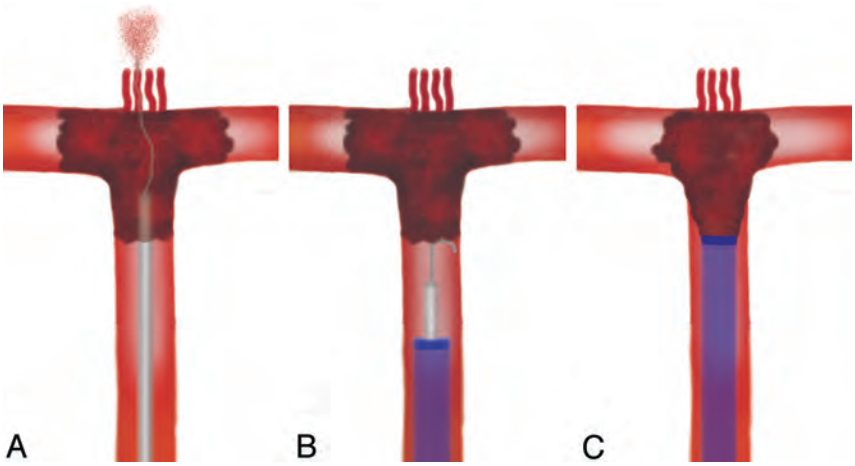

FIG 3. Schematic drawings of endovascular treatment for acute BAO. *A*, Arterial branches are obscured above the occlusive site, and inadvertent hemorrhagic complications can occur when a microwire and microcatheter must be navigated distal to the occlusive site. *B* and *C*, The FAST method can avoid this risk because the tip of the Penumbra reperfusion catheter is located only at the proximal end of the clot.

tients. Specifically, intracranial stent placement was performed in 19% and 28% of patients in the FAST and fibrinolysis groups, respectively.

DISCUSSION

In this series, we have demonstrated that the FAST method with the Penumbra aspiration catheter can rapidly and effectively restore blood flow in acute BAO and can improve patient outcome in comparison with the traditional IA fibrinolysis method. Better clinical outcome was attributed to higher performance in terms of the revascularization rate and shorter procedural duration. This study is the first to report the efficacy of FAST with the Penumbra reperfusion catheter for the treatment of acute BAO in comparison with IA fibrinolysis.

Acute BAO is a devastating disease, which has been associated with a poor clinical outcome and a high mortality rate.[1,2] Treatment with intravenous thrombolysis has been shown to be ineffective for the recanalization of BAO or carotid T occlusion.[18,19] On the basis of these limitations, IA injection of fibrinolytic agents has been adopted in standard protocols to treat BAO by many stroke centers, and several randomized trials and numerous case series have demonstrated the benefits of this therapy.[2,7,20-22] However, despite the high recanalization rate of intra-arterial fibrinolysis therapy, clinical outcome has not improved.[23-25] In the past several years, the introduction of mechanical thrombectomy devices has offered a new option for the treatment of large-vessel occlusion, achieving higher recanalization rates and favorable clinical outcomes.[5,10,12,13,26,27]

At the start of the endovascular treatment era for BAO, Hacke et al[2] published findings in 1988 demonstrating better outcomes and higher survival rates in patients who underwent IA fibrinolysis compared with those who received conventional treatment. On the basis of that report, IA fibrinolysis has been considered an additional treatment option for patients with acute BAO. Recently, several studies have described the performance and efficacy of new mechanical thrombectomy devices for the treatment of BAO. The Merci retrieval system (Concentric Medical, Mountain View, California) was reported as a feasible option for the revascularization of acute BAO, with a recanalization rate of 68%.[13] Several studies using the Solitaire retrieval stent (Covidien, Irvine, California) in acute BAO have also been reported.[11,12,26-29] The latest studies have achieved revascularization rates of 74%–94% and mortality rates of 22%–32% by using stent-retrieval systems.[27,28] Previous studies of endovascular treatment for BAO are summarized in Table 4.[10,13,28,30,31]

Limited literature is available on use of the Penumbra system for acute BAO. In one study, 12 patients with acute BAO were treated with the standard Penumbra System, with a recanalization rate of 75% and a mortality rate of 33%.[10] In the present study, a successful revascularization rate of 79% and a 21% mortality rate were observed with the FAST method. Compared with traditional IA fibrinolysis, which had a successful revascularization rate of 36% and a mortality rate of 68%, outcomes of the FAST method were substantially better. Compared with the standard Penumbra System,[10] outcomes appeared to be slightly better, particularly with respect to mortality.

The interpretation of clinical outcomes in our cohort should be cautious. In contrast to cohorts in Western countries, the rate of atherosclerosis among stroke etiologies in our patients was relatively high, up to 50%. After patients were treated with the first endovascular method, intractable severe stenosis still caused the blood flow to be stagnated, necessitating secondary angioplasty and/or stent placement, in approximately 20% of our patients. These additional procedures may delay the final revascularization

time and worsen clinical outcomes. On this basis, investigators should consider that intracranial stenosis may be observed often when Asian patients are studied in clinical trials of endovascular treatment. Furthermore, a specific strategy of endovascular treatment should be established for Asian patients.

The FAST method is theoretically considered safe because it can avoid inadvertent hemorrhagic complications resulting from the perforation of small arteries originating from the top of the basilar artery (Fig 3). These complications may cause further decrease of mental status and new neurologic deficits. In most cases of BAO, the distal portion above the proximal end of the occlusion is obscured. When a microwire and microcatheter must be navigated to select a posterior cerebral artery, those instruments risk perforating small arteries that are located directly beyond the basilar artery. In the FAST method, the reperfusion catheter is placed immediately proximal to the clot, and negative pressure is applied to aspirate the thrombus. Without any procedure through the thrombus, the risk of perforation is decreased (Fig 3). Recent reports on A Direct Aspiration first Pass Technique (ADAPT) have indicated that it is similar to the FAST method[32,33]; this technique was especially well-illustrated in a previous report.[33] However, the microwire and microcatheter should be selectively traversed because this may cause a subarachnoid hemorrhage, particularly through the perforators at the top of the basilar artery.

The current study has some limitations. First, it was retrospective. A further comparative study in which both groups are randomly assigned should be performed to confirm our results. Second, both methods were not performed in the same time period. The FAST method was introduced more recently; therefore, progress in the systematic treatment for acute ischemic stroke and the development of newer intracranial microwires and microcatheters may have influenced our results. Nonetheless, major baseline characteristics and clinical events that have a substantial influence on outcomes were similar between the groups. Additionally, data were collected from 2 large hospitals and combined so that unforeseen confounding factors were less likely to have significantly affected our results. Finally, additional treatment for intracranial arterial stenosis was not considered in our analyses. Stenosis of the vertebrobasilar artery system is often observed, especially in Asians. The revascularization methods for stenosis should be applied differently. On the basis of our observations, FAST methods are better suited to embolic BAO than to atherosclerosis.

CONCLUSIONS

The FAST method by using the Penumbra reperfusion catheter demonstrated superior performance and was associated with better outcomes in patients with acute BAO compared with intra-arterial fibrinolysis. Moreover, the Penumbra system has recently been enhanced. However, additional clinical trials with newer generation devices, such as Penumbra ACE and MAX, are required to confirm the conclusions of this study.

REFERENCES

1. Caplan LR, Wityk RJ, Glass TA, et al. **New England Medical Center Posterior Circulation registry.** *Ann Neurol* 2004;56:389–98
2. Hacke W, Zeumer H, Ferbert A, et al. **Intra-arterial thrombolytic therapy improves outcome in patients with acute vertebrobasilar occlusive disease.** *Stroke* 1988;19:1216–22
3. Davis SM, Donnan GA. **Basilar artery thrombosis: recanalization is the key.** *Stroke* 2006;37:2440
4. Kim HY, Chung CS, Moon SY, et al. **Complete nonvisualization of basilar artery on MR angiography in patients with vertebrobasilar ischemic stroke: favorable outcome factors.** *Cerebrovasc Dis* 2004;18:269–76
5. Pfefferkorn T, Holtmannspotter M, Schmidt C, et al. **Drip, ship, and retrieve: cooperative recanalization therapy in acute basilar artery occlusion.** *Stroke* 2010;41:722–26
6. Pfefferkorn T, Mayer TE, Opherk C, et al. **Staged escalation therapy in acute basilar artery occlusion: intravenous thrombolysis and on-demand consecutive endovascular mechanical thrombectomy—preliminary experience in 16 patients.** *Stroke* 2008;39:1496–500
7. Eckert B, Kucinski T, Pfeiffer G, et al. **Endovascular therapy of acute vertebrobasilar occlusion: early treatment onset as the most important factor.** *Cerebrovasc Dis* 2002;14:42–50
8. Furlan A, Higashida R, Wechsler L, et al. **Intra-arterial prourokinase for acute ischemic stroke: the PROACT II study—a randomized controlled trial. Prolyse in Acute Cerebral Thromboembolism.** *JAMA* 1999;282:2003–11
9. Schonewille WJ, Wijman CA, Michel P, et al. **Treatment and outcomes of acute basilar artery occlusion in the Basilar Artery International Cooperation Study (BASICS): a prospective registry study.** *Lancet Neurol* 2009;8:724–30
10. Roth C, Mielke A, Siekmann R, et al. **First experiences with a new device for mechanical thrombectomy in acute basilar artery occlusion.** *Cerebrovasc Dis* 2011;32:28–34
11. Machi P, Costalat V, Lobotesis K, et al. **Solitaire FR thrombectomy system: immediate results in 56 consecutive acute ischemic stroke patients.** *J Neurointerv Surg* 2012;4:62–66
12. Mordasini P, Brekenfeld C, Byrne JV, et al. **Technical feasibility and application of mechanical thrombectomy with the Solitaire FR revascularization device in acute basilar artery occlusion**. *AJNR Am J Neuroradiol* 2013;34:159–63
13. Lutsep HL, Rymer MM, Nesbit GM. **Vertebrobasilar revascularization rates and outcomes in the MERCI and multi-MERCI trials.** *J Stroke Cerebrovasc Dis* 2008;17:55–57
14. Kang DH, Hwang YH, Kim YS, et al. **Direct thrombus retrieval using the reperfusion catheter of the Penumbra system: forced-suction thrombectomy in acute ischemic stroke.** *AJNR Am J Neuroradiol* 2011;32:283–87
15. Lee JS, Hong JM, Lee SJ, et al. **The combined use of mechanical thrombectomy devices is feasible for treating acute carotid terminus occlusion.** *Acta Neurochir (Wien)* 2013;155:635–41
16. Kang DH, Kim YS, Park J, et al. **Rescue forced-suction thrombectomy using the reperfusion catheter of the Penumbra System for thromboembolism during coil embolization of ruptured cerebral aneurysms.** *Neurosurgery* 2012;70(1 suppl operative):89–93, discussion 93–94
17. Kim YW, Kang DH, Hwang JH, et al. **Rescue strategy for acute carotid stent thrombosis during carotid stenting with distal filter protection using forced arterial suction thrombectomy with a reperfusion catheter of the Penumbra system: a technical note.** *Acta Neurochir (Wien)* 2013;155:1583–88
18. Arnold M, Nedeltchev K, Mattle HP, et al. **Intra-arterial thrombolysis in 24 consecutive patients with internal carotid artery T occlusions.** *J Neurol Neurosurg Psychiatry* 2003;74:739–42
19. Kucinski T, Koch C, Grzyska U, et al. **The predictive value of early CT and angiography for fatal hemispheric swelling in acute stroke.** *AJNR Am J Neuroradiol* 1998;19:839–46
20. Chandra RV, Law CP, Yan B, et al. **Glasgow coma scale does not predict outcome post-intra-arterial treatment for basilar artery thrombosis.** *AJNR Am J Neuroradiol* 2011;32:576–80
21. Eckert B, Koch C, Thomalla G, et al. **Aggressive therapy with intravenous abciximab and intra-arterial rtPA and additional PTA/stenting improves clinical outcome in acute vertebrobasilar**

occlusion: combined local fibrinolysis and intravenous abciximab in acute vertebrobasilar stroke treatment (FAST): results of a multicenter study. *Stroke* 2005;36:1160–65
22. Kashiwagi J, Kiyosue H, Hori Y, et al. **Endovascular recanalization of acute intracranial vertebrobasilar artery occlusion using local fibrinolysis and additional balloon angioplasty.** *Neuroradiology* 2010; 52:361–70
23. Barlinn K, Becker U, Puetz V, et al. **Combined treatment with intravenous abciximab and intraarterial tPA yields high recanalization rate in patients with acute basilar artery occlusion.** *J Neuroimaging* 2012;22:167–71
24. Lindsberg PJ, Mattle HP. **Therapy of basilar artery occlusion: a systematic analysis comparing intra-arterial and intravenous thrombolysis.** *Stroke* 2006;37:922–28
25. Nagel S, Schellinger PD, Hartmann M, et al. **Therapy of acute basilar artery occlusion: intraarterial thrombolysis alone vs bridging therapy.** *Stroke* 2009;40:140–46
26. Miteff F, Faulder KC, Goh AC, et al. **Mechanical thrombectomy with a self-expanding retrievable intracranial stent (Solitaire AB): experience in 26 patients with acute cerebral artery occlusion.** *AJNR Am J Neuroradiol* 2011;32:1078–81
27. Mourand I, Machi P, Milhaud D, et al. **Mechanical thrombectomy with the Solitaire device in acute basilar artery occlusion.** *J Neurointerv Surg* 2014;6:200–04
28. Espinosa de Rueda M, Parrilla G, Zamarro J, et al. **Treatment of acute vertebrobasilar occlusion using thrombectomy with stent retrievers: initial experience with 18 patients.** *AJNR Am J Neuroradiol* 2013; 34:1044–48
29. Roth C, Papanagiotou P, Behnke S, et al. **Stent-assisted mechanical recanalization for treatment of acute intracerebral artery occlusions.** *Stroke* 2010;41:2559–67
30. Mourand I, Machi P, Milhaud D, et al. **Mechanical thrombectomy with the Solitaire device in acute basilar artery occlusion.** *J Neurointerv Surg* 2014;6:200–44
31. Arnold M, Nedeltchev K, Schroth G, et al. **Clinical and radiological predictors of recanalisation and outcome of 40 patients with acute basilar artery occlusion treated with intra-arterial thrombolysis.** *J Neurol Neurosurg Psychiatry* 2004;75:857–62
32. Turk AS, Frei D, Fiorella D, et al. **ADAPT FAST study: a direct aspiration first pass technique for acute stroke thrombectomy.** *J Neurointerv Surg* 2014;6:260–64
33. Turk AS, Spiotta A, Frei D, et al. **Initial clinical experience with the ADAPT technique: a direct aspiration first pass technique for stroke thrombectomy.** *J Neurointerv Surg* 2014;6:231–37
34. Adams HP Jr, Bendixen BH, Kappelle LJ, et al. **Classification of subtype of acute ischemic stroke: definitions for use in a multicenter clinical trial–TOAST. Trial of Org 10172 in Acute Stroke Treatment.** *Stroke* 1993;24:35–41

Detection of Carotid Artery Stenosis: A Comparison between 2 Unenhanced MRAs and Dual-Source CTA

P. Lv, J. Lin, D. Guo, H. Liu, X. Tang, C. Fu, and J. Hu

ABSTRACT

BACKGROUND AND PURPOSE: Dual-source CTA and black-blood MRA are recently developed techniques for evaluating carotid stenosis. The purpose of this study was to compare dual-source CTA with black-blood MRA and conventional TOF MRA in both detecting carotid stenosis by using DSA as a reference standard and demonstrating plaque morphology.

MATERIALS AND METHODS: Thirty patients with suspected carotid artery stenosis underwent unenhanced MRA by using black-blood and TOF MRA and dual-source CTA. Source images from unenhanced MRAs and dual-source CTA were reconstructed with MIP or curved planar reconstruction. The degree of carotid artery stenosis was measured, and plaque surface morphology at the stenosis was analyzed and compared among different techniques.

RESULTS: Good correlation was observed for measuring the degree of carotid stenosis among dual-source CTA, black-blood MRA, TOF MRA, and DSA. Sensitivity and specificity for detecting severe stenosis were 100% and 97% with dual-source CTA, 100% and 95% with black-blood MRA, and 79% and 95% with TOF MRA. None of the 3 technologies resulted in stenosis of <50% being overestimated. Plaque surface irregularity or ulceration was more frequently detected with dual-source CTA and black-blood MRA than with TOF MRA and DSA.

CONCLUSIONS: This preliminary study shows that black-blood MRA is a promising technique, comparable with dual-source CTA and DSA, but better than TOF MRA, in the evaluation of carotid stenosis. Unlike dual-source CTA, black-blood MRA requires no intravenous contrast or radiation.

ABBREVIATIONS: BB MRA = black-blood MRA; DSCTA = dual-source CTA

Carotid artery atherosclerosis is a major cause of ischemic cerebrovascular disease.[1,2] Measurement of carotid stenosis and demonstration of plaque morphology are critical for the management of patients with carotid atherosclerosis. DSA is the current reference standard for evaluating carotid artery stenosis. The diagnostic role of DSA has largely been replaced, however, by noninvasive techniques such as sonography, CTA, and MRA.

Sonography has been the most commonly performed technique but may be restricted by its operator dependence and limited coverage. CTA is another widely used technique for the evaluation of carotid artery stenosis with high accuracy.[3] Dual-source CTA (DSCTA) uses 2 x-ray sources and 2 detectors at the same time. With this technique, 2 images can be simultaneously acquired with different tube voltages; this feature has been shown to be an advantage for the evaluation of densely calcified carotid stenosis.[4,5] Contrast-enhanced MRA has been established as an alternative for carotid imaging with a diagnostic accuracy similar to that of CTA.[6,7] Both CTA and contrast-enhanced MRA use contrast media and are restricted in patients with impaired renal function, and CTA also requires ionizing radiation. As a result, unenhanced MRA without gadolinium is a desirable alternative, especially in patients with renal failure. Conventional TOF MRA has been widely used in clinical practice for carotid visualization, but it is limited by local reduction of signal intensity related to slow and turbulent flow and also prolonged imaging time.[8] T2-weighted black-blood MRA (BB MRA) is a newly developed technique showing potential in the evaluation of both the lumen and the wall of the carotid artery after optimal suppression of the

Received April 23, 2014; accepted after revision May 26.

From the Department of Radiology (P.L., J.L., H.L.), Zhongshan Hospital, Shanghai Medical College of Fudan University and Shanghai Institute of Medical Imaging, Shanghai, China; Department of Vascular Surgery (D.G., X.T.), Zhongshan Hospital, Fudan University and Institute of Vascular Surgery, Shanghai, China; Siemens Shenzhen Magnetic Resonance (C.F.), Shenzhen, China; and Department of Cardiology (J.H.), Zhongshan Hospital, Fudan University, Shanghai, China.

Please address correspondence to Jiang Lin, MD, Department of Radiology, Zhongshan Hospital, Shanghai Medical College of Fudan University and Shanghai Institute of Medical Imaging, Fenglin Rd 180, Shanghai 200032, China; e-mail: lin.jiang@zs-hospital.sh.cn; and Daqiao Guo, MD, Department of Vascular Surgery, Zhongshan Hospital, Fudan University and Institute of Vascular Surgery, Fudan University, Fenglin Rd 180, Shanghai 200032, China; e-mail: guo.daqiao@zs-hospital.sh.cn

http://dx.doi.org/10.3174/ajnr.A4073

signal from flowing blood.[9,10] Few studies, to our knowledge however, have compared DSCTA with BB MRA and conventional TOF MRA in evaluating carotid stenosis.

The aim of this study was to prospectively and intraindividually compare these 2 unenhanced MRA methods with DSCTA in detecting carotid artery stenosis by using DSA as the standard of reference and in demonstrating plaque morphology.

MATERIALS AND METHODS

Patients

Between December 2013 and March 2014, 30 patients (mean age, 65 ± 13 years; 22 men and 8 women) suspected of having carotid atherosclerotic disease were prospectively enrolled in the study. All patients underwent DSCTA, TOF and BB MRA, and DSA sequentially within 2 weeks. The examinations were approved by the local medical ethics committee, and informed consent was obtained from each patient.

DSCTA

All examinations were performed on a dual-source CT system (Somatom Definition; Siemens, Erlangen, Germany). With a power injector, 50–70 mL (according to the patient's body weight) of nonionic iodinated contrast media (iopamidol, Iopamiron 370; Bracco, Milan, Italy) was injected into an antecubital vein at a flow rate of 5.0 mL/s followed by a 25-mL saline flush. CT was initiated by using a bolus-tracking technique at the level of the aortic arch with a trigger threshold of 100 HU. Acquisition parameters were 140 kV and 80 mAs_{eff} on tube A and 80 kV and 234 mAs_{eff} on tube B. Each detector was collimated to 32 × 0.6 mm with a flying focal spot, and a pitch of 0.65 was applied. Images were reconstructed with a dedicated D30 reconstruction algorithm. Section thickness and increment were 1.0 and 0.7 mm, respectively. Two individual stacks of images for each detector (80 kV and 140 kV images) and dual energy mixed images were reconstructed. The latter contained weighted information from both detectors with a weighting factor of 0.3, thus approximating regular 120-kV images.

The raw DSCTA images were transferred to a workstation with commercially available dual-energy postprocessing software (syngo Dual Energy; Siemens). Automatic bone removal was performed without further manual adjustments of the algorithm. The DSCTA images before and after bone removal were used for both reconstruction and diagnostic reading. The DSCTA images after bone removal were considered supplements in case calcified plaque affected the evaluation of carotid stenosis.

MRA

All examinations were performed on a 3T MR imaging system (Magnetom Verio; Siemens) using a head and neck coil. 3D TOF was acquired first with the following parameters: TR = 19 ms; TE = 3.6 ms; flip angle = 18°; FOV = 240 ×240 mm; matrix = 256 × 256; section thickness = 0.8 mm; section number = 40; mean acquisition time = 5:33 minutes. After that, 3D BB MRA was performed with a fat-saturated T2-sampling perfection with application-optimized contrast by using different flip angle evolution sequence in the coronal plane. Imaging parameters were as follows: TR = 1800 ms; TE = 168 ms; FOV = 240 × 240 mm; matrix = 256 × 256; section thickness = 0.8 mm; section number = 50; mean acquisition time = 5:47 minutes.

DSA

DSA was performed via femoral artery catheterization by using the digital subtraction technique (Axiom Artis dTA; Siemens). Common carotid arteries were selectively catheterized. Images were obtained in anteroposterior, lateral, and 2 oblique projections for each catheterization.

Image Analysis

Commercially available 3D software (syngo, Siemens) was used to create MIP, MPR, and curved planar reconstructions from the raw DSCTA and MRA images.

An experienced vascular radiologist reviewed the image quality of DSCTA and MRA in 2 separate sessions. Image quality was evaluated on the basis of the following features: vascular attenuation or signal intensity, homogeneity of enhancement, and the presence of artifacts. It was scored on a 4-point scale as follows: 1, excellent; 2, good; 3, moderate; and 4, poor visualization or nondiagnostic.

Each MRA and DSCTA image was assessed by another 2 experienced vascular radiologists (with 5 and 8 years of experience) independently in terms of stenosis and plaque morphology. A third interventional radiologist with 15 years of experience, who was unaware of the findings of the other examinations, assessed the stenosis and plaque surface on DSA. The patient's basic information was hidden, and all datasets were analyzed in random order. DSCTA, BB MRA, and TOF MRA images were evaluated separately with an interval of 1 week.

The degree of stenosis of each ICA was quantified on DSCTA, MRA, and DSA images on a similar plane. The diameter of the most severe stenosis was divided by the diameter of the ICA well beyond the bulb. The degree of stenosis was graded according to the NASCET criteria[11]: I (1%–29%), mild stenosis; II (30%–49%) and III (50%–69%), moderate stenosis; IV (70%–99%), severe stenosis; and V, occlusion. Plaque surface morphology was classified as regular, irregular, or ulcerated.[12,13] Ulcer was seen as a crater penetrating into a plaque. A relatively smooth outpouching between 2 smooth narrowings that was most consistent with the expected position of the carotid wall would be regarded as a normal lumen and not ulceration.

Statistical Assessment

The relationship among DSCTA, BB MRA, TOF MRA, and DSA in grading stenosis was analyzed by using the Spearman rank correlation coefficient. For each unenhanced MRA and DSCTA, interobserver agreement in the evaluation of stenosis and plaque surface morphology was assessed by using the Cohen κ test. Agreement was defined as mild ($\kappa > 0.40–0.69$), good ($\kappa > 0.70–0.89$), or excellent ($\kappa > 0.90–1.00$).

RESULTS

In 30 patients, 55 stenoses at the carotid bifurcation were detected by DSA; 5 patients had unilateral carotid stenosis and 25 had bilateral carotid stenosis. The quality of DSCTA images was graded as either excellent (28 cases) or good (2 cases). No relevant

Comparison of the degree of stenosis with CTA, BB MRA, TOF MRA, and DSA

Stenosis Degree on DSCTA/BB MRA/TOF MRA	Stenosis Degree on DSA				
	1%–29%	30%–49%	50%–69%	70%–99%	100%
1%–29%	23/23/23	0/0/0	0/0/0	0/0/0	0/0/0
30%–49%	0/0/0	7/7/7	0/0/0	0/0/0	0/0/0
50%–69%	0/0/0	0/0/0	7/6/6	0/0/1	0/0/0
70%–99%	0/0/0	0/0/0	1/2/2	14/14/11	0/0/0
100%	0/0/0	0/0/0	0/0/0	0/0/2	1/1/1

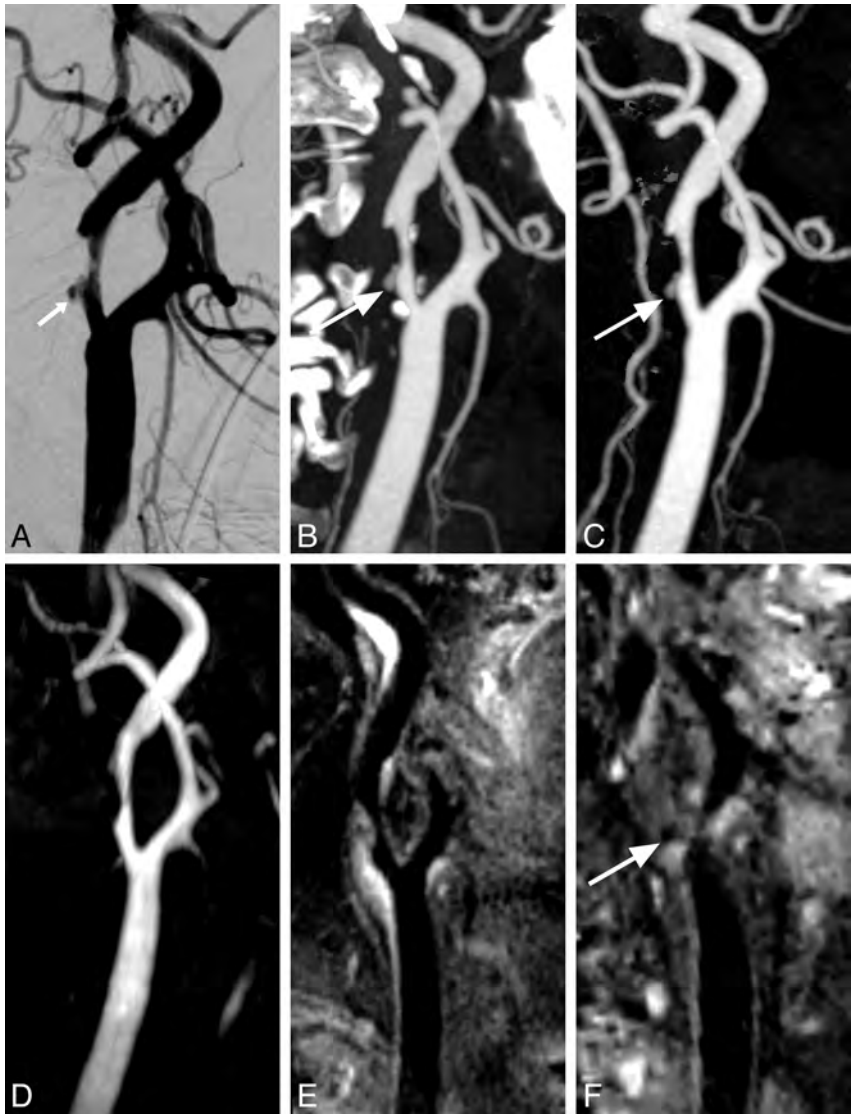

FIG 1. *A*, DSA depicts a moderate stenosis of the ICA. *B*, Dense calcification on standard DSCTA interferes with the display of the vascular lumen. *C*, DSCTA after removal of calcification and bone clearly demonstrates the stenosis. TOF MRA (*D*) and BB MRA (*E*) both accurately depict the degree of carotid stenosis. An ulcer (*white arrows*) is detected by all of the examinations except TOF MRA. *F*, MPR of BB MRA in a different perspective shows the ulcer.

motion artifacts diminished the quality of the DSCTA images. The TOF MRA was graded as either excellent (15 cases) or good (15 cases). The quality of BB MRA images was graded as excellent in 10 cases and good in 18 cases. In 2 cases, BB MRA was rated as poor visualization or nondiagnostic because of a limited signal-to-noise ratio or motion artifacts. These 2 cases with unilateral carotid stenosis shown on DSA were excluded from further evaluation and comparison.

The Table summarizes the results of stenosis measured with DSCTA, BB MRA, and TOF MRA in comparison with DSA (Figs 1-3). For the measured carotid stenosis, good correlation was observed among these 3 techniques and DSA (r^2 = 0.988, 0.986, 0.967, respectively) (Fig 4). None of the 3 techniques resulted in the degree of stenosis <50% being overestimated. Overestimation occurred in 1 case of moderate stenosis (50%–69%) with DSCTA and in 2 cases of moderate stenosis with both BB MRA and TOF MRA. TOF MRA misinterpreted severe stenosis (70%–99%) as occlusion in 2 cases.

Sensitivity and specificity for detecting severe stenosis was 100% and 97% with DSCTA, 100% and 95% with BB MRA, and 79% and 95% with TOF MRA. Interobserver agreement for the evaluation of the degree of stenosis was excellent for DSCTA (κ = 0.94) and good for BB MRA (κ = 0.81) and TOF MRA (κ = 0.85).

Plaque surface irregularity or ulcer was more frequently identified on DSCTA (18 irregularities and 7 ulcers) and BB MRA (19 irregularities and 6 ulcers) than on TOF MRA (15 irregularities and 3 ulcers) and DSA (16 irregularities and 4 ulcers). Three plaque ulcers all depicted by DSCTA, BB MRA, and DSA were not seen on TOF MRA (Fig 1). Interobserver agreement for the evaluation of plaque surface morphology was good for DSCTA (κ = 0.80), BB MRA (κ = 0.76), and TOF MRA (κ = 0.71).

DISCUSSION

Accurate evaluation of the degree of carotid stenosis is essential for guiding clinical treatment. Although DSA is still considered the criterion standard for the evaluation of carotid artery stenosis, there are some well-known limitations, including its invasiveness, risk of neurologic complications, and the potential for variability in the quantification of stenosis, especially if limited projections are acquired.

Noninvasive vascular imaging techniques have gradually replaced DSA for the diagnosis of carotid artery stenosis. Previous studies have already proved the capabilities of both CTA and MRA to reliably determine the degree of carotid stenosis.[6,14-17] In addition, studies have shown that CT and MR imaging may provide supplemental information about the composition and morphology of plaque.[18-22]

Due to its high spatial resolution and fast imaging, CTA has been widely used in the examination of the carotid artery. Identification of calcified plaque is another advantage of CT, which is

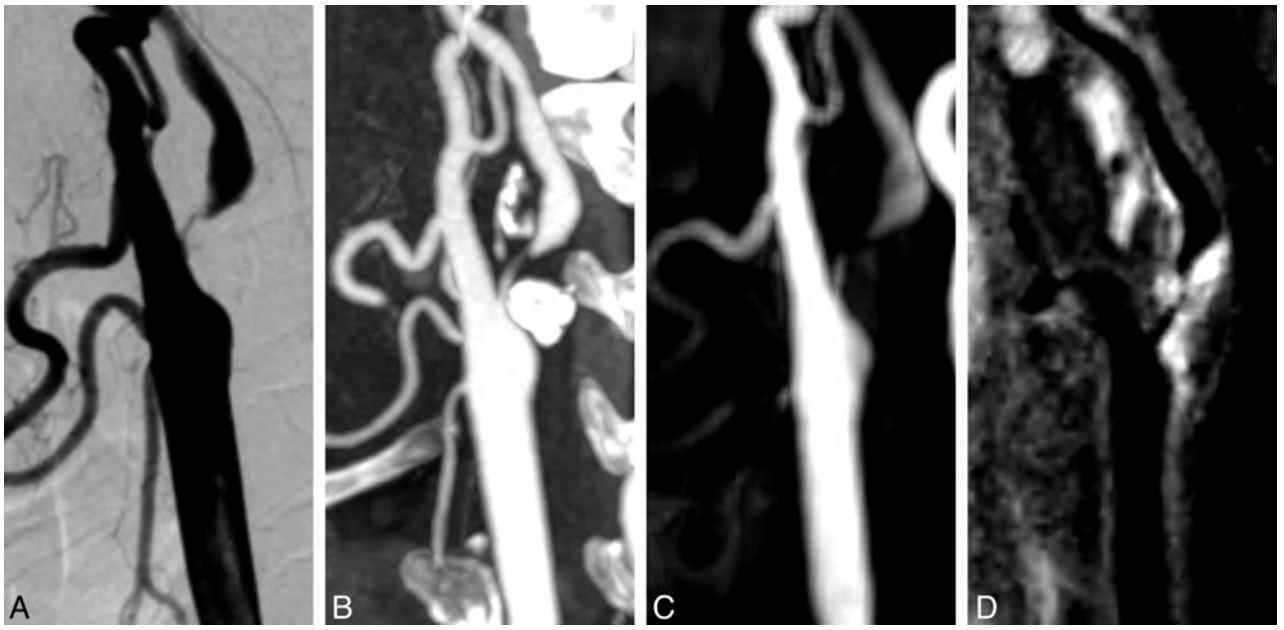

FIG 2. DSA (*A*) and DSCTA (*B*) depict a severe and irregular stenosis of the ICA. *C*, TOF MRA overestimates this stenosis as an occlusion because of local luminal nonvisualization. *D*, BB MRA clearly detects this severe stenosis with an irregular plaque surface.

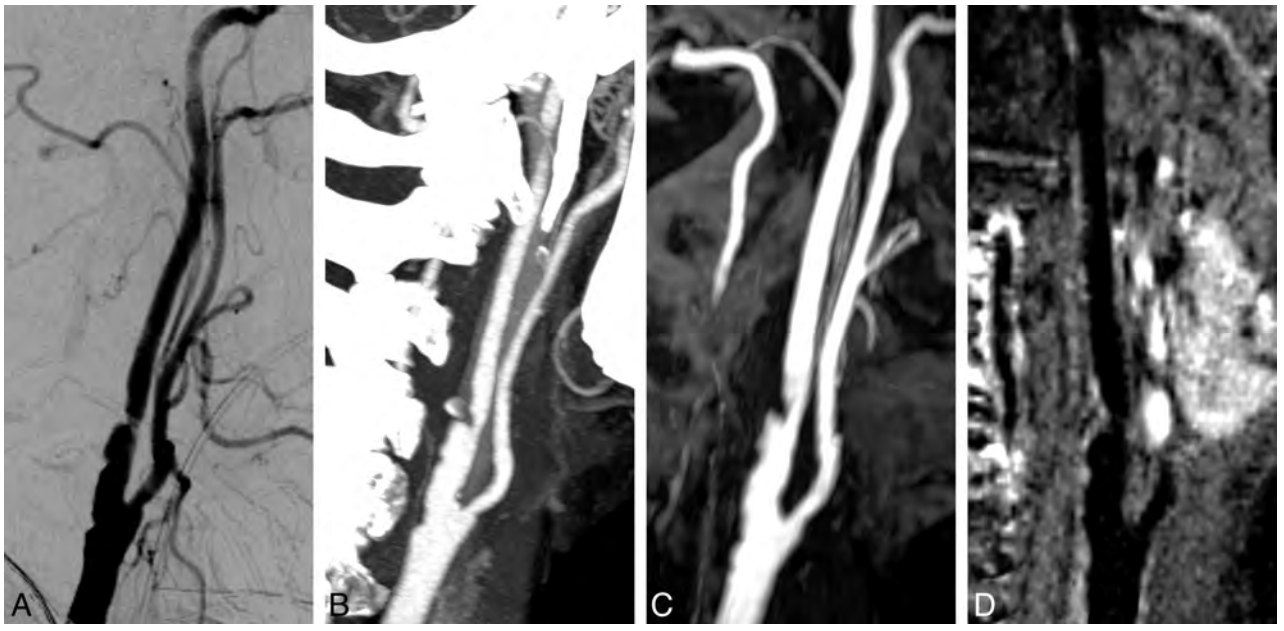

FIG 3. DSA (*A*), DSCTA (*B*), TOF MRA (*C*), and BB MRA (*D*) all depict a moderate and irregular stenosis at the ICA with close correlation.

helpful in the preinterventional assessment of carotid disease. However, in cases with severe calcification on the vessel wall, the demonstration of the lumen may be compromised; this compromise affects accurate evaluation of the degree of carotid stenosis.[23,24]

The application of conventional bone subtraction or automatic bone removal with DSCT greatly improves carotid assessment without overlay of calcified plaques. The dual-energy technique on DSCTA distinguishes contrast media from calcified plaques by exploiting the differences in attenuation of iodine and calcium at different x-ray energies.[25] The radiation dose of a dual-source scan is only slightly higher than that of a normal single-source scan.[23] Compared with conventional subtraction, DSCTA reduces the radiation dose and avoids motion artifacts by sparing the unenhanced acquisition.[23] With the dual-energy technique, we achieved the best image quality and accuracy of DSCTA in the demonstration of carotid stenosis. Sensitivity and specificity for detecting severe stenosis were 100% and 97% with DSCTA in our study, which was similar to that in the previous literature.[23] Overestimation occurred in only 1 case because of excessive deletion of calcified plaque, which might be due to blooming artifacts and partial volume effects.

Although slightly inferior to CTA in the evaluation accuracy of carotid stenosis, contrast-enhanced MRA is also a robust technique.[6] In recent years, however, nephrogenic systemic fibrosis in patients with renal failure associated with gadolinium chelates has

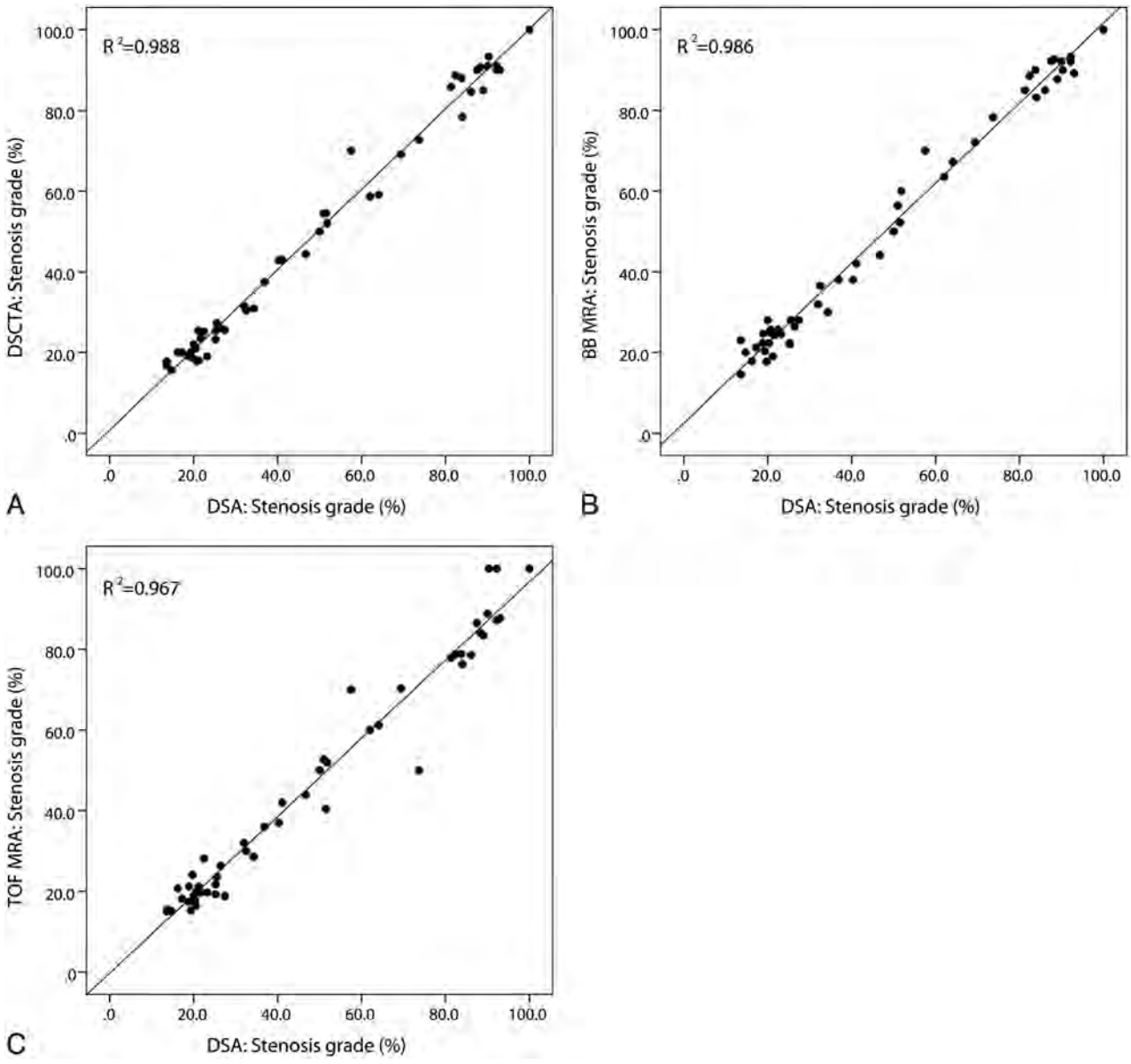

FIG 4. Linear regression among DSCTA, BB MRA, TOF MRA, and DSA for the stenosis measurement.

received increasing attention.[26] As an alternative option, traditional TOF MRA is still widely in use despite signal loss resulting from slow and turbulent flow at the carotid bifurcation region.[8] In this study, overestimation occurred on TOF MRA in 2 cases with moderate stenosis and in 2 cases with severe stenosis.

Black-blood MR imaging has been used to define carotid plaque composition and morphology.[20,27] In recent years, it is being refined to visualize and quantify the lumen of the carotid artery.[10,28] By selectively suppressing the signals coming from the artery lumen, BB MRA can better delineate the structure of the arterial wall and detect the degree of carotid stenosis. 3D sampling perfection with the application of optimized contrast by using different flip angle evolution is a recently developed T2-weighted MR imaging technique with high spatial resolution. Good T2-weighted images can be obtained by using different flip angles, which enable a low specific absorption rate value. Use of a parallel acquisition technique makes it possible to obtain thin-section images in a reasonable acquisition time.[29] One previous study showed that 3D BB MRA could allow accurate measurement of carotid stenosis in comparison with contrast-enhanced MRA.[10] Our study showed that its sensitivity and specificity for the detection of severe carotid stenosis were comparable with DSCTA but better than TOF, though the image quality was slightly inferior to that of DSCTA. Overestimation occurred in 2 cases of moderate stenosis, which was due to heterogeneous signals from the lumen.

Detecting plaque morphology is also important. Ulceration and irregularity of carotid plaque are strong predictors of overall carotid plaque instability.[12] Furthermore, they have been shown to predict the risk of future stroke and to be associated with acute coronary events.[30] Because of the limited projection angles, DSA has limitations in detecting irregular plaque or small ulcers.

In our study, irregularities of plaques and ulcers were more frequently observed on DSCTA and BB MRA because both allowed better visualization of the plaque through multiple perspectives. TOF MRA, however, was insensitive to the surface ulcer

of the carotid plaque, which might be due to the local loss of signal intensity as mentioned above.

This study has several limitations. First, the sample size was relatively small, and further studies are warranted to verify the accuracy of BB MRA in evaluating carotid stenosis. Second, no surgical and histologic confirmation was available for plaque morphology in our study. We assumed that the number of ulcers detected in this study is likely be underestimated because small ulcers might not be obvious on all images or appeared as plaque irregularities. Finally, the acquisition time of BB MRA was still long, and further technical optimization of BB MRA was still needed because 2 cases were excluded from our study owing to motion artifacts or reduced signal-to-noise ratio.

CONCLUSIONS

BB MRA is a promising technique that is comparable with DSCTA and DSA in the evaluation of carotid stenosis. In addition, BB MRA and DSCTA are better than TOF MRA in demonstrating stenosis and plaque morphology. The clinical application of BB MRA may be valuable, given that it does not use ionizing radiation and contrast medium.

REFERENCES

1. Inzitari D, Eliasziw M, Gates P, et al. **The causes and risk of stroke in patients with asymptomatic internal-carotid-artery stenosis: North American Symptomatic Carotid Endarterectomy Trial Collaborators.** *N Engl J Med* 2000;342:1693–700
2. Barnett HJ, Gunton RW, Eliasziw M, et al. **Causes and severity of ischemic stroke in patients with internal carotid artery stenosis.** *JAMA* 2000;283:1429–36
3. Koelemay MJ, Nederkoorn PJ, Reitsma JB, et al. **Systematic review of computed tomographic angiography for assessment of carotid artery disease.** *Stroke* 2004;35:2306–12
4. Korn A, Bender B, Thomas C, et al. **Dual energy CTA of the carotid bifurcation: advantage of plaque subtraction for assessment of grade of the stenosis and morphology.** *Eur J Radiol* 2011;80:e120–25
5. Vlahos I, Chung R, Nair A, et al. **Dual-energy CT: vascular applications.** *AJR Am J Roentgenol* 2012;199:S87–97
6. Randoux B, Marro B, Koskas F, et al. **Carotid artery stenosis: prospective comparison of CT, three-dimensional gadolinium-enhanced MR, and conventional angiography.** *Radiology* 2001;220:179–85
7. Villablanca JP, Nael K, Habibi R, et al. **3 T contrast-enhanced magnetic resonance angiography for evaluation of the intracranial arteries: comparison with time-of-flight magnetic resonance angiography and multislice computed tomography angiography.** *Invest Radiol* 2006;41:799–805
8. Miyazaki M, Lee VS. **Nonenhanced MR angiography.** *Radiology* 2008;248:20–43
9. Balu N, Yarnykh VL, Chu B, et al. **Carotid plaque assessment using fast 3D isotropic resolution black-blood MRI.** *Magn Reson Med* 2011;65:627–37
10. Mihai G, Winner MW, Raman SV, et al. **Assessment of carotid stenosis using three-dimensional T2-weighted dark blood imaging: initial experience.** *J Magn Reson Imaging* 2012;35:449–55
11. **North American Symptomatic Carotid Endarterectomy Trial: methods, patient characteristics and progress.** *Stroke* 1991;22:711–20
12. Lovett JK, Gallagher PJ, Hands LJ, et al. **Histological correlates of carotid plaque surface morphology on lumen contrast imaging.** *Circulation* 2004;110:2190–97
13. Streifler JY, Eliasziw M, Fox AJ, et al. **Angiographic detection of carotid plaque ulceration: comparison with surgical observations in a multicenter study: North American Symptomatic Carotid Endarterectomy Trial.** *Stroke* 1994;25:1130–32
14. Remonda L, Senn P, Barth A, et al. **Contrast-enhanced 3D MR angiography of the carotid artery: comparison with conventional digital subtraction angiography.** *AJNR Am J Neuroradiol* 2002;23:213–19
15. Josephson SA, Bryant SO, Mak HK, et al. **Evaluation of carotid stenosis using CT angiography in the initial evaluation of stroke and TIA.** *Neurology* 2004;63:457–60
16. Cumming MJ, Morrow IM. **Carotid artery stenosis: a prospective comparison of CT angiography and conventional angiography.** *AJR Am J Roentgenol* 1994;163:517–23
17. Huston JR, Fain SB, Wald JT, et al. **Carotid artery: elliptic centric contrast-enhanced MR angiography compared with conventional angiography.** *Radiology* 2001;218:138–43
18. Wintermark M, Jawadi SS, Rapp JH, et al. **High-resolution CT imaging of carotid artery atherosclerotic plaques.** *AJNR Am J Neuroradiol* 2008;29:875–82
19. Cormode DP, Roessl E, Thran A, et al. **Atherosclerotic plaque composition: analysis with multicolor CT and targeted gold nanoparticles.** *Radiology* 2010;256:774–82
20. Saam T, Hatsukami TS, Takaya N, et al. **The vulnerable, or high-risk, atherosclerotic plaque: noninvasive MR imaging for characterization and assessment.** *Radiology* 2007;244:64–77
21. Qiao Y, Etesami M, Astor BC, et al. **Carotid plaque neovascularization and hemorrhage detected by MR imaging are associated with recent cerebrovascular ischemic events.** *AJNR Am J Neuroradiol* 2012;33:755–60
22. van den Bouwhuijsen QJ, Vernooij MW, Hofman A, et al. **Determinants of magnetic resonance imaging detected carotid plaque components: the Rotterdam Study.** *Eur Heart J* 2012;33:221–29
23. Uotani K, Watanabe Y, Higashi M, et al. **Dual-energy CT head bone and hard plaque removal for quantification of calcified carotid stenosis: utility and comparison with digital subtraction angiography.** *Eur Radiol* 2009;19:2060–65
24. Deng K, Liu C, Ma R, et al. **Clinical evaluation of dual-energy bone removal in CT angiography of the head and neck: comparison with conventional bone-subtraction CT angiography.** *Clin Radiol* 2009;64:534–41
25. Johnson TR, Krauss B, Sedlmair M, et al. **Material differentiation by dual energy CT: initial experience.** *Eur Radiol* 2007;17:1510–17
26. Thomsen HS. **Nephrogenic systemic fibrosis: a serious late adverse reaction to gadodiamide.** *Eur Radiol* 2006;16:2619–21
27. Kerwin WS, Hatsukami T, Yuan C, et al. **MRI of carotid atherosclerosis.** *AJR Am J Roentgenol* 2013;200:W304–13
28. Kramer H, Runge VM, Morelli JN, et al. **Magnetic resonance angiography of the carotid arteries: comparison of unenhanced and contrast enhanced techniques.** *Eur Radiol* 2011;21:1667–76
29. Haystead CM, Dale BM, Merkle EM. **N/2 ghosting artifacts: elimination at 3.0-T MR cholangiography with SPACE pulse sequence.** *Radiology* 2008;246:589–95
30. Rothwell PM, Villagra R, Gibson R, et al. **Evidence of a chronic systemic cause of instability of atherosclerotic plaques.** *Lancet* 2000;355:19–24

Diagnostic Accuracy of Screening MR Imaging Using Unenhanced Axial CISS and Coronal T2WI for Detection of Small Internal Auditory Canal Lesions

T.A. Abele, D.A. Besachio, E.P. Quigley, R.K. Gurgel, C. Shelton, H.R. Harnsberger, and R.H. Wiggins III

ABSTRACT

BACKGROUND AND PURPOSE: While enhanced T1WI is considered the "gold standard" for detection of internal auditory canal pathology, unenhanced fluid-sensitive sequences have shown high sensitivity for lesion identification. Our purpose was to evaluate the diagnostic accuracy of an unenhanced MR imaging protocol using axial CISS and coronal T2WI for detection of small (10 mm or less) internal auditory canal lesions.

MATERIALS AND METHODS: Twenty-three patients with small internal auditory canal lesions and 13 patients without lesions who had undergone MR imaging using the screening protocol and confirmatory gadolinium-enhanced thin section T1WI were identified. Two blinded neuroradiologists retrospectively evaluated all examinations using 1) only axial CISS, 2) only coronal T2WI, and 3) axial and coronal sequences together. Accuracy, specificity, sensitivity, and interobserver agreement were assessed.

RESULTS: Median maximum lesion dimension was 4 mm (range, 2–10 mm). Accuracy, specificity, and sensitivity for axial CISS alone were 0.94, 0.96, and 0.91 for observer 1 and 0.94, 0.92, and 1.00 for observer 2. The data for the coronal T2WI sequence only were 0.94, 0.96, and 0.91 for observer 1, and 0.99, 1.00, and 0.96 for observer 2. Using axial and coronal sequences, the data were 0.97, 0.96, and 1.00 for observer 1, and 0.99, 0.98, and 1.00 for observer 2. κ coefficients were 0.84 for the axial sequence only, 0.90 for coronal only, and 0.91 for axial and coronal both.

CONCLUSIONS: Screening noncontrast MR imaging using a combination of axial CISS and coronal T2WI sequences can detect small internal auditory canal lesions with 100% sensitivity and excellent interobserver agreement.

ABBREVIATION: IAC = internal auditory canal

Vestibular schwannoma is the most common lesion diagnosed during MR imaging evaluation of unilateral sensorineural hearing loss.[1,2] Nevertheless, only 2.7%–4.7% of contrast-enhanced MRIs performed for audiovestibular symptoms will diagnose vestibular schwannomas.[3,4] Although gadolinium-enhanced thin section MR imaging has historically been considered the "gold standard" for detection of internal auditory canal (IAC) tumors such as vestibular schwannomas, lower cost unenhanced, fluid-sensitive sequences have demonstrated pooled sensitivities ranging from 96% to 98% for detection of IAC lesions ranging from 2 mm to >20 mm in diameter.[5] In the era of rising health care costs, especially for diagnostic imaging, the cost savings associated with a low-cost screening IAC MR imaging may become an important factor in decision-making.

At our institution, we have performed screening MR imaging of the IACs since the 1990s using fluid-sensitive axial and coronal sequences. In 1996, Allen et al[6] demonstrated 98% accuracy of an axial and coronal T2-weighted IAC screening MR imaging protocol in 25 patients whose lesions had a mean diameter of 12 mm. Two lesions measuring <5 mm were missed. In 2006, the axial T2 FSE sequence at our institution was replaced by an axial dual-excitation balanced steady-state interference sequence termed CISS (Siemens, Erlangen, Germany), as 3D CISS had been reported to have twice the contrast-to-noise ratio compared with 3D T2WI.[7] As no study has evaluated the accuracy of a 2-plane screening IAC MR imaging protocol using CISS for detection of small (≤10 mm) lesions, we chose to evaluate the diagnostic accuracy of a 2-sequence screening MR imaging protocol

Received March 10, 2014; accepted after revision May 24.

From the Departments of Radiology (T.A.A., E.P.Q., H.R.H., R.H.W.), Biomedical Informatics (R.H.W.), and Division of Otolaryngology—Head and Neck Surgery (R.K.G., C.S., R.H.W.), University of Utah, Salt Lake City, Utah; and Department of Radiology (D.A.B.), Naval Medical Center Portsmouth, Portsmouth, Virginia.

Paper previously presented at: Annual Meeting of the American Society of Head and Neck Radiology, September 26, 2013; Milwaukee, Wisconsin.

Please address correspondence to Travis A. Abele, MD, Department of Radiology, University of Utah, 30 North 1900 East #1A071, Salt Lake City, UT 84132; e-mail: travis.abele@hsc.utah.edu

http://dx.doi.org/10.3174/ajnr.A4041

using unenhanced axial CISS and coronal T2WI for detection of small IAC lesions.

MATERIALS AND METHODS

The study was approved by the institutional review board and was compliant with the Health Insurance Portability and Accountability Act. Our institutional radiologic information system database was reviewed from February 2006 to April 2013 for patients who had undergone both 1) the unenhanced screening IAC MR imaging protocol and 2) the contrast-enhanced thin section T1-weighted MR imaging of the IACs. Patients were included if their examinations were within 13 months of each other or the contrast-enhanced MR imaging was performed after the screening MR imaging. The cases with IAC lesions >10 mm, prior surgery, and/or inadequate diagnostic quality secondary to motion or other artifacts were then excluded. Two lesions located in the cochlea that were readily visible on the noncontrast screening MR imaging were excluded because they were few in number and because this study was focused on IAC lesions.

The remaining cases, including 23 patients with IAC lesions and 13 patients without lesions, were then reviewed by 2 Certificate of Added Qualification neuroradiologists who were blinded to the original interpretations. One observer was an assistant professor with 5 years of neuroradiology experience after fellowship, and the other observer was a professor of neuroradiology with 14 years of experience. Each observer retrospectively evaluated both IACs 3 separate times from the screening IAC MR imaging study. First, only the axial CISS sequence was reviewed for all IACs, then only the coronal T2 sequence was reviewed, and then both sequences were reviewed together. At least a 24-hour interval and study rerandomization was performed between each review to decrease recollection bias. Observers were asked to identify if there was a lesion within the IAC that warranted further evaluation with contrast-enhanced MR imaging. The absence of pathology was determined when both the vestibulocochlear and facial nerves were visualized from their root entry/exit zones to the fundus of the IAC without adjacent mass. Observers were also asked to identify the location of the lesions as being: 1) intracanalicular (located within the IAC without contacting the fundus of the IAC), or 2) fundal (within the IAC with any portion of the lesion in contact with the fundus). All examinations were interpreted on a diagnostic PACS workstation during a normal work day in between clinical examinations to simulate a routine study interpretation by the neuroradiologists. All answers were recorded by a third party. After all reading sessions of the studies, the noncontrast interpretations were compared with the correlating postcontrast studies to confirm the presence or absence of a lesion. The greatest lesion diameter in either the transverse, anteroposterior, or craniocaudal dimension was measured on contrast-enhanced MR imaging as part of the inclusion criteria.

All MRIs were performed on a 1.5T or 3T MR imaging scanner. With a few exceptions, all axial 3D CISS sequences were performed with the following parameters: TR, 5.91–7.85; TE, 2.96–3.93; averages, 1–2; flip angle, 37°–80°; and voxel size, 0.3 × 0.3 × 0.8 mm or larger. With a few exceptions, coronal 3D T2 sequences were performed with the following parameters: TR, 750; TE, 110–15; averages, 1; flip angle, 170°; and voxel size, 0.3 × 0.3 × 1.24 mm or larger. The standard body coil was used to transmit radiofrequency pulses, and a 16-channel head coil was used to receive signal in all patients. In general, the axial 3D CISS sequence was 2 minutes 45 seconds to 4 minutes 30 seconds in acquisition time and the coronal 3D T2 sequence was 4 minutes 35 seconds to 4 minutes 59 seconds in acquisition time. Including the 3 plane localizers, the average total scan time was 10 minutes 2 seconds to 10 minutes 43 seconds.

Statistical analysis included assessment of sensitivity, specificity, and accuracy of the axial CISS sequence only, the coronal T2 sequence only, and both sequences together, using the T1 postgadolinium correlating studies as a "gold standard." Interobserver agreement was assessed with κ coefficient analysis.

Table 1: Diagnostic data for observer 1

	Axial CISS	Coronal T2WI	CISS + T2WI
Accuracy	0.94	0.94	0.97
Specificity	0.96 (0.85–0.99)	0.96 (0.85–0.99)	0.96 (0.85–0.99)
Sensitivity	0.91 (0.70–0.98)	0.91 (0.70–0.94)	1.00 (0.82–1.00)

Note:—All data are percentage (95% CI).

Table 2: Diagnostic data for observer 2

	Axial CISS	Coronal T2WI	CISS + T2WI
Accuracy	0.94	0.99	0.99
Specificity	0.92 (0.80–0.97)	1.00 (0.94–1.00)	0.98 (0.88–1.00)
Sensitivity	1.00 (0.82–1.00)	0.96 (0.76–1.00)	1.00 (0.82–1.00)

Note:—All data are percentage (95% CI).

RESULTS

Of 865 screening IAC examinations performed between February 2006 and April 2013, 36 cases had both the screening MR imaging and the postcontrast MR imaging that met the inclusion criteria. These included 23 patients with radiologically identified IAC lesions measuring ≤10 mm in greatest diameter and 13 control patients without lesions on contrast-enhanced T1-weighted MR imaging. Thus, a total of 72 IACs were included: 23 with a lesion and 49 without pathology. The ages of patients with an IAC lesion ranged from 29 to 81 years (median 65 years); 12 patients were women and 11 were men. The patients without pathology were considered the control group and ranged in age from 36 to 85 years (median 53 years). Six were women and 7 were men.

Fourteen lesions were intracanalicular and 9 were fundal in location. The lesion size ranged from 2 to 10 mm in greatest diameter, the mean greatest diameter was 4.7 mm, and the median greatest diameter was 4 mm. Four of 23 lesions were resected. Three were vestibular schwannomas, and 1 was a ganglioneuroma. One lesion was treated with radiation therapy, and the others were followed and thus had no histologic evaluation.

Accuracy, specificity, and sensitivity were calculated for both observers using the axial CISS alone, coronal T2WI alone, and both sequences together, and are detailed in Tables 1 and 2. Observer 1 achieved less than 100% sensitivity with either sequence alone, but did achieve 100% sensitivity when evaluating the 2 sequences together. Observer 2 performed with 100% sensitivity using the axial CISS sequence alone and with both sequences together. The 2 lesions undetected by observer 1 on the axial sequence alone were at the fundus of the IAC and measured 3 and 4 mm in maximum diameter. These lesions were more conspicuous on the coronal sequences (Fig 1). On the coronal sequence alone,

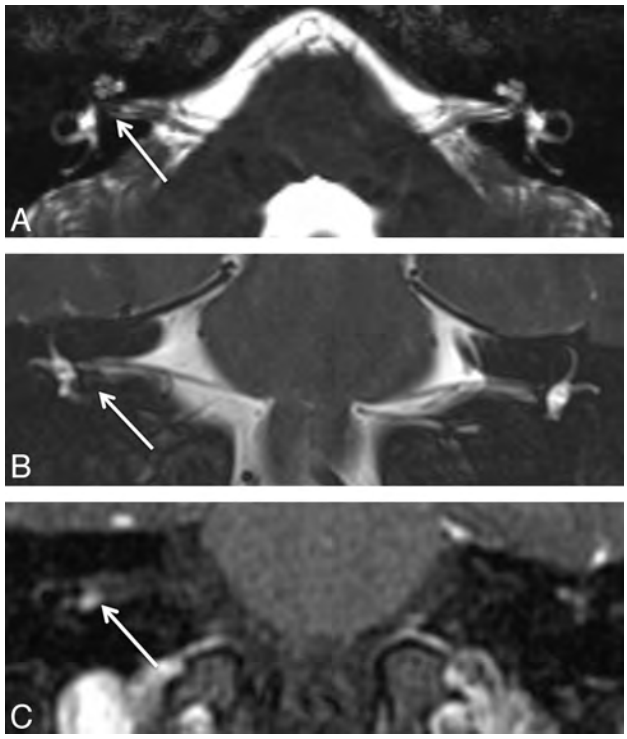

FIG 1. A 29-year-old man with hearing loss on the right. *A*, Axial CISS image shows subtle asymmetric hypointense signal within the fundus of the right IAC (*arrow*), which could be dismissed as volume averaging. *B*, Coronal T2WI better demonstrates the hypointense lesion (*arrow*) along the inferior right IAC fundus, which is confirmed to be a 4-mm enhancing mass (*arrow*) on postcontrast coronal T1WI (*C*).

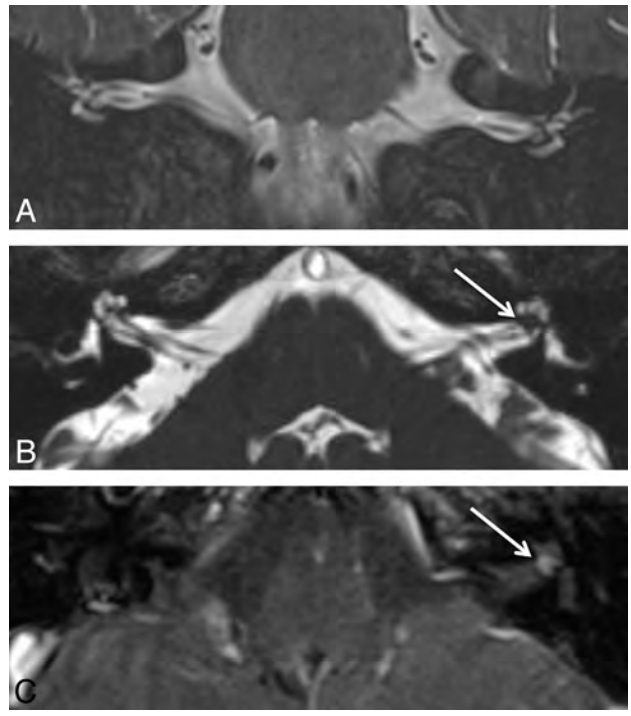

FIG 2. A 65-year-old woman who presented with left-sided hearing loss. *A*, Coronal T2WI shows the intracanalicular bilateral vestibulocochlear and facial nerves without associated lesion. *B*, Axial CISS image demonstrates a hypointense lesion (*arrow*) to better advantage located within the fundus of the left IAC. *C*, Postcontrast axial T1WI confirms the enhancing 2-mm lesion (*arrow*).

observers 1 and 2 missed the same fundal IAC lesion and observer 1 missed an additional fundal lesion. These lesions were more apparent on the axial sequences (Fig 2).

Observer 1 had 2 false-positives on the axial sequence and 2 false-positives on the coronal sequence, whereas observer 2 had 4 false-positives on the axial and 0 false-positives on the coronal sequence. Using both sequences, observer 1 had 2 false-positives and observer 2 had 1 false-positive, which was a different patient from observer 1. On retrospective review, the 3 false-positives generated on evaluation of both sequences were felt to be secondary to volume averaging from the adjacent wall of the IAC, banding artifact on the axial CISS that was not resolved on the coronal T2WI, and volume averaging from the anterior inferior cerebellar artery within the IAC (Fig 3).

κ coefficients for interobserver reliability were 0.84 for the axial CISS alone and 0.90 for coronal T2WI alone. For both sequences together, the κ coefficient was 0.91.

DISCUSSION

In this study, we showed that a 2-sequence screening MR imaging protocol using axial CISS and coronal T2WI can reliably detect IAC lesions with 100% sensitivity, high accuracy and specificity, and excellent interobserver reliability. Screening diagnostic tools are intended to have a high sensitivity. The high sensitivity, however, creates a small number of false-positives, which may necessitate confirmatory imaging with contrast administration.

Early detection of vestibular schwannomas and other IAC lesions is important to reduce treatment morbidity because larger tumors cause more treatment-related complications, particularly with regard to facial nerve outcomes.[8] Early detection is particularly important if surgery is attempted to preserve hearing; this is because the size of the tumor correlates with hearing outcomes.[9,10] As the trend moves to less audiometric testing and more initial imaging evaluation, a smaller percentage of IAC MRIs will be positive for vestibular schwannoma. While gadolinium-enhanced MR imaging is considered a standard and embraced by many, in the era of rising health care costs, adoption of a less expensive and less time intensive screening protocol is warranted. This study proves that unenhanced MR imaging can detect even small subcentimeter IAC lesions, which have been considered by many to require gadolinium administration for detection.

The measure of a screening examination is its ability to detect mild or early forms of disease, which for this study translates into recognition of very small IAC lesions. In the late 1990s and early 2000s, at least 8 studies[3,4,6,11-15] evaluated the diagnostic value of unenhanced fluid-sensitive MR imaging sequences (T2WI or CISS) for the evaluation of IAC lesions. Five of those studies reported the number of lesions measuring $\leq$10 mm.[6,11-14] Of the 5, 2 had 100% sensitivity using axial 2D fast spin-echo T2WI alone and axial 3D fast asymmetric spin-echo T2WI alone and included 10 and 11 patients, respectively.[12,14] Of the remaining 3 studies, Allen et al[6] included 12 small lesions, in which 2 lesions (measuring less than 4 mm) were missed by 2 of 4 observers in small internal auditory canals using axial and coronal T2 fast spin-echo with voxel size of approximately $0.3 \times 0.4 \times 3$ mm. Stuckey et al[11] evaluated 4 lesions measuring $\leq$10 mm in which a 4-mm IAC

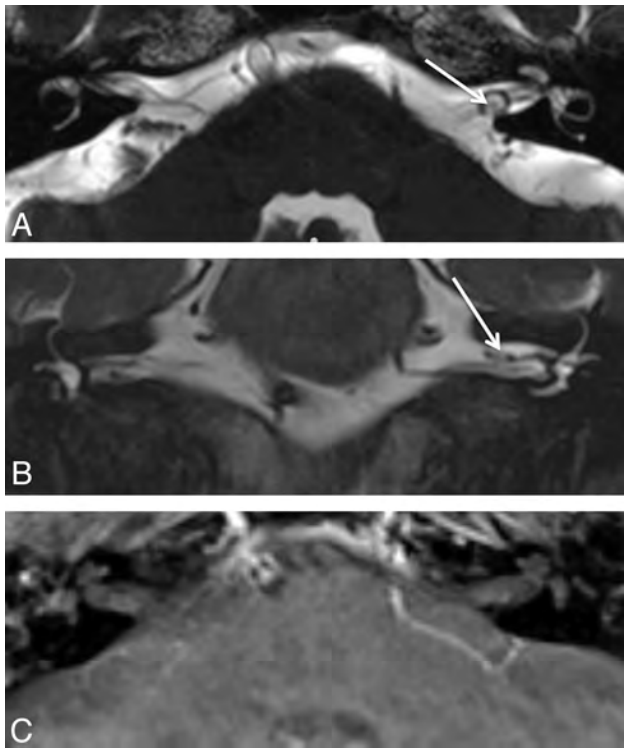

FIG 3. A 71-year-old man with vertigo. *A*, Axial CISS image demonstrates a hypointense focus surrounded by a loop of the anterior inferior cerebellar artery, which was thought to represent a small IAC lesion. *B*, Coronal T2WI shows the same hypointense focus. *C*, Postcontrast axial T1WI shows no enhancing lesion, indicating that the hypointense focus on the screening study was volume averaging related to the adjacent artery.

lesion was undetected by 1 of 2 observers on axial 3D CISS with voxel size of approximately 0.7 mm isotropic. Hermans et al[13] imaged 9 small lesions in which a 3-mm IAC lesion was missed by both observers, and a 6-mm intralabyrinthine lesion was missed by 1 observer using a $0.7 \times 0.7 \times 3.0$ mm axial 3D CISS sequence.

Comparing our data to prior studies supports a diagnostic benefit of the 2 plane, 2-sequence screening protocol using coronal T2WI and axial CISS. Two planes mitigate the effects of artifact from volume averaging, which can be especially limiting in small IACs. In the Hermans et al[13] study, both observers attributed misses and uncertainty primarily to volume averaging, but also to artifacts and suboptimal techniques. In the Allen et al[6] publication, 2 lesions measuring 2 and 3 mm in maximum diameter were missed likely because of volume averaging because they were specifically noted to be found in small IACs.[6]

Another advantage of the 2-sequence protocol is the benefit of superior contrast-to-noise ratio provided by CISS imaging in addition to having the T2 sequence to mitigate the banding artifact, which may limit balanced steady-state free precession sequences such as CISS. The 3D CISS imaging has twice the contrast-to-noise ratio for the intracanalicular nerves and CSF compared with the 3D fast recovery fast spin-echo T2WI sequence,[7] which is likely why it has replaced T2WI for evaluation of the IACs in many institutions. However, CISS sequences are limited by banding artifact resulting from magnetic field inhomogeneity,[16] which can lead to the appearance of pseudolesions in the evaluation of the IACs. T2WI can be used to confirm or exclude suspected lesions on CISS that may be artifactual.

Unenhanced screening sequences provide significant cost and time savings compared with gadolinium-enhanced IAC MR imaging. The institutional charge of our screening IAC protocol is $850 less than our contrast-enhanced IAC MR imaging protocol, which is due to a lack of gadolinium contrast, reduced scan time, and reduced professional fee. The screening protocol takes approximately 11 minutes versus 30 minutes for the contrast-enhanced examination. Over 1 year from April 2012 to April 2013, 127 screening IAC studies were performed for asymmetric hearing loss at our institution. Of those, 101 were normal, 20 were performed to follow already diagnosed IAC or intralabyrinthine lesions, 5 had incidental lesions unrelated to hearing symptoms, and 1 study had an IAC lesion that will be further characterized by a contrast-enhanced MR imaging. Using the screening protocol rather than the contrast-enhanced IAC protocol over that year, we saved at least $107,100 ($126 \times $850), which is a slight overestimate because it does not account for the redundant screening examination performed on the 1 patient with an IAC lesion. Three studies[6,17,18] demonstrated similar cost saving per examination with the difference in unenhanced and enhanced protocols equaling $550–$800. MR imaging time savings over that same year equal approximately 2394 minutes (126×19 minutes) or 99.75 hours of MR imaging scan time.

A 2009 meta-analysis[5] supported by the United Kingdom National Institute for Health Research reviewed over 11 studies from 1996 to 2001 assessing the diagnostic accuracy and cost-effectiveness of noncontrast T2 or T2* sequences in the identification of vestibular schwannoma. Fortnum et al[5] found that fluid-sensitive sequences have pooled sensitivities ranging from 96%–98% for detection of IAC lesions measuring 2 mm to >20 mm in diameter. They concluded that noncontrast fluid-sensitive MR imaging sequences allow for accurate evaluation of the facial and vestibulocochlear nerves within the cerebellopontine angle and IAC, and that including contrast-enhanced sequences is less cost effective and not likely to add information that would change management in a screening population.

While unenhanced screening MR imaging is sufficient to exclude lesions of the IAC, noncontrast-enhanced MR imaging could potentially miss some pathology of the IAC or labyrinth that would be detected with contrast. As Jackler[19] addressed in his response to the screening studies published in the late 1990s, noncontrast screening MR imaging may not reliably detect labyrinthitis, vestibular neuritis, sarcoidosis, or leptomeningeal metastases. In the case of the first 2 diagnoses, however, treatment is based on clinical symptoms, not radiologic appearance. For patients who present with symptoms of acute vertigo with or without sudden sensorineural hearing loss, the optimal treatment will be a short course of high-dose steroids, regardless of the imaging findings.[20,21] In the setting of suspected sarcoidosis or primary malignancy, a contrast-enhanced examination is warranted rather than a screening examination. Furthermore, sarcoidosis or leptomeningeal metastases rarely present as isolated sensorineural hearing loss. Clinical judgment on the part of the ordering clinician is still required to select the best examination and to determine when a screening scan is appropriate. The unenhanced screening MR im-

aging protocol is meant for patients with audiovestibular symptoms without other comorbidities that might affect the IAC or inner ear.

Limitations of this study include its small sample size, few controls, retrospective nature, and lack of pathologic confirmation in most cases. The small sample size was unavoidable given the rare incidence of IAC lesions in the population, especially lesions measuring ≤10 mm in diameter. Similarly, a prospective study of this sample size would be difficult given the time necessary to recruit patients with such a rare lesion. Few controls were available because the unenhanced screening examination was almost exclusively used during the surveyed time span. Patients who had a normal noncontrast screening examination rarely underwent a "gold standard" contrast-enhanced examination and vice versa. Pathologic confirmation could not be obtained in most of the cases because the lesions were small enough and lacking in symptoms to permit follow-up rather than surgery.

Lastly, it could be argued that similar sensitivity data would not be achieved with general radiologists as observers rather than experienced neuroradiologists. We contend that although there may be a brief learning curve, a general radiologist can just as easily trace unaffected vestibulocochlear nerves or detect an asymmetric hypointense mass on a background of hyperintense CSF in the IAC as a Certificate of Added Qualification–holding neuroradiologist.

CONCLUSIONS

Screening MR imaging using a combination of unenhanced axial CISS and coronal T2WI sequences can reliably detect small (≤10 mm) IAC schwannomas with 100% sensitivity and excellent interobserver reliability. The high sensitivity creates a small number of false-positives, which may necessitate confirmatory imaging with contrast administration. Fundal lesions may be missed on an axial or coronal sequence alone because of volume averaging.

Disclosures: Clough Shelton—*UNRELATED: Grants/Grants Pending:* Sonitus,* Cochlear Corp,* *Comments*: Research into bone conduction hearing aid (Sonitus); research into cochlear implants (Cochlear Corp). H. Ric Harnsberger—*UNRELATED: Board Membership:* Amirsys, *Comments*: Work has no relationship to peer-reviewed articles; *Employment:* Amirsys, *Comments*: Work has no relationship to peer-reviewed articles; *Stock/Stock Options:* Amirsys, *Comments*: Work has no relationship to peer-reviewed articles. *Money paid to the institution.

REFERENCES

1. Kumar A, Maudelonde C, Mafee M. **Unilateral sensorineural hearing loss.** *Laryngoscope* 1986;96:14–18
2. Armington WG, Harnsberger HR, Smoker WR, et al. **Normal and diseased acoustic pathway: evaluation with MR imaging.** *Radiology* 1988;167:509–15
3. Zealley IA, Cooper RC, Clifford KM, et al. **MRI screening for acoustic neuroma: a comparison of fast spin echo and contrast enhanced imaging in 1233 patients.** *Br J Radiol* 2000;73:242–47
4. Annesley-Williams DJ, Laitt RD, Jenkins JP, et al. **Magnetic resonance imaging in the investigation of sensorineural hearing loss: is contrast enhancement still necessary?** *J Laryngol Otol* 2001;115:14–21
5. Fortnum H, O'Neill C, Taylor R, et al. **The role of magnetic resonance imaging in the identification of suspected acoustic neuroma: a systematic review of clinical and cost effectiveness and natural history.** *Health Technol Assess* 2009;13:iii–iv, ix–xi, 1–154
6. Allen RW, Harnsberger HR, Shelton C, et al. **Low-cost high-resolution fast spin-echo MR of acoustic schwannoma: an alternative to enhanced conventional spin-echo MR?** *AJNR Am J Neuroradiol* 1996;17:1205–10
7. Lane JI, Ward H, Witte RJ, et al. **3-T imaging of the cochlear nerve and labyrinth in cochlear-implant candidates: 3D fast recovery fast spin-echo versus 3D constructive interference in the steady state techniques.** *AJNR Am J Neuroradiol* 2004;25:618–22
8. Gurgel RK, Dogru S, Amdur RL, et al. **Facial nerve outcomes after surgery for large vestibular schwannomas: do surgical approach and extent of resection matter?** *Neurosurg Focus* 2012;33:E16
9. Yates PD, Jackler RK, Satar B, et al. **Is it worthwhile to attempt hearing preservation in larger acoustic neuromas?** *Otol Neurotol* 2003;24:460–64
10. Meyer TA, Canty PA, Wilkinson EP, et al. **Small acoustic neuromas: surgical outcomes versus observation or radiation.** *Otol Neurotol* 2006;27:380–92
11. Stuckey SL, Harris AJ, Mannolini SM. **Detection of acoustic schwannoma: use of constructive interference in the steady state three-dimensional MR.** *AJNR Am J Neuroradiol* 1996;17:1219–25
12. Soulié D, Cordoliani YS, Vignaud J, et al. **MR imaging of acoustic neuroma with high resolution fast spin echo T2-weighted sequence.** *Eur J Radiol* 1997;24:61–65
13. Hermans R, Van der Goten A, De Foer B, et al. **MRI screening for acoustic neuroma without gadolinium: value of 3DFT-CISS sequence.** *Neuroradiology* 1997;39:593–98
14. Naganawa S, Ito T, Fukatsu H, et al. **MR imaging of the inner ear: comparison of a three-dimensional fast spin-echo sequence with use of a dedicated quadrature-surface coil with a gadolinium-enhanced spoiled gradient-recalled sequence.** *Radiology* 1998;208:679–85
15. Marx SV, Langman AW, Crane RC. **Accuracy of fast spin echo magnetic resonance imaging in the diagnosis of vestibular schwannoma.** *Am J Otolaryngol* 1999;20:211–16
16. Bangerter NK, Hargreaves BA, Vasanawala SS, et al. **Analysis of multiple-acquisition SSFP.** *Magn Reson Med* 2004;51:1038–47
17. Daniels RL, Shelton C, Harnsberger HR. **Ultra high resolution nonenhanced fast spin echo magnetic resonance imaging: cost-effective screening for acoustic neuroma in patients with sudden sensorineural hearing loss.** *Otolaryngol Head Neck Surg* 1998;119:364–69
18. Tan TY. **Non-contrast high resolution fast spin echo magnetic resonance imaging of acoustic schwannoma**. *Singapore Med J* 1999;40:27–31
19. Jackler RK. **Cost-effective screening for acoustic neuroma with unenhanced MR: a clinician's perspective.** *AJNR Am J Neuroradiol* 1996;17:1226–28
20. Strupp M, Zingler VC, Arbusow V, et al. **Methylprednisolone, valacyclovir, or the combination for vestibular neuritis.** *N Engl J Med* 2004;351:354–61
21. Rauch SD, Halpin CF, Antonelli PJ, et al. **Oral vs intratympanic corticosteroid therapy for idiopathic sudden sensorineural hearing loss: a randomized trial.** *JAMA* 2011;305:2071–79

Transorbital Sonography in Acute Optic Neuritis: A Case-Control Study

P. Lochner, R. Cantello, F. Brigo, L. Coppo, R. Nardone, F. Tezzon, O. Raymkulova, G. Strigaro, C. Comi, and M.A. Leone

ABSTRACT

BACKGROUND AND PURPOSE: Acute unilateral optic neuritis is associated with a thickening of the retrobulbar portion of the optic nerve as revealed by transorbital sonography, but no comparison has been made between nerve sheath diameter and optic nerve diameter in patients with acute optic neuritis versus healthy controls. We evaluated optic nerve sheath diameter and optic nerve diameter in patients with acute optic neuritis and healthy controls and compared optic nerve sheath diameter and optic nerve diameter with visual-evoked potentials in patients.

MATERIALS AND METHODS: A case-control study was performed in 2 centers. Twenty-one consecutive patients with onset of visual loss during the prior 10 days and established acute noncompressive unilateral optic neuritis were compared with 21 healthy controls, matched for sex and age (±5 years). Two experienced vascular sonographers performed the study by using B-mode transorbital sonography. Visual-evoked potentials were performed on the same day as the transorbital sonography and were evaluated by an expert neurophysiologist. Sonographers and the neurophysiologist were blinded to the status of the patient or control and to clinical information, including the side of the affected eye.

RESULTS: The median optic nerve sheath diameter was thicker on the affected side (6.3 mm; interquartile range, 5.9–7.2 mm) compared with the nonaffected side (5.5 mm; interquartile range, 5.1–6.2 mm; $P < .0001$) and controls (5.2 mm; interquartile range, 4.8–5.5 mm; $P < .0001$). The median optic nerve diameter was 3.0 mm (range, 2.8–3.1 mm) on the affected side and 2.9 mm (range, 2.8–3.1 mm) on the nonaffected side (P = not significant.). Both sides were thicker than those in controls (2.7 mm; interquartile range, 2.5–2.8 mm; $P = .001$ and .009). No correlation was found between optic nerve sheath diameter and optic nerve diameter and amplitude and latency of visual-evoked potentials in patients with optic neuritis.

CONCLUSIONS: Transorbital sonography is a promising tool to support the clinical diagnosis of acute optic neuritis. Further studies are needed to define its specific role in the diagnosis and follow-up of optic neuritis.

ABBREVIATIONS: ON = optic neuritis; OND = optic nerve diameter; ONSD = optic nerve sheath diameter; TOS = transorbital sonography; VEP = visual-evoked potentials

Optic neuritis (ON) is an acute inflammation of the optic nerve that may cause a complete or partial loss of vision. The classic triad for its clinical diagnosis is visual loss, periocular pain, and dyschromatopsia.[1] ON typically occurs in young adults with an approximately 3:1 female-male ratio. ON is mostly idiopathic but may be associated with autoimmune disorders and infectious, inflammatory, and demyelinating diseases, especially multiple sclerosis. It is diagnosed through a complete ophthalmologic and neurologic evaluation and a prolonged latency of the visual-evoked potentials (VEP). MR imaging with gadolinium is valuable for differential diagnosis.[2]

Previous studies have shown that transorbital sonography (TOS) reliably investigates the optic nerve owing to its low reflectivity and the high reflectivity of the perineural sheath and orbital fat.[3] TOS has been recognized as an accurate, noninvasive method to identify papilledema.[4,5] Some TOS studies have shown that the optic nerve may be enlarged in acute ON,[6-11] though the validity of this technique for the diagnosis of ON has not yet been recog-

Received March 24, 2014; accepted after revision May 22.

From the Department of Neurology (P.L., F.B., F.T.), General Hospital, Merano, Italy; Section of Neurology (P.L., R.C., L.C., G.S., C.C.), Department of Translational Medicine, University of Piemonte Orientale "A. Avogadro," Novara, Italy; Department of Neurological and Movement Sciences (F.B.), Section of Clinical Neurology, University of Verona, Verona, Italy; Department of Neurology (R.N.), Christian Doppler Clinic, Paracelsus Medical University, Salzburg, Austria; Head and Neck Department (O.R.), SCDU Neurology, MS Centre, AOU "Maggiore della Carità," Novara, Italy; and Interdisciplinary Research Center of Autoimmune Diseases (C.C., M.A.L.), Novara, Italy.

Please address correspondence to Piergiorgio Lochner, MD, Department of Neurology, General Hospital Tappeiner, Rossinistr 5, 39012 Merano (Bolzano) Italy; e-mail: piergiorgio.lochner@gmail.com

http://dx.doi.org/10.3174/ajnr.A4051

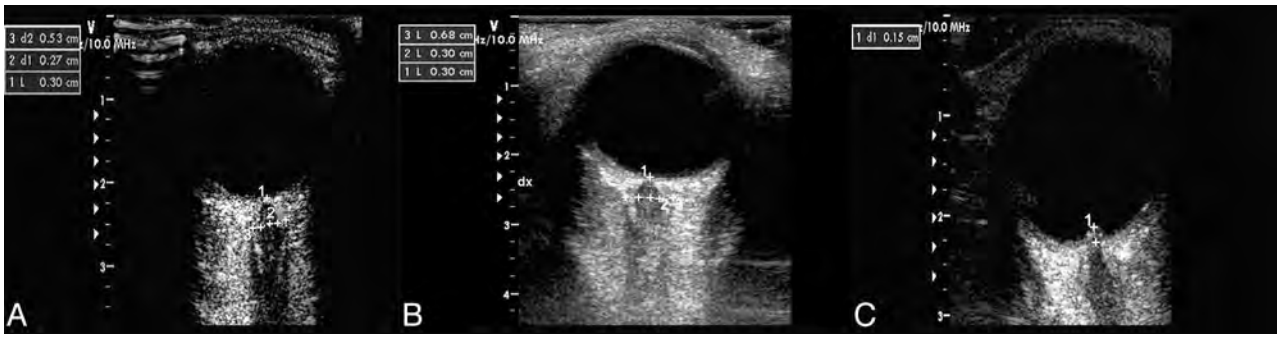

FIG 1. Transorbital sonography in optic neuritis. *A–C*, Sonographic examinations of the eye are performed in B-mode imaging in a control subject. *A*, Optic nerve sheath diameter in the control eye is 3 mm behind the papilla (*1*) (*dotted arrow*) in an axial plane showing the optic nerve (*2*) in its longitudinal course. The *dotted arrow* (*3*) denotes the ONSD. *B*, B-scan shows an optic neuritis increase of ONSD (left, 6.8 mm). *C*, In patients with optic neuritis with disc swelling, optic disc elevation is gauged between the fundus and the dome of the papilla.

nized.[12] No sonographic data are available to distinguish enlargement of the nerve itself from that of its sheath, though an enlargement of the sheath in acute ON has been described with MR imaging.[13]

Previous studies did demonstrate good accuracy and reliability of sonographic quantification of optic nerve sheath diameter (ONSD).[14,15]

The primary aim of this study was to use TOS to assess enlargement of the optic nerve and its sheath in acute ON by measuring optic nerve diameter (OND) and ONSD. The second aim was to identify whether OND and ONSD values were associated with any VEP abnormalities in cases of acute ON.

MATERIALS AND METHODS

Patients

All consecutive patients presenting to the Neurology Outpatient Clinics of the Novara and Merano Hospitals between December 2012 and October 2013 with a diagnosis of the first acute episode of demyelinating unilateral ON were invited to enter the study. The study was approved by the local ethics committees and was performed in accordance with the Declaration of Helsinki. Written informed consent was obtained from all persons before entering the study.

All patients underwent neurologic and ophthalmologic examinations, including visual acuity assessment, direct ophthalmoscopy, and laboratory examinations, including vasculitis screening and antineuromyelitis optica antibodies. MR imaging was performed to exclude other causes of ON or compressive lesions. Inclusion criteria were 18–50 years of age, visual loss with onset <10 days before the visit, and diagnosis of ON according to the Optic Neuritis Study Group.[16] Exclusion criteria were bilateral or recurrent ON, suspected ischemic optic neuropathy, recent steroid treatment, and recent lumbar puncture.

Controls were 21 healthy volunteers, matched to patients by sex and age (±5 years) and selected among students, university personnel, relatives of patients admitted to the hospital, and their friends. Controls were examined to exclude a diagnosis of MS, ON, or other neurologic diseases; those with a relative affected by MS were excluded.

Patients and controls with a history of any major systemic diseases, including cardiovascular disease, arterial hypertension, hyperlipidemia, or diabetes, and pregnant or breast-feeding women were excluded. The interval from the onset of symptoms was calculated from the first day the patient experienced visual loss or retro-orbital pain to the date of TOS.

Procedure

TOS was performed in patients and age- and sex-matched controls by 2 expert sonographers (P.L. and L.C.). VEP were performed only in patients, to avoid discomfort due to needle electrode placement in healthy controls, and were evaluated by an expert neurophysiologist (G.S.). TOS and VEP were always performed on the same day and before the onset of steroid treatment. Operators were unaware of the side involved (sonographers, VEP technicians, neurophysiologist) and of the condition of patients or controls (sonographers). To ensure blinding, we asked patients and healthy controls not to reveal their affected side (or their status) during examinations, and they were always placed on the tilt table before the arrival of the sonographer.

Transorbital Sonography

TOS was performed in B-mode by using a Vivid 7 sonography system with a 7- to 11-MHz linear array transducer (GE Healthcare, Milwaukee, Wisconsin) and an Aplio XG equipped with a 4- to 11-MHz 5 S1 Linear Probe (Toshiba Medical Systems, Nasu, Japan). A procedure described previously in the literature was used.[14,15] Subjects were examined in the supine position with the upper part of the body and the head elevated to 20°–30° to avoid any pressure on the eye and were asked to keep their eyes in a midposition and to suppress eye movements.

For safety reasons due to possible biomechanical side effects, the mechanical index was reduced to 0.2. The probe was placed on the temporal part of the closed upper eyelid by using a thick layer of sonography gel. The anterior part of the optic nerve was depicted in an axial plane showing the papilla and the optic nerve in its longitudinal course. ONSD and OND were assessed 3 mm behind the papilla. To measure the ONSD, we quantified the distance between the external borders of the hyperechogenic area surrounding the optic nerve. We measured the OND, marking the internal borders of this formation (Fig 1). To minimize intraobserver variability, we examined each bulb 3 times and calculated the means. Sonography was also used to evaluate the presence of papilledema.[4,5] The presence of papilledema, evaluated by assessing optic disc elevation, was measured between the fundus and the

Clinical and sonographic features of patients with optic neuritis and healthy control subjects

Characteristic	ON	Controls[a]	*P* Value[b]	ON-MS	Isolated ON	*P* Value[c]
No. of patients	21	21		11	10	
Age (mean) (SD) (yr)	30.3, 10.7	34.2, 8.7	NS	26.9, 9.5	34.0, 11.1	NS
Time to US examination: (median) (IQR) (days)	5, 3–7			7, 3–10	4, 3–7	NS
BMI (mean) (SD) (Kg/m^2)	24.6, 4.8	23.6, 4.1	NS			
Optic nerve sheath diameter (mm)[d]						
Affected eye (median) (IQR)	6.3, 5.9–7.2	5.2, 4.8–5.5	<.0001	6.2, 5.8–7.8	6.3, 5.9–7.0	NS
Fellow eye (median) (IQR)	5.5, 5.1–6.2		NS	5.5, 5.0–6.2	5.6, 5.1–6.4	NS
Optic nerve diameter (mm)[e]						
Affected eye (median) (IQR)	3.0, 2.8–3.2	2.7, 2.5–2.8	.001	2.9, 2.8–3.0	3.1, 2.8–3.2	NS
Fellow eye (median) (IQR)	2.9, 2.8–3.1		.009	2.9, 2.7–2.9	3.0, 2.8–3.2	NS
VEP amplitude (μV)						
Affected eye (median) (IQR)	5.2, 2.2–12.2			7.1, 2.2–12.2	4.0, 2.6–9.3	NS
Fellow eye (median) (IQR)	8.4, 3.2–11.5			4.5, 2.8–8.7	11.1, 9.1–15.1	NS
VEP latency (ms)						
Affected eye (median) (IQR)	124, 115–139			119, 115–128	134, 119–142	NS
Fellow eye (median) (IQR)	107, 103–114			104, 103–114	108, 106–113	NS

Note:—IQR indicates interquartile range; ON-MS, optic neuritis in patients with prior relapses of multiple sclerosis; US, ultrasound; BMI, body mass index; NS, not significant.
[a] The average value between the right and left eye was used as a measure of OND and ONSD in healthy controls.
[b] Level of significance at .01, according to the Bonferroni correction for multiple comparisons.
[c] Level of significance at .006, according to the Bonferroni correction for multiple comparisons.
[d] The comparison of the affected and fellow eye was significant ($P < .0001$) in all ON, ON-MS, and isolated ON.
[e] The comparison of the affected and fellow eye was not significant in all ON, ON-MS, and isolated ON.

dome of the papilla (Fig 1). Agreement between the 2 sonographers was preliminarily assessed for ONSD and OND by using the same device in 9 healthy subjects (see "Statistical Evaluation").

Pattern-Reversal Visual-Evoked Potentials

Standard pattern-reversal VEP were performed according to recent guidelines[17] with 4-channel equipment (Medtronic Keypoint, Denmark). The visual stimulus was a black-and-white pattern checkerboard (24 × 32) with 90% contrast, generated on an LED monitor (17-inch, high-resolution display; Acer, New Taipei City, Taiwan), with stimulus frequency, 2 Hz; observation distance, 100 cm. Patients were preadapted to the room lighting, and all recordings were performed under dim room lights. Patients were instructed to fix on the red point in the center of the screen with their best refractive correction during the monocular stimulation. The recording electrode was placed on Oz, the reference electrode was placed on Cz, and the ground electrode, on Fz according to the International 10–20 System. The impedance was kept below 3 kΩ on all electrodes. Signals were amplified and filtered with a bandpass filter from 0.2 to 3 kHz. One hundred responses were averaged for each side. Latencies of the N75, P100, and N145 waves and amplitude of the N75-P100 complex were analyzed.

Statistical Evaluation

If one assumed a median ONSD in controls of 5.0 mm, the sample needed to detect a mean difference of 1 mm was 10 patients and 10 controls with an α error of .05 and a β error of 0.20. Continuous variables were described by their median with the interquartile range. Comparisons between groups were assessed by using parametric (Student *t* test) and nonparametric methods (Wilcoxon test, Fisher exact test, and Spearman correlation) when appropriate (deviation from normal distribution according to the Shapiro-Wilk test). In view of the large number of comparisons, the Bonferroni correction for statistical significance was used.

Interobserver agreement between the ONSD and OND evaluations made by the 2 sonographers was preliminarily assessed with intraclass correlation coefficients.

RESULTS

We analyzed 21 patients with a first episode of ON, 17 women and 4 men; a visual loss >3/10 was present in 18 (85.7%). The right eye was affected in 16, and the left, in 5. Eleven patients had prior MS relapses (ON-MS), though never involving ON, and 10 had isolated ON. We enrolled 21 healthy controls. Mean age and body mass index were not different between patients and controls (Table). The Table reports clinical features and ONSD and OND values of patients and controls. Interobserver agreement was high for both ONSD (intraclass correlation coefficient, 0.98; 95% CI, 0.93–1.00) and OND (intraclass correlation coefficient, 0.98; 95% CI, 0.92–1.00). The main finding of our study was the statistically significant thickening of the ONSD on the affected side (intraclass correlation coefficient, 6.3 mm; 95% CI, 5.9–7.2 mm) compared with the nonaffected side (intraclass correlation coefficient, 5.5 mm; 95% CI, 5.1–6.2 mm; $P < .0001$) between patients and controls (Table). The median OND in the affected side (3.0 mm; range, 2.8–3.1 mm) was similar to that in the nonaffected side (2.9 mm; range, 2.8–3.1 mm) (P = not significant). Both sides were thicker than those in controls (median, 2.7 mm; range, 2.5–2.8 mm; $P = .001$ and .009). The OND and ONSD were strictly correlated both in healthy controls ($r = 0.63$, $P = .002$) and the nonaffected eye ($r = 0.45$, $P = .039$) but not in the affected eye ($r = -0.15$, $P = .51$).

Among controls, the ONSD or OND was similar in men and women. The median ONSD was 4.8 mm (interquartile range = 4.8–5.3 mm) in men and 5.3 mm (interquartile range = 4.8–5.6 mm) in women ($P = .16$); the median OND was 2.5 mm (interquartile range = 2.3–2.8 mm) in men and 2.7 mm (interquartile range = 2.5–2.9 mm) in women ($P = .17$). Neither ONSD ($r = 0.37$) nor OND ($r = 0.13$) was correlated with age (P = not significant).

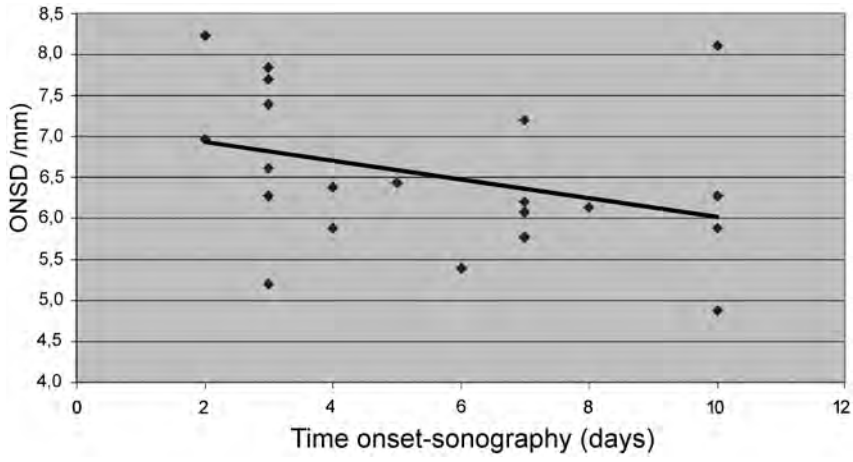

FIG 2. Optic nerve sheath diameter and delay from symptom onset. Correlation between the delay of the transorbital sonography examination (days from symptom onset) and optic nerve sheath diameter in the affected eye ($r = -0.42$, $P = .06$).

We did not find any significant difference between the ONSD and OND in patients with ON-MS and in those with isolated ON (Table).

An almost significant inverse correlation between the delay of TOS examination and ONSD diameter in the affected eye was found, suggesting that the earlier the examination, the larger was the diameter ($r = -0.42$, $P = .06$) (Fig 2). No correlation was found between delay and OND ($r = -0.11$, $P = .62$).

TOS revealed papilledema in 9 patients (43%), 8 on the right side, and in none of the controls. There was no statistical difference between patients with and without this elevation in terms of age, body mass index, ONSD, OND, VEP latency, and VEP amplitude (data not shown).

No correlation (P = not significant) was found between the ONSD and either latency or amplitude of VEP both in the affected (latency, $r = -0.01$; amplitude, $r = 0.07$) and the fellow eye (latency, $r = 0.05$; amplitude, $r = 0.09$). No correlation (P = not significant) was found between the OND and either latency or amplitude of VEP both in the affected ($r = 0.22$; -0.16, respectively) and the fellow eye ($r = 0.23$; 0.31, respectively).

DISCUSSION

Our study is the first to report transorbital sonographic measurement of both the ONSD and OND in patients with acute ON. Patients with ON had significantly increased ONSD values in the affected eye compared with the other eye and with values in age-matched controls. The thickening of the perineural space surrounding the optic nerve is probably related to inflammation of the optic nerve, resulting in an increase of the perineural subarachnoid fluid or edema caused by an impairment of axoplasmic flow, depending on the acute demyelinating plaque. Most interesting, it has been reported that narrowed optic canals, occurring for instance in osteopetrosis, may lead to compressive optic neuropathy.[18,19] It is, therefore, possible that within the anatomic variability among different subjects, a tendency toward reduced diameter of the optic canals may lead to a further increase in perineural subarachnoid fluid and edema, with subsequent worsening of visual dysfunction. Our results, therefore, suggest that ONSD has a high sensitivity for the diagnosis of acute ON. Our study was not designed to assess the specificity and predictive value of ONSD, which would require a larger sample size and controls with different diseases and different settings. Most interesting, although our patient population is not different from that in previous studies,[6-11] the mean ONSD was slightly higher and corresponded to the ONSD values of patients with either chronically[4] (6.4 mm) or acutely elevated intracranial pressure (6.2 mm).[20] We believe that this discrepancy could be explained by a different resolution of the sonography system, different probes, or by variability in the evaluation of sonographic anatomy and time of insonation. We also found that the sooner TOS is performed after symptom onset, the higher is the probability of detecting an increased ONSD. This observation supports the planning of further studies aiming to evaluate TOS for monitoring the evolution of inflammation.

The measurement of optic disc elevation is useful for detecting the presence of disc swelling (papilledema). Papilledema results from transmission of increased intracranial pressure to the subarachnoid space of the optic nerve, with compression of the nerve, stasis of axonal transport, and subsequent swelling of the optic nerve axons, particularly in patients with a narrow optic canal.[21] In our study, we found a percentage of papilledema (45%) higher than that in previous studies (ranging from 6% to 37%).[6-8,10]

Although the OND in the affected eye was not thicker than that in the contralateral eye, both were slightly thicker than that in matched controls. We have no clear explanation for this finding. Such a difference may be due to chance alone, or it may suggest a subclinical involvement of the fellow nerve. We did not find any correlation between TOS and VEP measures, though VEP were performed only in patients. VEP specifically evaluate the conduction time of the visual pathways, including the optic nerve tract: A slow conduction time (ie, prolonged latency of P100) is primarily due to a demyelinating process affecting the optic nerve. TOS instead evaluates the optic nerve and a different structure, its perineural space. Thus, these 2 techniques provide different, though complementary, information on the pathophysiology of ON.

This study is limited by the relatively small number of patients, the impossibility of obtaining a complete blinding of the clinical status of the patients, and the VEP performed only in patients. This study has several strengths, however, because we always performed sonographic assessments before starting steroid therapy and close to the onset of symptoms, and examiners were blinded to both clinical diagnosis and the side of ON. Furthermore, preliminary assessment of interobserver agreement between the ONSD and OND evaluations made by the 2 sonographers was high and similar to that found in a previous study by Bäuerle et al[14] ($r = 0.92–0.97$). These findings indicate that sonographic

ONSD quantification can be performed with good accuracy and reliability.

CONCLUSIONS

ONSD measured by TOS is a noninvasive, inexpensive, and easy procedure, which may represent a promising tool to support and confirm the clinical diagnosis of acute ON, even if it can only examine the anterior portion of the optic nerve. Further investigations with larger sample sizes and longitudinal studies are required to confirm our results.

Disclosures: Francesco Brigo—*UNRELATED*: *Payment for Lectures (including service on Speakers Bureaus)*: UCB Pharma. Cristoforo Comi—*UNRELATED: Grants/Grants Pending*: Italian Ministry of Health,* Guillain-Barré Syndrome - Chronic Inflammatory Demyelinating Polyneuropathy Foundation International,* *Comments*: grants for research in neuroimmunology (€300,000), *Travel/Accommodations/Meeting Expenses Unrelated to Activities Listed*: Biogen, UCB Pharma, Novartis, AbbVie, *Comments*: meeting expenses (€5000). Maurizio A. Leone—*UNRELATED*: *Board Membership*: *European Journal of Neurology*, *Comments*: Associate Editor, *Grants/Grants Pending*: Fondazion Comunità del Novarese,* *Comments*: grant for home-care project in multiple sclerosis. *Money paid to the institution.

REFERENCES

1. Shams PN, Plant GT. **Optic neuritis: a review.** *Int MS J* 2009; 16:82–89
2. Korsholm K, Madsen KH, Frederiksen JL, et al. **Recovery from optic neuritis: an ROI-based analysis of LGN and visual cortical areas.** *Brain* 2007;130:1244–53
3. Hansen HC, Helmke K, Kunze K. **Optic nerve sheath enlargement in acute intracranial hypertension.** *Neuro-Ophtalmology* 1994;6: 345–54
4. Bäuerle J, Nedelmann M. **Sonographic assessment of the optic nerve sheath in idiopathic intracranial hypertension.** *J Neurol* 2011;258:2014–19
5. Lochner P, Nardone R, Tezzon F, et al. **Optic nerve sonography to monitor treatment efficacy in idiopathic intracranial hypertension: a case report.** *J Neuroimaging* 2013;23:533–34
6. Gerling J, Janknecht P, Hansen LL, et al. **Diameter of the optic nerve in idiopathic optic neuritis and in anterior ischemic optic neuropathy.** *Int Ophthalmol* 1997;21:131–35
7. Stefanović IB, I Jovanović M, Krnjaja BD, et al. **Influence of retrobulbar neuritis and papillitis on echographically measured optic nerve sheath diameter.** *Vojnosanit Pregl* 2010;67:32–35
8. Neroev VV, Karlova IZ, Zaĭtseva OV, et al. **Role of ultrasonic B-scanning in differential diagnosis and prognosis of the course of optic neuritis** [in Russian]. *Vestn Oftalmol* 2001;117:25–29
9. Elvin A, Andersson T, Söderström M. **Optic neuritis: Doppler ultrasonography compared with MR and correlated with visual evoked potential assessments.** *Acta Radiol* 1998;39:243–48
10. Karami M, Janghorbani M, Dehghani A, et al. **Orbital Doppler evaluation of blood flow velocities in optic neuritis.** *Korean J Ophthalmol* 2012;26:116–22
11. Dehghani A, Giti M, Akhlaghi MR, et al. **Ultrasonography in distinguishing optic neuritis from nonarteritic anterior ischemic optic neuropathy.** *Adv Biomed Res* 2012;1:3
12. Kolappan M, Henderson AP, Jenkins TM, et al. **Assessing structure and function of the afferent visual pathway in multiple sclerosis and associated optic neuritis.** *J Neurol* 2009;256:305–19
13. Hickmann SJ, Miszkiei KA, Plant GT, et al. **The optic nerve on MRI in acute optic neuritis.** *Neuroradiology* 2005;47:51–55
14. Bäuerle J, Lochner P, Kaps M, et al. **Intra- and interobserver reliability of sonographic assessment of the optic nerve sheath diameter in healthy adults.** *J Neuroimaging* 2012;22:42–45
15. Bäuerle J, Schuchardt F, Schroeder L, et al. **Reproducibility and accuracy of optic nerve sheath diameter assessment using ultrasound compared to magnetic resonance imaging.** *BMC Neurol* 2013;13:187
16. **The clinical profile of optic neuritis: experience of the optic neuritis treatment trial—Optic Neuritis Study Group.** *Arch Ophthalmol* 1991;109:1673–78
17. Holder GE, Celesia GG, Miyake Y, et al. **International Federation of Clinical Neurophysiology: recommendations for visual system testing.** *Clin Neurophysiol* 2010;121:1393–409
18. Vanier V, Miller NR, Carson BS. **Bilateral visual improvement after unilateral optic canal decompression and cranial vault expansion in a patient with osteopetrosis, narrowed optic canals, and increased intracranial pressure.** *J Neurol Neurosurg Psychiatry* 2000;69: 405–06
19. Nardone R, Brigo F, Orioli A, et al. **Optic nerve sonography in a patient with osteopetrosis.** *Can J Neurol Sci* 2014;41:400–01
20. Moretti R, Pizzi B, Cassini F, et al. **Reliability of the optic nerve ultrasound for the evaluation of patients with spontaneous intracranial hemorrhage.** *Neurocritic Care* 2009;11:406–10
21. Boynton JR, Pheasant TR, Levine MR. **Hypoplastic optic nerves studied with B-scan ultrasonography and axial tomography of the optic canals.** *Can J Ophtahmol* 1975;10:473–81

Low-Tube-Voltage 80-kVp Neck CT: Evaluation of Diagnostic Accuracy and Interobserver Agreement

J.L. Wichmann, J. Kraft, E.-M. Nöske, B. Bodelle, I. Burck, J.-E. Scholtz, C. Frellesen, J. Wagenblast, J.M. Kerl, R.W. Bauer, T. Lehnert, T.J. Vogl, and B. Schulz

ABSTRACT

BACKGROUND AND PURPOSE: Low-tube-voltage acquisition has been shown to facilitate substantial dose savings for neck CT with similar image contrast compared with standard 120-kVp acquisition. However, its potential for the detection of neck pathologies is uncertain. Our aim was to evaluate the effects of low-tube-voltage 80-kV(peak) acquisitions for neck CT on diagnostic accuracy and interobserver agreement.

MATERIALS AND METHODS: Three radiologists individually analyzed 80-kVp and linearly blended 120-kVp image series of 170 patients with a variety of pathologies who underwent dual-energy neck CT. Reviewers were unblinded to the clinical indication for CT but were otherwise blinded to any other data or images and were asked to state a final main diagnosis. Findings were compared with medical record charts, CT reports, and pathology results. Sensitivity, specificity, positive predictive value, and negative predictive value were calculated for each observer. Interobserver agreement was evaluated by using intraclass correlation coefficients.

RESULTS: Diagnoses were grouped as squamous cell carcinoma–related ($n = 107$, presence/absence of primary/recurrent squamous cell carcinoma), lymphoma-related ($n = 40$, presence/absence of primary/recurrent lymphoma), and benign ($n = 23$, eg, abscess). Cumulative sensitivity, specificity, positive predictive value, and negative predictive value for 80-kVp and blended 120-kVp images were 94.8%, 93.0%, 95.9%, and 91.1%, respectively. Results were also consistently high for squamous cell carcinoma–related (94.8%/95.3%, 89.1%/89.1%, 94.3%/94.4%, 90.1%/91.0%) and lymphoma-related (95.0%, 100.0%, 100.0%, 95.2%) 80-kVp/120-kVp image series. Global interobserver agreement was almost perfect (intraclass correlation coefficient, 0.82, 0.80; 95% CI, 0.76–0.74, 0.86–0.85). Calculated dose-length product was reduced by 48% with 80-kVp acquisitions compared with the standard 120-kVp scans (135.5 versus 282.2 mGy × cm).

CONCLUSIONS: Low-tube-voltage 80-kVp CT of the neck provides sufficient image quality with high diagnostic accuracy in routine clinical practice and has the potential to substantially decrease radiation exposure.

ABBREVIATIONS: $CTDI_{vol}$ = volume CT dose index; DECT = dual-energy CT; DLP = dose-length product; ICC = intraclass correlation coefficient; NPV = negative predictive value; PPV = positive predictive value; SCC = squamous cell carcinoma

CT is a standard imaging technique in routine clinical practice for detection, staging, and follow-up evaluation of various pathologies of the neck, including squamous cell carcinoma (SCC), cervical lymphoma or lymphadenopathy, and parapharyngeal or retropharyngeal abscess.[1-5] CT examinations contribute a substantial amount of cumulative radiation exposure to patients with cervical pathologies, especially if follow-up CT is required.[6] Thus, various approaches for dose reduction of CT of the neck, brain, paranasal sinus, and the facial skeleton have been proposed, including reduction of tube current and tube potential, high-pitch acquisition, and application of automated exposure-control software.[7-10] The combination of such techniques with an iterative reconstruction algorithm can also provide similar image quality while substantially reducing exposure to ionizing radiation compared with the standard 120-kVp acquisitions.[11,12]

Several studies have demonstrated that low-tube-voltage acquisitions at 80 kVp can increase iodine attenuation and image contrast of soft-tissue structures and reduce radiation exposure.[13-15] However, only a few studies have investigated low-tube-voltage acquisition CT techniques for imaging of the neck.[16-18] We hypothesized that an 80-kVp acquisition may provide comparable image quality for evaluation of the neck region. To evaluate the efficacy of this technique in simulated routine clinical practice, we retrospectively assessed the diagnostic accuracy of

Received April 25, 2014; accepted after revision June 2.

From the Departments of Diagnostic and Interventional Radiology (J.L.W., J.K., E.-M.N., B.B., I.B., J.-E.S, C.F., J.M.K., R.W.B., T.L., T.J.V., B.S.) and Otolaryngology, Head and Neck Surgery (J.W.), University Hospital Frankfurt, Frankfurt, Germany.

Please address correspondence to Julian L. Wichmann, MD, Universitätsklinikum Frankfurt am Main, Institut für Diagnostische und Interventionelle Radiologie, Theodor-Stern-Kai 7, 60590 Frankfurt; e-mail: docwichmann@gmail.com

http://dx.doi.org/10.3174/ajnr.A4052

low-tube-voltage 80-kVp image series from dual-energy neck CT (DECT) for evaluation of a variety of cervical pathologies, and the results were compared with linearly blended images representing a standard 120-kVp acquisition. We also assessed interobserver agreement and calculated the potential radiation dose reduction.

MATERIALS AND METHODS

Patient Selection and Study Design

This retrospective study was approved by the ethics committee of our hospital, and written informed consent was waived. Of 404 clinically indicated neck DECT examinations performed between February 2010 and November 2010 at our institution, we included 170 consecutive examinations. During that timeframe, neck CT examinations were performed by using 2 different CT systems at our facility; only the patients scanned by using the dual-source system capable of DECT mode were included in this study. However, assignment to either scanner was completely random on the basis of available timeslots and was not influenced for research purposes.

Contraindications for DECT imaging were known allergies to iodinated contrast material, pregnancy, and impaired renal function (estimated glomerular filtration rate below 40 mL/min). Exclusion criteria for this study were age younger than 18 years (n = 15), noncontrast studies (n = 4), CT angiography examinations (n = 26), and severe motion (n = 21) or metal artifacts (n = 49) in case-relevant anatomic regions. Furthermore, to retain study group homogeneity, we excluded patients referred for evaluation of cervical metastasis from distal neoplasms (n = 6). In case a patient underwent multiple DECT examinations during this timeframe, we included only the first examination and excluded subsequent studies (n = 113).

To simulate routine clinical practice, we aggregated 3 main groups of indications for imaging: SCC-related (group 1, n = 107), lymphoma-related (group 2, n = 40), and benign conditions (group 3, n = 23). Groups 1 and 2 included CT examinations for the primary staging of known malignancy, detection of suspected malignancy, and follow-up CT to rule out recurrence. Patients with follow-up DECT were only included if the prior non-DECT scan did not show a recurrent SCC or pathologically enlarged lymph nodes in patients with known lymphoma to avoid miscategorizing patients with tumor remnants as having recurrent tumors. Group 3 consisted of patients referred for detection or evaluation of suspected benign conditions (eg, para-/retropharyngeal abscess, sialadenitis with possible sialolithiasis, Warthin tumor). A detailed list of indications for CT is summarized in Table 1.

The criterion standard in this study for comparison of observer results was based on the combination of the electronic medical records, results from histopathology, and the original CT imaging report, ranked in that order. However, because the original CT imaging reports of the evaluated scans may have resulted in false-positive or false-negative findings, especially in initial and follow-up examinations of patients with SCC, we ranked the final clinical diagnosis first because it also included clinical knowledge from physical examinations and biopsy; correlation with clinical diagnosis is especially important in SCC of the oral cavity, for example, which may be missed on neck CT. Thus, a final diagnosis of recurrent head-neck SCC based on histopathologic findings overruled a false-negative or uncertain finding in the original CT imaging report.

Table 1: Indications for neck CT imaging (n = 170)

Indication	No.
Squamous cell carcinoma	107
Primary staging or detection of suspected squamous cell carcinoma	66
Follow-up to detect tumor recurrence	41
Lymphoma	40
Primary staging or detection of suspected lymphoma	19
Follow-up to detect lymphoma recurrence	21
Benign conditions	23
Suspected benign cervical mass (eg, Warthin tumor, adenoma)	5
Suspected cervical abscess	13
Suspected sialadenitis	3
Suspected branchial cleft cyst	2

DECT Protocol

All CT examinations in this study were performed by using a second-generation 128-section dual-source CT in dual-energy mode (Somatom Definition Flash; Siemens, Erlangen, Germany). Both x-ray tubes were operated at a different tube potential. Examination parameters were as follows: tube A: 80 kVp, reference current-time product of 302 mAs per rotation; tube B: Sn140 kVp with a tin filter; 151 mAs per rotation; rotation time, 0.5 seconds; pitch, 0.9; collimation, 2 × 64 × 0.6 mm. Real-time automatic milliampere-second-modulation software (CareDose4D; Siemens) was used to regulate the tube current, depending on the patient's anatomy. Images were acquired in a craniocaudal direction in expiratory breath-hold with the patient in a supine position. The scan range extended from the upper orbital rim to the aortic arch. DECT imaging was initiated 70 seconds after the start of intravenous administration of 100 mL of nonionic iodinated contrast agent (iopamidol, Imeron 400; Bracco-Altana Pharma, Konstanz, Germany) through an antecubital vein at a flow rate of 2 mL/s.

On the basis of the DECT raw data, the scanner automatically reconstructed an image series with a standard linear blending setting (M_0.3), merging 30% of the 80-kVp and 70% of the 140-kVp data spectrum, representing a 120-kVp acquisition. All images were reconstructed with a dedicated dual-energy medium-soft convolution kernel (D30f) and a section thickness of 2.0 mm. Evaluation of image series was limited to axial images, and multiplanar reformations were not assessed. Quantitative DECT data were also not analyzed in this study.

Image Analysis

Initially only the 80-kVp image series was evaluated on a regular PACS workstation by 3 radiologists with 7, 3, and 2 years of experience in neck CT, respectively. All image series were assessed in random order. To avoid potential recall bias, readers were aware of the indication for CT imaging but were blinded to any other clinical information or auxiliary image series (ie, prior imaging studies). Readers were allowed to scroll through the whole stack of CT images. Window settings were automatically set to predetermined standard values for evaluation of soft tissue (width, 400

Hounsfield units; level, 80 Hounsfield units) but were freely adjustable. After a time interval of 12 weeks, all blended 120-kVp images from these cases were evaluated by the same readers in the same fashion and random order to allow an assessment of the diagnostic accuracy of a standard 120-kVp acquisition.

Radiation Dose Estimations

Examination protocols were evaluated, and the resulting volume CT dose index ($CTDI_{vol}$) and dose-length-product (DLP) were recorded for each scan. Currently, examination protocols provided by the second-generation dual-source CT scanner used in this study only display cumulative $CTDI_{vol}$ and DLP values when scans are obtained in dual-energy mode and do not allow a further division of emitted radiation between both tubes with different voltage settings. However, to allow an intraindividual analysis of the estimated radiation dose without additional radiation exposure and to avoid potential bias among different study groups, we used dedicated software designed specifically for this study so that all DICOM datasets and $CTDI_{vol}$ values of each of the 80-kVp series were extracted and averaged. $CTDI_{vol}$ values are, in great part, also present in the patient protocols of each examination, which are usually used for analysis of the radiation dose. The given DLP of the cumulative DECT examination was divided by the cumulative $CTDI_{vol}$ to calculate a conversion factor. The calculated mean $CTDI_{vol}$ of the 80-kVp series based on the extracted data was then multiplied by this conversion factor to calculate the resulting estimated DLP for the low-tube-voltage acquisition.

Statistical Analysis

All statistical analyses were conducted by using dedicated software (SPSS, Version 21; IBM, Armonk, New York; and MedCalc for Windows, Version 13; MedCalc Software, Mariakerke, Belgium). Sensitivity, specificity, positive predictive value (PPV), and negative predictive value (NPV) were calculated for each observer and type of image series. The means and SDs of metric data were calculated. The paired *t* test was used to compare the $CTDI_{vol}$ and DLP between the calculated values of the 80-kVp tube and the cumulative dual-energy CT examination. A P value $< .05$ indicated a statistically significant difference for all used tests.

Interobserver agreement among the 3 radiologists was evaluated by using intraclass correlation coefficient (ICC) statistics. Cumulative and subgroup-related ICC values were calculated. The ICC value was interpreted in the following way: ICC < 0.20, slight agreement; ICC = 0.21–0.40, fair agreement; ICC = 0.41–0.60, moderate agreement; ICC = 0.61–0.80, substantial agreement; ICC = 0.81–1.0, almost perfect agreement.

RESULTS

The study group consisted of 170 patients (57.2 ± 16.3 years [range, 18–94 years]), comprising 114 male (56.3 ± 16.2 years [range, 18–94 years]) and 56 female (58.9 ± 16.6 years [range, 23–89 years]) patients.

All DECT examinations were performed without any complications, and no severe motion or metal artifacts were present. The mean cumulative $CTDI_{vol}$ of all examinations was 10.04 ± 0.80 mGy, and the calculated isolated $CTDI_{vol}$ of the 80-kVp tube was 4.82 ± 0.41 mGy ($P < .001$). The mean cumulative DLP was 282.2 ± 30.2 mGy × cm, and the mean calculated isolated 80-kVp DLP was 135.5 ± 14.7 mGy × cm ($P < .001$), resulting in an estimated dose reduction of approximately 48.0%.

Criterion Standard Final Clinical Diagnoses

One hundred seven patients underwent SCC-related neck DECT. The findings of the 3 observers for 80-kVp and blended 120-kVp images were compared with the criterion standard on the basis of the combination of the electronic medical records, results from histopathology, and the original CT imaging report. Primary neck SCC was present in 50 cases and absent in 16 cases. SCC recurrence was diagnosed in 15 cases and ruled out in 26 cases. The primary and recurrent SCC sites were the hypopharynx and larynx ($n = 21$), oropharynx ($n = 17$), nasopharynx ($n = 11$), buccal soft tissue ($n = 6$), floor of mouth ($n = 5$), tongue ($n = 3$), and nose ($n = 2$). On the basis of the Tumor, Node, Metastasis classification, we evaluated 15 T1 tumors, 17 T2 tumors, 12 T3 tumors, and 21 T4 tumors. Data for the degree of spread to the lymph nodes were not available for all cases and thus were not included. Average follow-up of SCC-related cases was 21.3 months.

Forty patients completed lymphoma-related neck DECT. Primary lymphoma was diagnosed in 12 patients and ruled out in 7. Recurrent cervical lymphoma was present in 8 patients and ruled out in 13.

Twenty-three patients underwent neck DECT to assess suspected benign conditions. A primary benign tumor (eg, Warthin tumor, adenoma) was present in 5 patients. Primary abscess was diagnosed in 7 patients and ruled out in 4. Abscess recurrence was present in 1 patient and ruled out in 1. Findings of sialadenitis or sialolithiasis as the main diagnosis were present in 3 patients. A branchial cleft cyst was diagnosed in 2 patients.

Diagnostic Accuracy of 80-kVp and Blended 120-kVp Scans

The mean global (and individual) sensitivity and NPV for all 3 observers for evaluation of 80-kVp and blended 120-kVp image series in this study were 94.8% and 91.1%, respectively. Specificity and PPV were 93.0% and 95.9% for both image series. Summarized results regarding the analysis of diagnostic accuracy are listed in Table 2.

Compared with the global scores, diagnostic accuracy for the evaluation of the subgroup of SCC showed a similarly high sensitivity for 80-kVp and 120-kVp images (94.8%, 95.3%), a decreased specificity (both 89.1%), and slightly lower PPV (94.3%, 94.4%) and NPV (90.1%, 91.0%).

Diagnostic accuracy was consistently higher for lymphoma-related imaging with a sensitivity of 95.0%, a specificity and PPV of 100.0%, and an NPV of 95.2% for both image series.

Evaluation of 80- and 120-kVp image series from examinations performed due to benign indications showed a sensitivity of 94.3%/92.5%, a specificity of 93.3%/93.3%, a PPV of 98.2%/98.1%, and an NPV of 85.7%/79.0%.

Interobserver Agreement

The global ICC score for all 3 reviewers for 80-kVp images was 0.82 (95% CI, 0.76–0.86), and for blended 120-kVp images, it was

Table 2: Comparison of diagnostic accuracy of the 3 observers[a]

Value	Global (*n* = 170)	SCC-Related (*n* = 107)	Lymphoma-Related (*n* = 40)[b]	Benign Conditions (*n* = 23)
80-kVp image series				
Sensitivity	94.8% (93.5%–95.4%)	94.8% (91.4%–97.2%)	95.0%	94.3% (88.9%–100.0%)
Specificity	93.0% (91.9%–95.1%)	89.1% (86.5%–91.7%)	100.0%	93.3% (80.0%–100.0%)
PPV	95.9% (95.3%–97.2%)	94.3% (93.1%–95.8%)	100.0%	98.2% (94.7%–100.0%)
NPV	91.1% (89.1%–92.1%)	90.1% (84.6%–94.3%)	95.2%	85.7% (71.4%–100.0%)
120-kVp image series				
Sensitivity	94.8% (92.6%–96.3%)	95.3% (91.4%–97.2%)	95.0%	92.5% (88.9%–94.4%)
Specificity	93.0% (91.9%–95.1%)	89.1% (86.5%–91.7%)	100.0%	93.3% (80.0%–100.0%
PPV	95.9% (95.3%–97.2%)	94.4% (93.2%–95.8%)	100.0%	98.1% (94.4%–100.0%)
NPV	91.1% (87.7%–93.5%	91.0% (84.6%–94.3%)	95.2%	79.0% (71.4%–85.7%)

[a] Values are given as mean (range).
[b] No interobserver differences, therefore no ranges, are given.

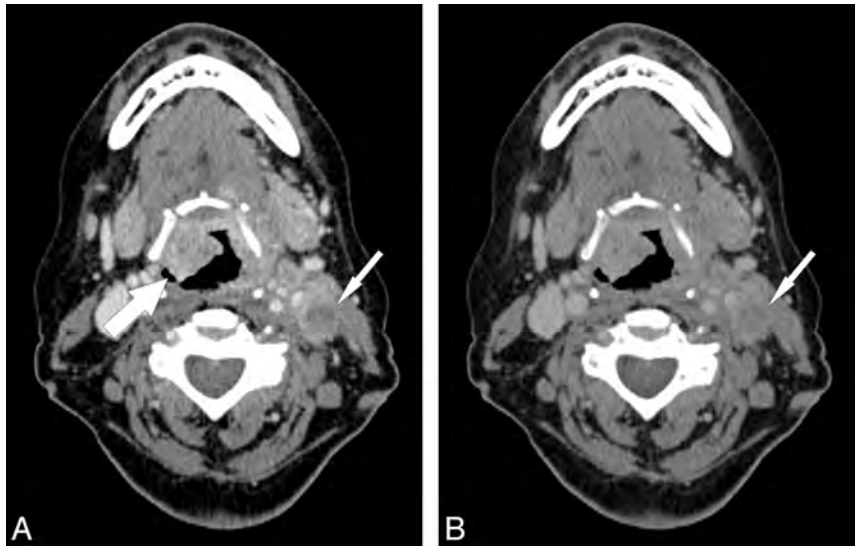

FIG 1. A 61-year-old female patient with a primary supraglottic laryngeal carcinoma (T4a N2c). Low-tube-voltage acquisition (*A*) improves tumor attenuation (*large arrow*) compared with the standard blended 120-kVp image series (*B*) and also shows a higher contrast and improved depiction of cervical lymph node metastasis (*small arrows*) (window settings: width, 400 HU; level, 80 HU).

0.80 (95% CI, 0.74–0.85), interpreted as almost perfect agreement. Interobserver agreement for SCC-related CT examinations was substantial for 80-kVp image series with an ICC score of 0.79 (95% CI, 0.70–0.85) and for blended 120-kVp images with an ICC of 0.76 (95% CI, 0.66–0.82). Evaluation of lymphoma-related examinations resulted in a perfect interobserver agreement with an ICC score of 1.0 for both image series. The 80-kVp imaging for the evaluation of benign conditions showed a substantial interobserver agreement for the 80-kVp image series with an ICC score of 0.72 (95% CI, 0.45–0.87) and for the blended 120-kVp images with an ICC of 0.69 (95% CI, 0.41–0.83).

DISCUSSION

The findings of our study indicate that compared with standard 120-kVp imaging, low-tube-voltage 80-kVp CT provides sufficient image quality for evaluation of the neck region in routine clinical practice and simultaneously allows a distinct reduction of radiation exposure. We found very high global sensitivity, specificity, PPV, and NPV and substantial interobserver agreement for the 3 reviewers with varying levels of experience with neck CT. Our results suggest that low-tube-voltage 80-kVp acquisitions may be used in routine clinical practice to substantially lower the cumulative radiation dose for patients undergoing neck CT.

While clinicians unacquainted with low-tube-voltage acquisitions might be concerned about false-negative findings regarding the detection of cervical malignancy, our results indicate that cervical SCC can be reliably diagnosed by using this technique with a consistently high sensitivity, though malignancy and especially SCC recurrence in the early stages may be present but undetectable on CT as a general limitation of the technique.[19] The high NPV in our study also indicates that neck SCC was reliably ruled out with this technique in our patient population. The additional evaluation of blended 120-kVp images representing standard acquisitions showed no significant differences for this subgroup. Furthermore, we found that low-tube-voltage acquisitions provided an increased signal attenuation and consequently improved SCC border contrast (Fig 1). Consequently, necrotic metastatic lymph nodes may also be better depicted with low-tube-voltage acquisitions as demonstrated in Fig 1. Nevertheless, the increased signal attenuation usually requires modifying the window width and level settings for evaluation of 80-kVp studies compared with standard 120-kVp examinations. In addition, low-tube-voltage

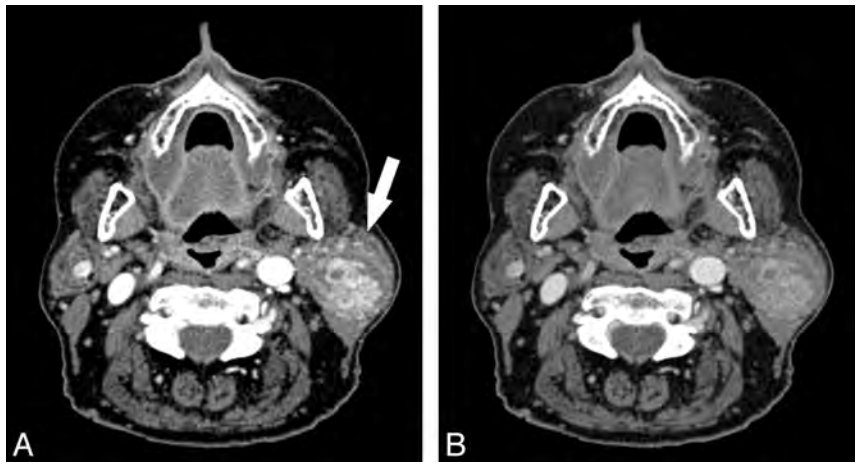

FIG 2. A 66-year-old female patient with a vascularized mass (*arrow*) in the left parotid gland. She underwent excision, and a Warthin tumor was confirmed by histopathology. The increased iodine attenuation with an 80-kVp acquisition (*A*) results in a distinctly increased image contrast of the mass compared with the standard 120-kVp acquisition (*B*) (window settings: width, 400 HU; level, 80 HU).

acquisitions may result in an increased focal spot blooming and more severe metal artifacts. Nevertheless, these limitations may be mitigated with the recently introduced third-generation dual-source CT.[20]

Prior studies have also demonstrated that low-tube-voltage neck CT results in a superior contrast-to-noise ratio compared with 120-kVp scans.[16,18] Because patients with neck SCC often undergo multiple CT examinations and radiation therapy, the benefit for this specific patient group from low-tube-voltage acquisitions may be limited. Nevertheless, younger patients with suspected or known lymphoma and patients in whom primary neck SCC can be ruled out on the basis of CT findings may particularly benefit from a dose-saving 80-kVp CT technique.

Several previous studies have demonstrated that the radiation dose during head and neck CT angiography can be substantially reduced with low-tube-voltage acquisitions.[21-23] Intravenously administered iodinated contrast material shows an increased signal attenuation when exposed to lower tube voltages, which can also improve soft-tissue contrast (Fig 2).[13-15] However, only a few prior studies evaluated low-tube-voltage CT acquisitions for imaging the soft-tissue structures of the neck region.[16-18] Gnannt et al[16] demonstrated that the consecutive increase in soft-tissue attenuation on 70-kVp scans is higher than the corresponding increase in image noise, therefore resulting in a superior contrast-to-noise ratio for neck imaging. They reported a dose reduction of 34% with 70-kVp acquisitions compared with standard 120-kVp acquisitions. We found an estimated dose reduction of 48% with 80-kVp acquisitions based on extraction of $CTDI_{vol}$ values from DECT datasets, but the actual dose savings may be less with single-energy 80-kVp acquisitions. Toepker et al[18] reported a peak in image quality for the 80-kVp images of neck DECT in patients with oral cancer, emphasizing the clinical applicability of low-tube-voltage acquisitions.

The results of this study should be interpreted in the context of the study design and consequent limitations. First, although a study group of 170 patients was reasonable for this initial study, further re-evaluation of our findings with low-tube-voltage acquisitions in larger patient cohorts is necessary. Second, there may be differences regarding the average radiation exposure of neck DECT among various dual-source CT systems. We also expect differences between single- or dual-source 80-kVp CT, and our results from retrospective analysis of the 80-kVp images from DECT should be evaluated in additional studies with phantom measurements. Especially single-source 80-kVp CT may also show a different image quality because the 140-kVp tube in DECT may have an effect on the 80-kVp DECT images. However, 80-kVp neck CT can still be expected to result in a distinct dose reduction.[16] DECT may result in a slower scan speed than certain single- or dual-source CT systems, which may lead to more motion artifacts, which were a potential exclusion criterion in our study. Third, there were far more SCC-related examinations included than the other subgroups. While we also excluded patients undergoing neck CT for evaluation of cervical metastasis from distant neoplasm, we assumed that our results regarding the detection of cervical lymphoma can be transferred to the detection of metastatic cervical lymph nodes. Fourth, although the mathematic calculations of the DICOM-reading software used in our study are ordinary and only use data that are included in the DICOM headers per se and are included in the patient protocols, the diagnostic accuracy of this technique for the estimation of low-tube-voltage radiation exposure from DECT examinations has not been validated in prior studies. Fifth, to allow an optimal comparability, we compared image series from the same patients, which may have led to potential bias though there was a 12-week interval between evaluations of both series. In addition, reviewers were blinded to any auxiliary previous imaging studies and only assessed axial images; this process does not reflect routine clinical practice for follow-up CT in patients with known neck malignancy and may have influenced diagnostic accuracy.

CONCLUSIONS

Our results demonstrate that low-tube-voltage 80-kVp neck CT provides a high diagnostic accuracy and interobserver agreement for the evaluation of various cervical pathologies and suggests that this technique may be used in routine clinical practice to substantially reduce cumulative radiation exposure for patients.

Disclosures: J. Matthias Kerl—*UNRELATED: Payment for Lectures (including service on Speakers Bureaus)*: Siemens. Ralf W. Bauer—*UNRELATED: Payment for Lectures (including service on Speakers Bureaus)*: Siemens.

REFERENCES

1. Sadick M, Schoenberg SO, Hoermann K, et al. **Current oncologic concepts and emerging techniques for imaging of head and neck squamous cell cancer.** *GMS Curr Top Otorhinolaryngol Head Neck Surg* 2012;11:Doc08
2. Hermans R. **Staging of laryngeal and hypopharyngeal cancer: value of imaging studies.** *Eur Radiol* 2006;16:2386–400
3. Castelijns JA, van den Brekel MW. **Imaging of lymphadenopathy in the neck.** *Eur Radiol* 2002;12:727–38
4. Hoang JK, Branstetter BF 4th, Eastwood JD, et al. **Multiplanar CT and MRI of collections in the retropharyngeal space: is it an abscess?** *AJR Am J Roentgenol* 2011;196:W426–32
5. Clavel S, Charron MP, Bélair M, et al. **The role of computed tomography in the management of the neck after chemoradiotherapy in patients with head-and-neck cancer.** *Int J Radiat Oncol Biol Phys* 2012;82:567–73
6. Brenner DJ, Hall EJ. **Computed tomography: an increasing source of radiation exposure.** *N Engl J Med* 2007;357:2277–84
7. Kalra MK, Maher MM, Toth TL, et al. **Techniques and applications of automatic tube current modulation for CT.** *Radiology* 2004;233:649–57
8. Bodelle B, Bauer RW, Holthaus L, et al. **Dose and image quality of high-pitch dual source computed tomography for the evaluation of cervical lymph node status: comparison to regular 128-slice single source computed tomography.** *Eur J Radiol* 2013;82:e281–85
9. Schell B, Bauer RW, Lehnert T, et al. **Low-dose computed tomography of the paranasal sinus and facial skull using a high-pitch dual-source system–first clinical results.** *Eur Radiol* 2011;21:107–12
10. Becker HC, Augart D, Karpitschka M, et al. **Radiation exposure and image quality of normal computed tomography brain images acquired with automated and organ-based tube current modulation multiband filtering and iterative reconstruction.** *Invest Radiol* 2012;47:202–07
11. Bodelle B, Klein E, Naguib NN, et al. **Acute intracranial hemorrhage in CT: benefits of sinogram-affirmed iterative reconstruction techniques.** *AJNR Am J Neuroradiol* 2014;35:445–49
12. Schulz B, Beeres M, Bodelle B, et al. **Performance of iterative image reconstruction in CT of the paranasal sinuses: a phantom study.** *AJNR Am J Neuroradiol* 2013;34:1072–76
13. Nakayama Y, Awai K, Funama Y, et al. **Abdominal CT with low tube voltage: preliminary observations about radiation dose, contrast enhancement, image quality, and noise.** *Radiology* 2005;237:945–51
14. Macari M, Spieler B, Kim D, et al. **Dual-source dual-energy MDCT of pancreatic adenocarcinoma: initial observations with data generated at 80 kVp and at simulated weighted-average 120 kVp.** *AJR Am J Roentgenol* 2010;194:W27–32
15. Nakaura T, Awai K, Oda S, et al. **Low-kilovoltage, high-tube-current MDCT of liver in thin adults: pilot study evaluating radiation dose, image quality, and display settings.** *AJR Am J Roentgenol* 2011;196:1332–38
16. Gnannt R, Winklehner A, Goetti R, et al. **Low kilovoltage CT of the neck with 70 kVp: comparison with a standard protocol.** *AJNR Am J Neuroradiol* 2012;33:1014–19
17. Hoang JK, Yoshizumi TT, Nguyen G, et al. **Variation in tube voltage for adult neck MDCT: effect on radiation dose and image quality.** *AJR Am J Roentgenol* 2012;198:621–27
18. Toepker M, Czerny C, Ringl H, et al. **Can dual-energy CT improve the assessment of tumor margins in oral cancer?** *Oral Oncol* 2014;50:221–27
19. Sullivan BP, Parks KA, Dean NR, et al. **Utility of CT surveillance for primary site recurrence of squamous cell carcinoma of the head and neck.** *Head Neck* 2011;33:1547–50
20. Meinel FG, Canstein C, Schoepf UJ, et al. **Image quality and radiation dose of low tube voltage 3(rd) generation dual-source coronary CT angiography in obese patients: a phantom study.** *Eur Radiol* 2014;24:1643–50
21. Zhang WL, Li M, Zhang B, et al. **CT angiography of the head-and-neck vessels acquired with low tube voltage, low iodine, and iterative image reconstruction: clinical evaluation of radiation dose and image quality.** *PLoS One* 2013;8:e81486
22. Xia W, Wu JT, Yin XR, et al. **CT angiography of the neck: value of contrast medium dose reduction with low tube voltage and high tube current in a 64-detector row CT.** *Clin Radiol* 2014;69:e183–89
23. Kayan M, Köroğlu M, Yeşildağ A, et al. **Carotid CT-angiography: low versus standard volume contrast media and low kV protocol for 128-slice MDCT.** *Eur J Radiol* 2012;81:2144–47

3T Intraoperative MRI for Management of Pediatric CNS Neoplasms

A.F. Choudhri, P. Klimo Jr, T.S. Auschwitz, M.T. Whitehead, and F.A. Boop

ABSTRACT

BACKGROUND AND PURPOSE: High-field-strength intraoperative MR imaging has emerged as a powerful adjunct for resection of brain tumors. However, its exact role has not been firmly established. We sought to determine the impact of 3T-intraoperative MRI on the surgical management of childhood CNS tumors.

MATERIALS AND METHODS: We evaluated patient data from a single academic children's hospital during a consecutive 24-month period after installation of a 3T-intraoperative MRI. Tumor location, histology, surgical approach, operating room time, presence and volume of residual tumor, need for tumor and non-tumor-related reoperation, and anesthesia- and MR imaging–related complications were evaluated. Comparison with pre-intraoperative MRI controls was performed.

RESULTS: One hundred ninety-four patients underwent intraoperative MRI–guided surgery. Of these, 168 were 18 years or younger (mean, 8.9 ± 5.0 years; 108 males/60 females). There were 65 posterior fossa tumors. The most common tumors were pilocytic astrocytoma (n = 31, 19%), low-grade glioma (n = 31, 19%), and medulloblastoma (n = 20, 12%). An average of 1.2 scanning sessions was performed per patient (maximum, 3). There were no MR imaging–related safety issues. Additional tumor was resected after scanning in 21% of patients. Among patients with a preoperative goal of gross total resection, 93% achieved this goal. The 30-day reoperation rate was <1% (n = 1), and no patient required additional postoperative MR imaging during the same hospital stay.

CONCLUSIONS: Intraoperative MRI is safe and increases the likelihood of gross total resection, albeit with increased operating room time, and reduces the need for early reoperation or repeat sedation for postoperative scans in children with brain tumors.

ABBREVIATIONS: FSPGR = fast-spoiled gradient recalled; iMRI = intraoperative MRI

Brain tumors are the second most common type of pediatric cancer, affecting more than 4000 children per year in the United States.[1] For many tumors, such as ependymoma and medulloblastoma, maximal cytoreductive resection offers the greatest chance for long-term survival.[2] Intraoperative MR imaging (iMRI) has been proposed as an adjunctive technique to achieve maximal tumor resection while limiting iatrogenic neurologic injury.[3-11] However, the benefits of this expensive technology have not been uniformly demonstrated in the literature.[11-14] With respect to high-field-strength iMRI, typically defined as 1.5T or higher, its impact on operating room and anesthesia time and the incidence of MR imaging–related complications, particularly in the pediatric population, have been the topic of limited publications.[3,15-17] We performed a retrospective review of our 24-month experience with a 3T-iMRI at a tertiary care children's hospital to determine the impact of this tool on surgical planning, workflow, and patient outcomes. Comparison was made with a cohort of pediatric patients with brain tumor at our institution from before installation of the iMRI scanner.

MATERIALS AND METHODS

This Health Insurance Portability and Accountability Act–compliant retrospective study was performed after institutional review board approval. We evaluated 3T-iMRI patient data for a consecutive 24-month period (February 2011 to February 2013) from a single academic children's hospital, identifying patients 18

Received January 30, 2014; accepted after revision May 26.

From the Departments of Radiology (A.F.C., M.T.W.), Neurosurgery (A.F.C., P.K., T.S.A., F.A.B.), and Ophthalmology (A.F.C.), University of Tennessee Health Science Center, Memphis, Tennessee; Le Bonheur Neuroscience Institute (A.F.C., P.K., M.T.W., F.A.B.), Le Bonheur Children's Hospital, Memphis, Tennessee; Semmes-Murphey Neurologic and Spine Institute (P.K., F.A.B.), Memphis, Tennessee; Division of Neurosurgery (P.K., F.A.B.), and Department of Surgery, St. Jude Children's Hospital, Memphis, Tennessee; and Department of Radiology (M.T.W.), Children's National Medical Center, Washington, DC.

This work was supported, in part, by a grant from Le Bonheur Children's Hospital and Children's Research Foundation to A.F.C.

Please address correspondence to Asim F. Choudhri, MD, Department of Radiology, Le Bonheur Children's Hospital, 848 Adams Ave-G216, Memphis, TN 38103; e-mail: achoudhri@uthsc.edu; @AsimChoudhriMD

http://dx.doi.org/10.3174/ajnr.A4040

years or younger who underwent iMRI-guided resection. Preoperative, intraoperative, MR imaging–related, and postoperative parameters and outcomes were recorded.

Preoperative parameters evaluated included the age, sex, number of prior tumor resections or biopsies, and the presence of a preoperative shunt. Intraoperative parameters evaluated included operating room entry time, time of initial skin incision and skin closure, operating room exit time, patient position, surgical approach, estimated blood loss, and anesthesia-related complications. We determined whether frameless stereotactic navigation was used and whether this was performed by using scans obtained in the operating room or before arrival in the operating room.

MR imaging parameters evaluated included the number of intraoperative scans, the time required to place the MR imaging coils and bring the scanner into the room, the number of scout-localizers required, the total amount of intravenous contrast administered, and any MR imaging–related complications. The presence of residual tumor on MR imaging scans was also documented. The extent of resection was graded as gross total resection if >98% of the tumor was resected, near-total if >90% was resected, and subtotal if <90% was resected.

Postoperative parameters included tumor histology, length of stay (intensive care, total hospital admission), disposition at time of discharge (home versus other facility), 7- and 30-day reoperation rates, mortality, and surgical site complications.

MR Imaging Scanner and Imaging Protocol

iMRI scans were performed with a 3T unit (Magnetom Verio 3T; Siemens, Erlangen, Germany), which was brought into the operating room via a ceiling-mounted track system (IMRIS-neuro; IMRIS, Winnipeg, Manitoba, Canada). A 2-part split-array 8-channel head coil (HC-300; IMRIS-neuro) was used, with one 4-channel component of the coil placed inferior to the patient's head and one 4-channel component placed superior to the patient's head.

For the first 12 months, the routine intraoperative scanning protocol included axial and coronal T1-weighted images before and after contrast administration and an axial T2-weighted sequence and diffusion-weighted imaging. Additional planes were used in select cases as needed, most often sagittal T1 postcontrast for posterior fossa tumors. After 12 months, the protocol was revised to include axial 3D fast-spoiled gradient recalled (FSPGR) images before and after contrast administration, an axial T2-weighted image, and axial diffusion-weighted images. The axial T2-weighted image was obtained immediately after contrast administration to allow a contrast agent infusion delay before the FSPGR images. Subtraction imaging was performed between the pre- and postcontrast FSPGR sequence, and FSPGR reformats were performed in the sagittal and coronal planes.

Imaging studies were interpreted at the time of scanning by 1 of 2 fellowship-trained board-certified neuroradiologists (A.F.C. or M.T.W.) and were reviewed in direct consultation with the attending neurosurgeon (F.A.B. or P.K.).

Historical Comparison

A hospital neuro-oncology data base was queried to evaluate the incidence of tumor-related reoperations at our hospital in the time before institution of the iMRI program.

Table 1: Tumor location

	No.	(%)
Supratentorial (NOS)	64	38
Infratentorial (not brain stem)	43	26
Brain stem	22	13
Midbrain/pineal	13	8
Third ventricular/suprasellar	12	7
Deep gray nuclei	9	5
Cervical spine/skull base	5	3

Note:—NOS indicates not otherwise specified.

Table 2: Tumor histology

Histology	No.	(%)
Pilocytic astrocytoma	31	19
Low-grade glioma	31	19
Medulloblastoma/PNET	20	12
Ependymoma	15	9
High-grade glioma	14	8
Ganglioglioma	10	6
Other	47	28

Note:—PNET indicates primitive neuroectodermal tumor.

Data Collection and Statistics

Data were stored on a spreadsheet (Excel 2011; Microsoft, Redmond, Washington). Data were analyzed by using Excel and SPSS, Version 20 (IBM, Armonk, New York). Discrete variables were compared by using the Fisher exact test. Continuous variables were compared by using the Kruskall-Wallis test, with a nonparametric posttest, or a Student *t* test when data followed a Gaussian distribution. A P value $< .05$ was considered significant.

RESULTS

Patient Demographics

One hundred ninety-four patients underwent iMRI-guided surgery at our institution in the 24 months after installation. Of these, 168 (87%) were 18 years or younger (mean, 8.9 ± 5.0; range, 1.2–18.5 years; median, 8.0 years). There were 60 females and 108 males. Sixty-five (39%) tumors were located in the posterior fossa (Table 1). The most common tumors were pilocytic astrocytoma ($n = 31$, 19%), low-grade glioma ($n = 31$, 19%), and medulloblastoma ($n = 20$, 12%) (Table 2). Prior tumor resection was performed in 60 patients (38%), and 34 (21%) had pre-existing CSF shunts. The prone position was used in 79 patients; supine, in 70; and lateral decubitus, in 19.

MR Imaging Scans

Within the pediatric subset of patients, an average of 1.2 intraoperative scanning sessions per patient was performed (median, 1; maximum, 3 scan sessions). There were no MR imaging–related safety issues. Intraoperative gadolinium was administered in 152 patients (90%). For patients receiving gadolinium for the intraoperative scan, an average of 1.1 doses was administered (median, 1; range, 1–3). The dose for the first 2 administrations was 0.1 mmol/kg of gadopentetate dimeglumine. When required, the third administration was a half-dose (0.05-mmol/kg gadopentetate dimeglumine).

Operating Room Workflow

The mean time in the operating room, from the patient entering the room to exiting the room, was 428 ± 143 minutes (range,

158–958 minutes; median, 415 minutes) (Table 3). The time from operating room entry to initial skin incision was 91 ± 40 minutes (range, 19–237 minutes; median, 78 minutes).

Thirty-four patients underwent a stereotactic MR imaging scan in the operating room before starting the case, with a time from entering the operating room to initial skin incision of 145 ± 36 minutes (median, 145 minutes). Compared with the 134 patients who did not have a stereotactic MR imaging scan in the operating room before starting the procedure, which included 98 patients with previously performed stereotactic scans and 36 performed without stereotactic guidance, the mean time from entering the room to initial skin incision was 69 ± 20 minutes (median, 63 minutes; $P < .0001$).

Table 3: Mean time in the operating room[a]

	Total OR Time	OR Entry to Skin	Skin to Skin
All patients	428 ± 142 (415)	91 ± 40 (78)	316 ± 130 (315)
Group 1	491 ± 173 (469)	145 ± 36 (145)	323 ± 157 (330)
Group 2 (all pts)	450 ± 141 (439)	98 ± 40 (82)	331 ± 129 (329)
Group 2a	482 ± 126 (483)	75 ± 19 (70)	389 ± 114 (387)
Group 2b	415 ± 120 (412)	82 ± 24 (77)	312 ± 113 (302)
P (g1 vs g2)	.08	<.0001	NS (.67)
p (g2a vs g2b)	.03	.21	0.008

Note:—OR indicates operating room; pts, patients; g1, group 1; g2, group 2; g2a, group 2a; g2b, group 2b; NS, not significant.

[a] Time is listed in minutes; numbers in parentheses are the median values. Group 1 indicates those with an intraoperative stereotactic scan; group 2, no intraoperative stereotactic scan; group 2a, no stereotactic navigation used; group 2b, stereotactic scan obtained prior to arrival in the operating room.

Peri- and Postoperative Outcomes

The preoperative surgical goal was individualized, primarily depending on the tumor location: gross total resection ($n = 112$), debulking ($n = 40$), biopsy ($n = 12$), and other ($n = 4$).

Additional tumor was resected in 35 (21%) patients (Fig 1) after scanning. Intraoperatively acquired volumetric images were merged with the stereotactic navigation study in 22 patients to correct for brain shift and guide continuation of resection. Of 112 with a goal of gross total resection, 26 (23%) had further resection of the lesion, and at the end of the procedure, 104 of these patients (93%) had gross total resection, with 6 having near-total resection and 2 having subtotal resection. Of 40 patients with a preoperative goal of debulking, 2 had gross total resection, 20 had near-total resection, 16 had subtotal resection, and 2 had biopsy. Estimated

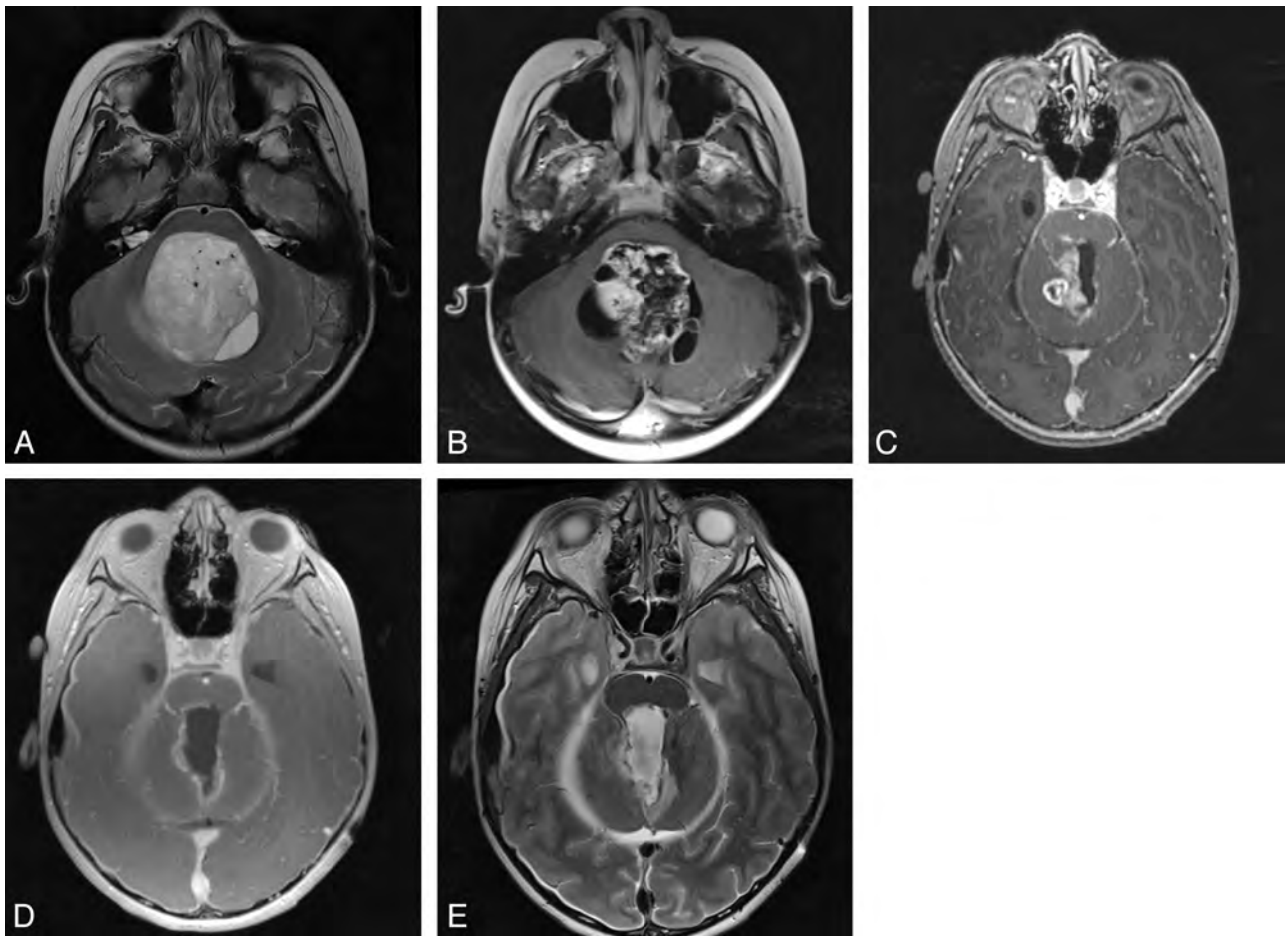

FIG 1. *A*, Axial T2-weighted image shows a mass in the fourth ventricle in a 9-year-old boy. *B*, Axial T1-weighted image after gadolinium administration shows heterogeneous enhancement within the lesion. *C*, Axial T1 postgadolinium image from intraoperative MRI shows residual tumor along the right superolateral aspect of the resection cavity. *D*, Axial T1 postgadolinium image from intraoperative MRI after continuation of resection shows removal of the previously seen residual lesion. A rim of enhancement was seen along the margins of the resection cavity; however, no discrete lesion was identified on surgical inspection of the margins. *E*, Axial T2WI shows a margin of T2 shortening with subjacent edema in the areas of enhancement, a pattern that corresponds to recent use of bipolar electrocautery. On this basis, no further resection was performed.

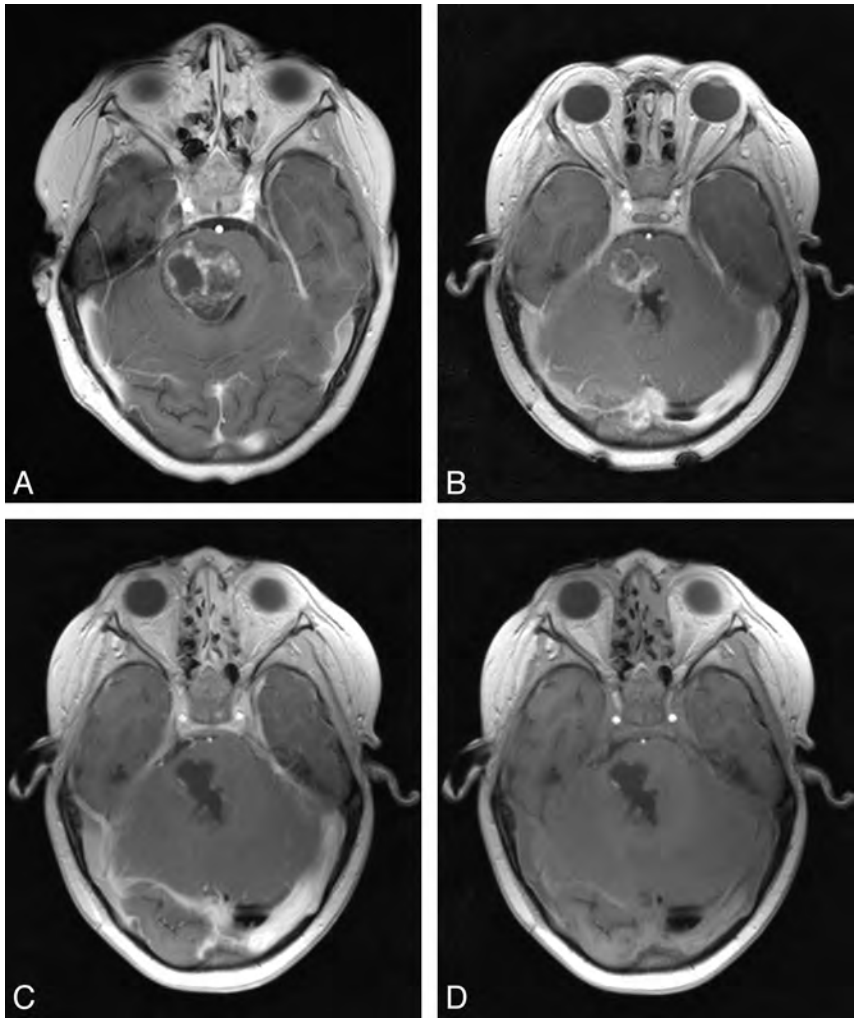

FIG 2. *A*, Axial T1WI postgadolinium image at the level of the midpons in a 3-year-old girl shows a heterogeneously enhancing mass, which causes near-complete effacement of the fourth ventricle. *B*, Axial T1WI postgadolinium iMRI obtained after initial resection of the lesion shows decreased bulk of the lesion and decreased mass effect on the fourth ventricle. Volumetric T1 images were merged to the stereotactic dataset to guide further resection; this step allowed the procedure to go forward, accounting for intraoperative "brain-shift" from ventricular decompression and tumor debulking. *C*, Axial T1WI postgadolinium iMRI image after continuation of resection shows several areas of T1 shortening along the posterior margin of the resection cavity. Review of the resection cavity under an operating microscope showed no macroscopic blood products in this location. *D*, Axial T1WI iMRI after continuation of resection prior to contrast administration shows a similar pattern of T1 shortening; this represents intrinsic T1 shortening (presumably related to electrocautery use). Accordingly, there was no abnormal enhancement on the second postcontrast iMRI scan.

blood loss was 141 ± 137 mL (range, 10–1000 mL; median, 100 mL).

One hundred fifty-one patients went to the intensive care unit after surgery, and 17 did not. The average intensive care unit length of stay was 2.3 ± 3.9 days (range, 0–35 days; median, 1 day). The total hospital length of stay for all patients was 7.6 ± 5.3 days (range, 1–35 days; median, 6 days). Discharge disposition was most commonly to home ($n = 99$). Twenty-nine patients were transferred to a partner institution ($n = 29$) for continued convalescence and others to a hospital-partnered family temporary housing ($n = 23$).

The tumor-related reoperation rate was 0% at 7 days and 1% at 30 days (1 of 168). The one patient who required reoperation was an 11-year-old boy who had a right frontal lesion originally postulated to be a low-grade lesion. After pathologic determination of a high-grade glioma, the decision was made to further extend the margins to ensure the removal of nonenhancing T2/FLAIR signal abnormality that was originally thought to represent edema. The all-cause reoperation rate was 6% at 7 days ($n = 10$) and 7% at 30 days ($n = 11$), with reoperations for shunt placement/revision ($n = 6$), pseudomeningocele ($n = 3$), and intracranial pressure monitor placement ($n = 1$) within the first 7 days and for additional tumor resection ($n = 1$) within the first 30 days.

The 30-day mortality rate after iMRI-guided tumor resection was 0%. At 30 days, 2 patients developed superficial wound infections and a third patient developed a deep infection. There have been no clinical signs of contrast-induced nephrogenic systemic fibrosis in any of the patients.

In the 12 months before instituting the iMRI program, 104 patients underwent tumor resection at our institution (63 males, 41 females). The 30-day tumor-related reoperation rate was 8% (8 of 104 patients) ($P = .002$ versus the iMRI cohort).

DISCUSSION

We have demonstrated that high-field-strength iMRI in children is safe; negates the need for sedation and postoperative MR imaging requiring travel from the safe confines of the intensive care unit; and markedly reduces the need for early reoperation by maximizing tumor resectability. The price of this technology is added operating room time, with an intraoperative scan adding approximately 45–60 minutes to a case, including the time for safety checks, patient preparation, moving the MR imaging scanner, and performing the scan. Performing stereotactic navigation sequences in the operating room before skin incision further prolongs operating room time. The preoperative preparation time, from entering the room to initial skin incision, was approximately 55 minutes longer when an intraoperative stereotactic scan was performed compared with use of a pre-existing scan. However, we have had no anesthesia or MR imaging–related complications, and our wound infection rates are no greater than those in historical controls. Continued follow-up is needed to assess the incidence of tumor recurrence, postoperative neurologic and cognitive deficits, and ultimately survival.

There are unique challenges in evaluating and interpreting intraoperative MR images. Gross changes in lesional signal inten-

sity, diffusion characteristics, and enhancement patterns between the preoperative MR imaging and iMRI are often postoperative in nature rather than a reflection of residual tumor. For example, there are often thin areas of enhancement marginating the operative cavity (Fig 2), even in locations where there was no enhancing tumor on preoperative imaging. In most cases, these areas of enhancement most likely represent hyperemia/engorged vasculature and regional small-vessel permeability, especially if electrocautery (ie, bipolar) was performed. Intrinsic T1 shortening from blood products can be mistaken for enhancement if comparison with precontrast T1 imaging is not performed (Fig 2*D*), and subtraction imaging can help confirm this. Granulation tissue does not develop in the immediate intraoperative setting. Distinction of vascular enhancement from trace residual tumor may be difficult or impossible, particularly if the tumor shows marked preprocedural enhancement or if the enhancement is nodular in character. In equivocal cases, these areas should be explored intraoperatively or subject to higher scrutiny on follow-up examinations.

Multiple iterations of intraoperative scanning in patients with enhancing lesions requires repeat administration of intravenous gadolinium. Accordingly, care must be taken to ensure that there are no secondary signs of acute renal dysfunction, such as decreased urine output, to reduce the risk of nephrogenic systemic fibrosis. Use of half-dose (0.05 mmol/kg) contrast, possibly with high relaxivity and/or macrocyclic gadolinium chelates, may help mitigate this risk.

Little is known about the normal appearance of an active operative cavity after multiple contrast agent doses. The imaging appearance is complicated by the presence of an admixture of contrast material injected at 2 different time points. Theoretically, both false-positive and false-negative findings of residual tumor could be possible in patients who have received >1 contrast agent dose during a short time. Nonetheless, there have been no known instances of false-positive or false-negative tumor residual in our experience thus far.

For various reasons, image distortion may be present in patients undergoing iMRI. First, suboptimal patient positioning with respect to the magnet isocenter can result in spatial-resolution distortions.[18] Paramagnetic susceptibility artifacts from blood products and gas can cause image distortion. These entities have major implications for iMRI. Even subtle differences between apparent and actual lesion location because of image distortion could alter the expected surgical outcome.

Performing an intraoperative MR imaging decreases the need for postoperative imaging and, in the case of CT, radiation exposure. Some patients without visible complications on the iMRI scan may be able to be followed in a step-down bed as opposed to a full intensive care unit bed. No repeat MR imaging scans were performed during the first week after resection in patients who had an iMRI after tumor resection.

Alternative intraoperative imaging modalities have been described, in particular sonography, however predominantly related to adult gliomas.[19-23] Few uses of sonography have been shown in pediatric tumors.[24,25] Sonography is highly operator-dependent, and proper orientation with respect to the resection cavity can be difficult. iMRI allows spatial localization of the resection cavity and possible residual tumor, in a manner that easily compares with preoperative imaging and can serve as a comparison study for postoperative follow-up scans.

In addition to brain tumor resection, iMRI may have other roles in the pediatric population. It can be used to confirm shunt placement, perhaps in a patient with multiloculated hydrocephalus; to confirm biopsy location in a suspected demyelinating disorder or vasculitis; in surgery for vascular lesions; and for confirmation of resection margins in epilepsy surgery.[26-28]

Success of high-field-strength iMRI requires careful attention to safety, and accordingly, patients with some implanted medical devices may not be able to safely undergo iMRI-guided surgery. Several patients at our institution were unable to undergo iMRI-guided surgery because they had implanted devices that were not cleared for 3T scanning.

The large-bore scanner (70 cm) allowed patients to be scanned in various positions; however, upright surgery is not possible with this system. Additionally, the patient cannot fully enter the bore of the magnet, and tumors of the lower cervical spine and thoracic spine could not be imaged with current technology.

Successful implementation of an iMRI program requires collaboration, and accordingly, all cases at our institution are reviewed by the neuroradiologist and neurosurgeon before the operation to identify the goals of the operation and the intended approach. All iMRI scans are interpreted with the neuroradiologist in the operative suite at the time of scanning, providing real-time consultation with the neurosurgeon.

Future work will include outcome analysis looking at long-term disease-free survival and mortality. Additionally, a detailed cost-analysis will be helpful to account for the expenditures on the device itself and the increased operating room time.

CONCLUSIONS

In this series, the early tumor reoperation rate reduced from 8% to <1% after instituting an iMRI program, which may result in reduced tumor recurrence and improved survival. If successful, an iMRI program can create a new paradigm for tumor treatment and establish the role for integrated real-time neuroradiology-neurosurgery collaboration for the resection of pediatric CNS tumors, which will translate into achieving optimal patient outcomes.

REFERENCES

1. Ostrom QT, Gittleman H, Farah P, et al. **CBTRUS Statistical Report: primary brain and central nervous system tumors diagnosed in the United States in 2006–2010.** *Neuro Oncol* 2013;15(suppl 2):ii1–ii56
2. Finlay JL, Wisoff JH. **The impact of extent of resection in the management of malignant gliomas of childhood.** *Childs Nerv Syst* 1999;15:786–88
3. Levy R, Cox RG, Hader WJ, et al. **Application of intraoperative high-field magnetic resonance imaging in pediatric neurosurgery.** *J Neurosurg Pediatr* 2009;4:467–74
4. Nimsky C, Ganslandt O, Von Keller B, et al. **Intraoperative high-field-strength MR imaging: implementation and experience in 200 patients.** *Radiology* 2004;233:67–78
5. Claus EB, Horlacher A, Hsu L, et al. **Survival rates in patients with low-grade glioma after intraoperative magnetic resonance image guidance.** *Cancer* 2005;103:1227–33
6. Knauth M, Wirtz CR, Tronnier VM, et al. **Intraoperative MR imag-**

ing increases the extent of tumor resection in patients with high-grade gliomas. *AJNR Am J Neuroradiol* 1999;20:1642–46
7. Hall WA, Martin AJ, Liu H, et al. **High-field strength interventional magnetic resonance imaging for pediatric neurosurgery.** *Pediatr Neurosurg* 1998;29:253–59
8. Hall WA, Liu H, Martin AJ, et al. **Safety, efficacy, and functionality of high-field strength interventional magnetic resonance imaging for neurosurgery.** *Neurosurgery* 2000;46:632–41, discussion 641–42
9. Alexander E 3rd, Moriarty TM, Kikinis R, et al. **The present and future role of intraoperative MRI in neurosurgical procedures.** *Stereotact Funct Neurosurg* 1997;68(1–4 pt 1):10–17
10. Moriarty TM, Kikinis R, Jolesz FA, et al. **Magnetic resonance imaging therapy; intraoperative MR imaging.** *Neurosurg Clin N Am* 1996;7:323–31
11. Black PM, Alexander E, Martin C, et al. **Craniotomy for tumor treatment in an intraoperative magnetic resonance imaging unit.** *Neurosurgery* 1999;45:423–31, discussion 431–33
12. Roth J, Beni Adani L, Biyani N, et al. **Intraoperative portable 0.12-Tesla MRI in pediatric neurosurgery.** *Pediatr Neurosurg* 2006;42:74–80
13. Black PM, Moriarty T, Alexander E, et al. **Development and implementation of intraoperative magnetic resonance imaging and its neurosurgical applications.** *Neurosurgery* 1997;41:831–42, discussion 842–45
14. Samdani AF, Schulder M, Catrambone JE, et al. **Use of a compact intraoperative low-field magnetic imager in pediatric neurosurgery.** *Childs Nerv Syst* 2005;21:108–13, discussion 114
15. Souweidane MM. **Intraoperative magnetic resonance imaging.** *J Neurosurg Pediatr* 2009;4:465–66, discussion 466
16. Abernethy LJ, Avula S, Hughes GM, et al. **Intra-operative 3-T MRI for paediatric brain tumours: challenges and perspectives.** *Pediatr Radiol* 2012;42:147–57
17. Avula S, Mallucci CL, Pizer B, et al. **Intraoperative 3-Tesla MRI in the management of paediatric cranial tumours: initial experience.** *Pediatr Radiol* 2012;42:158–67
18. Choudhri AF, Chin EM, Klimo P, et al. **Spatial distortion due to field inhomogeneity in 3.0 Tesla intraoperative MRI.** *Neuroradiol J* 2014;27:387–92
19. Hammoud MA, Ligon BL, elSouki R, et al. **Use of intraoperative ultrasound for localizing tumors and determining the extent of resection: a comparative study with magnetic resonance imaging.** *J Neurosurg* 1996;84:737–41
20. Regelsberger J, Lohmann F, Helmke K, et al. **Ultrasound-guided surgery of deep seated brain lesions.** *Eur J Ultrasound* 2000;12:115–21
21. Chen SY, Chiou TL, Chiu WT, et al. **Application of intraoperative ultrasound for brain surgery.** *Tzu Chi Med J* 2004;16:85–92
22. Cui LG, Jiang L, Zhang HB, et al. **Monitoring of cerebrospinal fluid flow by intraoperative ultrasound in patients with Chiari I malformation.** *Clin Neurol Neurosurg* 2011;113:173–76
23. Comeau RM, Fenster A, Peters TM. **Intraoperative ultrasound in interactive neurosurgery.** *Radiographics* 1998;18:1019–27
24. El Beltagy MA, Aggag M, Kamal M. **Role of intraoperative ultrasound in resection of pediatric brain tumors.** *Childs Nerv Syst* 2010; 26:1189–93
25. Ulrich NH, Burkhardt JK, Serra C, et al. **Resection of pediatric intracerebral tumors with the aid of intraoperative real-time 3-D ultrasound.** *Childs Nerv Syst* 2012;28:101–19
26. Roessler K, Sommer B, Grummich P, et al. **Improved resection in lesional temporal lobe epilepsy surgery using neuronavigation and intraoperative MR imaging: favourable long term surgical and seizure outcome in 88 consecutive cases.** *Seizure* 2014;23:201–07
27. Sommer B, Kasper BS, Coras R, et al. **Surgical management of epilepsy due to cerebral cavernomas using neuronavigation and intraoperative MR imaging.** *Neurol Res* 2013;35:1076–83
28. Sun GC, Chen XL, Zhao Y, et al. **Intraoperative MRI with integrated functional neuronavigation-guided resection of supratentorial cavernous malformations in eloquent brain areas.** *J Clin Neurosci* 2011;18:1350–54

MRI–Based Radiologic Scoring System for Extent of Brain Injury in Children with Hemiplegia

S.I. Shiran, M. Weinstein, C. Sirota-Cohen, V. Myers, D. Ben Bashat, A. Fattal-Valevski, D. Green, and M. Schertz

ABSTRACT

BACKGROUND AND PURPOSE: Brain MR imaging is recommended in children with cerebral palsy. Descriptions of MR imaging findings lack uniformity, due to the absence of a validated quantitative approach. We developed a quantitative scoring method for brain injury based on anatomic MR imaging and examined the reliability and validity in correlation to motor function in children with hemiplegia.

MATERIALS AND METHODS: Twenty-seven children with hemiplegia underwent MR imaging (T1, T2-weighted sequences, DTI) and motor assessment (Manual Ability Classification System, Gross Motor Functional Classification System, Assisting Hand Assessment, Jebsen Taylor Test of Hand Function, and Children's Hand Experience Questionnaire). A scoring system devised in our center was applied to all scans. Radiologic score covered 4 domains: number of affected lobes, volume and type of white matter injury, extent of gray matter damage, and major white matter tract injury. Inter- and intrarater reliability was evaluated and the relationship between radiologic score and motor assessments determined.

RESULTS: Mean total radiologic score was 11.3 ± 4.5 (range 4–18). Good inter- ($\rho = 0.909$, $P < .001$) and intrarater ($\rho = 0.926$, $P = < .001$) reliability was demonstrated. Radiologic score correlated significantly with manual ability classification systems ($\rho = 0.708$, $P < .001$), and with motor assessments (assisting hand assessment [$\rho = -0.753$, $P < .001$]; Jebsen Taylor test of hand function [$\rho = 0.766$, $P < .001$]; children's hand experience questionnaire [$\rho = -0.716$, $P < .001$]), as well as with DTI parameters.

CONCLUSIONS: We present a novel MR imaging–based scoring system that demonstrated high inter- and intrarater reliability and significant associations with manual ability classification systems and motor evaluations. This score provides a standardized radiologic assessment of brain injury extent in hemiplegic patients with predominantly unilateral injury, allowing comparison between groups, and providing an additional tool for counseling families.

ABBREVIATIONS: CP = cerebral palsy; GMFCS = Gross Motor Functional Classification System; MACS = Manual Ability Classification System; AHA = Assisting Hand Assessment; JTTHF = Jebsen Taylor Test of Hand Function; CHEQ = Children's Hand Experience Questionnaire

The role of neuroimaging in assessing patterns of injury in patients with cerebral palsy (CP) is well established. MR imaging of the brain for evaluation of children with CP is a practice recommended by the American Academy of Neurology since 2004.[1] Major reviews of the literature support this practice guideline.[2-4] Korzeniewski et al[2] concluded that neuroradiologic imaging modalities are making significant contributions to our understanding of CP. However, there are significant inconsistencies in descriptions of radiologic findings. In their systematic review of the literature, 42 studies relating to neuroimaging evaluation of patients with CP were assessed and were found to use more than 100 different terms to describe brain injury in these patients, making comparison between studies very difficult. In their review, Krägeloh-Mann and Horber[3] highlighted the potential of MR imaging to elucidate etiology and pathogenesis in CP but found a lack of consensus on classification of MR imaging results. In their opinion, a standardized classification of MR imaging results would be helpful for data collection in CP registries. This was acknowledged by the Surveillance of Cerebral Palsy in Europe network, which developed a recommended standardized method for reporting brain MR

Received November 27, 2013; accepted after revision January 30, 2014.

From the Pediatric Radiology Unit (S.I.S.), Department of Radiology (C.S.-C.), and Functional Brain Center, The Wohl Institute for Advanced Imaging (M.W., V.M., D.B.B.), Tel Aviv Sourasky Medical Center, Tel Aviv, Israel; Department of Psychology (M.W.), Gonda Multidisciplinary Brain Research Centre, Bar Ilan University, Ramat Gan, Israel; Sackler Faculty of Medicine (D.B.B., A.F.-V.), Tel Aviv University, Tel Aviv, Israel; Sagol School of Neuroscience (D.B.B.), Tel Aviv University, Tel Aviv, Israel; Department of Child Neurology (A.F.-V., M.S.), Dana-Dwek Hospital, Tel Aviv Sourasky Medical Center, Tel Aviv, Israel; Center for Rehabilitation (D.G.), Oxford Brookes University, Oxford, UK; and Pediatric Neurology and Child Development Service-Meuhedet North (M.S.), Haifa, Israel.

Please address correspondence to Shelly I. Shiran, MD, Pediatric Radiology, Tel Aviv Sourasky Medical Center, 6 Weizman St, 64239 Tel Aviv, Israel, e-mail: shellyshiran@gmail.com

Indicates article with supplemental on-line appendix and table.

http://dx.doi.org/10.3174/ajnr.A3950

imaging results.[5,6] Arnfield et al[4] investigated the relationship between the brain structure on MR imaging and motor outcomes in children with CP by reviewing the related literature. They found a relationship between the type of brain lesion as seen on MR imaging and 2 clinical outcomes: Gross Motor Functional Classification System (GMFCS)[7,8] and type of CP. The difficulties they encountered in comparing MR imaging results between different studies led them to emphasize the importance of developing a validated quantitative approach to classification of brain injury on MR imaging.

In our medical center, we developed a quantitative scoring method for brain injury based on anatomic MR imaging of the brain. The purpose of this study was to examine the reliability and validity of the scoring system in correlation to motor function status in a cohort of children with hemiplegia.

MATERIALS AND METHODS

Participants

The study group comprised 27 children with clinical signs of hemiplegia, recruited from the Regional Pediatric Neurology Unit at the Tel Aviv Sourasky Medical Center and Guy's and St Thomas' NHS Foundation Trust and affiliated Child Development Centres, as part of a study examining motor intervention in children with hemiplegia.[9] Inclusion criteria were clinical signs of spastic hemiplegia as assessed by a neurologist, attendance at a mainstream educational institution, and independence of mobility. Exclusion criteria were intractable seizures, prior surgical intervention, and any contraindications to MR imaging.

This study was approved by the Institutional Review Board and National Research Ethics Committee of the respective hospitals, and fully informed consent was obtained from parents and/or children over 18 years of age.

Motor Function Assessment

Motor classification included rating according to the Manual Ability Classification System (MACS) and the GMFCS. The MACS classifies ability to handle objects in important daily activities across a 5-point scale; children at level I handle most objects easily and at level V are severely limited in their ability.[10] The GMFCS is a measure of spontaneous functional mobility.[7] Participants were also assessed with the Assisting Hand Assessment (AHA; version 4.3),[11] the Jebsen Taylor Test of Hand Function (JTTHF),[12] and the Children's Hand Experience Questionnaire (CHEQ).[13] AHA tests spontaneous use and performance of the affected hand in functional/play-based tasks; higher scores represent better bimanual skills. JTTHF is a timed test of manual dexterity where higher scores represent poorer unimanual skills. CHEQ is a 29-item questionnaire of affected hand use in daily bimanual activities; higher scores represent better hand use.

MR Imaging

All participants underwent MR imaging and motor assessment on the same day, with training in a mock scanner before the actual scan. MR imaging scans were performed on 1 of 2 3T scanners (Signa Excite, Milwaukee, Wisconsin), the first at Tel Aviv Sourasky Medical Center, Israel (19 participants), and the second at the Institute of Psychiatry, London, United Kingdom (8 participants). The scanning protocol, which was matched between sites, included:

- 2D sagittal T1-weighted conventional spin-echo. TR = 400 ms, TE = 10 ms; 21 × 5 mm sections with a 1.5 mm gap; matrix size 256 × 160 over a 240 mm FOV.
- 2D axial T2-weighted fast spin echo. TR = 4000 ms, TE = 137 ms; 36 × 4 mm sections with no section gap; matrix size 384 × 224 over a 240 mm FOV.
- 2D axial FLAIR. TR = 9000 ms, TE = 144 ms, TI = 2100 ms; 32 × 4 mm sections with no section gap; matrix size 256 × 192 over a 240-mm FOV.
- Gradient-echo $T2^*$. FOV/matrix = 240 mm^2/512 × 512; TR/TE = 320/20 ms.
- Axial 3D high-resolution anatomic T1-weighted fast spoiled gradient-echo imaging. (FOV)/matrix = 240–256 mm^2/256 × 256; TR/TE = 8.6/3.3 ms.
- DTI acquired along 19 diffusion gradient directions (b = 1000 s/mm^2) and 1 with no applied diffusion gradient, (FOV/matrix = 220 mm^2/acquired matrix of 128 × 128; reconstructed to 256 × 256; TR/TE = 11,000/91 ms).

Radiologic Scoring

A scoring system was devised, adding points for positive findings, as shown in the On-line Appendix. The score covered 7 aspects across 4 domains: 1) number of affected lobes, 2) volume and type of white matter injury, 3) extent of gray matter damage, and 4) major white matter tract injury. Scoring was dichotomous, with 1 point for pathology and 0 for normal structure, with the exception of white matter volume loss, which was graded as explained below. Total radiologic score was obtained by summing all points. Thus, a child with a completely normal scan would get a score of 0. Brain injury with unilateral hemispheric involvement may reach a maximum score of 18. In the presence of bilateral brain injury, each hemisphere was scored separately and summed to give the total score. The following aspects of brain injury were assessed:

1. Number of affected lobes: for each lobe affected, 1 point was scored, up to a maximum of 4 points if all 4 lobes in the injured hemisphere were affected.

2. White matter injury:
   a. Volume loss of white matter in the affected regions was assessed in comparison with the unaffected side, by averaging a few measurements of white matter width at the region of abnormality and comparing them with the unaffected hemisphere. Extent of white matter volume loss was described as none (0 points), mild (1 point) if less than 40% decrease in volume, moderate (2 points) if approximately 40%–60% decrease in volume, and severe (3 points) for greater than 60% decrease in volume (Fig 1).
   b. Presence of T2 signal changes reflecting gliosis, regardless of extent, was scored 1 point and absence of gliosis 0 points. (Fig 2*A*, -*B*).
   c. Presence of parenchymal cystic changes (not including ex-vacuo dilation of the ventricle) was scored 1 point and absence of cystic changes 0 points. (Fig 2*C*).

3. Gray matter injury:
   a. Cortical gray matter abnormality was scored 1 point, regardless of extent. Cortical gray matter abnormality was reflected by thinning and/or signal abnormality in case of injury (Fig

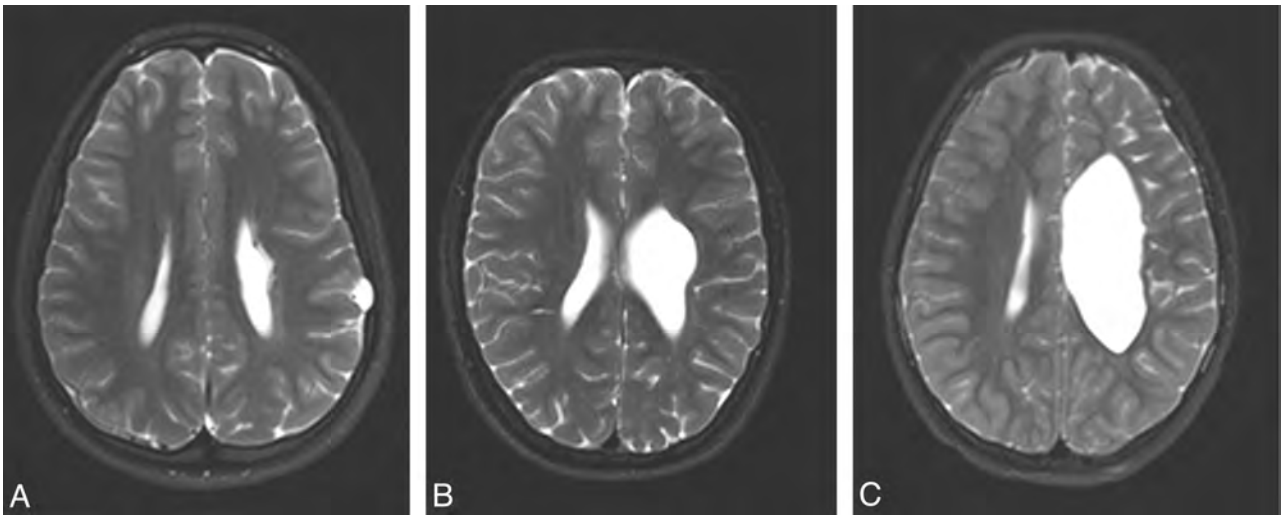

FIG 1. Axial T2-weighted images at the level of the lateral ventricles from 3 different patients demonstrating different levels of white matter loss: *A* indicates mild; *B*, moderate; and *C*, severe.

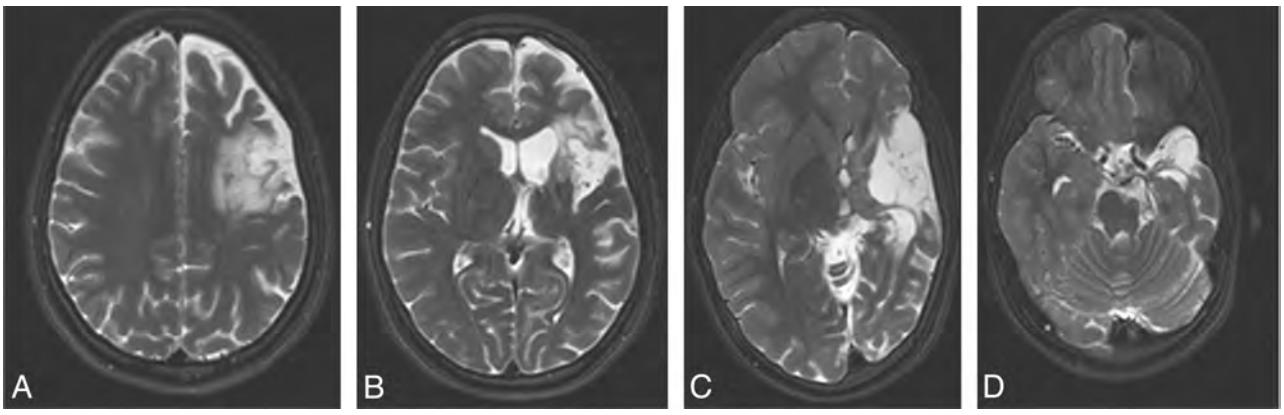

FIG 2. *A* and *B*, Axial T2-weighted images demonstrate high T2 signal in the frontal subcortical white matter consistent with white matter gliosis. There is thinning and high T2 signal in the frontal cortex consistent with cortical gray matter injury. *C*, Axial T2-weighted image at the level of the basal ganglia of a different patient demonstrates cystic changes involving both cortical and deep gray matter, with extensive involvement of the basal ganglia, thalamus, and adjacent major white matter tracts. *D*, Axial T2-weighted image at the level of midbrain-pons junction demonstrating significant asymmetry of cerebral peduncles, reflecting left sided Wallerian degeneration.

2*A*–*C*), and by thickening and abnormal structure in case of congenital malformation.

b. Deep gray matter injury was evaluated for extent of basal ganglia and thalami involvement by assigning 1 point for each to a maximal score of 4 points if caudate, putamen, globus palidus, and thalamus were affected (Fig 2*C*).

4. Major white matter tract injury was scored by assigning 1 point for presence of signal changes in each of the following: the internal capsule anterior limb, internal capsule posterior limb, and external capsule (Fig 2*C*). In addition, presence of cerebral peduncles asymmetry at the level of the midbrain was also scored 1 point (Fig 2*D*).

Application of the radiologic scoring method in 2 different children is presented in Figs 3 and 4.

Scoring was performed by a pediatric radiologist with 6 years' experience in pediatric neuroradiology. The scoring was performed a second time, with a period of at least 6 months between assessments, to evaluate intraobserver variability. An additional assessment was performed in all cases by a second radiologist at the beginning of her neuroradiology training to evaluate interobserver variability.

DTI Analysis

DTIStudio software (Johns Hopkins University, Baltimore, Maryland) was used for DTI analyses as per our published protocol.[14] In brief, tractography analysis was performed to reconstruct the corpus callosum by using a streamline fiber-tracking method with the fiber assignment by continuous tracking algorithm.[15] The Witelson parcellation scheme[16] was used to segment the corpus callosum into 3 segments: genu, midbody, and splenium. Region of interest analysis was performed for the left and right posterior limbs of the internal capsule by using ROIEditor software (Johns Hopkins University, Baltimore, Maryland). Mean values of axial diffusivity, radial diffusivity, mean diffusivity, and fractional anisotropy were calculated for each fiber/region of interest.

Statistical Analysis

Spearman correlations were used to assess inter- and intrarater reliability of total radiologic score (continuous item), whereas

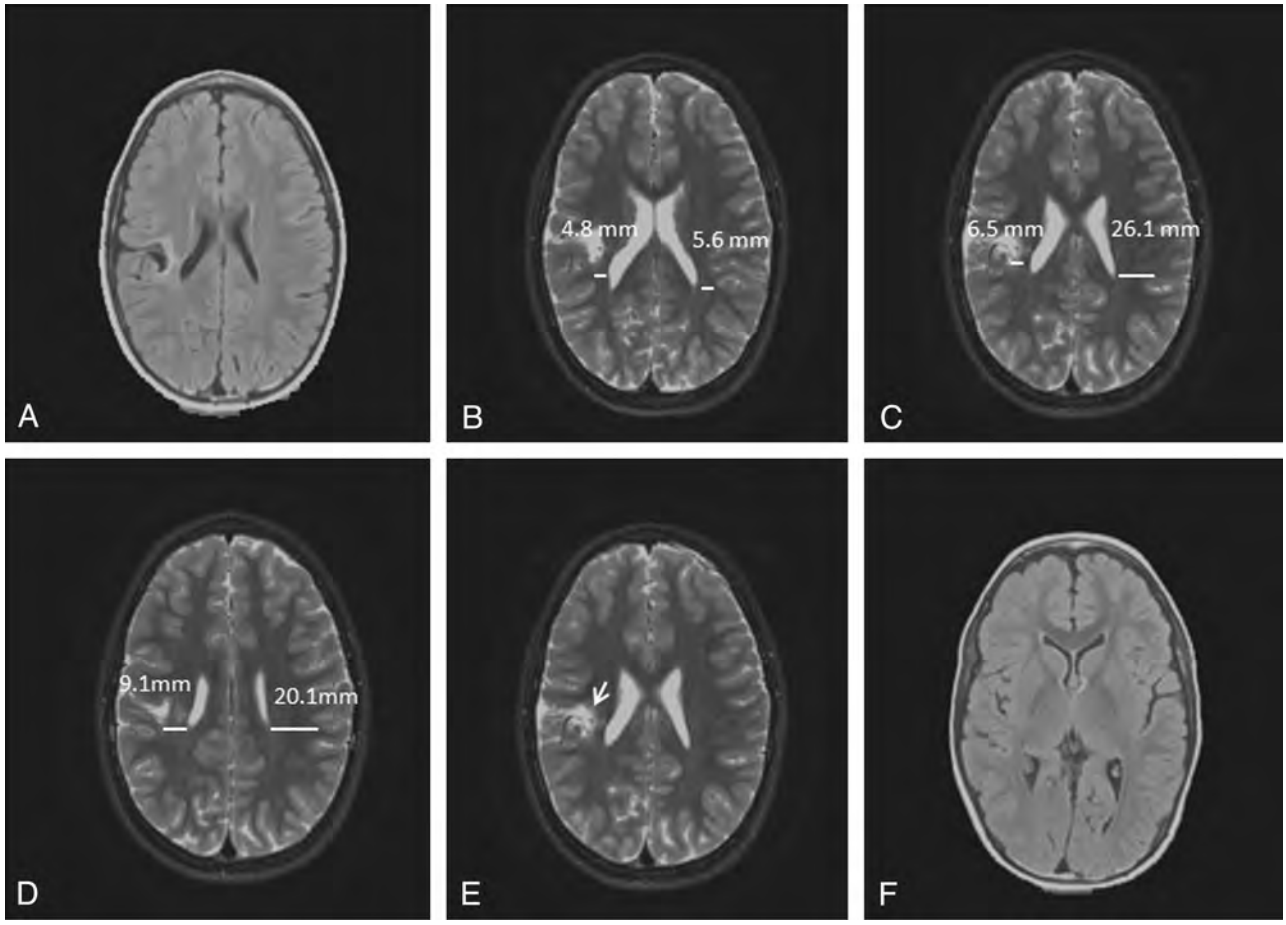

FIG 3. A series of axial T2-weighted images from a 7-year-old boy with left hemiplegia and MACS score of 1, with prematurity-related brain injury (periventricular leukomalacia + focal infarct). *A*, Right-sided perirolandic encephalomalacia involving frontal and parietal lobes (2 points); white matter changes include gliosis (1 point), no cystic changes. *B–D*, Assessment of white matter volume loss: the width of white matter was measured in the affected area and compared with the contralateral side, calculating percentage of volume loss. At least 3 measurements were performed and averaged; in this case, the average was in the range of moderate volume loss (40%–60%) (2 points). *E*, Presence of cortical gray matter changes (1 point). *F*, No involvement of deep gray matter and major white matter tracts. The total score was 6.

Cohen κ was used to evaluate inter- and intrarater reliability of each individual item (dichotomous or ranked items), accounting for the effects of chance agreement.[17] A score of at least 0.6 is taken as substantial agreement, whereas 0.8 and greater represents a very high level of agreement.[18]

ANOVA test and Scheffe post hoc tests were used to examine differences in radiologic score according to MACS and GMFCS classification. Spearman correlation was used to further assess this relationship. Spearman correlations were applied and scatterplots plotted to determine the relationship between radiologic score and motor assessments including the AHA, JTTHF, and CHEQ scores. Means and standard deviations were calculated for each fiber tract/region of interest. Pearson correlations were calculated between fractional anisotropy and diffusivity parameters of each fiber tract/region of interest and the total radiologic scores. Data were analyzed using SPSS version 17.0 (IBM, Armonk, New York).

RESULTS

The study group comprised 27 children (15 male, 12 female), mean age 10.9 ± 3.2 years (range 7.0–18.7 years). Seven children (26%) were born prematurely (mean gestational age = 29 ± 3 weeks). Of the remaining term born children, 13 had perinatal brain injury, 3 presented with congenital malformation, 1 child had traumatic brain injury at 3 months of age, and 3 children had stroke at a later age, at 18 months, 2.5 years, and 7.5 years of age. Most subjects had right hemiplegia (70%; $n = 19$). GMFCS score ranged from 1 (40%) to 2 (60%) whereas MACS score ranged from 1 to 3, with a mean score of 2.0 ± 0.7. Mean total radiologic score (mean of 3 ratings from 2 radiologists) was 11.3 ± 4.5, with a range of 4–18 (On-line Table).

Correlation analyses showed good inter- ($\rho = 0.909$, $P < .001$) and intrarater ($\rho = 0.926$, $P < .001$) reliability for total radiologic score. When analyzed item-by-item, substantial agreement was found, with mean κ score 0.687 for intrarater, and 0.676 for interrater variability (Table 1).

A strong positive correlation was evident between radiologic score and MACS severity ($\rho = 0.708$, $P = < .0001$). On further analysis, a 1-way ANOVA showed that mean radiologic score differed significantly between the 3 MACS classifications, with lower MACS score (representing less impairment) corresponding to lower radiologic score [$F(2,24) = 11.571$, $P = .003$] (representing less brain injury based on imaging). Post hoc tests showed a significant difference between MACS 1 and 3 according to radiologic score, differentiating the 2 groups (Fig 5). No significant correla-

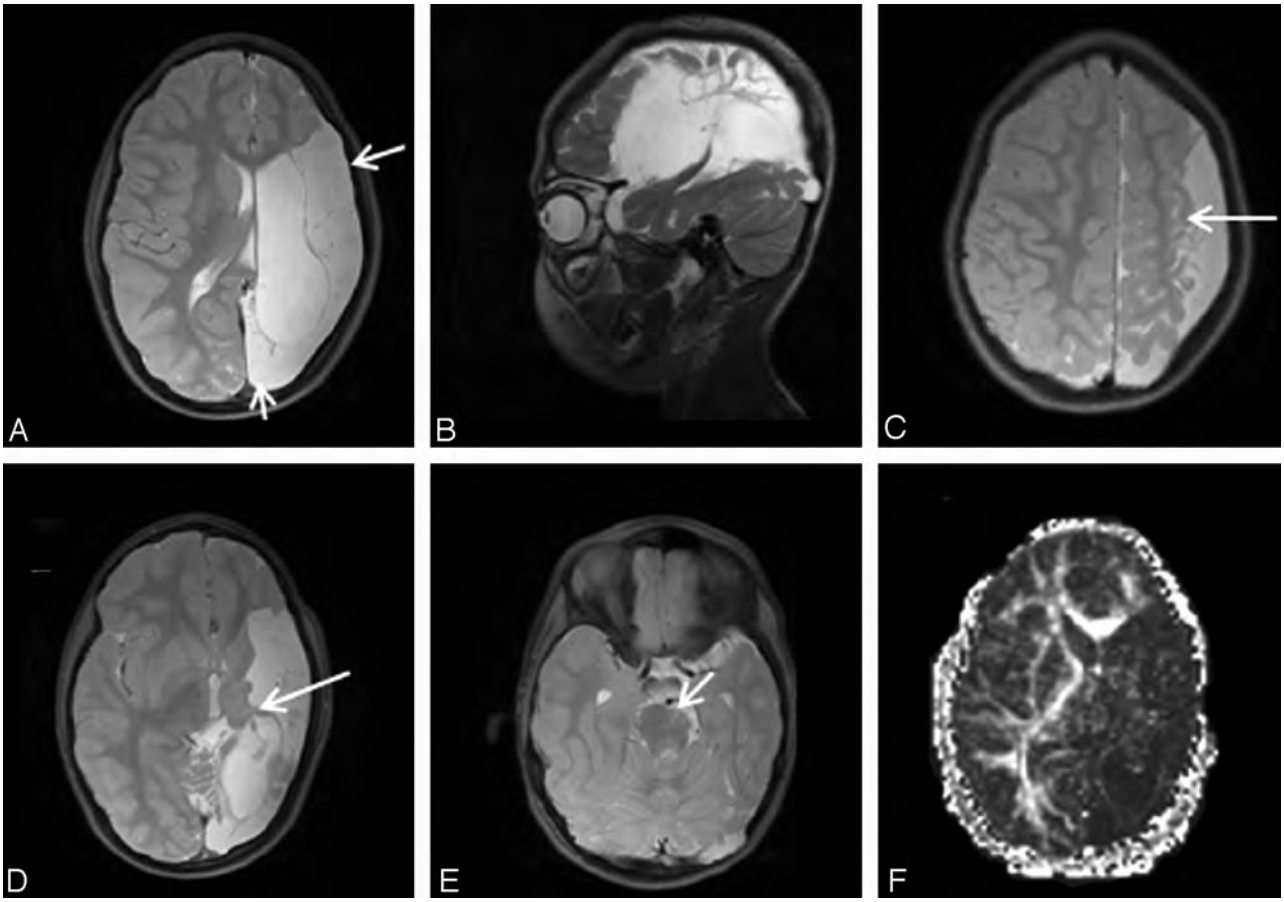

FIG 4. Images from an 8-year-old boy with right hemiplegia and MACS score of 3, with a background of left MCA infarct, born at term. *A*, Axial T2-weighted image, and *B*, sagital T2-weighted image, both demonstrate involvement of all 4 lobes (4 points). Extensive cystic and gliotic changes are present (2 points). In this case there is obvious severe white matter volume loss, which makes actual measurement redundant (3 points). There is extensive loss of cortical gray matter with thinning and gliosis in adjacent gray matter (1 point) as shown in *C*. *D*, Extensive involvement of deep gray matter structures (4 points), as well as major white matter tracts including external capsule and anterior and posterior limbs of the internal capsule (3 points). *E*, Asymmetry of the pyramids (1 point). When DTI is available, the anisotropy map can help in delineating the white matter tract involvement as seen in *F*. The total score was 18.

Table 1: Intra- and interrater reliability

	Intrarater		Interrater	
Item	κ	Significance	κ	Significance
Frontal involvement	0.649	.001	0.65	<.001
Parietal involvement	−0.102	.595	0.780	<.001
Temporal involvement	0.772	<.001	0.778	<.001
Occipital involvement	0.742	<.001	0.767	<.001
Gliosis	0.835	<.001	0.514	.006
Cystic changes	0.629	.001	0.695	<.001
WM volume loss	0.435	.002	0.469	.001
GM involvement	0.761	<.001	0.767	<.001
Caudate	0.611	.002	.773	<.001
Putamen	0.752	<.001	0.922	<.001
Globus pallidus	0.830	<.001	0.743	<.001
Thalamus	0.806	<.001	0.539	.005
External capsule	0.843	<.001	0.485	.010
Anterior limb	0.819	<.001	0.599	.001
Posterior limb	0.660	.001	0.615	.001
Pyramids	0.906	<.001	0.727	<.001
Mean	0.684		0.676	

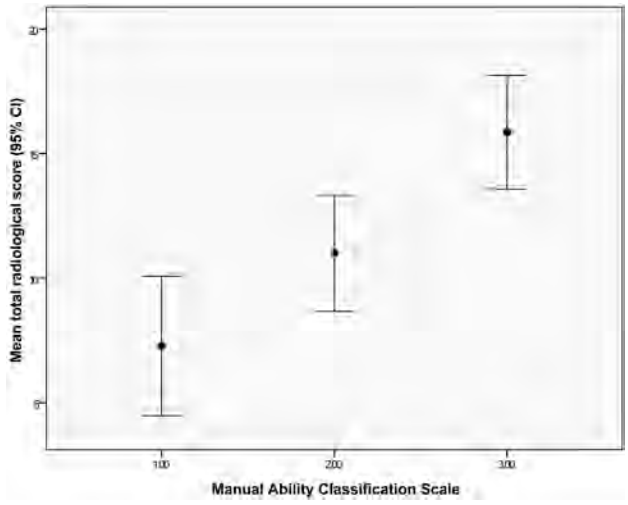

FIG 5. Mean and 95% confidence intervals of radiologic scores according to MACS classification.

tion was detected between radiologic score and GMFCS ($\rho = 0.281$; $P = .156$).

Strong, significant correlations were further detected between radiologic score and motor assessments, including the AHA ($\rho = -0.753$, $P < .001$), JTTHF ($\rho = 0.766$, $P < .001$), and CHEQ ($\rho = -0.716$, $P < .001$) (Fig 6). As radiologic score increased (repre-

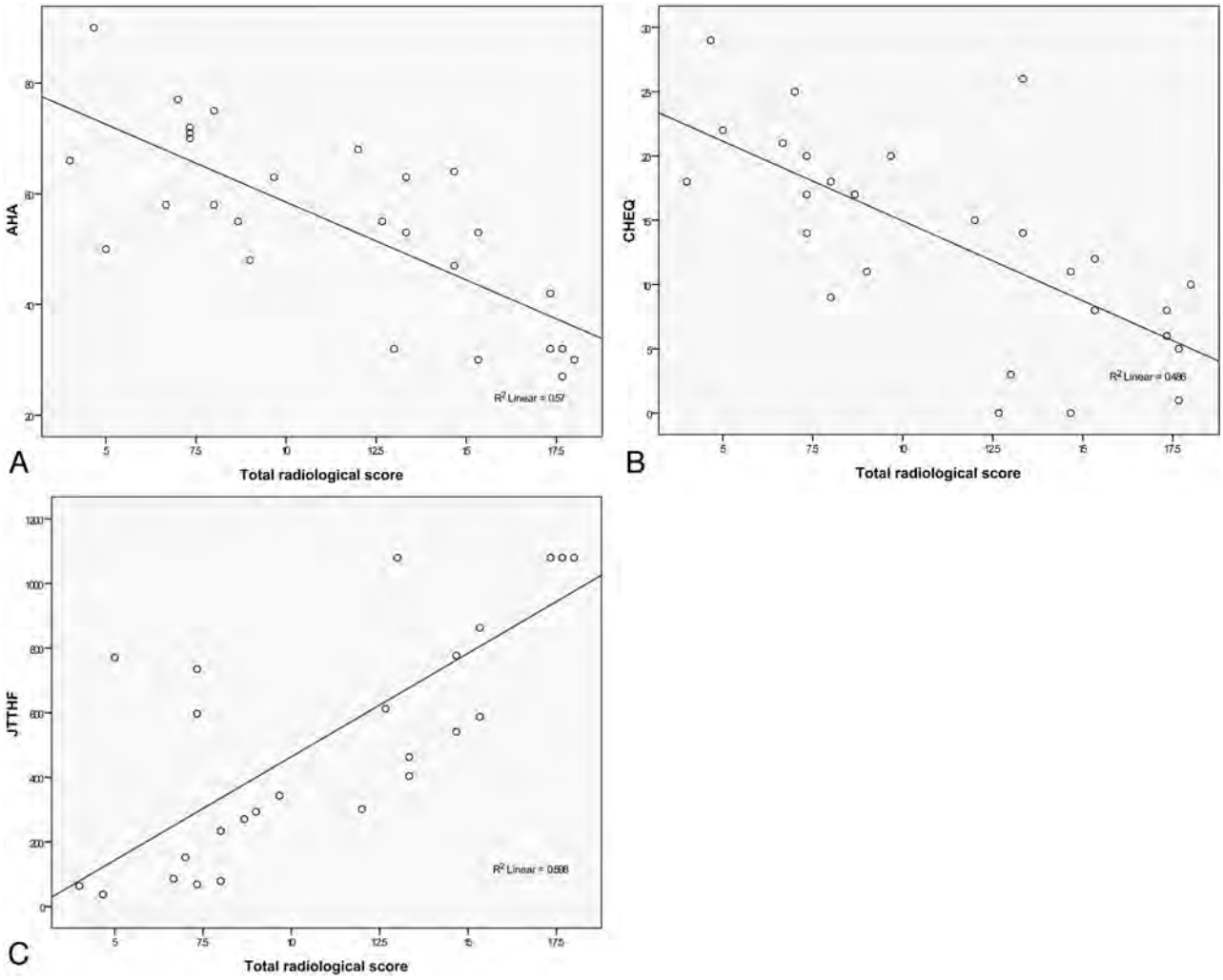

FIG 6. Scatterplots showing correlation between radiologic score and motor assessments on the AHA, JTTHF, and CHEQ scores.

senting increased brain injury), motor performance decreased, indicated by lower AHA and CHEQ scores and longer JTTHF reaction times.

Total Radiologic Score and White Matter Integrity

Two children did not undergo the DTI scan (subjects 15 and 24) and 1 child (subject 21) was excluded due to movement artifacts. In 2 children (subjects 1 and 7), all segments of the corpus callosum and the affected posterior limbs of the internal capsule could not be reconstructed due to the large size of the lesion. In 1 child (subject 12), the midbody of the corpus callosum, and in another (subject 9), the affected posterior limbs of the internal capsule could not be reconstructed due to the lesion. These children were excluded, leaving 20 children whose DTI data could be analyzed.

Significant correlations were found between the white matter integrity of the corpus callosum and the total radiologic score, in the genu, midbody, and splenium. Higher diffusivity values, reflecting reduced white matter integrity, were associated with higher radiologic score (Table 2).

Significant correlations were also found between the white matter integrity of the affected posterior limbs of the internal capsule and the total radiologic score. The lower the fractional anisotropy in the affected posterior limbs of the internal capsule (indicating reduced white matter integrity), the higher the total radiologic score ($r = -0.668$, $P < .001$) (Fig 7). There were no significant correlations between the total radiologic score and the white matter integrity of the less affected posterior limbs of the internal capsule.

Table 2: Correlations between DTI values in the corpus callosum and total radiologic score

	Diffusivity Parameter	Correlation with Total Radiologic Score (r)	*P* Value
Genu	MD	0.59	.004
	Da	0.45	.036
Midbody	MD	0.55	.011
	Da	0.48	.029
Splenium	MD	0.67	.001
	Da	0.58	.004

Note:—MD indicates mean diffusivity; Da, axial diffusivity.

DISCUSSION

We present a novel scoring system, based on diagnostic MR imaging study of the brain, developed to describe the extent of brain injury in a quantitative fashion. Our results show high inter- and intrarater reliability and significant correlation with motor classification and function on motor assessments of hand function of children with hemiplegia.

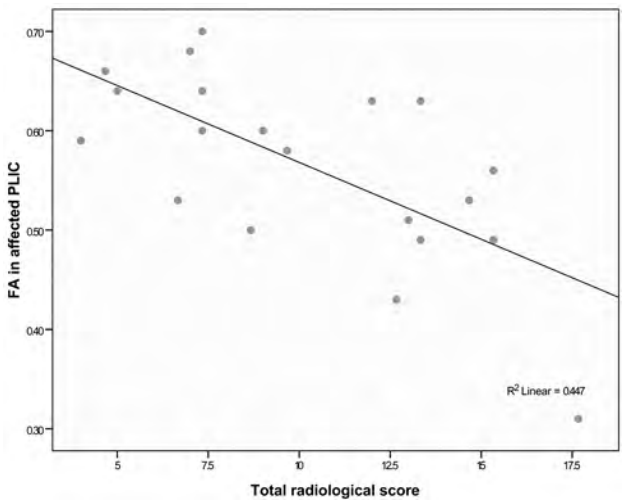

FIG 7. Scatterplot showing correlation between radiologic score and fractional anisotropy in the affected posterior limbs of the internal capsule.

In recent years, studies have suggested that the combination of type, location, and extent of brain lesion in patients with CP is a stronger predictor of hand function than lesion type alone.[19,20] These studies highlight the importance of a standardized approach for assessing extent of brain damage. In this study, we report on a point value MR imaging–based scoring method to estimate extent of brain injury in children with hemiplegia and to determine its correlation to clinical status, independent of the underlying etiology.

Feys et al[21] reported a systematic approach to describing brain injury in addition to pattern recognition; they used a checklist of anatomic structures involved in brain injury, assigning 1 point for pathology and 0 for normal structure. These data were used to investigate the association between each affected neuroanatomic structure to upper limb function. Their study highlighted the importance of lesion location to upper limb function; however, they did not assign a score profile per child, thus preventing comparison between patients.

A methodical scoring system for pediatric brain injury was reported by Woodward et al,[22] who proposed a standardized scoring system of neonatal brain injury. The authors found significant associations between the qualitative measures of cerebral white matter and gray matter abnormalities on MR imaging at term-equivalent age and the subsequent risks of adverse neurodevelopmental outcomes at 2 years of age among very preterm infants. Additional studies reported qualitative and quantitative methods for assessing the extent of injury to the premature brain at term equivalent age.[23–25] Using these scoring systems in our population was not possible as they rely on the unique imaging features of the immature neonatal brain which do not apply to MR imaging studies performed on older children with mature brains.

In our scoring method, we aimed to simplify the brain MR imaging evaluation and minimize interrater variability by using dichotomous items; each brain injury characteristic was scored 1 for a positive finding and 0 if no pathology was noted. Only white matter volume loss was graded for extent with point values ranging from 0, if no volume loss was noted, to 3 for most severe volume loss, adding an element of qualitative evaluation. This method appears reliable and reproducible as reflected by very good intra- and interobserver correlation. The fact that the second rater had recently finished her residency and was at the beginning of her neuroradiology fellowship suggests that this method is simple and does not require extensive experience to use.

Furthermore, the system we developed is consistent with the classification of MR imaging recommended by the Surveillance of Cerebral Palsy in Europe network,[6] but goes further in quantifying the extent of brain damage to enable comparison between children and across studies.

Correlation between DTI measurements and clinical status was previously reported by our group,[14] though this is a larger cohort with additional children that were not included in the previous study. The strong correlation we found between total radiologic score and DTI measurements further supports the reliability of this method, as it seems the scoring based on anatomic imaging reflects well the microstructural changes that are measured in the DTI evaluation.

Several studies demonstrated significant correlation between deep gray matter involvement and worse upper limb motor function.[19,21,26] Holmefur et al[19] reported worse hand function to be associated with combined involvement of both basal ganglia and thalamus, independent of the basic type of brain lesion. Based on diffusion MR imaging studies, Holmström et al[27] suggested significant changes in major white matter tracts also correlate with hand function. Our radiologic score took this into account by giving detailed scoring to each aspect of the deep gray matter and major white matter tracts rather than clumping these structures together for a single score. This embedded relative "weighting" of extent of deep gray matter involvement may explain the good correlation between the radiologic score and the functional status of patients.

Looking at the correlation between the radiologic scores and the MACS grades (Fig 5) it appears that the children with MACS 3 have a radiologic score above 11, and children with MACS 1 have a radiologic score below 13, which suggests good discrimination between MACS 1 and 3. Children with MACS 2 have more variable injury scores that overlap with 1 and 3. Although this assessment is limited by the lack of higher MACS grades in this group of patients, and by the small sample, these preliminary results do suggest possible prediction of MACS grade by radiologic score.

Our study did not find a correlation between the radiologic score and GMFCS. This is likely related to the relatively similar high function that children with hemiplegia have in regards to gross motor function, as measured by GMFCS scores of I and II only in our study group.

In this study group, children had predominantly unilateral abnormalities. Only 1 child had bilateral abnormalities (subject 27). The combined radiologic score from each hemisphere was used for the statistical analysis. Feys et al[21] demonstrated a lack of impact of bilateral abnormalities on the use of the hemiplegic hand. For this specific child, with a high MACS rating, the radiologic score of the hemisphere responsible for the hemiplegic hand alone fell below the 95% CI range when correlating with MACS, suggesting a possible impact of bilateral abnormalities on the use of the hemiplegic hand. However, no conclusions can be made based on a single case. Other studies have described bilateral abnormalities in larger numbers of children with unilateral hemi-

plegia.[19,21] The lack of significant bilateral abnormalities in our study group reflects the purposive sampling of children with clinical presentation of predominant unilateral impairment in view of the motor intervention protocol. In addition, the sample had a smaller percentage of patients with prematurity-related brain injury, compared with other studies, which tends to cause higher percentage of bilateral injury. Our results support further research to validate this scoring method in the presence of bilateral abnormalities in a greater number of children.

The main limitations of this study are the relatively small sample and the fact that all participants exhibited predominantly unilateral hemiplegia with relatively good gross motor functional status. It should be noted that most studies involving imaging/neurophysiology of children with brain injury are by nature small,[28-32] hence the need for a reliable scale that can be used to compare results. Although it remains to be seen whether the scoring method is effective in other types of motor disorders or with significant bilateral brain abnormalities, our results are promising and we believe justify further validation of the scoring method with a larger number of patients with variable subtypes of CP and acquired brain injury.

CONCLUSIONS

We present a novel MR imaging–based scoring system to describe brain injury in children with hemiplegia, which demonstrated high inter- and intrarater reliability and was significantly associated with MACS classification and motor evaluations. The significant correlations demonstrated between the proposed score and motor function status are a promising first step for the validation of this scoring system in children with hemiplegia. This scoring system may fill an important gap by providing a standardized radiologic assessment of brain injury extent in patients with predominantly unilateral brain injury and thus will allow comparison between registries or study groups. It may also provide the clinician an additional tool for counseling families regarding prognosis. Further studies will allow for better characterization of the properties of this instrument.

ACKNOWLEDGMENTS

We thank the children and families who participated, the Guy's and St Thomas' Charity and Marnie Kimelman Trust for funding, and Geoff Charles-Edwards from the Biomedical Engineering Department and Gareth Barker of the Department of Neuroimaging, Institute of Psychiatry at Kings College London, for providing the data from the UK participants.

Disclosures: Dido Green—*RELATED: Grant:* Guy's and St Thomas' Charity,* Marnie Kimelman Trust,* *Comments:* These monies were paid directly to institute for project expenses of venue, equipment, and delivery of project. I received no salary payment or any funds for this project. **Money paid to institution.*

REFERENCES

1. Ashwal S, Russman BS, Blasco PA, et al. **Practice Parameter: Diagnostic assessment of the child with cerebral palsy. Report of the Quality Standards Subcommittee of the American Academy of Neurology and the Practice Committee of the Child Neurology Society.** *Neurology* 2004;62:851–63
2. Korzeniewski SJ, Birbeck G, DeLano MC, et al. **A systematic review of neuroimaging for cerebral palsy.** *J Child Neurol* 2008;23:216–27
3. Krägeloh-Mann I, Horber V. **The role of magnetic resonance imaging in elucidating the pathogenesis of cerebral palsy: a systematic review.** *Dev Med Child Neurol* 2007;49:144–51
4. Arnfield E, Guzzetta A, Boyd R. **Relationship between brain structure on magnetic resonance imaging and motor outcomes in children with cerebral palsy: a systematic review.** *Res Dev Disabil* 2013;34:2234–50
5. Krageloh-Mann I, Cans C. **Cerebral palsy update.** *Brain Dev* 2009;31:537–44
6. Krageloh-Mann I, Horber V, Petruch UR, et al. **Surveillance of cerebral palsy in Europe: reference and training manual, SCPE, Editor. 2013.** Available at: http://www.scpenetwork.eu/en/my-scpe/rtm/neuroimaging/. Accessed October 17, 2013
7. Palisano RJ, Gorter JW, Morris C, et al. **The creation and purpose of a classification system of children's abilities: gross motor function classification system (GMFCS).** *J Intell Disab Res* 2004;48:346
8. Palisano RJ, Rosenbaum P, Bartlett D, et al. **Content validity of the expanded and revised gross motor function classification system.** *Dev Med Child Neurol* 2008;50:744–50
9. Green D, Schertz M, Gordon AM, et al. **A multi-site study of functional outcomes following a themed approach to hand-arm bimanual intensive therapy for children with hemiplegia.** *Dev Med Child Neurol* 2013;55:527–33
10. Eliasson AC, Krumlinde-Sundholm L, Rosblad B, et al. **The manual ability classification system (MACS) for children with cerebral palsy: scale development and evidence of validity and reliability.** *Dev Med Child Neurol* 2006;48:549–54
11. Krumlinde-Sundholm L, Holmefur M, Kottorp A, et al. **The assisting hand assessment: current evidence of validity, reliability, and responsiveness to change.** *Dev Med Child Neurol* 2007;49:259–64
12. Jebsen RH, Taylor N, Trieschmann RB, et al. **An objective and standardized test of hand function.** *Arch Phys Med Rehabil* 1969;50:311–19
13. Skold A, Hermansson LN, Krumlinde-Sundholm L, et al. **Development and evidence of validity for the children's hand-use experience questionnaire (CHEQ).** *Dev Med Child Neurol* 2011;53:436–42
14. Weinstein M, Green D, Geva R, et al. **Interhemispheric and intrahemispheric connectivity and manual skills in children with unilateral cerebral palsy.** *Brain Struct Funct* 2014;219:1025–40
15. Mori S, Crain BJ, Chacko VP, et al. **Three-dimensional tracking of axonal projections in the brain by magnetic resonance imaging.** *Ann Neurol* 1999;45:265–69
16. Witelson SF. **Hand and sex differences in the isthmus and genu of the human corpus callosum. A postmortem morphological study.** *Brain* 1989;112:799–835
17. Cohen J. **A coefficient of agreement for nominal scales.** *Ed Psych Meas* 1960;20:37–46
18. Landis JR, Koch GG. **The measurement of observer agreement for categorical data.** *Biometrics* 1977;33:159–74
19. Holmefur M, Kits A, Bergstrom J, et al. **Neuroradiology can predict the development of hand function in children with unilateral cerebral palsy.** *Neurorehabil Neural Repair* 2013;27:72–78
20. Holmström L, Vollmer B, Tedroff K, et al. **Hand function in relation to brain lesions and corticomotor-projection pattern in children with unilateral cerebral palsy.** *Dev Med Child Neurol* 2010;52:145–52
21. Feys H, Eyssen M, Jaspers E, et al. **Relation between neuroradiological findings and upper limb function in hemiplegic cerebral palsy.** *Eur J Paediatr Neurol* 2010;14:169–77
22. Woodward LJ, Anderson PJ, Austin NC, et al. **Neonatal MRI to predict neurodevelopmental outcomes in preterm infants.** *N Engl J Med* 2006;355:685–94
23. Inder TE, Wells SJ, Mogridge NB, et al. **Defining the nature of the cerebral abnormalities in the premature infant: a qualitative magnetic resonance imaging study.** *J Pediatr* 2003;143:171–79
24. Kidokoro H, Neil JJ, Inder TE. **New MR imaging assessment tool to define brain abnormalities in very preterm infants at term.** *Pediatrics* 2013;34:2208–14
25. Nguyen TTS, Anderson PJ, Shimony JS, et al. **A novel quantitative**

simple brain metric using MR imaging for preterm infants. *AJNR Am J Neuroradiol* 2009;30:125–31
26. Holmefur M, Aarts P, Hoare B, et al. **Test-retest and alternate forms reliability of the assisting hand assessment.** *J Rehabil Med* 2009; 41:886–91
27. Holmström L, Lennartsson F, Eliasson AC, et al. **Diffusion MRI in corticofugal fibers correlates with hand function in unilateral cerebral palsy.** *Neurology* 2011;77:775–83
28. Walther M, Juenger H, Kuhnke N, et al. **Motor cortex plasticity in ischemic perinatal stroke: a transcranial magnetic stimulation and functional MRI study.** *Pediatr Neurol* 2009;41:171–78
29. Kuhnke N, Juenger H, Walther M, et al. **Do patients with congenital hemiparesis and ipsilateral corticospinal projections respond differently to constraint-induced movement therapy?** *Dev Med Child Neurol* 2008;50:898–903
30. Sellier E, Horber V, Krageloh-Mann I, et al. **Interrater reliability study of cerebral palsy diagnosis, neurological subtype, and gross motor function.** *Dev Med Child Neurol* 2012;54:815–21
31. Dinomais M, Groeschel S, Staudt M, et al. **Relationship between functional connectivity and sensory impairment: red flag or red herring?** *Hum Brain Mapp* 2012;33:628–38
32. Juenger H, de Haan B, Krageloh-Mann I, et al. **Early determination of somatosensory cortex in the human brain.** *Cereb Cortex* 2011;21: 1827–31

Racial and Health Insurance Disparities of Inpatient Spine Augmentation for Osteoporotic Vertebral Fractures from 2005 to 2010

C.N. Gu, W. Brinjikji, A.M. El-Sayed, H. Cloft, J.S. McDonald, and D.F. Kallmes

ABSTRACT

BACKGROUND AND PURPOSE: Vertebroplasty and kyphoplasty are frequently utilized in the treatment of symptomatic vertebral body fractures. While prior studies have demonstrated disparities in the treatment of back pain and care for osteoporotic patients, disparities in spine augmentation have not been investigated. We investigated racial and health insurance status differences in the use of spine augmentation for the treatment of osteoporotic vertebral fractures in the United States.

MATERIALS AND METHODS: Using the Nationwide Inpatient Sample from 2005 to 2010, we selected all discharges with a primary diagnosis of vertebral fracture (International Classification of Diseases-9 code 733.13). Patients who received spine augmentation were identified by using International Classification of Diseases-9 procedure code 81.65 for vertebroplasty and 81.66 for kyphoplasty. Patients with a diagnosis of cancer were excluded. We compared usage rates of spine augmentation by race/ethnicity (white, black, Hispanic, and Asian/Pacific Islander) and insurance status (Medicare, Medicaid, self-pay, and private). Comparisons among groups were made by using χ^2 tests. A multivariate logistic regression analysis was fit to determine variables associated with spine augmentation use.

RESULTS: A total of 228,329 patients were included in this analysis, of whom 129,206 (56.6%) received spine augmentation. Among patients with spine augmentation, 97,022 (75%) received kyphoplasty and 32,184 (25%) received vertebroplasty; 57.5% (92,779/161,281) of white patients received spine augmentation compared with 38.7% (1405/3631) of black patients ($P < .001$). Hispanic patients had significantly lower spine augmentation rates compared with white patients (52.3%, 3777/7222, $P < .001$) as did Asian/Pacific Islander patients (53.1%, 1784/3361, $P < .001$). The spine augmentation usage rate was 57.2% (114,768/200,662) among patients with Medicare, significantly higher than that of those with Medicaid (43.9%, 1907/4341, $P < .001$) and those who self-pay (40.2%, 488/1214, $P < .001$).

CONCLUSIONS: Our findings demonstrate substantial racial and health insurance–based disparities in the inpatient use of spinal augmentation for the treatment of osteoporotic vertebral fracture.

ABBREVIATIONS: NIS = Nationwide Inpatient Sample; ICD = International Classification of Diseases

Vertebroplasty and kyphoplasty are frequently used in the treatment of symptomatic vertebral body fractures.[1] Prior studies have demonstrated that minority patients are significantly less likely to receive spine procedures such as cervical diskectomy for the treatment of pain compared with whites.[2] The Nationwide Inpatient Sample (NIS) has been used in a number of prior studies to demonstrate racial and health insurance status disparities in access to treatment of a variety of diseases such as deep brain stimulation for Parkinson disease,[3] revascularization for lower extremity ischemia,[4] and surgical/endovascular treatment for intracranial aneurysms.[5] The goal of this study was to investigate what, if any, racial or health insurance status disparities existed in the use of spine augmentation for the treatment of osteoporotic fractures in the United States by analyzing the NIS, a large public data base containing discharge information for nearly 8 million hospitals stays per year.

MATERIALS AND METHODS

Patient Population

We purchased the NIS hospital discharge data base for 2005–2010 from the Healthcare Cost and Utilization Project of the Agency for Healthcare Research and Quality, Rockville, Maryland.[6] The NIS is a hospital discharge data base representing 20% of all inpatient admissions to nonfederal hospitals in the United States. Inclusion criteria were the following: 1) adult patients who had a primary diagnosis of vertebral fracture (International Classification of Diseases [ICD]-9 diagnosis code 733.13), and 2) patients treated at centers that performed spine augmentation. Exclusion criteria were the following: 1)

Received March 24, 2014; accepted after revision May 7.

From the Departments of Radiology (C.N.G., W.B., H.C., J.S.M., D.F.K.) and Neurosurgery (H.C., D.F.K.), Mayo Clinic, Rochester, Minnesota; and Department of Epidemiology (A.M.E.-S.), Columbia University, New York, New York.

Please address correspondence to Chris Gu, MD, Mayo Clinic, Department of Radiology, 200 1st St SW, Rochester, MN 55905; e-mail: gu.chris@mayo.edu

http://dx.doi.org/10.3174/ajnr.A4044

patients with a diagnosis of cancer (ICD-9, 1400-1991, 2000-2089), and 2) patients treated at centers not performing spine augmentation procedures. Patients with vertebroplasty were identified by using the ICD-9 procedure code 81.65, and patients with kyphoplasty were identified by using the ICD-9 procedure code 81.66. Hospitals performing spine augmentation were identified by cross-matching ICD-9 procedure codes with hospital identifier codes. If a hospital performed ≥1 spine augmentation procedure in a given year, patients discharged from that hospital were included in this analysis. In addition to race and insurance, other demographic variables collected included age, Charlson Comorbidity Index (which predicts the 10-year mortality for patients with a variety of comorbid conditions),[7] sex, and the presence of the following comorbidities: congestive heart failure, coronary artery disease, hypertension, hyperlipidemia, osteoporosis, diabetes mellitus, obesity, and smoking.

Usage

The usage rate of spine augmentation (combined vertebroplasty and kyphoplasty) was compared across racial/ethnic groups and insurance status. Racial/ethnic groups specified in our analysis included the following categories: white, black, Hispanic, and Asian/Pacific Islander. Patient insurance status groups specified in our analysis included Medicare, private insurance, Medicaid, and self-pay. Two sets of subgroup analyses were performed. First, we compared the ratio of kyphoplasty and vertebroplasty by racial/ethnic categories and by insurance category among patients receiving spine augmentation. Patients who did not receive spine augmentation were excluded from this analysis. Second, we compared spine augmentation usage rates by race/ethnicity among patients whose primary payer was Medicare. The analysis was performed because Medicare was the primary payer for most patients.

Statistical Analysis

First, χ^2 testing was used to study the usage rates of spine augmentation, vertebroplasty, and kyphoplasty. The white race was specified as the reference for analyses concerned with racial differences; Medicare was specified as the reference for analyses concerned with differences by insurance status. Odds ratios are presented with their corresponding 95% confidence intervals. Discharge weights were applied throughout our analyses. *P* values < .05 were considered statistically significant.

Second, a multivariable logistic regression model of spine augmentation use was fit by insurance status, race, age, Charlson Comorbidity Index, and sex to assess mutually adjusted disparities in spine augmentation rates. A second multivariate logic regression model comparing the odds of kyphoplasty use versus vertebroplasty among patients receiving spine augmentation was fit by insurance status, race, age, Charlson Comorbidity Index, and sex. This analysis was performed to assess mutually adjusted disparities in kyphoplasty usage rates compared with vertebroplasty. All statistical analyses were performed by using SAS-based JMP 9.0 software (www.jmp.com).

RESULTS

Spine Augmentation Use and Demographics

Between 2005 and 2010, a total of 228,329 patients were identified who were hospitalized with a primary diagnosis of vertebral fracture. Of these patients, 56.6% (129,206/228,329) underwent any form of spine augmentation. Among patients with spine augmentation, 97,022 (75%) received kyphoplasty and 32,184 patients (25%) received vertebroplasty. Overall, 79.4% of patients were women (181,372/228,329), 91.9% (161,281/175,495) were white, and 88.8% (200,662/225,962) had Medicare. The mean age of the overall patient population was 78.9 years. The mean age among patients with spine augmentation was slightly younger (78.6 years) than the mean age of patients without spine augmentation (79.3 years). Patients with spine augmentation had lower mean Charlson Comorbidity scores than those without spine augmentation (0.8 ± 2.2 versus 0.9 ± 2.4, $P < .001$). Patients with spine augmentation had significantly lower rates of congestive heart failure (11.9% versus 16.1%, $P < .001$) and significantly higher rates of osteoporosis (71.5% versus 63.1%, $P < .001$). Demographic and comorbidity characteristics of the patients in this study are summarized in Table 1.

Overall Spine Augmentation Use

The spine augmentation usage rate was 57.5% (92,779/161,281) for white patients, significantly higher than that of black patients (38.7%, 1405/3631, $P < .001$), Hispanic patients (52.3%, 3777/7222, $P < .001$), and Asian/Pacific Islander patients (53.1%, 1784/3361, $P < .001$). The spine augmentation usage rate for patients with Medicare was 57.2% (114,768/200,662), significantly higher than that among patients with private insurance (54.2%, 10,766/19,745, $P < .001$), those with Medicaid (43.9%, 1907/4341, $P < .001$), and those who self-pay (40.2%, 488/1214, $P < .001$). These data are summarized in Table 2.

Medicare Subgroup Analysis

In our subgroup analysis considering only patients whose primary payer was Medicare, we found that black patients with Medicare had a spine augmentation usage rate of 40.7% (1083/2660), significantly lower than that among white patients (57.9%, 83,477/144,263, $P < .001$). Hispanic patients also had significantly lower rates of spine augmentation use compared with white patients (53.0%, 2870/5326, $P < .001$) as did Asian/Pacific Islander patients (54.9%, 1484/2703, $P < .001$). These data are summarized in Table 3.

Comparative Use of Kyphoplasty and Vertebroplasty among Patients with Spine Augmentation

Among white patients receiving spine augmentation procedures, 78.8% (73,059/92,779) underwent kyphoplasty and 21.3% (19,720/97,779) underwent vertebroplasty. Among black patients receiving spine augmentation procedures, 78.0% (1096/1405) underwent kyphoplasty and 22.0% (309/1405) underwent vertebroplasty ($P = .52$ compared with white patients). Hispanic patients with spine augmentation were less likely to receive kyphoplasty compared with white patients as 74.0% (2795/3777) of Hispanic patients received kyphoplasty and 26.0% (982/3777) received vertebroplasty ($P < .001$). Asian/Pacific Islander patients were also significantly less likely to receive kyphoplasty as 76.4% (1362/1784) received kyphoplasty and 23.6% (422/1784) received vertebroplasty ($P = .02$).

Among patients with Medicare, 76.8% (88,187/114,768) re-

Table 1: Summary of patient demographics for inpatients with vertebral spinal fractures from 2005 to 2010

Variable	All Patients	Patients without Spine Augmentation	Patients with Spine Augmentation	*P*
Mean age (SD) (yr)	78.9 (24.0)	78.6 (21.7)	79.3 (26.6)	<.001
Female (No.) (%)	18,1372 (79.5)	79,467 (80.2)	10,1905 (78.9)	<.001
Mean (SD) (CCI) comorbidities	0.8 (2.3)	0.9 (2.4)	0.8 (2.2)	<.001
Congestive heart failure	31,377 (13.7)	15,953 (16.1)	15,424 (11.9)	<.001
Coronary artery disease	53,902 (23.6)	23,347 (23.6)	30,555 (23.7)	.60
Diabetes mellitus	41,551 (18.2)	18,065 (18.2)	23,487 (18.2)	.77
Hypertension	14,0843 (61.7)	61,020 (61.6)	79,824 (61.8)	.28
Hyperlipidemia	52,651 (23.1)	22,126 (22.3)	30,525 (23.6)	<.001
Smoking	14,656 (6.4)	5804 (5.9)	8853 (6.9)	<.001
Obesity	7968 (3.5)	3589 (3.6)	4380 (3.4)	.003
Osteoporosis	15,4941 (67.9)	62,528 (63.1)	92,313 (71.5)	<.001
Race (No.) (%)				
White	16,1281 (91.9)	68,502 (90.4)	92,779 (93.0)	<.001
Black	3631 (2.7)	2226 (2.9)	1405 (1.4)	
Hispanic	7222 (4.1)	3445 (4.5)	3777 (3.8)	
Asian/Pacific Islander	3361 (1.9)	1577 (2.1)	1784 (1.8)	
Insurance status (No.) (%)				
Medicare	20,0662 (88.8)	85,893 (87.6)	11,4768 (89.7)	<.001
Private	19,745 (8.7)	8979 (9.2)	10,766 (8.4)	
Medicaid	4341 (1.9)	2434 (2.5)	1907 (1.5)	
Self-Pay	1214 (0.5)	725 (0.7)	488 (0.4)	

Note:—CCI indicates Charlson Comorbidity Index.

Table 2: Use of spine augmentation among 228,329 patients presenting with a primary diagnosis of vertebral fracture

	No. (%) Not Receiving Spine Augmentation	No. (%) Receiving Spine Augmentation	*P*
Race			
White	68,502 (42.5)	92,779 (57.5)	Ref
Black	2226 (61.3)	1405 (38.7)	<.001
Hispanic	3445 (47.7)	3777 (52.3)	<.001
Asian/Pacific Islander	1577 (46.9)	1784 (53.1)	<.001
Insurance			
Medicare	85,893 (42.8)	11,4768 (57.2)	Ref
Private	8979 (45.5)	10,766 (54.2)	<.001
Medicaid	2434 (56.1)	1907 (43.9)	<.001
Self-Pay	725 (59.8)	488 (40.2)	<.001

Note:—Ref indicates reference.

Table 3: Comparative usage rate of spine augmentation among patients on Medicare

	No. (%) Receiving Spine Augmentation	*P* Value
Race		
White	83,477 (57.9)	Ref
Black	1083 (40.7)	<.001
Hispanic	2870 (53.0)	<.001
Asian/Pacific Islander	1484 (54.9)	<.001

Note:—Ref indicates reference.

ceived kyphoplasty and 23.2% (26,582/114,768) received vertebroplasty. Among patients with private insurance, 77.6% (8352/10,766) received kyphoplasty and 22.4% (2414/10,766) received vertebroplasty ($P = .08$ compared with Medicare). Patients with Medicaid had significantly lower relative use of kyphoplasty compared with those with Medicare as 71.3% (1360/1907) received kyphoplasty and 28.7% (547/1360) received vertebroplasty ($P < .001$). The same was true for self-pay patients as 60.2% (294/488) received kyphoplasty and 39.8% (195/488) received vertebroplasty ($P < .001$). These data are summarized in Table 4.

Table 4: Comparative usage rate of kyphoplasty versus vertebroplasty among patients with spine augmentation

	No. (%) Receiving Kyphoplasty	No. (%) Receiving Vertebroplasty	*P* Value
Race			
White	73,059 (78.8)	19,720 (21.3)	Ref
Black	1096 (78.0)	309 (22.0)	.52
Hispanic	2795 (74.0)	982 (26.0)	<.001
Asian/Pacific Islander	1362 (76.4)	422 (23.6)	.02
Insurance			
Medicare	88,187 (76.8)	26,582 (23.2)	Ref
Private	8352 (77.6)	2414 (22.4)	.08
Medicaid	1360 (71.3)	547 (28.7)	<.001
Self-Pay	294 (60.2)	195 (39.8)	<.001

Note:—Ref indicates reference.

Multivariable Analysis

After we performed multivariable analysis, black patients had lower odds of receiving any spine augmentation compared with whites (OR = 0.46; 95% CI, 0.43–0.49; $P < .001$). The same was true for Hispanic patients (OR = 0.83; 95% CI, 0.79–0.99; $P < .001$). Patients with private insurance had significantly lower odds of spine augmentation compared with those with Medicare (OR = −0.77; 95% CI, 0.75–0.80; $P < .001$) and Medicaid (OR = 0.50; 95% CI, 0.47–0.53; $P < .001$) and those who self-pay (OR = 0.41; 95% CI, 0.37–0.56; $P < .001$).

Among patients receiving spine augmentation, comparative use of kyphoplasty was similar between black and white patients (OR = 0.90; 95% CI, 0.79–1.02; $P = .11$), though Hispanic patients had significantly lower use of kyphoplasty compared with white patients (OR = 0.76; 95% CI, 0.70–0.82; $P < .001$). Patients with private insurance (OR = 0.85; 95% CI, 0.80–0.89; $P < .001$), those with Medicaid (OR = 0.53, 95% CI, 0.48–0.59; $P < .001$), and those who self-paid (OR = 0.35; 95% CI, 0.29–0.42; $P < .001$) had significantly lower odds of kyphoplasty use compared with those with Medicare. These data are summarized in Table 5.

Table 5: Multivariate analysis

	Odds of Spine Augmentation		Odds of Kyphoplasty[a]	
	OR (95% CI)	*P*	OR (95% CI)	*P*
Race				
White	Ref	Ref	Ref	Ref
Black	0.46 (0.43–0.49)	<.001	0.90 (0.79–1.02)	.11
Hispanic	0.83 (0.79–0.99)	<.001	0.76 (0.70–0.82)	<.001
Asian/Pacific Islander	0.89 (0.84–0.96)	.002	0.93 (0.84–1.04)	.23
Insurance status				
Medicare	Ref	Ref	Ref	Ref
Private	0.77 (0.75–0.80)	<.001	0.85 (0.80–0.89)	<.001
Medicaid	0.50 (0.47–0.53)	<.001	0.53 (0.48–0.59)	<.001
Self-Pay	0.41 (0.37–0.56)	<.001	0.35 (0.29–0.42)	<.001

Note:—Ref indicates reference.

[a] Only patients receiving spine augmentation were included in this analysis.

DISCUSSION

Our study demonstrated significant racial and health insurance–based disparities in the use of spinal augmentation for the treatment of osteoporotic vertebral fracture. Compared with white patients, all racial and ethnic minority groups had significantly lower rates of inpatient spine augmentation. Indeed, less than one-half of black patients admitted with a primary diagnosis of vertebral fracture were treated with spine augmentation, while nearly two-thirds of white patients underwent spine augmentation. Differences in spine augmentation use among Hispanic and Asian/Pacific Islander patients compared with white patients were also statistically significant, but the degree of difference was much less marked than that seen in black-versus-white patients. Conversely, when implemented, the type of augmentation used, either kypho- or vertebroplasty, was quite similar among racial groups. Despite the large sample size in our study, there is significant under-representation of patients who were not white as black patients composed only 2.7%, Hispanic patients composed 4.1%, and Asian/Pacific Islander patients composed 1.9% of the sample size. The reason for this difference is unclear and may be multifactorial, including lower fracture rates for black, Hispanic, and Asian women compared with white women[8] and disparities in osteoporosis treatment in these minority groups.[9]

Similar to race, the insurance provider also had a profound impact on the use of spine augmentation, with patients with Medicare and private insurance having augmentation at markedly higher rates than either patients with Medicaid or those who self-paid. In our multivariate analysis, the differences noted above were as great or greater than those in the univariate analyses. Overall, these findings suggest that significant health insurance status disparities exist in the use of spine augmentation procedures, findings consistent with the already reported disparities in access to health care by minorities and the uninsured.[5,10-15]

These current findings are potentially clinically relevant because prior studies have shown that patients receiving spine augmentation procedures demonstrate improved survival and quality of life compared with patients receiving nonoperative treatment.[16,17] In a study of the 2006 Medicare Provider Analysis and Review File data base, Chen et al[16] demonstrated that patients who underwent vertebroplasty and kyphoplasty had significantly higher 3-year survival rates compared with patients receiving nonoperative management. The Fracture Reduction Evaluation study, which randomized patients into balloon kyphoplasty and nonsurgical management, demonstrated that kyphoplasty was associated with improved quality of life.[17]

While this study was not designed to determine the specific causes behind racial and insurance-based disparities, we believe that the causes of such disparities are multiple, including but not limited to physician bias, access to care, patient preferences, and communication barriers.[18-23] While high costs of spine augmentation procedures could contribute to the lower rates of spine augmentation in some groups, our subgroup analysis of patients with Medicare demonstrated that racial minorities still had lower rates of spine augmentation despite having the same type of insurance as their white counterparts. Racial disparities in the care of patients with osteoporosis have been previously identified. In a study of patients with Medicare and osteoporotic fractures, Liu et al[24] demonstrated that black patients were significantly less likely to receive both prefracture and postfracture care compared with white patients. Yoo et al[25] demonstrated significant racial disparities in osteoporosis drug maintenance therapy between black and white patients, especially among patients with Medicare, among whom supplementary health insurance was not affordable.

Insurance-based disparities in spine augmentation use may, at least in part, be explained by costs. In general, Medicare provides higher reimbursement rates for all medical services compared with Medicaid. In 2013, the Medicaid-to-Medicare fee index was 0.66 across the entire United States.[26] The inability of patients who self-pay and those with Medicaid to pay for the costs associated with spine augmentation could contribute to their lower rate of spine augmentation use overall. Cost differences may also explain our finding that patients with Medicaid and those who self-pay had significantly lower usage rates of kyphoplasty compared with patients who were privately insured, because kyphoplasty has been reported to cost between 2 and 20 times more than vertebroplasty.[27,28] It is unclear to us as to why patients who were privately insured used spine augmentation less than those with Medicare in our study; one theory may be that there are preauthorization barriers that discourage the use of spine augmentation in this population.

Several prior studies have demonstrated disparities in the surgical treatment of back pain. Carey et al demonstrated that hospitalization and surgery rates were significantly lower in black patients with chronic back pain.[29] In a study of the Nationwide Inpatient Sample, Alosh et al[30] found that racial minorities were significantly less likely to receive cervical spine surgery for the treatment of degenerative cervical spine disease. The Alosh et al study also demonstrated that patients with Medicaid were significantly less likely to receive surgery compared with those with private insurance.[30] In a study of Workers' Compensation claims in Missouri, Chibnall et al[31] found that white patients were significantly more likely to receive a diagnosis of a herniated disk and

that among those with such a diagnosis, whites were significantly more likely to undergo surgery compared with black patients. These studies further support our findings that minorities and the underinsured are treated differently for spine disease.

There are several limitations to our study. Our use of broad racial designations (white, black, Hispanic, Asian/Pacific Islander) in an effort to maintain consistency within the NIS data base may have limited our sample population because some racial groups are heterogeneous. Despite our ability to demonstrate usage disparities, we did not analyze outcome data for these procedures and cannot comment on morbidity or postoperative functional status across groups. Our study only examined disparities among inpatients diagnosed with osteoporotic vertebral fractures. However, a prior study of Medicare enrollees found that only 40% of vertebroplasties between 2001 and 2005 were performed as inpatient procedures. In addition, while the NIS is a large inpatient data base, it does not include federally funded health care facilities. It is unclear to us as to why privately insured patients used spine augmentation less than Medicare patients in our study; one theory may be that there are preauthorization barriers that discourage the use of spine augmentation in this population. As with any analysis of a large data base, errors in coding are also a potential limitation,[32] though error rates are likely similar between racial and insurance groups. Finally, given the very large size of the data base, numerous comparisons reach statistical significance yet have a very small, absolute difference; we have attempted throughout the article to highlight differences that may be clinically relevant.

CONCLUSIONS

Our study demonstrated significant racial and health insurance–based disparities in the use of spine augmentation for the treatment of osteoporotic vertebral fractures. Significantly more white patients received spine augmentation compared with black, Hispanic, and Asian/Pacific Islander patients and significantly more patients with Medicare received spine augmentation compared with those with Medicaid and those who self-pay. While our findings echo many of the already reported disparities in surgical care, further research is needed to explain the underlying cause.

Disclosures: Harry Cloft—*UNRELATED*: *Grants/Grants Pending*: Site Principal Investigator at the enrolling site for the Stenting and Angioplasty with Protection in Patients at HIgh Risk for Endarterectomy registry sponsored by Cordis Endovascular.* Jennifer S. McDonald—*UNRELATED*: *Grants/Grants Pending:* GE Healthcare,* *Comments*: investigator-initiated research grant to study contrast-induced nephropathy. David F. Kallmes—*UNRELATED*: *Consultancy*: ev3/Covidien, Medtronic, *Comments*: planning and implementation of clinical trials, *Grants/Grants Pending*: MicroVention,* Benvenue Medical,* ev3/Covidien,* Codman,* Sequent Medical,* SurModics,* *Comments*: preclinical and clinical research, *Royalties*: University of Virginia Patent Foundation, *Comments*: spine fusion. *Money paid to the institution.

REFERENCES

1. Leake CB, Brinjikji W, Cloft HJ, et al. **Trends of inpatient spine augmentation: 2001–08.** *AJNR Am J Neuroradiol* 2011;32:1464–68
2. Romano PS, Campa DR, Rainwater JA. **Elective cervical discectomy in California: postoperative in-hospital complications and their risk factors.** *Spine (Phila Pa 1976)* 1997;22:2677–92
3. Chan AK, McGovern RA, Brown LT, et al. **Disparities in access to deep brain stimulation surgery for Parkinson disease: interaction between African American race and Medicaid use.** *JAMA Neurol* 2014;71:291–99
4. Durazzo TS, Frencher S, Gusberg R. **Influence of race on the management of lower extremity ischemia: revascularization vs amputation.** *JAMA Surg* 2013;148:617–23
5. Brinjikji W, Rabinstein AA, Lanzino G, et al. **Racial and ethnic disparities in the treatment of unruptured intracranial aneurysms: a study of the Nationwide Inpatient Sample 2001–2009.** *Stroke* 2012;43:3200–06
6. HCUP Nationwide Inpatient Sample (NIS). Healthcare Cost and Utilization Project (HCUP). 2005–2010. Rockville: Agency for Healthcare Research and Quality. Published 2011. http://www.hcup-us.ahrq.gov/nisoverview.jsp. Accessed October 26, 2013
7. Charlson ME, Pompei P, Ales KL, et al. **A new method of classifying prognostic comorbidity in longitudinal studies: development and validation.** *J Chronic Dis* 1987;40:373–83
8. Cauley JA, Wu L, Wampler NS, et al. **Clinical risk factors for fractures in multi-ethnic women: the Women's Health Initiative.** *J Bone Miner Res* 2007;22:1816–26
9. Cauley JA. **Defining ethnic and racial differences in osteoporosis and fragility fractures.** *Clin Orthop Relat Res* 2011;469:1891–99
10. Hughes K, Seetahal S, Oyetunji T, et al. **Racial/ethnic disparities in amputation and revascularization: a Nationwide Inpatient Sample study.** *Vasc Endovascular Surg* 2013;48:34–37
11. Brinjikji W, Rabinstein AA, McDonald JS, et al. **Socioeconomic disparities in the utilization of mechanical thrombectomy for acute ischemic stroke in US hospitals.** *AJNR Am J Neuroradiol* 2014;35:553–56
12. DeNavas-Walt C, Proctor BD, Smith JC. Income, poverty, and health insurance coverage in the United States: 2011. Issued September 2012. http://www.census.gov/prod/2012pubs/p60-243.pdf. Accessed October 26, 2013
13. Agency for Healthcare Research and Quality. National healthcare quality and disparities reports. http://www.ahrq.gov/research/findings/nhqrdr. Accessed October 26, 2013
14. The Henry J. Kaiser Family Foundation. Racial and ethnic disparities in access to health insurance and health care. July 30, 2000. http://kff.org/disparities-policy/fact-sheet/racial-and-ethnic-disparities-in-access-to. Accessed October 26, 2013
15. Escarce JJ. Racial and ethnic disparities in access to and quality of health care. Research Synthesis Report No 12. Robert Wood Johnson Foundation. September 2007. http://www.cahpf.org/GoDocUserFiles/446.RWJF_Research_Report_11.7.07.pdf. Accessed October 26, 2013
16. Chen AT, Cohen DB, Skolasky RL. **Impact of nonoperative treatment, vertebroplasty, and kyphoplasty on survival and morbidity after vertebral compression fracture in the Medicare population.** *J Bone Joint Surg Am* 2013;95:1729–36
17. Van Meirhaeghe J, Bastian L, Boonen S, et al. **A randomized trial of balloon kyphoplasty and non-surgical management for treating acute vertebral compression fractures: vertebral body kyphosis correction and surgical parameters.** *Spine (Phila Pa 1976)* 2013;38:971–83
18. Stepanikova I, Cook KS. **Effects of poverty and lack of insurance on perceptions of racial and ethnic bias in health care.** *Health Serv Res* 2008;43:915–30
19. Green AR, Carney DR, Pallin DJ, et al. **Implicit bias among physicians and its prediction of thrombolysis decisions for black and white patients.** *J Gen Intern Med* 2007;22:1231–38
20. Evans K, Coresh J, Bash LD, et al. **Race differences in access to health care and disparities in incident chronic kidney disease in the US.** *Nephrol Dial Transplant* 2011;26:899–908
21. Whittle J, Conigliaro J, Good CB, et al. **Do patient preferences contribute to racial differences in cardiovascular procedure use?** *J Gen Intern Med* 1997;12:267–73
22. Saha S, Arbelaez JJ, Cooper LA. **Patient-physician relationships and racial disparities in the quality of health care.** *Am J Public Health* 2003;93:1713–19
23. Morales LS, Cunningham WE, Brown JA, et al. **Are Latinos less satisfied with communication by health care providers?** *J Gen Intern Med* 1999;14:409–17

24. Liu SK, Munson JC, Bell JE, et al. **Quality of osteoporosis care of older Medicare recipients with fragility fractures: 2006 to 2010.** *J Am Geriatr Soc* 2013;61:1855–62
25. Yoo JW, Kim S, Kim SJ, et al. **Effects of health insurance on racial disparity in osteoporosis medication adherence.** *J Am Pharm Assoc (2003)* 2013;53:626–31
26. The Henry J. Kaiser Family Foundation. How much will Medicaid physician fees for primary care rise in 2013? Evidence from a 2012 survey of Medicaid physician fees. December 13, 2013. http://kff.org/medicaid/issue-brief/how-much-will-medicaid-physician-fees-for/. Accessed October 26, 2013
27. Mathis JM, Ortiz AO, Zoarski GH. **Vertebroplasty versus kyphoplasty: a comparison and contrast.** *AJNR Am J Neuroradiol* 2004;25:840–45
28. Gray DT, Hollingworth W, Onwudiwe N, et al. **Costs and state-specific rates of thoracic and lumbar vertebroplasty, 2001–2005.** *Spine (Phila Pa 1976)* 2008;33:1905–12
29. Carry TS, Garrett JM, et al. **The relation of race to outcomes and the use of health care services for acute low back pain.** *Spine* 2003;28:390–94
30. Alosh H, Riley LH, 3rd, Skolasky RL. **Insurance status, geography, race, and ethnicity as predictors of anterior cervical spine surgery rates and in-hospital mortality: an examination of United States trends from 1992 to 2005.** *Spine (Phila Pa 1976)* 2009;34:1956–62
31. Chibnall JT, Tait RC, Andresen EM, et al. **Race differences in diagnosis and surgery for occupational low back injuries.** *Spine (Phila Pa 1976)* 2006;31:1272–75
32. Hertzer NR. **The Nationwide Inpatient Sample may contain inaccurate data for carotid endarterectomy and carotid stenting.** *J Vasc Surg* 2012;55:263–66

21st Annual Blood-Brain Barrier Consortium Meeting
March 19-21, 2015
Skamania Lodge in Stevenson, Washington

The 2015 Annual Blood-Brain Barrier Consortium Meeting will be held March 19-21 at Skamania Lodge in Stevenson, Washington. The meeting will include a state-of-the-art pre-clinical and clinical neuroimaging session titled "Imaging the Neurovascular Unit: Permeability, Blood Volume, and Functional Imaging". The meeting is partially funded by a National Institutes of Health R13 grant, with support from the National Cancer Institute, National Institute of Neurological Disorders and Stroke, and National Institute of Deafness and Communication Disorders, and is organized in collaboration with the International Brain Barriers Society.

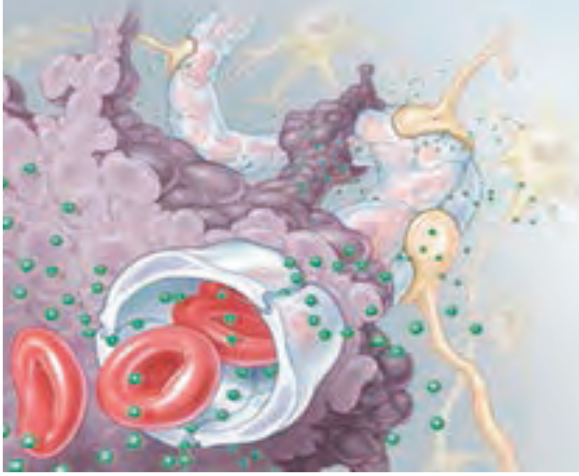

For more information, please visit www.ohsu.edu/bbb

OREGON HEALTH & SCIENCE UNIVERSITY

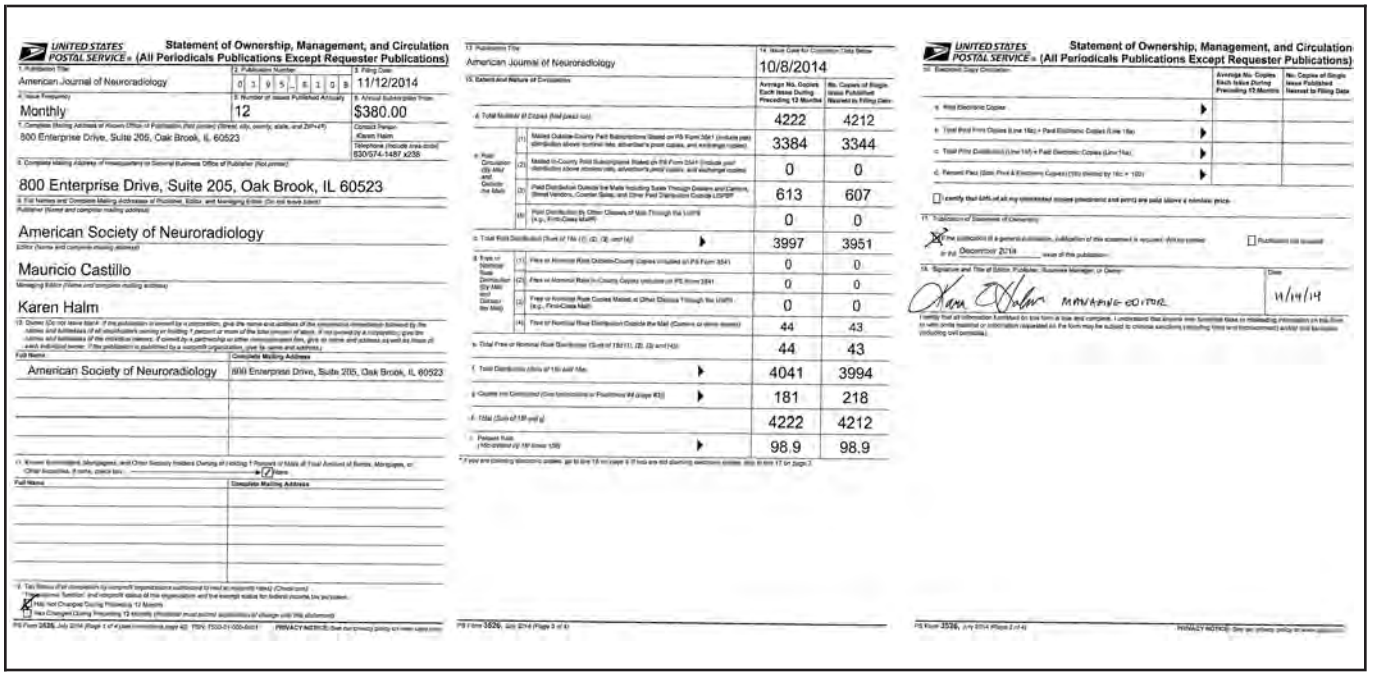

UNITED STATES POSTAL SERVICE® Statement of Ownership, Management, and Circulation (All Periodicals Publications Except Requester Publications)

1. Publication Title	2. Publication Number	3. Filing Date
American Journal of Neuroradiology	0 3 9 5 - 6 1 0 8	11/12/2014
4. Issue Frequency	5. Number of Issues Published Annually	6. Annual Subscription Price
Monthly	12	$380.00

7. Complete Mailing Address of Known Office of Publication (Not printer) (Street, city, county, state, and ZIP+4®): 800 Enterprise Drive, Suite 205, Oak Brook, IL 60523 — Contact Person: Karen Halm; Telephone (Include area code): 630/574-1487 x238

8. Complete Mailing Address of Headquarters or General Business Office of Publisher (Not printer): 800 Enterprise Drive, Suite 205, Oak Brook, IL 60523

9. Full Names and Complete Mailing Addresses of Publisher, Editor, and Managing Editor (Do not leave blank)
Publisher (Name and complete mailing address): American Society of Neuroradiology
Editor (Name and complete mailing address): Mauricio Castillo
Managing Editor (Name and complete mailing address): Karen Halm

10. Owner (Do not leave blank. If the publication is owned by a corporation, give the name and address of the corporation immediately followed by the names and addresses of all stockholders owning or holding 1 percent or more of the total amount of stock. If not owned by a corporation, give the names and addresses of the individual owners. If owned by a partnership or other unincorporated firm, give its name and address as well as those of each individual owner. If the publication is published by a nonprofit organization, give its name and address.)

Full Name	Complete Mailing Address
American Society of Neuroradiology	800 Enterprise Drive, Suite 205, Oak Brook, IL 60523

11. Known Bondholders, Mortgagees, and Other Security Holders Owning or Holding 1 Percent or More of Total Amount of Bonds, Mortgages, or Other Securities. If none, check box: → ☑ None

Full Name	Complete Mailing Address

12. Tax Status (For completion by nonprofit organizations authorized to mail at nonprofit rates) (Check one)
The purpose, function, and nonprofit status of this organization and the exempt status for federal income tax purposes:
☒ Has Not Changed During Preceding 12 Months
☐ Has Changed During Preceding 12 Months (Publisher must submit explanation of change with this statement)

PS Form 3526, July 2014 (Page 1 of 4 (see instructions page 4)) PSN: 7530-01-000-9931 PRIVACY NOTICE: See our privacy policy on www.usps.com

13. Publication Title: American Journal of Neuroradiology
14. Issue Date for Circulation Data Below: 10/8/2014

15. Extent and Nature of Circulation		Average No. Copies Each Issue During Preceding 12 Months	No. Copies of Single Issue Published Nearest to Filing Date
a. Total Number of Copies (Net press run)		4222	4212
b. Paid Circulation (By Mail and Outside the Mail)	(1) Mailed Outside-County Paid Subscriptions Stated on PS Form 3541 (Include paid distribution above nominal rate, advertiser's proof copies, and exchange copies)	3384	3344
	(2) Mailed In-County Paid Subscriptions Stated on PS Form 3541 (Include paid distribution above nominal rate, advertiser's proof copies, and exchange copies)	0	0
	(3) Paid Distribution Outside the Mails Including Sales Through Dealers and Carriers, Street Vendors, Counter Sales, and Other Paid Distribution Outside USPS®	613	607
	(4) Paid Distribution by Other Classes of Mail Through the USPS (e.g., First-Class Mail®)	0	0
c. Total Paid Distribution (Sum of 15b (1), (2), (3), and (4))		3997	3951
d. Free or Nominal Rate Distribution (By Mail and Outside the Mail)	(1) Free or Nominal Rate Outside-County Copies included on PS Form 3541	0	0
	(2) Free or Nominal Rate In-County Copies included on PS Form 3541	0	0
	(3) Free or Nominal Rate Copies Mailed at Other Classes Through the USPS (e.g., First-Class Mail)	0	0
	(4) Free or Nominal Rate Distribution Outside the Mail (Carriers or other means)	44	43
e. Total Free or Nominal Rate Distribution (Sum of 15d (1), (2), (3) and (4))		44	43
f. Total Distribution (Sum of 15c and 15e)		4041	3994
g. Copies not Distributed (See Instructions to Publishers #4 (page #3))		181	218
h. Total (Sum of 15f and g)		4222	4212
i. Percent Paid (15c divided by 15f times 100)		98.9	98.9

* If you are claiming electronic copies, go to line 16 on page 3. If you are not claiming electronic copies, skip to line 17 on page 3.

PS Form 3526, July 2014 (Page 3 of 4)

UNITED STATES POSTAL SERVICE® Statement of Ownership, Management, and Circulation (All Periodicals Publications Except Requester Publications)

16. Electronic Copy Circulation	Average No. Copies Each Issue During Preceding 12 Months	No. Copies of Single Issue Published Nearest to Filing Date
a. Paid Electronic Copies		
b. Total Paid Print Copies (Line 15c) + Paid Electronic Copies (Line 16a)		
c. Total Print Distribution (Line 15f) + Paid Electronic Copies (Line 16a)		
d. Percent Paid (Both Print & Electronic Copies) (16b divided by 16c × 100)		

☐ I certify that 50% of all my distributed copies (electronic and print) are paid above a nominal price.

17. Publication of Statement of Ownership
☒ If the publication is a general publication, publication of this statement is required. Will be printed in the December 2014 issue of this publication. ☐ Publication not required

18. Signature and Title of Editor, Publisher, Business Manager, or Owner: Karen Halm MANAGING EDITOR — Date: 11/14/14

I certify that all information furnished on this form is true and complete. I understand that anyone who furnishes false or misleading information on this form or who omits material or information requested on the form may be subject to criminal sanctions (including fines and imprisonment) and/or civil sanctions (including civil penalties).

PS Form 3526, July 2014 (Page 2 of 4) PRIVACY NOTICE: See our privacy policy on www.usps.com

Trevo® XP ProVue Retrievers

See package insert for complete indications, complications, warnings, and instructions for use.

INDICATIONS FOR USE

The Trevo Retriever is intended to restore blood flow in the neurovasculature by removing thrombus in patients experiencing ischemic stroke within 8 hours of symptom onset. Patients who are ineligible for intravenous tissue plasminogen activator (IV t-PA) or who fail IV t-PA therapy are candidates for treatment.

COMPLICATIONS

Procedures requiring percutaneous catheter introduction should not be attempted by physicians unfamiliar with possible complications which may occur during or after the procedure. Possible complications include, but are not limited to, the following: air embolism; hematoma or hemorrhage at puncture site; infection; distal embolization; pain/headache; vessel spasm, thrombosis, dissection, or perforation; emboli; acute occlusion; ischemia; intracranial hemorrhage; false aneurysm formation; neurological deficits including stroke; and death.

COMPATIBILITY

3x20 mm retrievers are compatible with Trevo® Pro 14 Microcatheters (REF 90231) and Trevo® Pro 18 Microcatheters (REF 90238).
4x20 mm retrievers are compatible with Trevo® Pro 18 Microcatheters (REF 90238). Compatibility of the Retriever with other microcatheters has not been established. Performance of the Retriever device may be impacted if a different microcatheter is used.
The Merci® Balloon Guide Catheters are recommended for use during thrombus removal procedures.
Retrievers are compatible with the Abbott Vascular DOC® Guide Wire Extension (REF 22260)

WARNINGS

- Contents supplied STERILE, using an ethylene oxide (EO) process.Nonpyrogenic.
- To reduce risk of vessel damage, adhere to the following recommendations:
  - Take care to appropriately size Retriever to vessel diameter at intended site of deployment.
  - Do not perform more than six (6) retrieval attempts in same vessel using Retriever devices.
  - Maintain Retriever position in vessel when removing or exchanging Microcatheter.
- To reduce risk of kinking/fracture, adhere to the following recommendations:
  - Immediately after unsheathing Retriever, position Microcatheter tip marker just proximal to shaped section. Maintain Microcatheter tip marker just proximal to shaped section of Retriever during manipulation and withdrawal.
  - Do not rotate or torque Retriever.
  - Use caution when passing Retriever through stented arteries.
- Do not resterilize and reuse. Structural integrity and/or function may be impaired by reuse or cleaning.
- The Retriever is a delicate instrument and should be handled carefully. Before use and when possible during procedure, inspect device carefully for damage. Do not use a device that shows signs of damage. Damage may prevent device from functioning and may cause complications.
- Do not advance or withdraw Retriever against resistance or significant vasospasm. Moving or torquing device against resistance or significant vasospasm may result in damage to vessel or device. Assess cause of resistance using fluoroscopy and if needed resheath the device to withdraw.
- If Retriever is difficult to withdraw from the vessel, do not torque Retriever. Advance Microcatheter distally, gently pull Retriever back into Microcatheter, and remove Retriever and Microcatheter as a unit. If undue resistance is met when withdrawing the Retriever into the Microcatheter, consider extending the Retriever using the Abbott Vascular DOC guidewire extension (REF 22260) so that the Microcatheter can be exchanged for a larger diameter catheter such as a DAC® catheter. Gently withdraw the Retriever into the larger diameter catheter.
- Administer anti-coagulation and anti-platelet medications per standard institutional guidelines.

PRECAUTIONS

- Prescription only – device restricted to use by or on order of a physician.
- Store in cool, dry, dark place.
- Do not use open or damaged packages.
- Use by "Use By" date.
- Exposure to temperatures above 54°C (130°F) may damage device and accessories. Do not autoclave.
- Do not expose Retriever to solvents.
- Use Retriever in conjunction with fluoroscopic visualization and proper anti-coagulation agents.
- To prevent thrombus formation and contrast media crystal formation, maintain a constant infusion of appropriate flush solution between guide catheter and Microcatheter and between Microcatheter and Retriever or guidewire.
- Do not attach a torque device to the shaped proximal end of DOC® Compatible Retriever. Damage may occur, preventing ability to attach DOC® Guide Wire Extension.

Concentric Medical
301 East Evelyn
Mountain View, CA 94041

EC REP

EMERGO Europe
Molenstraat 15
2513 BH, The Hague
The Netherlands

CE 0459

Stryker Neurovascular
47900 Bayside Parkway
Fremont, CA 94538

stryker.com/neurovascular
stryker.com/emea/neurovascular

Date of Release: JUN/2014

EX_EN_GL

NV00009028.AA

Trevo® XP

PROVUE RETRIEVER

Take Control. Capture More.

The newly designed Trevo® XP ProVue Retriever takes proven Trevo Retriever performance to new levels for **easy delivery, easy placement,** and **easy visualization.**

When you're in control, it's amazing what you can capture.

stryker® Neurovascular

Stroke: *Our Only Focus. Our Ongoing Promise.*

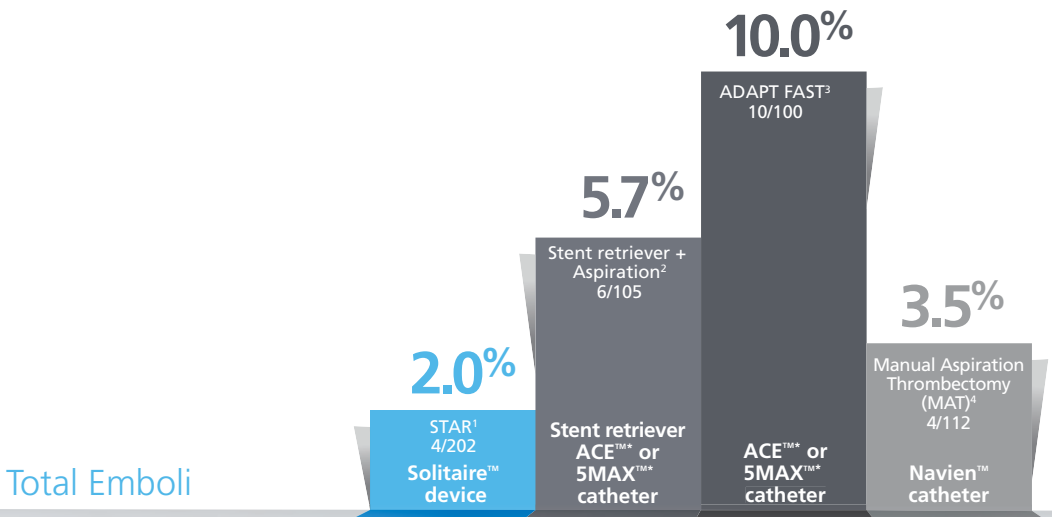

Numbers don't lie.

Using the Solitaire™ device first results in the lowest recorded instances of distal emboli, especially when compared to ADAPT.

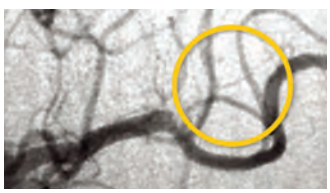

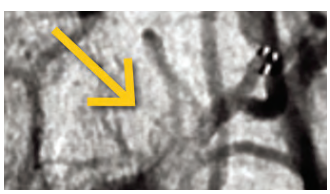

For you, and your acute ischemic stroke patients, outcomes make all the difference. That's why evaluating and understanding the differences in the data, across multiple clinical studies, is so important to delivering the best possible outcomes and quality of life after stroke.

The Solitaire™ revascularization device has been more rigorously tested[1-6] than any other mechanical thrombectomy device. With consistent results showing significantly lower total emboli[1-4], unrivaled* neurological outcomes[1-7], and the lowest observed mortality[1-7], **the Solitaire™ device is demonstrably the fastest route to better outcomes**.

[Solitaire™ Revascularization Device]

COVIDIEN

***** mRS ≤ 2 over 50% in a published study.

REFERENCES 1. Pereira V, Gralla J, Davalos A, et al. Prospective, Multicenter, Single-Arm Study of Mechanical Thrombectomy Using Solitaire Flow Restoration in Acute Ischemic Stroke. *Stroke.* 2013;44:2802-2807. **2.** Humphries W, Hoit D, Doss VT, et al. *J NeuroIntervent Surg.* doi:10.1136/neurintsurg-2013-010986. Data self reported. **3.** Turk AS, Frei D, Fiorella D, et al. *J NeuroIntervent Surg.* doi:10.1136/neurintsurg-2014-011125. Data self reported. **4.** Jankowitz B, Grandhi R, Horev A, et al. *J NeuroIntervent Surg.* doi:10.1136/neurintsurg-2013-011024. Data self reported. **5.** Saver JL, Jahan R, Levy EI, et al. SWIFT Trialists. Solitaire flow restoration device versus the Merci Retriever in patients with acute ischemic stroke (SWIFT): a randomized, parallel-group, non-inferiority trial. *Lancet.* 2012;380(9849):1241-1249. **6.** Jahan R, Liebeskind D, Nogueira R, et al.For SWIFT Investigators. Abstract 163: TICI success rates in SWIFT: comparison between randomized arms and correlation to 90 day neurologic outcome. *Stroke.* 2013;44:A163. **7.** Dávalos A, Pereira VM, Chapot R, et al. Solitaire Group. Retrospective multicenter study of Solitaire FR for revascularization in the treatment of acute ischemic stroke. *Stroke.* 2012;43(10):2699-2705.

The Solitaire™ revascularization device is intended to restore blood flow by removing thrombus from a large intracranial vessel in patients experiencing ischemic stroke within 8 hours of symptom onset. Patients who are ineligible for intravenous tissue plasminogen activator (IV t-PA) or who fail IV t-PA therapy are candidates for treatment. Indications, contraindications, warnings and instructions for use can be found on the product labeling supplied with each device. CAUTION: Federal (USA) law restricts this device to sale by or on the order of a physician.